

WISSENSCHAFTLICH-TECHNISCHE BERICHTE

**FZR-278**

November 1999

ISSN 1437-322X



**Archiv-Ex.:**

**International Workshop  
on Measuring Techniques  
for Liquid Metal Flows (MTLM)**

**Editors:**

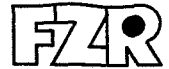
**Gunter Gerbeth and Sven Eckert**

Herausgeber:  
FORSCHUNGSZENTRUM ROSSENDORF  
Postfach 51 01 19  
D-01314 Dresden  
Telefon +49 351 26 00  
Telefax +49 351 2 69 04 61  
<http://www.fz-rossendorf.de/>

Als Manuskript gedruckt  
Alle Rechte beim Herausgeber

**FORSCHUNGSZENTRUM ROSSENDORF**

WISSENSCHAFTLICH-TECHNISCHE BERICHTE



**FZR-278**

November 1999

**International Workshop  
on Measuring Techniques  
for Liquid Metal Flows (MTLM)**

Dresden-Rossendorf, October 11-13, 1999

*Supported by:*

*Deutsche Forschungsgemeinschaft*

*(in framework of the „Dresden Innovationskolleg Magnetofluidynamik“)*

*and Volkswagen Foundation*

**Editors:**

**Gunter Gerbeth and Sven Eckert**

## List of Participants



Pietro Agostini	ENEA C.R. Brasimone	Italy
Thierry Alboussiere	University of Cambridge	Great Britain
Oleg Andreev	Institute of Physics Riga	Latvia
Egbert Baake	University of Hannover	Germany
Davide Batic	FZ Rossendorf	Germany
Reinhard Behrendt	Polytec GmbH Berlin	Germany
Remi Berriet	IMASONIC	France
Thomas Boeck	Dresden University of Technology	Germany
Andris Bojarevics	Institute of Physics Riga	Latvia
Philippe Cardin	LGIT, Universite J. Fourier Grenoble	France
Michael Christen	Dresden University of Technology	Germany
Andreas Cramer	FZ Rossendorf	Germany
Peter Dold	University of Freiburg	Germany
Kerstin Eckert	Dresden University of Technology	Germany
Sven Eckert	FZ Rossendorf	Germany
Jacqueline Etay	Laboratoire EPM-MADYLAM Grenoble	France
Gerd Fabritius	DaimlerChryslerAerospace Dornier Friedrichshafen	Germany
Frank Fellmoser	Forschungszentrum Karlsruhe	Germany
Bernd Fischer	University of Erlangen	Germany
Jean-Paul Garandet	CEA Grenoble	France
Annett Gebert	IFW Dresden	Germany
Yuri Gelfgat	Institute of Physics Riga	Latvia
Gunter Gerbeth	FZ Rossendorf	Germany



## Preface

The International Workshop on "Measuring Techniques in Liquid Metal Flows" (MTLM Workshop) was organised in frame of the Dresden "Innovationskolleg Magnetofluidodynamik". The subject of the MTLM Workshop was limited to methods to determine physical flow quantities such as velocity, pressure, void fraction, inclusion properties, crystallisation fronts etc. The present proceedings contain abstracts and viewgraphs of the oral presentations.

During the last decades numerical simulations have become an important tool in industry and research to study the structure of flows and the properties of heat and mass transfer. However, in case of liquid metal flows there exists a significant problem to validate the codes with experimental data due to the lack of available measuring techniques. Due to the material properties (opaque, hot, chemical aggressive) the measurement of flow quantities is much more delicate in liquid metals compared to ordinary water flows. The generalisation of results obtained by means of water models to real liquid metal flows has often to be considered as difficult due to the problems to meet the actual values of non-dimensional flow parameters ( $Re$ ,  $Pr$ ,  $Gr$ ,  $Ha$ , etc.). Moreover, a strong need has to be noted to make measuring techniques available to monitor and to control flow processes in real industrial facilities.

The objectives of the MTLM Workshop were to:

- Review of existing information on available techniques and experiences about the use in liquid metal flows,
- Initiate a discussion between developers and potential users with respect to the actual need of information about the flow structure as well as the capabilities of existing and developing measuring techniques,
- Explore opportunities for co-operative R&D projects to expedite new developments and results, to share expertise and resources.

The MTLM Workshop brought together scientists and engineers from universities, research institutes and the industry. The high response indicated by the large number of participants from a multiplicity of backgrounds and disciplines demonstrates the importance of the workshop subject.

The spectrum of measuring techniques presented at the workshop was broad. It covers local invasive probes such as electric potential or resistivity probes, mechano-optical probes etc. and non-invasive techniques which need to have a direct contact with the fluid container (ultrasonic methods) or being able to work fully contactless (X-ray radiography, velocity reconstruction from magnetic field measurements). Capabilities and restrictions of the particular methods and principles were discussed intensively.

In view of the large interest, the high number of interesting presentations, the fruitful discussions during the workshop as well as the new contacts between the participants the MTLM Workshop can be assessed as very successful.

written by           Gunter Gerbeth, Sven Eckert  
                          (Forschungszentrum Rossendorf e.V.)

Dresden, November 1999

## Scientific Programme

**October 11, 1999 (Monday)**

### **Morning Session**

- 9.30 Welcome and Opening  
Prof. F.-P. Weiß (FZ Rossendorf), Prof. R. Grundmann (TU Dresden)
- 10.00 **Invited Lecture**  
*J. Koster (University of Colorado at Boulder, USA)*  
In-situ solidification and metallic flow visualisations with X-rays
- 10.45 *T. Azami, S. Nakamura, T. Hibiya, K. Mukai (NEC Corporation, Japan)*  
The effect of oxygen partial pressure of ambient atmosphere on mode and velocity of Marangoni convection in molten silicon column
- 11.05 Coffee break
- 11.35 *C. Salvi, J.P. Garandet, A. Borgis and E. Rolland (CEA Grenoble, France)*  
High precision resistance measurement in directional solidification
- 11.55 *B. Drevet, P. Lehmann (EPM-MADYLAM Grenoble, France)*  
Seebeck effect as an in-situ detection technique in solidification of metallic alloys

# **In-situ solidification and metallic flow visualizations with X-rays**

*Jean N. Koster*

*University of Colorado at Boulder, USA*

Manufacturers of high performance metallic alloys and electronic crystals need to understand solidification from alloyed melts in order to improve processes. Predictive liquid metal modelling was considered necessary to improve material quality. The international microgravity programs heightened awareness of the impact the fluid flow in the melt has during solidification processing on properties of the solid. Numerical codes were developed for most processing systems. Validation was done by comparative benchmark problem solving and experiments with transparent model melts, without completely understanding its appropriateness. For a long time research on liquid metal fluid dynamics has been hampered by lack of flow and density visualization in the melt phase.

This presentation describes a radiosopic flow visualization technique. It will be shown that real-time liquid metal flow visualization and in-situ observation during solidification/ melting processing are very powerful and deliver results that need to be clarified. These include gravitational segregation in the melt, actual dissolution state of the melt above liquidus, a threshold in natural convective flow, and double diffusive flow patterns. So far, many experiments challenge some of the conjectures made in numerical simulations.



# In-situ solidification and metallic flow visualizations with X-rays

Jean N. Koster  
University of Colorado at Boulder

MTMIL-Workshop, Dresden, October 11-13, 1999



## Abstract

Manufacturers of high performance metallic alloys and electronic crystals need to understand solidification from alloyed melts in order to improve processes. Predictive liquid metal modeling was considered necessary to improve material quality. The international microgravity programs heightened awareness of the impact the fluid flow in the melt has during solidification processing on properties of the solid. Numerical codes were developed for most processing systems. Validation was done by comparative benchmark problem solving and experiments with transparent model melts, without completely understanding its appropriateness. For a long time research on liquid metal fluid dynamics has been hampered by lack of flow and density visualization in the melt phase.

This presentation describes a radioscopic flow visualization technique. It will be shown that real-time liquid metal flow visualization and in-situ observation during solidification melting processing are very powerful and deliver results that need to be clarified. These include gravitational segregation in the melt, actual dissolution state of the melt above liquidus, a threshold in natural convective flow, and double diffusive flow patterns. So far, many experiments challenge some of the conjectures made in numerical simulations.



## Outline

- Background Information
- Experimental Setup
- Pure Gallium Experiments
- Gallium Indium Alloy Experiments
- Aluminum Alloy Experiments
- Indium Antimony Crystal Growth
- Concluding Remarks

## Motivation

- Need for liquid metal thermofluiddynamic experiments.
- Industry reports unexplained segregation in castings and crystal growth
- Numerical models have not been validated with metallic melt experiments, and often do not reproduce simple flow situations
- Models and theory thrive on conjectures
- Visualization of temperature/density fields with energy absorptive X-ray systems provide benchmark data.

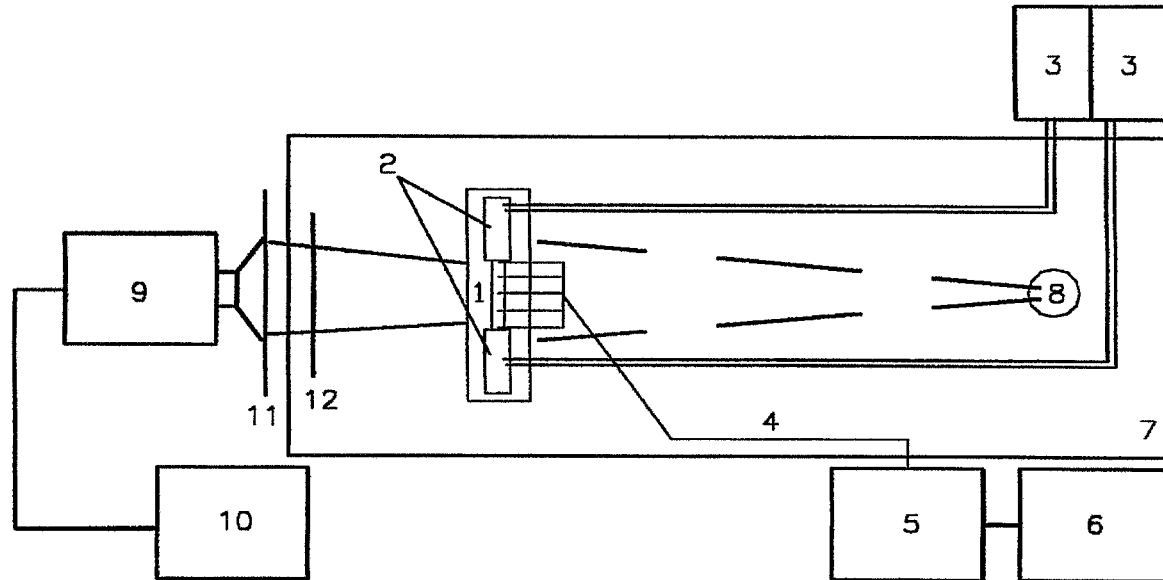


## Applications

- Turbine blade castings
- Sheet metal for aerospace/high-tech applications
- Compound crystal growth from melt for VLSI circuitry and MEMS
- Liquid metal cooling of
  - high performance computers
  - energy systems (space power, MHD)
  - astronaut gear



# X-ray setup



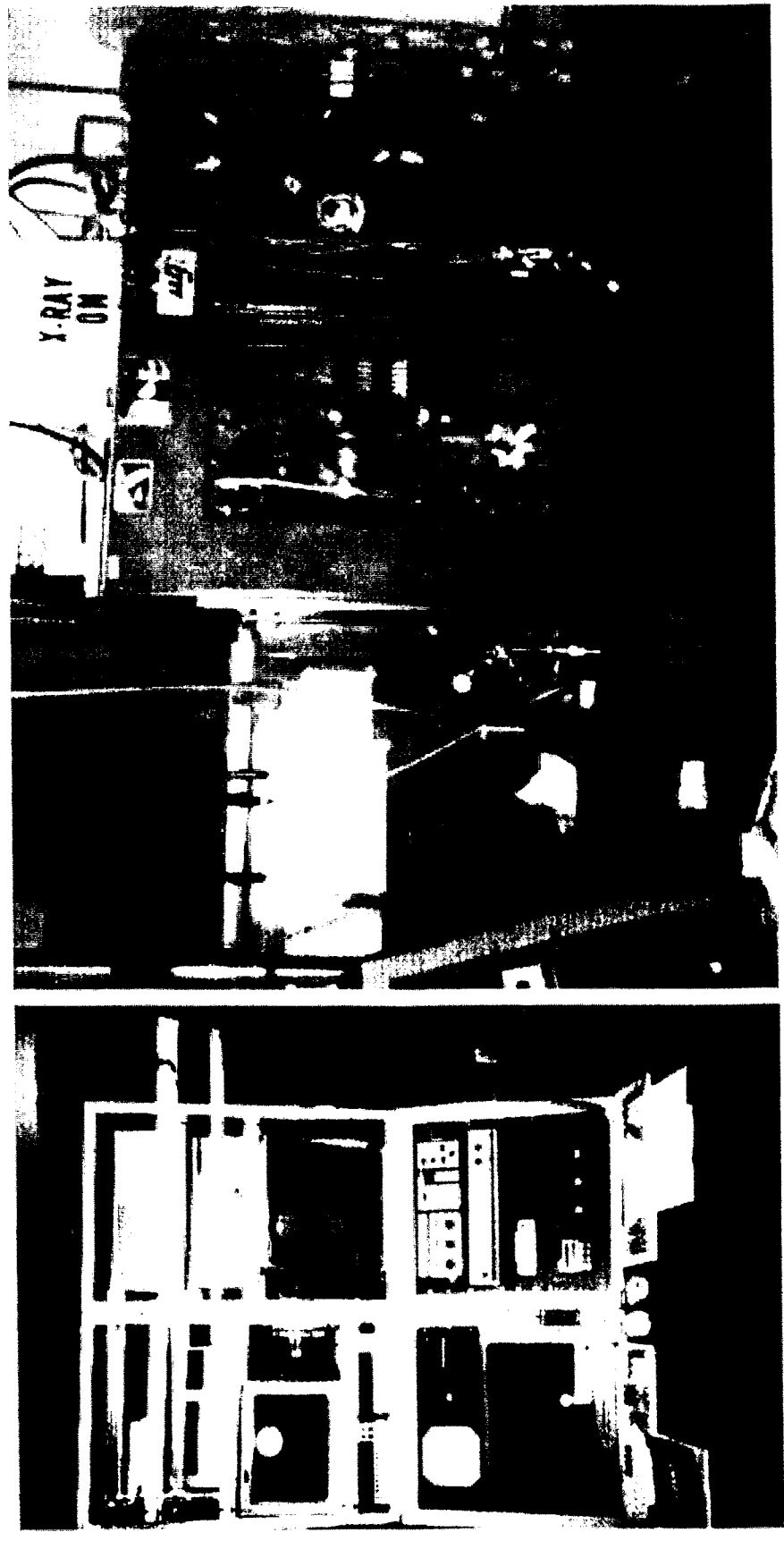
- |   |                                     |    |                         |
|---|-------------------------------------|----|-------------------------|
| 1 | Testcell with liquid metal          | 7  | Lead chamber            |
| 2 | Thermodes                           | 8  | X-ray source            |
| 3 | Waterbath temperature control       | 9  | CCD and Image processor |
| 4 | Thermocouples                       | 10 | PC #2                   |
| 5 | Temperature data acquisition system | 11 | Cesium Iodiode screen   |
| 6 | PC #1                               | 12 | Grid                    |



AEROSPACE ENGINEERING SCIENCES

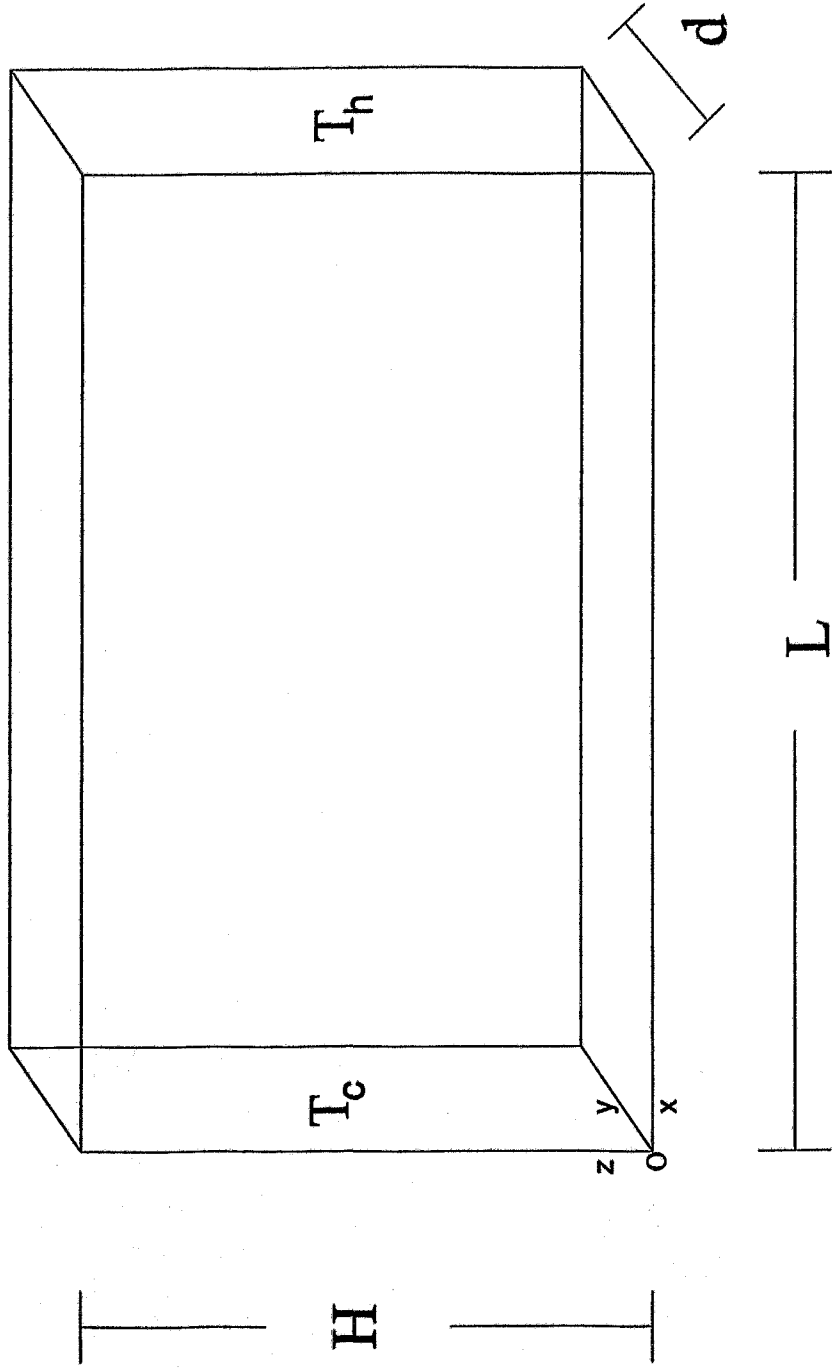


# X-Ray Flow Visualization Facility



Koster

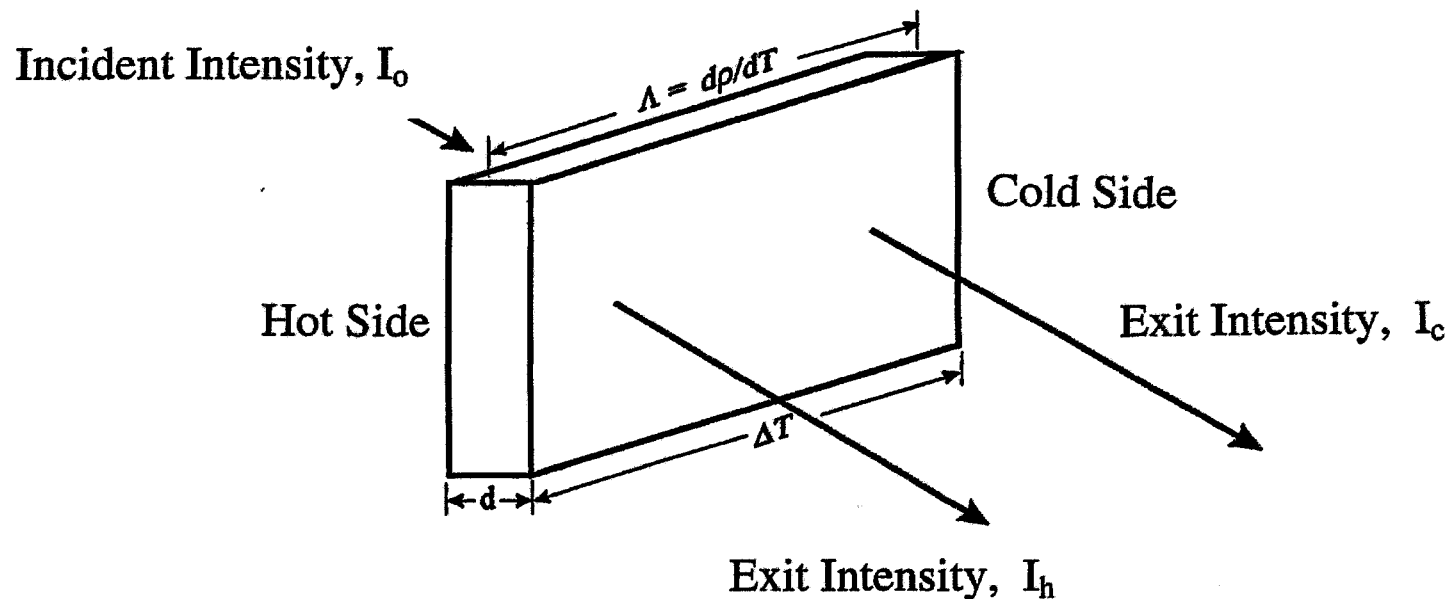
# Test Cavity: "Horizontal Bridgman Furnace" "Natural Convection Test Cell"





# Physics of X-ray absorption

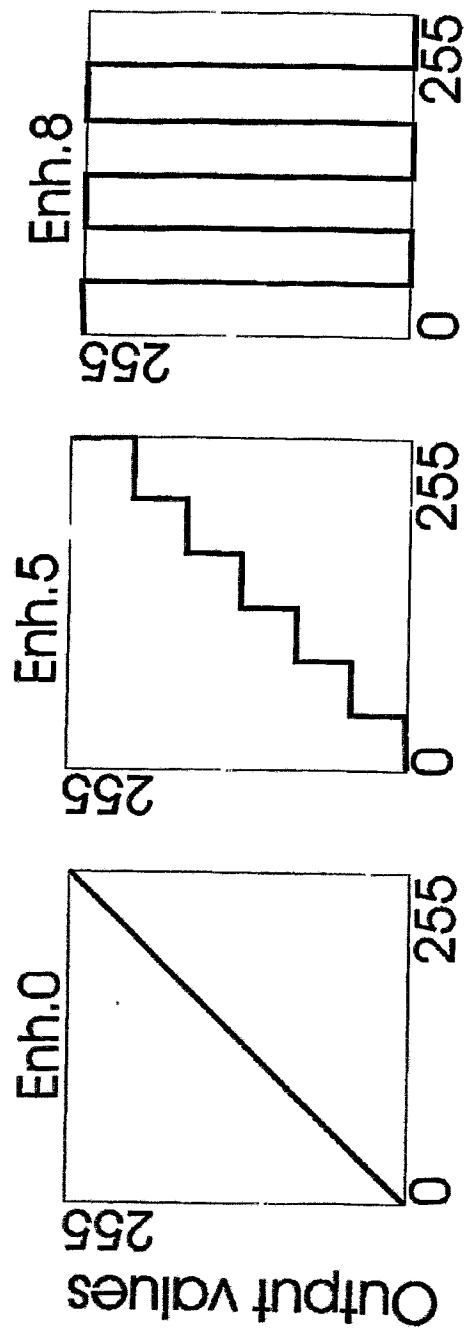
Pool, R.E., Koster, J.N., *Int. J. Heat Mass Transfer* 37 (1994), 2583.



$$\frac{I_c}{I_h} = \exp \left[ \left( \frac{\mu}{\rho} \right)_o (\Lambda \Delta T) d \right]$$



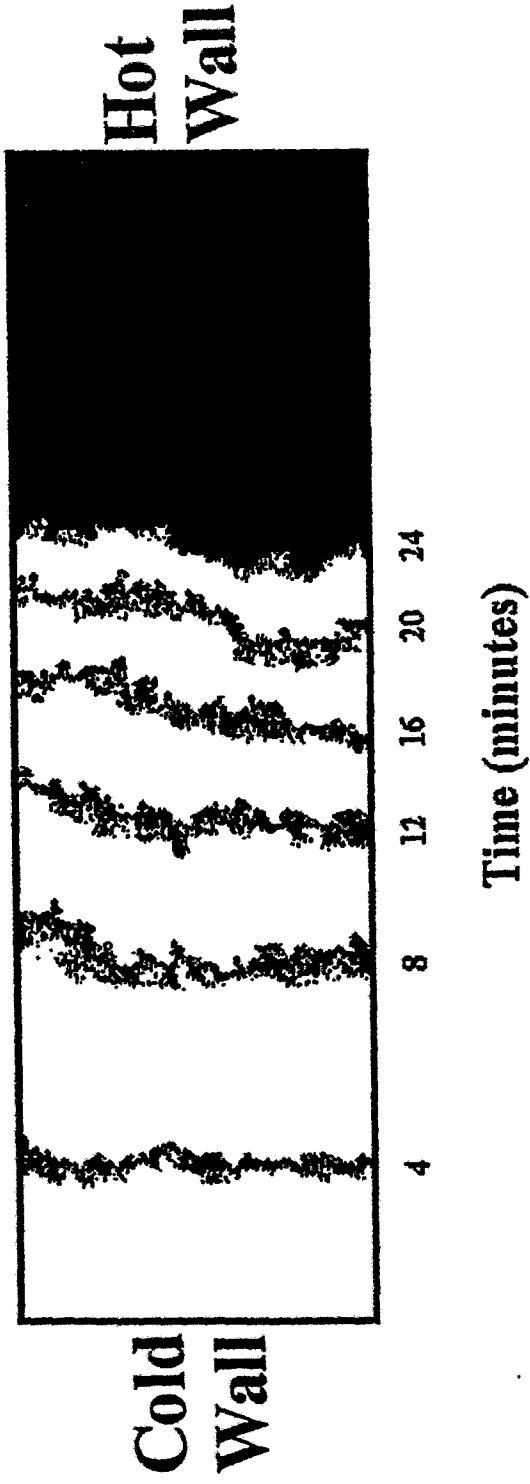
# Step-function transformation of the measured density profile to improve visualization: "Interferometric" fringes



A "fringe" is a mathematically averaged radiation intensity, and not a convecting fluid layer separated from the neighboring fringes!

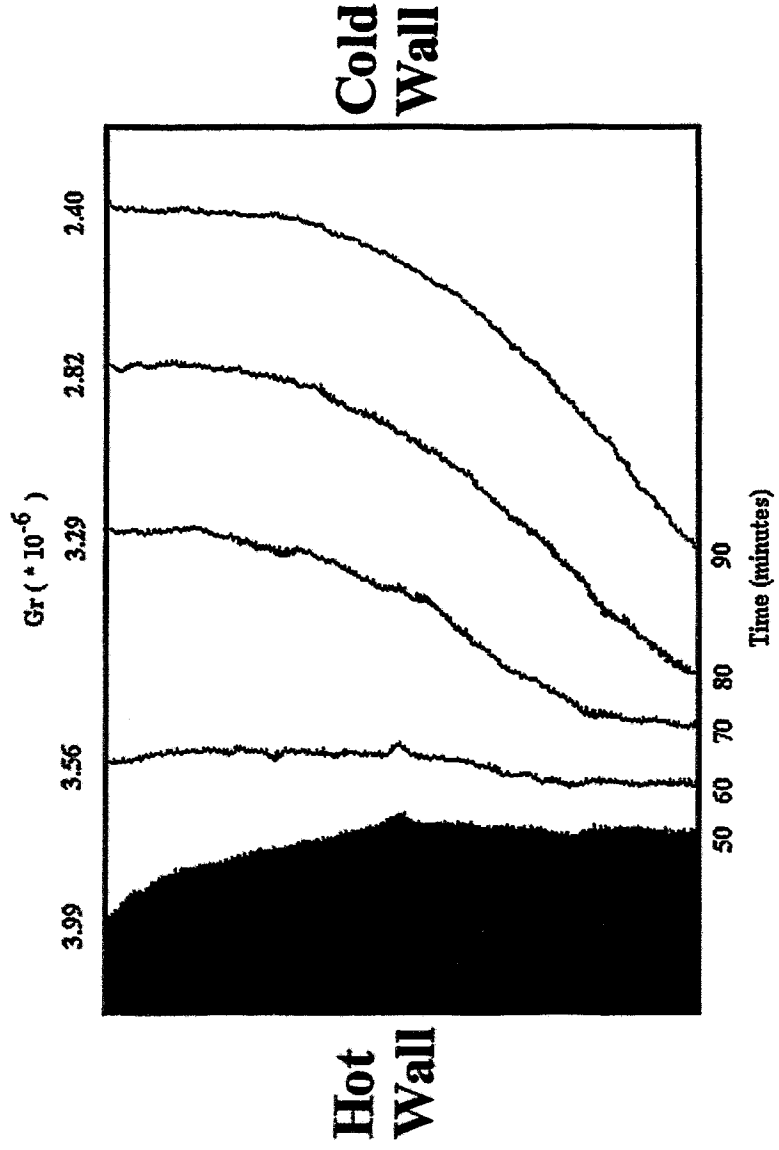


# Horizontal Solidification of pure Gallium



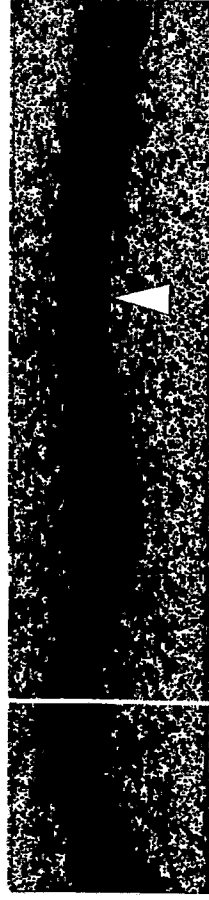


# Quasi-steady melting of pure Gallium





# Visualization of Rayleigh-Bénard convection in pure gallium



$Ra = 4.52 \times 10^4$   $a = 3.3$



$Ra = 4.96 \times 10^4$   $a = 2.92$



$Ra = 5.54 \times 10^4$   $a = 2.61$



$Ra = 6.76 \times 10^4$   $a = 2.51$





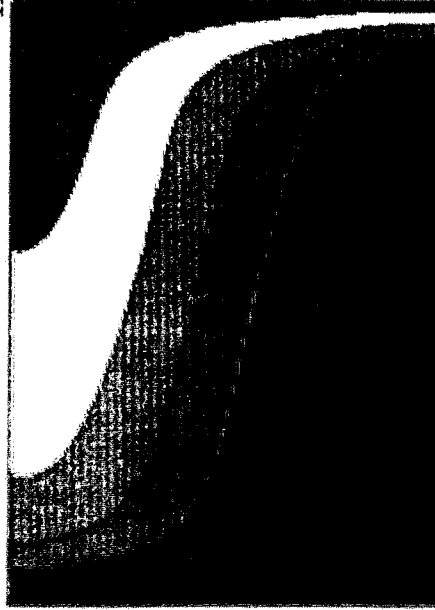
# Natural Convection in pure Gallium

## Comparison of numeric model and experiment

$$\Delta T = 50^{\circ}\text{C}, Gr = 1.56 \times 10^7$$

$$\Delta\rho/\text{fringe} = 4.9 \times 10^{-3} \text{ g/cm}^3$$

Cold



Hot

**Fidap® density modeling**



**Radioscopic density visualization**



# Temperature fields in liquid gallium with solid-liquid interface

$\Delta\rho/\text{fringe} = 1.3 \times 10^{-3} \text{ g/cm}^3$



$\Delta T = 4.9 \text{ K}$

$Gr = 2.3 \times 10^6$



$\Delta T = 7.1 \text{ K}$

$Gr = 2.7 \times 10^6$



$\Delta T = 11.5 \text{ K}$

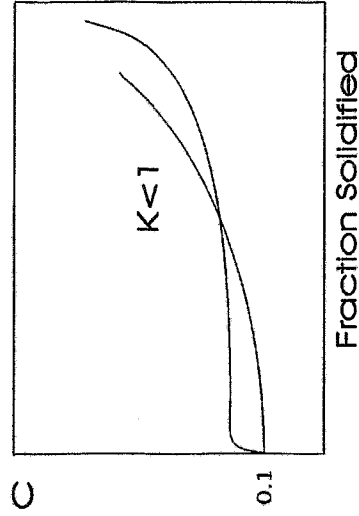
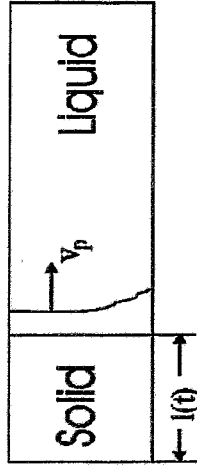
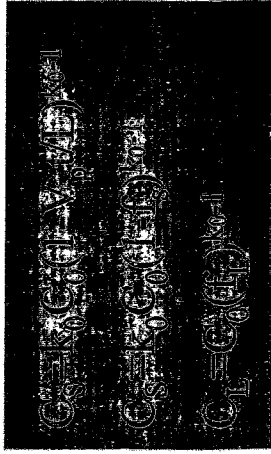
$Gr = 4.3 \times 10^6$



# Assumptions for Scheil equation

## Macrosegregation

- 1) segregation coefficient  $k$  is constant,
- 2) negligible diffusion in the solid,
- 3) steady growth rate is employed,
- 4) equal solid and liquid densities,
- 5) crystal-melt interface is planar and normal to the macroscopic solidification direction,
- 6) solute mixing in the melt is complete.



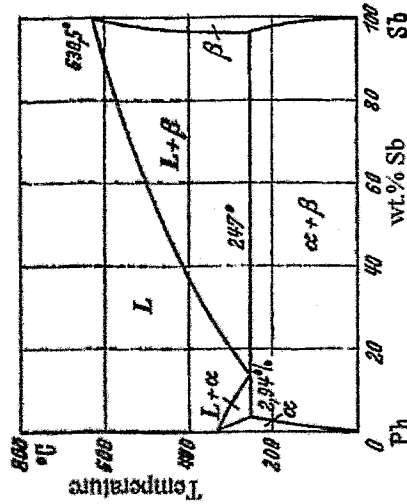


## Reports of unusual segregation

- Watson, J.H., *J. Inst Metals* **49** (1932), 347.
  - Silver-Copper
- Masing, G., *Lehrbuch der Allgemeinen Metallkunde*, Springer, Berlin (1950), 235.
  - Lead-Antimony hyper-eutectic
- Allen, B.C., Isserow, S., *Acta Metallurgica* **5** (1957), 465.
  - Uranium-Aluminum eutectic
- Reijonen, H., Forstén, J., *J. Cryst. Growth* **12** (1972), 61.
  - Tin-Cadmium
- Bardsley, W., Hurle, DTJ, Hart, M., Lang, A.R., *J. Cryst. Growth* **49** (1980), 612
  - Ga-doped Germanium; In-doped Germanium
- Rudolph, P., Neubert, M., Mühlberg, M. *J. Cryst. Growth* **128** (1993), 582.
  - Cadmium-Telluride
- Schilz, J., Romanenko, V.N. *J. Mat. Sci.: Materials in Electronics* **6** (1995), 265.
  - Germanium-Silicon
- Derebail, R., Koster, J.N., *Metal. Mat. Trans. B* **27B** (1996), 686.
  - Gallium-Indium eutectic
- Glazov, V., M., *et al.* In: *Centrifugal Materials Processing*, 3rd edition (1997).
  - Mercury-Cadmium-Telluride
- Koster, J.N., Derebail, R., *Heat Mass Transfer*, **32** (1997), 489.
  - Gallium-Indium hypo-eutectic



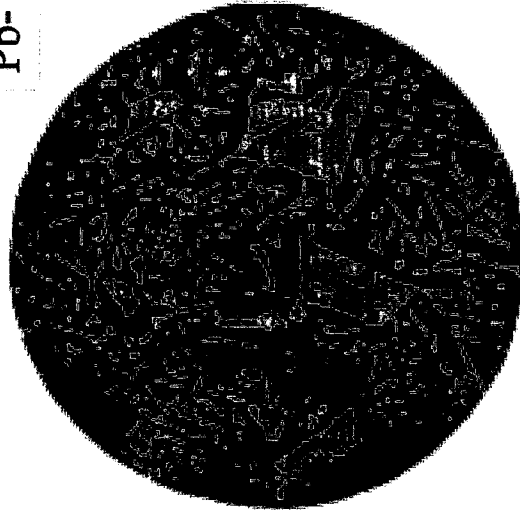
# Gravitational Segregation in Hyper-Eutectic Lead-Antimony



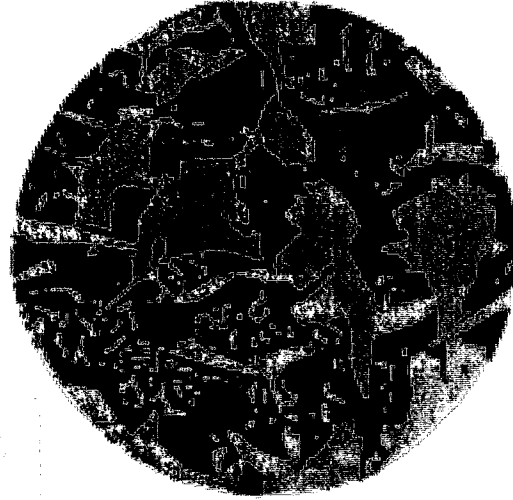
$$\rho_{Pb} = 11.36 \text{ g/cc}$$

$$\rho_{Sb} = 6.70 \text{ g/cc}$$

Pb-



bottom



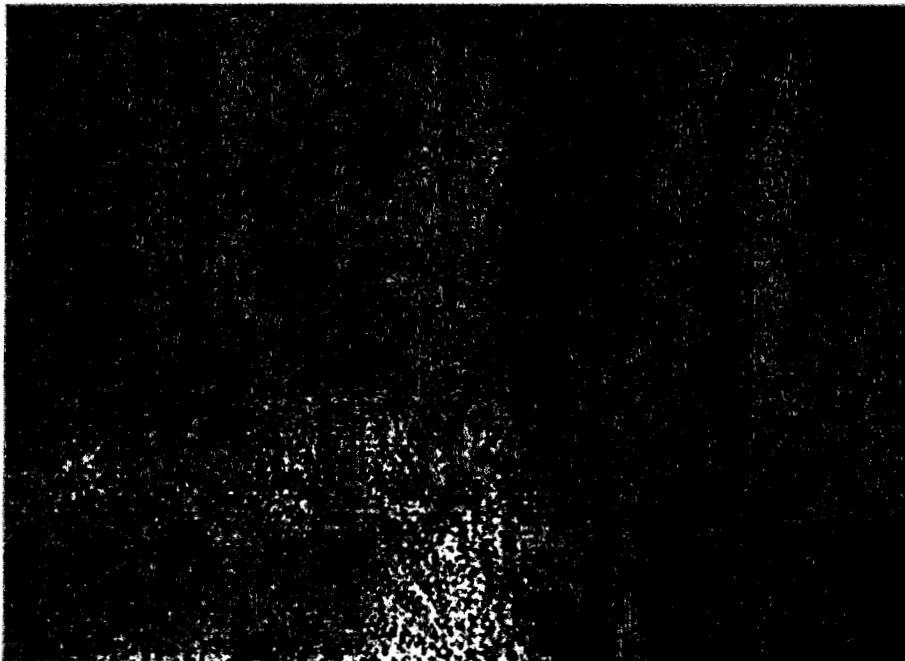
top

G. Masing, *Lehrbuch der Allgemeinen Metallkunde*, Springer Verlag, Berlin, 1950, p. 235



## Compositional Trails in Germanium Crystals

Bardsley, W., Hurle, DTJ, Hart, M., Lang, A.R., *J. Cryst. Growth* **49** (1980), 612



Ga-doped Germanium  
Dislocations and solute trails (~50  $\mu\text{m}$  wide).  
Ga-inclusions at end of trails



In-doped Germanium  
Vertical solute trails ending  
with In-inclusions.



Freckles around periphery of cylindrical  
Mar-M200 ingot



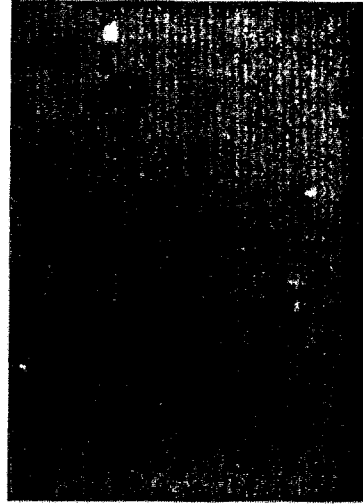
Giamei, A. F., and Kear, B. H., *Metall. Trans.* 1 (1970), 2185



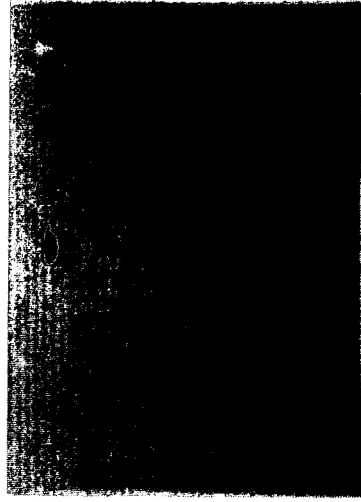




# Dissolution of 5 wt.% Indium in isothermal Gallium; $T = 40^{\circ}\text{C}$



$t = 0$  min



$t = 8$  min



$t = 24$  hrs



## Theoretical Gravitational Segregation

R.T. DeHoff, *Thermodynamics in Materials Science*, McGraw Hill, 1993.

J.N. Koster and R. Derebail, *Heat and Mass Transfer* **32** (1997), p.489.

$$d/dz \{ \ln X(z) \} = (g/RT)(M - M_2)$$

$$M = (1 - X) M_{1,Ga} + X \cdot M_{2,In}$$

$$X/(1-X) = \{ (X_0/1-X_0) \} \exp \{ g/RT (M_2 - M_1)(z - z_0) \}$$

$$C = m_{In}/(m_{In} + m_{Ga}) = M_{In} X / (M_{Ga} + (M_{In} - M_{Ga}) X)$$

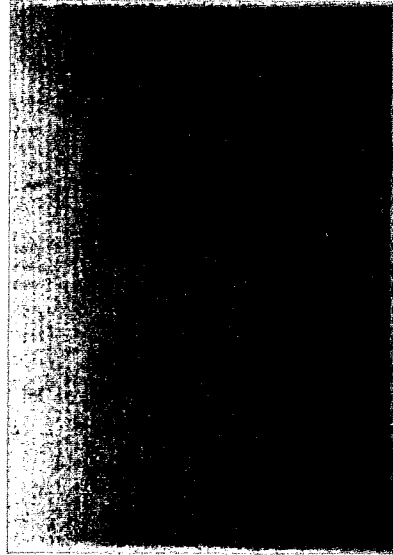
→  $\Delta X$  (3.5 cm) =  $2 \times 10^{-5}$  at%, or  $\Delta C = 3 \times 10^{-5}$  wt% Indium

\* which is negligible! → Boussinesq fluids

\*  $\Delta C$  *too small to be visualized by X-ray technique!*



# Transient Convective mixing of Ga-5In after dissolution and stratification



$\Delta T = 4.1\text{K},$   
 $Gr_1 = 1.3 \times 10^6$



$\Delta T = 7.6\text{K},$   
 $Gr_1 = 2.4 \times 10^6$



$\Delta T = 11.4\text{K},$   
 $Gr_1 = 3.6 \times 10^6$



# Typical Ga-5In solids



Fast solidification



$\Delta T = 1.4 \text{ K}, Gr_1 = 1.0 \times 10^6$



$\Delta T = 2.6 \text{ K}, Gr_1 = 1.7 \times 10^6$

## Development and disappearance of sub-layer convection in Ga-5In



$\Delta T = 3.3 \text{ K}, Gr_1 = 2.6 \times 10^6$



$\Delta T = 6.2 \text{ K}, Gr_1 = 2.1 \times 10^6$



$\Delta T = 5.5 \text{ K}, Gr_1 = 2.5 \times 10^6$



# Temperature fields in liquid gallium with solid-liquid interface

$$\Delta\rho/\text{fringe} = 1.3 \times 10^{-3} \text{ g/cm}^3$$



$$\Delta T = 4.9 \text{ K}$$

$$Gr = 2.3 \times 10^6$$



$$\Delta T = 7.1 \text{ K}$$

$$Gr = 2.7 \times 10^6$$



$$\Delta T = 11.5 \text{ K}$$

$$Gr = 4.3 \times 10^6$$



$\Delta T = 5.7 \text{ K}, Gr_1 = 2.3 \times 10^6$



$\Delta T = 5.6 \text{ K}, Gr_1 = 2.4 \times 10^6$

Development of full convection in Ga-5In.  
A threshold exists for onset of convection!



$\Delta T = 5.8 \text{ K}, Gr_1 = 2.6 \times 10^6$



$\Delta T = 7.3 \text{ K}, Gr_u = 4.2 \times 10^6$



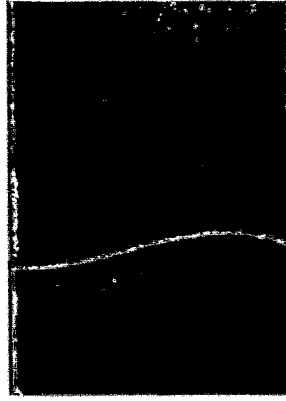
$\Delta T = 6.0 \text{ K}, Gr_1 = 3.3 \times 10^6$



## Concentration evaluation

J.N. Koster and R. Derebail, *Heat and Mass Transfer* 32 (1997), p.489.

Convectively mixed



$\Delta T_{\text{liq}} = 12.5 \text{ K}$

Ga-In Plate Model



$\Delta T_{\text{liq}} = 9 \text{ K}$

$$\rho_{\text{Ga-In}} = \rho_{\text{Ga-In}, T_0} (1 + \beta_T (T - T_0))$$

$$\Delta \rho_{\text{Ga-In}} = 9 \text{ kg/m}^3$$

$$\Delta I_1 / (I_0 d) = 0.0126 \text{ cm}^{-1}$$

Ga - 5 wt.% In

$$\Delta I_2 = \Delta I_{\text{In}} + \Delta I_{\text{Ga}} = I_0 d ((\mu/\rho)_{\text{In}} \Delta \rho_{\text{In}} + (\mu/\rho)_{\text{Ga}} \Delta \rho_{\text{Ga}})$$

$$\Delta I_2 = 10 \Delta I_1$$

$$\Delta \rho_{\text{In}} = 35.3 \text{ kgm}^{-3}$$

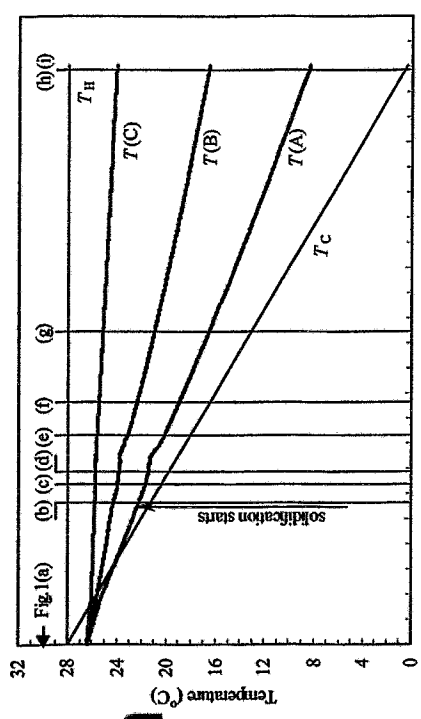
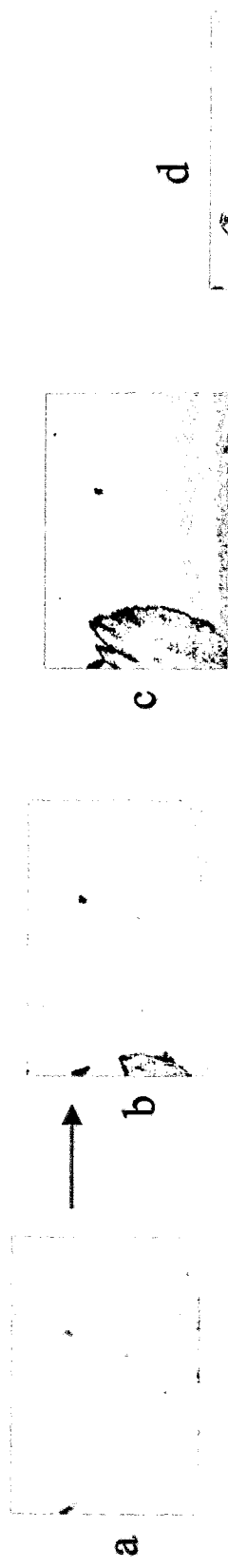
$$\Delta C = \Delta \rho_{\text{In}} / \rho_{\text{Ga}} = 5.8 \times 10^{-3}$$

or 0.58 wt.% vertical In-segregation

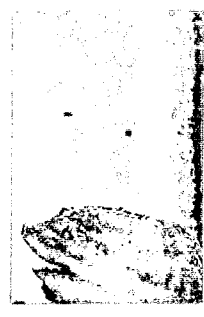
Top of melt: Ga-4.71In;

Bottom melt: Ga-5.29In





# Indium-stratification in melt during slow directional solidification



f



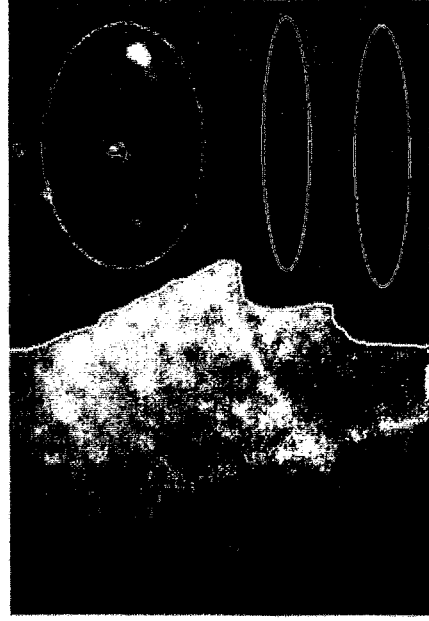
g



h



# Thermosolutal convection in Ga-5In



Multiple staggered roll cells after transient heating



53 min after heating start



92 min



142 min



177 min



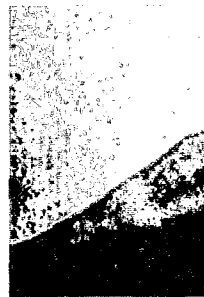
217 min



263 min



333 min



538 min

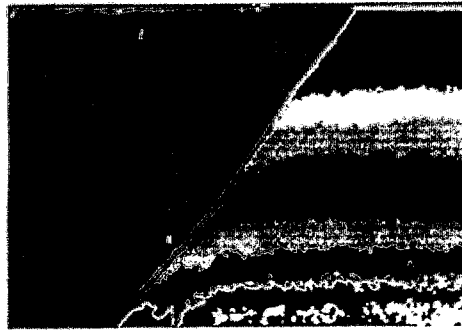
# Sequence of formation and merging of double-diffusive cells during fast melting

$Gr \approx 16 \times 10^6$



# Development of Thermosolutal Convection

$\Delta T_L < 9K$



Quasi-steady heating  
0.06 K/min

$\Delta T_L > 12K$

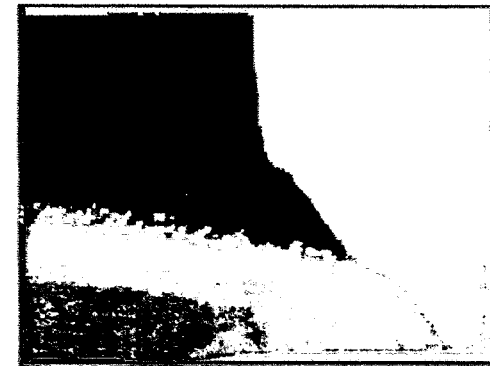
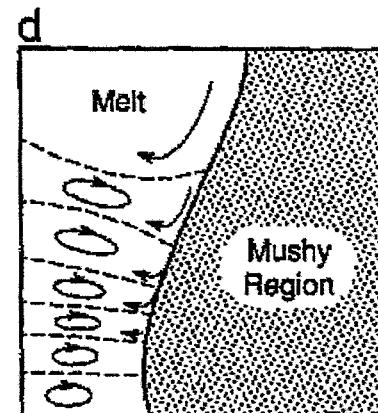
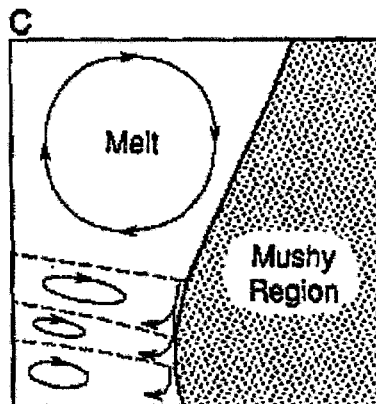
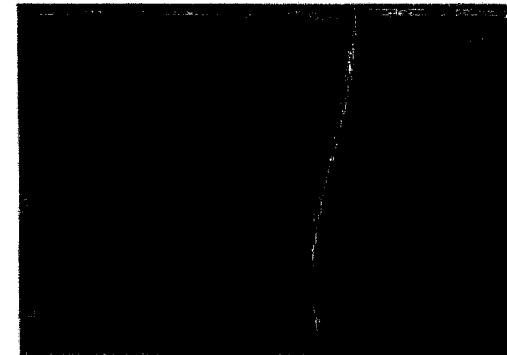
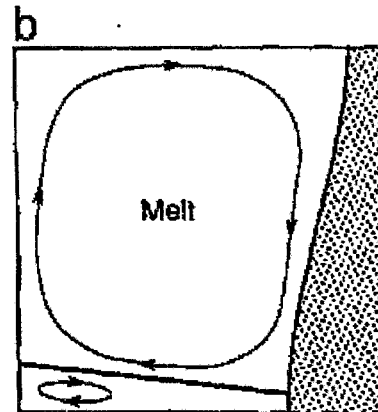
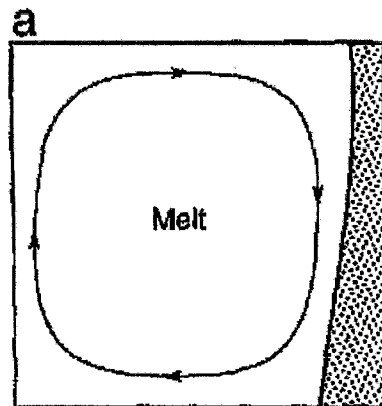


Transient heating  
1 K/min

$\Delta T_L \approx 14K$



## Comparison Theory-Experiment



Thompson, M.E. and Szekeley, J.,  
*J. Fluid Mech.*, **187** (1988), 409-433.

Ga-5In experiments



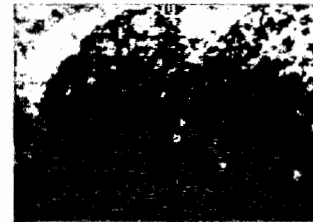
# Quasi-steady solidification of eutectic GaIn



A)  $Gr = 2.87 \times 10^6$   
( $\Delta T_h = 9.5$  K);



B)  $Gr = 3.82 \times 10^6$   
( $\Delta T_h = 11.6$  K);



C)  $Gr = 4.45 \times 10^6$   
( $\Delta T_h = 12.4$  K);



D)  $Gr = 4.51 \times 10^6$   
( $\Delta T_h = 12.1$  K);



E)  $Gr = 4.16 \times 10^6$   
( $\Delta T_h = 10.8$  K);



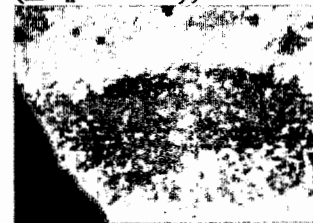
F)  $Gr = 3.66 \times 10^6$   
( $\Delta T_h = 9.1$  K);



G)  $Gr = 3.27 \times 10^6$   
( $\Delta T_h = 8.0$  K);



I)  $Gr = 2.80 \times 10^6$   
( $\Delta T_h = 6.6$  K).



H)  $Gr = 2.05 \times 10^6$   
( $\Delta T_h = 4.7$  K);



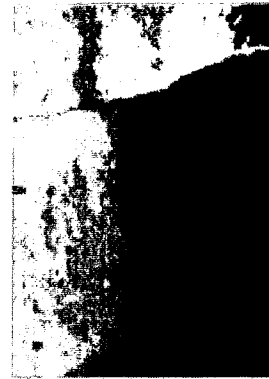
# Quasi-steady solidification of eutectic Galn



A)  $Gr_n = 6.16 \times 10^6$   
( $\Delta T_h = 10.9$  K);



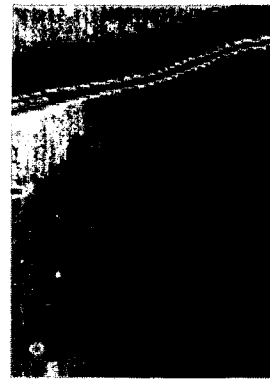
B)  $Gr_n = 3.77 \times 10^6$   
( $\Delta T_h = 3.8$  K);



C)  $Gr_n = 7.91 \times 10^6$ ,  
 $Gr_n = 3.27 \times 10^6$   
( $\Delta T_h = 3.5$  K);



D)  $Gr_n = 3.91 \times 10^6$   
( $\Delta T_h = 3.2$  K);



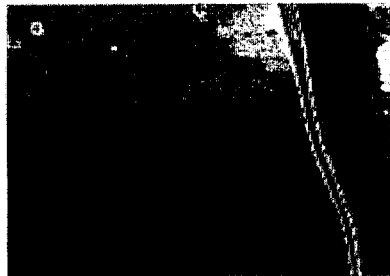
E)  $Gr_n = 2.43 \times 10^6$   
( $\Delta T_h = 2.6$  K);



F)  $Gr_n = 0.32 \times 10^6$   
( $\Delta T_h = 2.1$  K)



## Convection in melting eutectic GaIn, followed by convection breakdown



A)  $Gr_u = 1.89 \times 10^6$   
( $\Delta T_h = 2.9$  K);



B)  $Gr_u = 7.85 \times 10^6$   
( $\Delta T_h = 4.8$  K);



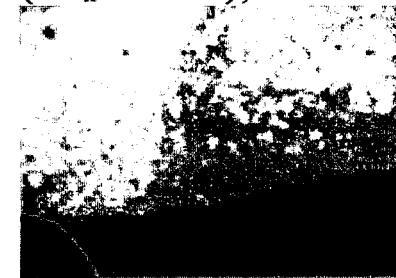
C)  $Gr_u = 9.95 \times 10^6$   
( $\Delta T_h = 8.6$  K);



D)  $Gr_u = 8.33 \times 10^6$   
( $\Delta T_h = 16.4$  K);



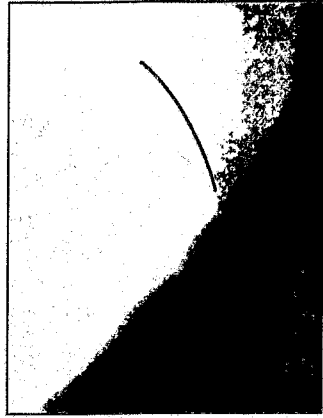
E)  $Gr_u = 5.86 \times 10^6$   
( $\Delta T_h = 17.9$  K);



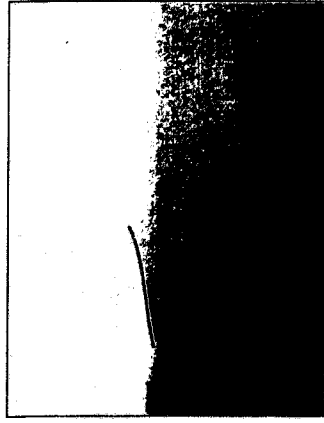
F)  $Gr_u = 6.50 \times 10^6$   
( $\Delta T_h = 16.7$  K);

Formation of partially immiscible double-diffusive convection layers (liquation)





$Gr = 5 * 10^6, t = 9 \text{ min}$

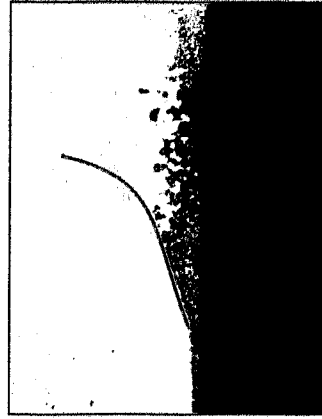


$Gr = 6.6 * 10^6, t = 20 \text{ min}$

Eutectic Ga-In solidification from left;  
Directional melting from left.  
Double-diffusive layers.



$Gr = 7.8 * 10^6, t = 145 \text{ min}$



$Gr = 7.8 * 10^6, t = 91 \text{ min}$



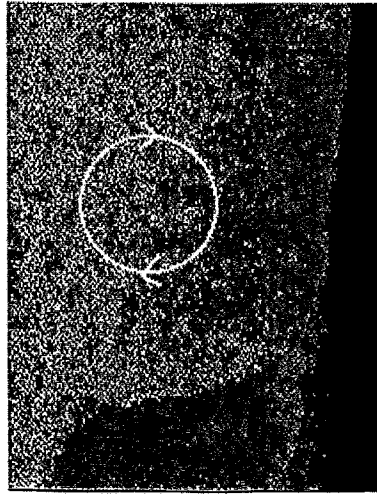
$Gr = 10.4 * 10^6, t = 40 \text{ min}$



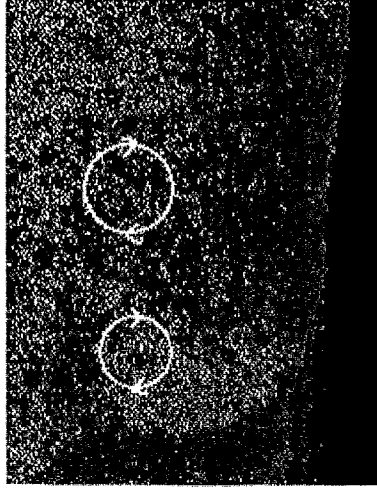
# Eddy release at heated left side

$$Gr = 14.4 \times 10^6, \Delta T = 50 \text{ K}$$

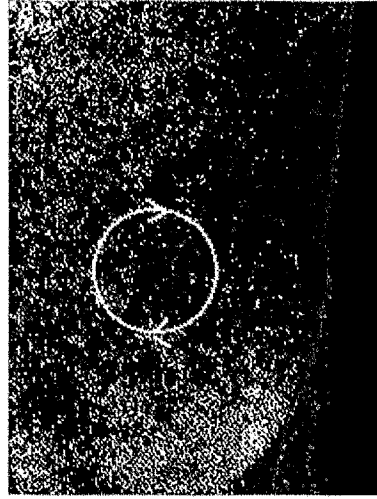
hot



t=0 sec



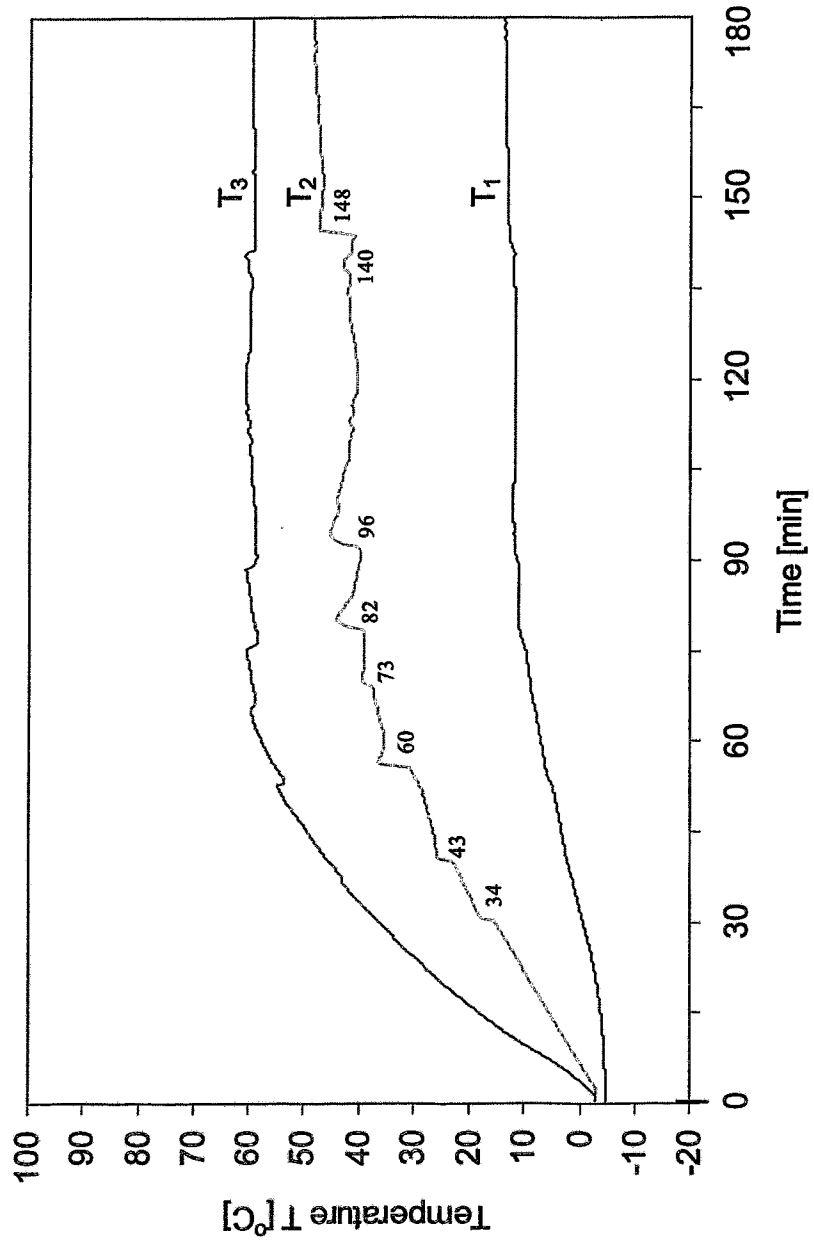
t=30 sec



t=44 sec

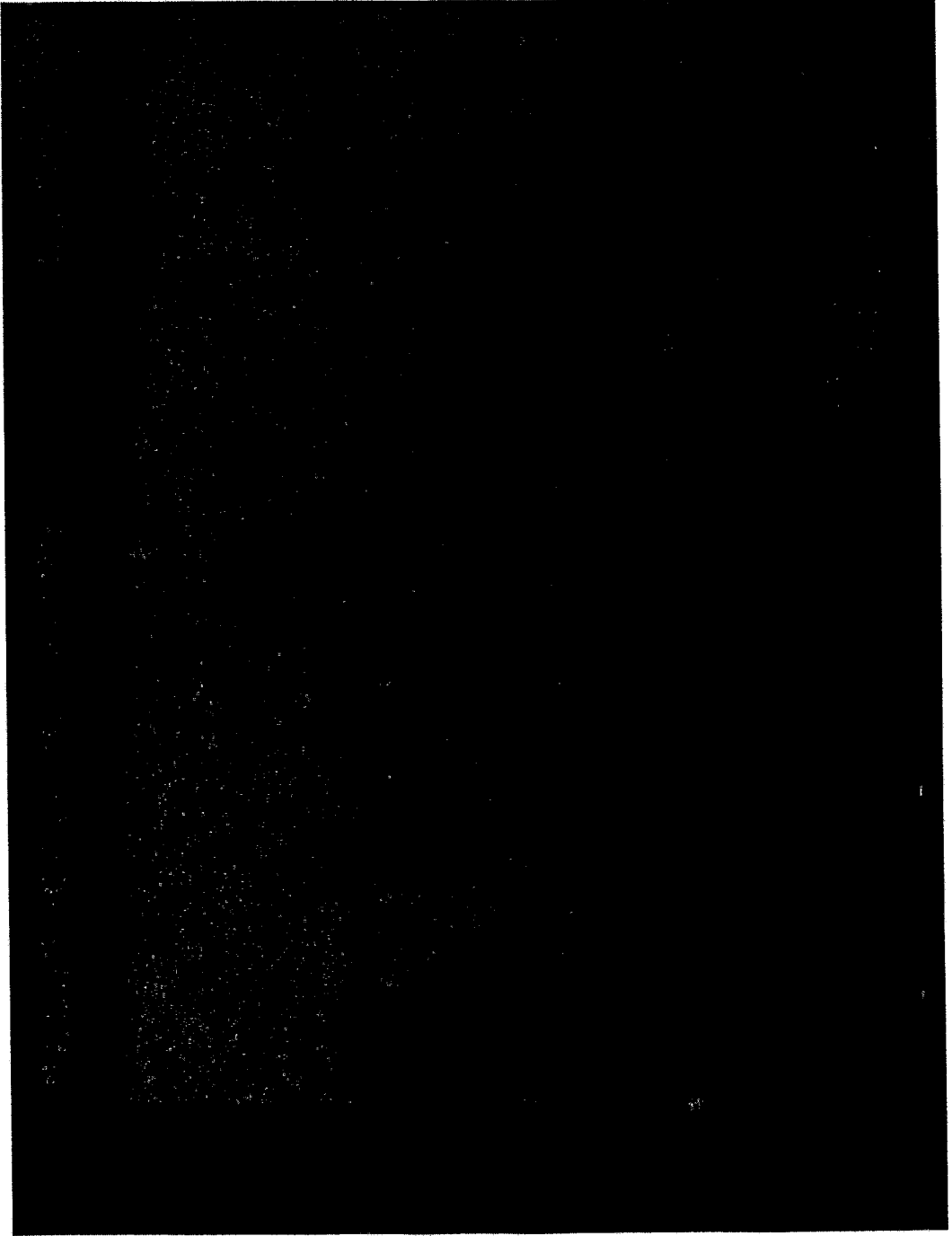


# Temperature-Time Trace leading to multiple eddy-formation





AEROSPACE ENGINEERING SCIENCES



Eddy

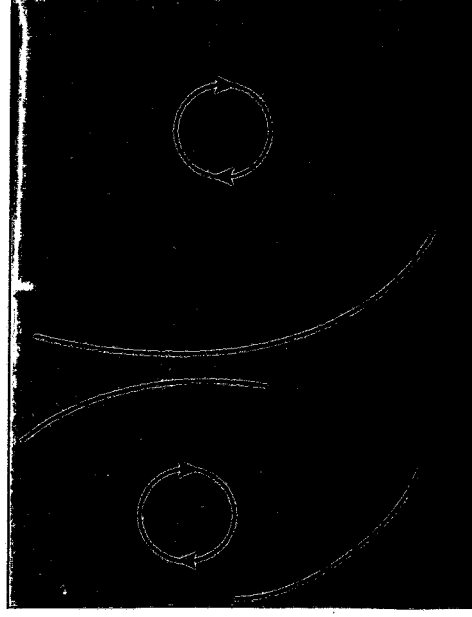
Koster



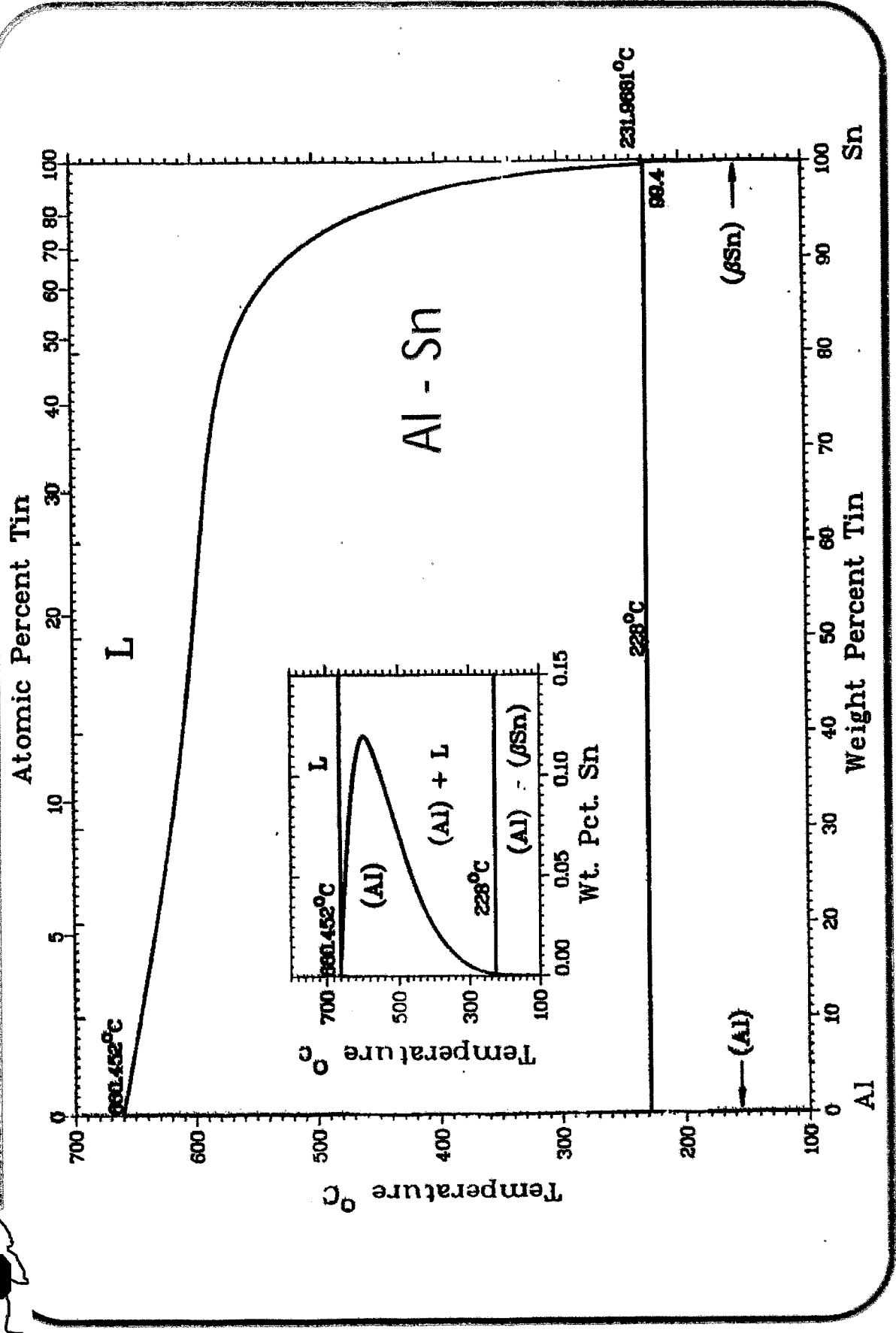
## Comparison with dispersion liquids



Benzylbenzoate-Paraffin-oil  
(dispersion fluid)

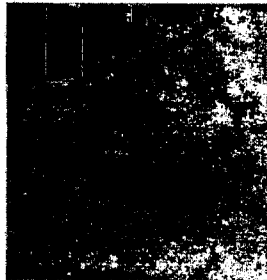


Gallium-Indium at  
end of solid dissolution

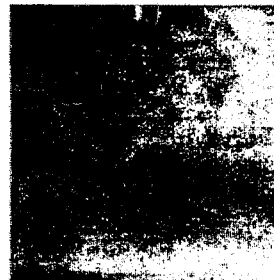




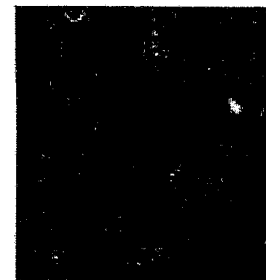
# Preparation of Al-2.4 wt.% Sn alloy



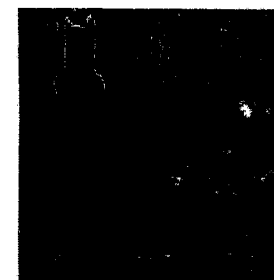
T = 20°C



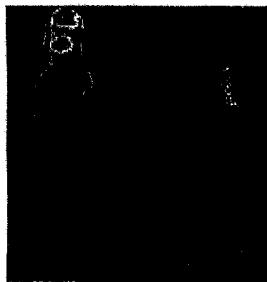
T = 668°C



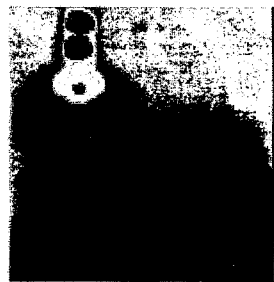
T = 595°C



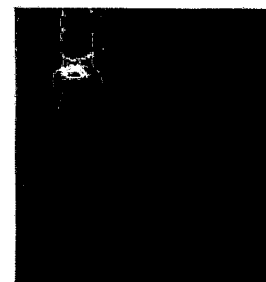
T = 598°C



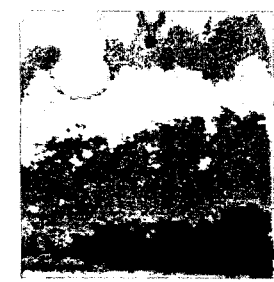
T = 605°C



T = 638°C



T = 644°C



T = 669°C



A)  $T_h=658^\circ\text{C}$ ,  $T_c=641^\circ\text{C}$   
 $Gr=2.7 \cdot 10^6$



$T_h=658^\circ\text{C}$ ,  $T_c=640^\circ\text{C}$



$T_h=658^\circ\text{C}$ ,  $T_c=640^\circ\text{C}$



$T_h=657^\circ\text{C}$ ,  $T_c=639^\circ\text{C}$

## Directional solidification and formation of vertical chemical segregation



$T_h=641^\circ\text{C}$ ,  $T_c=629^\circ\text{C}$



$T_h=649^\circ\text{C}$ ,  $T_c=634^\circ\text{C}$



$T_h=650^\circ\text{C}$ ,  $T_c=635^\circ\text{C}$



$T_h=654^\circ\text{C}$ ,  $T_c=636^\circ\text{C}$





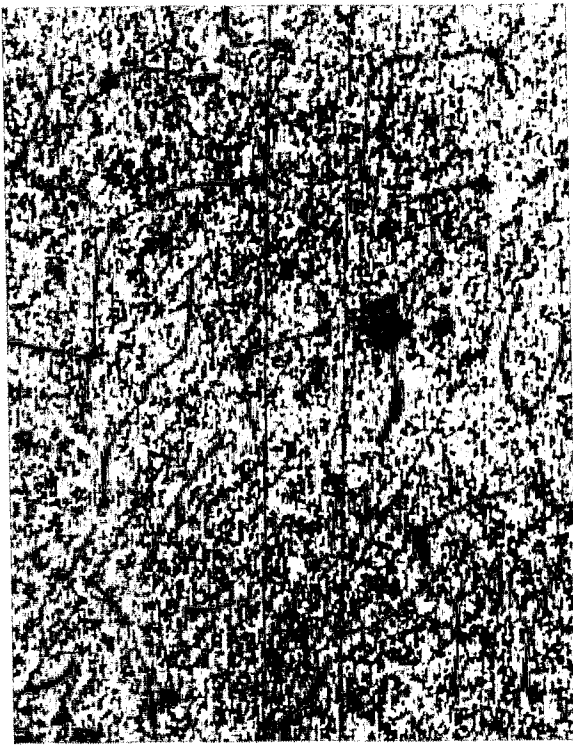
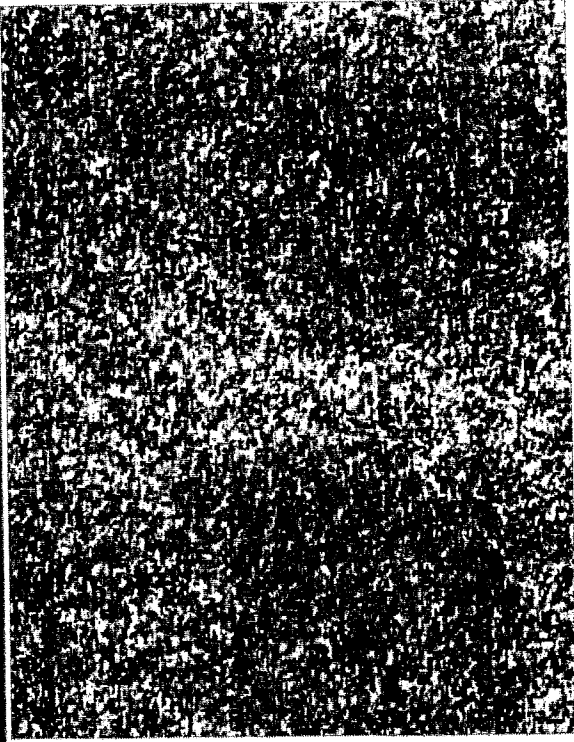
Top

# Gravitational Macrosegregation

Al-2.4Sn

Directional horizontal  
solidification

Vertical segregation of tin in melt  
& solid



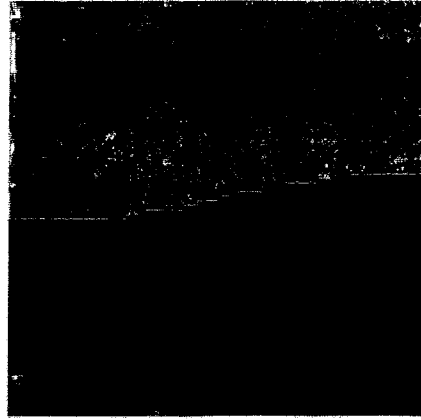
Bottom



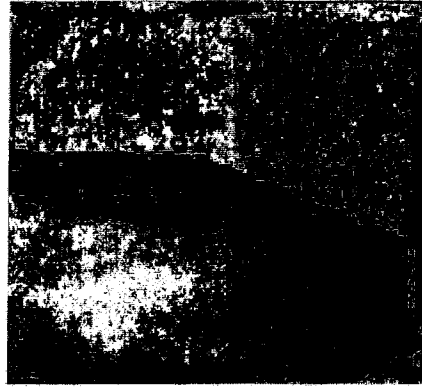


# Directional quasi-steady horizontal solidification of Al and Al-alloys

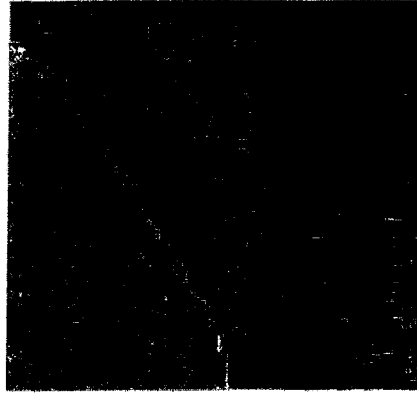
Solids in gray



Pure Al



Al-2.4Sn

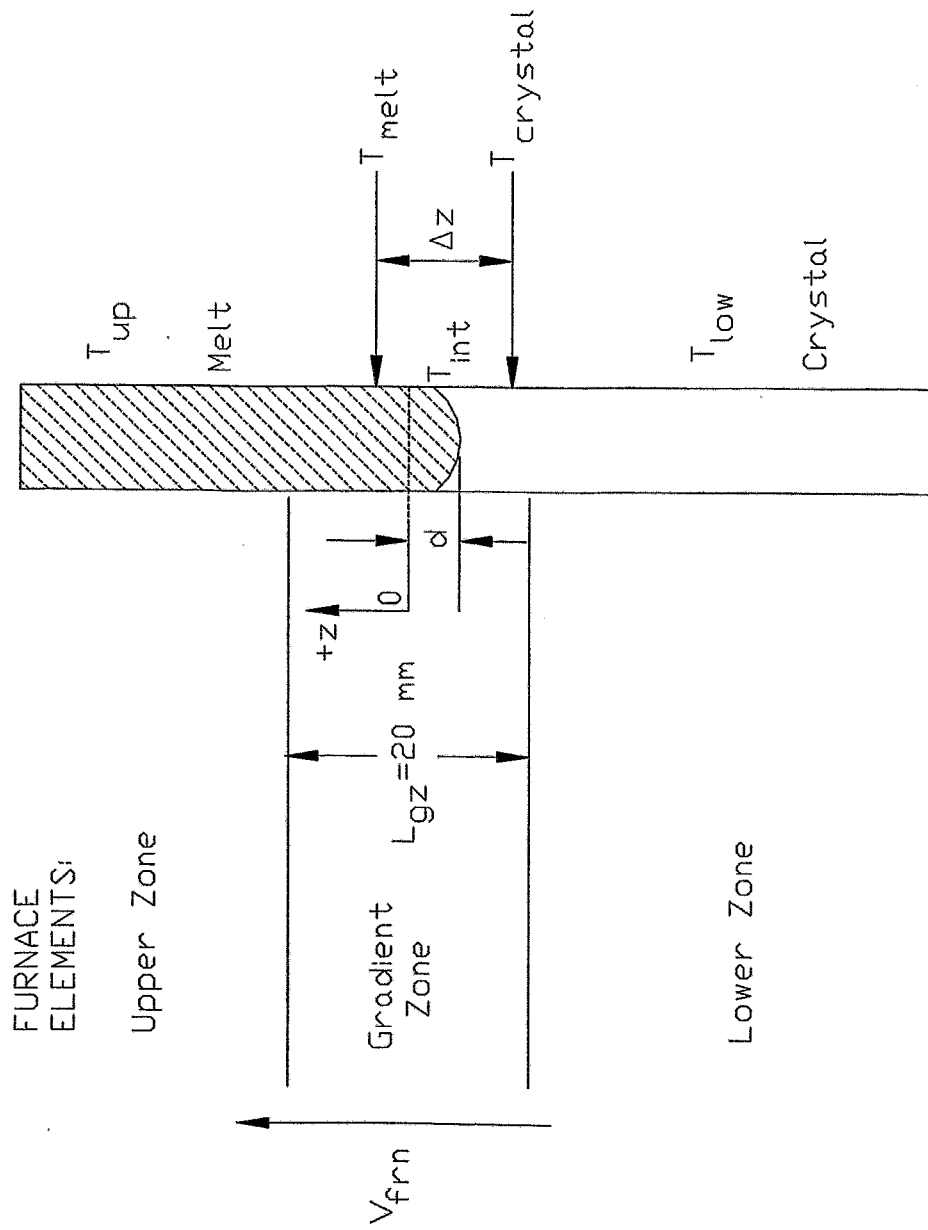


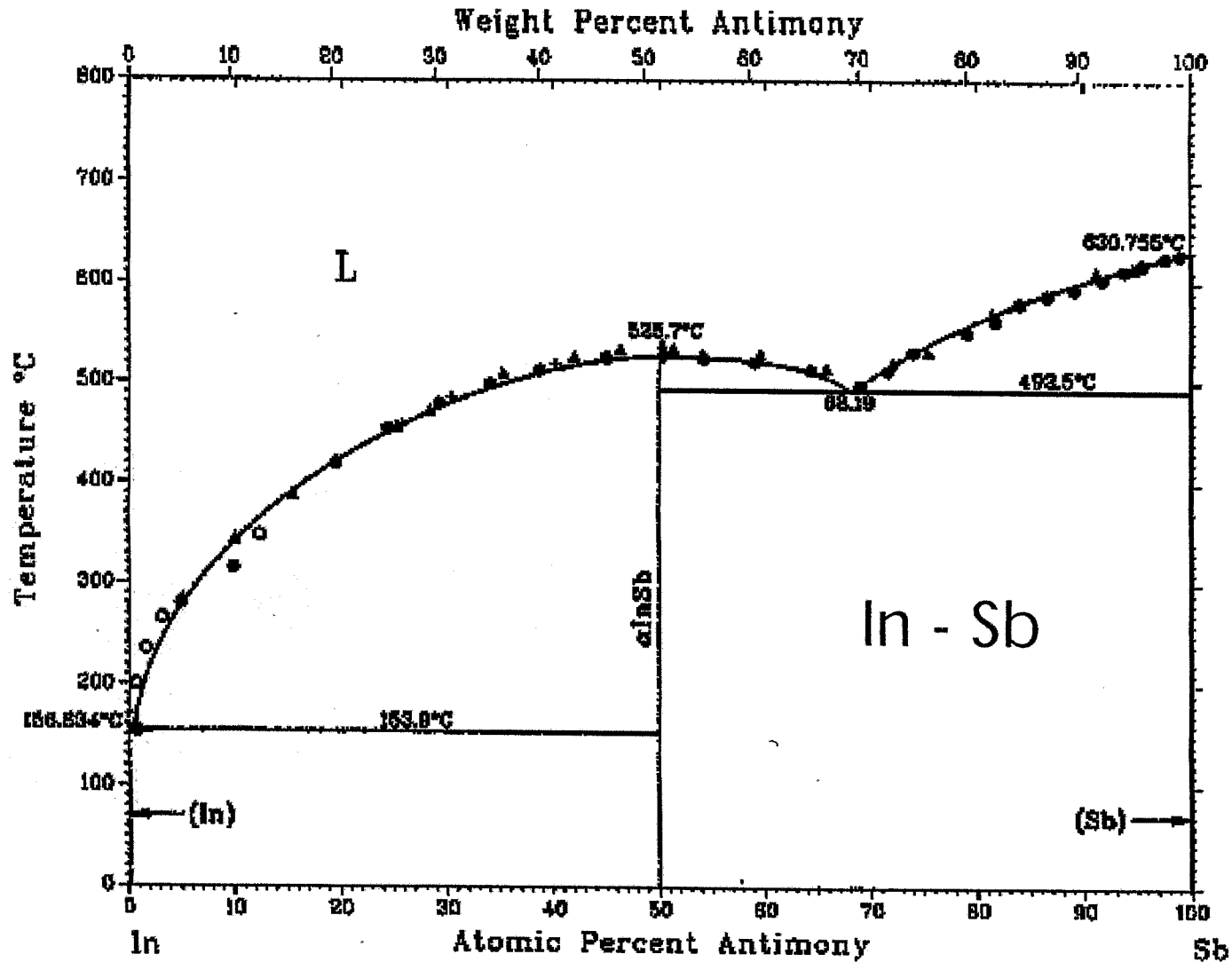
Al-4Cu

Same test cell for all 3 experiments; same thermal boundary conditions



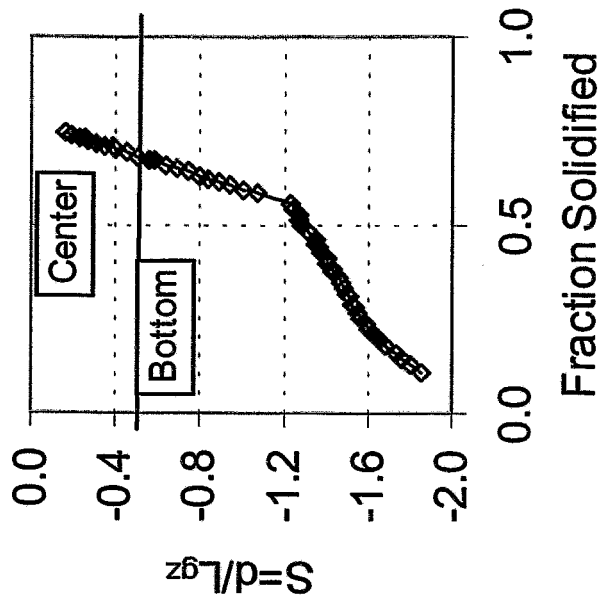
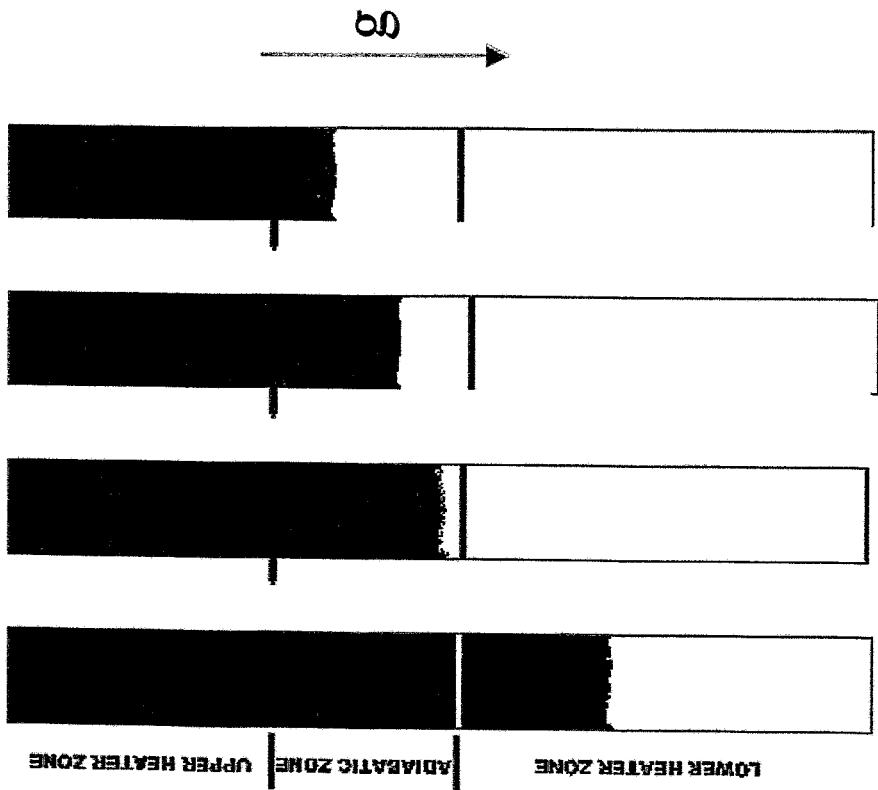
# Bridgman-Stockbarger Furnace - Variables







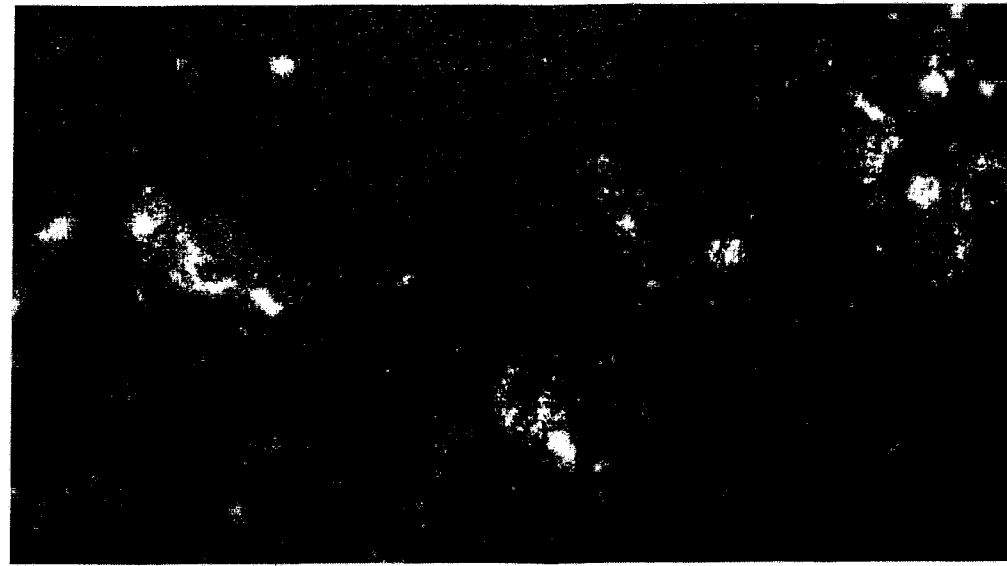
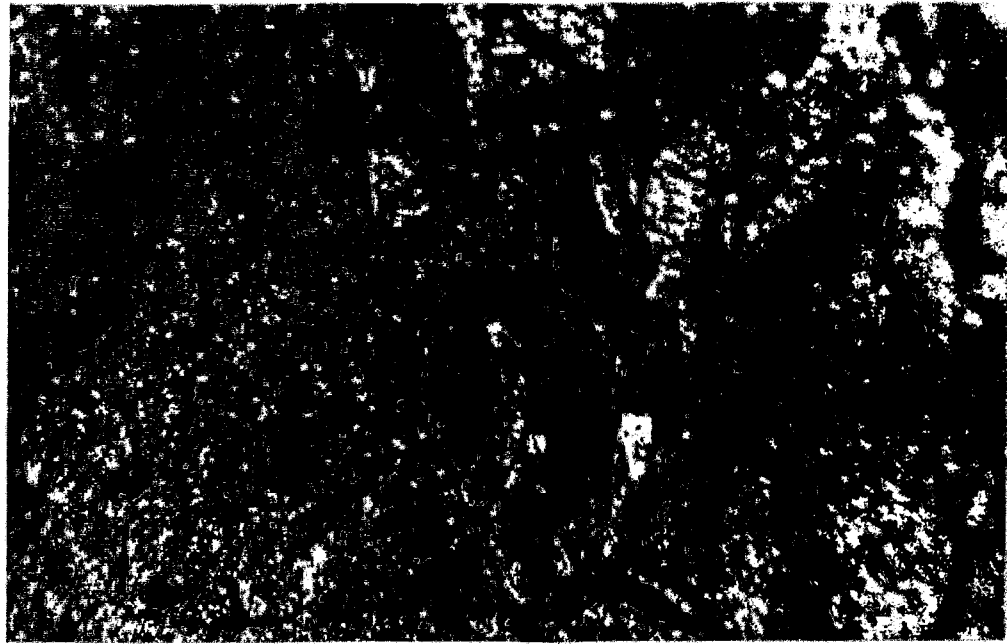
# Interface drops down into cold zone



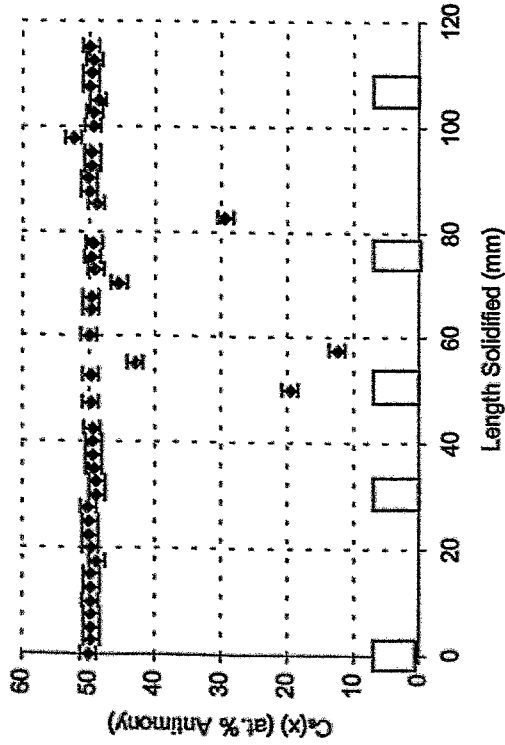


Solidification  
of  $\alpha$ InSb from  
Indium-rich  
(40 at.% Sb)  
solution

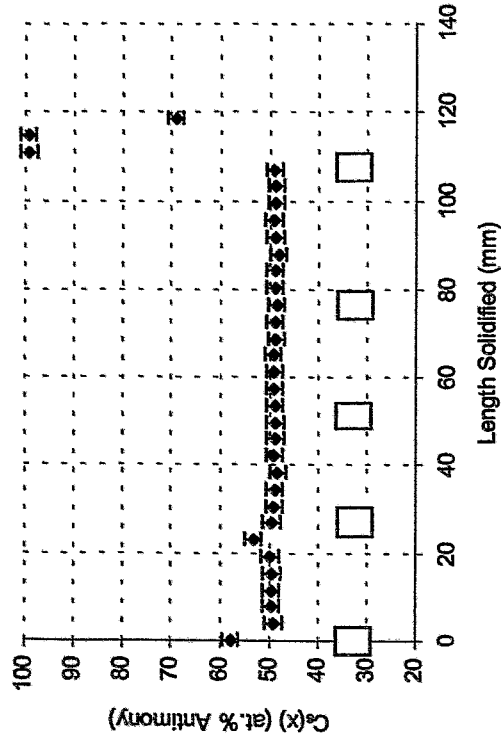
20X and 200X



# Concentration of Antimony in 2 InSb crystals grown from off-stoichiometric melts



In - 40 at.% Sb



In - 55 at.% Sb



## Consequences

Many numerical models do not simulate “simple” experiments: models need to be verified and validated.

Technologies need to be developed to avoid gravitational segregation of heavy elements in casting processes (turbine blade failure).

Cooling circuits have to be designed to prevent change in composition of coolant during operation (danger of clogging).

Compound crystal growth has to be done such that segregation in the melt does not impact stoichiometry of crystal (or, useless transistors and sensors).





## Conclusions

- Gravitational segregation in alloyed melts is observed to be more important than acceptable by current models
  - Macro-segregation in solid alloy, solidified after the horizontal Bridgman process, is a consequence of gravitational segregation in the melt phase.
- Melt may not readily form a fully dissolved liquid
  - Dissolution is slower than by diffusion alone, as particulates act as supercooled nucleation sites for higher melting elements or intermetallics.
  - Dissolution of elements may not be complete, or ideal.
- Physical Model of alloyed melt must be assessed
  - Current assumptions of ideal solutions may be more the academic exception than the production norm.
  - A thermodynamic non-equilibrium situation possible above liquidus.
- Numerical models for alloy melt solidification need to be revisited
  - Threshold conduction-convection because fluid is non-Boussinesq.



## X-Ray Research References

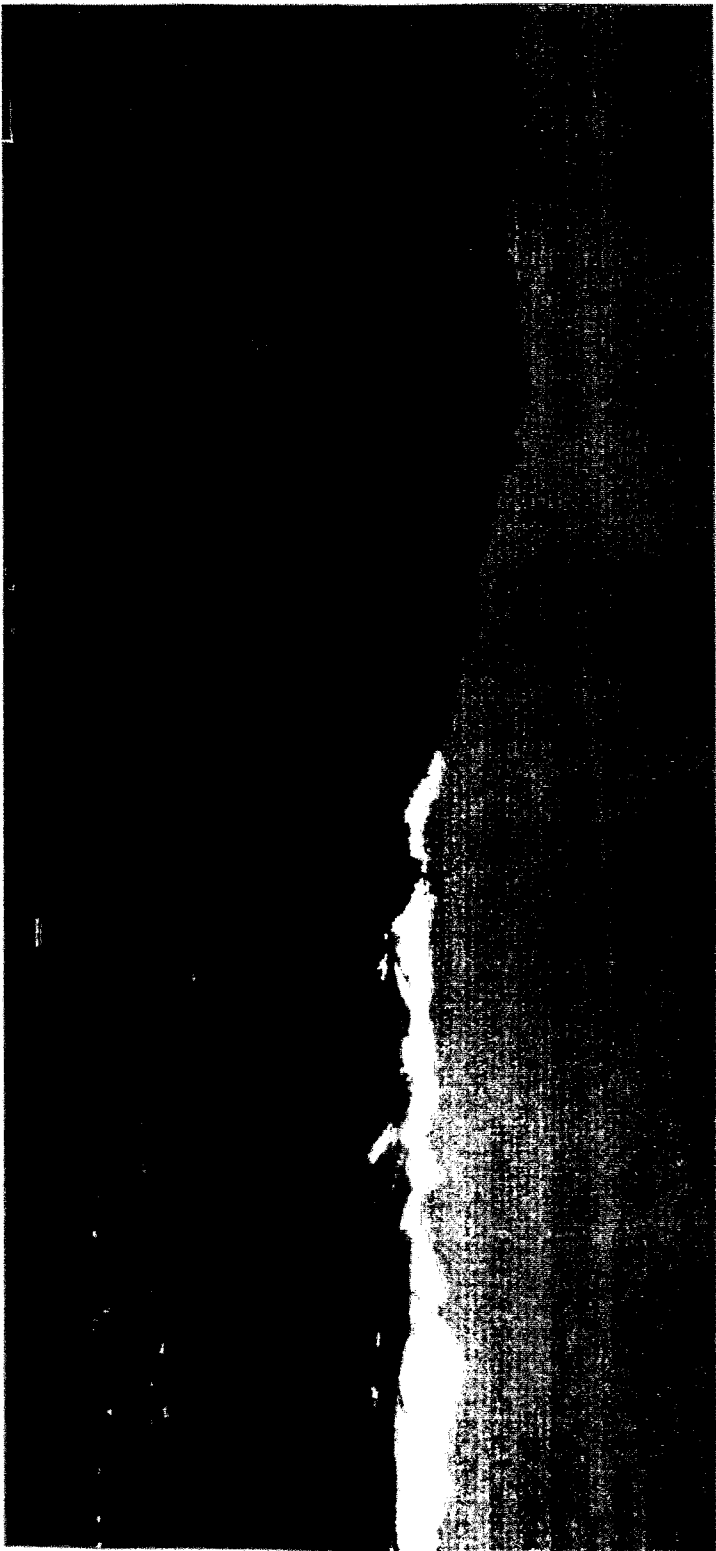
- Campbell, T.A., and Koster, J.N., "Visualization of Liquid/Solid Interface Morphologies in Gallium Subject to Natural Convection," *J. Crystal Growth*, **140**, 1994, 414-425.
- Pool, R.E., and Koster, J.N., "Visualization of Density Fields in Liquid Metals," *Int. J. Heat Mass Transfer*, **37**, 1994, 2583-2587.
- Campbell, T.A., and Koster, J.N., "Radioscopic Visualization of Indium Antimonide Growth by the Vertical Bridgman-Stockbarger Technique," *J. Crystal Growth*, **147**, 1995, 408-410.
- Campbell, T.A., and Koster, J.N., "A Novel Vertical Bridgman-Stockbarger Crystal Growth System with Visualization Capability", *Meas. Science and Technology*, **6**, 1995, 472-476.
- Derebail, R., and Koster, J.N., "Radioscopic Visualization of Isothermal Solidification of Eutectic Ga-In Alloy," *Met. Mat. Trans. B*, **27B**, 1996, 686-689.
- Derebail, R., and Koster, J.N., "Numerical Simulation of Natural Convection of Gallium in a Narrow Gap," *Int. J. Heat Mass Transfer*, **40** (5) 1997, 1169-1180.
- Koster, J.N., Derebail, R., and Grötzbach, "Visualization of Convective Solidification in a Vertical Layer of Eutectic Ga-In Melt," *Applied Physics A*, **64** (1), 1997, 45-54.
- Campbell, T., and Koster, J.N., "In-Situ Visualization of Constitutional Supercooling within a Bridgman-Stockbarger System." *J. Crystal Growth*, **171** (1-2), 1997, 1-11.
- Koster, J.N., "Visualizing convection and solidification in metallic alloys." *JOM*, March 1997, 31-35.
- Koster, J.N., "Visualization of Rayleigh-Bénard Convection in Liquid Metals." *Eur. J. Mech., B/Fluids*, **16** (3), 1997, 447-454.
- Koster, J.N., Seidel, T., Derebail, R., "A Radioscopic Technique to Study Convective Fluid Dynamics in Opaque Liquid Metals." *J. Fluid Mech.*, **343**, 1997, 29-41.
- Campbell, T.A., Koster, J.N., "In-situ Visualization of Off-Stoichiometric Equilibrium Crystal Growth within Indium Antimonide: Antimony-Rich Composition." *J. Cryst. Growth*, **174**, 1997, 238-244.
- Koster, J.N., Derebail, R., "A Threshold for Natural Convection in Binary Metallic Alloys," *Heat and Mass Transfer*, **32** (6), 1997, 489-498.
- Koster, J.N. "Experimental Study of Stability in a Layer of a Model Alloy with Liquid Miscibility Gap," *Heat Mass Transfer*, **33** (3), 1997, 193-199.
- Derebail, R. and Koster, J.N., "Visualization Study of Melting and Solidification in Convecting Hypoeutectic Ga-In Alloy," *Int. J. Heat Mass Transfer*, **41**(16), 1998, 2537-2548.
- Campbell, T.A., and Koster, J.N., "Compositional Effects on Solidification of Congruently Melting InSb," *Cryst. Res. & Technol.*, **33**(5), 1998, 707-716.
- Campbell, T.A., and Koster, J.N., "Interface Dynamics during Indium Antimonide Crystal Growth." *Cryst. Res & Technol.*, **33**(5), 1998, 717-732.
- Hongbin Yin and Koster, J.N., "In-situ observation of directional stratification and solid/liquid interface morphology during Ga-5%In alloy melt solidification," *J. Crystal Growth*, **205**(4), 1999, 590-606.
- Koster, J.N., "Directional solidification and melting of eutectic GaIn." *Cryst. Res. Technol.*, **34**(9), 1999, 1129-1140.



AEROSPACE ENGINEERING SCIENCES



# University of Colorado at Boulder



Koster

# The Effect of Oxygen Partial Pressure of Ambient Atmosphere on Mode and Velocity of Marangoni Convection in Molten Silicon Column

*T. Azami<sup>1</sup>, S. Nakamura<sup>1</sup>, T. Hibiya<sup>1</sup> and K. Mukai<sup>2</sup>*

*<sup>1</sup>Fundamental Research Laboratories, NEC Corporation,  
34 Miyukigaoka, Tsukuba 305-8501, Japan*

*<sup>2</sup>Department of Materials Science and Engineering, Kyushu Institute of Technology,  
1-1, Sensui-cho, Tobata-ku, Kita-Kyushu 804-8550, Japan*

Crystal growth of semiconductor silicon is controlled by a heat and mass transfer process at the crystal-melt interface. The Marangoni effect at the free surface is considered to play a significant role in this process. Moreover, Niu et al. reported that surface tension and its temperature coefficient of molten silicon are sensitive to oxygen partial pressure of ambient atmosphere [1]. However, there have been few reports on these subjects. The mode of temperature oscillation of a half-zone molten silicon column 5-mm high and 5-mm in diameter changed with increasing oxygen partial pressure of ambient atmosphere: oscillation with multiple frequencies (at  $P_{O_2} = 3.5 \times 10^{-7}$  MPa) changed to that with single frequency (at  $P_{O_2} = 1.8 \times 10^{-5}$  MPa). Also, velocity of the Marangoni flow, which was revealed by X-Ray radiography with a tracer particle under microgravity, decreased with increasing oxygen partial pressure. These experimental results can be explained by dependence of temperature coefficient of surface tension of molten silicon on oxygen partial pressure of ambient atmosphere: adsorbed oxygen atoms at the silicon melt surface significantly affect surface tension and its temperature coefficient.

[1] Z.-G. Niu, K. Mukai, Y. Shiraishi, T. Hibiya, K. Kakimoto, and M. Koyama, J. Jpn. Assoc. Crystal Growth, 24 (1997) 369.

This study was funded by a part of "Ground Research for Space Utilization" promoted by NASDA and Japan Space Forum.

# The Effect of Oxygen Partial Pressure of Ambient Atmosphere on Mode and Velocity of Marangoni Convection in Molten Silicon Column

T. Azami<sup>1</sup>, S. Nakamura<sup>1</sup>, T. Hibiya<sup>1</sup> and K. Mukai<sup>2</sup>

NEC Corporation,

<sup>2</sup>Kyushu Institute of Technology,

..... Oct 11, 1999, Dresden

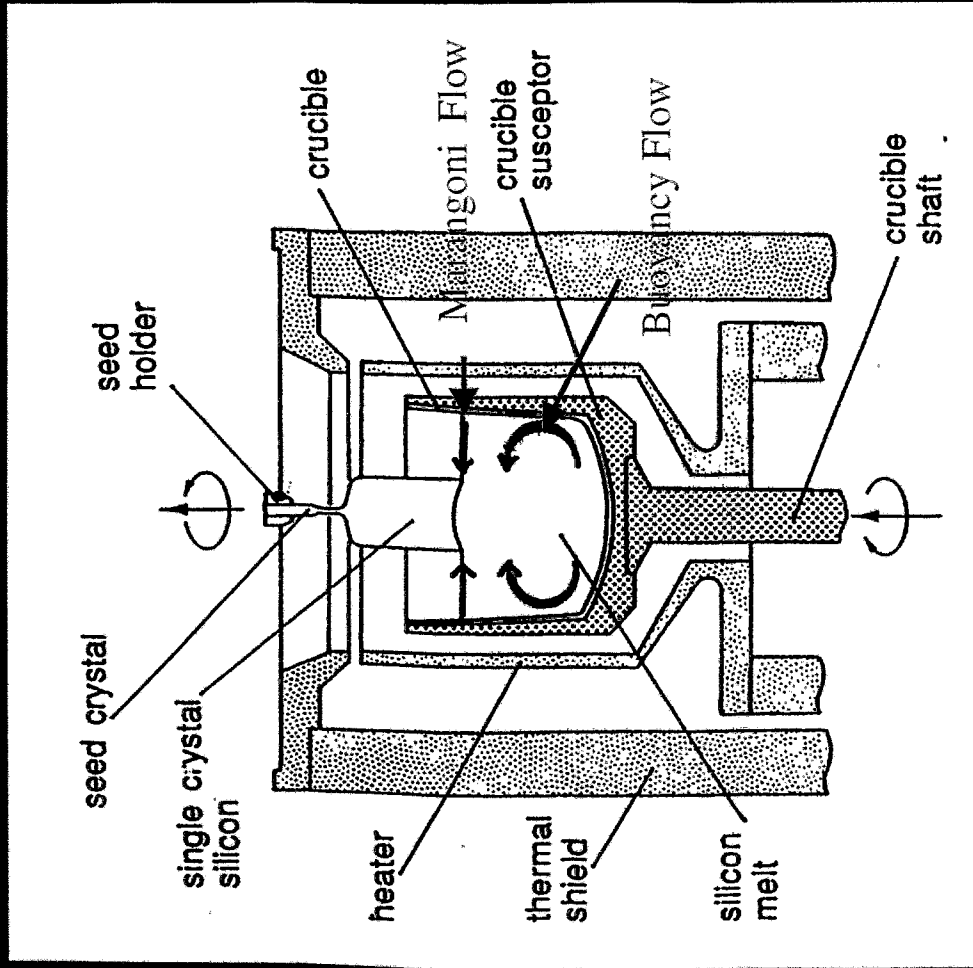
# Contents

- Motivation
- Marangoni Flow of Liquid Column
- Structure of Instability
- Flow Mode Transition
- Effect of Oxygen Partial Pressure
- Surface Oscillation
- Perspective

# Crystal Growth of Silicon

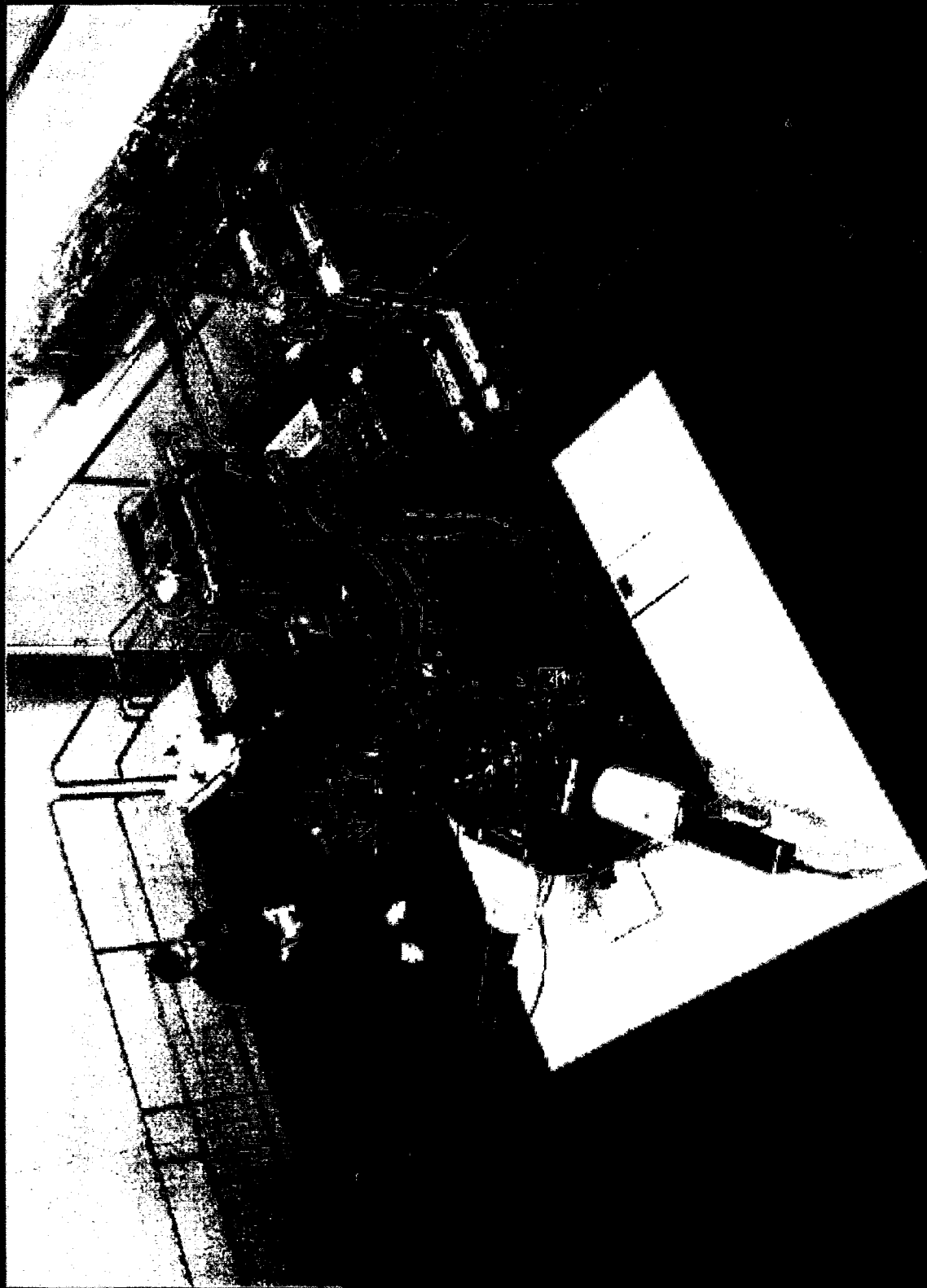
Controlled by a heat and mass transfer.

- Buoyancy Convection
- Marangoni Convection
- Diffusion

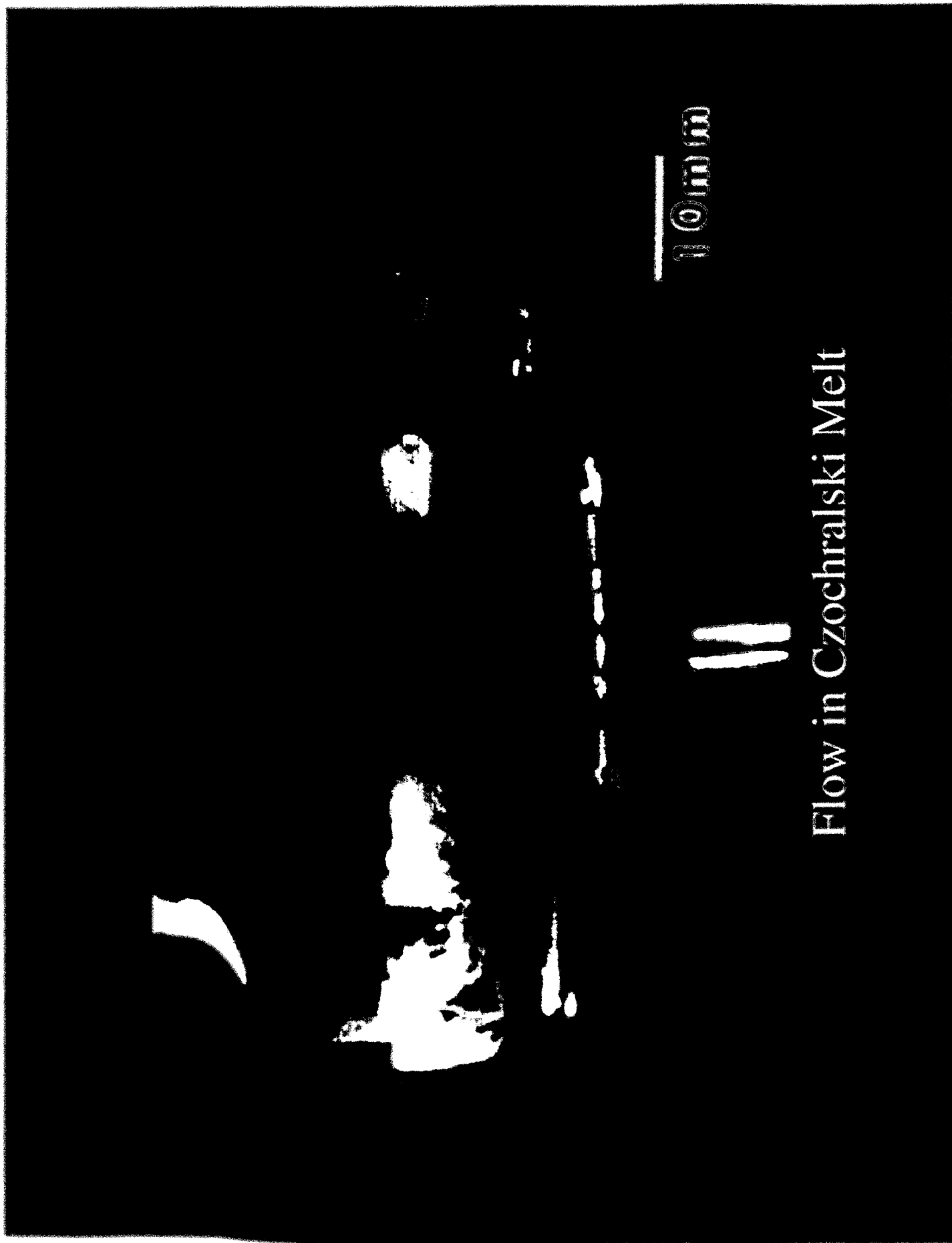


Heat and Mass Transfer in Crystal Growth





Czochralski Furnace with X-ray Visualization System



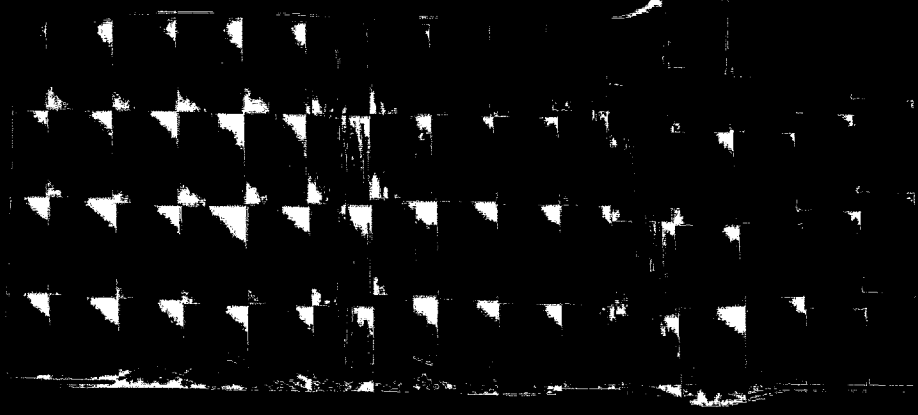
10000

11

## Flow in Czochralski Melt

## Marangoni Flow

- Reported by Nitsche et al (Freiburg)
- Striation induced even in Microgravity
- $Ma_{c_2} = 100 - 200$
- 3D-Stationary Flow:  $Ma_{c_1} < Ma < Ma_{c_2}$



5mm

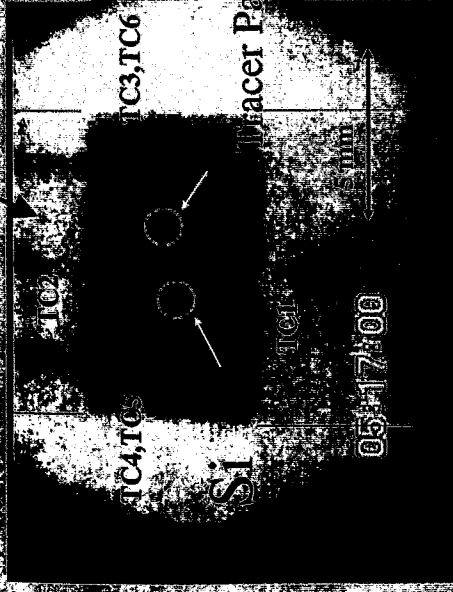
Growth striation induced in . -Gravity. after Cröll

## WHAT SHOULD WE OBSERVE?

- FLOW FIELD
- TEMPERATURE FIELD
- SURFACE OSCILLATION
- CRYSTAL GROWTH
- SIMULATION
- SURFACE TENSION

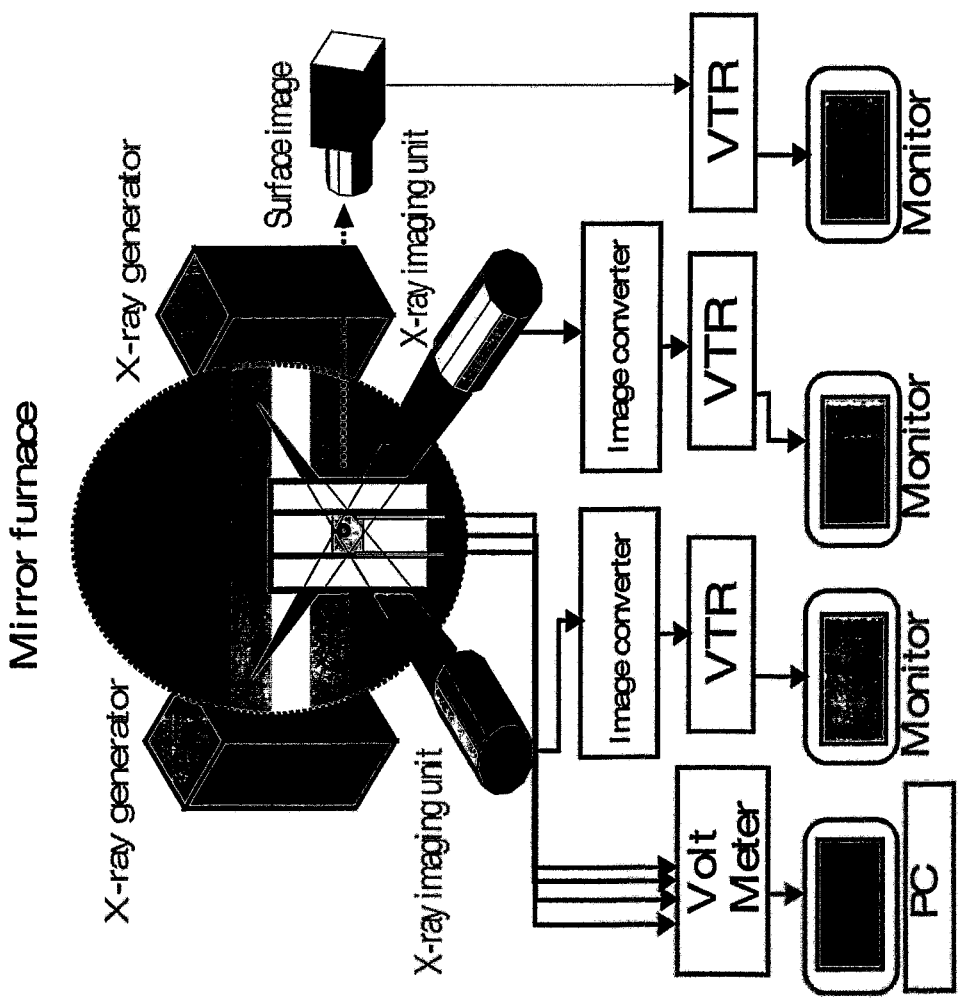


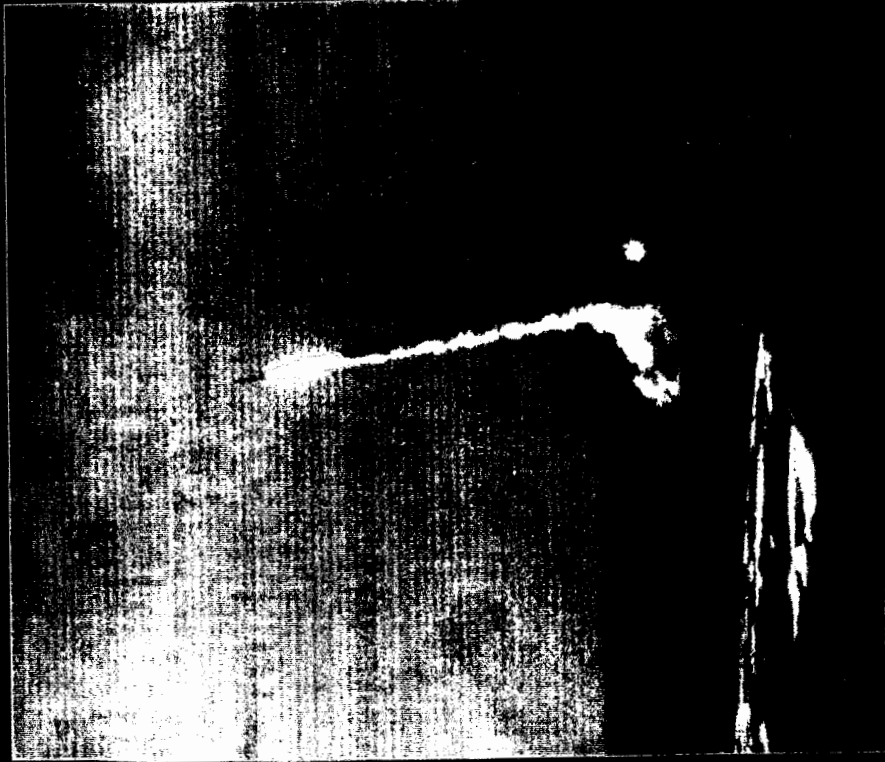
Carbon rod



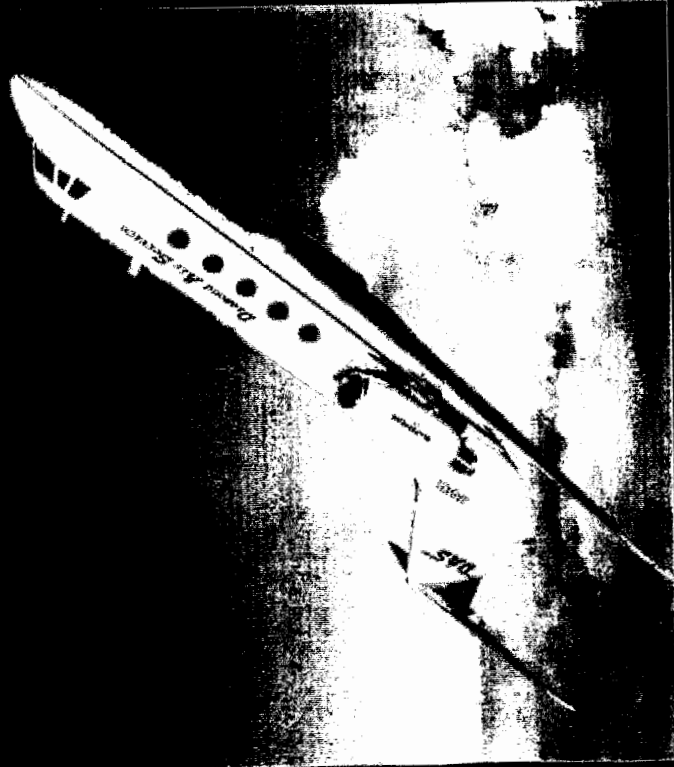
10 mm

Ampoule Configuration





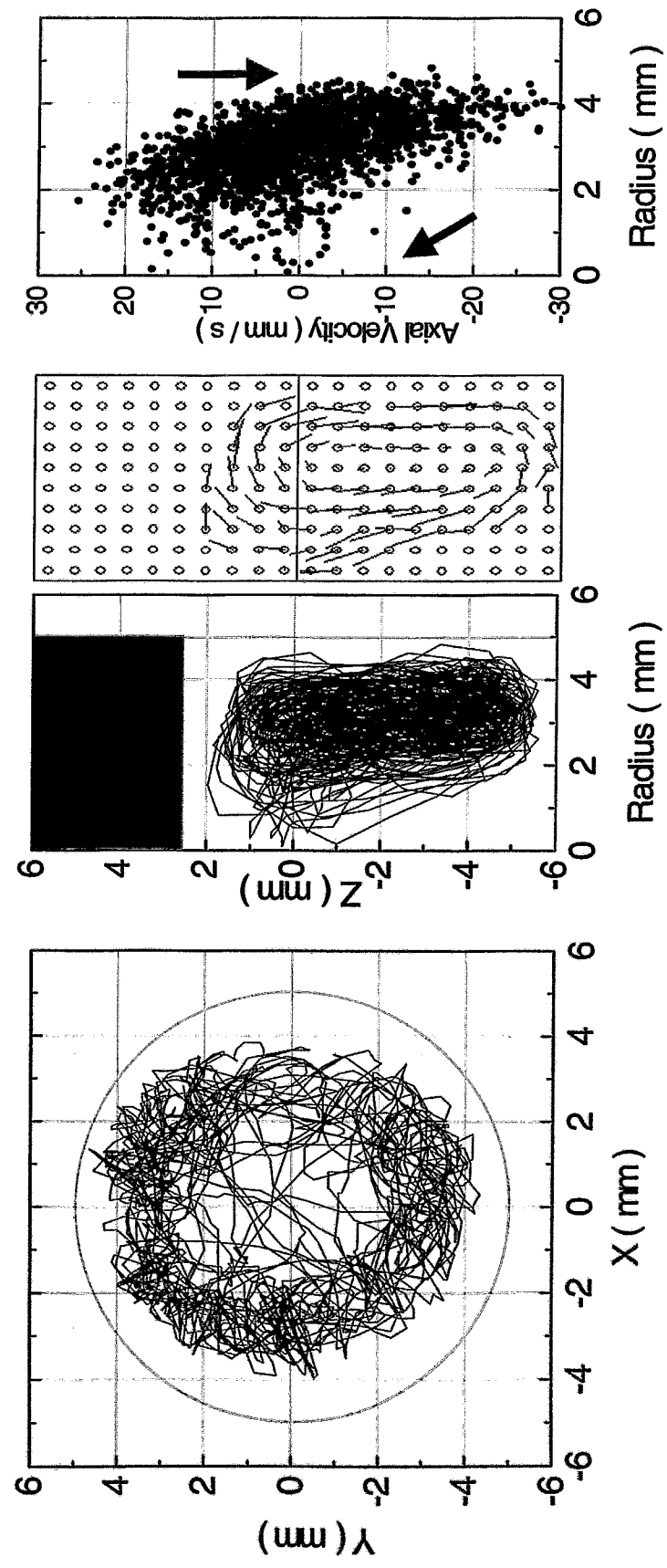
NASDA TR-IA-6



Gulf Stream II

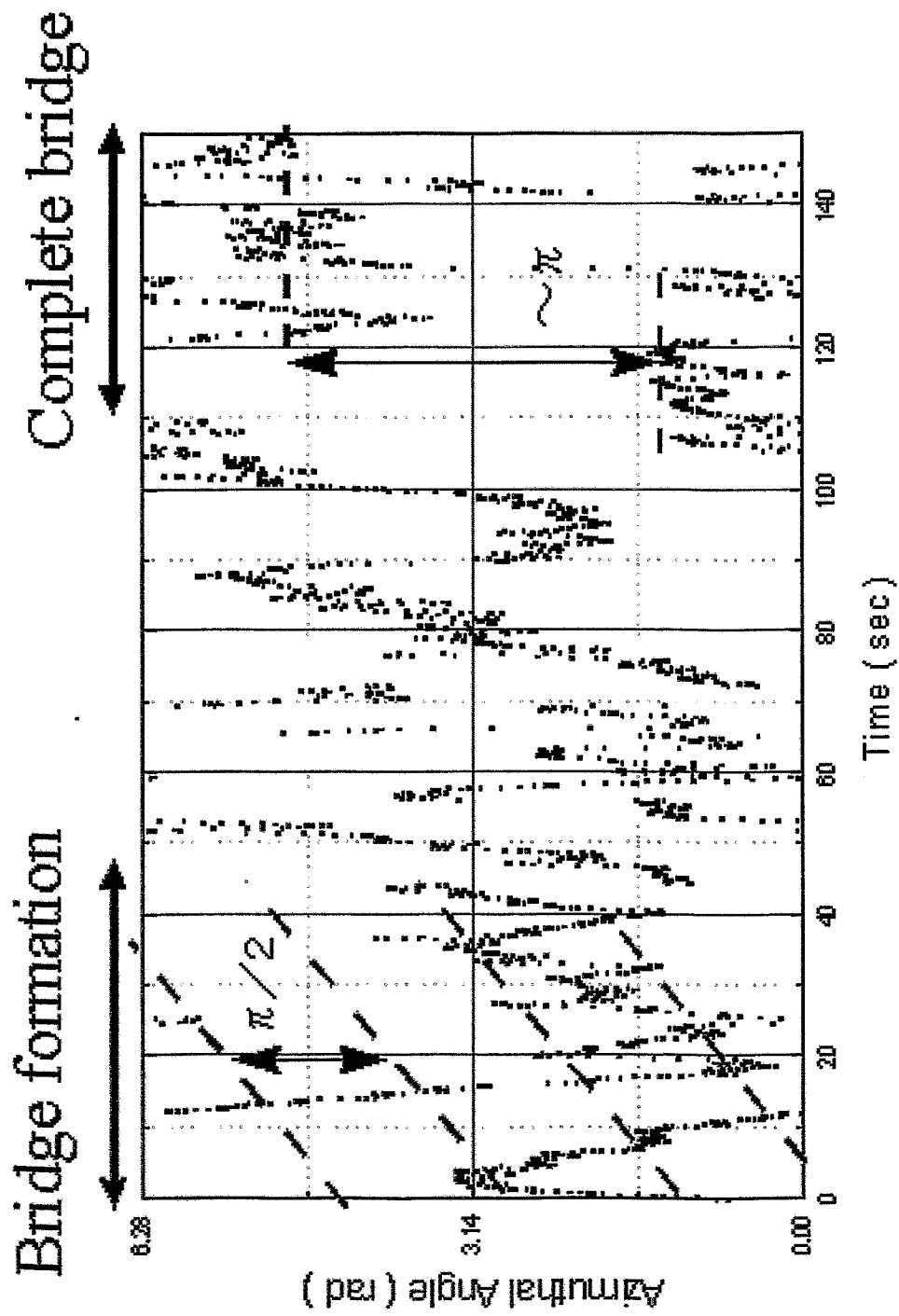


Flow structure for  $\sim 1.7$  (Complete bridge,  $Ma = 14900$ )



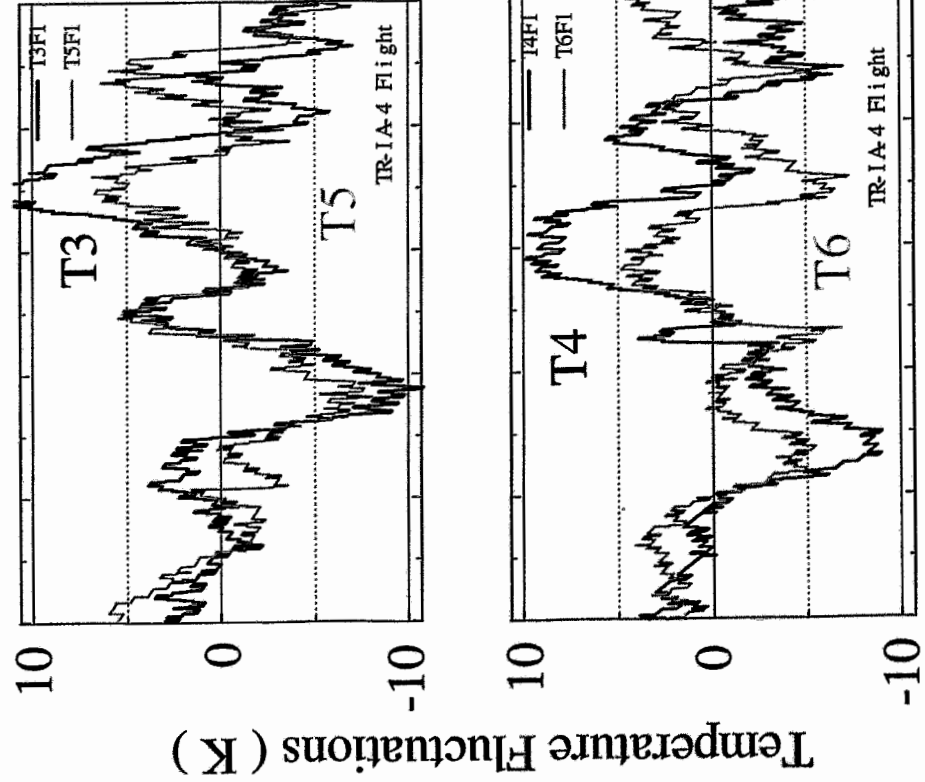
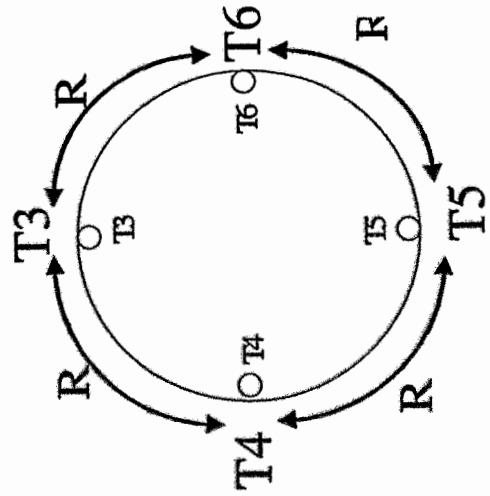
Particle Path and Flow Velocity

# Preferential Position of Tracer Particles



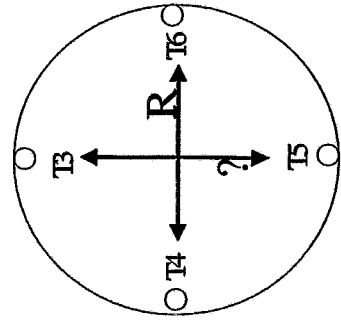
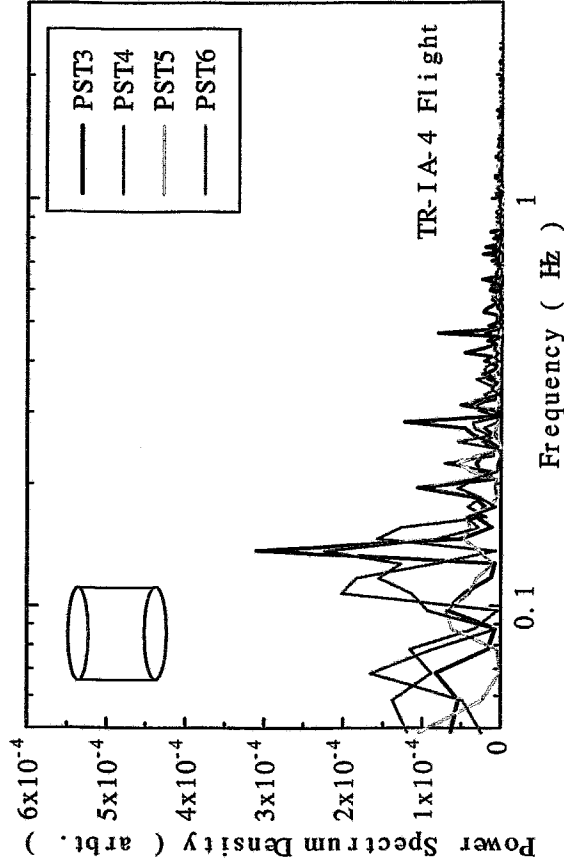
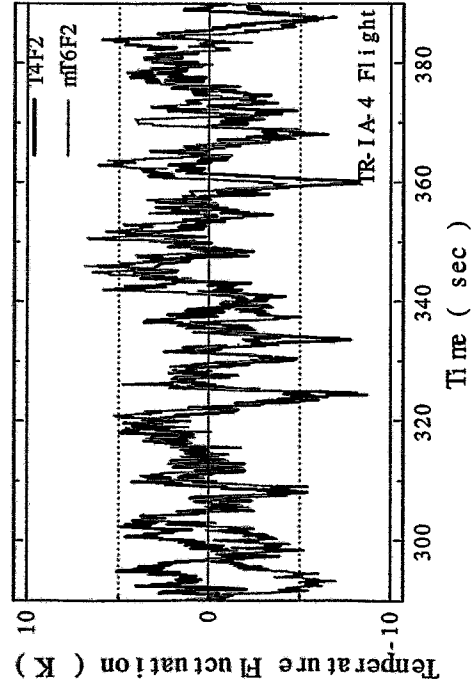
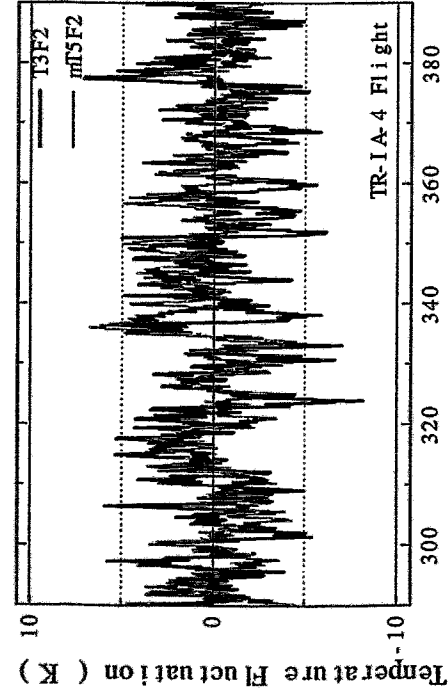
# Temperature oscillation during bridge formation (micro gravity condition)

Temperature oscillation frequency:  
 . . . . .  
 Antiphase correlation :  
 between 90 degree azimuthal angle.



180 200 220  
Time ( s )

# Temperature fluctuation in a complete bridge (microgravity condition, cylindrical)



Frequency characteristic  
0.15Hz

Antiphase correlation

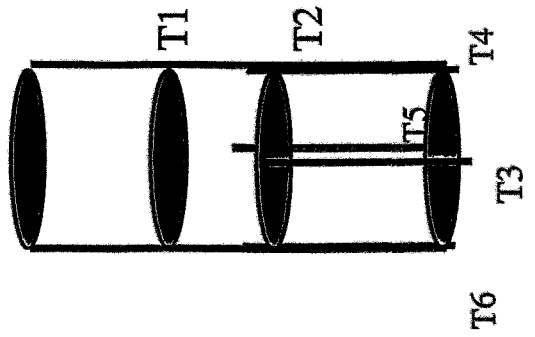
... ?  
... ?

# Inner temperature distribution in a cross section of bridge

Wave number vs.

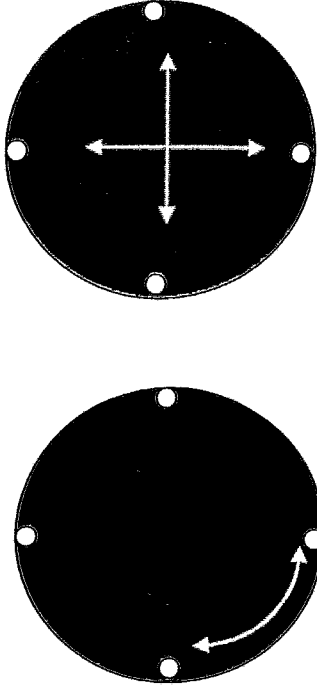
Aspect ratio

???



Bridge formation

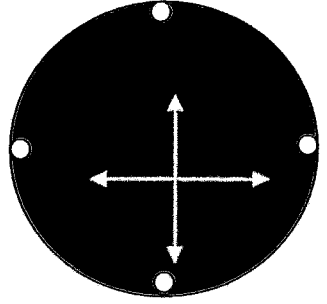
...  
...



Rotating . Pulsating

Complete bridge

...  
...



Translating

height / radius

# Marangoni Number

$$Ma = \frac{|\gamma_T| \Delta T L}{\mu \kappa}$$

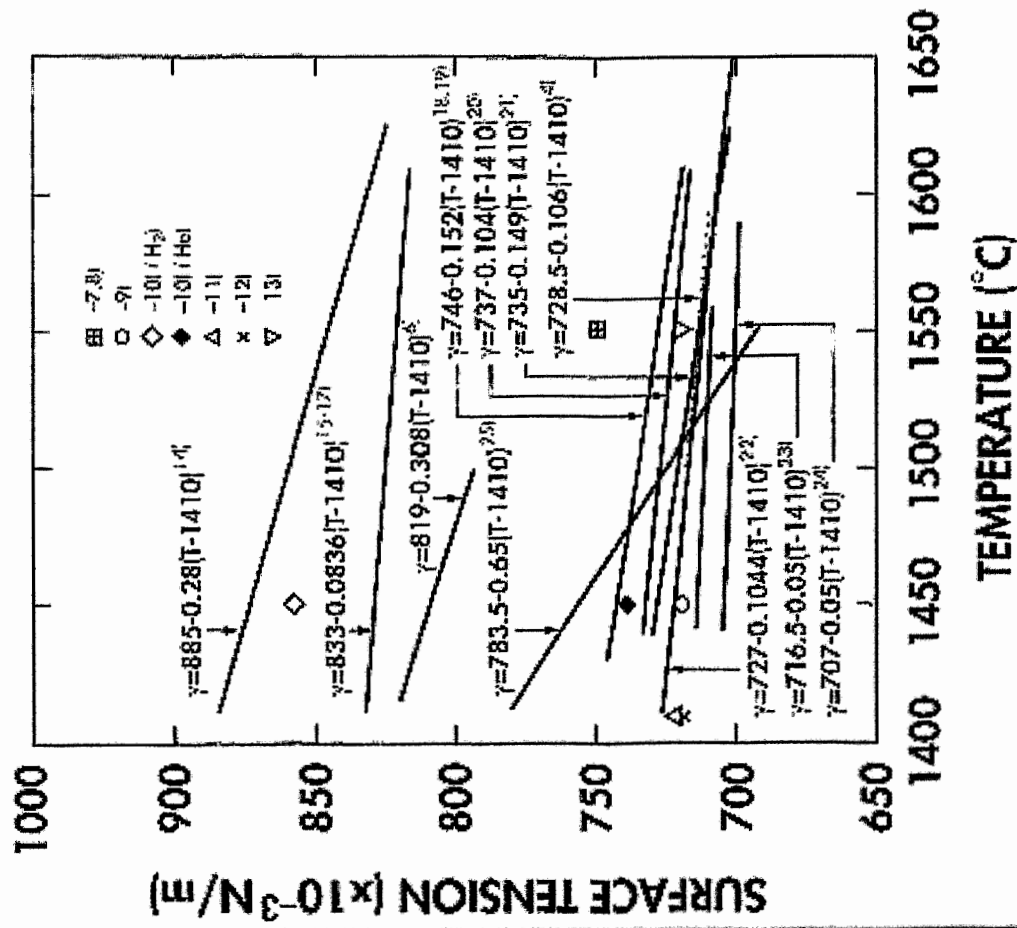
$|\gamma_T|$ : Temperature coefficient of surface tension

$\Delta T$ : Temperature difference

$L$ : Characteristic length

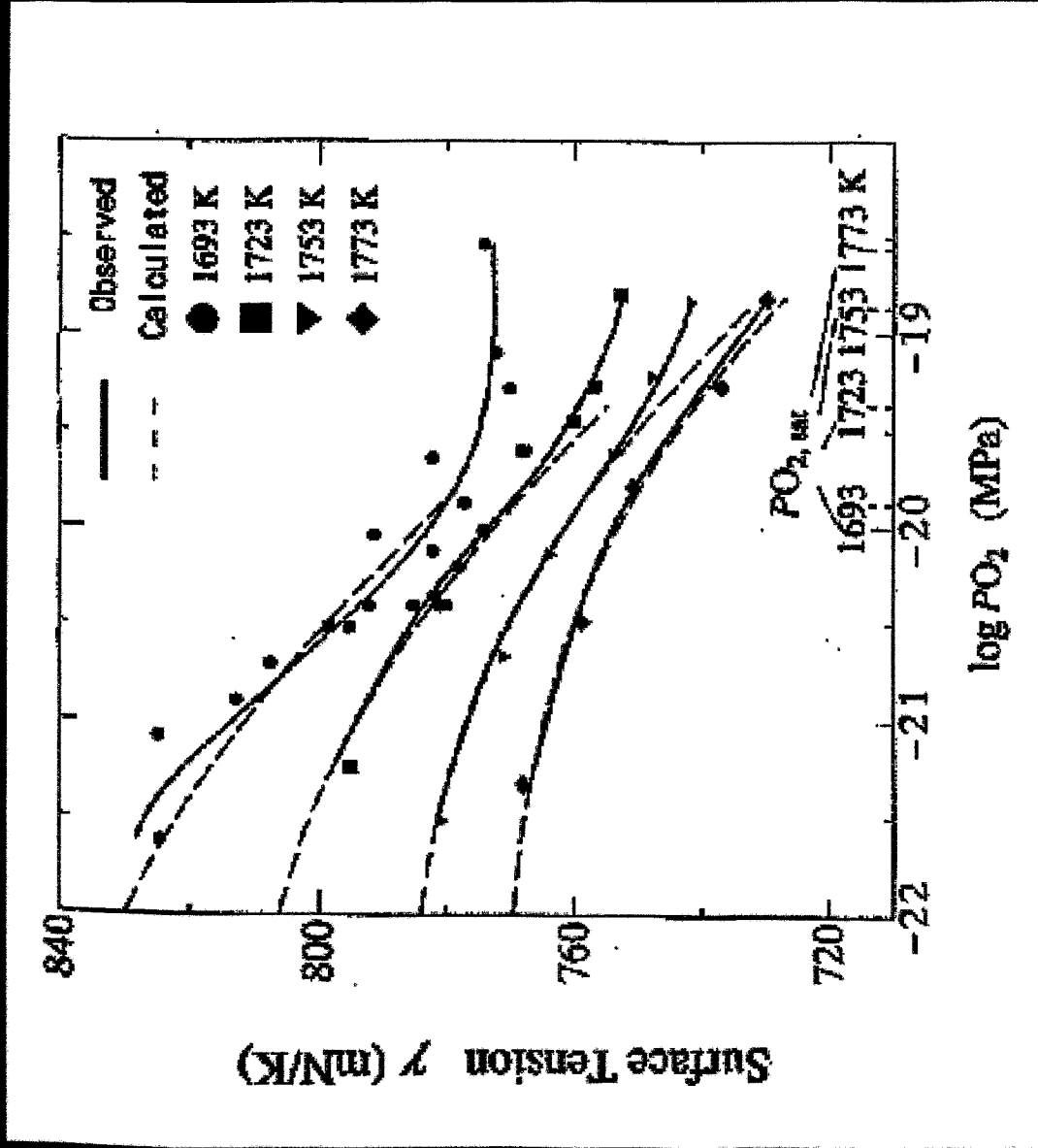
$\mu$ : Viscosity

$\kappa$ : Thermal diffusivity



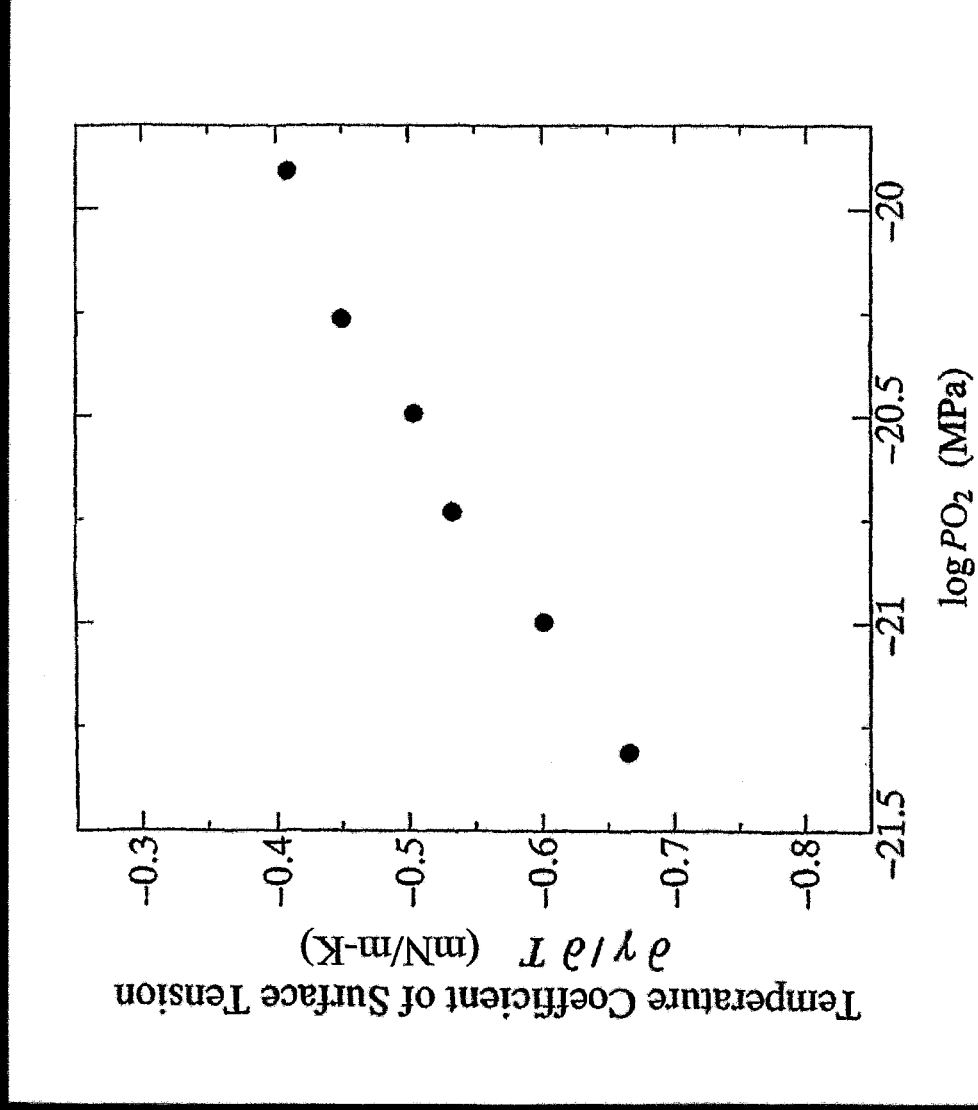
## Surface Tension of Molten Silicon

after Keene

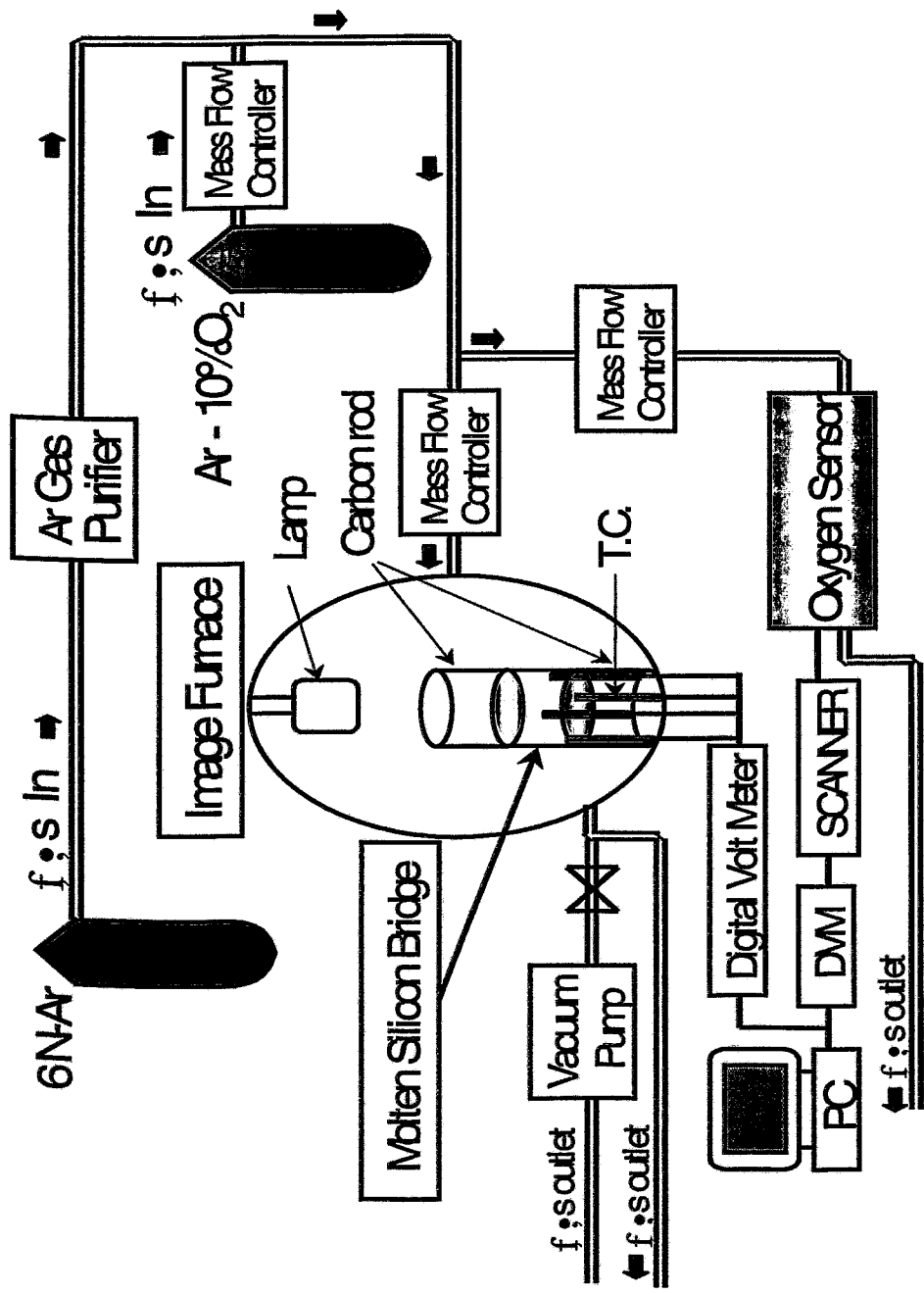


Surface Tension of Molten Si as a function of  $PO_2$

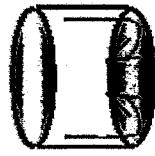




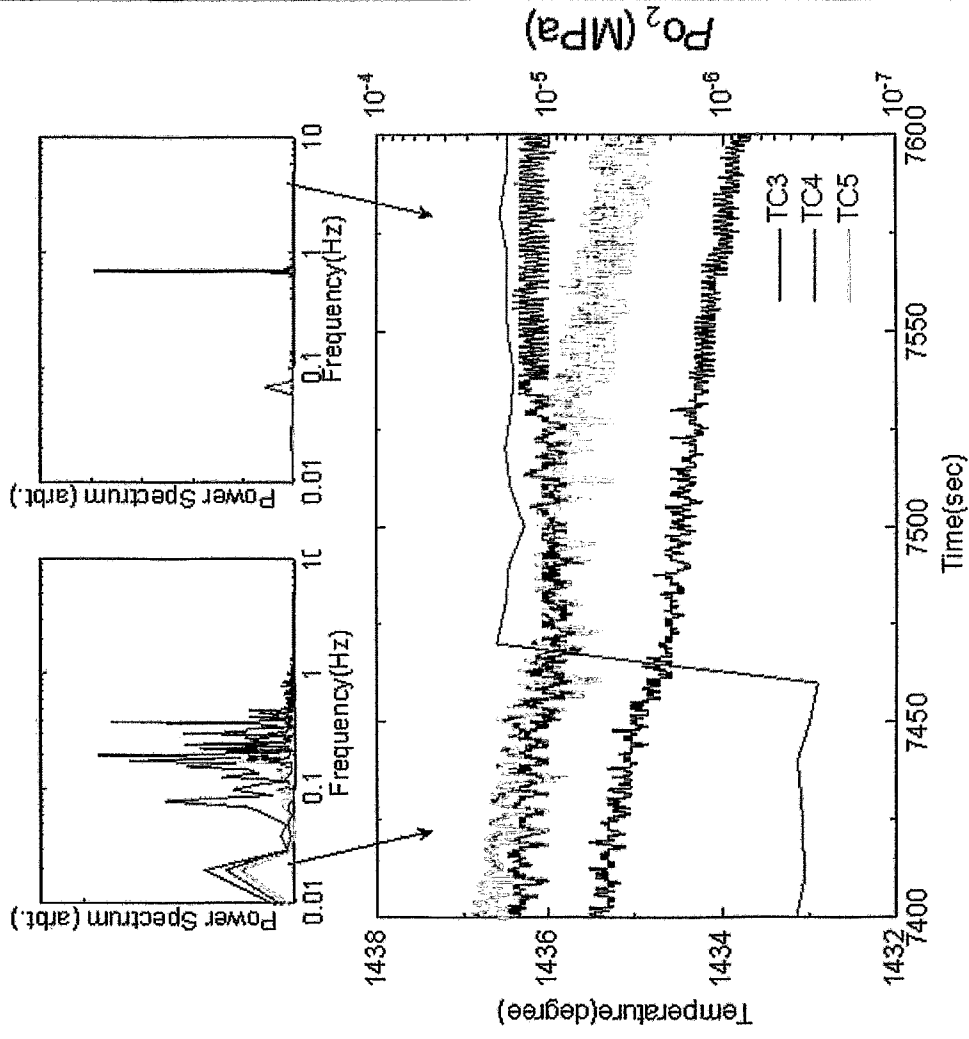
Temperature coefficient of Surface Tension  
of Silicon Melt



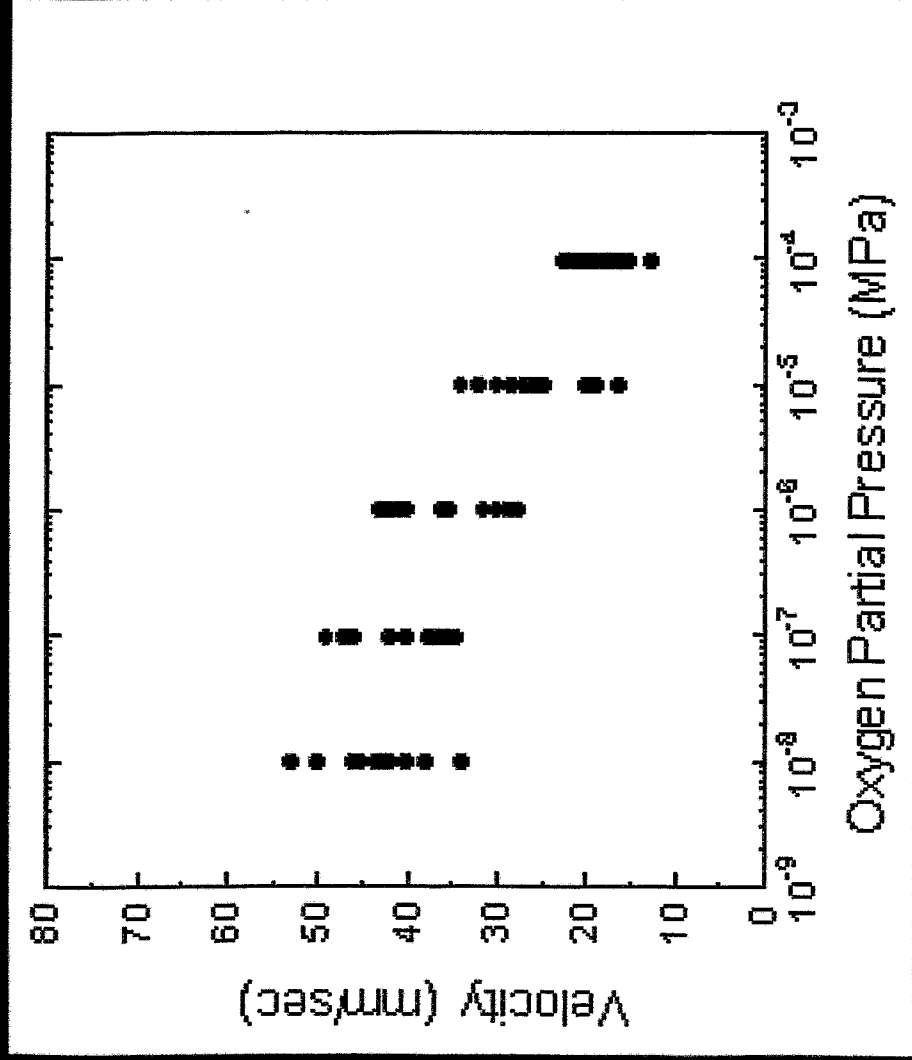
Aspect Ratio 1.0



$\Delta T = 52K$



# Effect of $Po_2$ on Temperature Oscillation



## Oxygen Partial Pressure Dependence of Tracer Velocity

## High precision resistance measurements in directional solidification

*C. Salvi, J.P. Garandet, A. Borgis and E. Rolland*

*Commissariat à l'Energie Atomique*

*DTA/CEREM/DEM/SPCM/LSP*

*CEA - Grenoble, 17 rue des Martyrs, F - 38054 Grenoble Cedex 9*

The interest of using *in situ* diagnostics to monitor directional solidification processes has long been recognized, *e.g.* by space agencies. In this communication, we shall present a novel differential resistance measurement technique that allows to track the position of the solid/liquid interface with an accuracy in the micrometer range in metallic alloys. By comparing prescribed and actual growth velocities, the thermal lag-time of the furnace can be characterized. More precisely, we were able to identify the transfer function of the furnace with a low pass filter. Another possible field of research is the detection of convective instabilities. The technique is also expected to be applicable to the case of semiconducting alloys.

***HIGH PRECISION RESISTANCE MEASUREMENTS IN  
DIRECTIONAL SOLIDIFICATION***

***C. Salvi, J.P. Garandet, A. Borgis and E. Rolland***

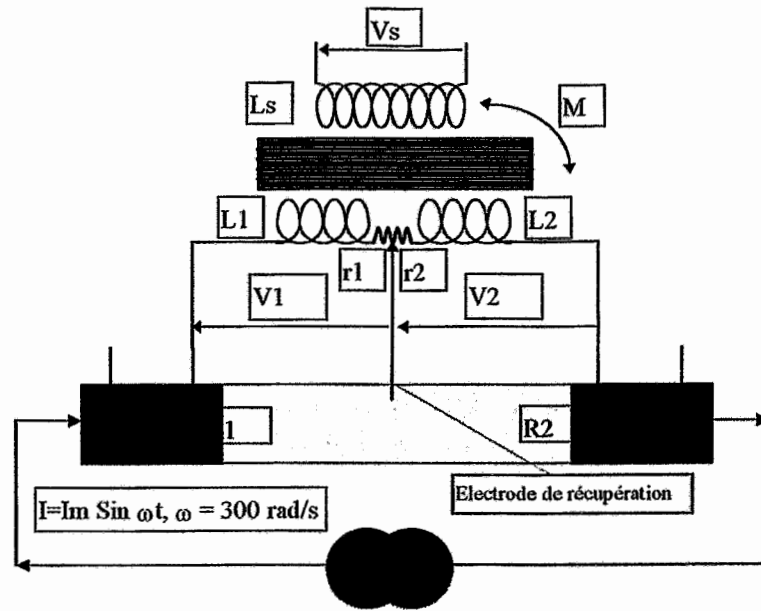
***CEREM, CEA - Grenoble, with support from CNES***

## ***SOLIDIFICATION DIAGNOSTICS***

- ♣ **Diagnostics allow a better control and an increase of scientific return, specially for microgravity experiments. Important feature for Space Station experimentation.**
- ♣ **Twenty years of experience in our laboratory in the field of electrical (resistance) and thermoelectrical (Seebeck) diagnostics : Mephisto program.**

## DIFFERENTIAL RESISTANCE MEASUREMENTS

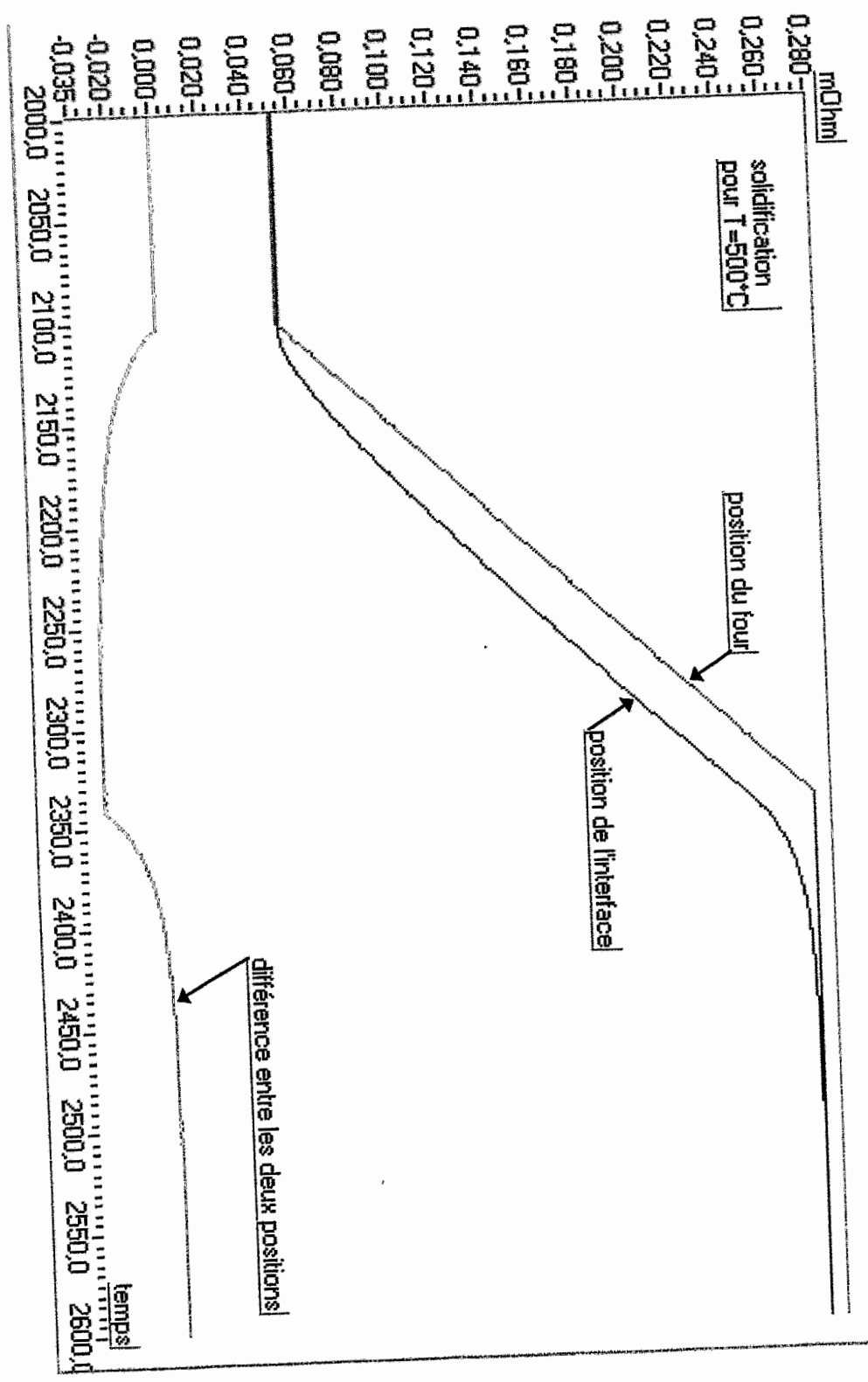
- ♣ Frame : Mephisto space program, double gradient configuration

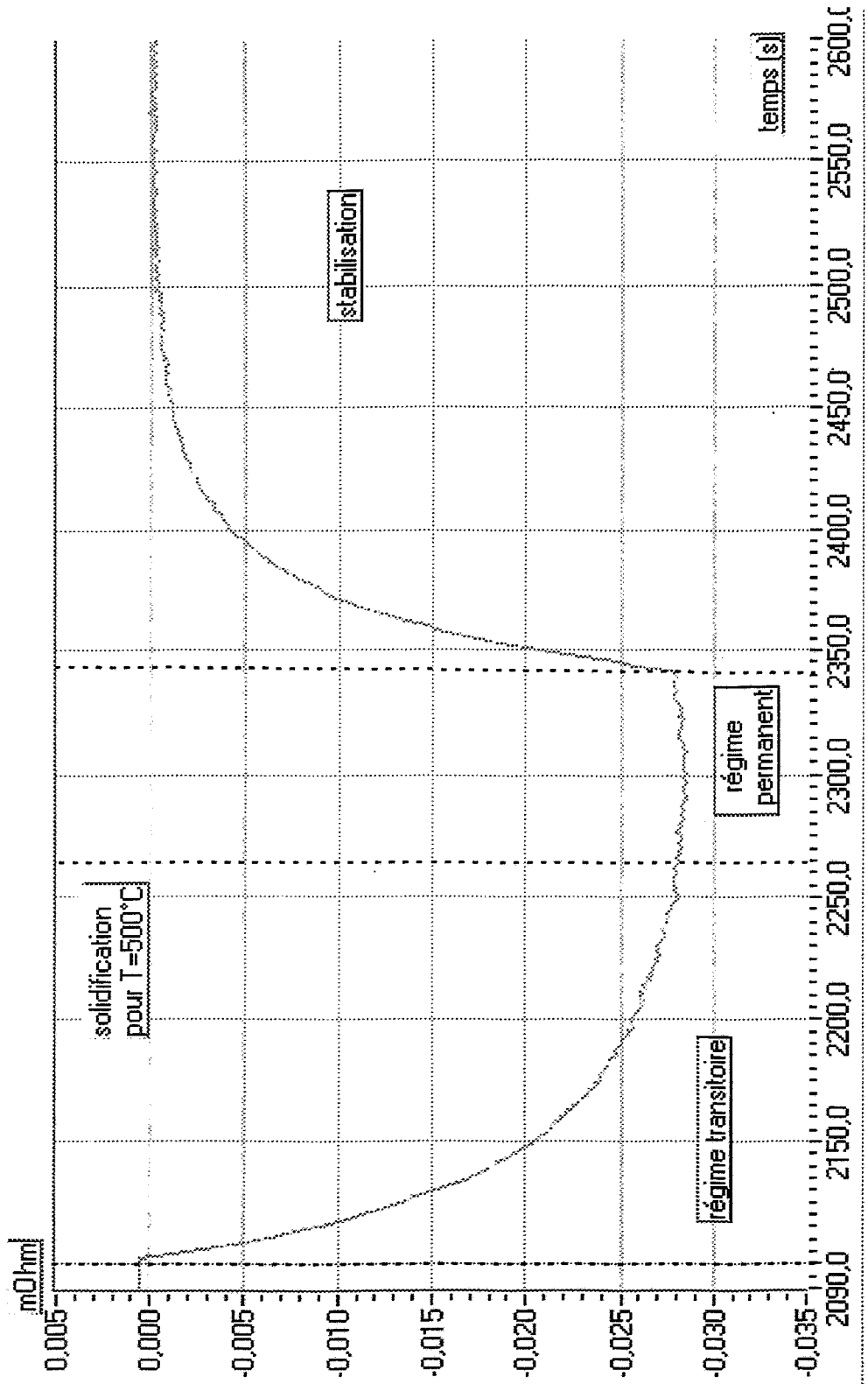


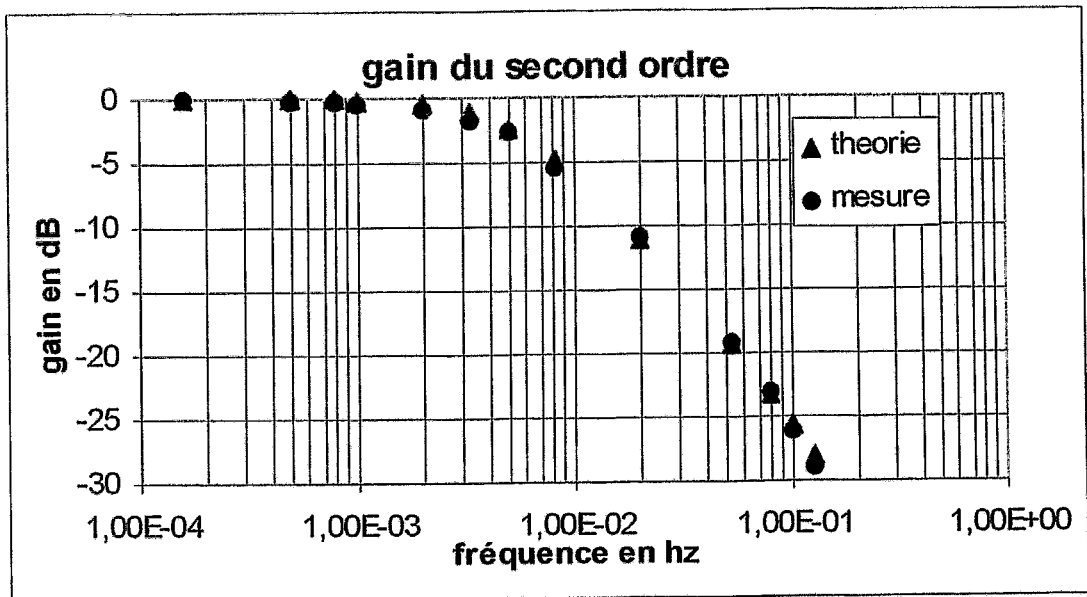


## ***EXPERIMENTAL PROCEDURE***

- ♣ **Objective : characterisation of interface kinetics and furnace thermal behaviour in initial solidification transients.**
  
- ♣ **Materials investigated : pure tin and tin based alloys ( $\Delta R = 1 \mu\Omega \approx \Delta L = 20 \mu\text{m}$ ).**
  
- ♣ **Sudden variations of pulling velocity (indicial response) : exponential like behaviour, identification of base frequency.**
  
- ♣ **Harmonic variations of pulling velocity : identification of higher order frequencies.**







$$H = \frac{1}{1 + j\omega\tau_1} \times \frac{1}{1 + j\omega\tau_2}$$

$$\tau_1 = 27s, \tau_2 = 0.8s$$

## ***TENTATIVE INTERPRETATION***

- ♣ Heat transfer kinetics may be limited either by propagation of temperature disturbance or heat flux extraction.
- ♣ Propagation kinetics :  $\tau \sim L^2 / \alpha$ ,  $L$  characteristic length,  $\alpha$  thermal diffusivity. In all cases, radial transfers are expected to be very fast, but longitudinal transfers may be much larger.
- ♣ Extraction kinetics :  $\tau \sim \Delta Q / \phi$ ,  $\Delta Q$  amount of heat to be extracted,  $\phi$  heat flux. Choice of phenomenological expression for  $\phi$  may be difficult.
- ♣ In directional solidification of alloys, the construction of the solutal boundary layer ahead of the growth front may also interfere with interface kinetics.

## ***CONCLUSIONS AND PERSPECTIVES***

- ♣ **Accurate resistance measurements allow to characterise the position, velocity, and acceleration of a directional solidification interface.**
- ♣ **Adaptation to classical single gradient furnaces (cartridge configuration) is being carried out with ESA support.**
- ♣ **Application to other directional solidification problems, such as microstructure formation, is under investigation.**

**Seebeck effect  
as an in-situ detection technique  
in solidification  
of metallic alloys.**

**A review.**

**B. Drevet\*, P. Lehmann\*\***

\*Commissariat à l'Energie Atomique DTA/CEREM/DEM/SPCM/LSP  
CEA - Grenoble, 17 rue des Martyrs, F - 38054 Grenoble Cedex 9, France

\*\* Lab EPM-MADYLAM, ENSHMG, BP 95 38402 St Martin d'Hères,  
France

# Seebeck effect as an in-situ detection technique in solidification of metallic alloys

*B. Drevet and P. Lehmann*

*EPM MADYLAM, ENSHMG, BP 95, 38402 St Martin d'Herès Cedex, France*

During the solidification of a metallic alloy, the interface between the solid and the liquid can be looked upon as a thermocouple junction, provided that the two phases show a difference of thermoelectric power. Several experimental devices (Mephisto, Ramses, Efaistos) have been realised to measure the voltage generated by the interface. Experiments have been performed both on earth and under microgravity conditions (i.e. with and without convection), with different solidification regimes such as planar, cellular, dendritic or eutectic front.

When the interface is planar, the measured signal is directly proportional to the temperature interface. However, when the interface is no longer isothermal (e.g. dendritic) or when the alloy is multiphase (e.g. eutectic), a local current density appears due to the coupling between thermoelectric effects and temperature gradient. This voltage drop must also be taken into account, and more information about the interface morphology can be obtained.

We propose to give here a review about the information (undercooling, segregation, microstructure transition...) that can be expected from this kind of measurements in most solidification conditions. Practical aspects and technical problems will also be discussed.

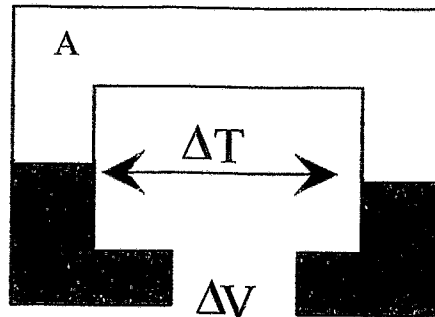


# Contents

- 1 – Principle of Seebeck measurements.
- 2 – “Isothermal interfaces” : crystal growth and eutectic solidification.
- 3 – Transitions : planar/cellular, planar/eutectic.
- 4 – Dendritic growth. Freckles and segregations.
- 5 – What configurations can Seebeck measurements be applied to? Technical constraints.
- 6 – Conclusions

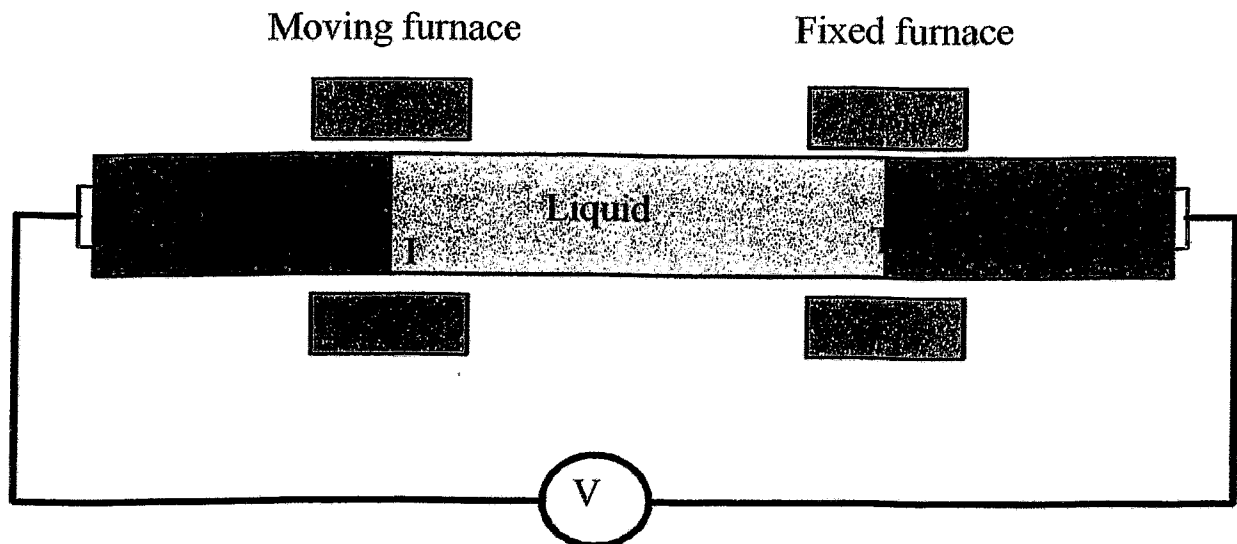
# Principle

From the thermocouple...



$$\Delta V = (\eta_A - \eta_B) \Delta T$$

...to solidification.



$$\Delta V = (\eta_s - \eta_l) (T_I - T_{\text{éq}})$$

Interest : measurements can be made several times on the same sample.

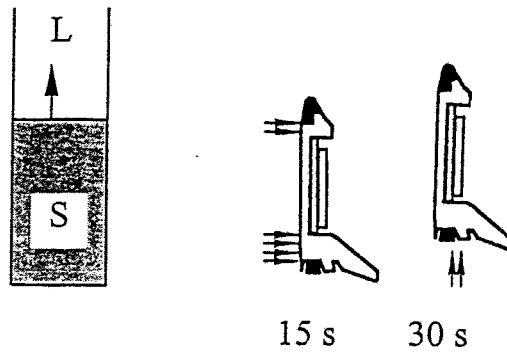
## Crystal growth / Isothermal interface

$$\Delta V = (\eta_s - \eta_l)(T_I - T_{\text{éq}})$$

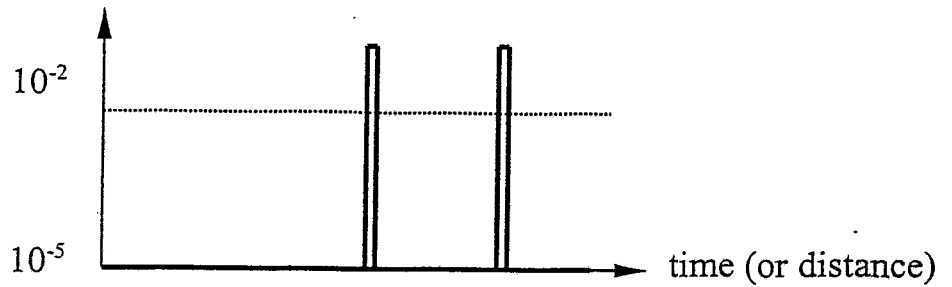
The measured voltage is proportional to the concentration.

*Measurement of striations due to convection. (SnBi 0.5 %at) (Rouzaud et al, 1993)*

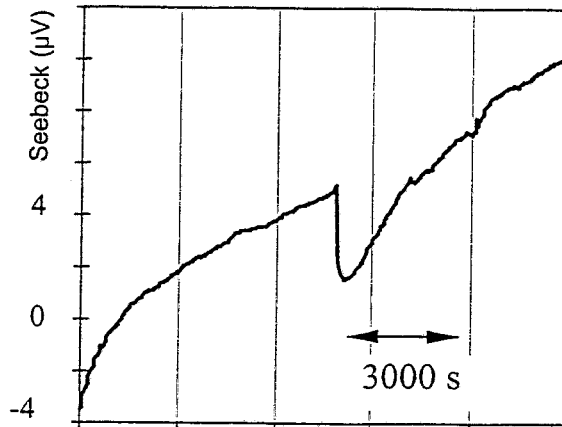
Effects of g-jitters on segregation (Sn-Bi,  $V=1.6 \mu\text{m/s}$ )



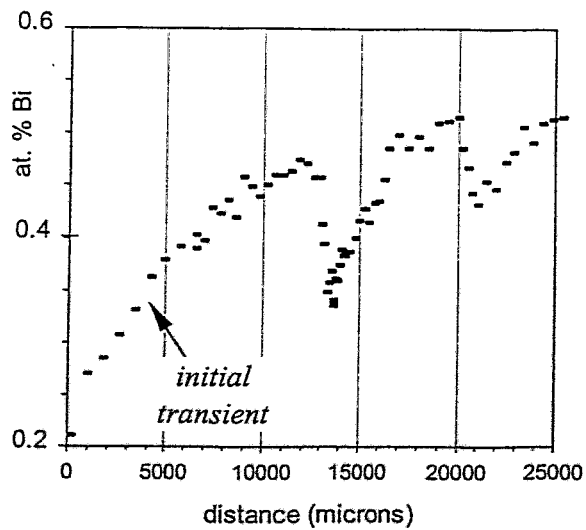
$g/g_0$



In situ diagnostic



Nuclear microprobe

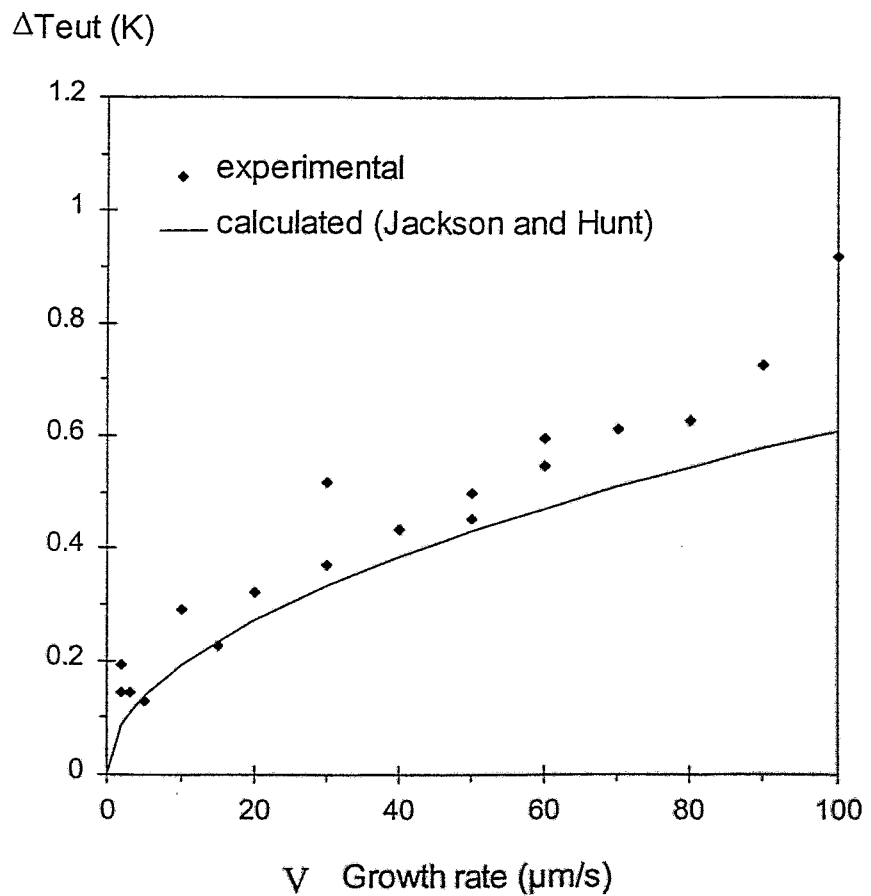


## Eutectic solidification

Sn-0.94 wt.% Cu

*Eutectic undercooling* :  $\Delta T_{\text{eut}} = K V^{1/2}$  [Jackson and Hunt model]

*Seebeck voltage* :  $\Delta V = \eta \Delta T_{\text{eut}}$

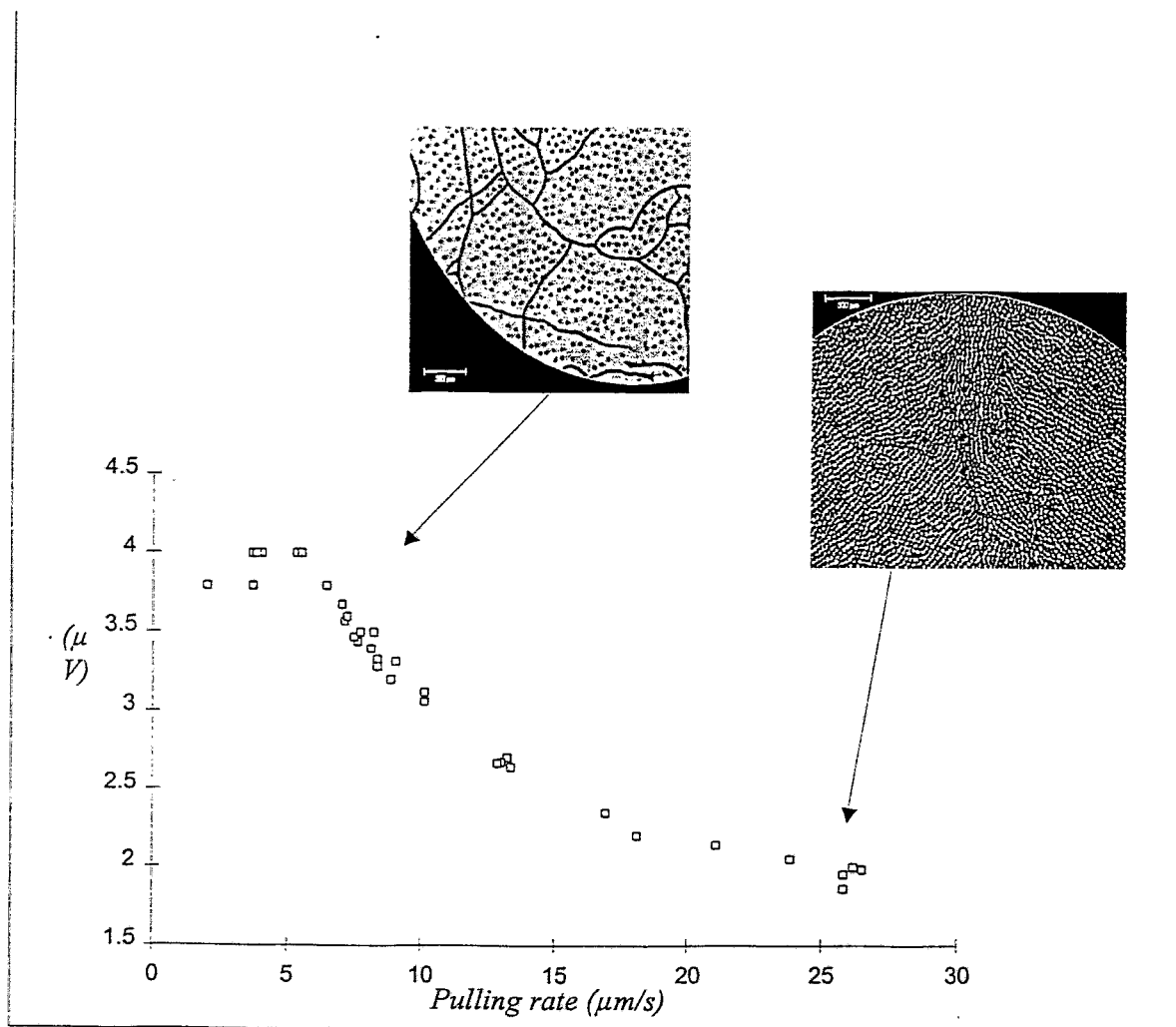


# Transitions

## Morphological instability

-Microgravity experiment USMP1

-Measurements at different velocities (SnBi0.5at%)

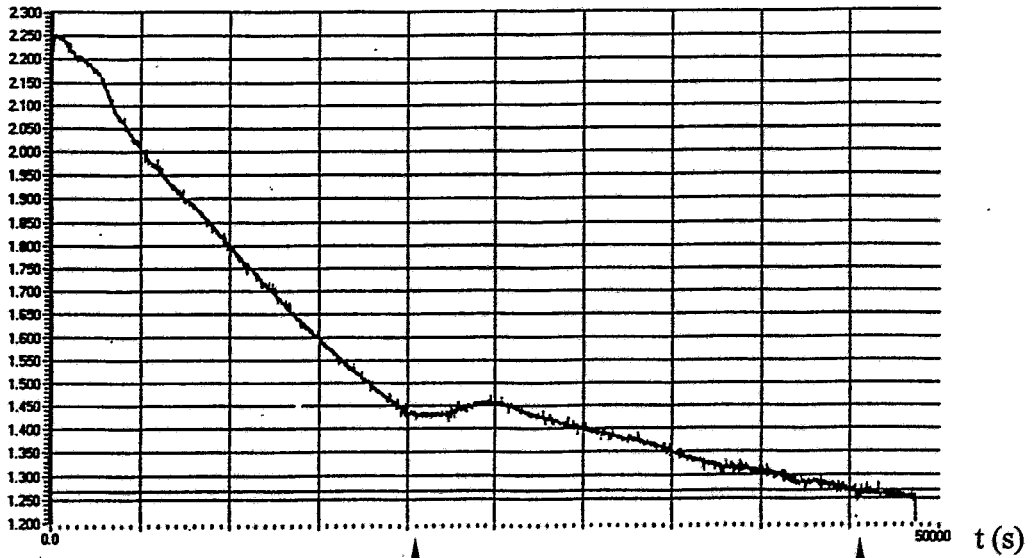


Test with the Mullins and Sekerka theory.

# Hypoeutectic solidification

Sn-0.8 wt.% Cu,  $V = 1 \mu\text{m/s}$

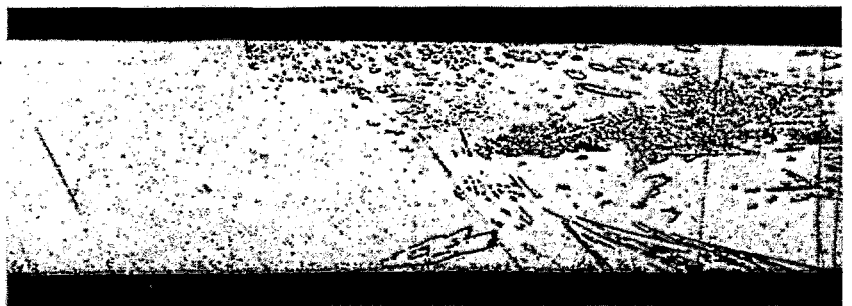
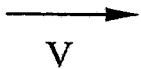
Seebeck voltage  
(x 10  $\mu\text{V}$ )



beginning  
of pulling

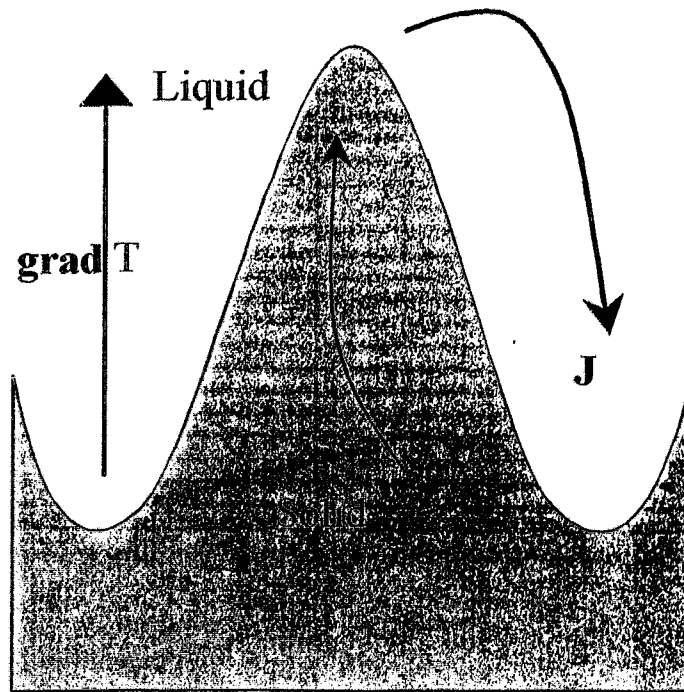
end of pulling

planar-eutectic transition  
at  $d = 22 \text{ mm}$



1 mm

## Non isothermal interface (dendrites, cells,...)



Coupling between temperature gradient and difference of thermoelectric power : thermoelectric current density.

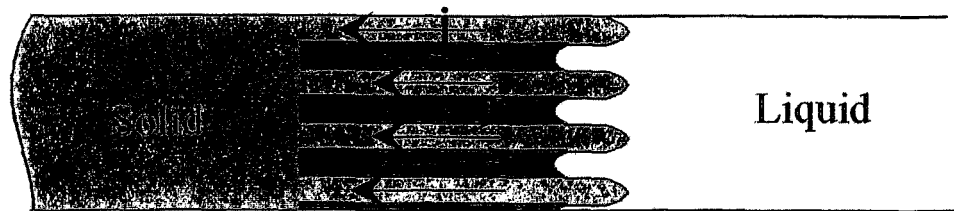
$$\Delta V = \Delta V(f_l, T_T, T_B)$$



## Solid phase contribution

Difference of composition in the solid:

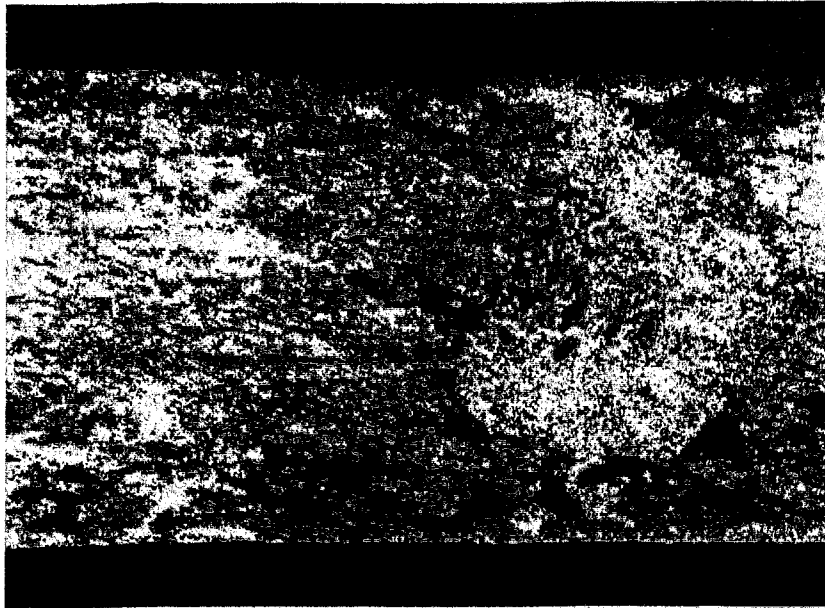
Thermoelectric currents



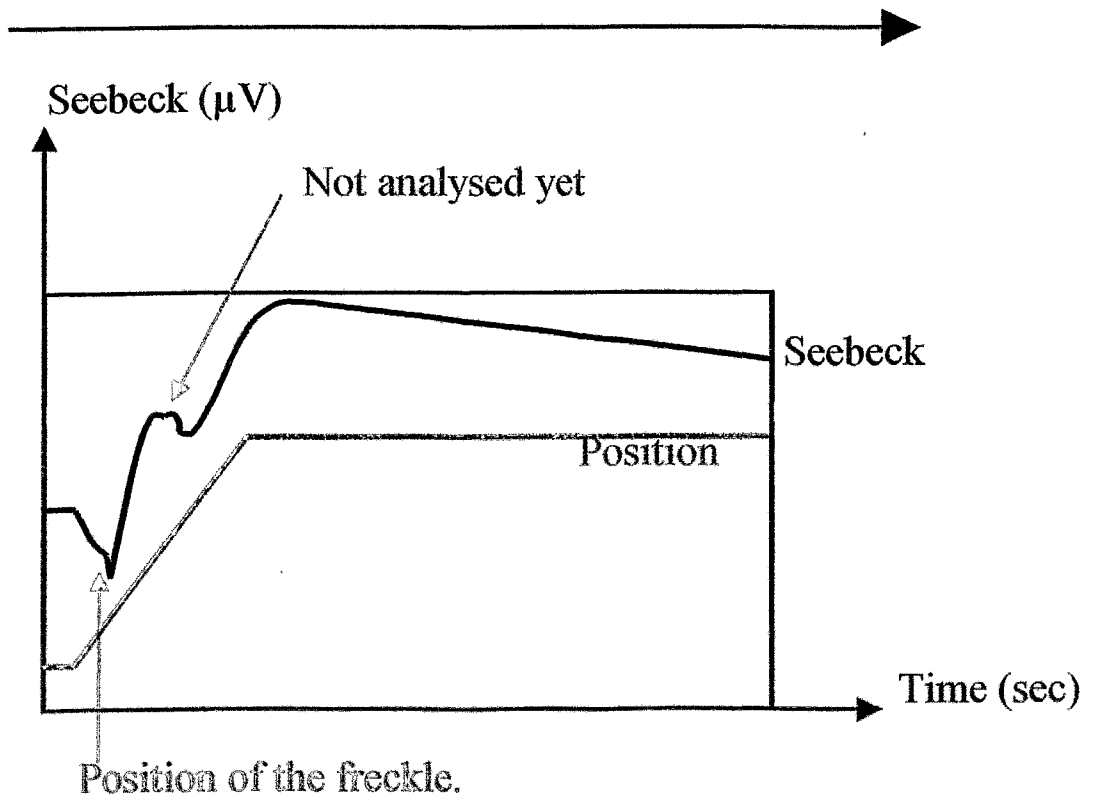
The voltage will depend on

- liquid fraction between the dendrites (freckles)
- composition of the solid phase (segregation)

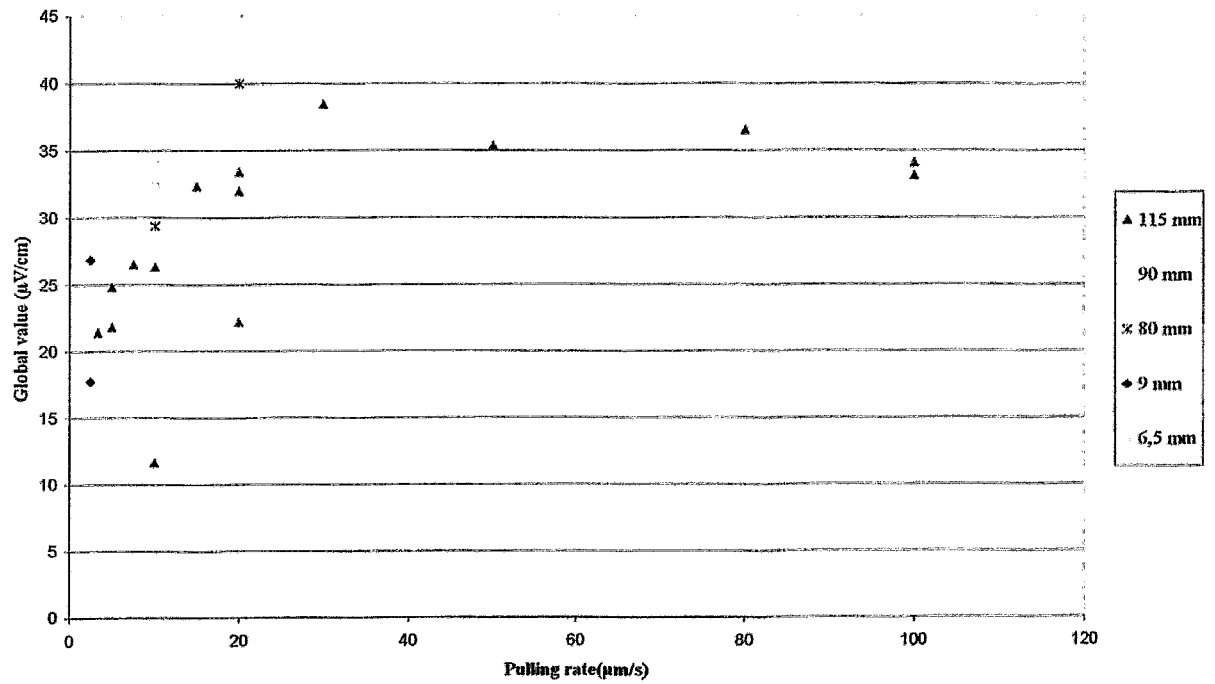
# Freckle detection (SnBi 25%mass)



Solidification direction



# Segregation measurements (Sn Bi 25%mass)

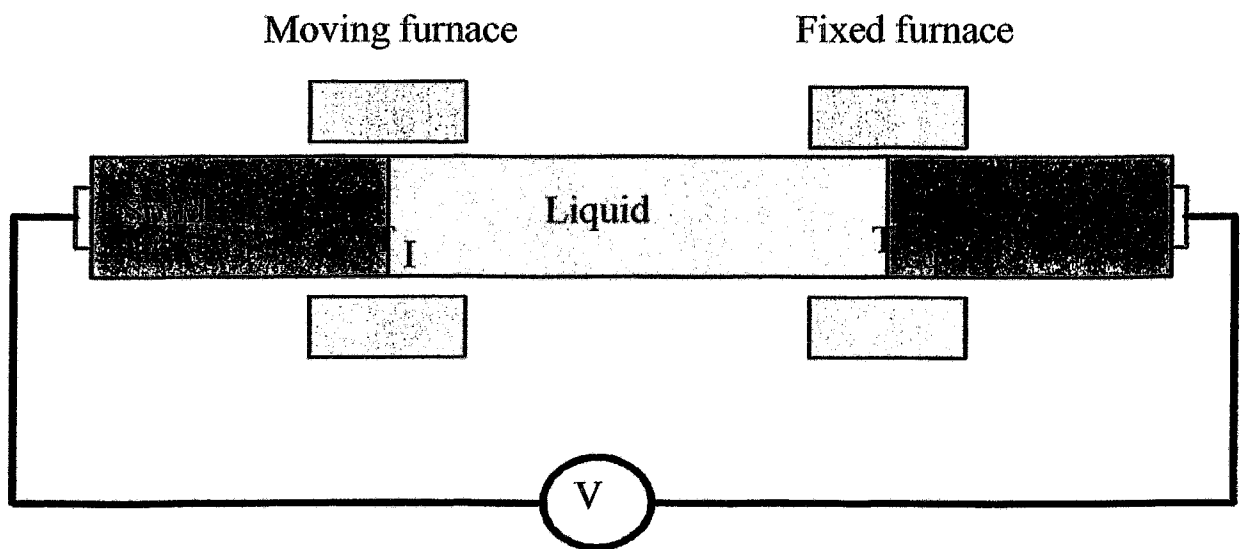


Increase of the incorporation of Bi with the pulling rate

# Solidification configuration and technical constraints.

Up to now : Bridgmann solidification. (directionnal)

Technical constraints : case of the Mephisto device



- Create a reference interface
- Stabilize the copper-metal junction
- Minimize electromagnetic perturbations.

## Conclusions

Seebeck effect allows an in situ diagnostic in solidification

It allows to measure : concentrations, undercooling, transitions, perturbations...

Some technical constraints....

## Scientific Programme

**October 11, 1999 (Monday)**

### **Afternoon Session**

- 14.00 **Invited Lecture**  
*E. Julius (AMEPA Aachen, Germany)*  
Flow velocity and two phase flow measurement in steel production
- 14.45 *F. Stefani, G. Gerbeth (FZ Rossendorf, Germany)*  
An inverse problem approach to velocity reconstruction from measurements of electromagnetic fields
- 15.05 *E. Baake, A. Mühlbauer (University of Hannover, Germany)*  
Experimental determination of turbulent flow characteristics, temperature and electromagnetic force density fields in the melt of induction furnaces
- 15.25 Coffee break
- 15.45 *S. Eckert, W. Witke, G. Gerbeth (FZ Rossendorf, Germany), L. Pisseloup (ENSHMG, France)*  
Local velocity measurements in high temperature liquid metals by means of mechano-optical probes
- 16.05 *A. Mühe, O. Gräbner (Fraunhofer IIS-B Erlangen, Germany), G. Müller (University Erlangen, Germany), E. Tomzig, W. v. Ammon (Wacker Siltronic Burghausen)*  
Determination of flow velocity in Silicon Melt during an Industrial Czochralski Process
- 16.25 *I. Platnieks (Institute of Physics Riga, Latvia)*  
Heat transfer investigation by specially designed heat emitting surfaces
- 16.45 *V. Ghilin, Y. Ivochkin, N. Razuvanov, L. Genin, A. Ustinov, V. Igumov (Institute of High Temperatures Moscow, Russia)*  
*V. Sviridov, E. Sviridov (Moscow Power Engineering Institute, Russia)*  
The automated complex for investigating hydrodynamics and heat transfer for a liquid metal flow under magnetic field with an opportunity of the remote access

# **Flow velocity and two phase flow measurement in steel production**

*E. Julius*

*AMEPA GmbH, Jülicher Straße 320, D-52070 Aachen*

Steel is and remains one of the most important manufacturing materials. The requirements regarding material characteristics and purity are constantly rising. The steel production process requires therefore an increasing effort regarding process control. Flow related influences on quality - positive and negative - have become a topic of great interest in the last years.

During the course of steel production the steel is poured several times from one vessel into another. But the slag which arises during each step of the process must not be transferred into the next vessel. Here electromagnetic slag detection systems have been successfully implemented. Equipped with high temperature sensors they detect the entrainment of slag into the discharged steel stream accurate and with high sensitivity. The amount of carried over slag is significantly reduced.

In the case of continuous casting the molten steel is poured from a tundish into a water cooled copper mould. The steel flow in the mould has an important influence on steel cleanliness. A lot of water model studies and computer simulations dealt with this problem. During the last years also several flow measuring techniques were developed and tested to determine the steel flow under production conditions. Most of them use a kind of a ceramic probe that is immersed into the steel.

A system that is able to monitor the flow velocity under production conditions was tested at Thyssen Krupp Stahl in Dortmund as well as in other steel plants. The electromagnetic sensors are mounted behind the walls of the mould. They consist of permanent magnets and sensitive receiver probes.

Metal flow measurements were carried out at a laboratory mould model using a kind of Woods metal and it was shown that the flow velocities were in close correspondence with results achieved with a conventional flow meter.

The steel plant operation of this flow monitoring system has shown significant correlation between casting parameters and mould flow pattern. Especially the influence of submerged nozzle position, nozzle outlet angle and argon rate have been investigated and the inclusion rate in a series of cold rolled strips has been correlated with the monitored mould flow pattern.

The results led to suggestions for improvements of the casting equipment.

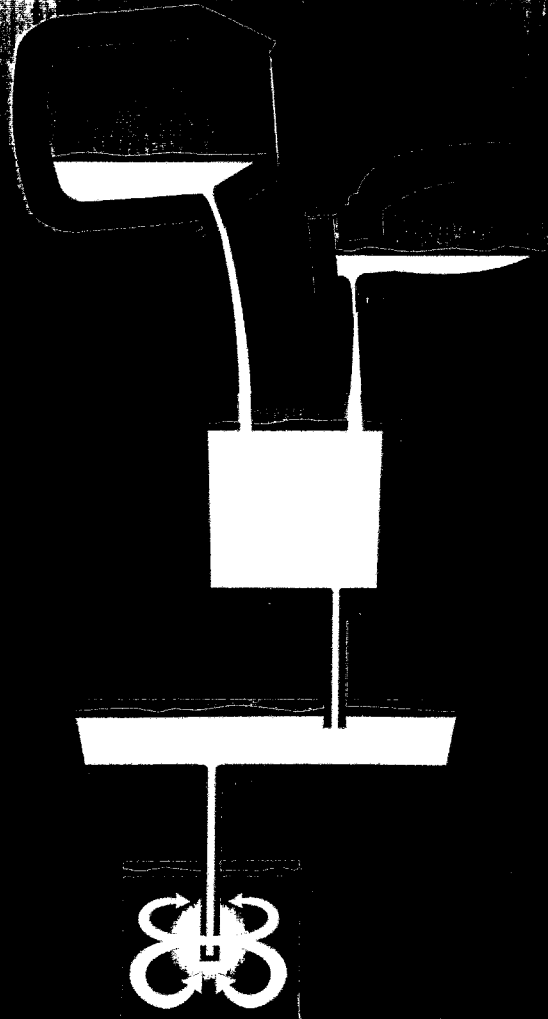
# **Flow Velocity And Two Phase Flow Measurement In Steel Production**

**E. Julius**

**AMEPA GmbH, Aachen, Germany**

- 1. Introduction**
  
- 2. Slag Carry Over Detection**
  - 2.1 Electromagnetic Slag Detection**
  - 2.2 Thermographic Slag Detection**
  
- 3. Steel Flow Velocity Measurement**
  - 3.1 Introduction**
  - 3.2 Different Steel Flow Measuring Methods**
  - 3.3 The AMEPA MFC System**
    - 3.3.1 The Measuring Principle**
    - 3.3.2 Laboratory Results**
    - 3.3.2 MFC Plant Application**
    - 3.3.4 Plant Measurement Results**
  
- 4. Conclusions and Outlook**





**BOF**

**EAF**

**LADLE**

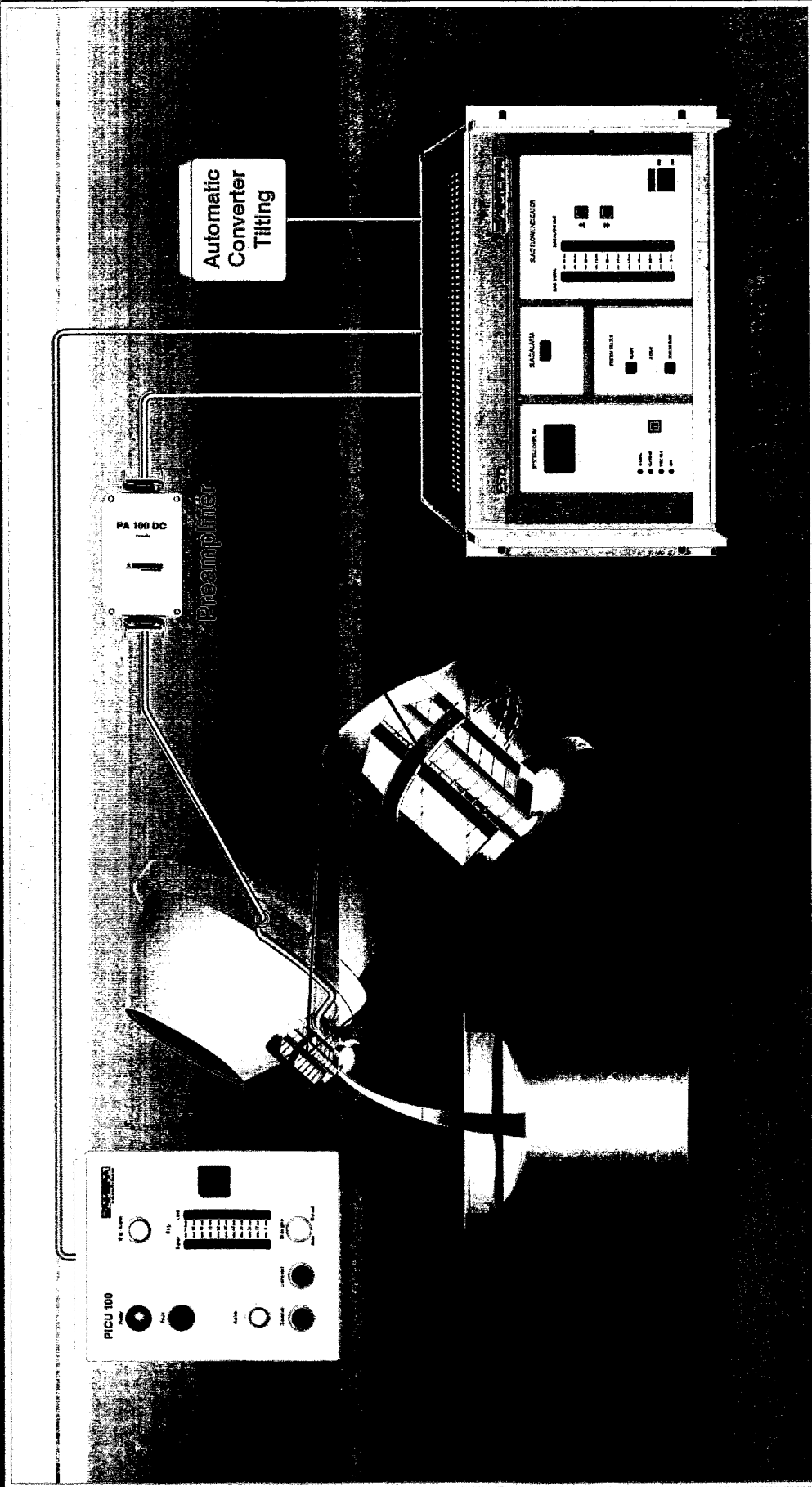
**TUNDISH**

**MOULD**

**MTLM 1999**

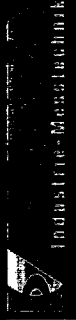
**Course of  
steel production**

 **Institute of Steel Technology**

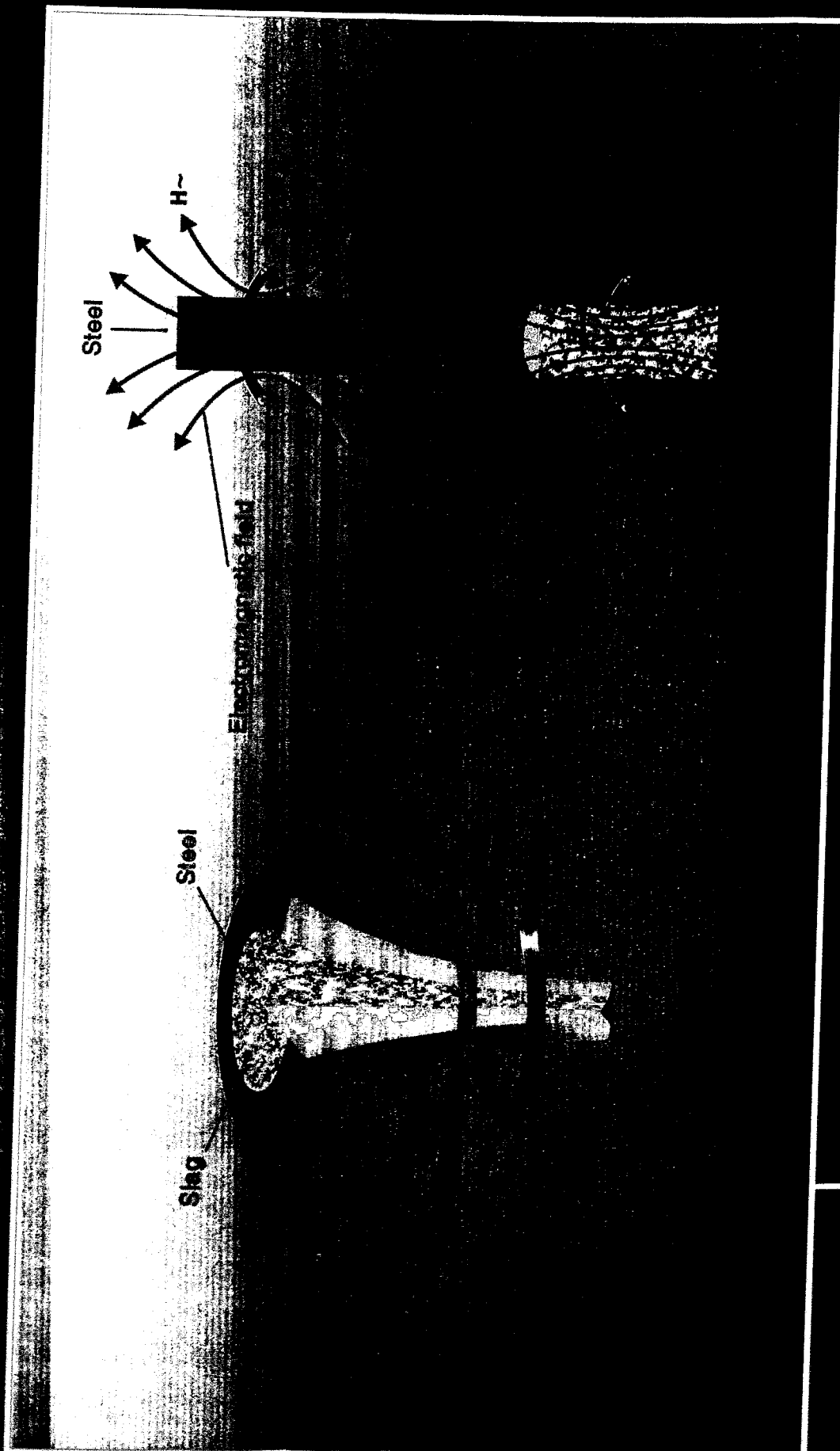


# Schematic layout at the BOF

MTLM 1999



Industrie-Messtechnik

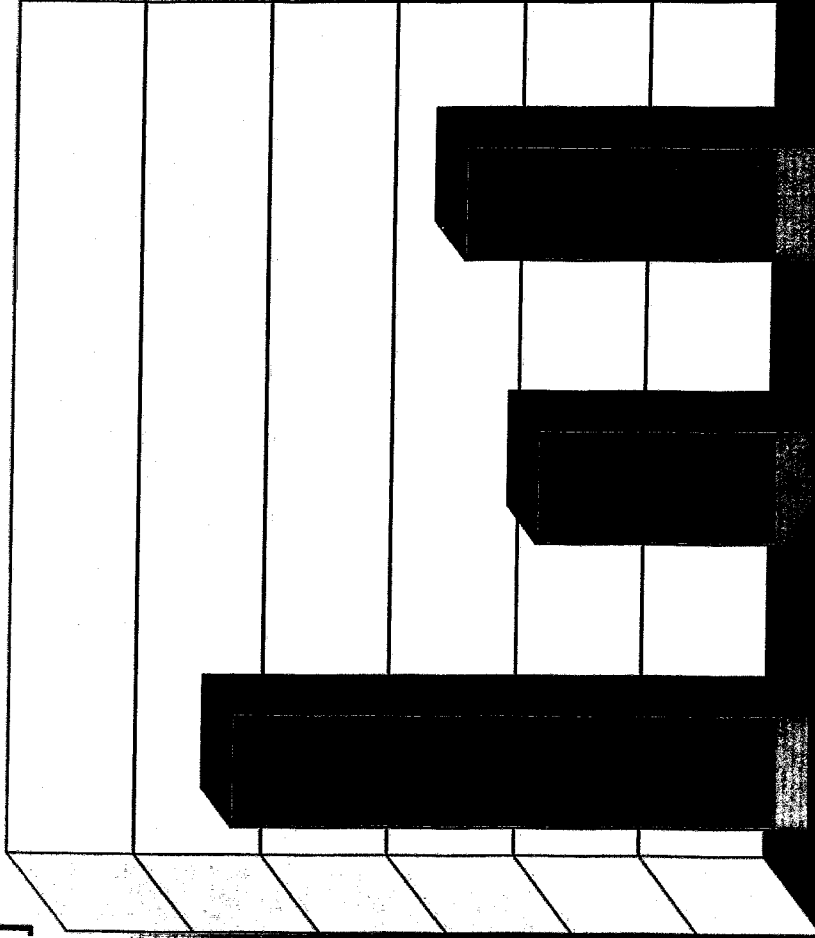


MTLM 1999

Measuring principle

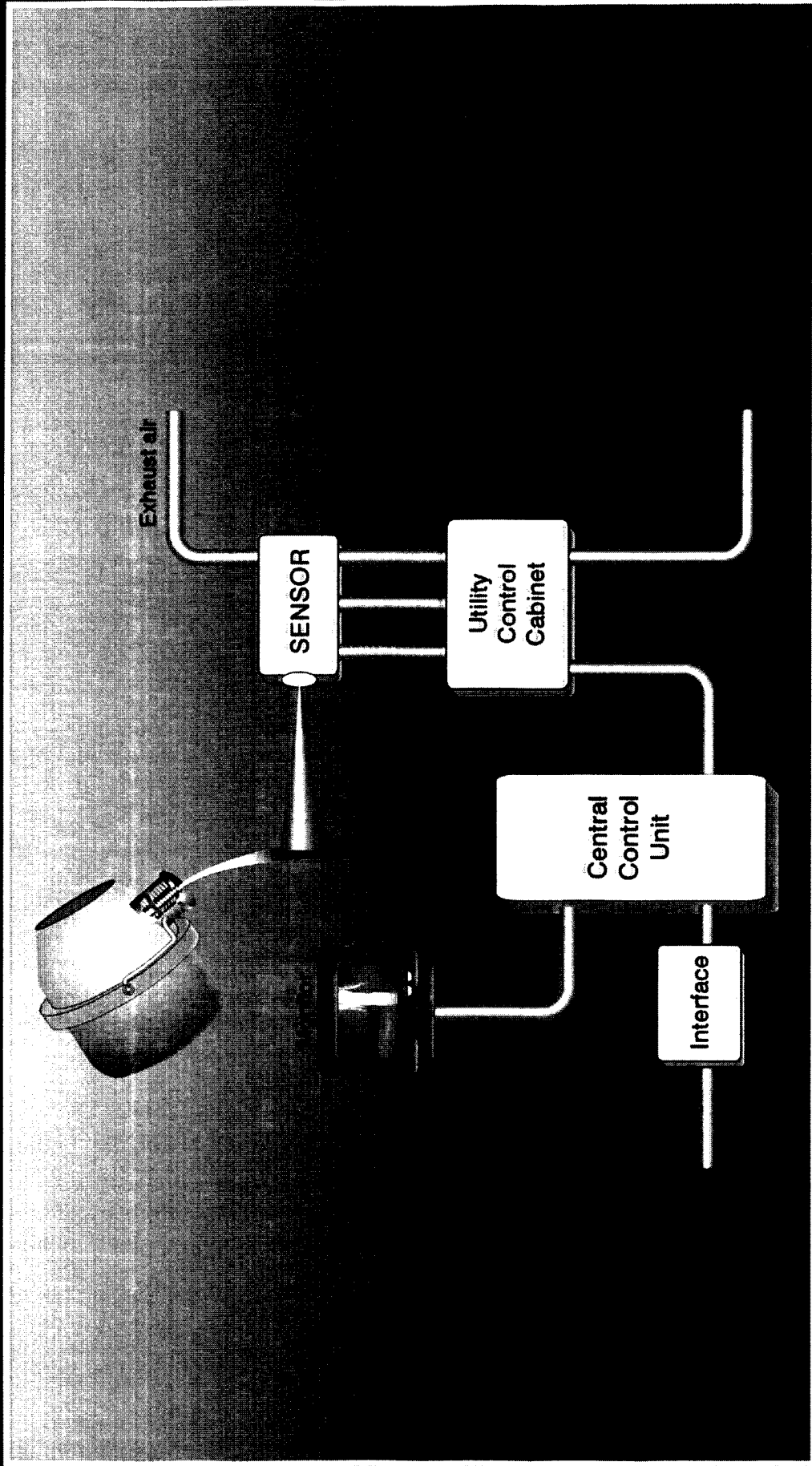
[kg/ton]

0.30



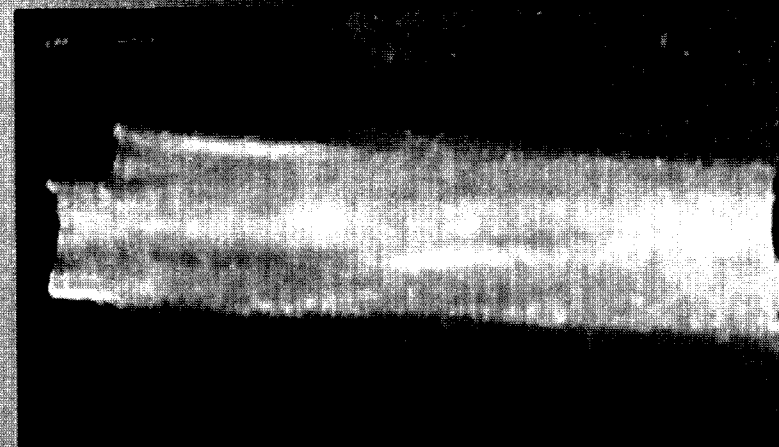
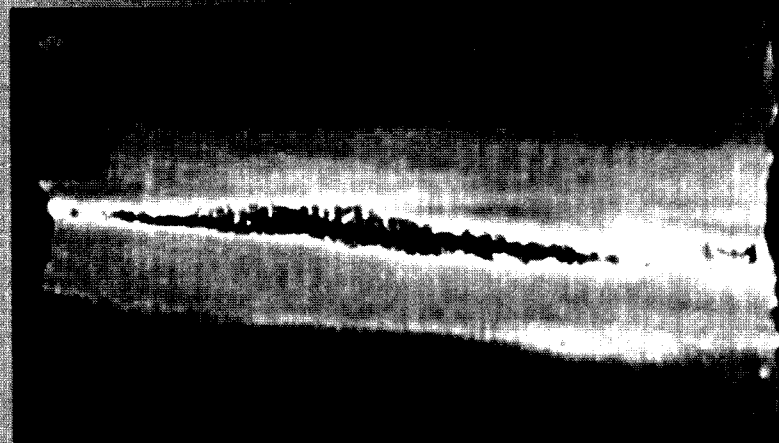
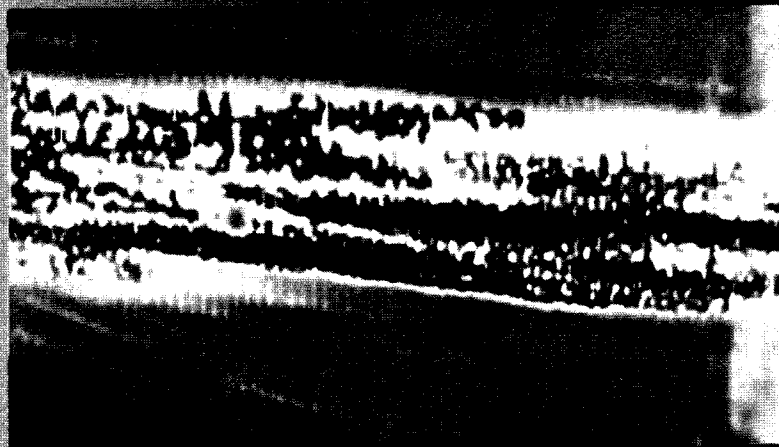
MTLM 1999

Economical slag detection benefits



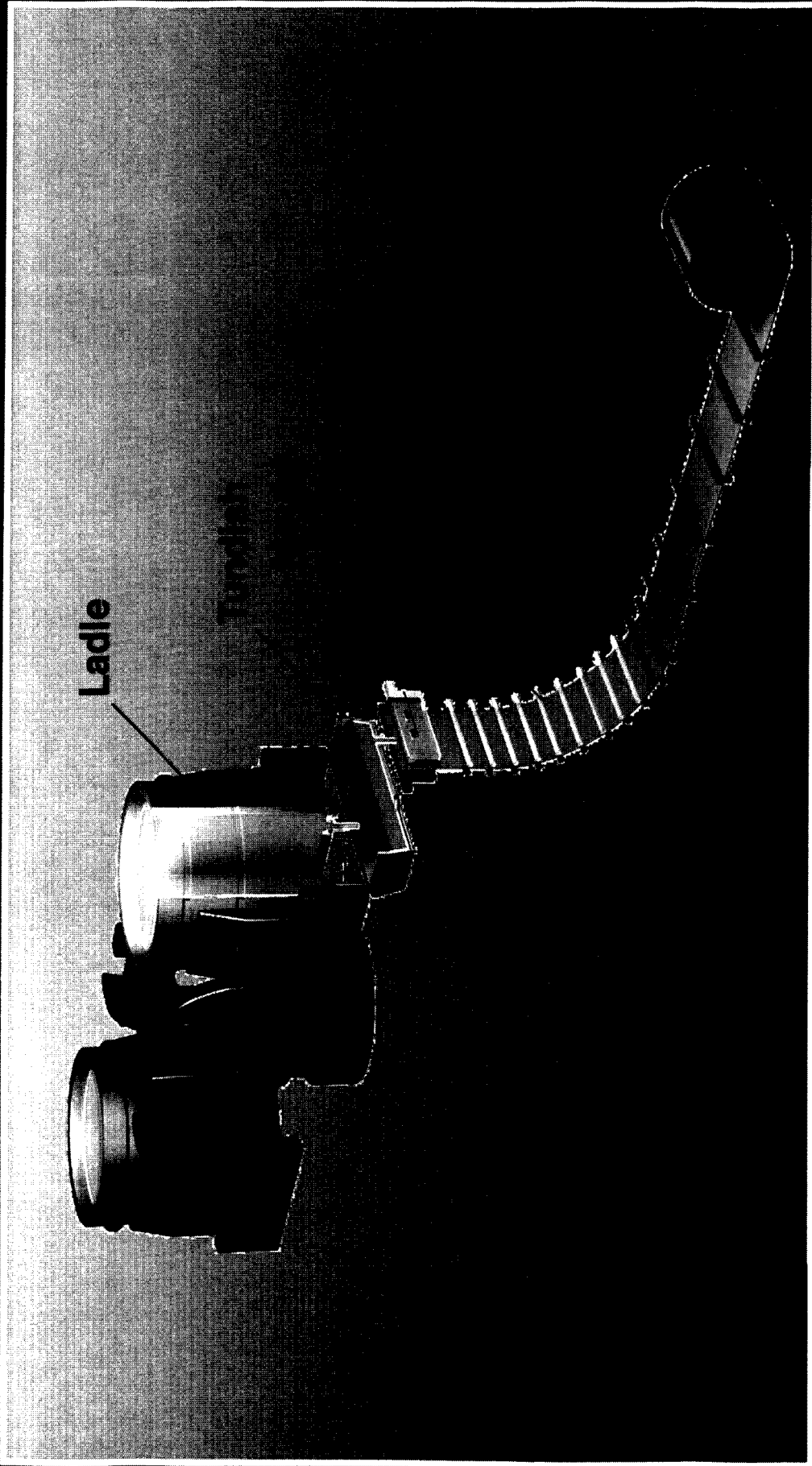
MTLM 1999

Thermographic slag detection



## Infrared slag detection image

MTLM 1999

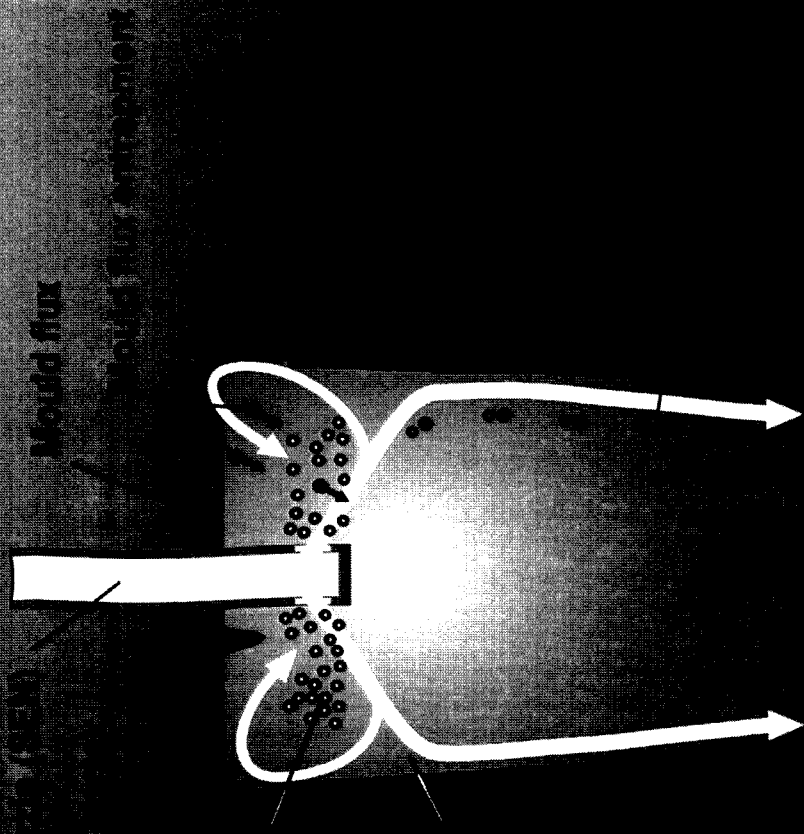


Ladle

MTLM 1999

Schematic continuous casting process

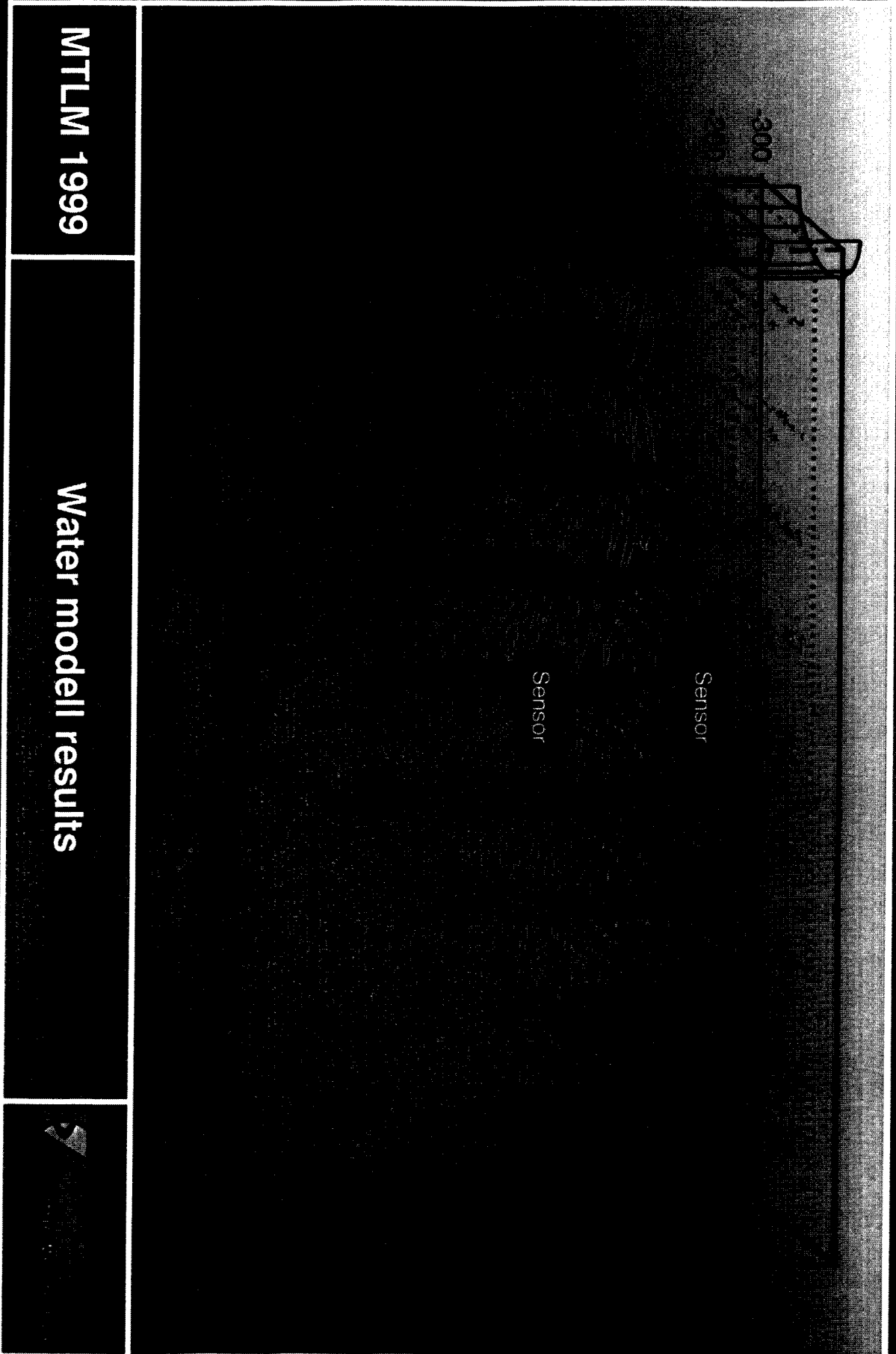




MTLM 1999

Mould flow related inclusion entrapment





**MTLM 1999**

**Water modell results**



**MEASURING METHODS**

**WITH CONTACT**

**REACTION**

**KARMAN  
VORTEX**

**MELTING  
TIME**

**NKK**

**AMEPA**

**WITHOUT CONTACT**

**MTLM 1999**

**Steel flow measuring methods**





Bridge

Dynamic  
Strain  
Meter

DRAG FORCE  $F_D = \frac{1}{2} C_D \cdot D \cdot H \cdot \rho \cdot V^2$

with  $C_D = f(R_e)$  with  $R_e = \frac{V \cdot D}{\nu}$

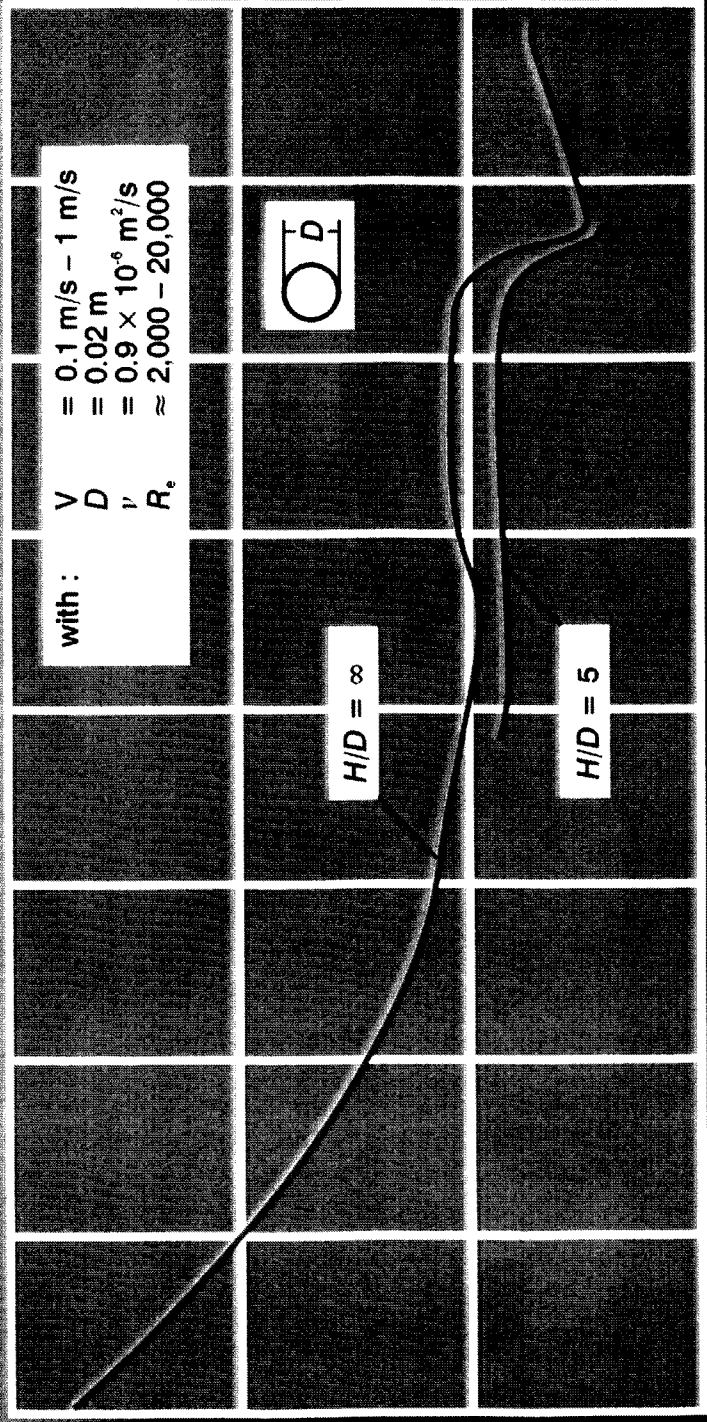
- $R_e$  = Reynolds number
- $V$  = Velocity of steel
- $C_D$  = Drag coefficient
- $\nu$  = Kinetic viscosity
- $\rho$  = Density of steel

MTLM 1999

Velocity measurement via drag force



10<sup>2</sup>

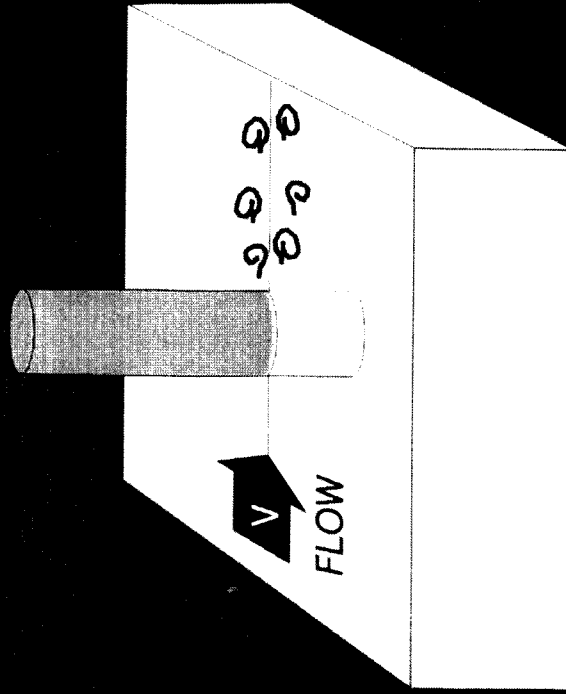


with :  
 $V = 0.1 \text{ m/s} - 1 \text{ m/s}$   
 $D = 0.02 \text{ m}$   
 $\nu = 0.9 \times 10^{-6} \text{ m}^2/\text{s}$   
 $R_e \approx 2,000 - 20,000$

MTLM 1999

Drag coefficient versus Reynolds number





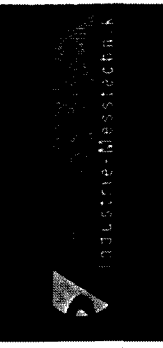
- Bridge
- Dynamic Strain Meter
- FFT

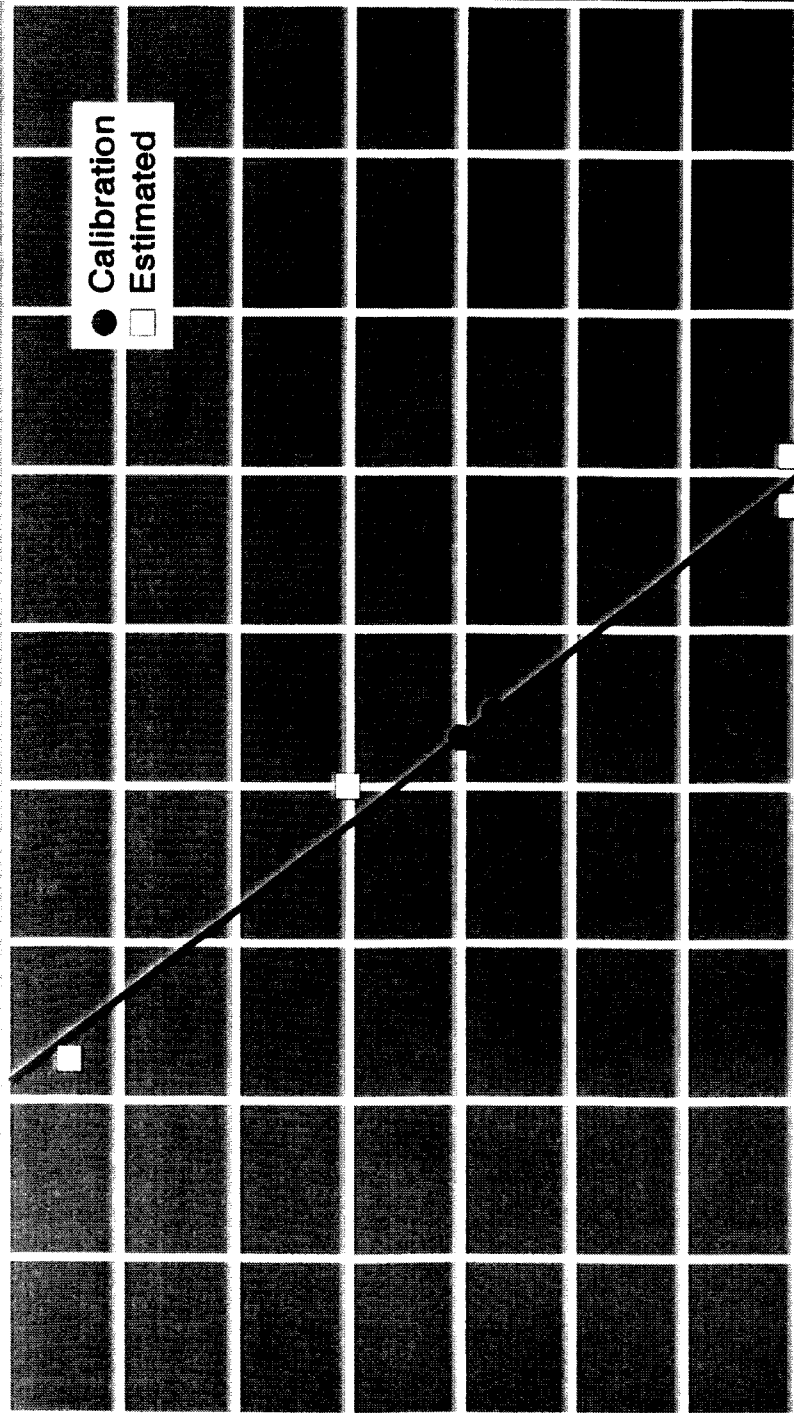
$$St = \frac{f \cdot D}{V}$$

$f$  = Shedding frequency

MTLM 1999

# Schematic of Karman Vortex probe



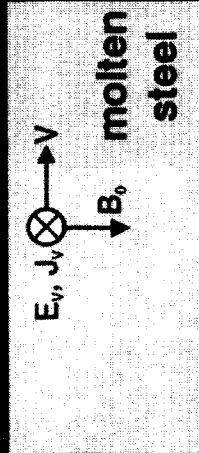
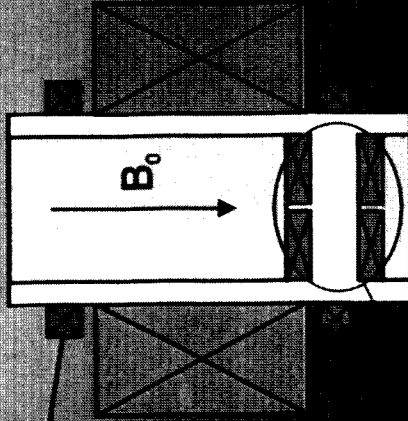


**Calibration results and actual flow velocity measurements at 1610° C**

**MTLM 1999**

Lift-off  
pick-up  
coils

Exciting  
coil



$$\vec{E}_v = \vec{V} \times \vec{B}_0$$

$$\Downarrow$$

$$\vec{J}_v = \sigma \cdot \vec{V} \times \vec{B}_0$$

$$\Downarrow$$

$$\vec{B}_v \propto \sigma \cdot \vec{V} \times \vec{B}_0$$

- $V$  = Flow velocity
- $\sigma$  = Conductivity
- $B_0$  = Existing magnetic field
- $E_v$  = Induced electric field
- $J_v$  = Induced current density
- $B_v$  = Induced magnetic field

MTLM 1999

# Schematic diagram of NKK sensor





The current density in a moving conductive fluid is given by:

$$\vec{j} = \sigma \cdot (\vec{V} \times \vec{E})$$

with:

$\vec{j}$  - Current density

$\sigma$  - Electric conductivity of the fluid

$\vec{V}$  - Velocity of the fluid

$\vec{E}$  - Electric field

MTLM 1999

Measuring principle



HTWK  
Hochschule  
Technische  
Wirtschaft



The current density in a moving conductive fluid is given by:

$$\vec{j} = \sigma \cdot (\vec{v} \times \vec{B})$$

Magnetic flux density  $\vec{B}$

with:

$\vec{j}$  = Current density

$\sigma$  = Electrical conductivity of the liquid

$\vec{v}$  = Flow velocity

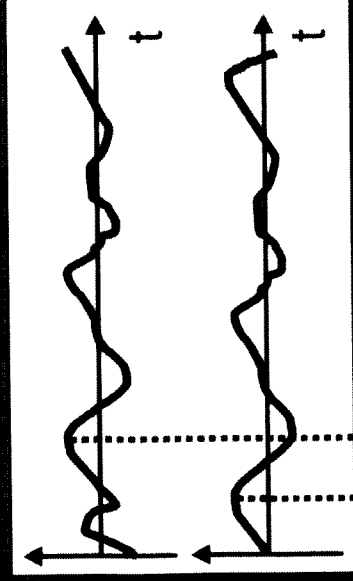
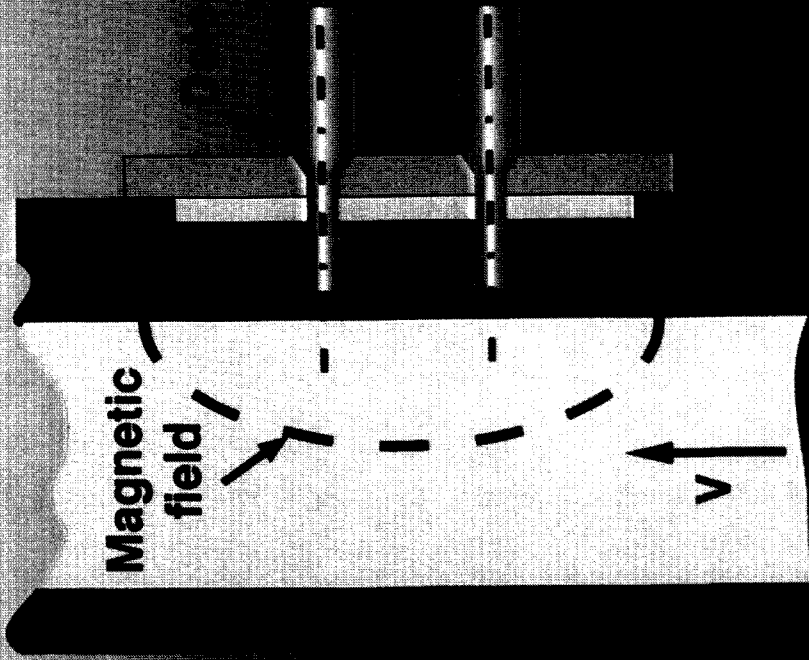
$\vec{B}$  = Magnetic flux density



MTLM 1999

Measuring principle





$$V = D / \tau$$

MTLM 1999

Measuring principle



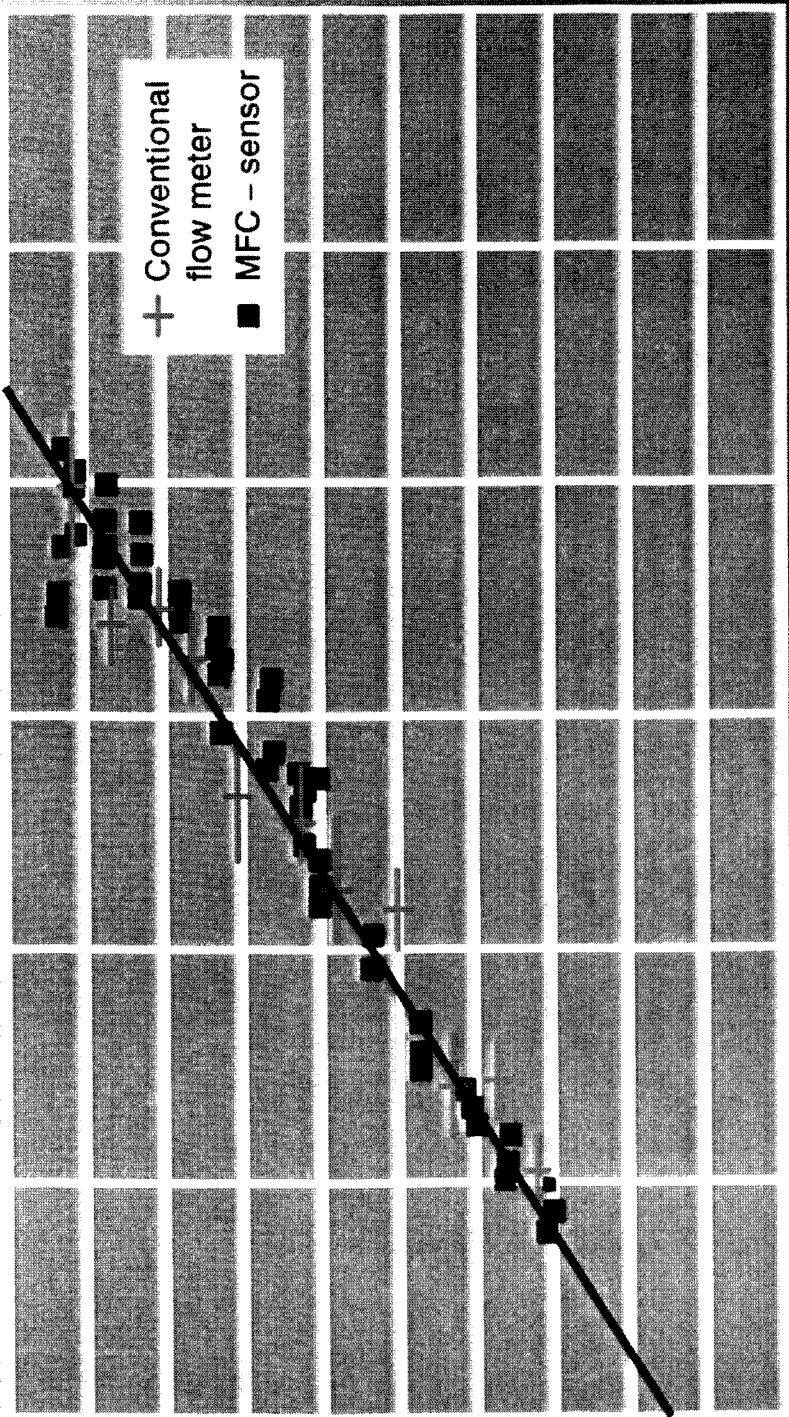
The mean flow velocity in front of the detectors can be calculated using the correlation method by calculating the time of flight  $\tau$ , for which the normalized cross-correlation  $P_{sg}(\tau)$  of the signals  $s(t)$  and  $g(t)$  has a maximum:

$$P_{sg}(\tau) = \frac{\int s(t) \cdot g(t + \tau) dt}{\sqrt{E_s \cdot E_g}}$$

with

$$E_s = \int s^2(t) dt \quad \text{and} \quad E_g = \int g^2(t) dt$$

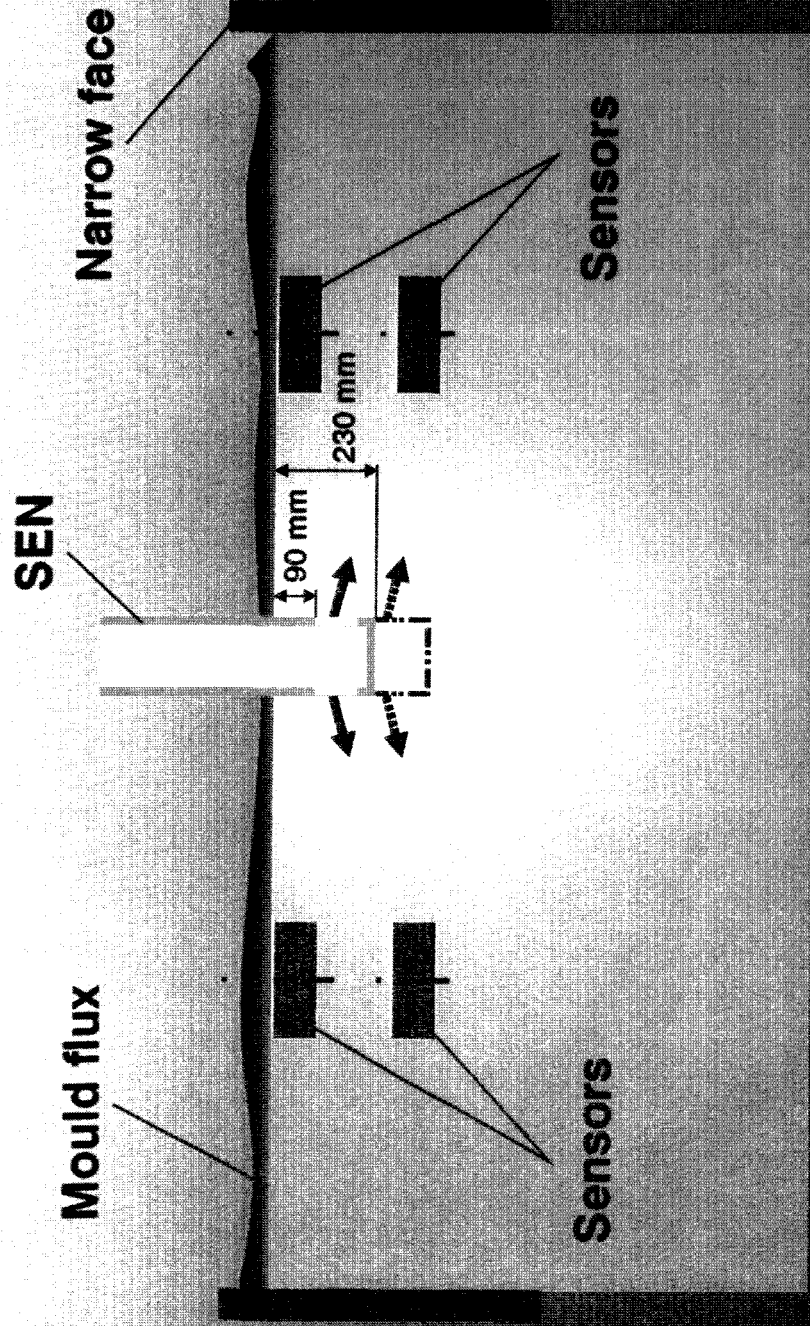
20



### MFC laboratory results



MTLM 1999

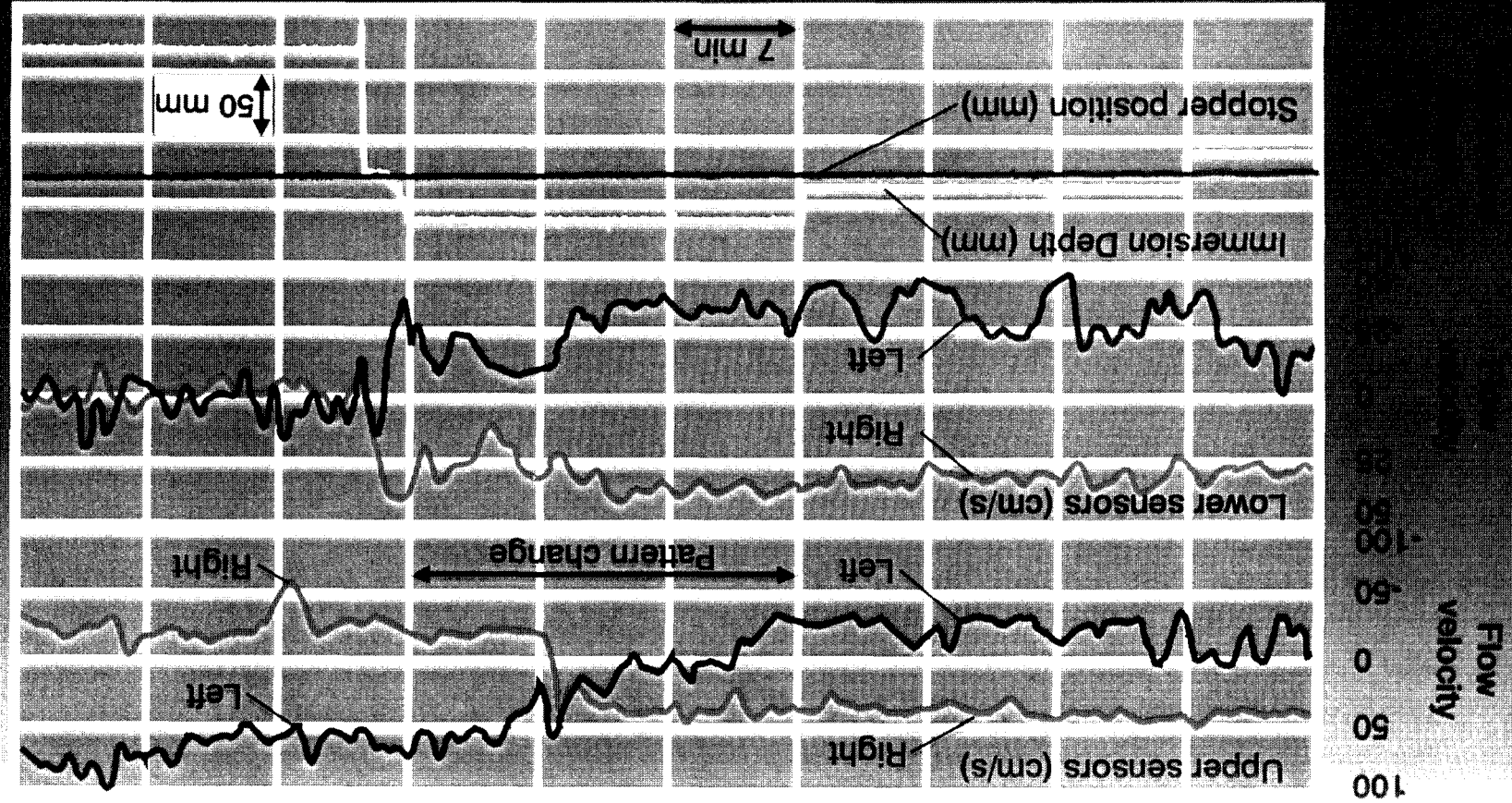


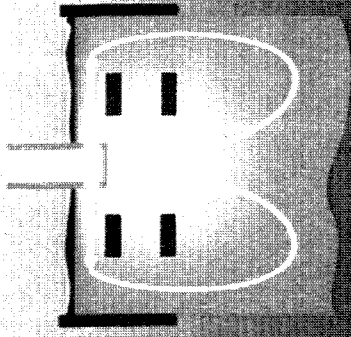
**MTLM 1999**

**Positions of the sensors in the mould**

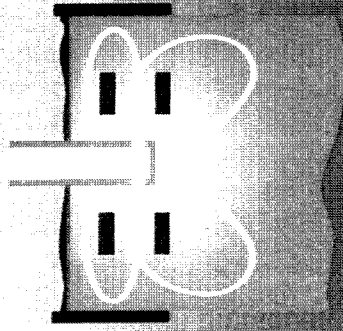


# Flow velocities in front of all 4 sensors and casting parameters

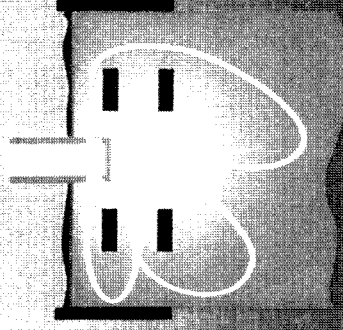




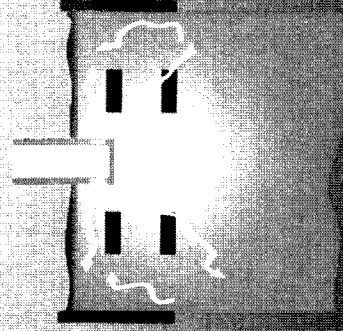
Single Roll



Double Roll



Meniscus Roll



Unstable Flow

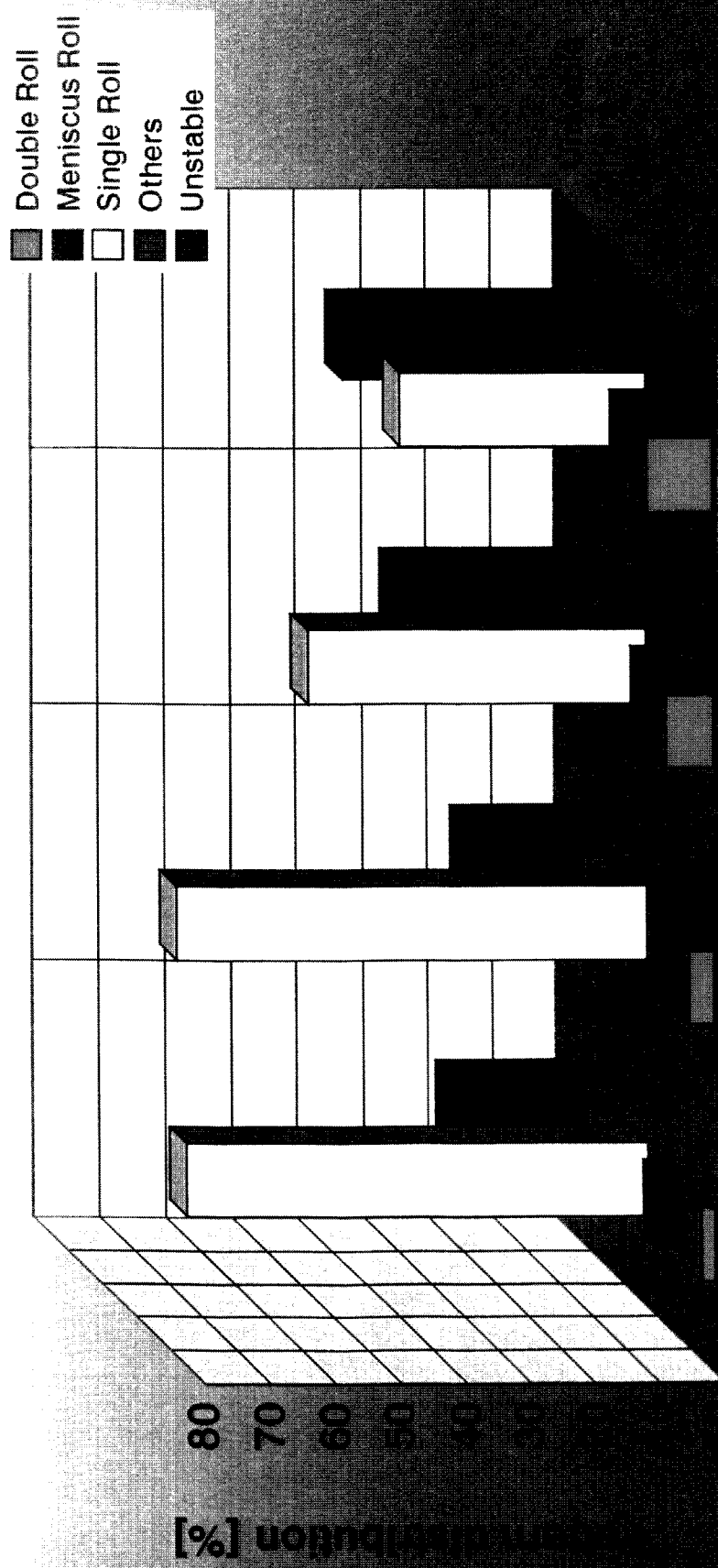
Designed by  
Prof. Dr. Ingrid Isenhardt  
© 1999 Fraunhofer IPA  
www.ipa.fraunhofer.de

Produced by  
Prof. Dr. Ingrid Isenhardt  
© 1999 Fraunhofer IPA  
www.ipa.fraunhofer.de

Produced by  
Prof. Dr. Ingrid Isenhardt  
© 1999 Fraunhofer IPA  
www.ipa.fraunhofer.de

MTLM 1999

Main flow patterns in the mould



**Flow pattern distribution  
versus casting speed**

**MTLM 1999**

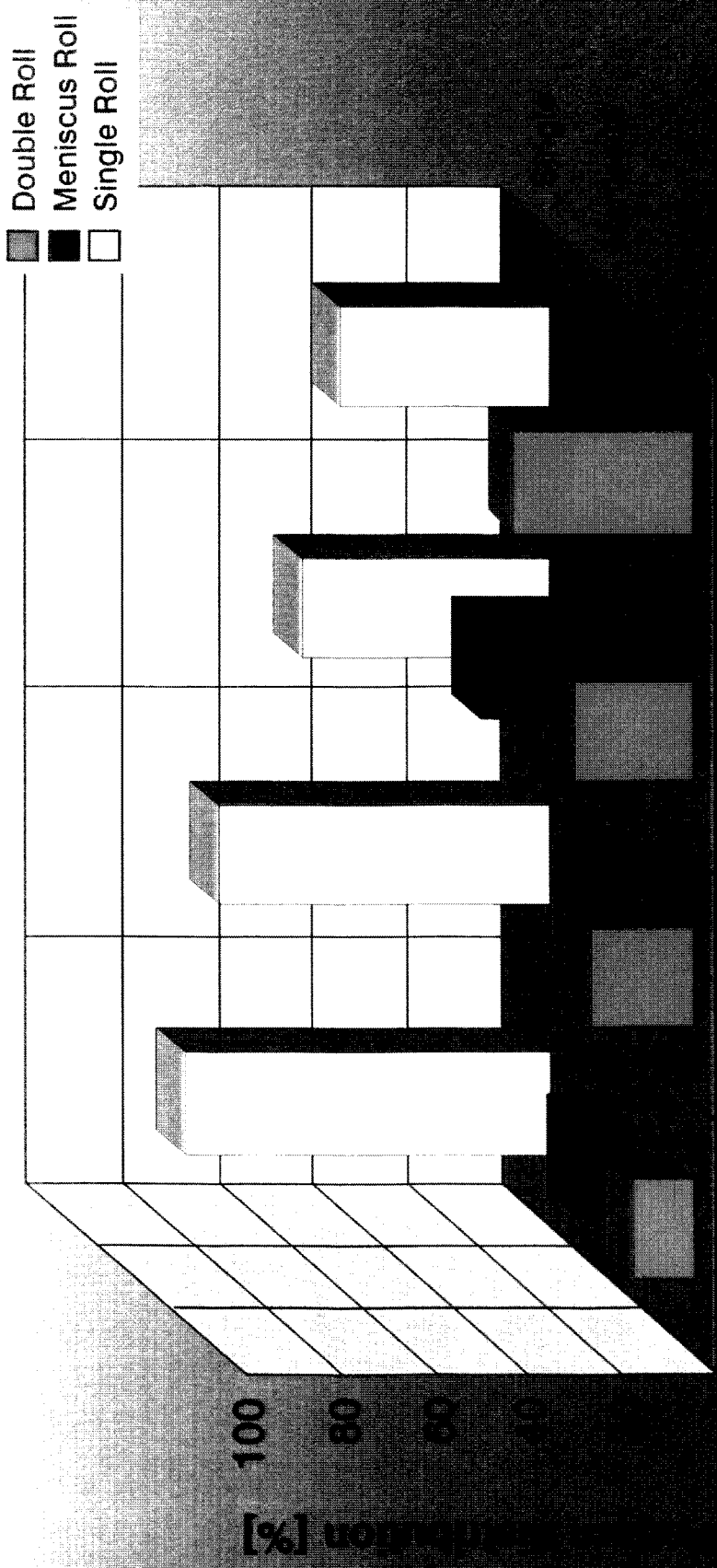






**Flow pattern distribution  
versus argon rate**

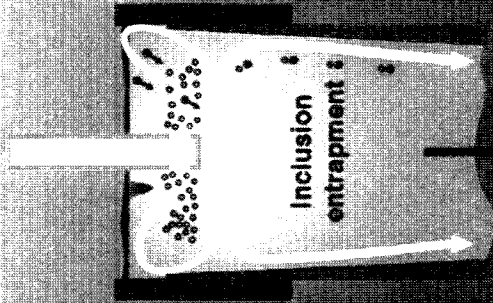
**MTLM 1999**



**Flow pattern distribution versus immersion depth (standard SEN)**

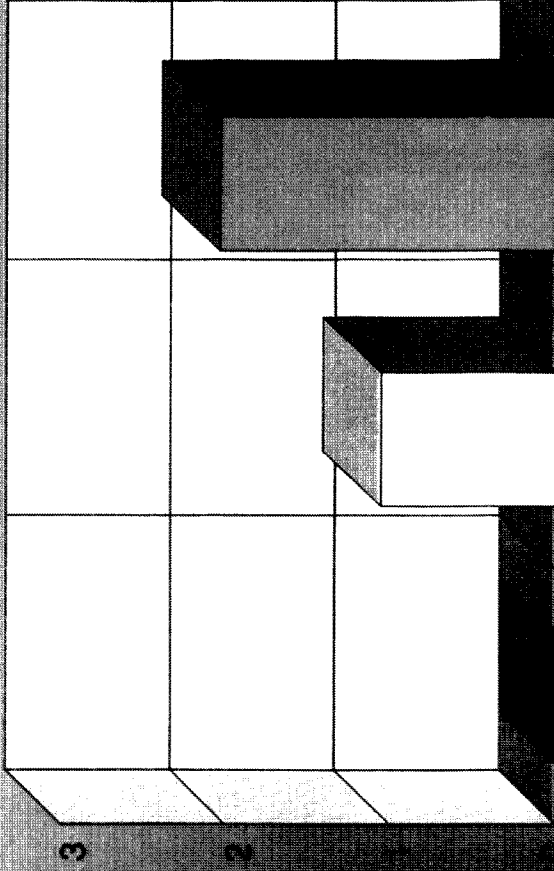
**MTLM 1999**





**Result**

Fine scale  
defect index

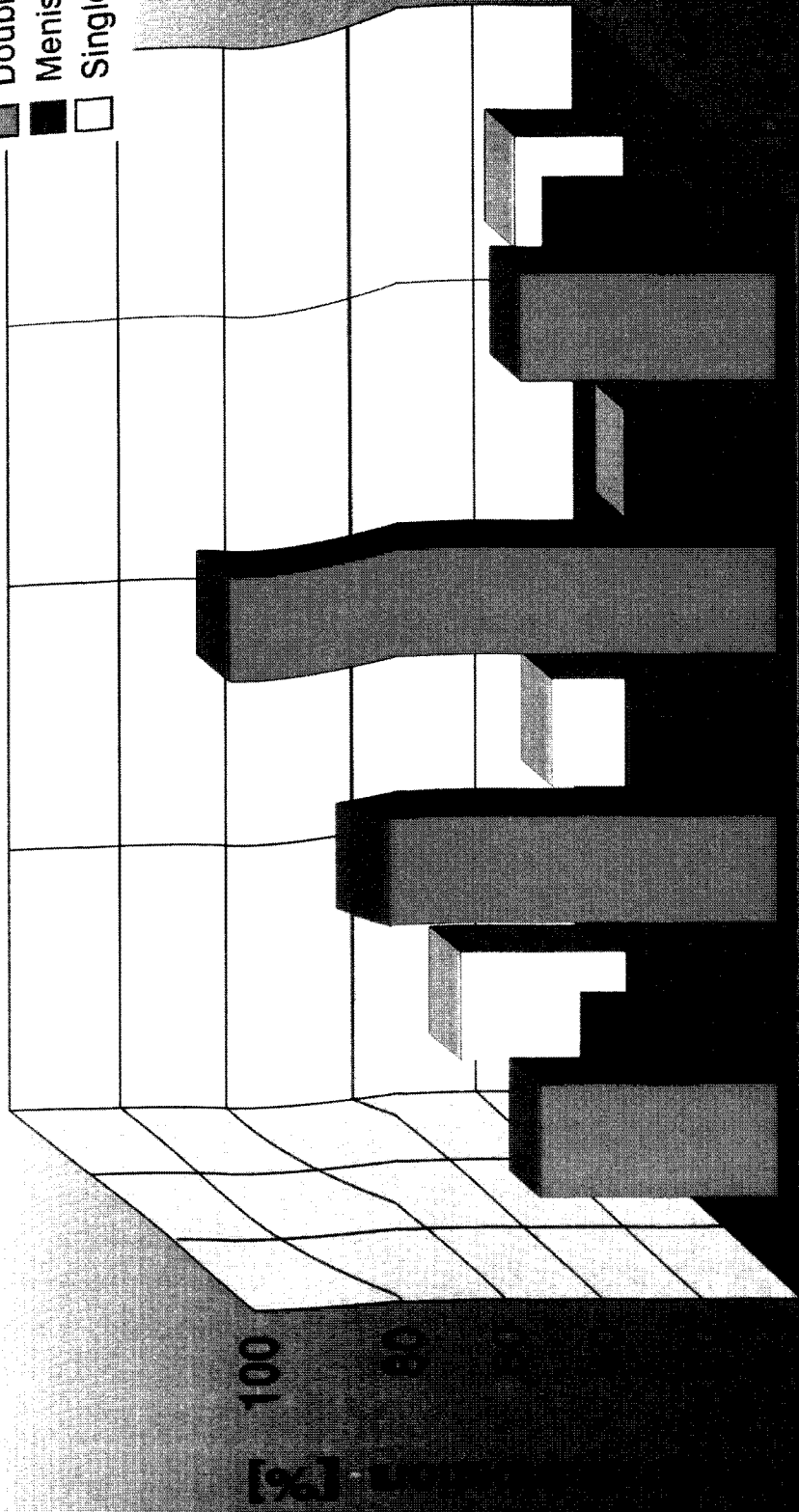


**MTLM 1999**

**Fine scale defect versus flow pattern**

**AMEPA**  
Industrie-Messtechnik

■ Double Roll  
 ■ Meniscus Roll  
 □ Single Roll



**Flow pattern distribution versus  
 immersion depth (long SEN)**

**MTLM 1999**

# Conclusions and Outlook

- **Electromagnetic slag detection is a standard in steel production.**
- **Thermographic slag detection may become an alternative at BOF/EAFs.**
- **Mould flow measurement has become a topic of high interest.**
- **There are some measurement methods available to measure steel flow. Most of them are only useful for short time trials.**
- **The MFC system can monitor the flow under casting conditions.**
- **The flow in a mould is much more unstable than it was expected from water model and computer modelling results.**
- **Correlations between product defects and flow conditions were observed.**
- **Based on the MFC results the SEN position and port angle could be improved.**
- **The next trial in a Belgium steel plant will focus on the correlation between flow pattern and product quality.**

# An inverse problem approach to velocity reconstruction from measurements of electromagnetic fields

Frank Stefani, Gunter Gerbeth  
Forschungszentrum Rossendorf

1. Introduction
2. Forward Problem
3. Inverse Problem
4. Uniqueness considerations
5. References and outlook

---

\*presented at: International Workshop on Measuring Techniques for Liquid Metal Flows (MTLM), Dresden, October 11-13, 1999

# **An inverse problems approach to velocity reconstruction from measurements of electromagnetic fields**

*Frank Stefani and Gunter Gerbeth*

*Forschungszentrum Rossendorf (FZR), P.O. Box 510119, D-01314 Dresden, Germany*

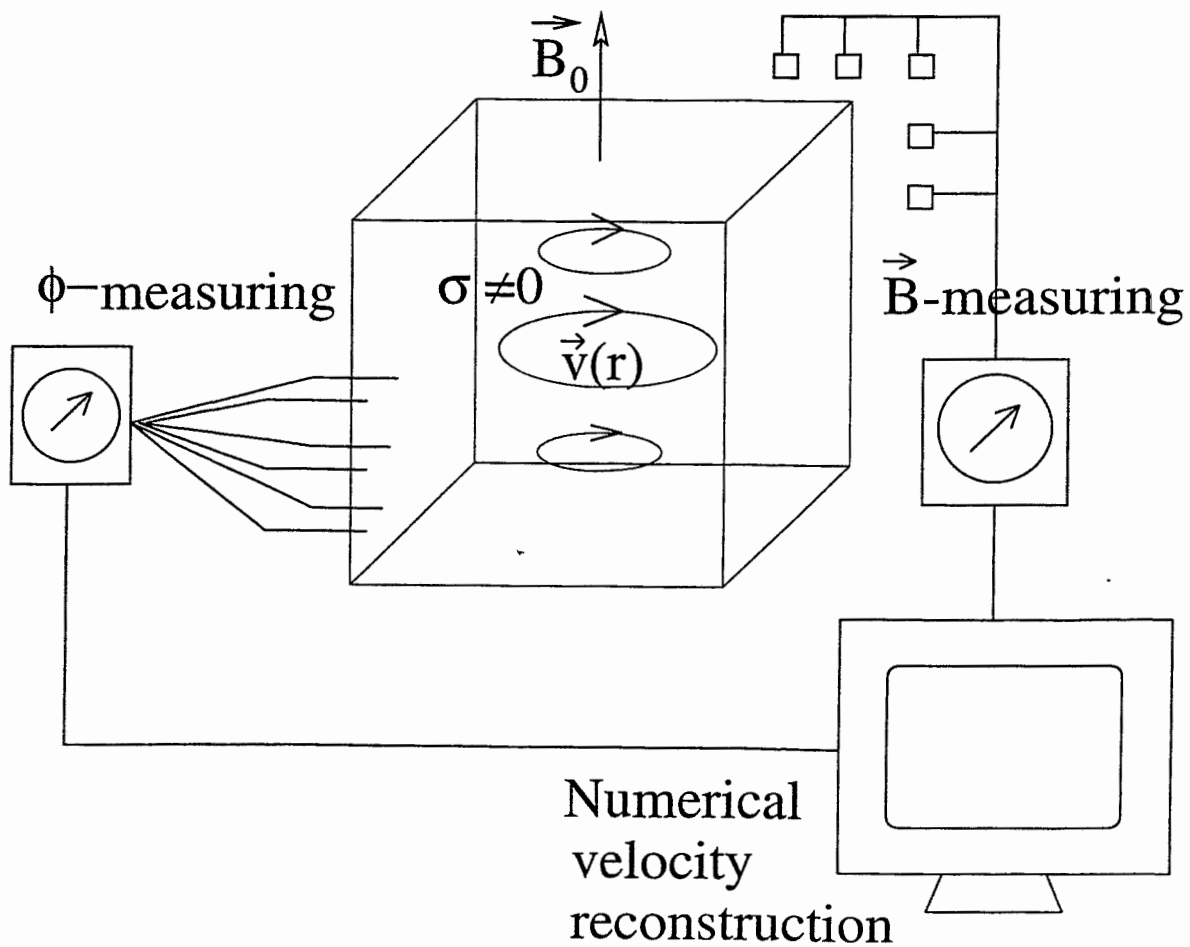
If a moving electrically conducting fluid is exposed to an external magnetic field electrical currents are induced. These currents give rise to an additional magnetic field which can be measured outside the fluid volume and to an electric potential measurable at the fluid boundary. From the viewpoint of inverse problems, we consider the possibility of velocity reconstruction from the measured electromagnetic fields. Possible applications for a contactless measuring technique are delineated.

# 1 Introduction

- Several measuring techniques for velocity determination in non-transparent fluids (ultrasonic and X-ray methods, hot wires, mechano-optical probes, magnetic probes, ....)
- Question: Is it possible to find a **non-intrusive** method to reconstruct (at least the global structure of) the velocity field in a conducting medium (exposed to an applied magnetic field) from the induced magnetic field in the outer space and the induced electric field at the fluid boundary?
- Preliminary work:
  - Baumgartl, Hubert, Müller (1993); Berkov, Gorn (1995); Kasuga, Fukai, Amano, Kumoyama (1993): Concentration on crystal growth applications, **Important disadvantage:** crucial influence of the **electric potential** at the fluid boundary on the magnetic field was not considered, Example:  $B_\phi$ -component for purely toroidal flow
  - Extensive work in biophysics, especially **Magnetoencephalography:** electric potential is correctly taken into account, many considerations about uniqueness, stability and regularization
  - Huge literature on inverse problems and regularization
- Aim of the present work: to apply the methods from magnetoencephalography to the MHD-case



● Scetch of a planned experiment



## 2 Forward problem

- Starting point: Induction equation for the magnetic field:

$$\frac{\partial \mathbf{B}}{\partial t} = \nabla \times (\mathbf{v} \times \mathbf{B}) + \frac{1}{\mu\sigma} \Delta \mathbf{B}$$

- Apply a steady magnetic field  $\mathbf{B}_0(\mathbf{r})$  and look for the deformation  $\mathbf{b}(\mathbf{r}, \mathbf{t})$ :

$$\frac{\partial \mathbf{b}}{\partial t} = \nabla \times (\mathbf{v} \times \mathbf{B}_0) + \nabla \times (\mathbf{v} \times \mathbf{b}) + \frac{1}{\mu\sigma} \Delta \mathbf{b}$$

- Two restrictions for the following work:

1. Steady (or slowly varying) flow :  $\frac{\partial \mathbf{b}}{\partial t} \rightarrow 0$
2.  $Rm = \mu\sigma vL < 1 \rightarrow$  Convective term  $\nabla \times (\mathbf{v} \times \mathbf{b})$  can be neglected

- Then: Poisson equation for the field  $\mathbf{b}(\mathbf{r})$ :

$$\Delta \mathbf{b}(\mathbf{r}) = -\mu\sigma \nabla \times (\mathbf{v} \times \mathbf{B}_0)$$

- Solution of the Poisson equation given in preliminary papers:

$$\begin{aligned} \mathbf{b}(\mathbf{r}) &= \frac{\mu\sigma}{4\pi} \int_V \frac{\nabla \times (\mathbf{v}(\mathbf{r}') \times \mathbf{B}_0(\mathbf{r}'))}{|\mathbf{r} - \mathbf{r}'|} dV' \\ &= \frac{\mu\sigma}{4\pi} \int_V (\mathbf{v}(\mathbf{r}') \times \mathbf{B}_0(\mathbf{r}')) \times \frac{\mathbf{r} - \mathbf{r}'}{|\mathbf{r} - \mathbf{r}'|^3} dV' \end{aligned}$$

is not general enough. It is only valid in an unbounded medium or for the special case  $\nabla \cdot (\mathbf{v} \times \mathbf{B}_0) = \mathbf{0}$ .

- Total current is:

$$\mathbf{j} = \sigma(\mathbf{E} + \mathbf{v} \times \mathbf{B}_0) = \sigma(-\nabla\varphi + \mathbf{v} \times \mathbf{B}_0)$$

- Biot-Savart law for  $\mathbf{b}$  has to take into account the total current:

$$\begin{aligned} \mathbf{b}(\mathbf{r}) &= \frac{\mu}{4\pi} \int_V \sigma(\mathbf{v}(\mathbf{r}') \times \mathbf{B}_0(\mathbf{r}') - \nabla\varphi(\mathbf{r}')) \times \frac{\mathbf{r} - \mathbf{r}'}{|\mathbf{r} - \mathbf{r}'|^3} dV' \\ &= \frac{\mu\sigma}{4\pi} \int_V (\mathbf{v}(\mathbf{r}') \times \mathbf{B}_0(\mathbf{r}')) \times \frac{\mathbf{r} - \mathbf{r}'}{|\mathbf{r} - \mathbf{r}'|^3} dV' \\ &\quad - \frac{\mu\sigma}{4\pi} \int_S \varphi(\mathbf{s}') \mathbf{n}(\mathbf{s}') \times \frac{\mathbf{r} - \mathbf{s}'}{|\mathbf{r} - \mathbf{s}'|^3} dS' \\ &= \mathbf{b}_V(\mathbf{r}) + \mathbf{b}_S(\mathbf{r}) \end{aligned}$$

- The total magnetic field distortion is a sum of a volume term and a surface term (coming from so-called "secondary currents")
- Electric potential must be computed additionally. Poisson equation for  $\varphi$  from continuity equation:

$$\begin{aligned} \nabla \cdot \mathbf{j} &= \nabla \cdot (\sigma(-\nabla\varphi + \mathbf{v} \times \mathbf{B}_0)) = 0 \\ \implies \Delta\varphi &= \nabla \cdot (\mathbf{v} \times \mathbf{B}_0) \end{aligned}$$

- Boundary conditions for  $\varphi$ : current must not leave the volume

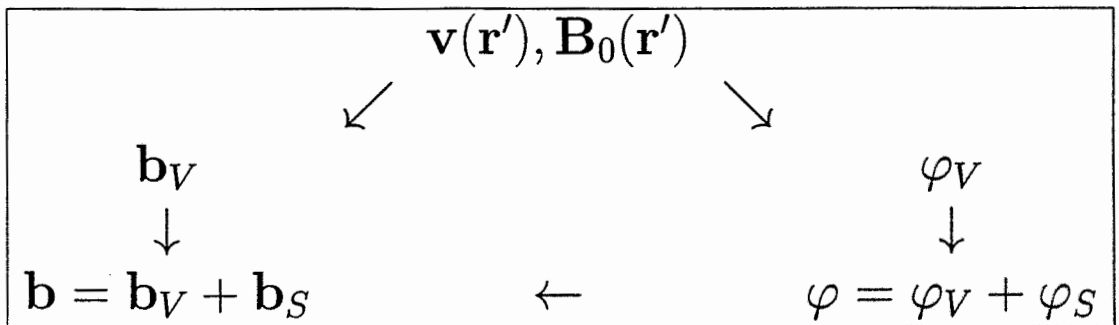
$$\frac{\partial\varphi}{\partial n} = 0$$

- If we are interested only in the potential at the boundary we can avoid the solution of the Poisson equation by using Greens identity.

⇒ Integral equation for  $\varphi$  (for  $\mathbf{s}$  at the boundary)

$$\begin{aligned} \varphi(\mathbf{s}) &= \frac{1}{2\pi G} \int (\mathbf{v}(\mathbf{r}') \times \mathbf{B}_0(\mathbf{r}')) \cdot \frac{\mathbf{s} - \mathbf{r}'}{|\mathbf{s} - \mathbf{r}'|^3} dV' \\ &\quad - \frac{1}{2\pi S} \int \varphi(\mathbf{s}') \mathbf{n}(\mathbf{s}') \cdot \frac{\mathbf{s} - \mathbf{s}'}{|\mathbf{s} - \mathbf{s}'|^3} dS' \\ &= \varphi_V + \varphi_S \end{aligned}$$

- General scheme for the forward problem



- Three examples of the forward problem: Poloidal, toroidal and mixed flow

- Total current is:

$$\mathbf{j} = \sigma(\mathbf{E} + \mathbf{v} \times \mathbf{B}_0) = \sigma(-\nabla\varphi + \mathbf{v} \times \mathbf{B}_0)$$

- Biot-Savart law for  $\mathbf{b}$  has to take into account the total current:

$$\begin{aligned} \mathbf{b}(\mathbf{r}) &= \frac{\mu}{4\pi} \int_V \sigma(\mathbf{v}(\mathbf{r}') \times \mathbf{B}_0(\mathbf{r}') - \nabla\varphi(\mathbf{r}')) \times \frac{\mathbf{r} - \mathbf{r}'}{|\mathbf{r} - \mathbf{r}'|^3} dV' \\ &= \frac{\mu\sigma}{4\pi} \int_V (\mathbf{v}(\mathbf{r}') \times \mathbf{B}_0(\mathbf{r}')) \times \frac{\mathbf{r} - \mathbf{r}'}{|\mathbf{r} - \mathbf{r}'|^3} dV' \\ &\quad - \frac{\mu\sigma}{4\pi} \int_S \varphi(\mathbf{s}') \mathbf{n}(\mathbf{s}') \times \frac{\mathbf{r} - \mathbf{s}'}{|\mathbf{r} - \mathbf{s}'|^3} dS' \\ &= \mathbf{b}_V(\mathbf{r}) + \mathbf{b}_S(\mathbf{r}) \end{aligned}$$

- The total magnetic field distortion is a sum of a volume term and a surface term (coming from so-called "secondary currents")
- Electric potential must be computed additionally. Poisson equation for  $\varphi$  from continuity equation:

$$\begin{aligned} \nabla \cdot \mathbf{j} &= \nabla \cdot (\sigma(-\nabla\varphi + \mathbf{v} \times \mathbf{B}_0)) = 0 \\ &\implies \Delta\varphi = \nabla \cdot (\mathbf{v} \times \mathbf{B}_0) \end{aligned}$$

- Boundary conditions for  $\varphi$ : current must not leave the volume

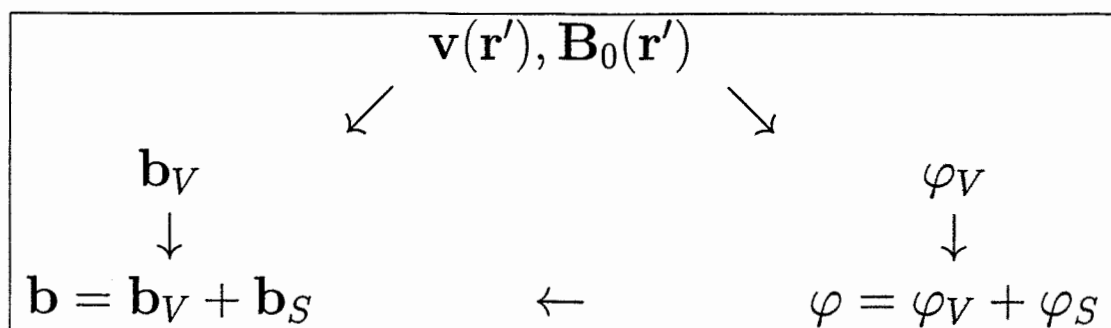
$$\frac{\partial\varphi}{\partial n} = 0$$

- If we are interested only in the potential at the boundary we can avoid the solution of the Poisson equation by using Greens identity.

⇒ Integral equation for  $\varphi$  (for  $\mathbf{s}$  at the boundary)

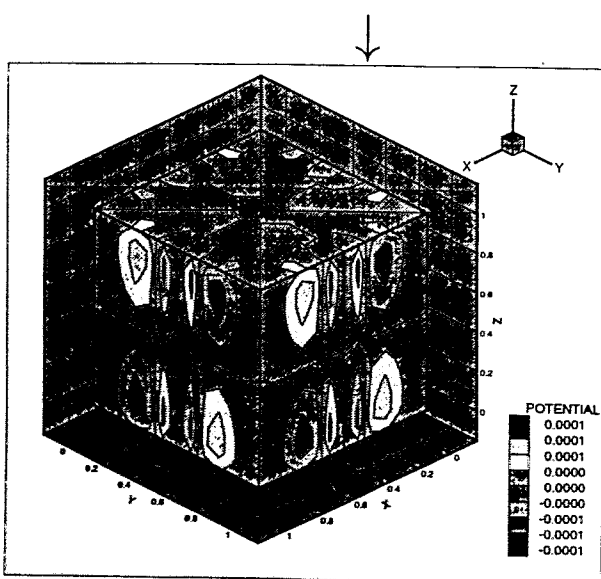
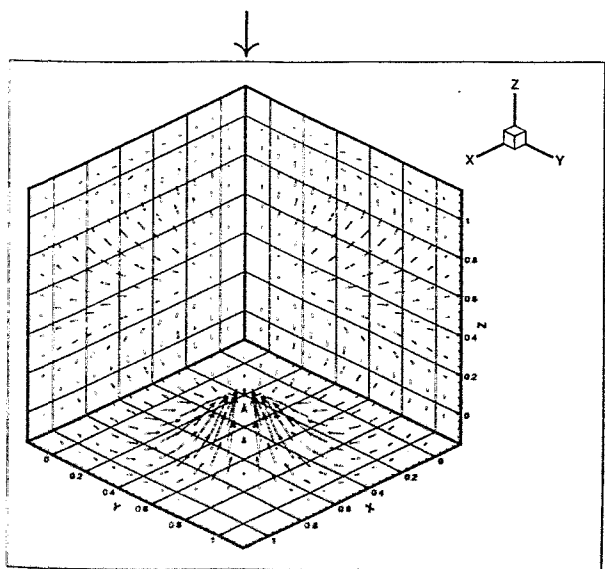
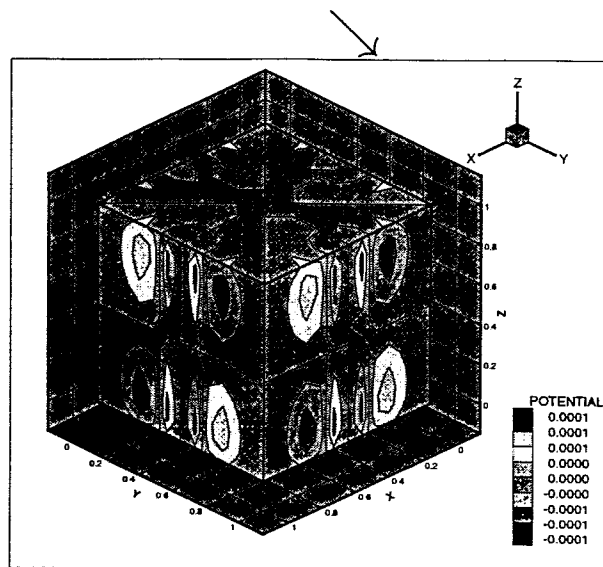
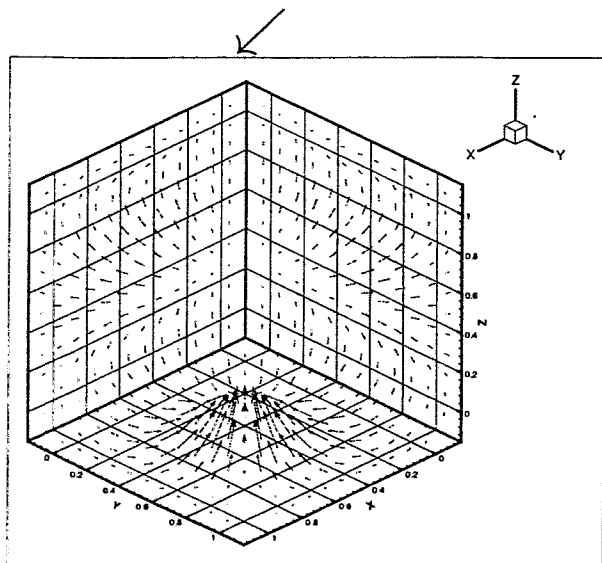
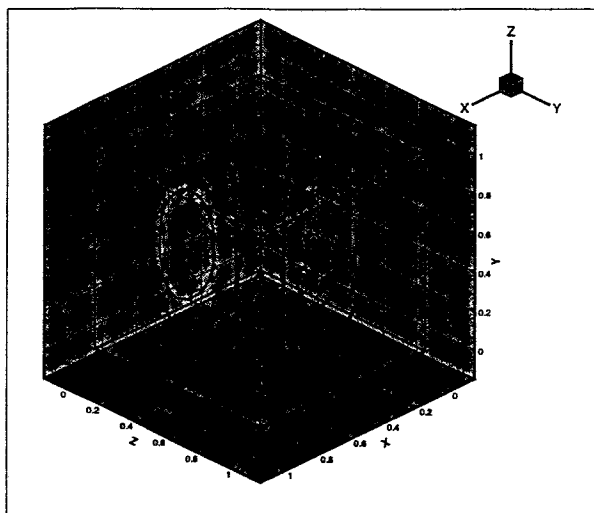
$$\begin{aligned} \varphi(\mathbf{s}) &= \frac{1}{2\pi G} \int (\mathbf{v}(\mathbf{r}') \times \mathbf{B}_0(\mathbf{r}')) \cdot \frac{\mathbf{s} - \mathbf{r}'}{|\mathbf{s} - \mathbf{r}'|^3} dV' \\ &\quad - \frac{1}{2\pi S} \int \varphi(\mathbf{s}') \mathbf{n}(\mathbf{s}') \cdot \frac{\mathbf{s} - \mathbf{s}'}{|\mathbf{s} - \mathbf{s}'|^3} dS' \\ &= \varphi_V + \varphi_S \end{aligned}$$

- General scheme for the forward problem

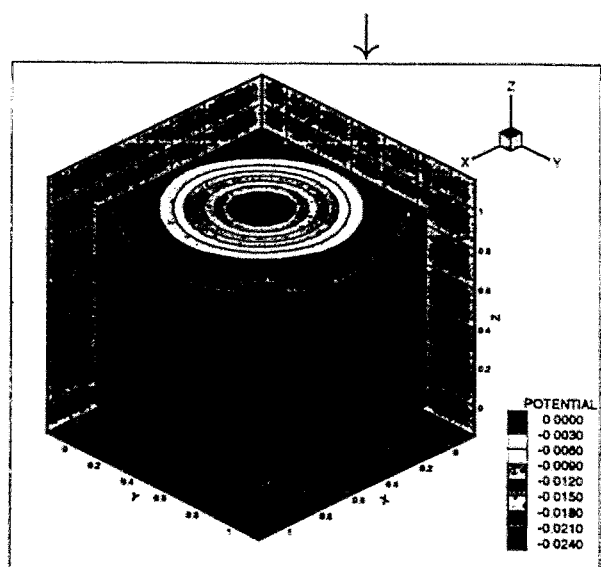
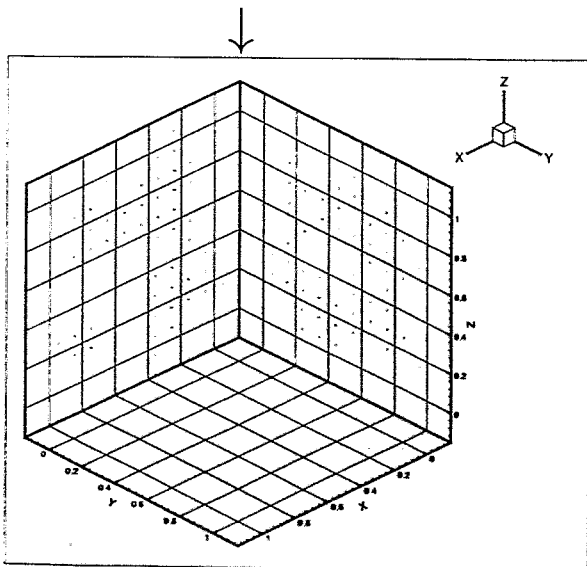
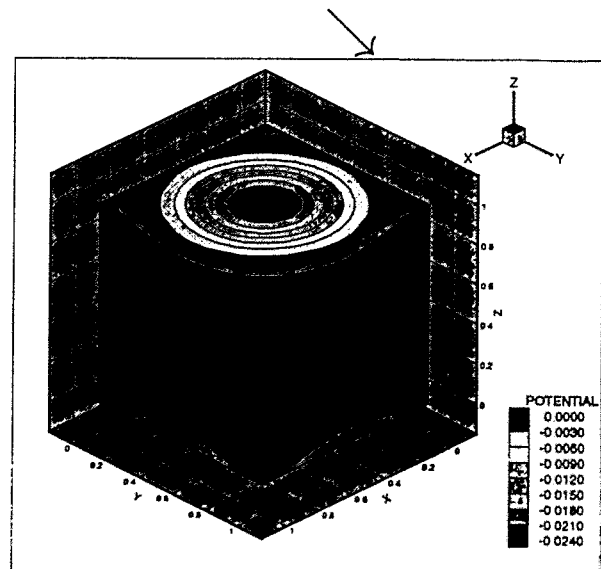
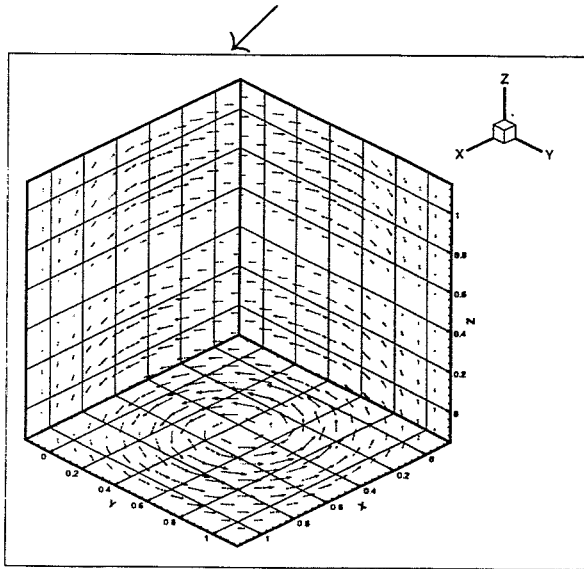
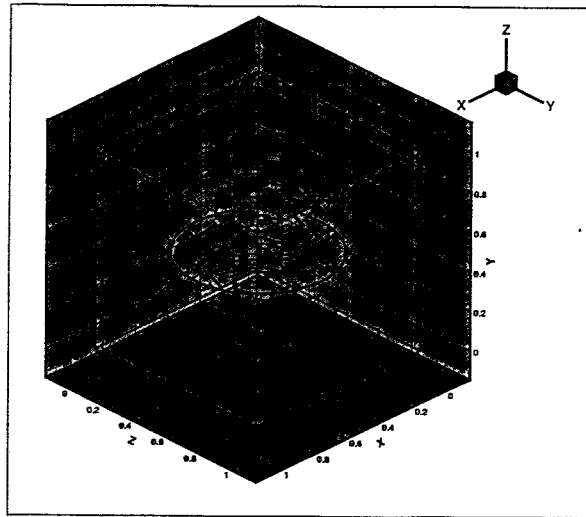


- Three examples of the forward problem: Poloidal, toroidal and mixed flow

● Example 1: Purely poloidal flow

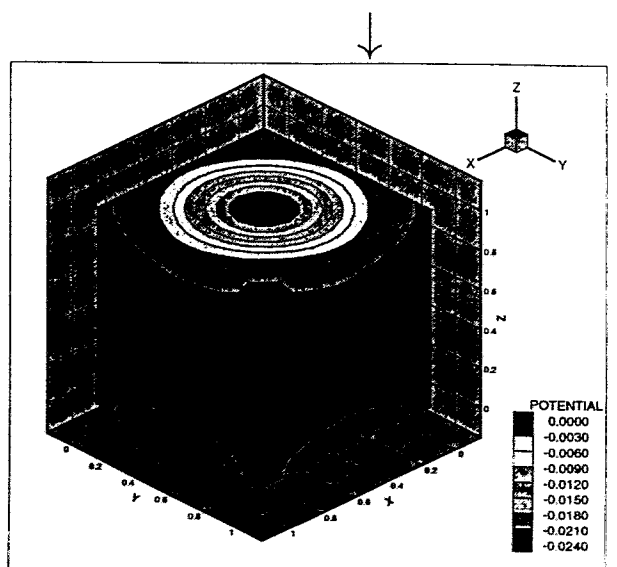
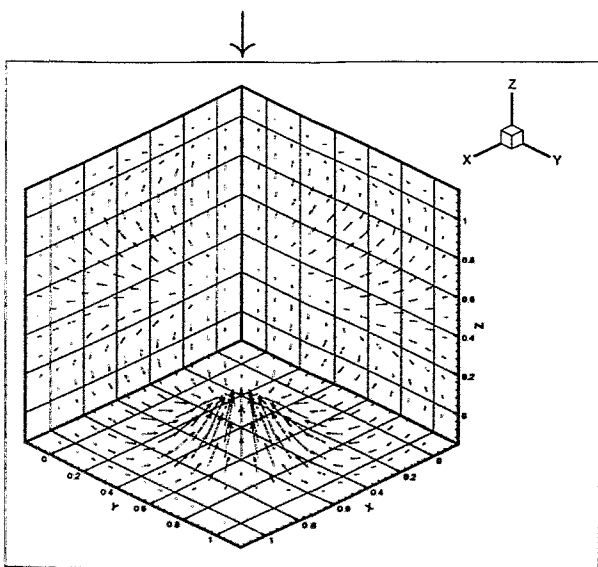
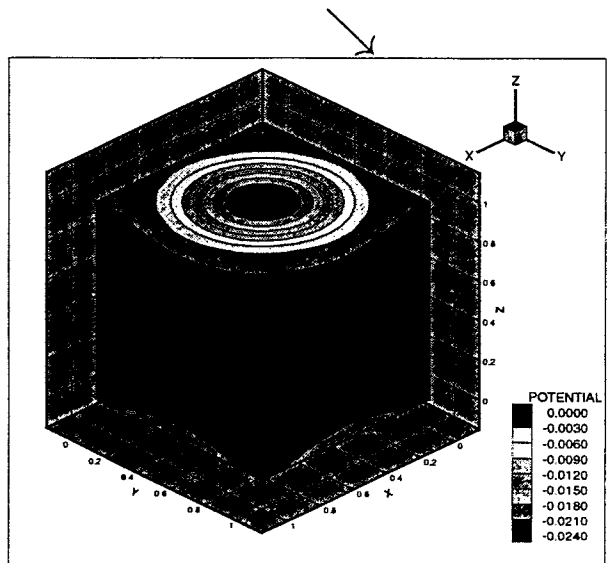
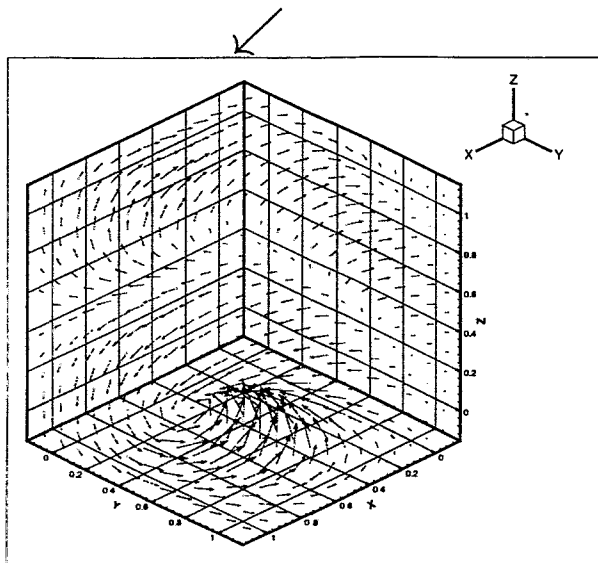
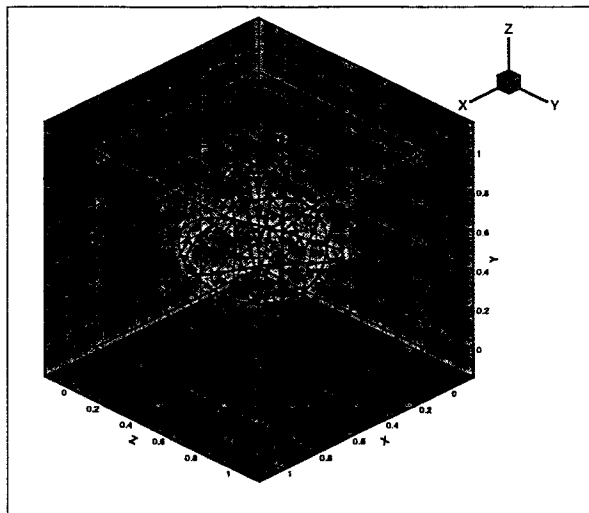


● Example 2: Purely toroidal flow





● Example 3: Addition of toroidal and poloidal flow



### 3 Inverse Problem

1. Magnetic field and electric potential are both measured values. Both are linearly dependent on the velocity field. But this dependence is complicated by means of the integral equation for  $\varphi$  at the surface and the dependence of  $\mathbf{b}$  on  $\varphi$ .

2. Problems of uniqueness and stability are typical for a wide class of inverse problems. A lot of different velocity fields provides (nearly) the same electric and magnetic field outside. Naive inversion yields unstable and unphysical solutions

1. Problem: What are the quantities the residual error of which can be minimized most easily? These are not the directly measurable quantities  $\mathbf{b}$  and  $\varphi$  but  $\mathbf{b}_V(\mathbf{r})$  and  $\varphi_V(\mathbf{r})$  for  $\mathbf{r}$  outside the fluid volume.

$$\begin{aligned}\mathbf{b}_V^m(\mathbf{r}) &= \mathbf{b}^m(\mathbf{r}) + \frac{\mu\sigma}{4\pi} \int_S \varphi^m(\mathbf{s}') \mathbf{n}(\mathbf{s}') \times \frac{\mathbf{r} - \mathbf{s}'}{|\mathbf{r} - \mathbf{s}'|^3} dS' \\ &= \frac{\mu\sigma}{4\pi} \int_V (\mathbf{v}(\mathbf{r}') \times \mathbf{B}_0(\mathbf{r}')) \times \frac{\mathbf{r} - \mathbf{r}'}{|\mathbf{r} - \mathbf{r}'|^3} dV'\end{aligned}$$

$$\begin{aligned}\varphi_V^m(\mathbf{r}) &= 0 + \frac{1}{4\pi} \int_S \varphi^m(\mathbf{s}') \mathbf{n}(\mathbf{s}') \cdot \frac{\mathbf{r} - \mathbf{s}'}{|\mathbf{r} - \mathbf{s}'|^3} dS' \\ &= \frac{1}{4\pi} \int_G (\mathbf{v}(\mathbf{r}') \times \mathbf{B}_0(\mathbf{r}')) \cdot \frac{\mathbf{r} - \mathbf{r}'}{|\mathbf{r} - \mathbf{r}'|^3} dV'\end{aligned}$$

2. Problem: For reasons of instabilities, it is not enough to minimize only the rms of the  $\mathbf{b}_V(\mathbf{r})$  and  $\varphi_V(\mathbf{r})$ . **Regularization** is needed in order to avoid unphysical solutions for  $\mathbf{v}$ . Examples for possible regularizing functionals: mean squared of the quantity itself, mean squared of the curvature.

- Total functional to be minimized:

$$F[\mathbf{v}] = F_B[\mathbf{v}] + F_\varphi[\mathbf{v}] + F_{div}[\mathbf{v}] + F_{pen}[\mathbf{v}] = Min$$

with

$$F_B[\mathbf{v}] = \frac{1}{\sigma_B^2} \sum_{i=1}^{NB} \left\{ \mathbf{b}_{V,i}^m - \frac{\mu\sigma}{4\pi} \sum_{k=1}^{NV} \left[ \Delta V_k (\mathbf{v}_k \times \mathbf{B}_{0k}) \times \frac{\mathbf{r}_i - \mathbf{r}_k}{|\mathbf{r}_i - \mathbf{r}_k|^3} \right] \right\}^2$$

$$F_\varphi[\mathbf{v}] = \frac{1}{\sigma_\varphi^2} \sum_{i=1}^{NP} \left\{ \varphi_{V,i}^m - \frac{1}{4\pi} \sum_{k=1}^{NV} \left[ \Delta V_k (\mathbf{v}_k \times \mathbf{B}_{0k}) \cdot \frac{\mathbf{r}_i - \mathbf{r}_k}{|\mathbf{r}_i - \mathbf{r}_k|^3} \right] \right\}^2$$

$$F_{div}[\mathbf{v}] = \frac{1}{\sigma_{div}^2} \sum_{k=1}^{NV} [\Delta V_k (\nabla \cdot \mathbf{v})_k]^2$$

$$F_{pen}[\mathbf{v}] = \frac{1}{\sigma_{pen}^2} \sum_{k=1}^{NV} [\Delta V_k (\nabla \cdot \nabla \mathbf{v})_k]^2$$

- Standard codes to solve the normal equations
- Scaling  $\sigma_{pen}^2$ , a curve

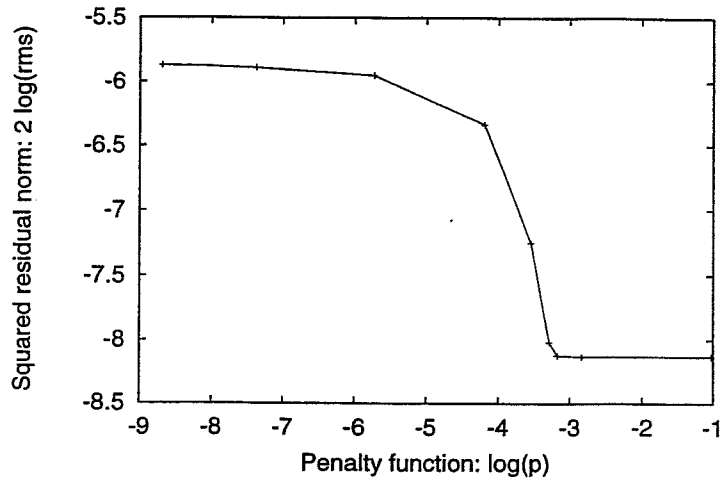
$$F_B[\mathbf{v}] + F_\varphi[\mathbf{v}] = F_{meas} [\sigma_{pen}^2 F_{pen}]$$

can be plotted (Tikhonov's L-curve). A reasonable solution  $\mathbf{v}$  is found at the point with the highest curvature of the L-curve. This can be checked by controlling the mean velocity and the empirical correlation coefficient

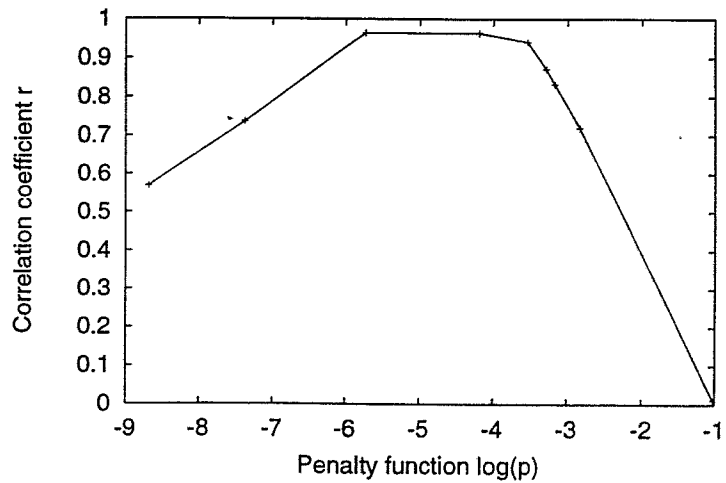
$$r = \frac{\sum_{k=1}^{NV} [(\mathbf{v}_k^{out} - \langle \mathbf{v}^{out} \rangle) \cdot (\mathbf{v}_k^{in} - \langle \mathbf{v}^{in} \rangle)]}{\sqrt{\sum_{k=1}^{NV} [(\mathbf{v}_k^{out} - \langle \mathbf{v}^{out} \rangle)]^2} \sqrt{\sum_{k=1}^{NV} [(\mathbf{v}_k^{in} - \langle \mathbf{v}^{in} \rangle)]^2}}$$

● Example 1: Purely poloidal flow

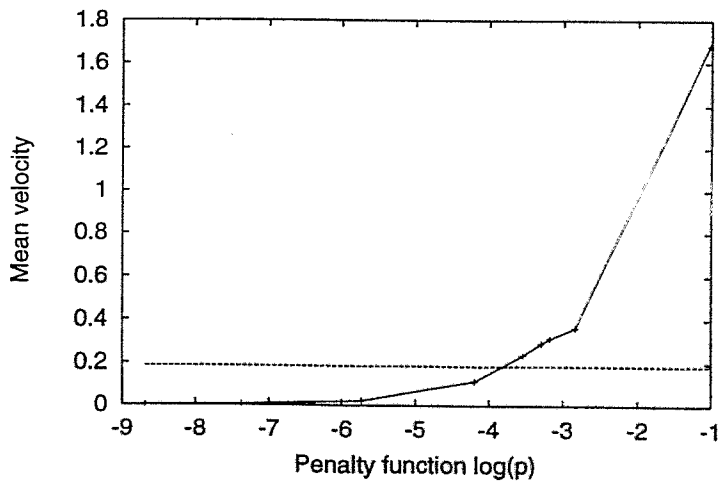
L-Curve:  
Squared residual norm



Empirical  
correlation  
coefficient

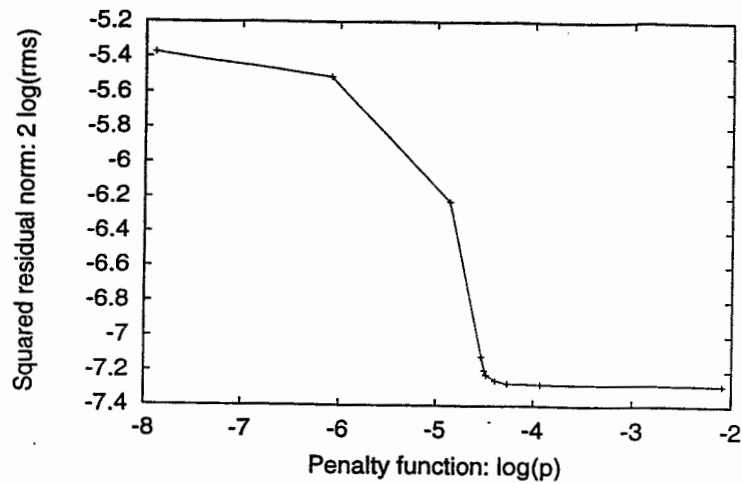


Mean velocity of the  
solution and  
real mean  
velocity

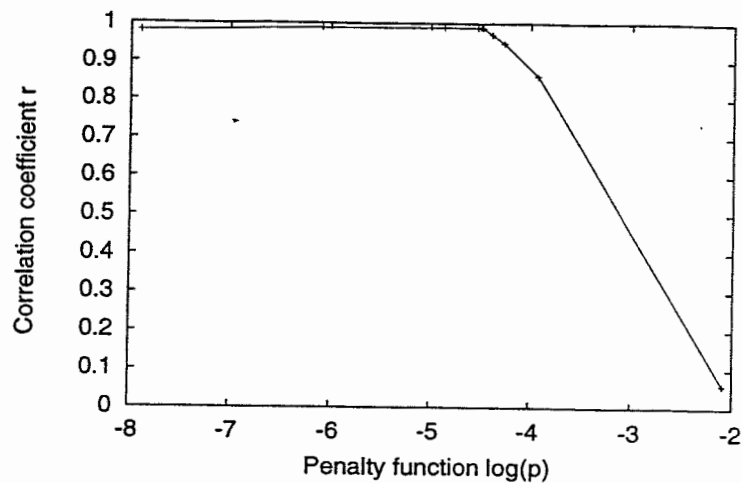


## ● Example 2: Purely toroidal flow

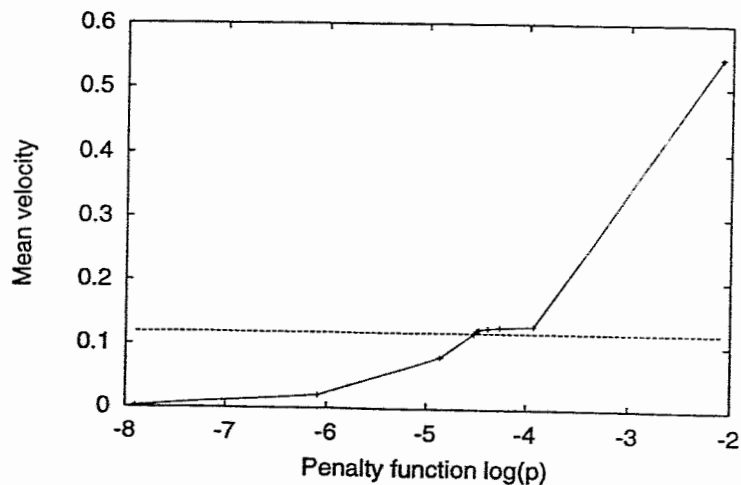
L-Curve:  
Squared residual norm



Empirical  
correlation  
coefficient

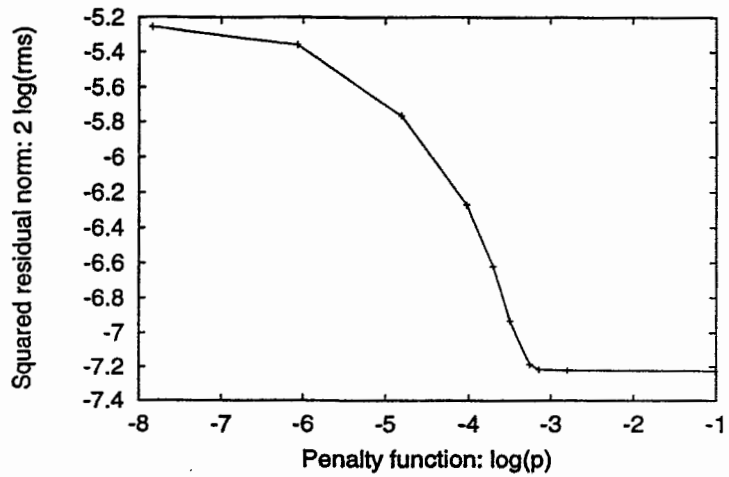


Mean velocity of the  
solution and  
real mean  
velocity

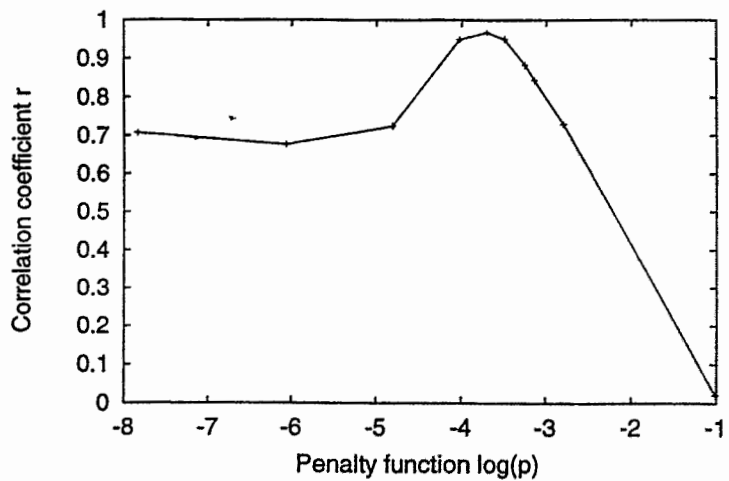


### ● Example 3: Addition of 1 and 2

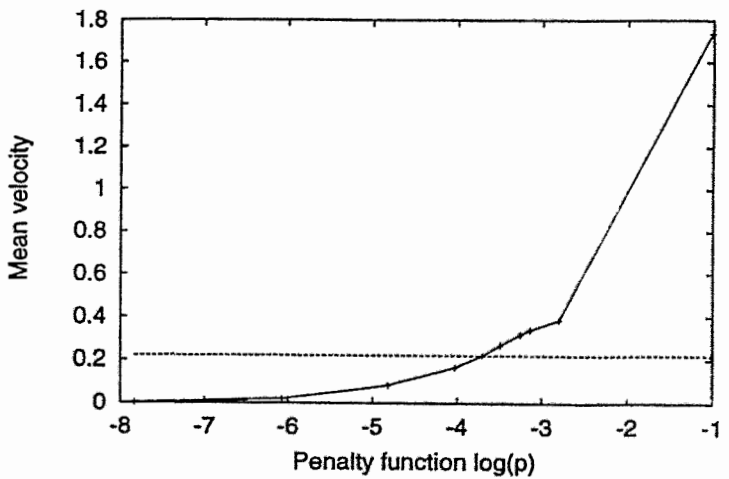
L-Curve:  
Squared residual norm



Empirical  
correlation  
coefficient



Mean velocity of the  
solution and  
real mean  
velocity



## 4 Uniqueness considerations

- Restriction to spherical geometry,  $\mathbf{B}_0 = B_0 \mathbf{e}_z$
- Representation of  $b_r$ ,  $\tilde{\varphi}$  with spherical harmonics:

$$b_r(r, \theta, \phi) = \sum_{l,m,\alpha} \frac{b_l^{m,\alpha}}{r^{(l+2)}} Y_l^{m,\alpha}(\theta, \phi), \quad \tilde{\varphi}(r, \theta, \phi) = \sum_{l,m,\alpha} \frac{\varphi_l^{m,\alpha}}{r^{(l+1)}} Y_l^{m,\alpha}(\theta, \phi)$$

- Representation of the velocity field in terms of defining scalars for the poloidal and the toroidal part:

$$\mathbf{v} = \mathbf{t} + \mathbf{s}, \quad \mathbf{t} = \nabla \times \left( T(r, \theta, \phi) \frac{\mathbf{r}}{r} \right), \quad \mathbf{s} = \nabla \times \nabla \times \left( S(r, \theta, \phi) \frac{\mathbf{r}}{r} \right)$$

$$T(r, \theta, \phi) = \sum_{l,m,\alpha} t_l^{m,\alpha}(r) Y_l^{m,\alpha}(\theta, \phi), \quad S(r, \theta, \phi) = \sum_{l,m,\alpha} s_l^{m,\alpha}(r) Y_l^{m,\alpha}(\theta, \phi)$$

- Information: two scalars in **2D**, Desired quantities: two scalars in **3D**  $\Rightarrow$  **Non-uniqueness**

- Resulting coupling equations for the quantities:

$$b_l^{m,\alpha} = \tilde{E}_l^{m,\alpha} \int_0^R dr r^{l+1} t_l^{m,\bar{\alpha}}(r) + \tilde{F}_l^{m,\alpha} \int_0^R dr r^l s_{l-1}^{m,\alpha}(r)$$

$$\varphi_l^{m,\alpha} = \tilde{G}_l^{m,\alpha} \int_0^R dr r^l t_{l-1}^{m,\alpha}(r) \quad \text{with some prefactors } \tilde{E}, \tilde{F}, \tilde{G}$$

- Using regularization (with kinetic energy as regularizing functional) a unique solution can be constructed:

$$t_l^{m,\alpha}(r) = \frac{\varphi_{l+1}^{m,\alpha}}{G_{l+1}^{m,\alpha}} r^{l+1}$$

$$s_l^{m,\alpha}(r) = \frac{1}{F_{l+1}^{m,\alpha}} \left[ b_{l+1}^{m,\alpha} - \frac{E_{l+1}^{m,\alpha}}{G_{l+2}^{m,\alpha}} \varphi_{l+2}^{m,\bar{\alpha}} \right] r^{l+1} \left( 1 - \frac{r^2}{R^2} \right)$$

with some factors  $E, F, G$

## 5 References and outlook

- Basic facts and numerical results:

Stefani, F., Gerbeth, G.: 1999, *Velocity reconstruction in conducting fluid from magnetic field and electric potential measurements*, Inverse Problems, **15**, 771-786

- Uniqueness considerations:

Stefani, F., Gerbeth, G.: 1999, *On the uniqueness of velocity reconstruction in conducting fluids from measurements of induced electromagnetic fields*, Inverse Problems, submitted

- Planned experiment with In-Ga-Sn, cylindrical vessel, 32 Hall sensors and potential probes

- A lot of remaining problems:

- Generalization for non-stationary flows
- Conducting walls
- Generalization to higher  $Rm \Rightarrow$  Inverse dynamo theory
- Can we go beyond regularization in order to get reliable information about the radial dependence?  $\Rightarrow$  Presumably yes, measuring decay times for different modes.



# Experimental determination of turbulent flow characteristics, temperature and electromagnetic force density fields in the melt of induction furnaces

Dr.-Ing. Egbert Baake

Prof. Dr.-Ing. Dr. h.c. Alfred Mühlbauer

Institute for Electroheat, University of Hannover

## Abstract:

The experimental determination of electromagnetic, hydrodynamic and thermal fields is indispensable for the evaluation of computer simulation results. For more than ten years the Institute for Electroheat, University of Hannover, has experience in the development and application of different measurement techniques for turbulent metal flows in induction furnaces. This paper describes the used measurement systems and presents various results along with selected examples of the determination of particular fluctuation rates and time averaged flow velocities, temperature and electromagnetic force density distributions in the melt of different induction furnaces, e.g. induction channel and induction crucible furnaces.

Wood's metal, which has a melting point of 72°C is used as a model melt. The hydrodynamic studies are carried out using permanent magnetic sensors [1]. The velocity sensors are calibrated with a self developed rotating channel. Due to the detected decrease of the magnetization of the permanent magnets by the influence of temperature and strong alternating magnetic fields in the melt, a remagnetization of the permanent magnet sensors is necessary. Therefore a self constructed remagnetization device is used and the magnetization is checked using a *Hall*-sensor. The use of two types of sensors allows three-dimensional investigations. The fluctuation rates are measured with a scanning rate of 20 Hz in order to determine the characteristics of the turbulence: the turbulent kinetic energy, the dissipation rate and the turbulent viscosity. The autocorrelation analysis of the local flow velocity components in different zones in the melt of the induction furnaces are investigated and show low frequency fluctuations with different, position dependent oscillation frequencies in the range of lower than 10 Hz.

In addition to the mainly used Wood's metal, local flow velocity measurements in the melt of Aluminium are carried out. Due to the high temperature level of 700°C, permanent magnet sensors are unsuitable. Therefore the velocity measurements in liquid aluminium are realized using a self developed electromagnetic sensor [2].

In parallel to the local flow velocities the temperature distribution in the melt is investigated using embedded thermocouples. By this way the correlation analysis between the local flow velocity and the local temperature fluctuations is carried out in order to analyse the heat and mass transfer in the melt.

The local current density and the magnetic flux density in the melt of induction furnaces are measured with a scanning rate of 10 kHz in order to determine the electromagnetic force density distribution. For this the phase angle between current density and magnetic flux density has to be defined by simultaneously measuring of the inductor current with a *Rogowski* belt.

## References:

- [1] Ricou, R., Vivés, C.: Local Velocity and Mass Transfer Measurements in Molten Metals using an incorporated Magnet Probe. *Int. Jo. Heat Transfer*, Vol. 25, 1982, No. 10, pp. 1579-1588.
- [2] Baake, E.: Grenzleistungs- und Aufkohlungsverhalten von Induktions-Tiegelöfen. VDI-Verlag, Düsseldorf, 1994, 42 pp.

# **Experimental determination of turbulent flow characteristics, temperature and electromagnetic force density fields in the melt of induction furnaces**

Egbert Baake, Alfred Mühlbauer  
Institute for Electroheat, University of Hannover

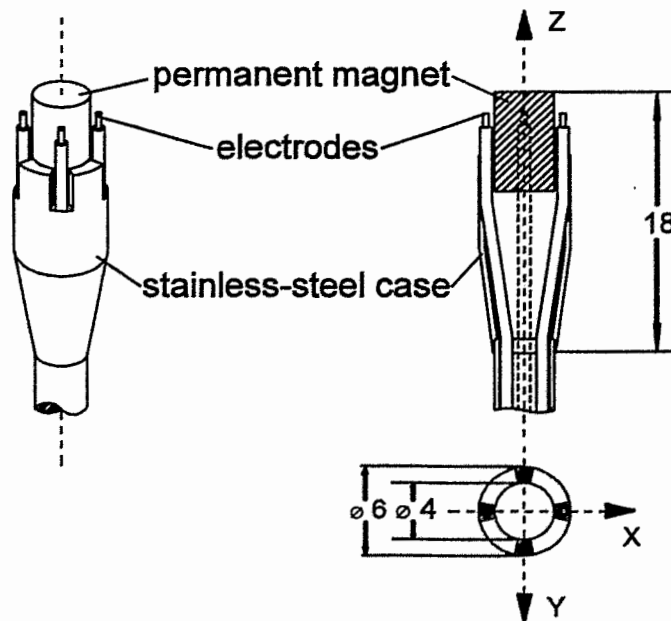
- Introduction
- Measurement systems
- Examples and results
- Conclusions

- Numerical simulation tools are of increasing importance in scientific research and development
- Experimental investigations are indispensable for the evaluation of computer simulation results
- Institute for Electroheat has many years of experience in the development and application of measuring techniques for liquid metal flows
- Turbulent melt flow velocity, temperature and electromagnetic force density fields in the melt of different induction furnaces

## Material properties of cast iron, aluminium and Wood's-metal

	cast iron	aluminium	Wood's-metal
density [ $10^3 \text{ kg/m}^3$ ]	6.8 (1700°C)	2.3 (900°C)	9.4 (85°C)
melting point [°C]	1500	660	74
electric conductivity [ $10^6 \text{ 1}/(\Omega \cdot \text{m})$ ]	0.72 (1535°C)	2.8 - 4.2 (700°C)	1 (80°C)
dynamic viscosity [ $10^{-3} \text{ Ns/m}^2$ ]	5.6 (1700°C)	1.29 (700°C)	4.2 (85°C)
kinematic viscosity [ $10^{-6} \text{ m}^2/\text{s}$ ]	0.82	0.56	0.45
specific heat [Ws/(kg·K)]	775 (1500°C)	1133 (800°C)	168 (85°C)

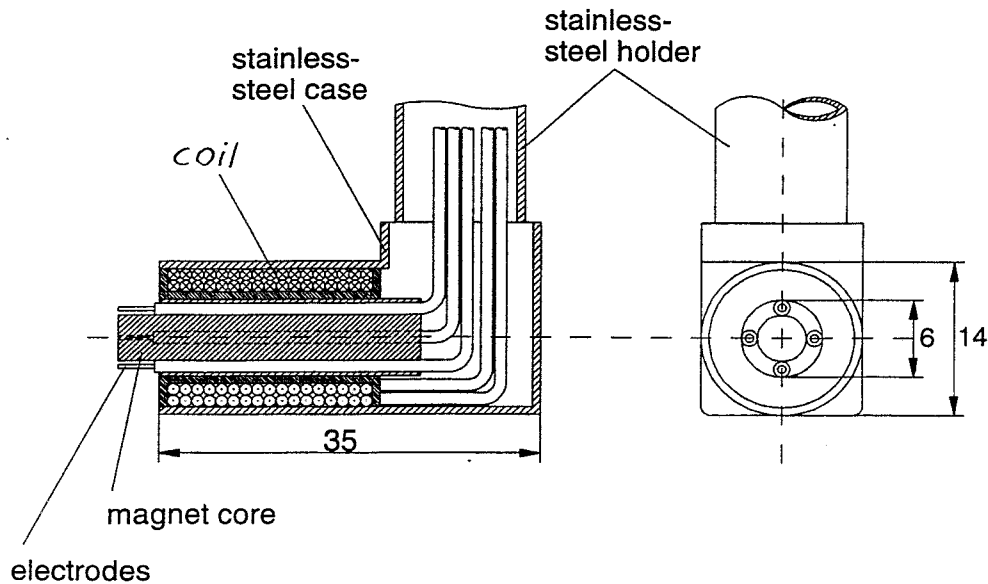
## Permanent magnet sensor (Vivés)



### Features of the permanent magnet sensor:

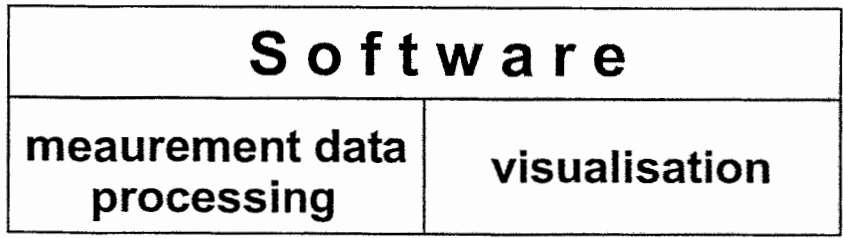
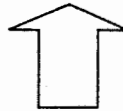
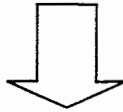
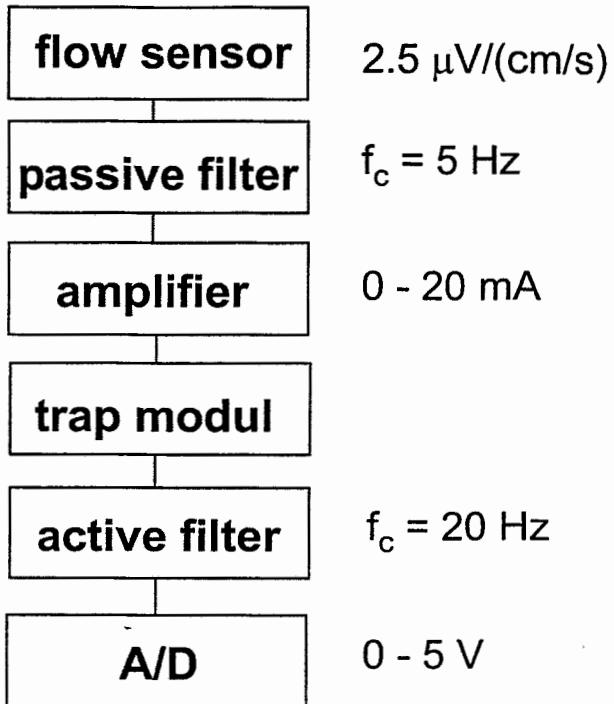
- type of magnet: Alnico 450
- calibrated with rotating channel
- use in Wood's metal up to  $150^{\circ}\text{C}$
- decrease of magnetization by temperature and magnetic field
- remagnetization by self constructed special DC-high current coil
- checking of magnetization using *Hall*-sensor
- well established, high reliability
- relatively easy to handle

## Electro magnet sensor

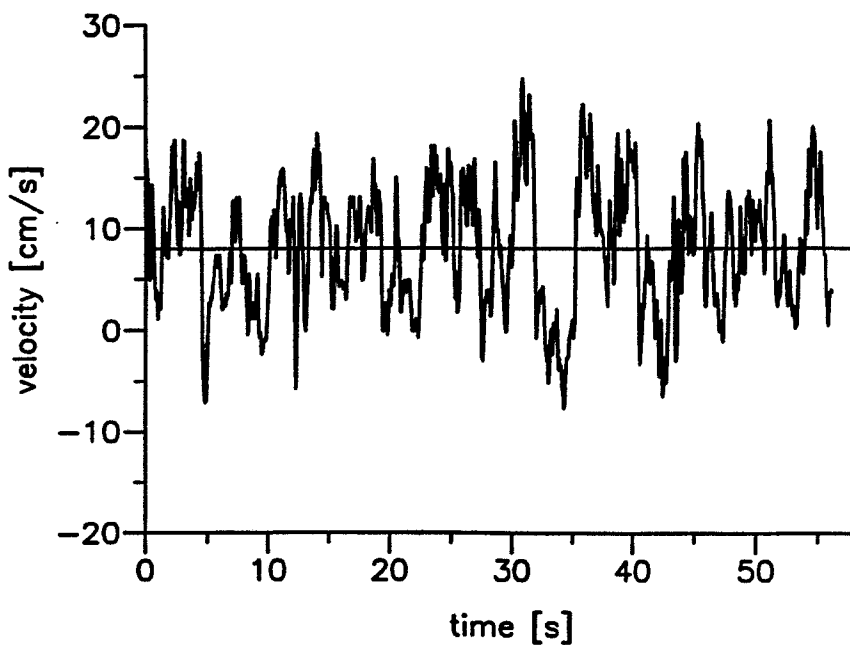


### Features of the electro magnet sensor:

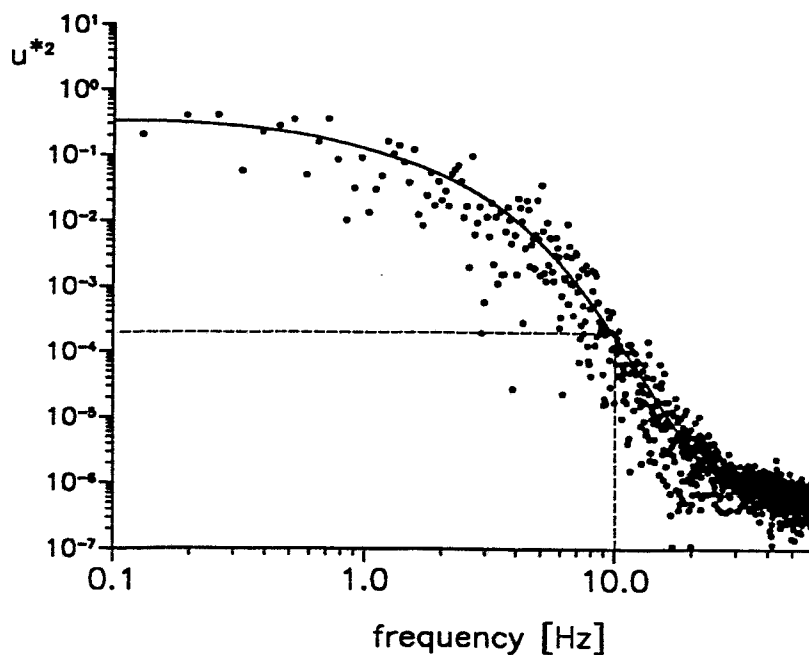
- self constructed and well tested
- coil feeded by DC current of 10 A
- sensitivity four times lower than the permanent magnet sensor
- used in Aluminium up to 750°C
- lifetime in a range of 15...30 min due to the aggressive aluminium melt
- not so easy to handle



### Chronological plot of the melt flow velocity

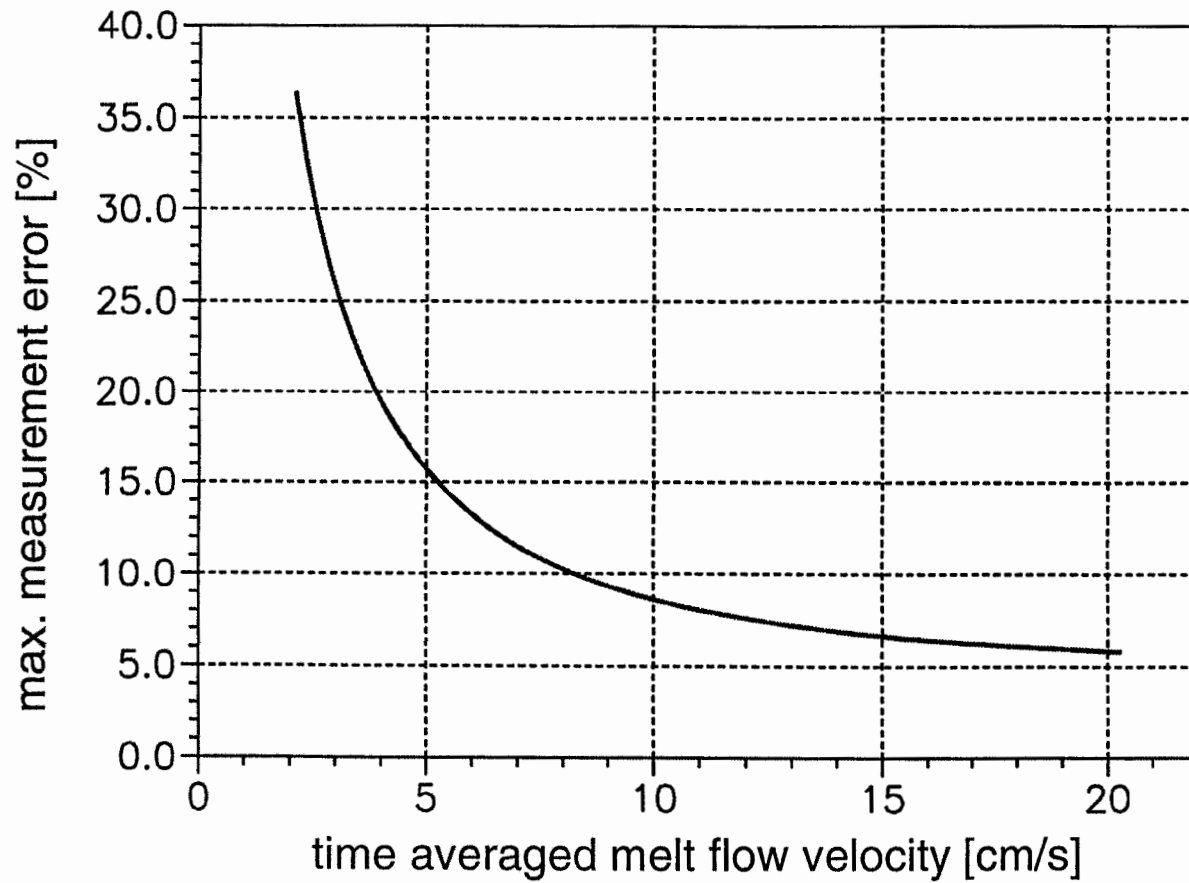


### Spectrum of the melt flow velocity





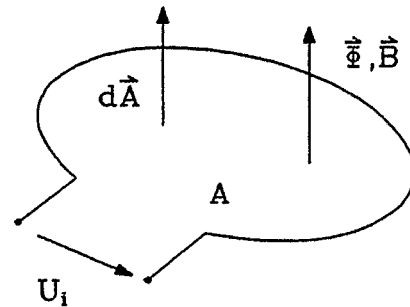
### Maximum of the measurement error in dependence on the time averaged flow velocity



## Determination of the electromagnetic force density in the melt of induction furnaces

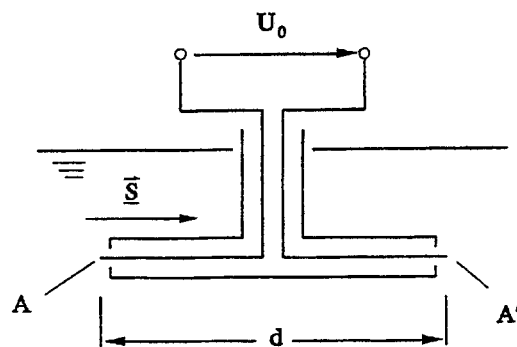
### magnetic flux density

- small measuring coils
- scanning rate 10 kHz



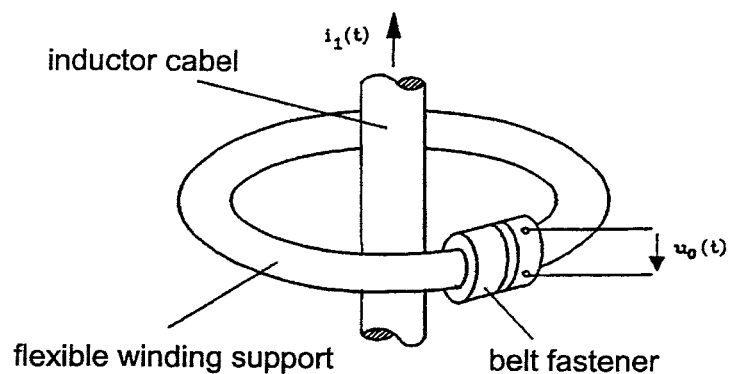
### current density

- potential sensor
- scanning rate 10 kHz



### inductor current

- magnetic voltage meter  
(*Rogowski-belt*)

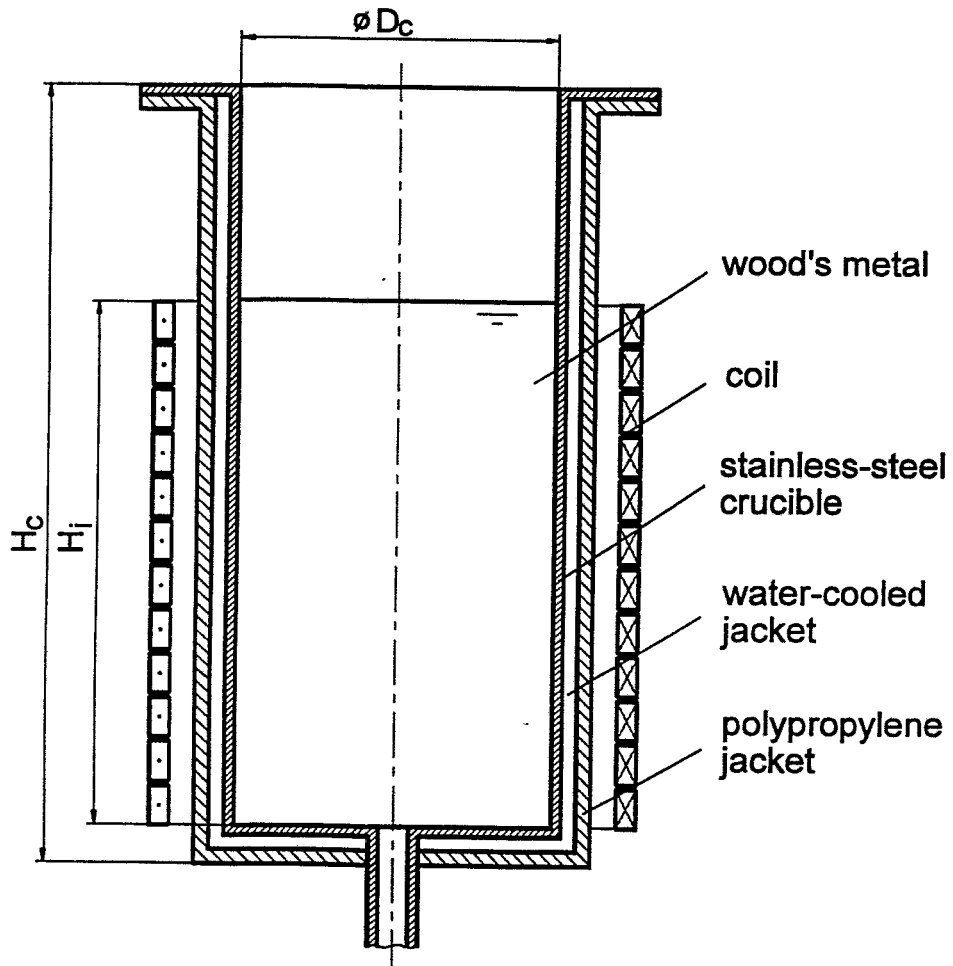


furnace model 1

$D_c = 316$  mm  
 $H_c = 756$  mm  
 $H_i = 570$  mm  
 $V = 45$  dm<sup>3</sup>  
 $m = 450$  kg  
 $P_{sp.} = 170$  kW/t

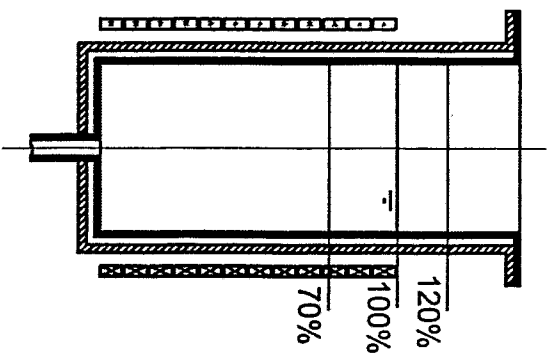
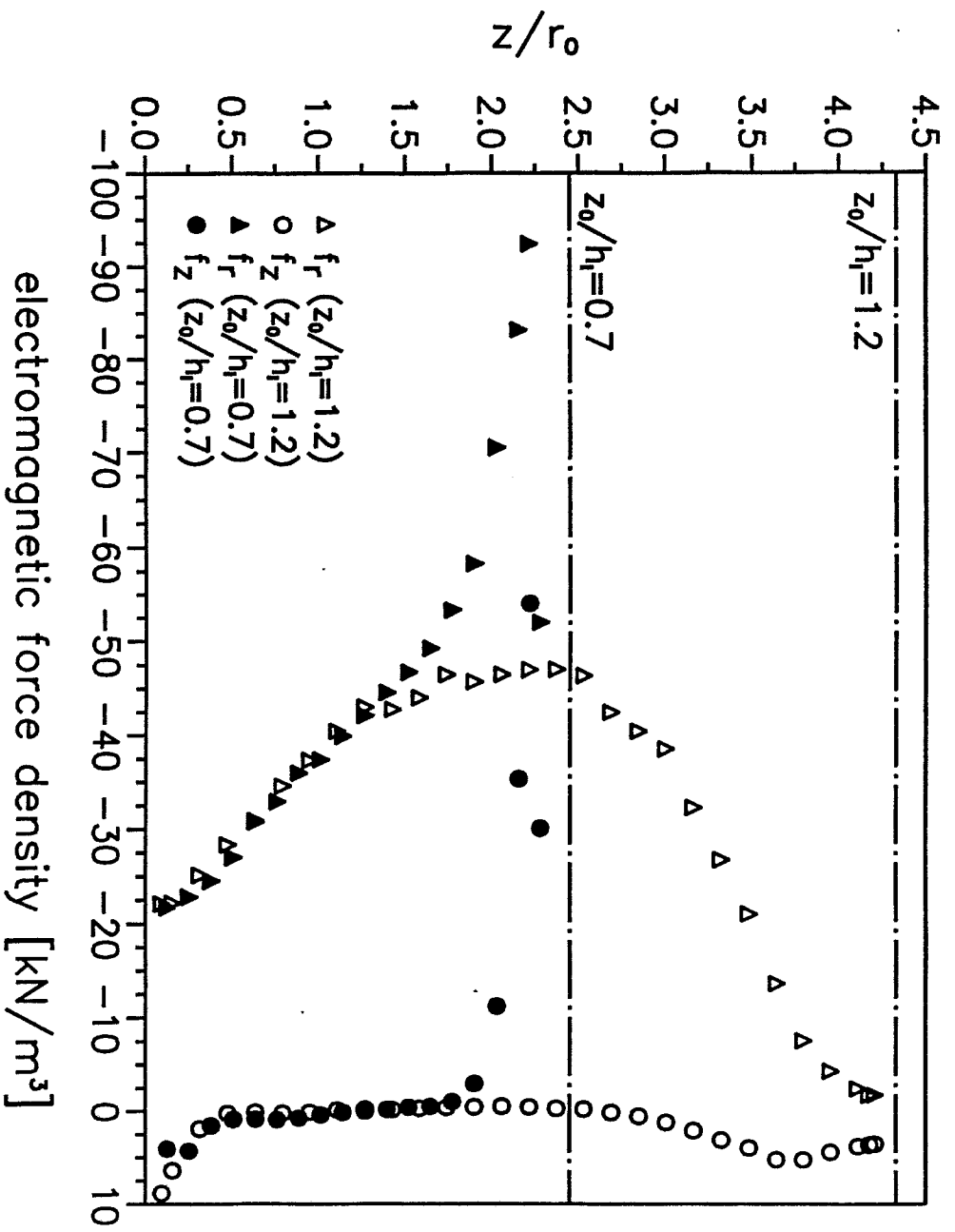
furnace model 2

$D_c = 170$  mm  
 $H_c = 383$  mm  
 $H_i = 235$  mm  
 $V = 5.3$  dm<sup>3</sup>  
 $m = 53$  kg  
 $P_{sp.} = 1600$  kW/t



power range :  $P = 10 - 100$  kW

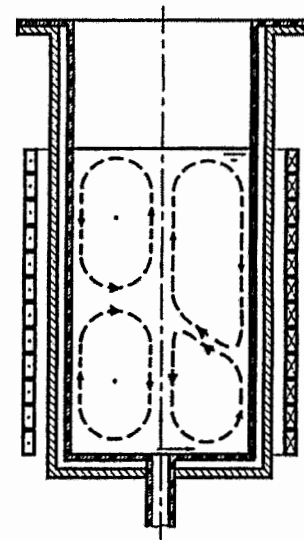
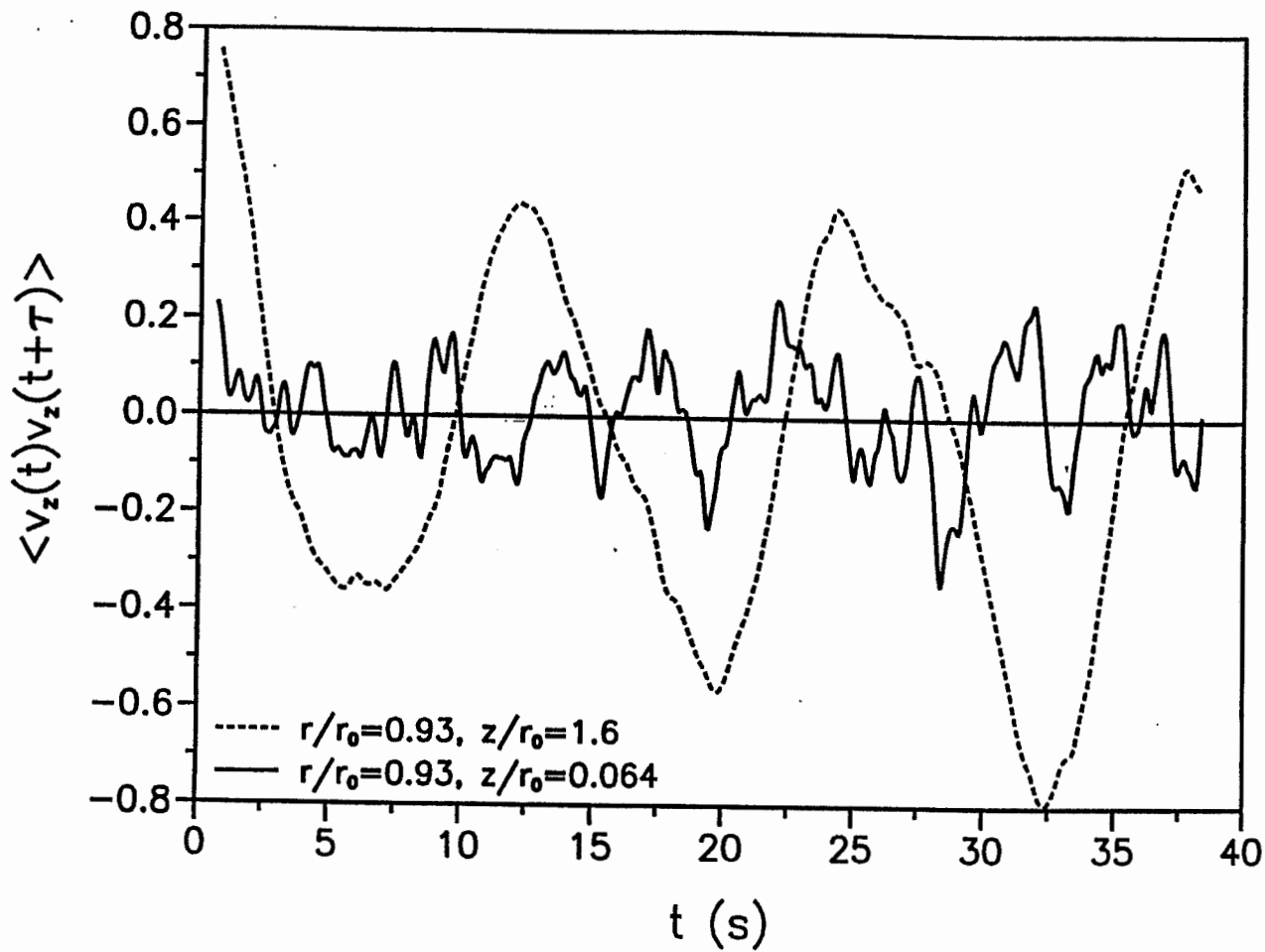
frequency range:  $f = 300 - 4000$  Hz  
 $\omega = 20 - 900$



**EWVH**

Experimentally determined axial distribution of the radial and axial components of the electromagnetic force density in the melt near the crucible wall

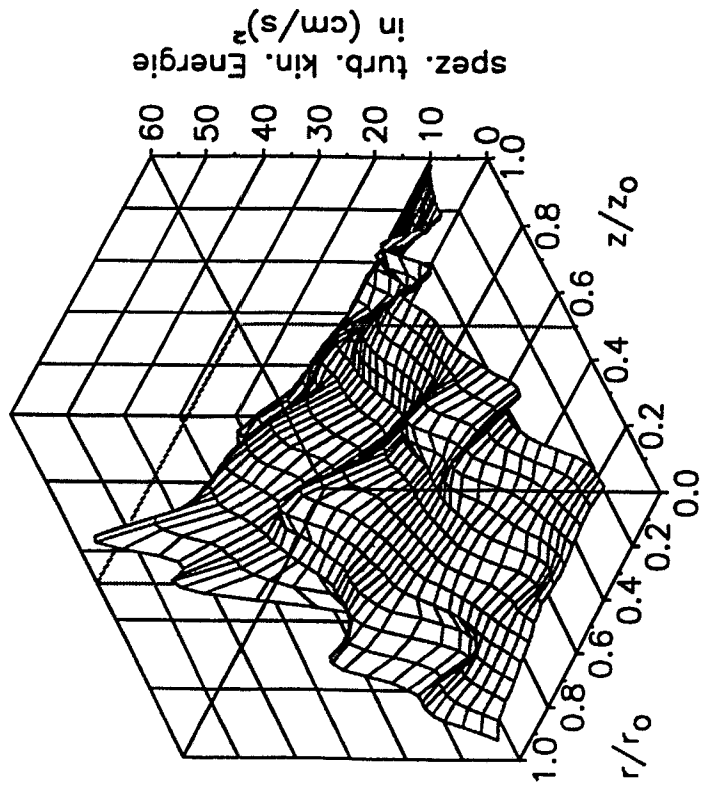
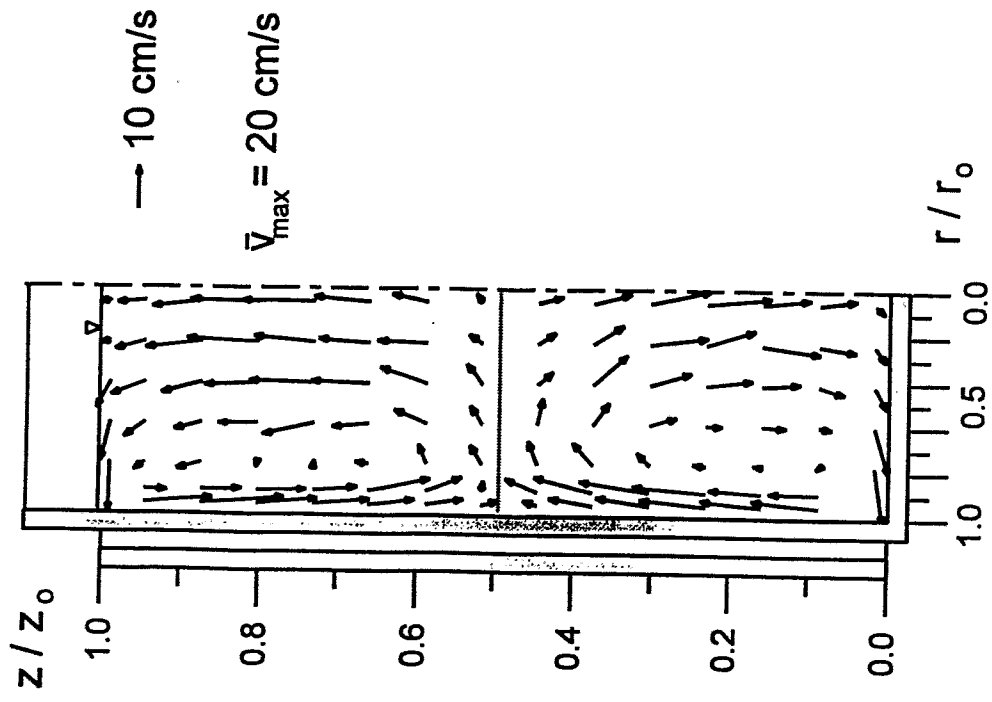
10/9 - 65



**EWH**

Autocorrelation analysis of the experimentally determined axial component of the local flow velocities in different regions of the melt

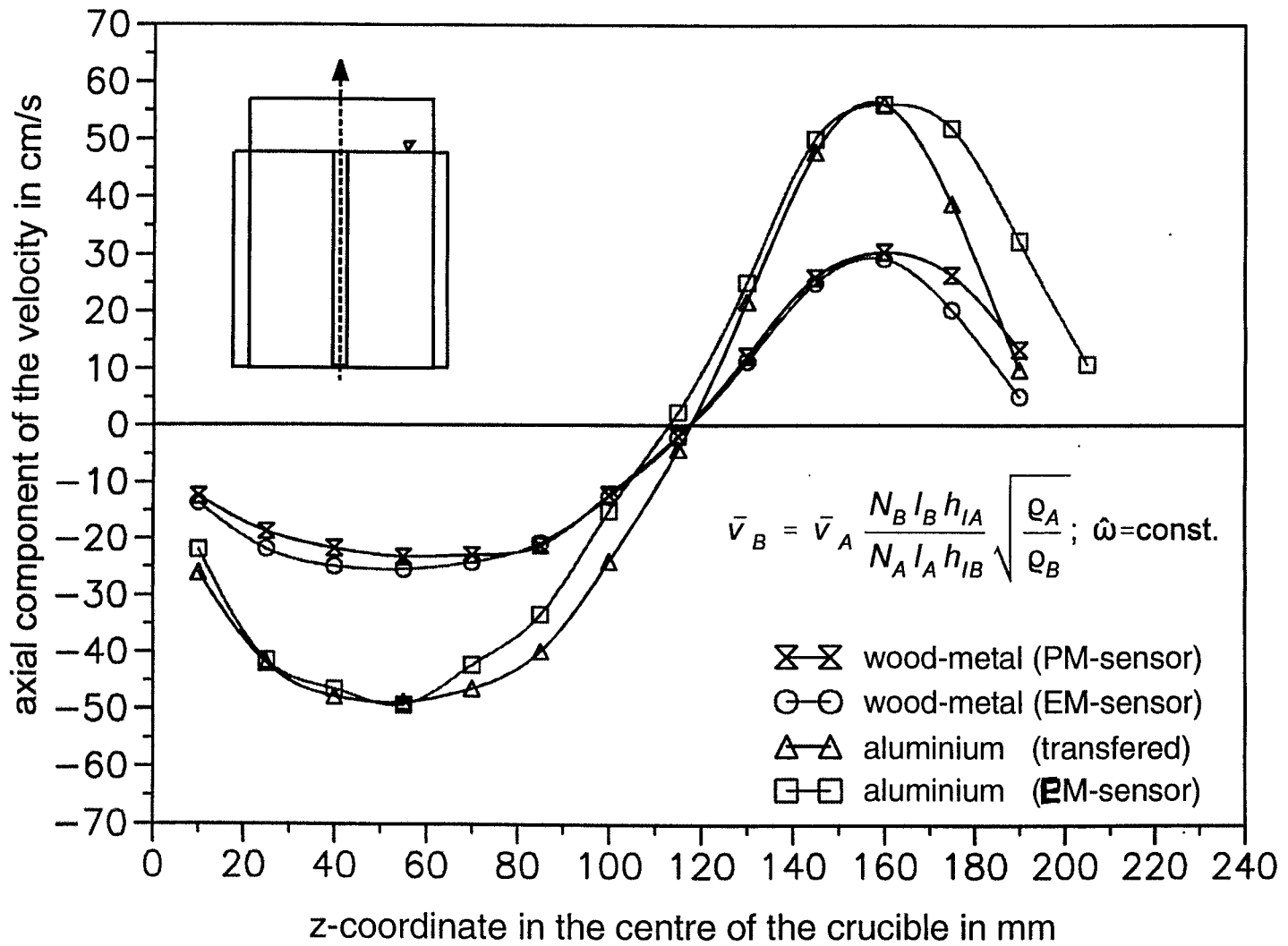
10/9 -55

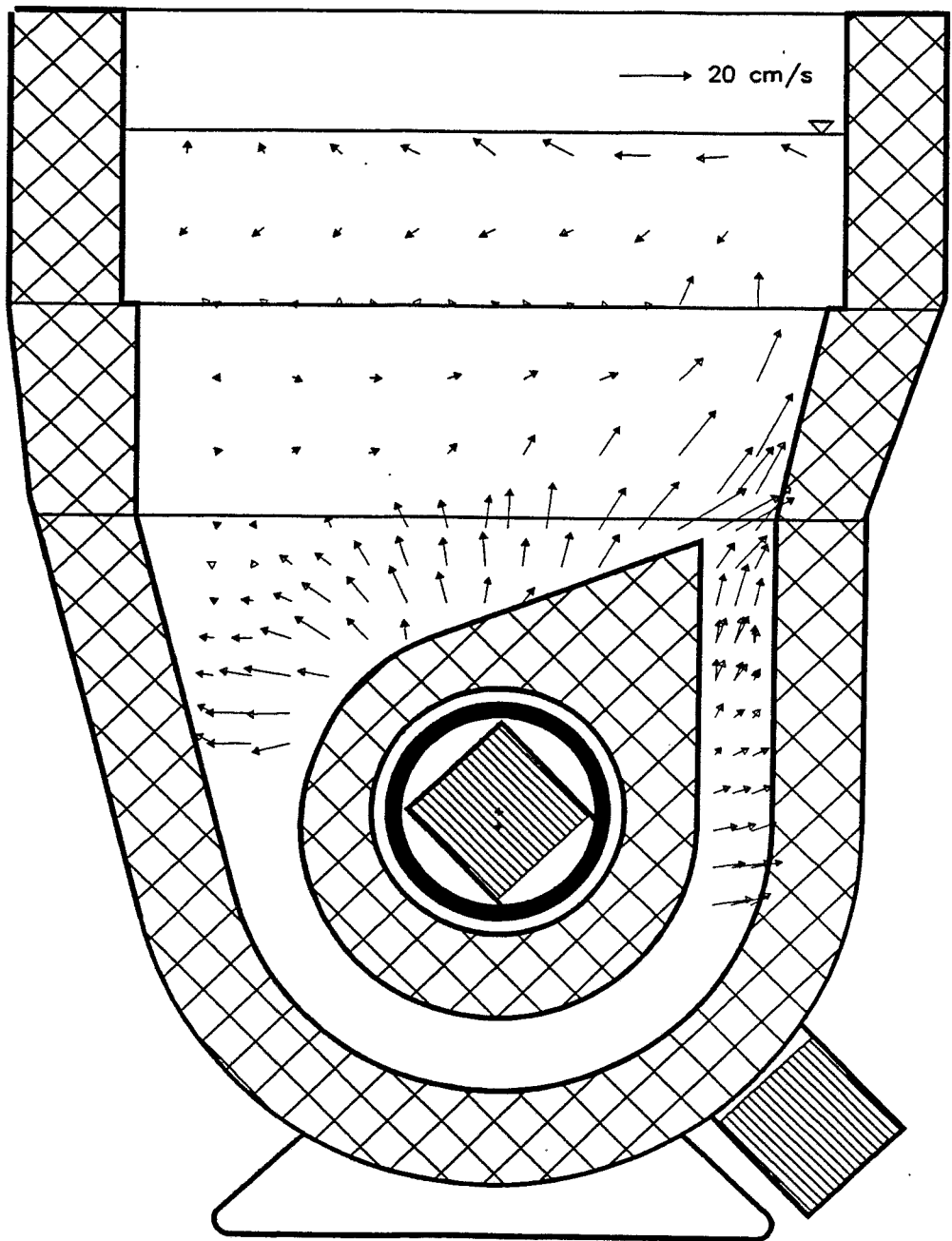


$I = 2000 A / f = 400 \text{ Hz}$

**EWH**

Time averaged velocity and specific kinetic energy of turbulence



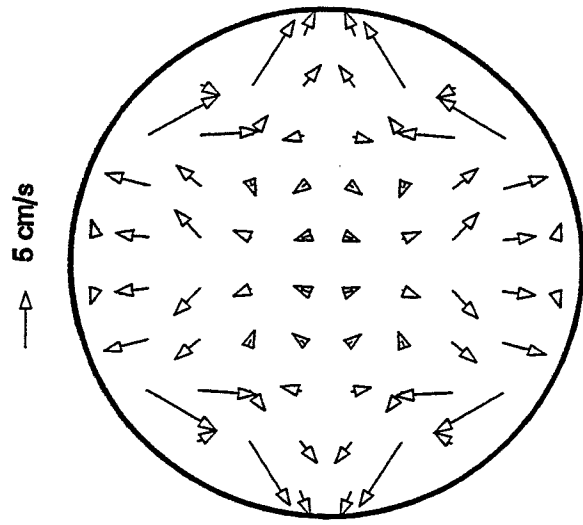
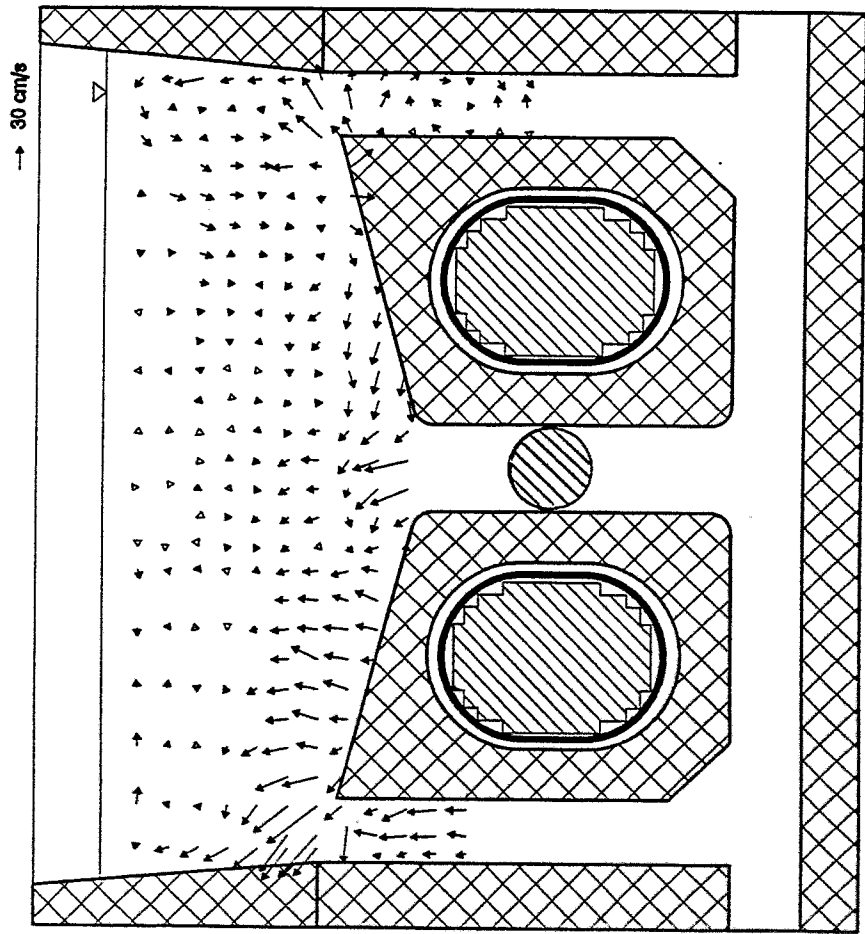


**EWH**

Measured melt flow velocity distribution in a  
single-loop induction channel furnace

10/9 - 90



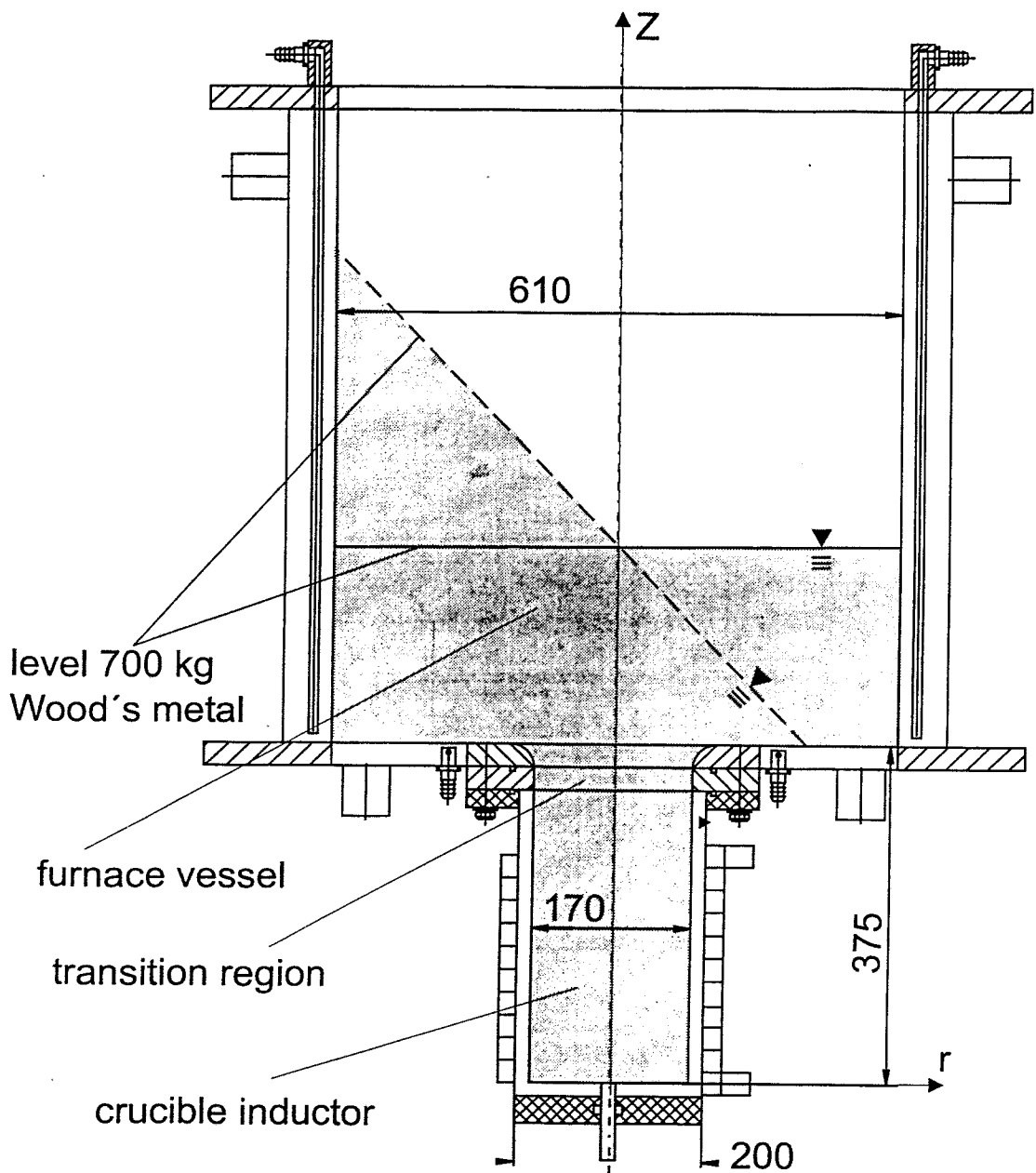


**EWH**

Measured melt flow velocity distribution in a double-loop induction channel furnace

10/9 - 95

# Experimental set-up

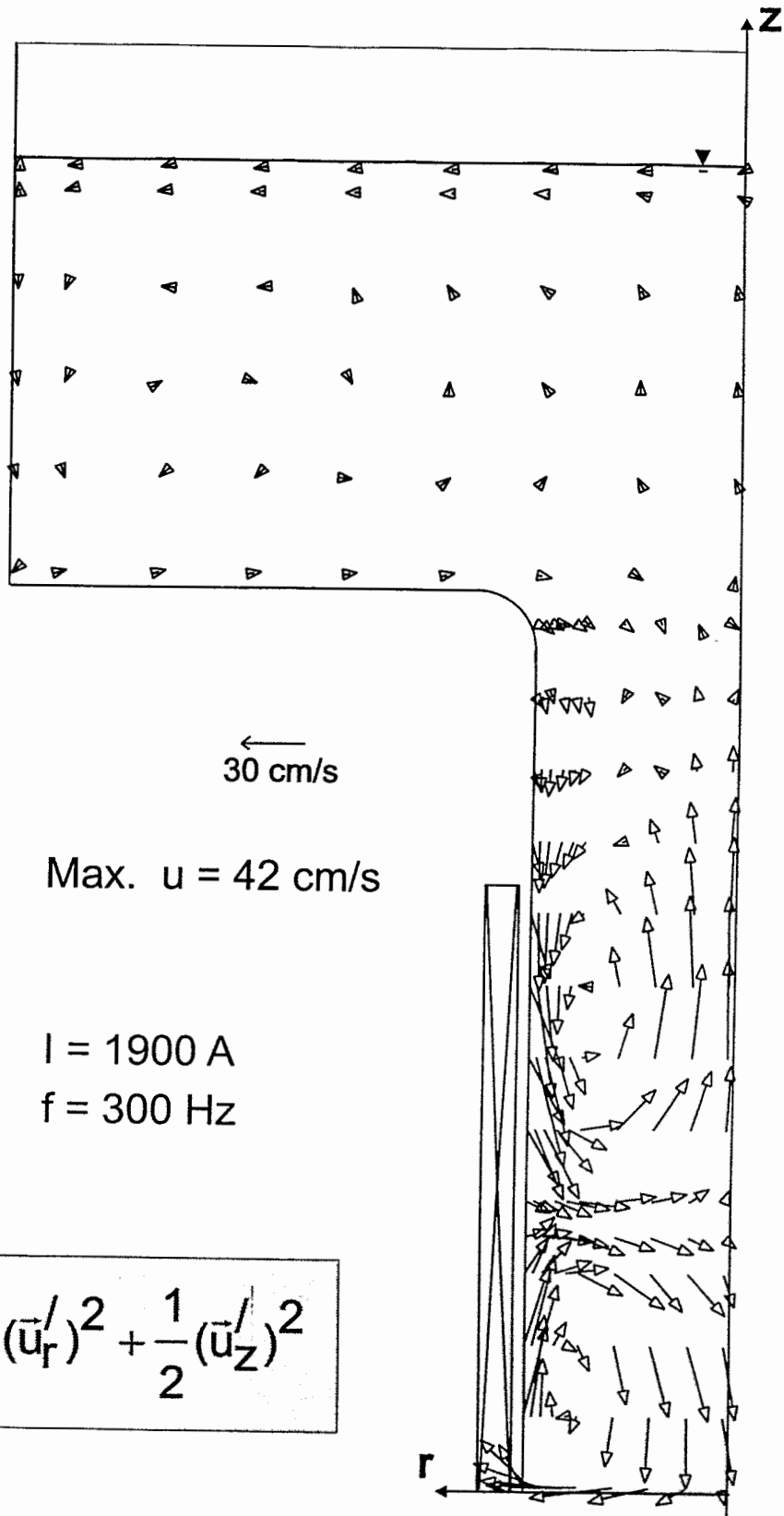


power: up to 100 kW  
frequency: 280 Hz...2 kHz

**EWH**

Model crucible inductor furnace

5/9 - 04

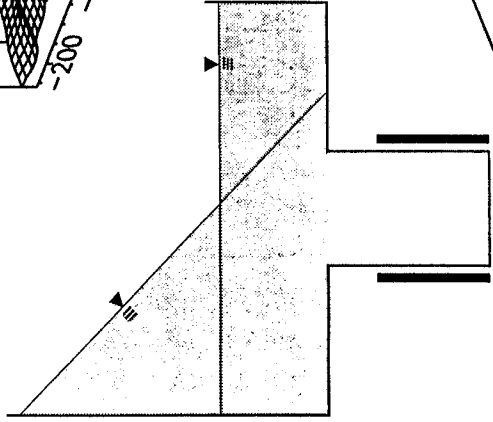
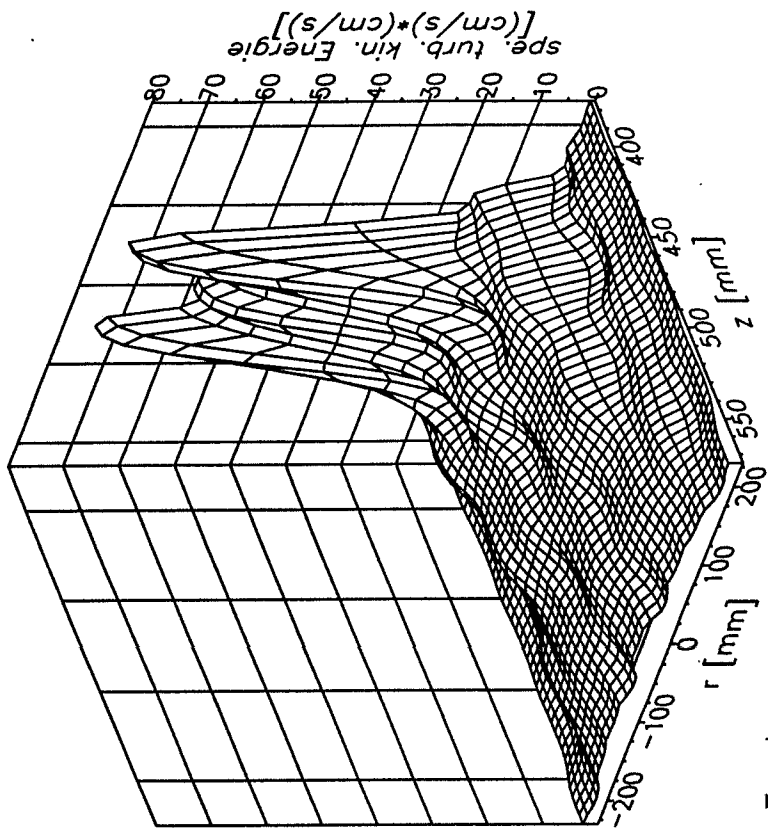


**EWH**

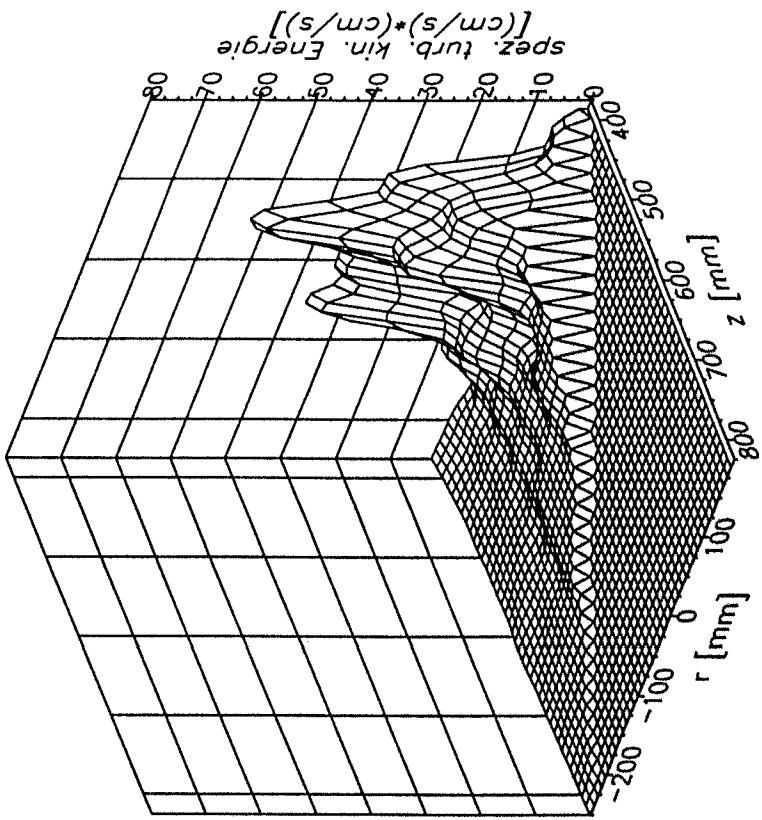
Measured time averaged melt  
 flow velocity distribution

5/9 - 05

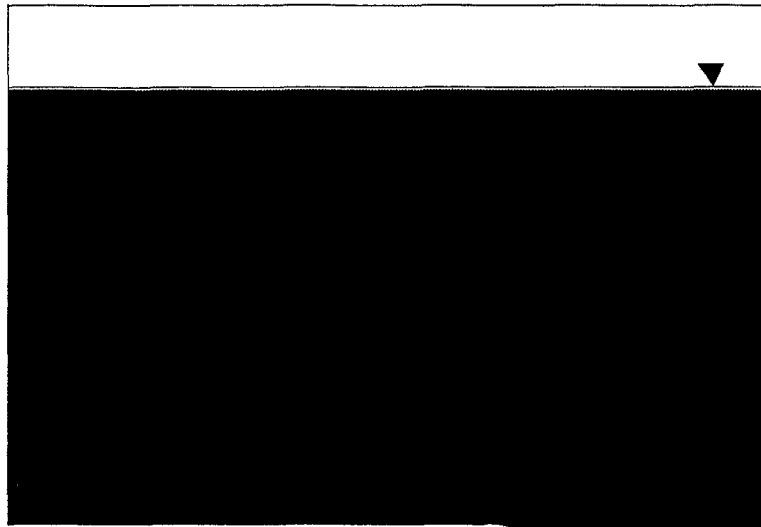
vertical  
position



















45° tilt  
position

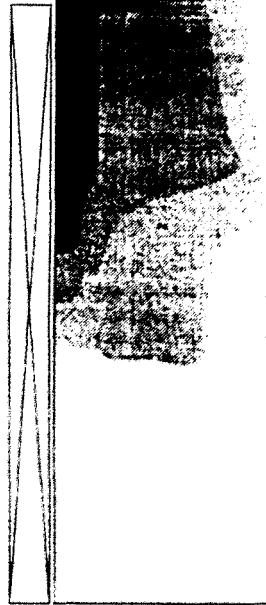


$I = 2200 A$   
 $f = 300 Hz$

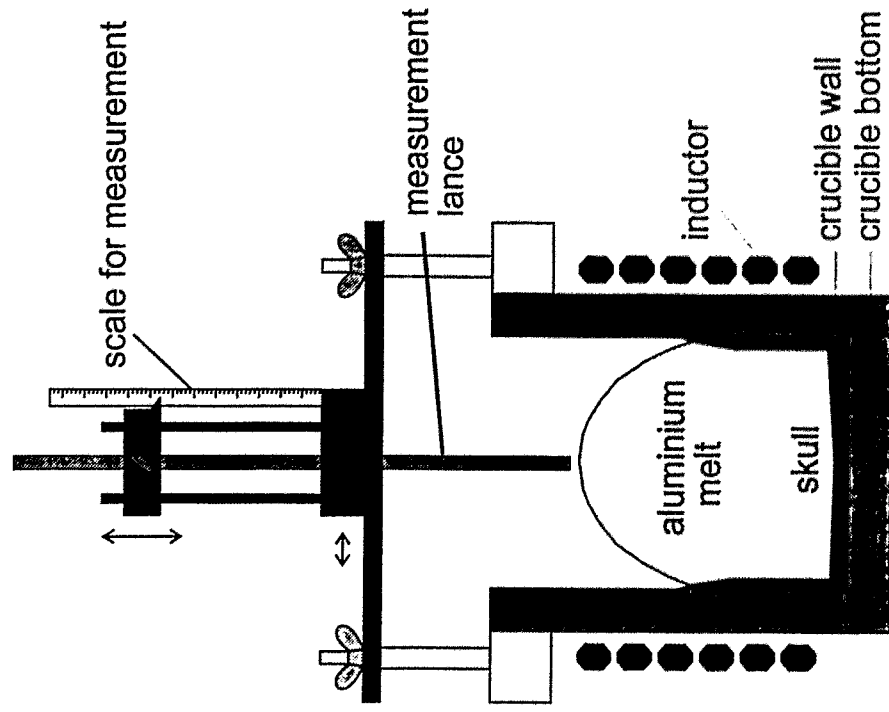
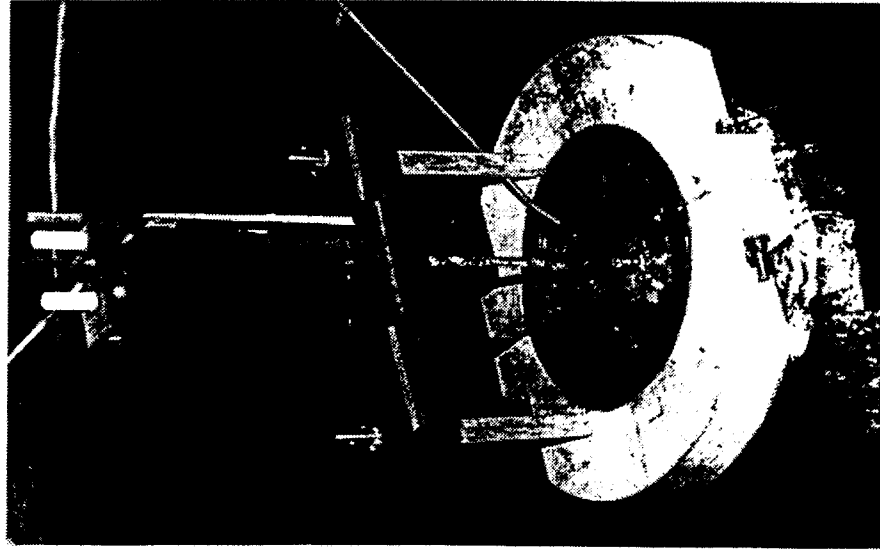


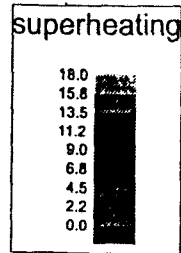
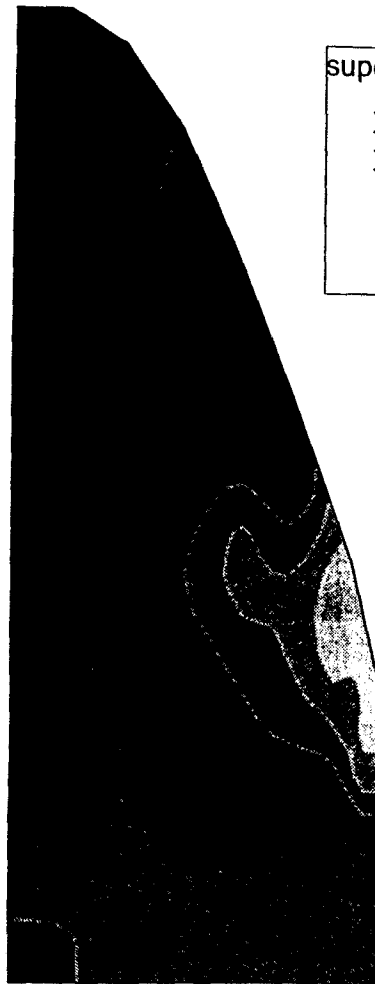
temperature scale [°C]

-  113.00 - 114.22
-  114.22 - 116.66
-  116.66 - 119.09
-  119.09 - 121.53
-  121.53 - 123.97
-  123.97 - 126.41
-  126.41 - 128.84
-  128.84 - 131.28
-  131.28 - 133.72
-  133.72 - 136.16
-  136.16 - 138.59
-  138.59 - 141.03
-  141.03 - 143.47
-  143.47 - 145.91
-  145.91 - 148.34
-  148.34 - 152.00



# Measurement of the melt temperature in a cold crucible induction furnace





## Measured temperature field

- 5 kg aluminium-melt
- Frequency-converter:  $f=8.3$  kHz,  $P=150$  kW
- NiCr-Ni thermo couple
- Measured values averaged over 30 sec.  
106 measurement points,  
measurement grid: 1 cm

not full-scaled

- The measuring of the current density and the magnetic flux density in the melt of induction furnaces using Wood's metal in order to determine the electromagnetic force density is well proved and leads to good results.
- The use of permanent magnet flow sensors is well-established and leads to reliable and reproducible results of the turbulent flow characteristics.
- Melt flow measurements have been carried out successfully in selected points in the aggressive aluminium-melt using a self developed electromagnetic sensor
- The results of the hydrodynamic investigations achieved using Wood's metal as a model melt are well transferable to typical metal melts used in practice

**EWH**

Conclusion

10/9 - 99



# Local velocity measurements in high temperature liquid metals by means of mechano-optical probes

*S. Eckert, W. Witke, <sup>1</sup>L. Pisseloup and G. Gerbeth*

*Forschungszentrum Rossendorf (FZR), P.O. Box 510119, D-01314 Dresden, Germany  
<sup>1</sup> ENSHMG, BP 95, 38402 St Martin d'Heres Cedex, France*

Model experiments are an important tool to understand the details of the flow structure and the transport properties of flows occurring in real-scale metallurgical facilities as well as to validate the multitude of numerical codes for flow simulation. Generally, water experiments are often performed to characterise the flow. Nevertheless, due to the large differences of material properties like density, heat conductivity, surface tension or electrical conductivity the use of liquid metals has clearly to be preferred if heat transfer phenomena, two-phase flows or the influence of electromagnetic fields on the flow should be investigated. The application of suitable alloys with low melting points, for instance PbBi ( $T_m = 125\text{ °C}$ ) or InGaSn ( $T_m = 5...10\text{ °C}$ ), makes such kind of experiments very flexible and offers the ability to measure the essential flow quantities like velocity, pressure or void fraction.

In this lecture we want to discuss a novel sensor which has been developed by the Rossendorf group to measure the local velocities in opaque liquid flows. The measuring principle is based on the separation of a direct mechanical interaction between flow and sensor tip and the optical acquisition and processing of the signal. In principle, this fact allows the extension of the range of applicability to higher temperatures. Furthermore, the insensitivity of the system to electrical noise and external magnetic fields can be considered as an important advantage. Until now, the sensor has been tested in metallic melts up to temperatures of about  $350\text{ °C}$ . In principle, an extension of the range of application up to temperatures of about  $1100\text{ °C}$  should be possible by the utilisation of quartz glass as material for the sensitive sensor tips. The first sensors have been manufactured and tested with low temperature melts.

We present measurements of the local velocity obtained in an eutectic InGaSn melt driven by a rotating magnetic field. The interest is focussed on geometry and parameters relevant for crystal growth technologies and mixing processes in metallurgical applications, respectively. Measured profiles of the azimuthal velocity have been obtained at different frequencies and field amplitudes.

# Local velocity measurements in high temperature liquid metals by means of a mechano-optical probe

*S. Eckert, W. Witke, G. Gerbeth  
Forschungszentrum Rossendorf, Germany*

*L. Pisseloup  
ENSHMG, France*

**International Workshop on  
Measuring Techniques for Liquid Metal Flows (MTLM)**

Rossendorf, October 11-13, 1999

# Local velocity measurements in liquid metals

## Difficulties

- opaque
- high temperatures
- chemical aggressive
- electromagnetic fields

## Methods

### invasive

Pitot-tube  
Hot-wire anemometer  
Permanent magnet probe  
Potential probe  
Karman vortex probe  
Mechano-optical probe

### non-invasive

Radiation techniques  
Ultrasonic Doppler technique  
Velocity reconstruction  
from b-field measurements

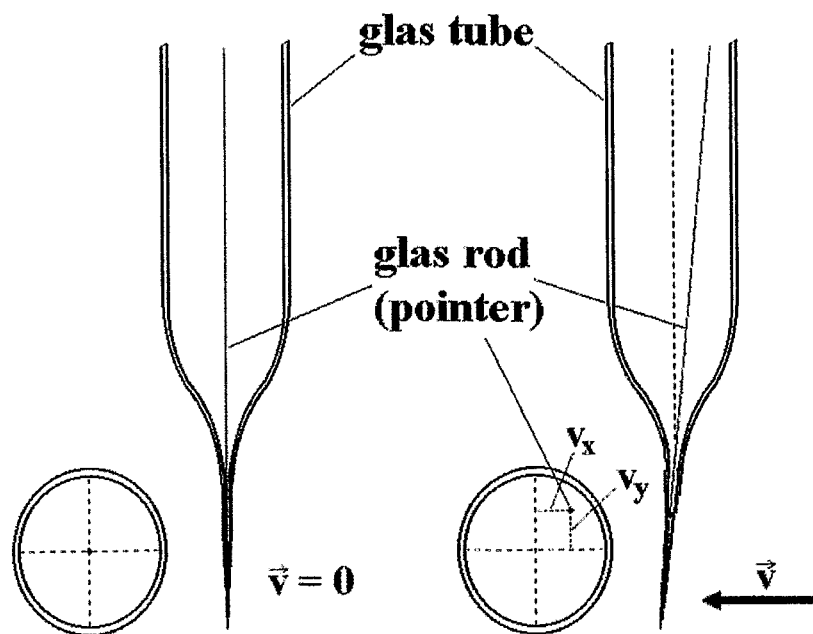
## Restrictions

- not available at high temperatures
- material properties (density, heat conductivity, ...)
- interfacial effects (wetting, impurities)
- poor accuracy, spatial and temporal resolution
- electromagnetic fields
- perturbation of the flow

## Wishes

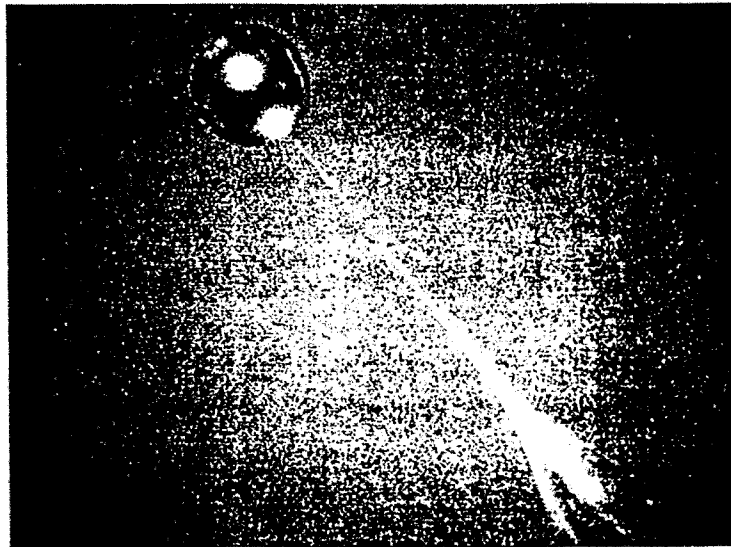
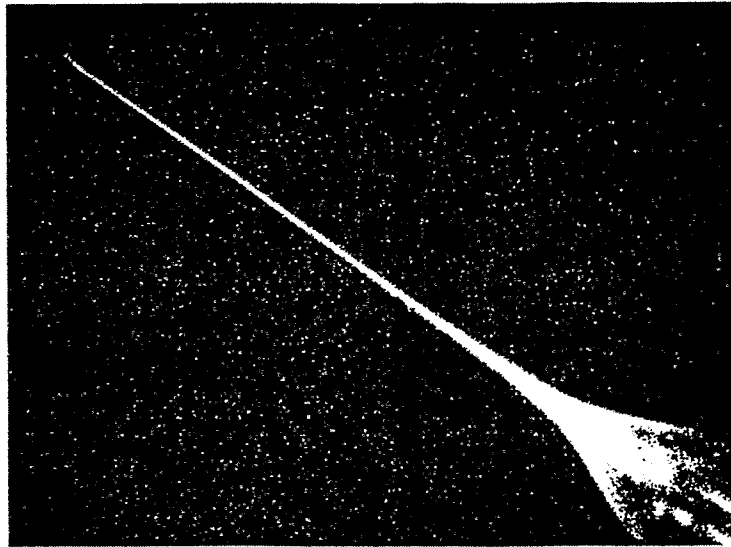
- suitable for local velocity measurements in opaque fluids at high temperatures
- signal should not be affected by electrical noise and external electromagnetic fields
- perturbation of the flow due to the sensor presence should be as small as possible
- wide velocity range should be covered
- reasonable costs

# Measuring Principle

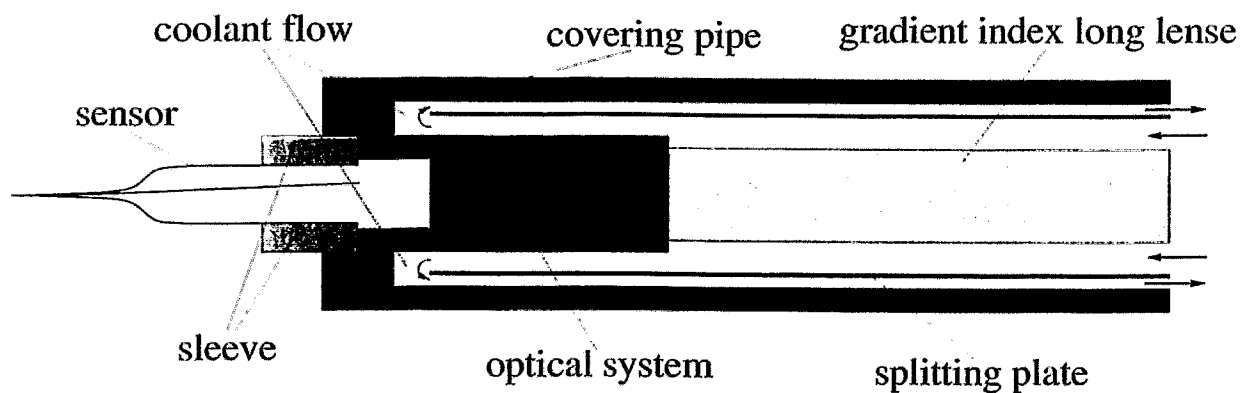


- force on a flexible body
- small elongations  $\rightarrow$  deformation =  $f(v)$
- signal acquisition by optical methods
- digital signal processing

Photographs obtained by means of a stereo microscope showing a probe tip with and without attached spherical body



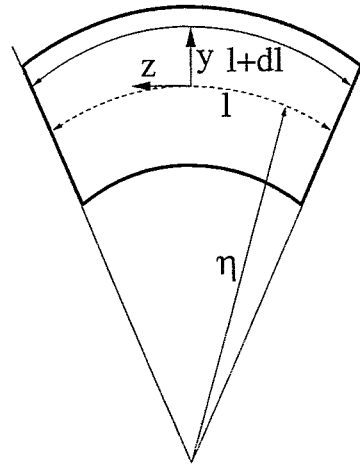
## Version for high temperature applications



- surrounding temperature about  $300^{\circ}\text{C}$
- penetration depth up to about 250 mm (500 mm)
- quartz glass sensor → go ahead up to temperatures of about  $700^{\circ}\text{C}$  should be possible

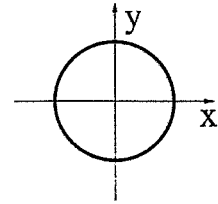
# Theoretical considerations

- rod element with length  $l$  is affected by torque  $M_x$



⇒ deformation  
(stretching, compressing)

'neutral' fiber  
with curvature  $\eta$



- geometrical relations:  $\frac{l}{\eta} = \frac{l + dl}{\eta + y} \Rightarrow \frac{dl}{l} = \frac{y}{\eta}$

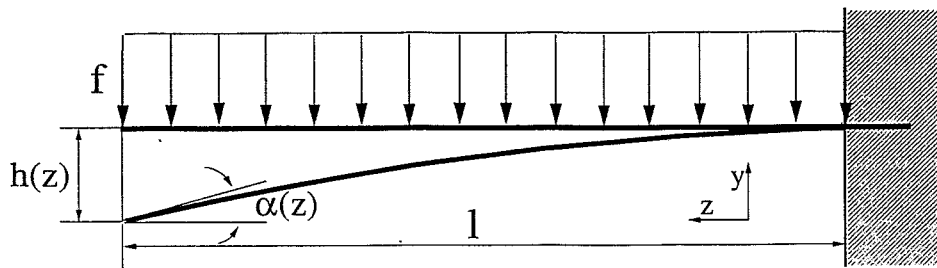
- Hooke's law:  $\sigma_z = E \frac{y}{\eta}$  (E - elastic modulus)

- torque  $M_x = \iint_A \sigma_z y dA = \frac{E}{\eta} \iint_A y^2 dA = \frac{E}{\eta} I_x$

- moment of inertia  $I_x = \iint_A y^2 dA,$

cylinder  $I_x = I_y = \frac{\pi}{4} r^4$





- $h(z)$  - displacement of the 'neutral' fiber

- small elongations:  $\frac{dh}{l} = \frac{dh}{dz} = \tan \alpha \approx \alpha \ll 1$

$$\Rightarrow -\frac{d^2 h}{dz^2} \approx \frac{1}{\eta}$$

- $E, I$  constant  $\Rightarrow M = EI \frac{d^2 h}{dz^2}$

$$F = EI \frac{d^3 h}{dz^3}$$

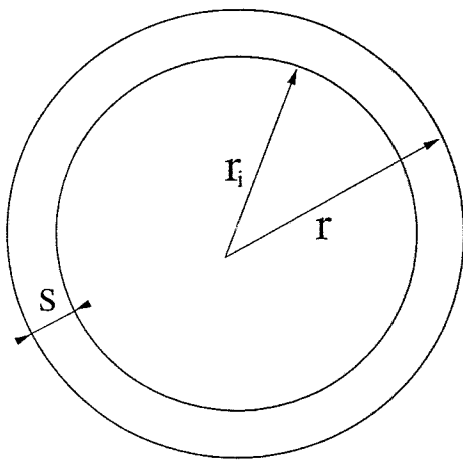
$$f = EI \frac{d^4 h}{dz^4}$$

- BC: fixed at  $z=0$ :  $h(0) = \frac{dh(0)}{dz} = 0$   
free at  $z=l$ :  $F(l)=M(l)=0$

$$\Rightarrow \alpha(l) = \frac{fl^3}{6EI} \quad h(l) = \frac{fl^4}{8EI}$$

# Bending of a cylinder affected by a flow

- drag force  $f = F/l = C_w \rho_l r v^2$
- moment of inertia  $I = \iint r^2 dA = \frac{\pi}{4} [r^4 - r_i^4]$   
 $\frac{\pi}{4} [r^4 - (r - s)^4]$



$$r \gg s \Rightarrow I \approx \pi r^3 s$$

$$\Rightarrow h(l) = \frac{C_w \rho_l v^2 l^4}{8\pi E r^2 s} \sim v^2$$

- flow of eutectic InGaSn

$$l = 15 \text{ mm}, r = 0.1 \text{ mm}, s = 0.025 \text{ mm}$$

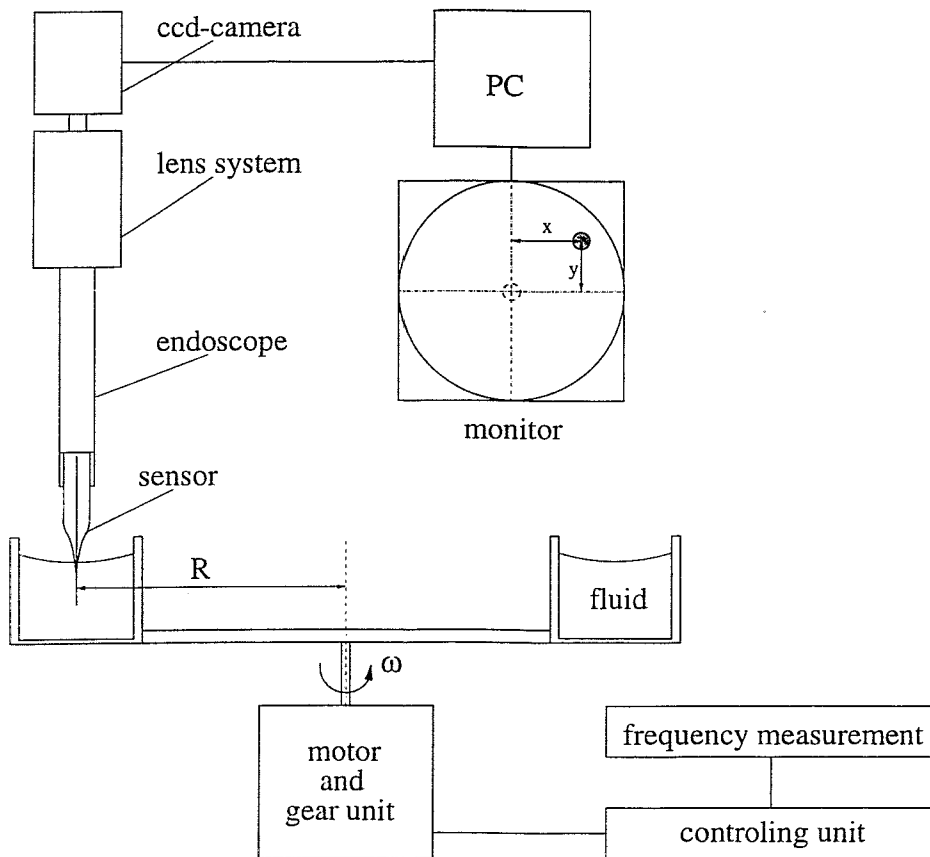
$$E = 6.18 \cdot 10^{10} \text{ N/m}^2 \text{ (borosilicate glass)}$$

$$\rho_l = 6360 \text{ kg/m}^3, v = 0.2 \text{ m/s}$$

$$C_w = f(\text{Re}), \text{Re} \approx 60 \rightarrow C_w \approx 1.5$$

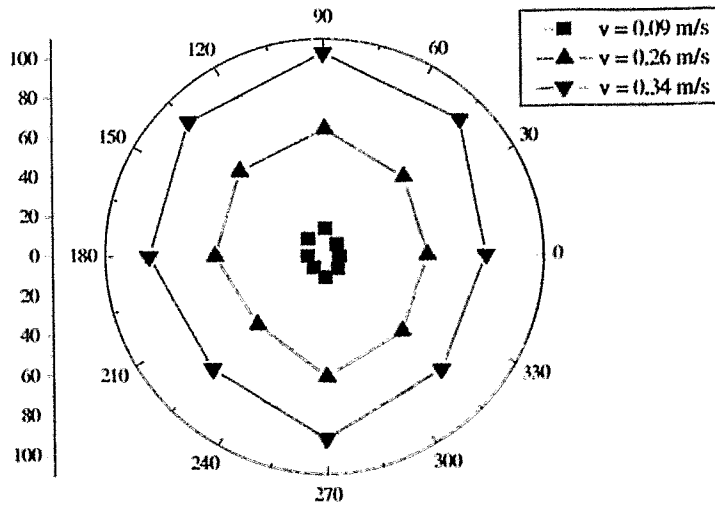
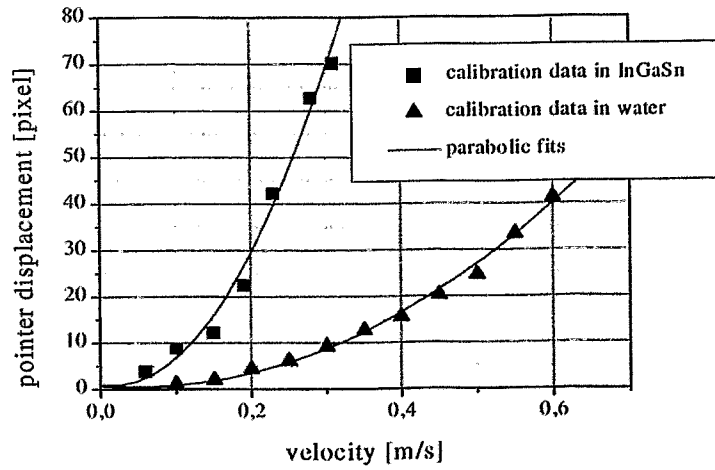
$$\Rightarrow h(l) \approx 0.06 \text{ mm}$$

# Sensor calibration

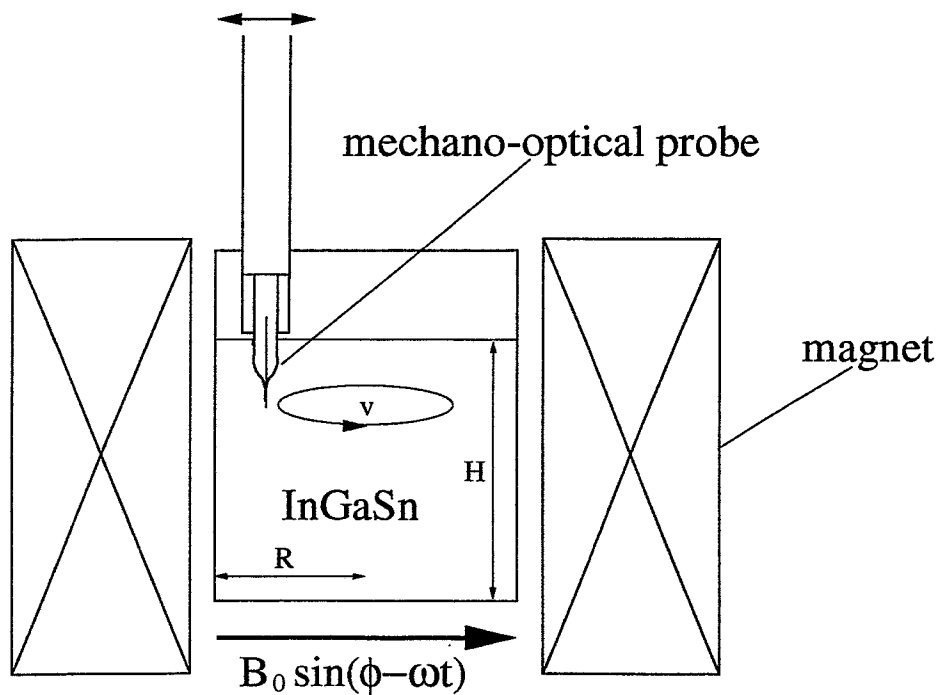


- rotating channel:  $v = \omega \cdot R$
- fluids: water, InGaSn (room temperature)  
PbBi, SnBi, SnPb (up to 350°C)

# Calibration curves

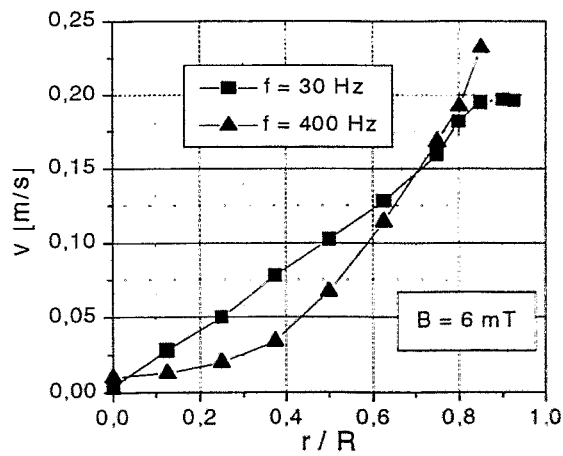
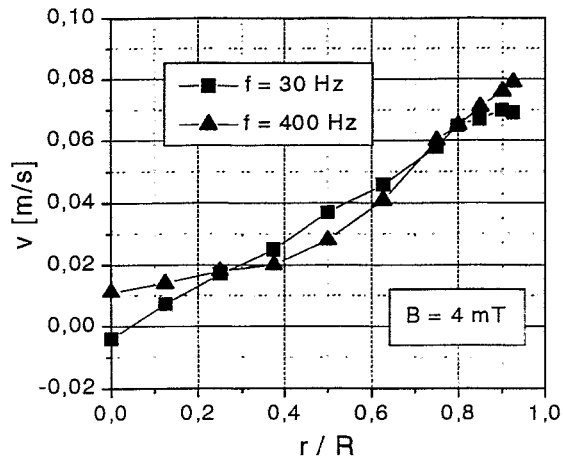


# Model experiment: Flow driven by a rotating magnetic field

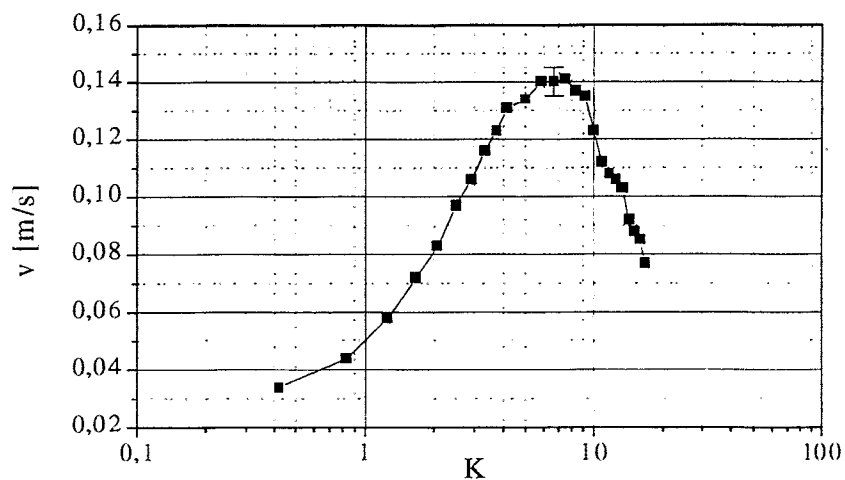


- eutectic InGa Sn melt, volume about 0.3l  
( $R = 4\text{cm}$ ,  $H = 5\text{cm}$ )
- b-field up to
- frequency between 10 and 400 Hz

# Radial profiles of the azimuthal velocity



## Azimuthal velocity depending on the frequency of the rotating field



- probe at a fixed position  $r/R = 0.75$
- nondim. frequency  $K = \mu\sigma\omega R^2 = 2\left(\frac{R}{\delta}\right)^2$
- skin depth  $\delta = \left(\frac{2}{\mu\sigma\omega}\right)^{\frac{1}{2}}$

## Evaluation of the method

- Applicability at high temperatures (about  $700^{\circ}C$ ) .
- not influenced by electric noise or electromagnetic fields
- Problems: - invasive method
  - spatial resolution along the sensor axis
  - influence of free surfaces
  - measurement of fluctuations



## **Determination of Flow - Velocity in Silicon Melt during an Industrial Czochralski Process**

*A. Mühe, O. Gräbner, G. Müller, E. Tomzig, W. v. Ammon*

*Fraunhofer IIS-B, Schottkystr. 10, D-91058 Erlangen, Germany*

In the industrial growth of Silicon single crystals by the Czochralski process melt sizes of up to 300 kg are used. Due to the low Prandtl-number of liquid Silicon and the strong influence of buoyancy convection, the flow in the Czochralski melts is usually 3-dimensional, time dependent and tends to become more and more turbulent with increasing melt sizes.

Fluctuations of the temperature and of the concentration of dissolved oxygen are detrimental to the quality of the devices made from the single crystal. However, the optimization of the process parameters like crucible- and crystal rotation rates or magnetic fields suffers from the lack of measurement techniques for the melt flow velocity.

At the high temperature of molten silicon (typically 1700 - 1750K) most mechanical approaches for velocity measurement are not applicable, while tracer methods in combination with X-ray cameras cannot be applied to the melt sizes of actual interest. The determination of flow velocity by the correlation of temperature signals from multiple thermocouple arrangements was successfully used for the analysis of baroclinic instabilities in Czochralski melts. The development of an optical fiber thermometer with high spatial and time resolution for the application under industrial silicon Czochralski conditions will be shown. Experimental results of flow evaluation in industrial size and laboratory scale silicon Czochralski melts will be shown. The combination of 3 or more temperature sensors for the 2- and 3-dimensional detection of the melt flow vector is discussed.

# Determination of Flow - Velocity in Silicon Melt during an Industrial Czochralski Process

A. Mühe, O. Gräbner, G. Müller  
Fraunhofer IIS-B, Erlangen

E. Tomzig, W. v. Ammon  
Wacker Siltronic AG, Burgausen

## Outline

Growth of Silicon Single Crystals by the  
Czochralski Method

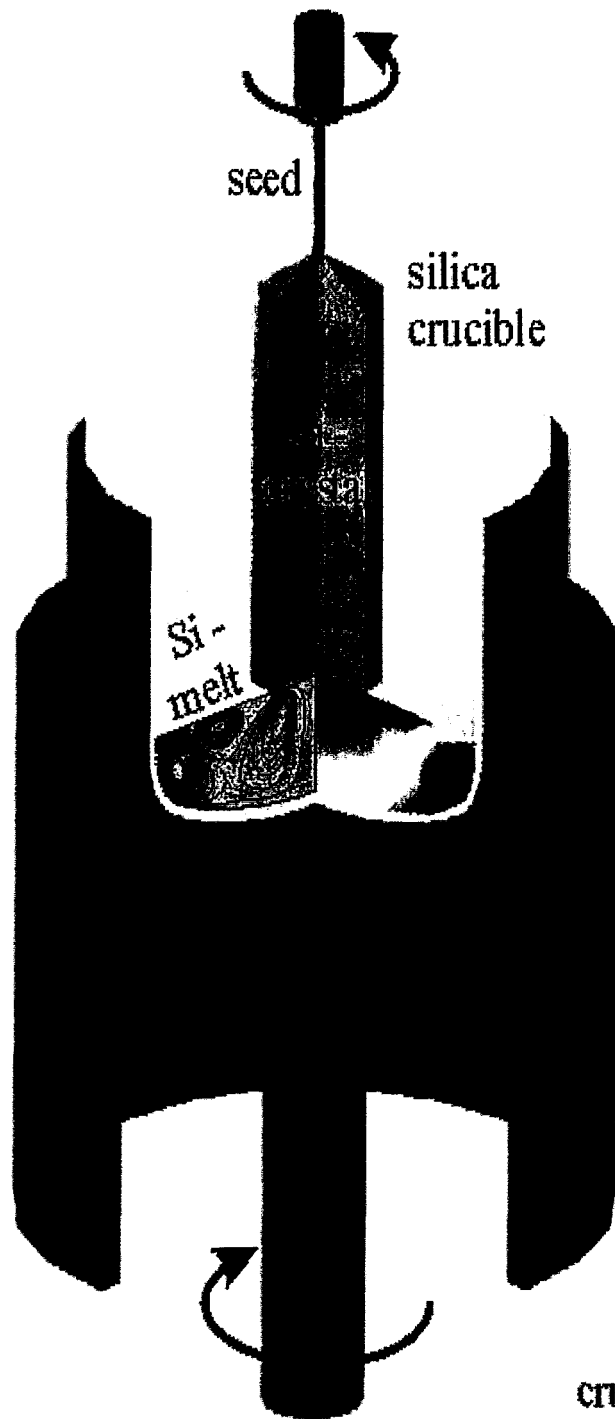
Determination of Flow - Velocity by the Correlation  
of Multiple Temperature Signals

*1st special case:* Analysis of Baroclinic Instabilities

*2nd special case:* Analysis of Flow beneath the  
Growing Crystal

Discussion of the Applicability as 3D Flow-Sensor

# Growth of Silicon Single Crystals by the Czochralski - Method



**problem:**

top-seeding method

non-stable  
temperature profile

strong buoyancy  
convection

(turbulent) fluctuation  
of temperature and  
impurity concentrations

problem for single-  
crystalline growth and  
homogeneity of crystals

**driving forces  
of flow**

buoyancy convection

marangoni convection

forced convection by  
crucible and crystal rotation

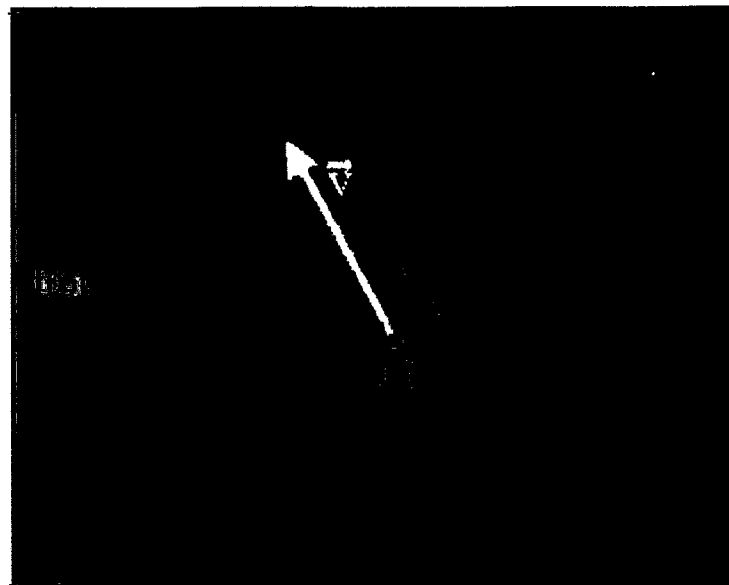
Grashof numbers up to  $10^{11}$ , melt temperature  $> 1700$  K

# Determination of Flow - Velocity by the Correlation of Multiple Temperature Signals

assumption:

heat transfer by conduction can be neglected

→ temperature distribution moves with the medium  
within a small portion of space and time



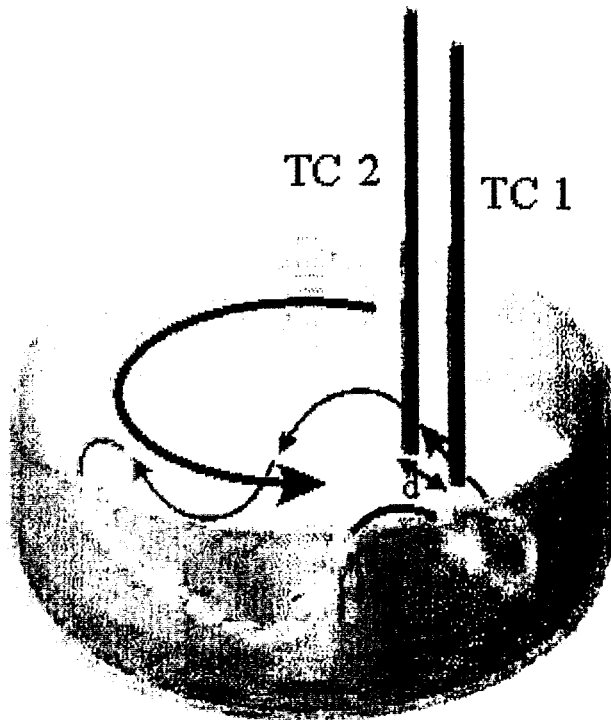
Temperature is recorded at positions  $T_1$  and  $T_2$ ,  
which are separated by the distance vector  $\vec{\Delta}$  of length  $d$ .  
 $\vec{v}$  describes the motion of the medium at velocity  $v$ .

$\vec{\nabla}T$  is the temperature gradient in the region where  
the temperature recordings are carried out.

cases:

- $\vec{v} \parallel \vec{\Delta} \perp \vec{\nabla}T$        $v = d / \text{time}$  can be detected
- $\vec{v} \perp \vec{\nabla}T$                       no information on  $v$

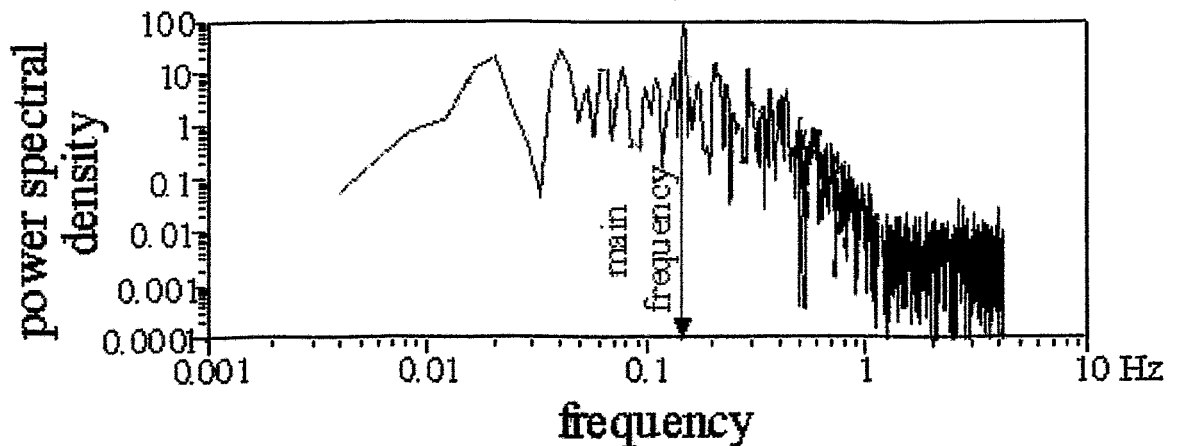
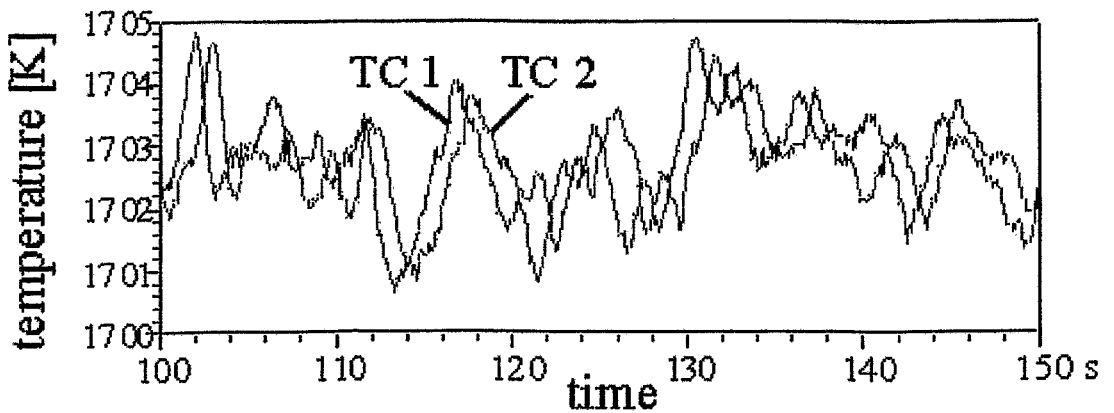
# 1st special case: Analysis of Baroclinic Instabilities



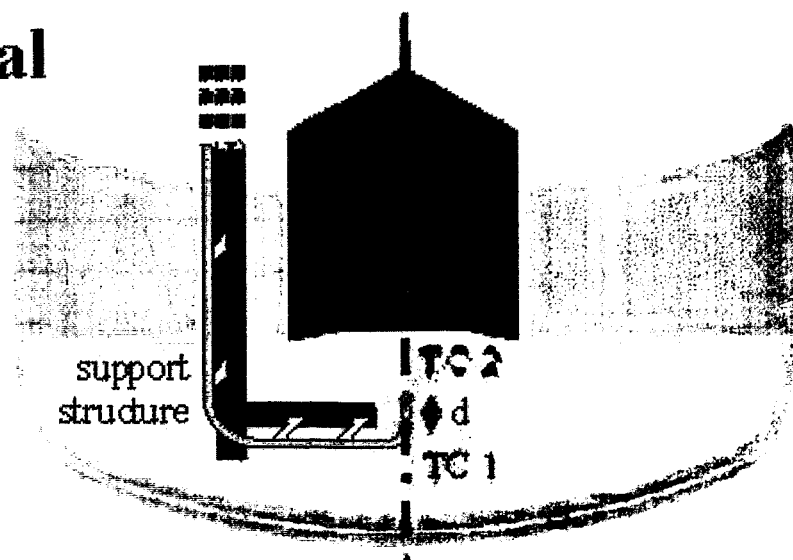
wavy temperature pattern causes periodic temperature oscillations

azimuthal flow velocity can be calculated by using frequency and phase shift from fourier analysis

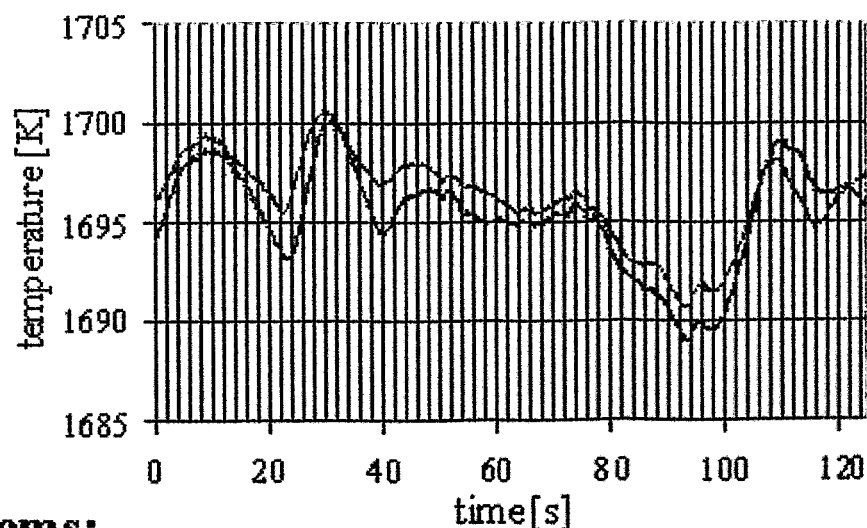
$$\vec{v} \parallel \vec{\Delta} \parallel \vec{\nabla} T \quad v = f * d / \phi$$



## *2nd special case:* Analysis of Flow beneath the Growing Crystal



**assumption:** flow pattern and temperature distribution have rotational symmetry in time average  $\rightarrow$  on the axis of symmetry only z-component is relevant



**problems:**

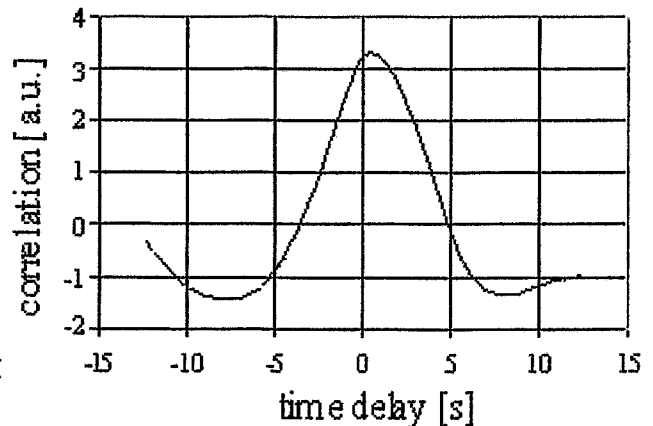
- 1) Signal is not periodical: How to evaluate time delay?
- 2) Dimension of structures in the temperature field is unknown  $\rightarrow$  Short distance  $d$  between measurement positions is desired  $\rightarrow$  Small sensors with high time resolution required

## solutions:

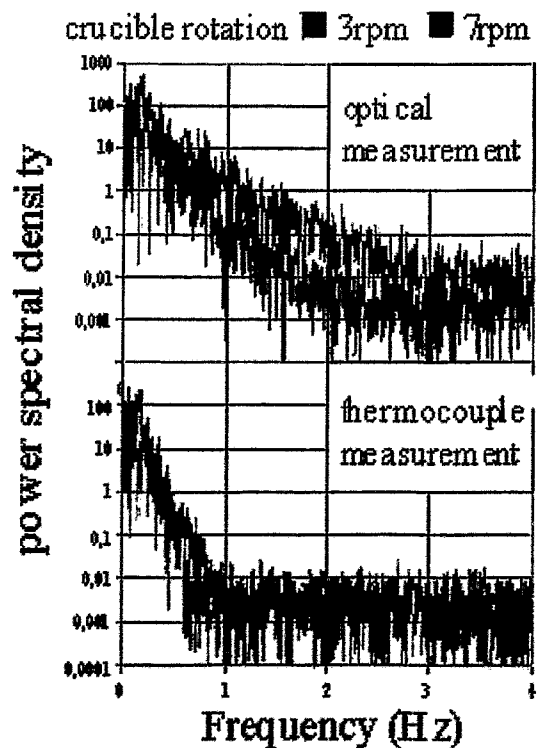
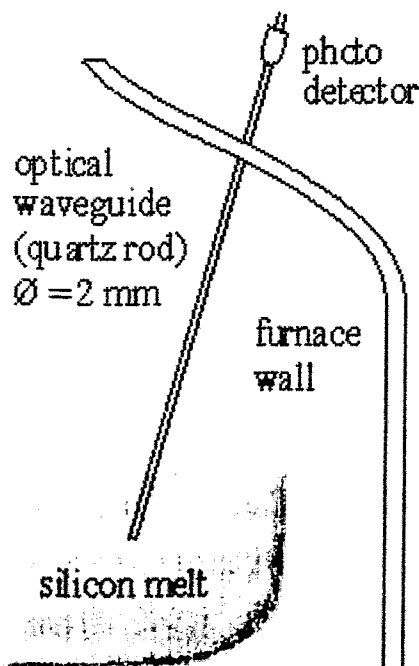
- 1) Application of the correlation function to evaluate the time-averaged delay between a pair of temperature signals

$$C(\tau) = \sum_{i=-n}^n T_i^1 * T_{(i+\tau)}^2$$

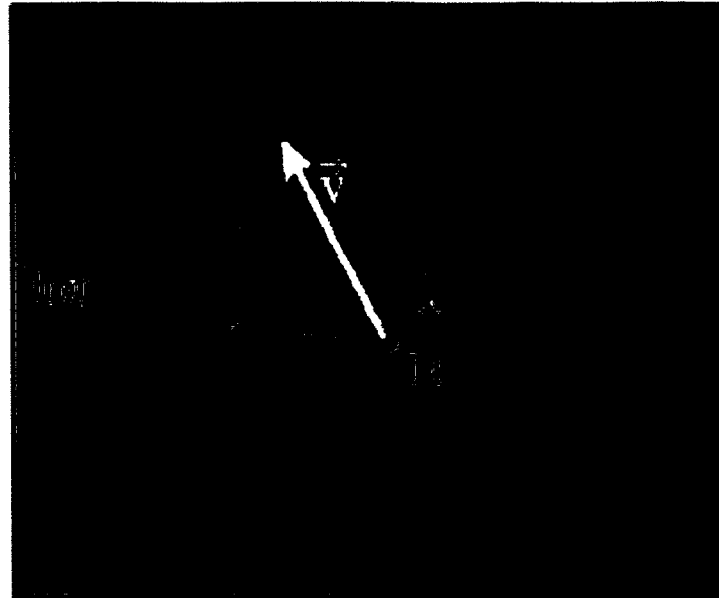
where  $C$  is the correlation,  $\tau$  is the time delay,  $T_i^1$  and  $T_i^2$  are discrete values from the temperature measurement at positions 1 and 2 and  $2n$  is the total number of temperature values taken into account.



- 2) Use of optical waveguide thermometry for temperature measurement at high spacial and time resolution



## Discussion of the Applicability as 3D Flow Sensor



3 measurement positions in 2D or 4 measurement positions in 3D → Temperature gradient is always known,

$$\vec{\nabla}T = \frac{1}{d} \begin{pmatrix} T2 - T1 \\ T3 - T1 \end{pmatrix}$$

If the direction of  $\vec{v}$  within the coordinates of  $\vec{\Delta}_1$ ,  $\vec{\Delta}_2$  was known, the velocity  $v$  could be calculated using

$$v \begin{pmatrix} \Delta t_1 \\ \Delta t_2 \end{pmatrix} = d \begin{pmatrix} \cos \varphi \\ \sin \varphi \end{pmatrix}$$

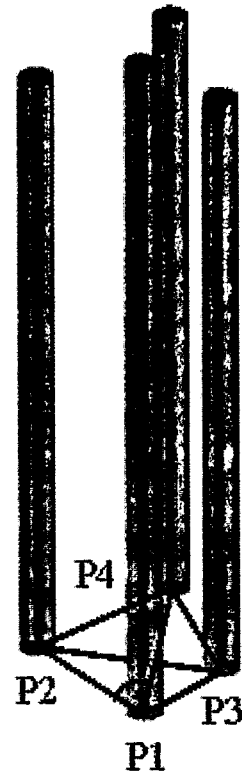
In the case of a convection-dominated heat transfer, one might assume that the time averaged heat flux has the same direction as the time averaged flow vector. Then, one might calculate  $\varphi$  using

$$\tan \varphi = \frac{T2 - T1}{T3 - T1}$$



# Proposed Proceeding for 3D-Measurement of Time Averaged Flow Velocity

- record temperatures at positions P1 through P4
- calculate time averaged temperature gradient
- calculate averaged time delays between P1/P2, P1/P3 and P1/P4 using correlation function
- calculate time averaged flow velocity in the direction of the time averaged temperature gradient



## conclusions:

The determination of the flow velocity by correlation of temperature measurements was carried out successfully in 1D for some special cases during industrial silicon Czochralski growth.

The generalization of the method for 3D flow measurement depends on the negligibility of heat transfer by conduction and can only be carried out in time averaged quantities.

# Heat transfer investigation by specially designed heat emitting surfaces

*Ilgvars Platnieks*

*Latvian Academy of Science, Institute of Physics, Miera iela, LV-2169 Salaspils, Latvia*

Heat Emitting Temperature Sensing Surface

HETSS

Content of the presentation.

- 1) HETSS idea
- 2) Technical designs
- 3) Examples of use
- 4) Elaboration of the technique for the SINQ target experiment
- 5) Conclusions

# Heat transfer investigation by specially designed heat emitting surfaces

*I. Platnieks*

*Latvian Academy of Science, Institute of Physics, Miera iela, LV-2169 Salaspils, Latvia*

The new technique was developed in Institute of Physics of Latvian University. It is possible to use the technique in two different versions.

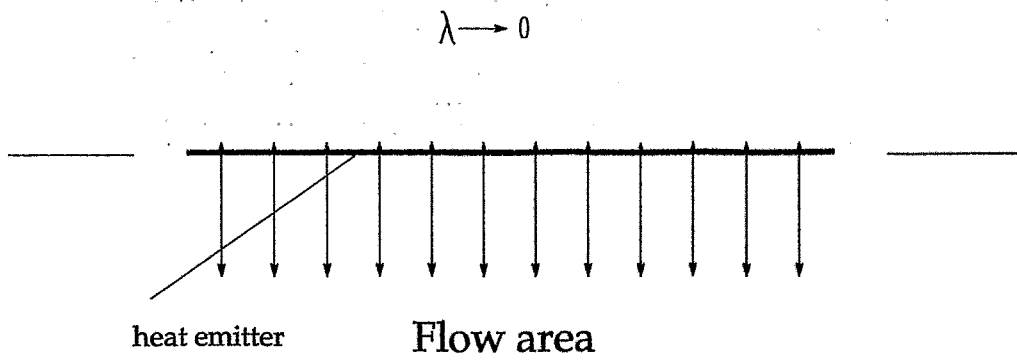
- 1) To fix a definite heat flux distribution from wall into the cooling flow and gain simultaneously the resulting temperature distribution on the wall.
- 2) To fix a definite temperature distribution on the wall with a simultaneous registration of the heat flux distribution which is necessary for keeping this temperature.

The technique provides direct local heat transfer coefficient measurements with definite spatial and time resolution.

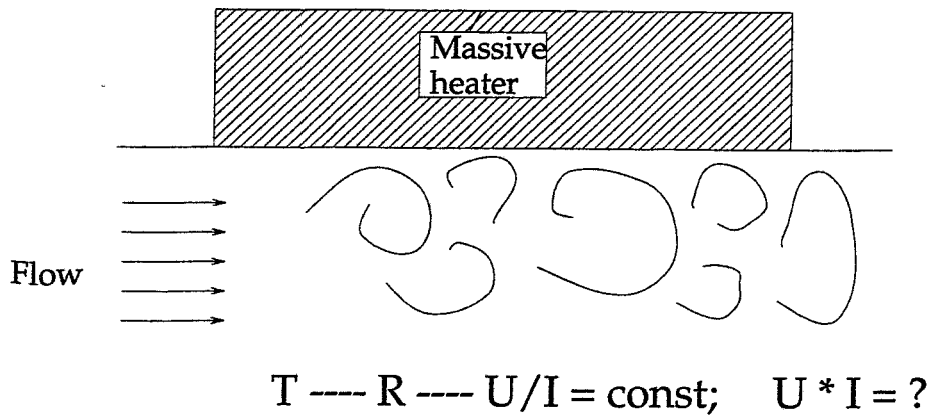
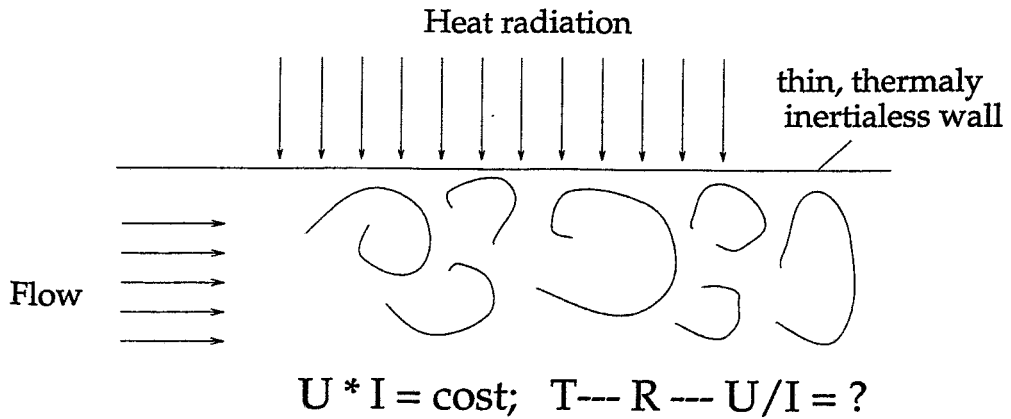
The local temperature registration at definite heat flux distribution is of great importance, for example, in situation when a thin wall is heated by radiation from one side and has contact with the cooling flow from other side. The situation is typical for high power facilities. Exploitation of the facilities at temperatures close to critical from material destruction point of view determines the temperature distribution as the item of the first importance. Presence of dead zones in cooling flow or other failures in cooling conditions will have indication in measured by the new method values.

The technique has demonstrated its usefulness in measurements of heat transfer at the beam window in a mockup target for SINQ (reported at 14th Meeting of the International Collaboration on Advanced Neutron Sources, Starved Rock Lodge, Utica Ill., USA June 14-19, 1998.)

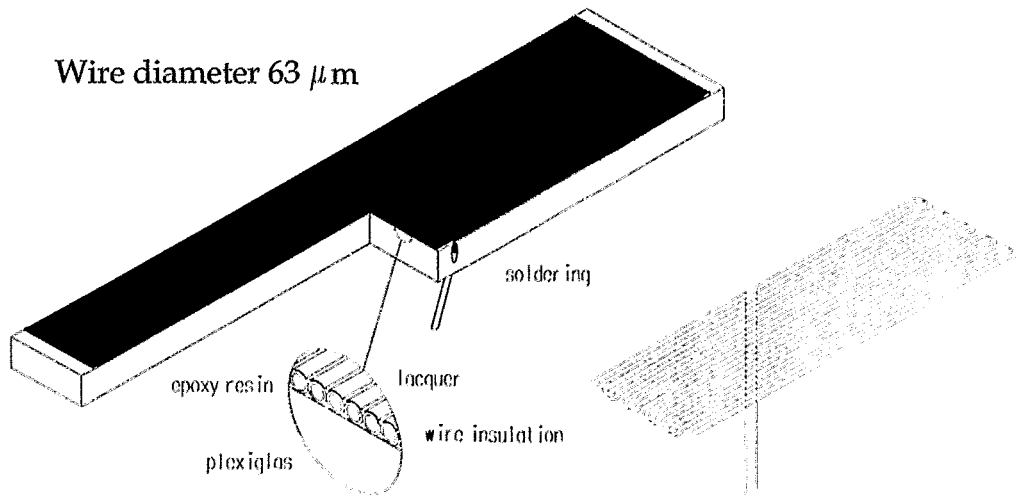
## General design of HETSS

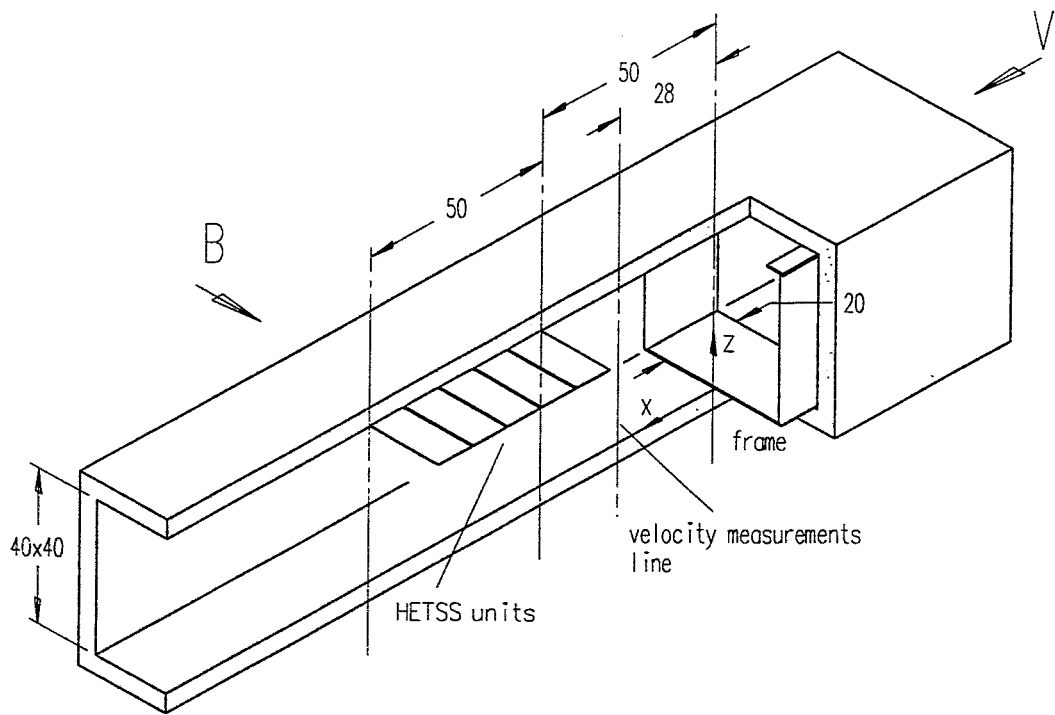


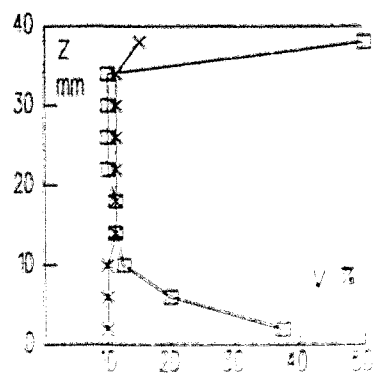
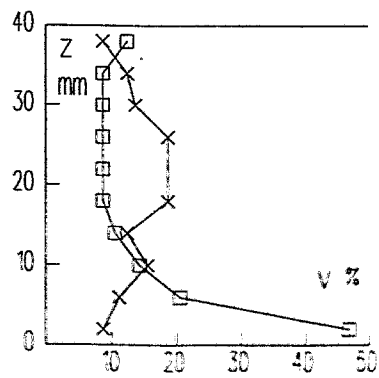
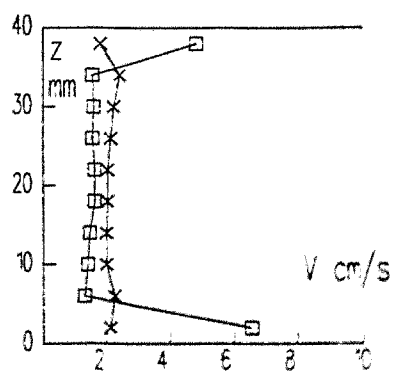
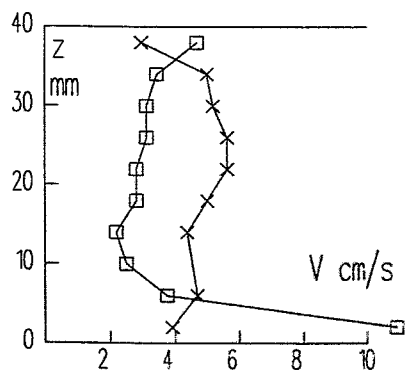
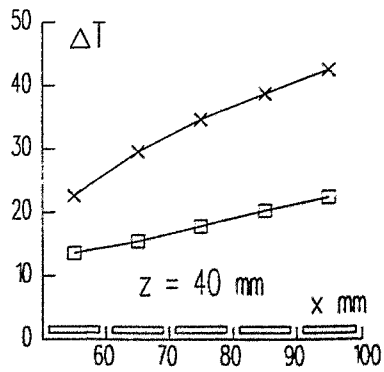
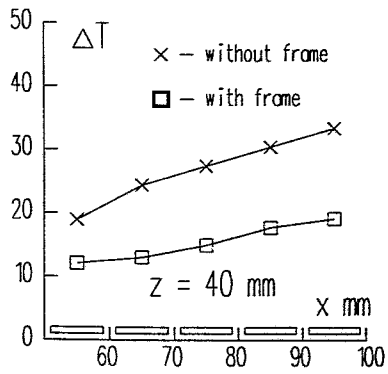
## Situations the HETSS simulate



# HETSS unit design

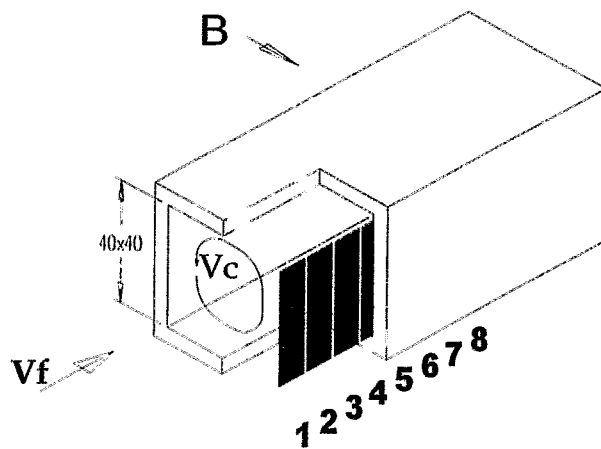
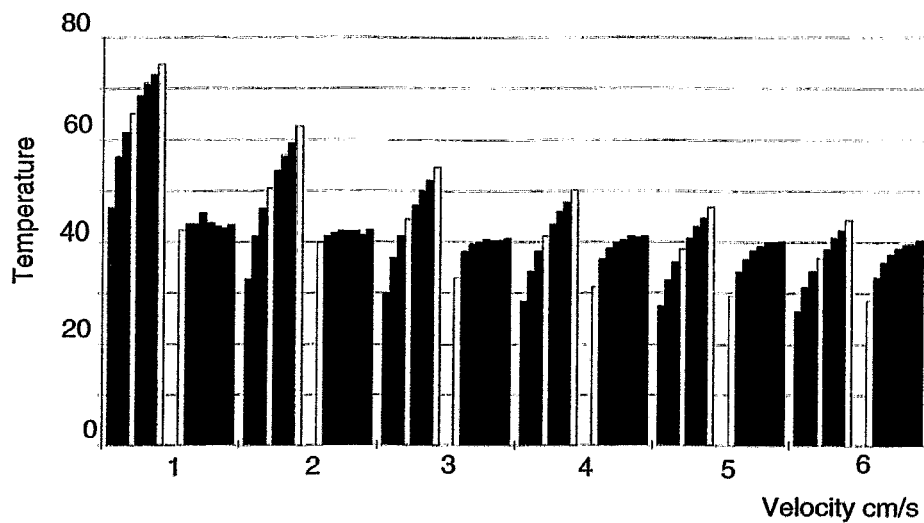


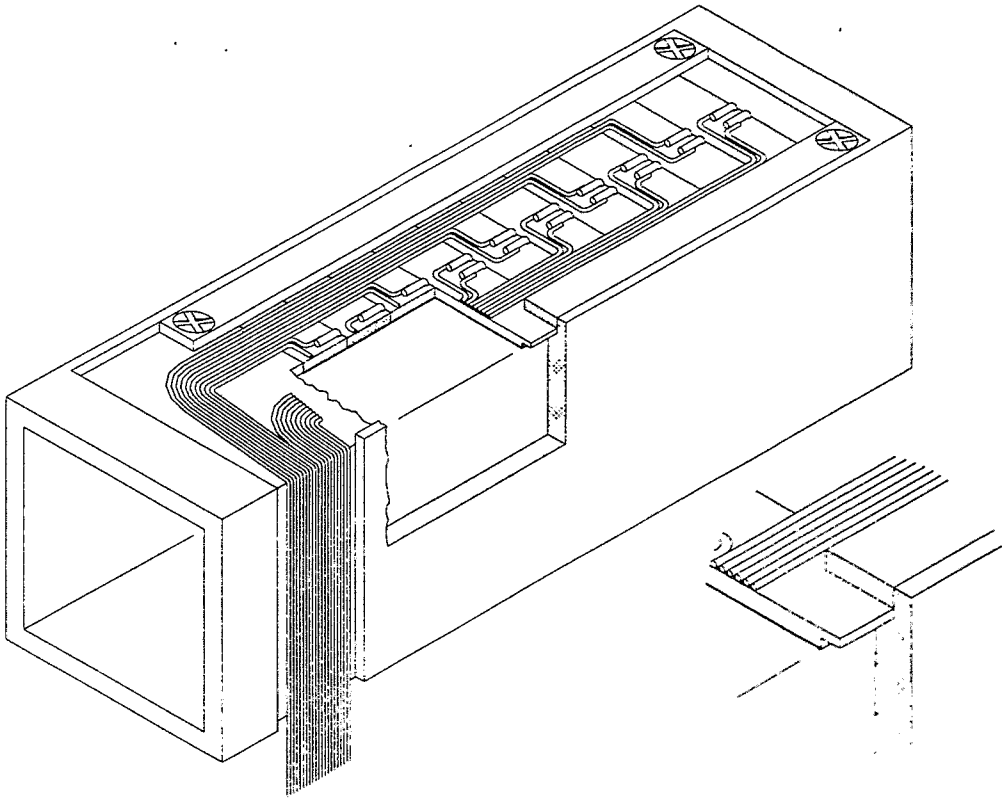


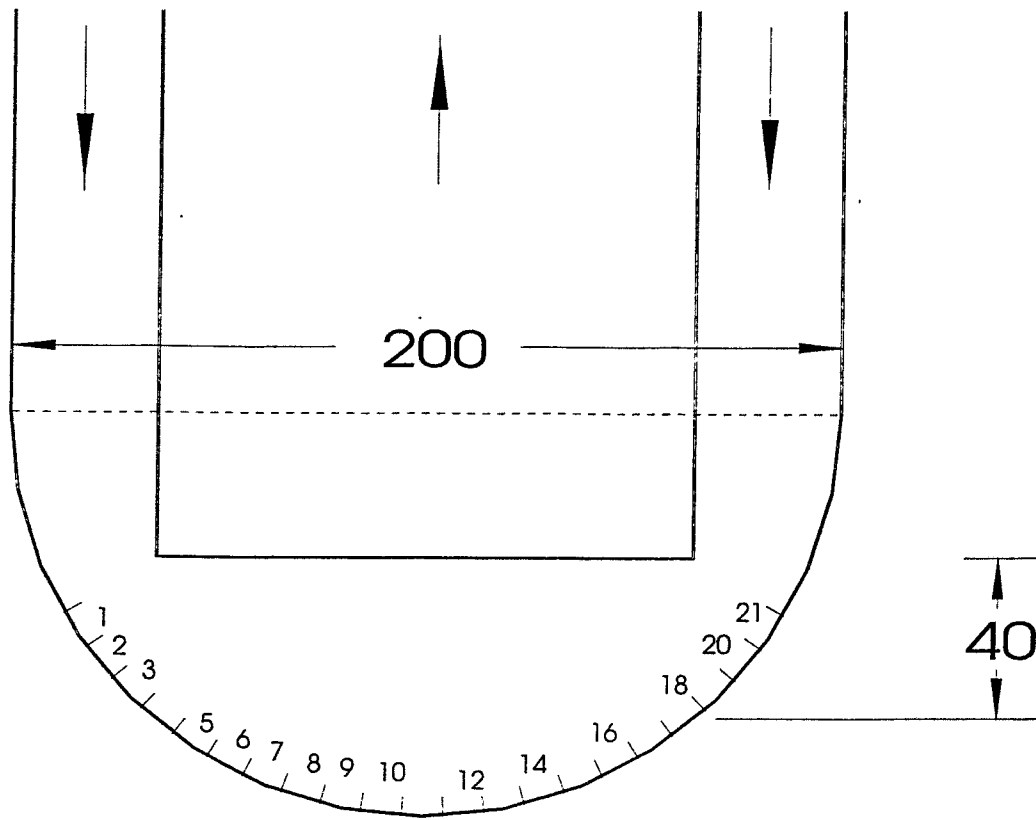




# Suppression of thermal convection by magnetic field

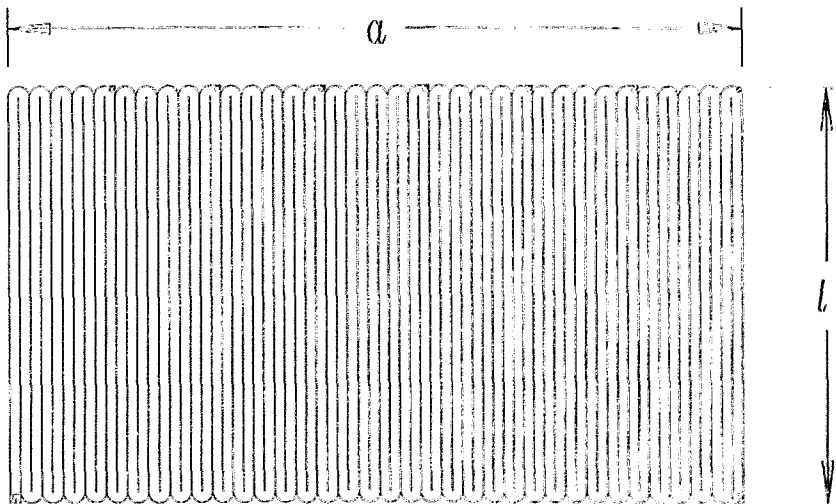






To calculate the number of segments per meander length unit the following parameters were taken in account:

- heat flux density  $\sim 7 \text{ w/cm}^2$  can provide suitable for electronics signal levels without reaching temperatures dangerous for insulation materials (from previous experience);  $Q = 70000 \text{ w/m}^2$
- the copper foil thickness on commercially available sheets for the etching technique is  $30 \mu\text{m}$ ;  $t = 0.00003 \text{ m}$
- the distance between bents equals the longest side of the HETSS unit -  $4 \text{ cm}$ ;  $l = 0.04 \text{ m}$
- area factor of current lead on HETSS surface;  $k = 0.9$
- desirable output signal voltage per meander ribbon length unit suitable for electronics is in range  $0.5 \div 3 \text{ v/cm}$ ;  $U = 50 \div 300 \text{ V/m}$
- The maximal current -  $10 \text{ A}$  (it is difficult to make an electrical connection to the very thin copper foil for higher currents);  $I = 10 \text{ A}$



*folly thickness*  $l$

If we are afraid about the level on measurement system input, for the calculation of the number of segments per meander length unit  $n$ , we use the formula:

$$n = \frac{U}{l} \sqrt{\frac{t \cdot k}{Q \cdot \rho}}, \text{ where } \rho \text{ is the electrical resistivity of copper.}$$

If we are afraid to exceed some current level we use for the  $n$  calculation

$$n = \frac{a}{l} \sqrt{\frac{Q \cdot t \cdot k}{\rho}}$$

(The formulae come from  $Q = \frac{U^2}{r \cdot a \cdot l}$  or  $Q = \frac{I^2 \cdot r}{a \cdot l}$  and  $r = \rho \frac{l \cdot n}{t \cdot k \cdot a/n}$ , where  $r$  is electrical resistance of all the current lead)

The second formula gives 10.65 segments per 1 cm for the 10 A electrical current. Using 10 segments we have space 1 mm for each. Having the area factor of current lead on HETSS surface  $k = 0.9$  the gaps between current leads will be 0.1 mm. It is difficult for the etching technique to make such gaps. Only 0.2 mm gap can ensure reliable electrical separation. Calculation of current for 0.8 mm wide current lead and 0.2 mm gap between them gives the 10 A, the maximum we have already accepted. The voltage on each cm (on each HETS unit) becomes 2.8 V and is acceptable too.

The quantity to be determined for each HETSS unit is the temperature rise per unit heat flux,  $h$  (in  $K/(W/cm^2)$ ), which is inverse of the heat transfer coefficient:

$$h = \Delta T_s / q$$

The temperature increase on the surface is calculated as

$$\Delta T_s = k_{af} (\Delta T_{Cu} - q \cdot d_i / \lambda_i),$$

where  $\Delta T_{Cu}$  - temperature of the copper foil forming the HETSS,  $k_{af}$  is the area factor of copper in the HETSS layout (0.8 in the present case),  $d_i$  is the thickness of insulation between copper and mercury ( $75 \mu m$ ),  $\lambda_i$  is the heat conductance of the insulation ( $0.39 W/mK^\circ$  for glass textolite as used).  
The heat flux density is calculated as

$$q = Q / S,$$

where  $Q$  denotes the electrical power supplied to the HETSS unit ( $\approx 28 W$  in the present experiment),  $S$  is the area of the HETSS unit ( $4 cm^2$ ).

The copper temperature increase then obtained as

$$\Delta T_{Cu} = (R - r) / r \cdot \alpha,$$

where  $R$  is the electrical resistance of the heated HETSS unit at full power,  $r$  is the electrical resistance of the same element at the temperature of the incoming fluid,  $\alpha$  is the temperature coefficient of resistance for copper ( $0.0044 1/^\circ K$ ).

Both the values of  $R$  and  $r$  for each HETSS unit  $n$  were calculated as a ratio of potential difference on the given to the current in the corresponding section. This current was obtained by means of measuring the potential difference on an instrumental shunt included in the current path. The shunt coefficient equals  $k_m = 0.0075 V/A$ .

$$R_n = (U_n / U_m) \cdot k_m \text{ and } r_n = (u_n / u_m) \cdot k_m$$

with  $n = 1, \dots, 21$ ,  $m = 1, \dots, 3$ .

The electrical resistance  $r$  of HETSS unit at the temperature of the incoming flow was obtained at the beginning of the experiment applying an electrical power which causes a negligible temperature increase ( $0.0015 W/cm^2$ ). The changes in the incoming flow temperature are taken into account by means of continuous measurement of the voltage drop on a special copper resistor. This resistor was connected to stabilized current source and fixed on the outer pipe of the Mockup where the incoming flow temperature can be determined. The ratio of the actual voltage drop on the resistor to that measured at the beginning of the experiment  $\varphi_r / \varphi_{r0}$  was used in computer evaluations as a correction coefficient. (The temperature of the incoming flow was in range  $18 \pm 1 C^\circ$  during the experiments.)

Heat flux from single HETSS element is

$$Q_n = U_n \cdot U_m / k_m$$

The final formula for computer calculations is then

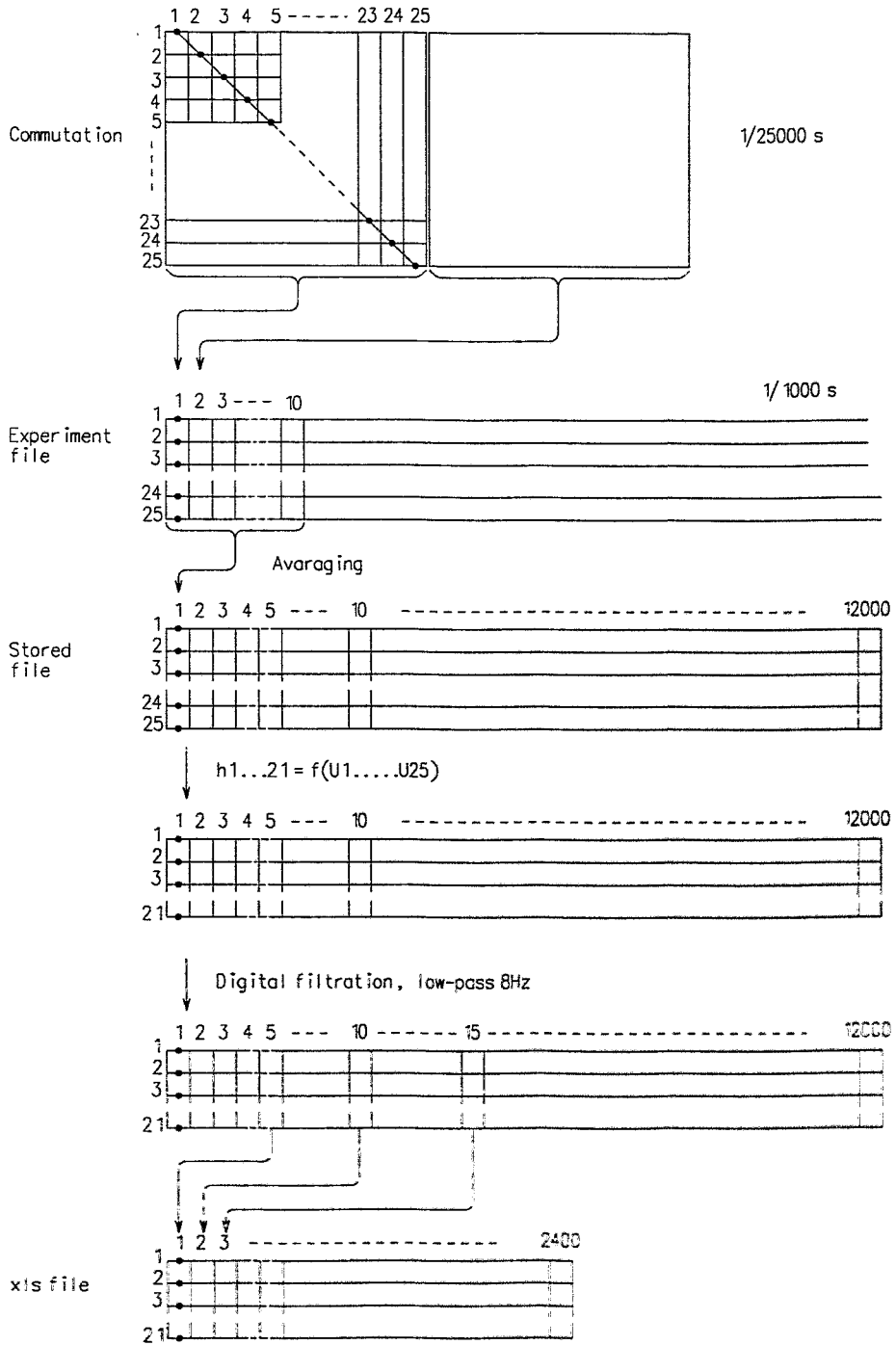
$$h_n = k_{af} \left( \frac{U_n}{U_m} - \frac{u_n \cdot \varphi_r}{u_m \cdot \varphi_{r0}} - \frac{U_n \cdot U_m \cdot d_i}{S[m^2] \cdot k_m \cdot \lambda_i} \right) / \frac{U_n \cdot U_m}{S[cm^2] \cdot k_m}$$

Inserting the fixed quantities for the present experiment, we have

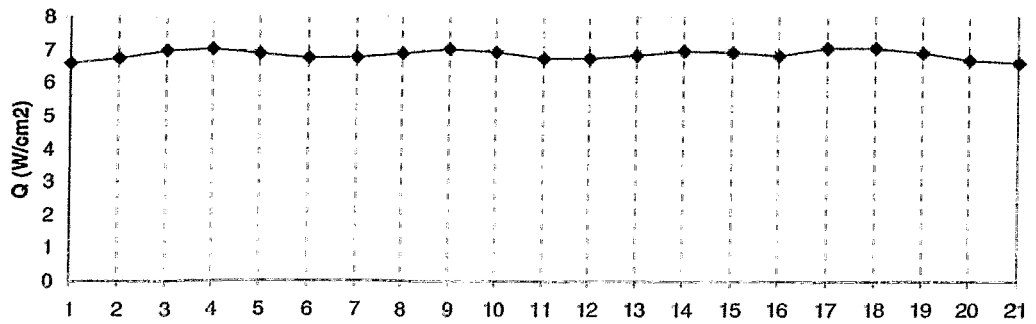
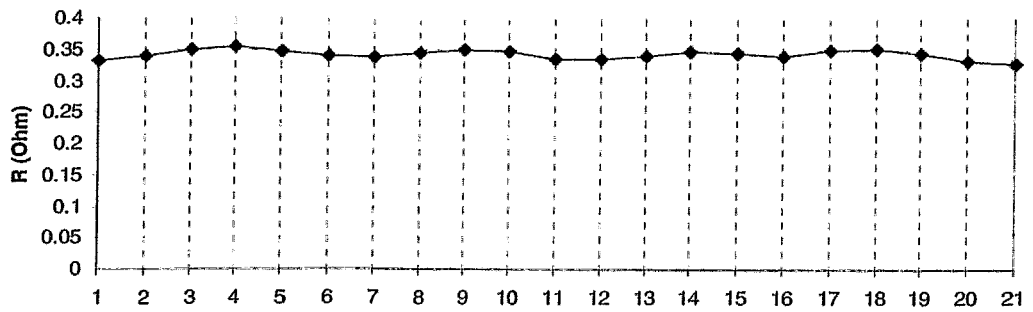
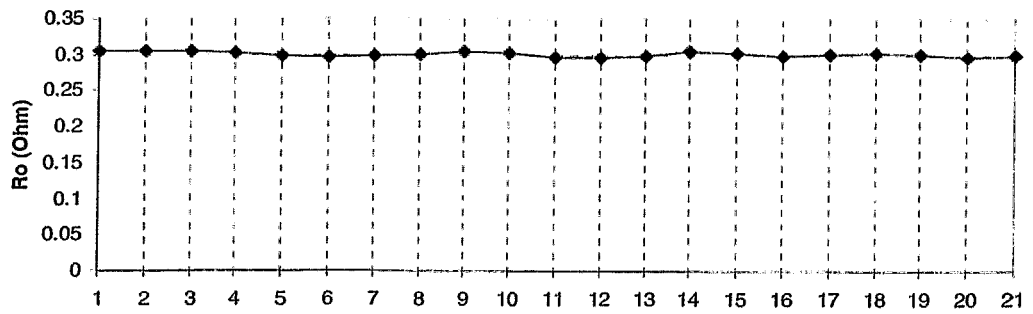
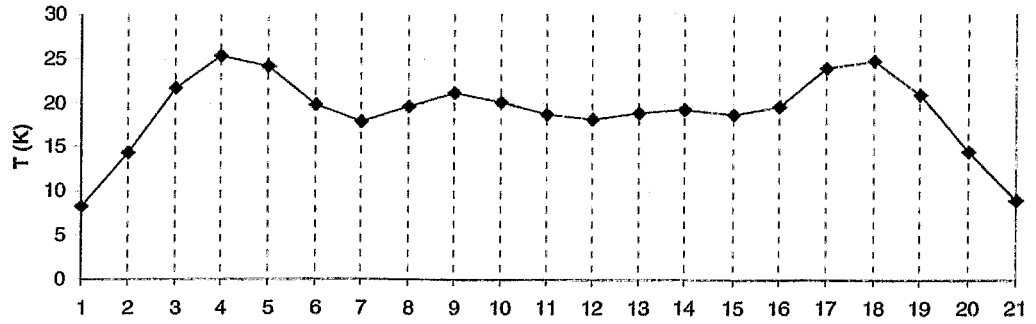
$$h_n = 0.8 \left( \frac{U_n}{U_m} - \frac{u_n \cdot \varphi_r}{u_m \cdot \varphi_{r0}} - 64.1 \cdot U_n \cdot U_m \right) / 33.3 \cdot U_n \cdot U_m$$

# Data processing

Made by Alexei Flerov  
"Test point"

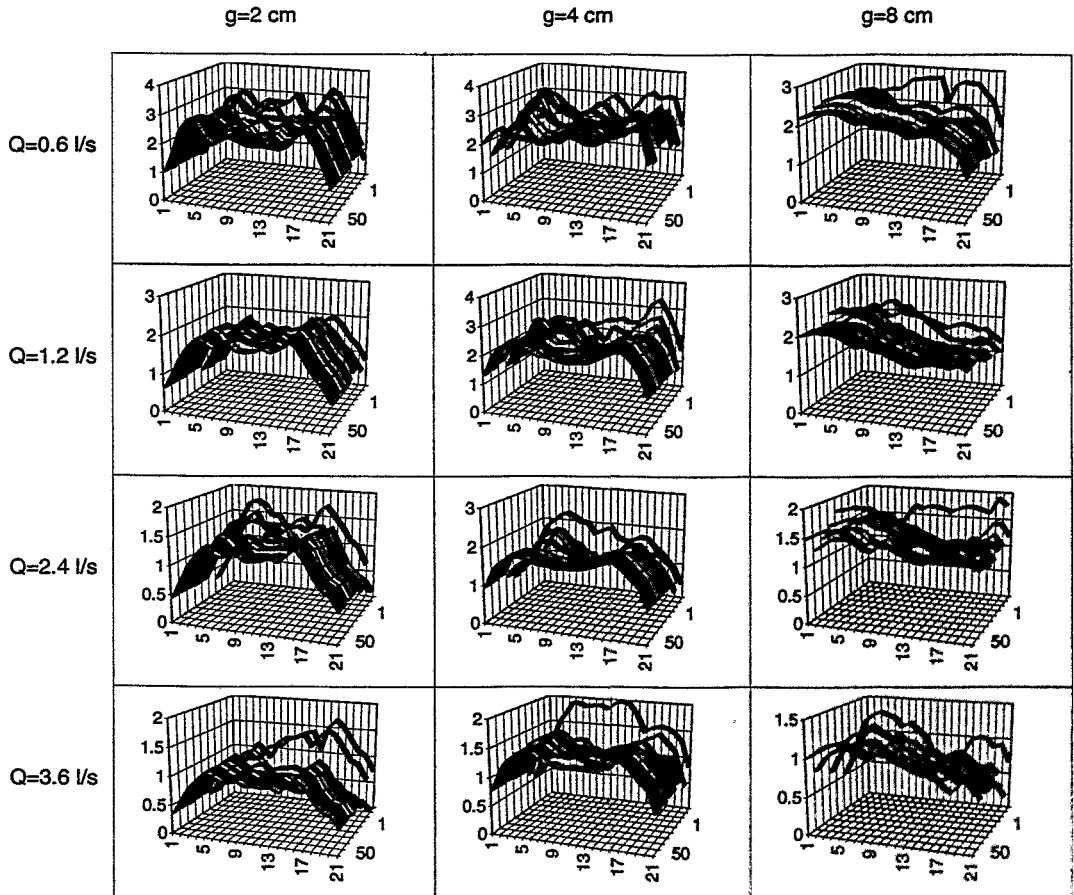


# Effect of temperature distribution on heat flux distribution

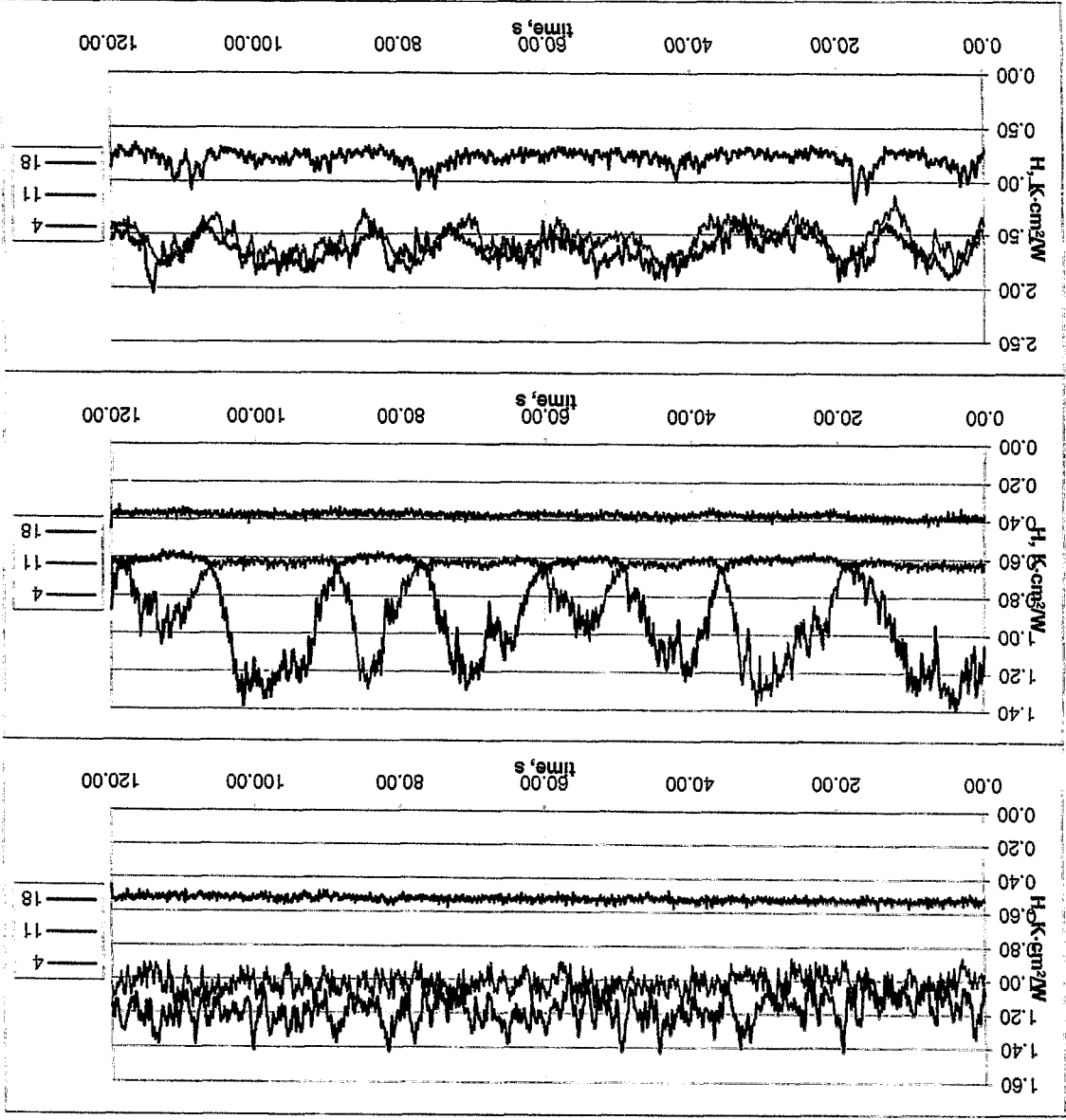


**Local thermal resistivity distribution  
along 21 HETSS elements**  
Measuring unit  $K \cdot cm^2/W$

Orientation  $0^\circ$  according Fig.1.







1.1/0.1

0.8/0.4

1.0/0.2

Q/q

Nozzle B  
Phase 3

Sheet 1

## THE AUTOMATED COMPLEX WITH REMOTE COMPUTER ACCESS FOR THE INVESTIGATIONS OF LIQUID METAL MHD HEAT TRANSFER

V.G. Ghilin, \* V.G. Sviridov, Yu.P. Ivotchkina, N.G. Razuvaev,  
\* L.G. Genin, \* E.V. Sviridov, \* A.V. Ustinov, V.S. Igumnov,  
(IIHT - Incorporated Institute of High Temperatures of the Russian Academy of Science,  
13/19 Igorskaya str., Moscow)  
(\*MPEI - Moscow Power Engineering Institute, 14 Krasnokazarmennaya str., Moscow)

The joint experimental complex are put into practice as a result of scientific cooperation between IIHI and MPEI. The complex make it possible to begin with joint program of MHD liquid metal (LM) heat transfer investigations applied to fusion TOKAMAK reactor. The complex consists of two experimental MHD facilities. The first one installed at MPEI is a LM (mercury) loop for investigations of hydrodynamics and heat transfer affected by LONGITUDINAL magnetic field (MF). The second facility at IIHI is generally the same LM loop in TRANSVERSE MF. Both facilities are automated. The specific feature of joint automated system: on the base of "Virtual Instruments" technology it enables the user to make experiments both directly at the facility or reportedly under conditions of remote computer access via LAN or Internet. We consider this approach to give wider opportunities for international scientific cooperation.

Various sensors and transducers were used at different stages of works, namely: microthermocouples, special film thermoanemometers for LM, optical fiber probes, correlation-type velocity sensor, electromagnetic velocity sensors. Two- and three-dimensional local measurements in LM flow are available.

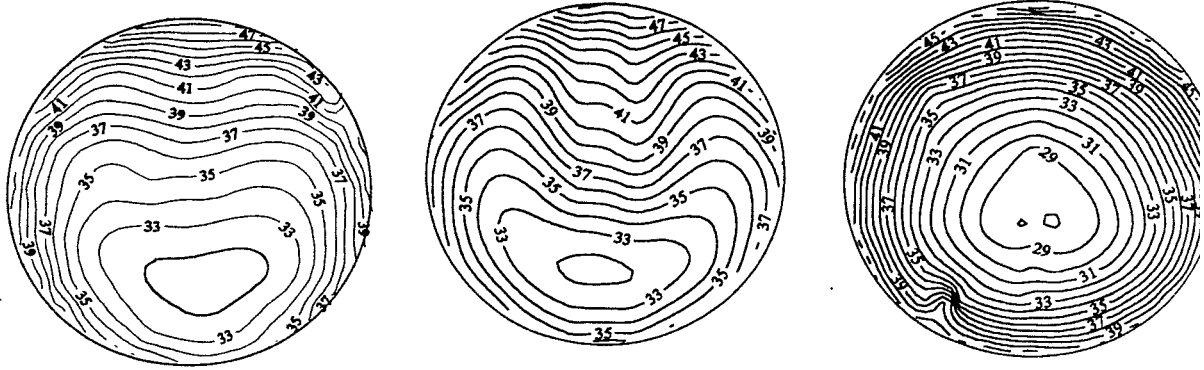
The current experimental program deals with temperature fields, local and averaged heat transfer intensities in a horizontal heated tube both in longitudinal and transverse MF applied to TOKAMAK reactor. The following regimes of heating are considered:

- 1) uniform wall heat flux distribution along the tube perimeter:  $q_1 = q_2 = \text{const}$ ;
- 2) non-uniform heating - heat flux on the left half of the tube is larger than on the right one  $q_1 > q_2$ ;
- 3) one-side heating - only one half of the tube is heated:  $q_1 \neq 0$ ;  $q_2 = 0$ .

The Reynolds, Hartman and Rayleigh criteria were as follows:  $Re = 5000 \div 120000$ ;  $Ha = 0 \div 500$ ;  $Ra = 0 \div 3 \cdot 10^6$ .

Some results of these current experiments are presented below:

1. The thermogravitational convection (TGC) affects LM heat transfer in a tube. Depending on the MHD-configuration, MF can enhance or weaken this effect (Fig.1). As a result of TGC affect local heat transfer intensity changes significantly along the tube perimeter. The zones with enhanced (at a bottom of a tube) and poorer (at a top) heat transfer intensities arise. The longitudinal MF makes this non-uniformity larger, while the transverse MF - smaller.
2. The TGC affect results in the appearance of secondary motion. The direct vertical components of the velocity measurements (Fig. 2) show the existence of one or two secondary vortices with axes parallel to main flow direction. Longitudinal MF makes these vortices more stable. Due to secondary motion the perimeter-averaged heat transfer intensity in MF can be even larger than without a MF.
3. Depending on the combination of electromagnetic and buoyancy forces acting on the flow, the turbulent velocity or temperature fluctuations (Fig.3) can be suppressed or increased. In some MHD configurations the regimes were found with abnormally high temperature fluctuations in a near-wall region. These fluctuations can be dangerous: on penetration into the wall they can cause high thermal stresses and fatigue failure of the wall material.



a) Without a magnetic field;      b) in longitudinal MF;      c) in transverse MF

Fig. 1. Mean temperatures in a cross-section of horizontal pipe. Uniform heating:  $q_1 = q_2$ .

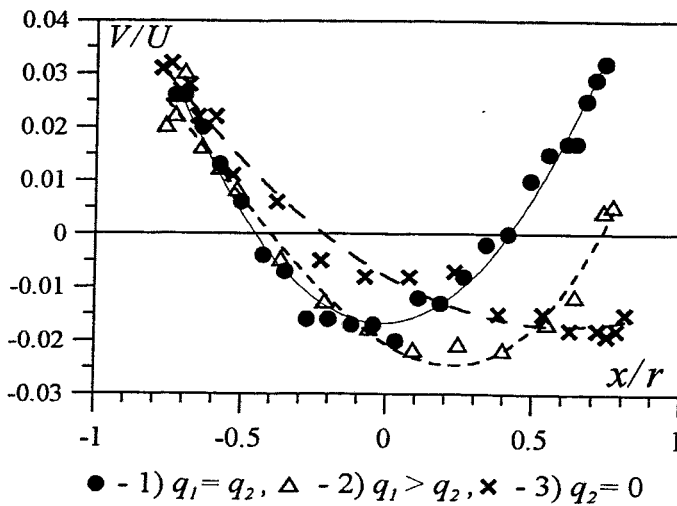


Fig. 2 Secondary motion -vertical velocity profiles ( $V$  - vertical velocity,  $U$  - mean longitudinal velocity).

$Re=3500$ ,  $Ha=450$

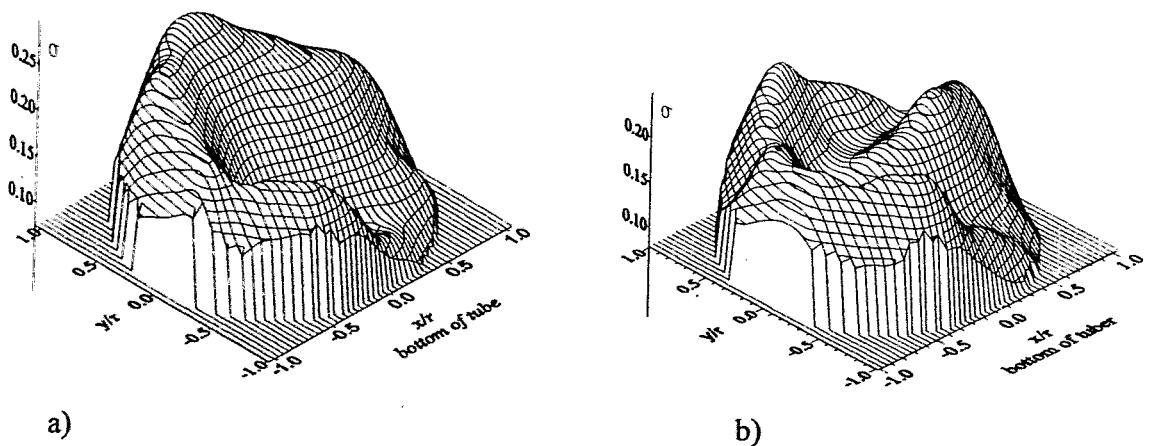
Heating regimes:

$q_1 = \text{const} = 35 \text{ kW/m}^2$ :

1)  $q_2 = 35 \text{ kW/m}^2$ ,

2)  $q_2 = 15 \text{ kW/m}^2$ ,

3)  $q_2 = 0 \text{ kW/m}^2$ ,



a)

b)

Fig. 3 Temperature intensity in tube cross-section (non-uniform heat flux  $q_1 = 35 \text{ kW/m}^2$ ,  $q_2 = 15 \text{ kW/m}^2$ ,  $Re = 24000$ ): a)  $Ha=0$ , b)  $Ha=300$ .

**THE AUTOMATED COMPLEX WITH REMOTE  
COMPUTER ACCESS FOR INVESTIGATIONS  
OF LIQUID METAL MHD HEAT TRANSFER**

*V.G. Sviridov, L.G. Genin, E.V. Sviridov, A.V. Ustinov,  
\* V.G. Ghilin, \* Yu.P. Ivotchkin, \* N.G. Razuvanov, \* V.S. Igumnov*

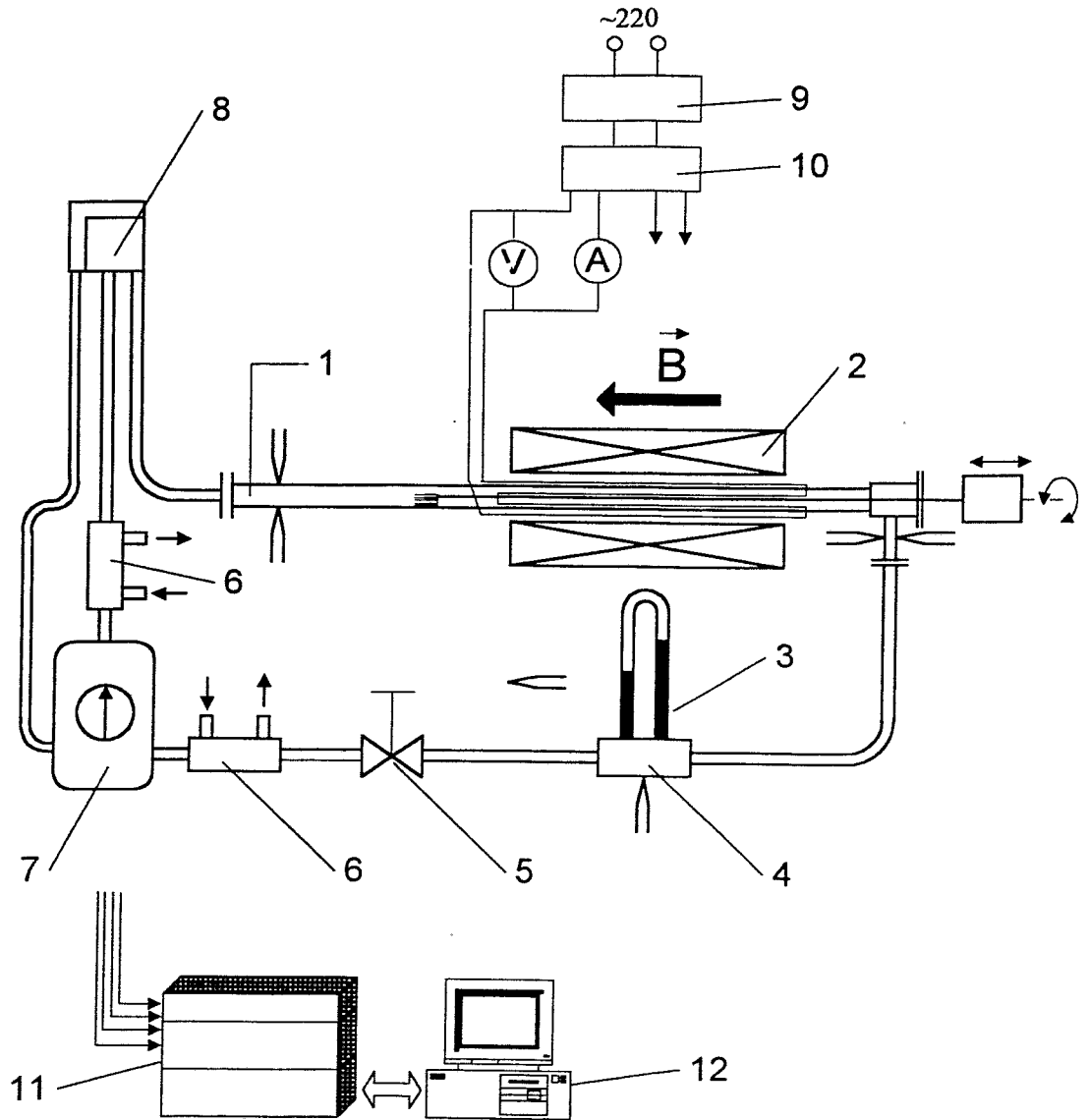
Moscow Power Engineering Institute (MPEI)

(14 Krasnokazarmennaya str., 111250 Moscow, Russia)

\* Incorporated Institute of High Temperatures  
of the Russian Academy of Science (IIHT RAS)

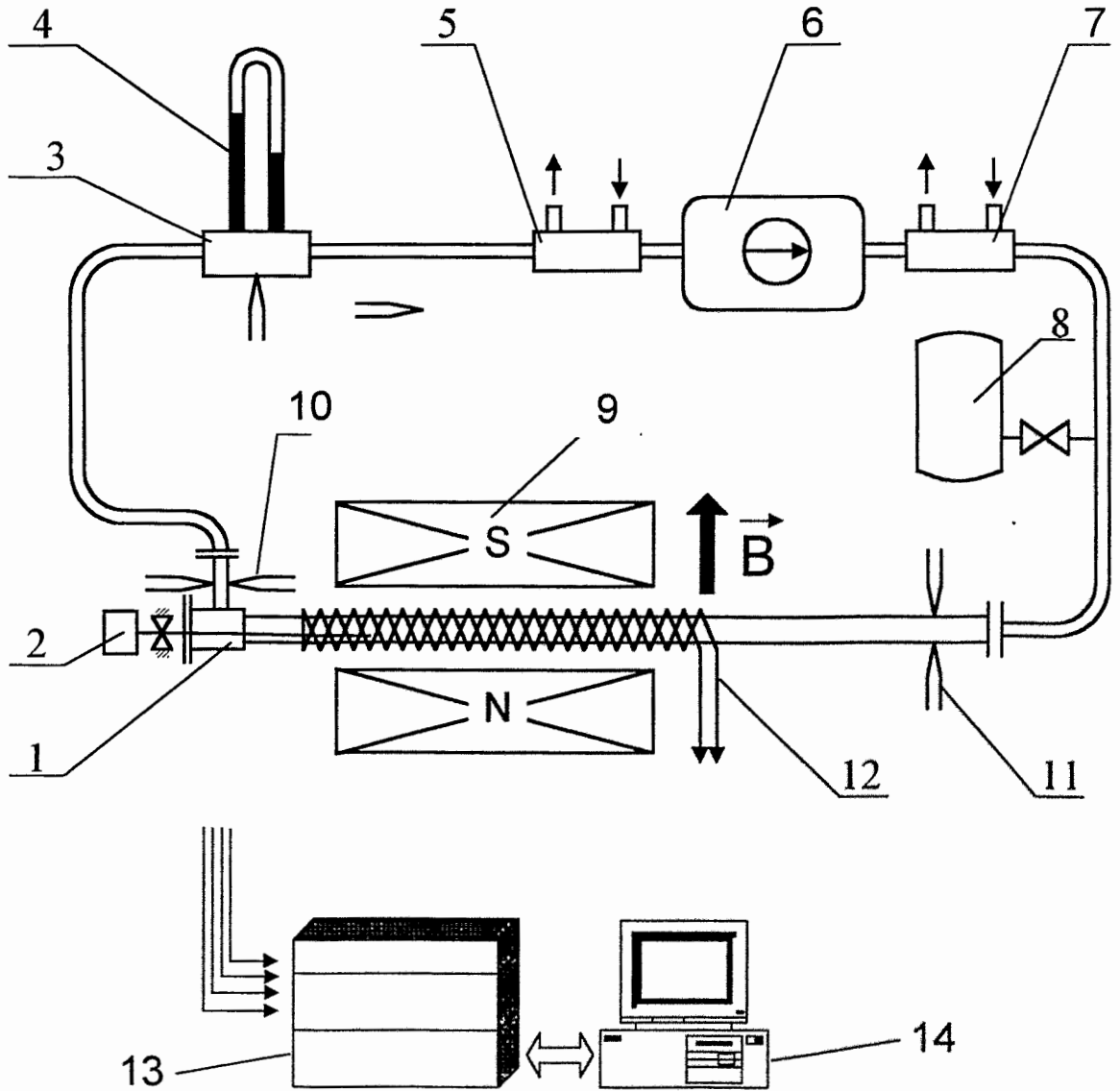
(13/19 Igorskaya str., 127412 Moscow, Russia)

**Experimental Facility at MPEI**  
**LM Loop for Investigations in LONGITUDINAL MF**



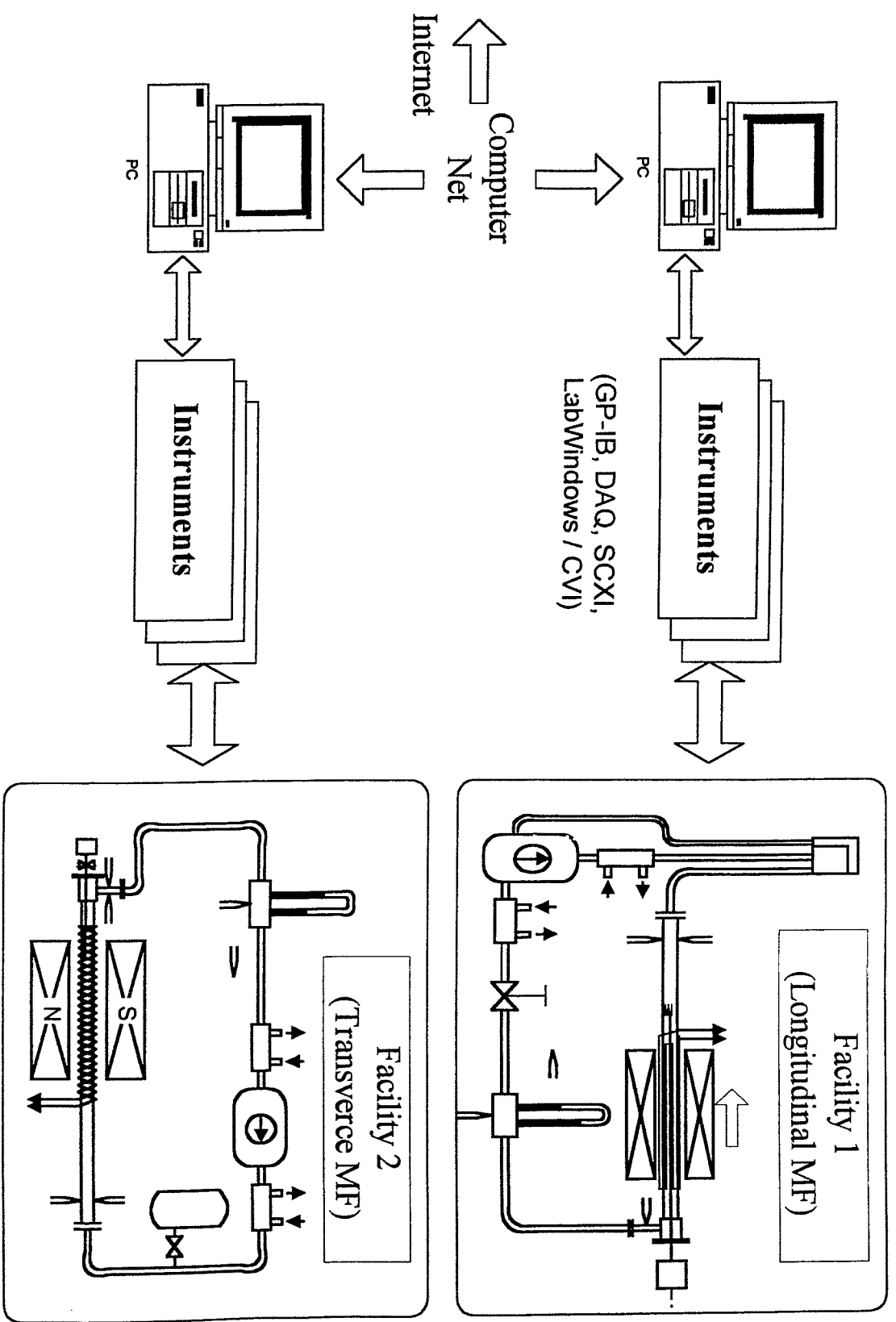
- 1 – Test-section, 2 – Solenoid, 3 – Differential manometer, 4 – Venturi tube,  
5 - Valve, 6 – Cooler, 7 – Pump, 8 – Constant level tank,  
9 – Stabilizer, 10 – Autotransformer, 11 – Data acquisition system,  
12 - Computer.

**Experimental Facility at IHI**  
**LM Loop for Investigations in TRANSVERCE MF**



- 1 – Test-section, 2 – Probe, 3 – Venturi tube, 4 – Differential manometer,  
 5, 7 – Cooler, 6 – Electromagnetic pump, 8 – Mercury tank,  
 9 – Electromagnet, 10 – Inlet thermocouples, 11 – Outlet thermocouples,  
 12 – Heater, 13 – Data acquisition system, 14 - Computer .

MPEL-IIH1 Joint Experimental MHD Facility  
with Remote Computer Access



## **SENSORS USED:**

- Thermocouples, Microthermocouples
- Electromagnetic Velocity Sensor
- Opto-mechanical Velocity Sensor
- Correlation Velocity Sensor
- Special Thermoanemometer for LMs

## **EXPERIMENTAL CONDITIONS**

**IIHT**  
(transverse MF)

**Re** – up to 120000,

**Pe** – up to 3000 ;

**Gr<sub>q</sub>** – up to  $3 \cdot 10^8$  ;

**Ra** – up to  $10^7$  ;

**Ha** - 0 ÷ 1000.

**MPEI**  
(longitudinal MF)

**Re** – up to 55000,

**Pe** – up to 1600 ;

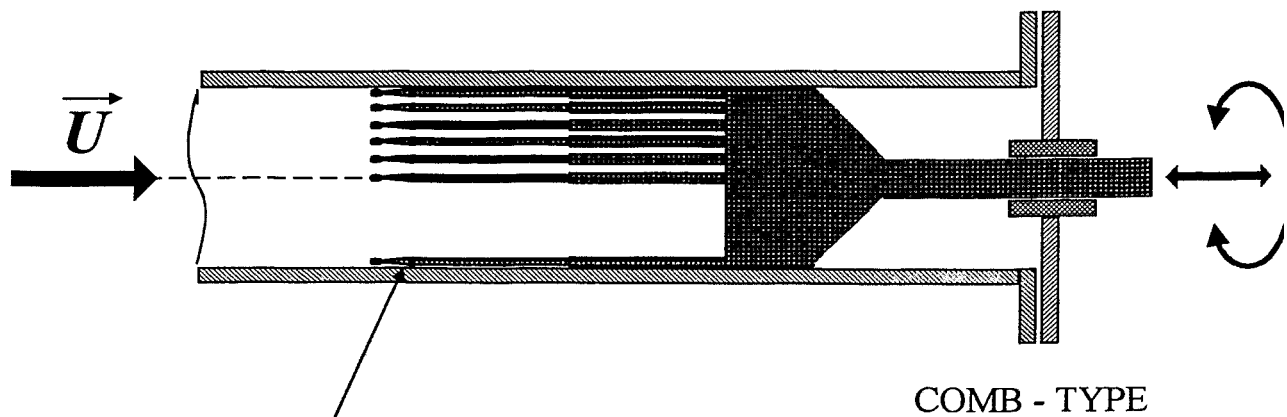
**Gr<sub>q</sub>** – up to  $3 \cdot 10^8$  ;

**Ra** – up to  $10^7$  ;

**Ha** - 0 ÷ 500.

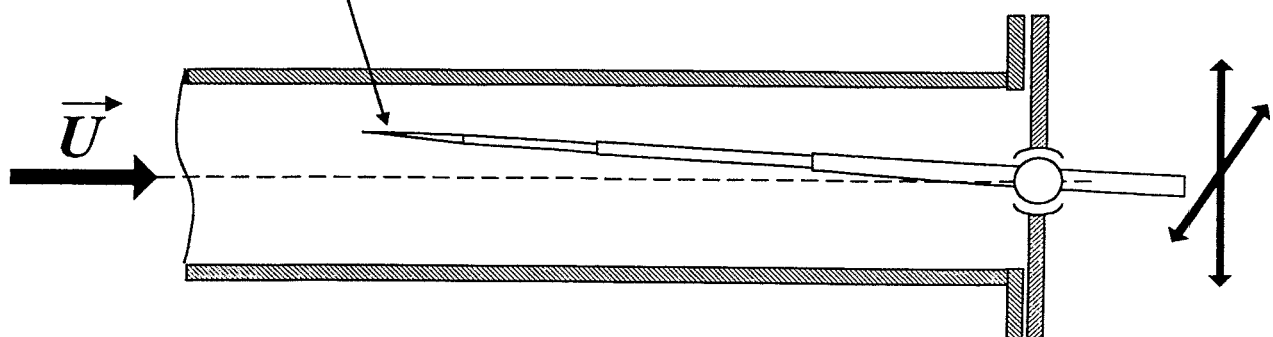


# Probe configurations

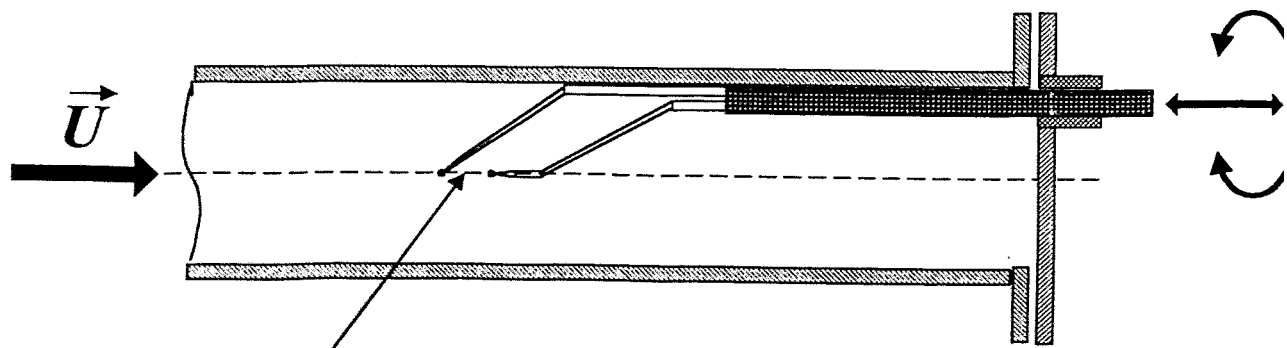


COMB - TYPE

Microthermocouple sensors



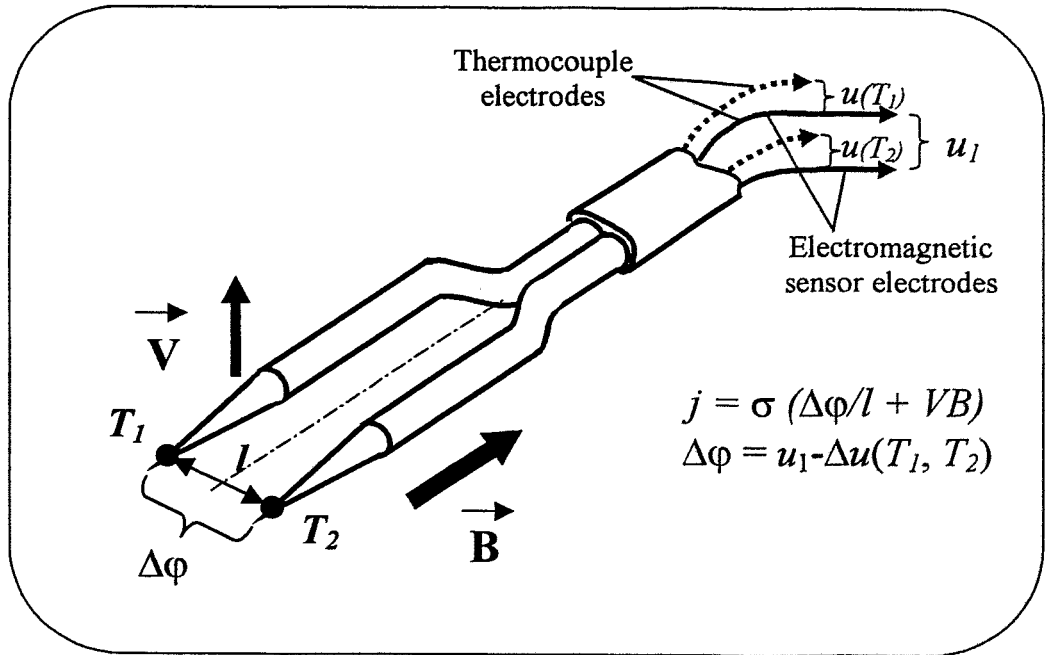
LEVER - TYPE



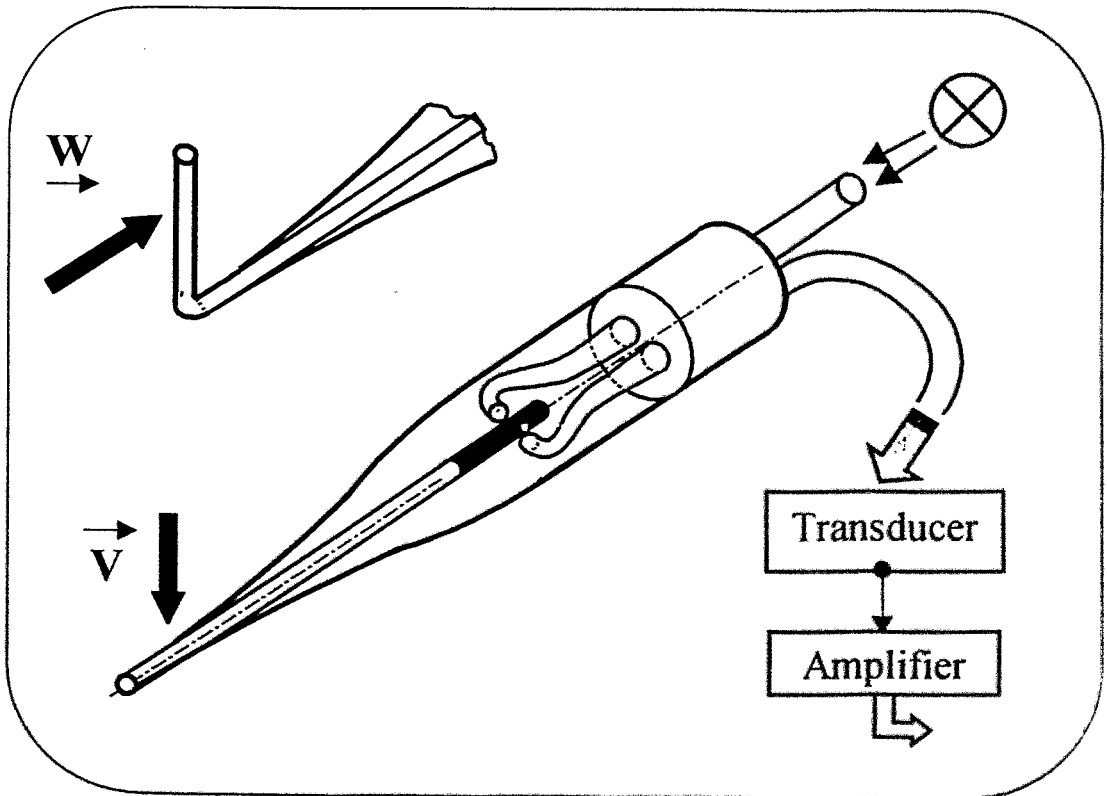
correlation velocity sensor

LONGITUDINAL WITH ASYMMETRIC BAR

### Electromagnetic velocity sensor with temperature compensation



### Opto-mechanical Velocity Sensors



# СИСТЕМА УРАВНЕНИЙ МАГНИТНОЙ ГИДРОДИНАМИКИ И ТЕПЛООБМЕНА

УРАВНЕНИЕ НЕРАЗРЫВНОСТИ:

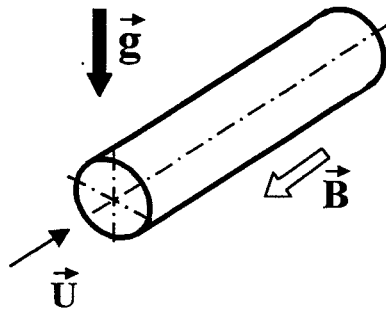
$$\frac{\partial \mathbf{w}_k}{\partial \mathbf{x}_k} = \mathbf{0}$$

УРАВНЕНИЯ ДВИЖЕНИЯ:

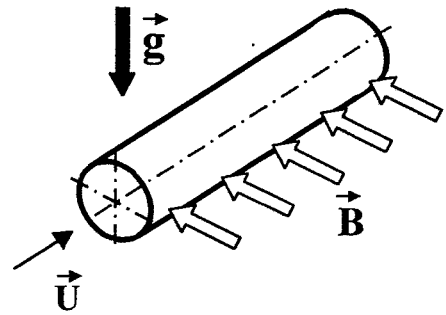
$$\left( \frac{\partial \mathbf{w}_i}{\partial \tau} + \mathbf{w}_k \frac{\partial \mathbf{w}_i}{\partial \mathbf{x}_k} \right) = - \frac{\partial p}{\partial \mathbf{x}_i} + \frac{1}{\text{Re}} \frac{\partial^2 \mathbf{w}_i}{\partial \mathbf{x}_k \partial \mathbf{x}_k} -$$
$$- \frac{\text{Gr}}{\text{Re}^2} (\text{T} - \text{T}_0) \mathbf{g}_i + \frac{\text{Ha}^2}{\text{Re}} \varepsilon_{ijk} \mathbf{j}_j \mathbf{B}_k$$

# Flow configurations

## Horizontal heated tube

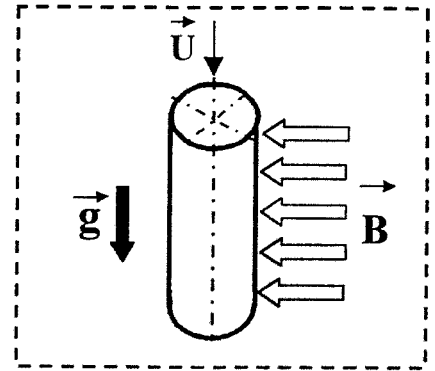
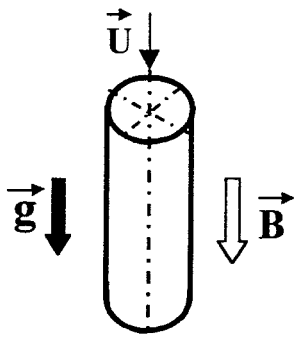


Longitudinal magnetic field

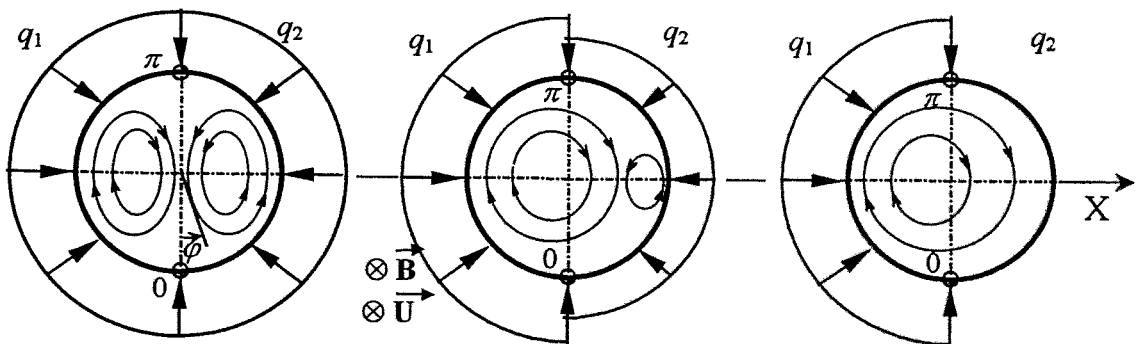


Transverse magnetic field

## Vertical heated tube



## Different cases of heating

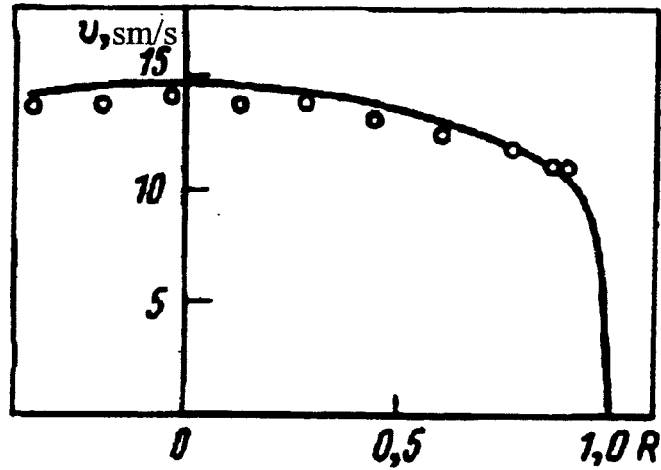


$q_1 = q_2 = \text{const}$   
1) Uniform heating

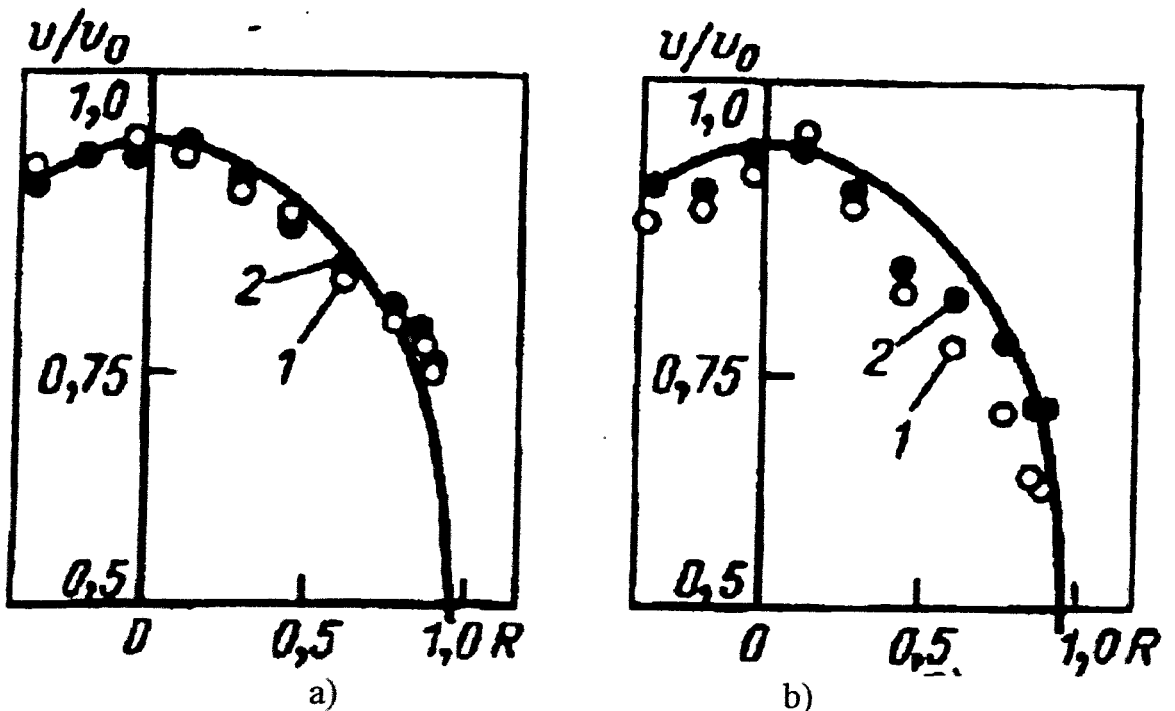
$q_1 > q_2$   
2) Non-uniform heating

$q_2 = 0$   
3) One-side heating

## The velocity correlation measurement results

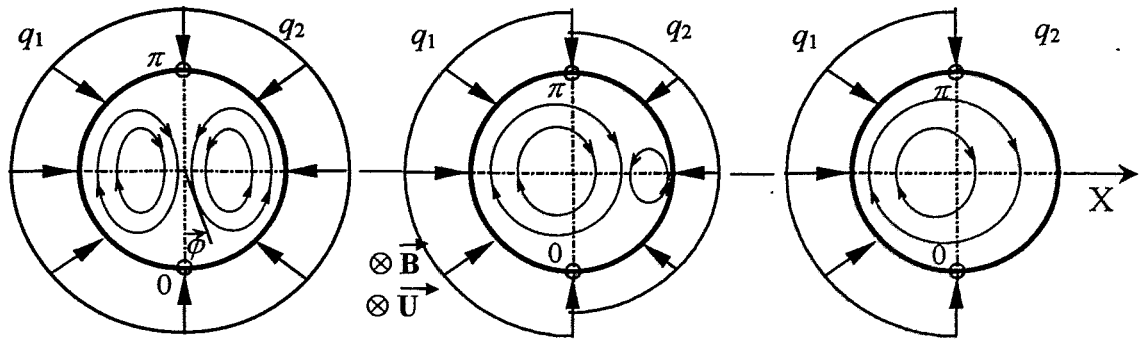


Experimental velocity profile (points) and theoretical Reichardt's profile (liquid line):  $Re = 2 \cdot 10^4$ .



The experimental velocity profile (points) in the vertical heated tube under longitudinal magnetic field:  $Re=10^4$ ; a) -  $Ha=0$ , b) - 300; 1 -  $Gr/Re^2=0.12$ , 2 - 0.25. Liquid line - Reichardt's profile.

Flow configuration.  
Different heating regimes.

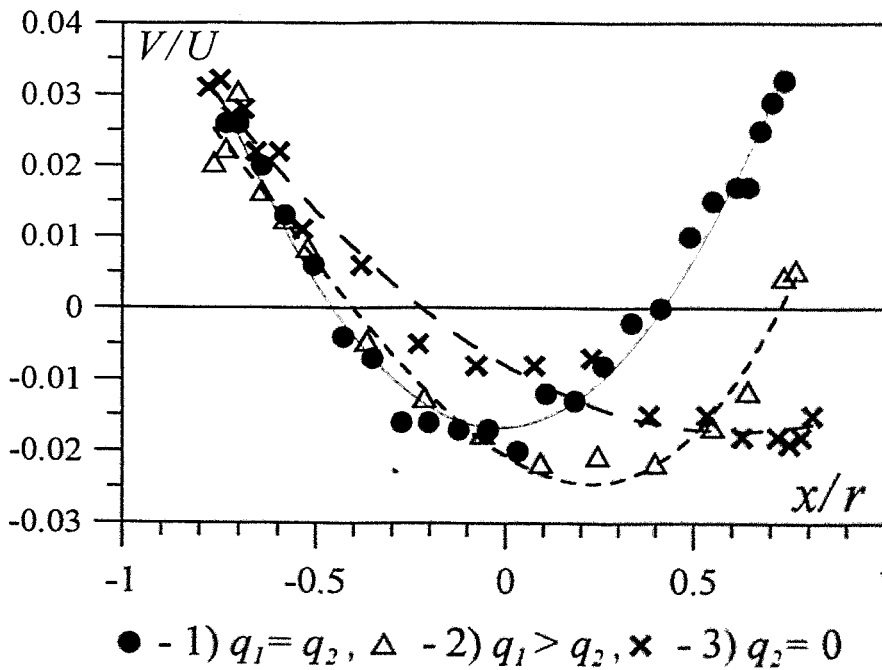


1)  $q_1 = q_2 = \text{const}$

2)  $q_1 > q_2$

3)  $q_2 = 0$

Secondary motion - vertical velocity profiles  
( $V$  - vertical velocity,  $U$  - mean longitudinal velocity).



$Re=3500$ ,

$Ha=450$

Heating regimes:

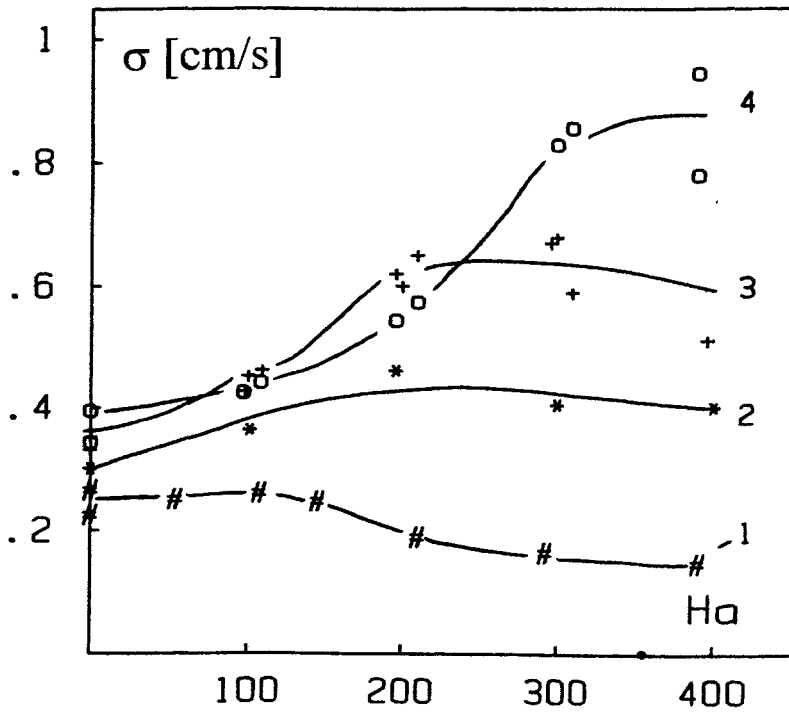
$q_1 = \text{const} = 35 \text{ kW/m}^2$

1)  $q_2 = 35 \text{ kW/m}^2$ ,

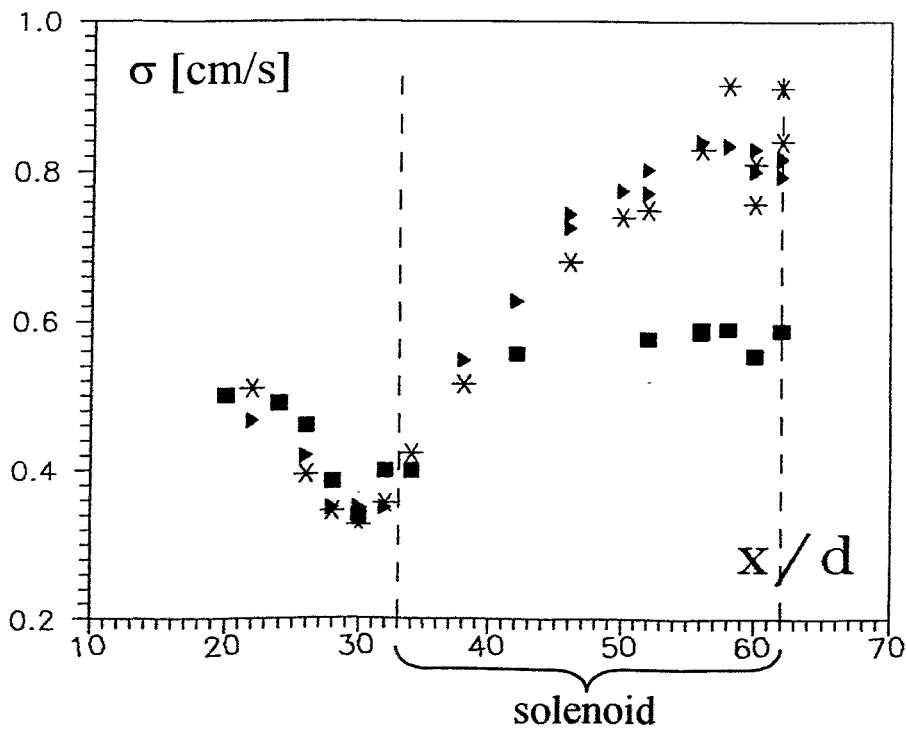
2)  $q_2 = 15 \text{ kW/m}^2$ ,

3)  $q_2 = 0 \text{ kW/m}^2$ ,

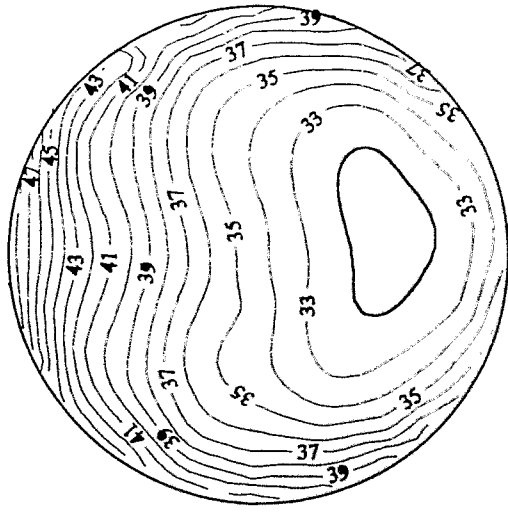
Velocity fluctuations intensity at the center of the liquid metal flow in vertical heated tube under longitudinal magnetic field



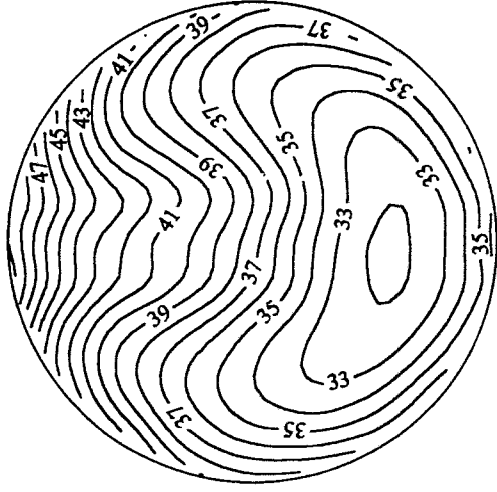
Velocity fluctuations intensity distribution along the tube



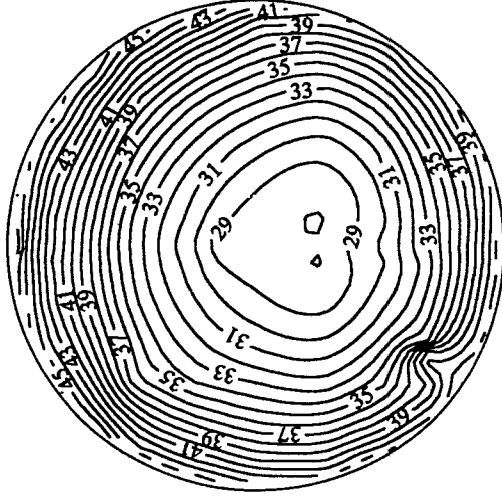
Mean temperatures in a cross-section of horizontal pipe. Uniform heating:  $q_1 = q_2$ .



a) Without a magnetic field;



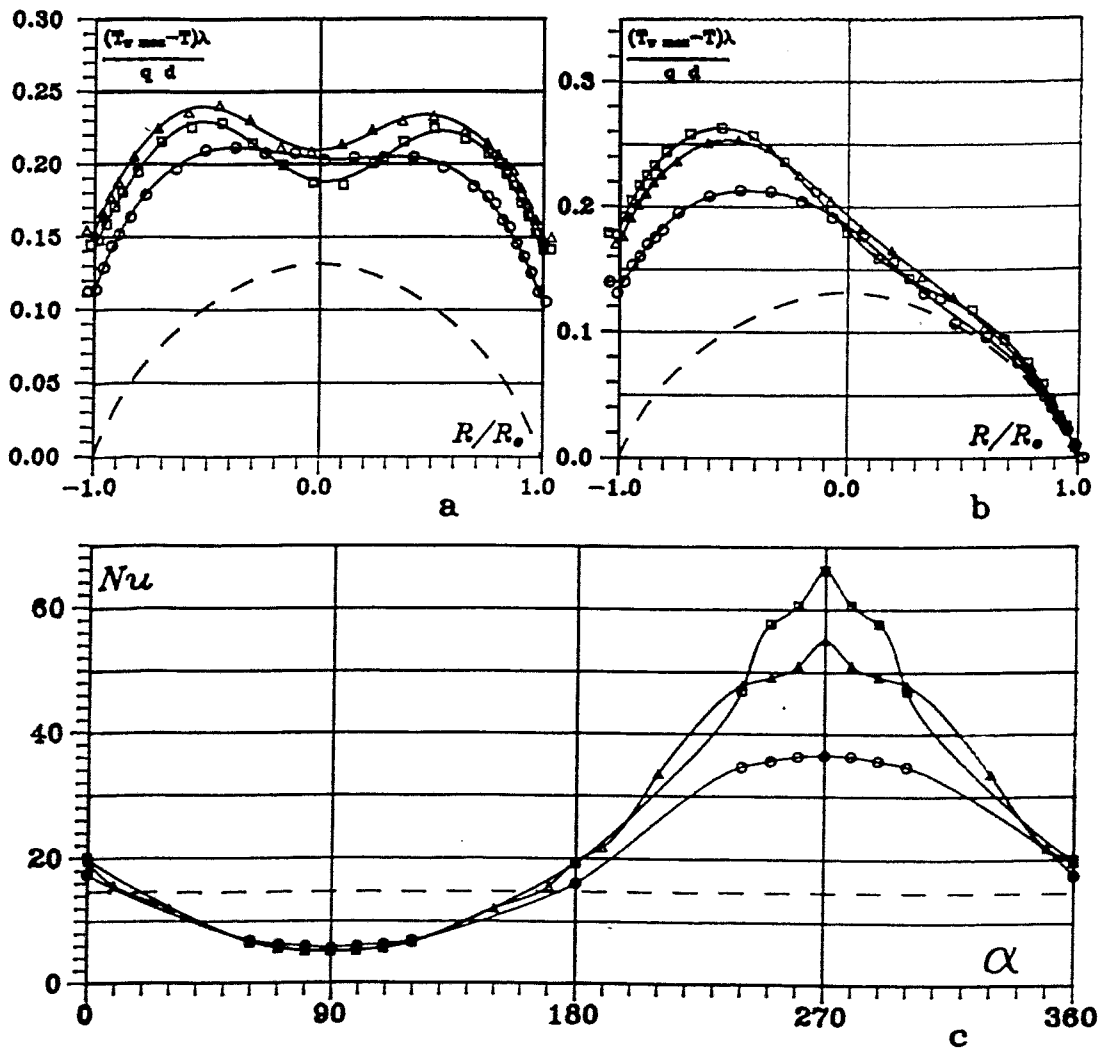
b) in longitudinal MF;



c) in transverse MF



Temperature profiles in horizontal (a) and vertical (b) planes, local  $Nu$  numbers (c) for identical  $Re$  numbers and heat fluxes and different  $Ha$  numbers

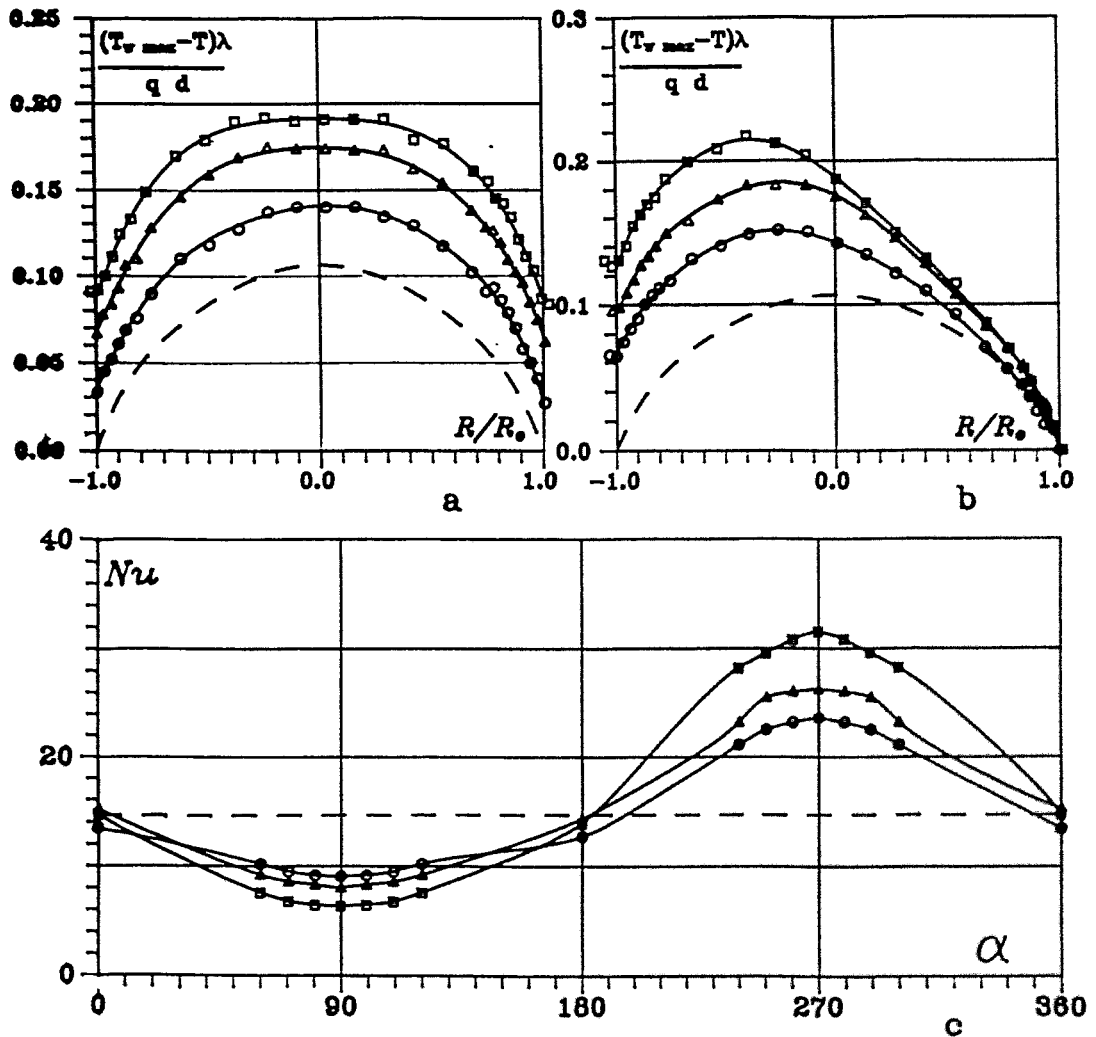


$Re=32000$ ;  $q=35000W/m^2$ ;  $Gr_q=7.2*10^7$ ;  $Ra=1.9*10^5$

- -  $Ha = 0$
- △ -  $Ha = 150$
- -  $Ha = 300$
- - Lion's profile for  $Re = 32000$

Fig.16

Temperature profiles in horizontal (a) and vertical (b) planes, local  $Nu$  numbers (c) for identical  $Re$  numbers and heat fluxes and different  $Ha$  numbers

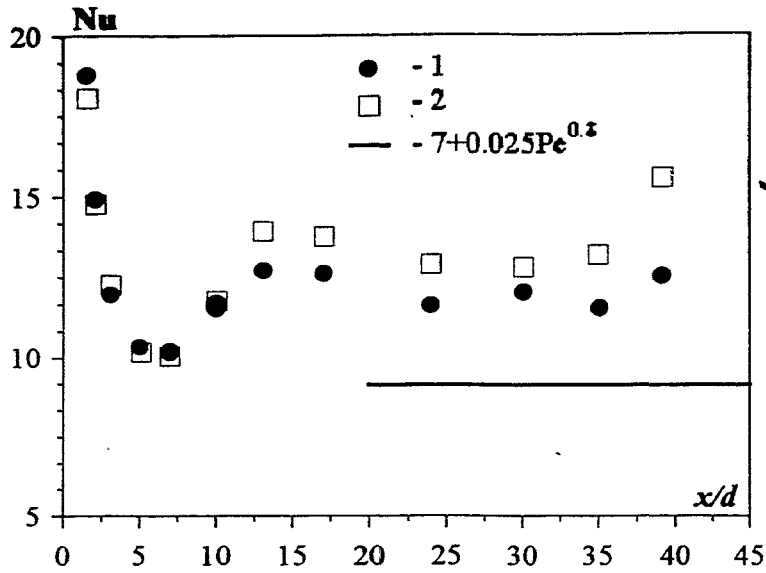


$Re=50000$ ;  $q=35000W/m^2$ ;  $Gr_v=7.2 \cdot 10^7$ ;  $Ra=1.9 \cdot 10^5$

- -  $Ha = 0$
- △ -  $Ha = 150$
- -  $Ha = 300$
- \* -  $Ha = 450$
- Lion's profile for  $Re = 50000$

Fig.15

Mean heat transfer intensity (Nusselt's number) along the tube.



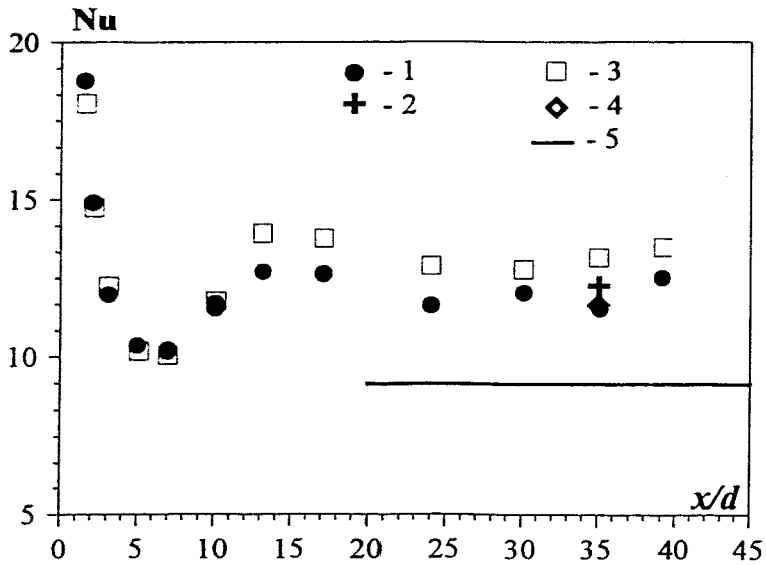
a) uniform heat flux

$$q_1 = q_2 = 24 \text{ kWt/m}^2,$$

$$Ra = 1.36 \cdot 10^6,$$

$$Pe = 261,$$

$$1 - Ha = 0, 2 - 300$$



b) non-uniform heat flux

$$q_1 = 35 \text{ kWt/m}^2,$$

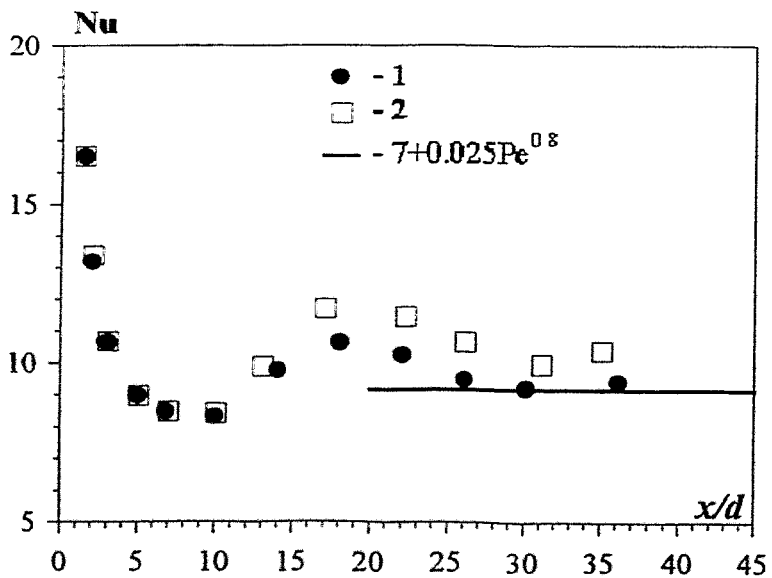
$$q_2 = 15 \text{ kWt/m}^2;$$

$$Ra = 1.4 \cdot 10^6; Pe = 261;$$

$$1 - Ha = 0, 2 - 150, 3 - 300,$$

$$4 - 450;$$

$$5 - Nu = 7 + 0.025Pe^{0.8}$$



c) heat flux from one side only

$$q_1 = 35 \text{ kWt/m}^2,$$

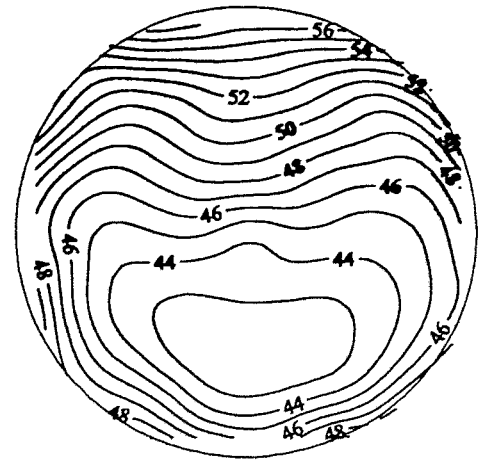
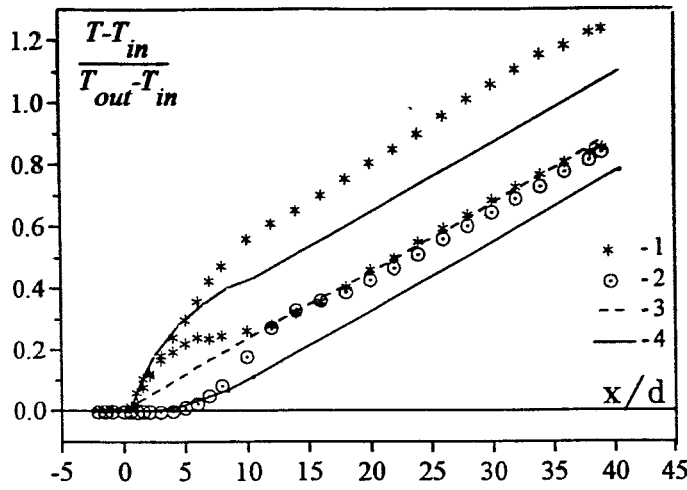
$$q_2 = 0 \text{ kWt/m}^2;$$

$$Ra = 0.96 \cdot 10^6;$$

$$Pe = 261;$$

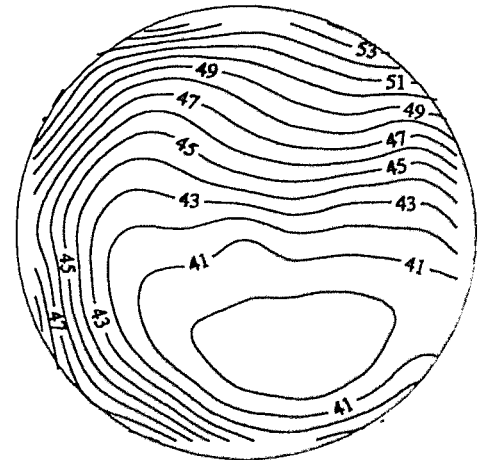
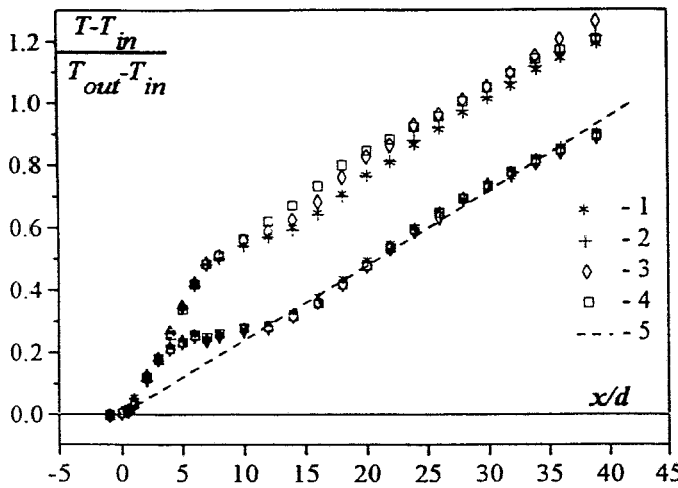
$$1 - Ha = 0, 2 - 300.$$

**Non-dimensionless wall temperature on the top and bottom point of cross-section along the tube and temperature fields.**



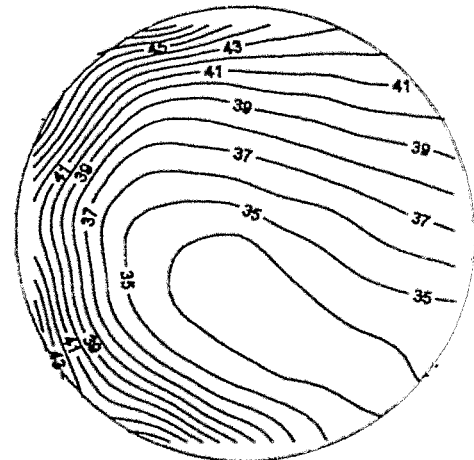
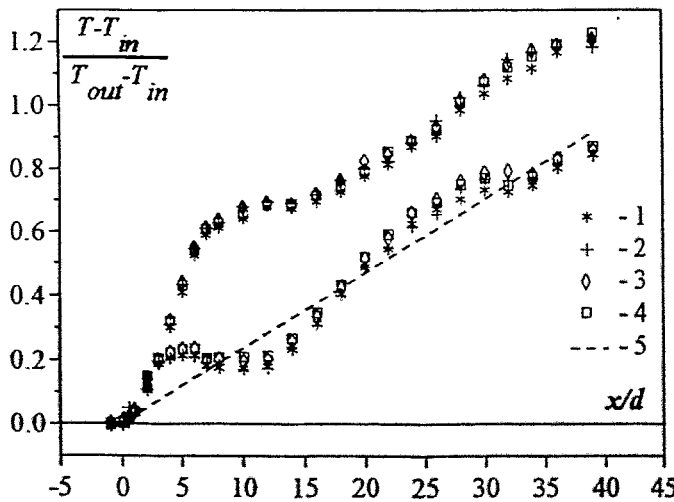
a)  $q_1 = q_2 = 24 \text{ kWt/m}^2$ ,  $Ra = 1.36 \cdot 10^6$ ,  $Pe = 261$ ,  $Ha = 0$ .  
 1 - top and bottom point of tube, 2 - bulk temperature, 3 - center of tube, 4 - wall and senter point of tube without free convection.

$x/d = 30$



b)  $q_1 = 35 \text{ kWt/m}^2$ ,  $q_2 = 15 \text{ kWt/m}^2$ ;  $Ra = 1.4 \cdot 10^6$ ,  $Pe = 261$ ;  
 1 -  $Ha = 0$ , 2 - 150, 3 - 300, 4 - 450, 5 - bulk temperature.

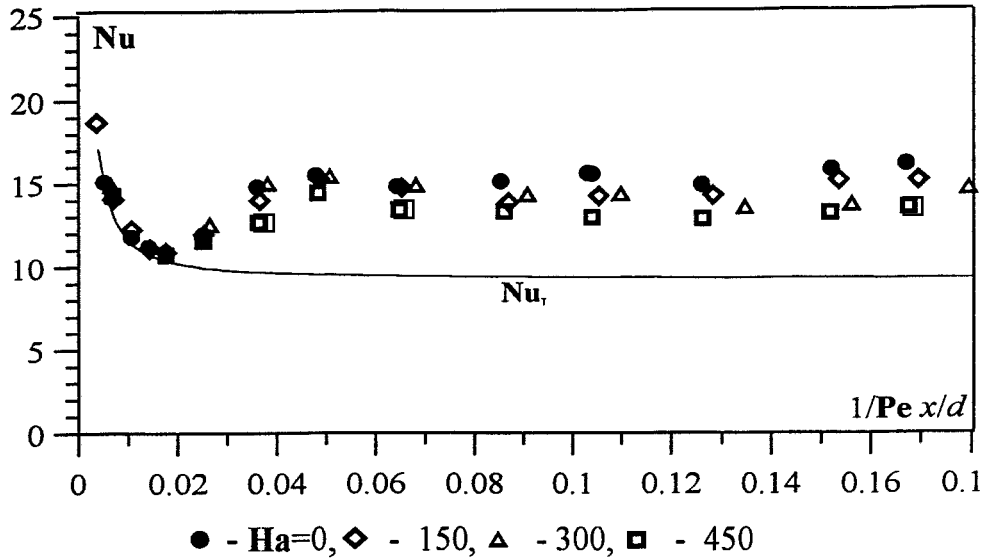
$x/d = 26$



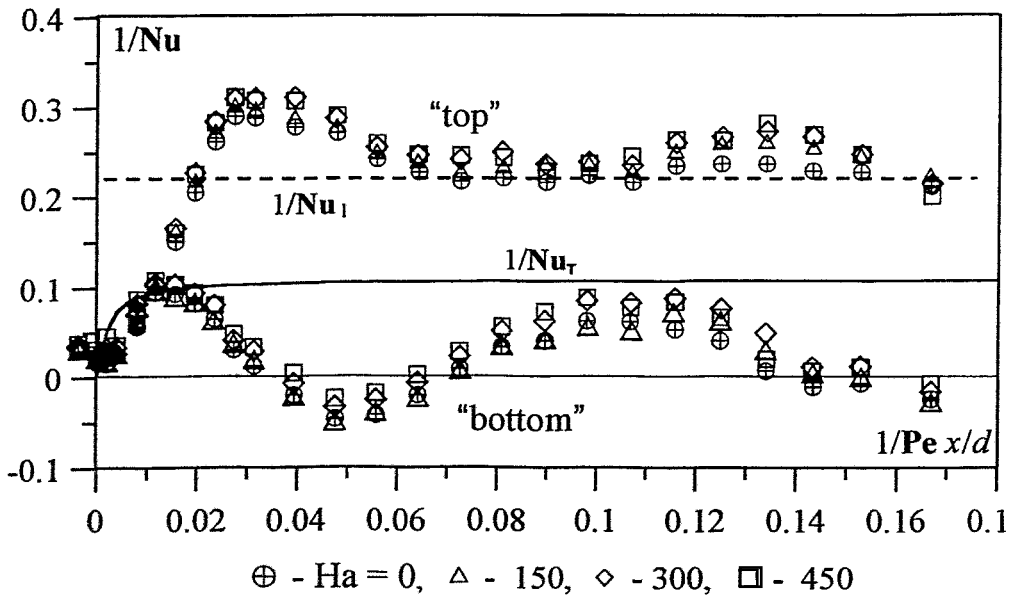
c)  $q_1 = 35 \text{ kWt/m}^2$ ,  $q_2 = 0 \text{ kWt/m}^2$ ,  $Ra = 0.96 \cdot 10^6$ ,  $Pe = 261$ ;  
 1 -  $Ha = 0$ , 2 - 150, 3 - 300, 4 - 450, 5 - bulk temperature.

$x/d = 26$

## EXPERIMENTAL RESULTS ON HEAT TRANSFER INTENSITY ALONG THE TUBE



Mean heat transfer intensity (Nusselt's number) along the tube  
(uniform heat flux  $q_1 = q_2 = 35 \text{ kWt/m}^2$ ,  $Pe = 243$ ,  $Ra = 1.36 \cdot 10^6$ ).

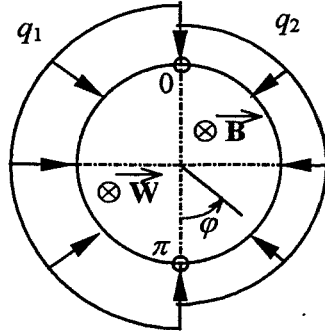


$$Nu_1 = 4.36$$

$$Nu_T - \text{Lyon equation}$$

Non-dimensionless wall temperature at the top ( $\varphi = \pi$ ) and bottom ( $\varphi = 0$ )  
point of cross-section along the tube (non-uniform heat flux:  
 $q_1 = 35 \text{ kWt/m}^2$ ,  $q_2 = 0 \text{ kWt/m}^2$ ;  $Pe = 261$ ;  $Ra = 0.96 \cdot 10^6$ ).

Temperature intensity in tube cross-section  
(non-uniform heat flux)

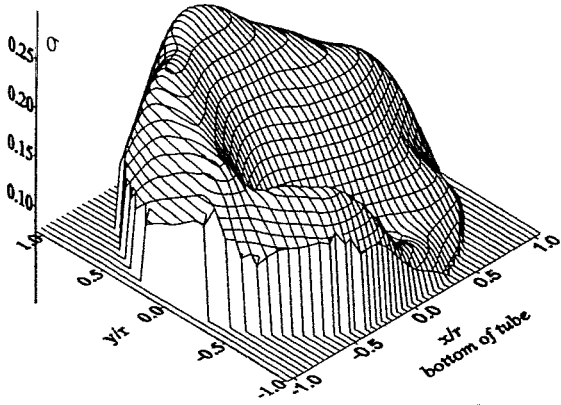


$q_1 = 35 \text{ kW/m}^2$ ,  
 $q_2 = 15 \text{ kW/m}^2$ ;

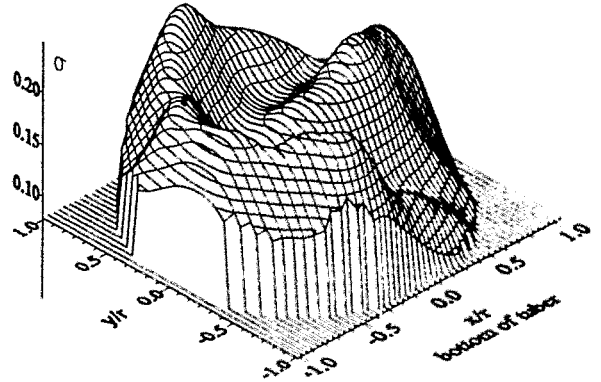
$\text{Re} = 24000$ );

a)  $\text{Ha} = 0$ ,

b)  $\text{Ha} = 300$ .



a) without MF



b) in longitudinal MF

## Scientific Programme

**October 12, 1999 (Tuesday)**

### **Morning Session**

**9.30 Invited Lecture**

*M. Iguchi (Hokkaido University, Japan)*

Measurement methods of bubble and molten metal flow characteristics in materials processing

**10.15 *I. Opstelten (Hoogovens R&D, The Netherlands)***

Measurement of multiphase flow in metallurgy

**10.35 *S. Eckert, G. Gerbeth (FZ Rossendorf, Germany), B. Guttek, H. Stechemesser (FZ Jülich, Germany), O. Lielausis (Institute of Physics Riga, Latvia)***

Investigation of liquid metal two phase flow characteristics by means of local resistivity probes and X-ray screening technique

**10.55 Coffee break**

**11.15 *P. Satyamurthy, N. Dixit, M. Quarishi, (Bhaba Atomic Research Centre, India) N. Venkatrami (Aligarh Muslim University, India)***

Void profile studies in vertical upward co-current churn mercury-nitrogen flow

**11.35 *B. Hofmann, E. Kaiser (Technical University Dresden, Germany)***

*S. Eckert, G. Gerbeth (FZ Rossendorf, Germany)*

Ultrasonic measurements of the motion of gas bubbles rising in a liquid metal

**11.55 *W. Grill, M. Schmachtl, J. Jahny (University Leipzig, Germany)***

Ultrasonic measuring techniques suitable for high temperature melts for Doppler imaging, for the determination of densities and temperatures and for the growth rate of the solidified fraction

**Measurement methods of bubble and  
molten metal flow characteristics  
in materials processing**

**October 11-13,1999  
Dresden**

**Manabu Iguchi**

**Division of Materials Science and Engineering  
Graduate School of Engineering  
Hokkaido University**



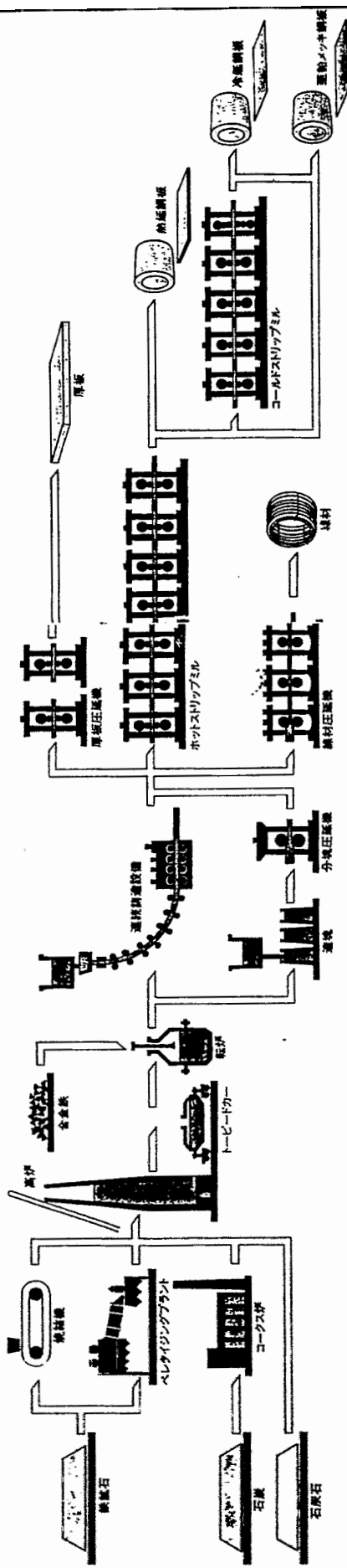
# Measurement methods of bubble and molten metal flow characteristics in materials processing

M. Iguchi

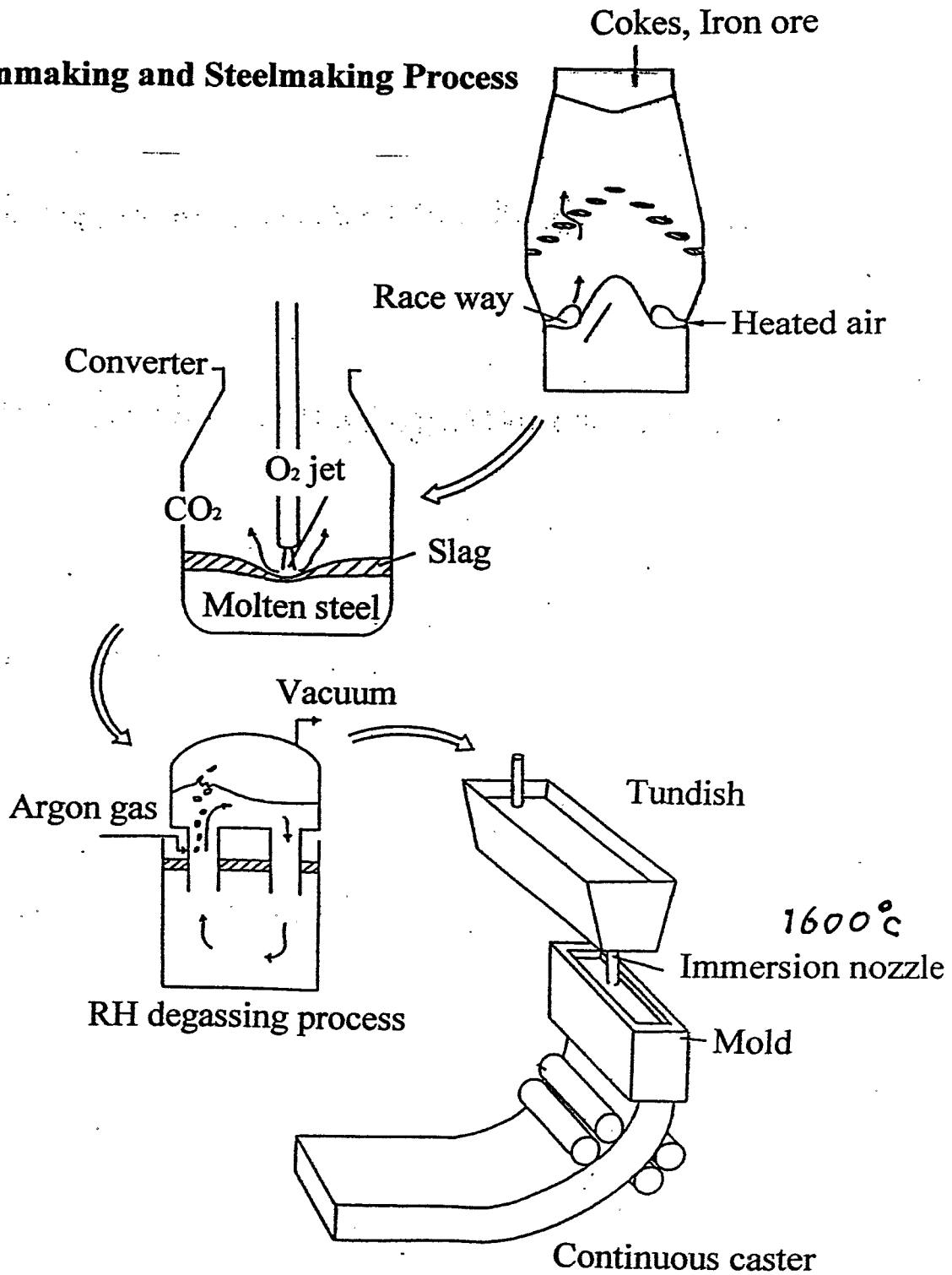
*Hokkaido University, Division of Materials Science and Engineering,  
Graduate School of Engineering, Hokkaido, 060-8628, Japan*

In many materials refining processes gas is injected into the molten metal bath of the processes to agitate the bath, and hence, homogenize the bath temperature and chemical compositions. The dispersion of bubbles and molten metal flow induced by the bubbles are responsible for the efficiency of the processes. An electroresistivity probe is usually used to measure the bubble characteristics represented by bubble frequency, gas holdup (void fraction), mean bubble rising velocity and mean chord length. This kind of probe is applicable to molten metal baths of a temperature up to 1873 K. On the other hand, it is very difficult to measure the mean velocities and turbulence components of molten metal flow at very high temperatures. The mean velocities of molten metal flows can be measured using a reaction probe or a Karman vortex probe even if the molten metal temperature is 1873 K as long as the surface flow on the bath is concerned. However, there exists no reliable velocimeter capable of measuring the turbulence components of molten metal flows at a temperature above 400 K. Below 400 K the Vives probe, i.e., magnet probe is widely used. In this paper some experimental results of the bubble and molten metal flow characteristics in a cylindrical bath agitated by bottom gas injection are introduced. The bath is filled with mercury, Wood's metal, molten copper or molten pig iron. Also, X-ray fluoroscopic observation of bubbles in a molten pig iron bath is discussed.

一貫工程図



# Ironmaking and Steelmaking Process



# **Current processes**

**Energy consumption is huge.**

**CO<sub>2</sub> emission**

**Enhancement of efficiency of current processes**

**Development of new processes**

**Fluid flow phenomena of molten steel :**

**No reliable sensor for the measurement of the fluid flow phenomena in practical applications**

# Flow in Materials Processing

**(1) Multiphase flow**

**(2) Highly turbulent**

$Tu > 100\%$

**(3) High temperature**

$1600^\circ\text{C}$

**Water model experiments**

**Numerical simulation**

**Purpose**

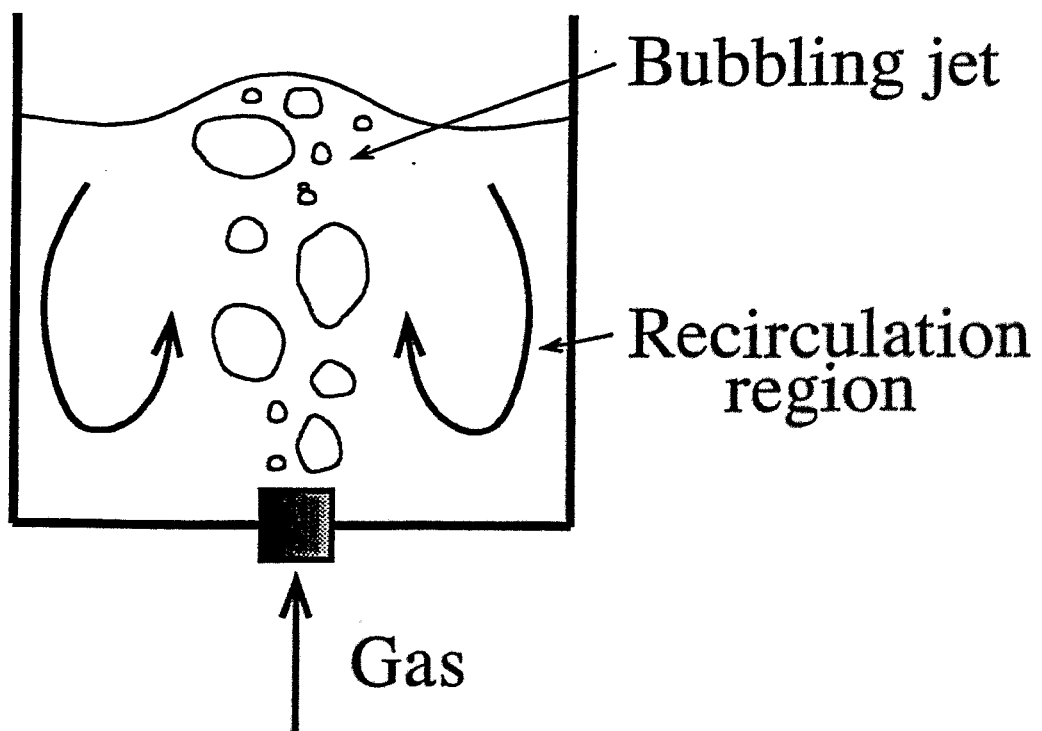
**Development of sensors applicable  
in actual processes**

**Measurement of bubble characteristics  
in bottom injection reactor**

**Measurement of molten steel flow  
in continuous casting mold**

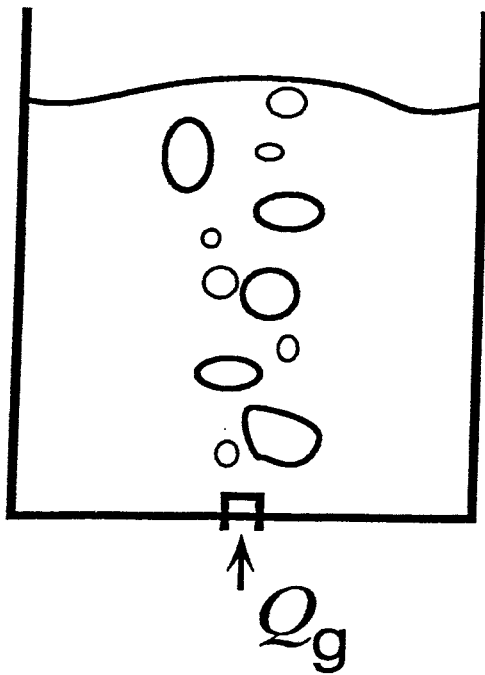
# 1. Effects of gas injection

- (1) **Mixing**
- (2) **Removal of impurities**
- (3) **Removal of nonmetallic inclusions**
- (4) **Enhancement of melting rate of scrap**

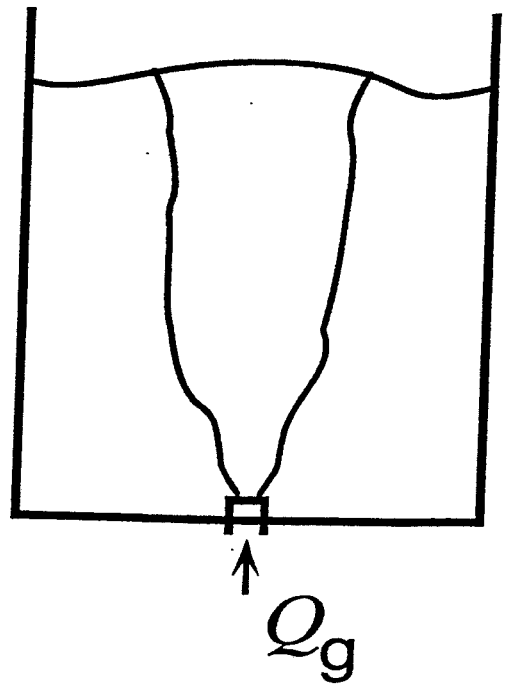




## Classification of flow pattern



Bubbling  
Mach number  
 $M < 1$



Jetting  
Mach number  
 $M \geq 1$

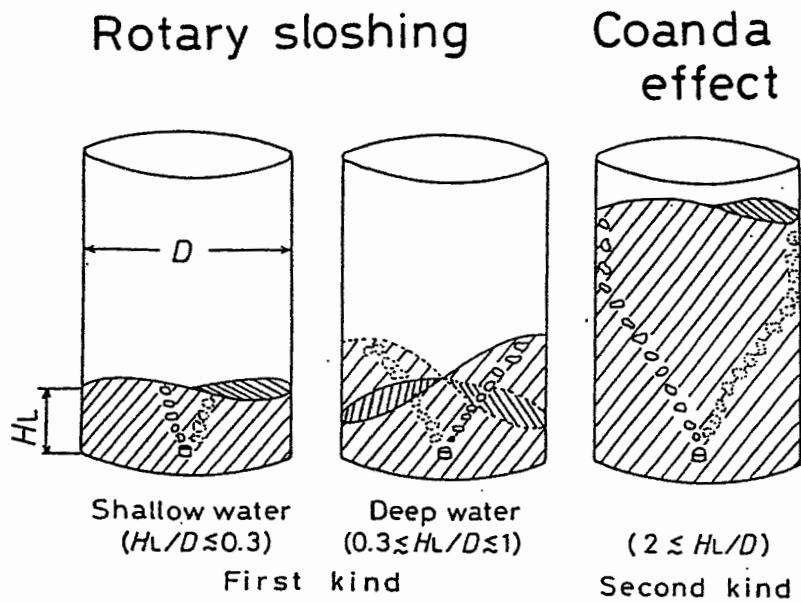


Fig. Classification of the swirl motions of bubbling jet in a cylindrical vessel.

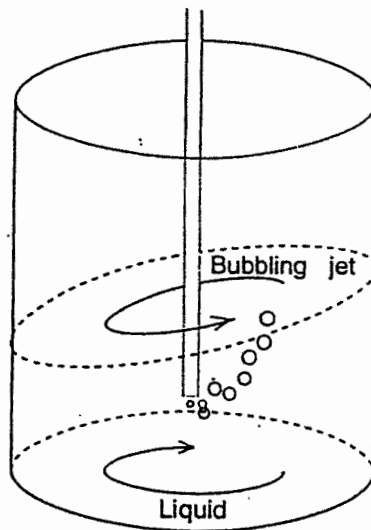
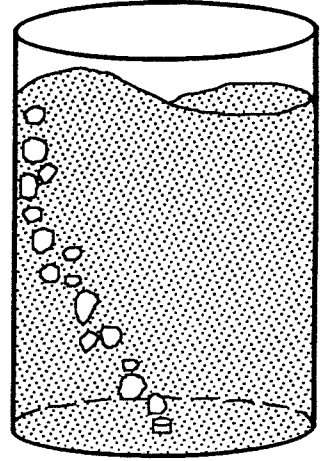
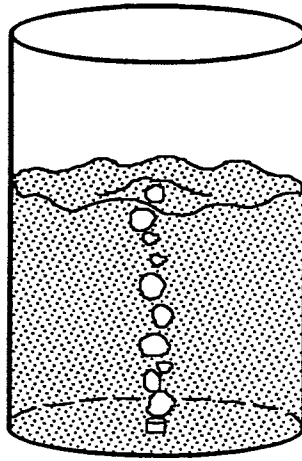
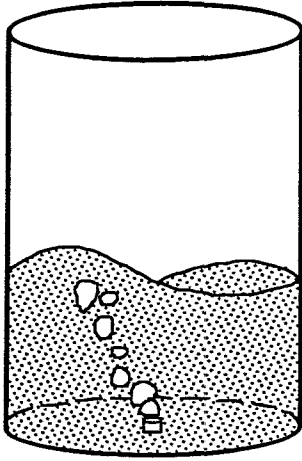
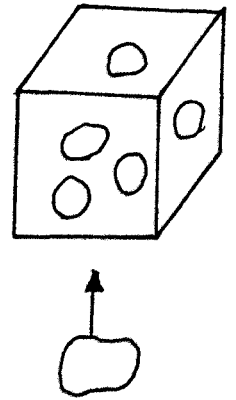


Fig. Schematic illustration of swirl motion caused by gas injection through an immersed top lance.



# Measurements of bubble characteristics

- (1) Gas holdup
- (2) Bubble frequency
- (3) Bubble rising velocity
- (4) Bubble chord length
- (5) Bubble shape



**Bubble**

## Transparent liquid

- (a) Still camera
- (b) High speed video camera
- (c) Electroresistivity probe
- (d) Image processing

---

**X ray fluoroscopic observation**

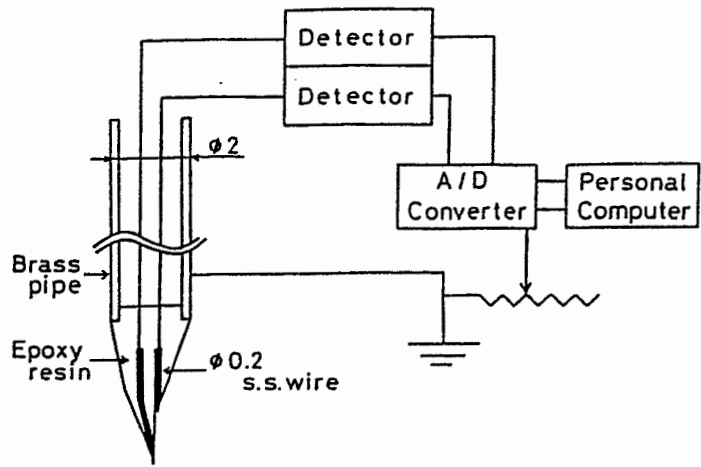
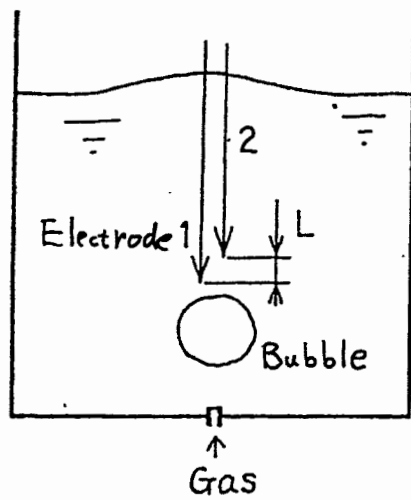


Figure Schematic of the two-element electro-resistivity probe.



- (1) Gas holdup (Void fraction)
- (2) Bubble frequency
- (3) Bubble rising velocity
- (4) Bubble chord length
- (5) Bubble shape

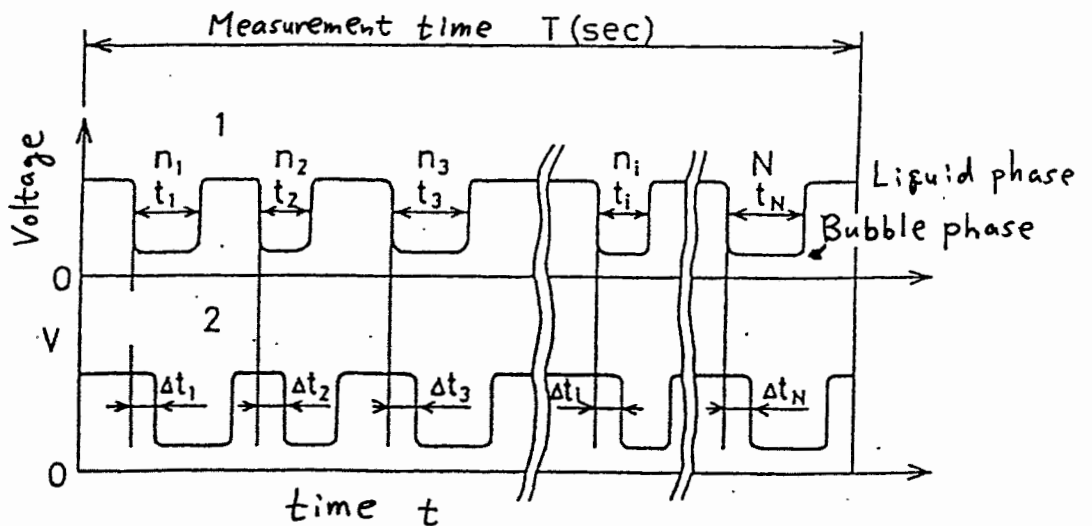


Fig. Definition of measuring bubble characteristics.

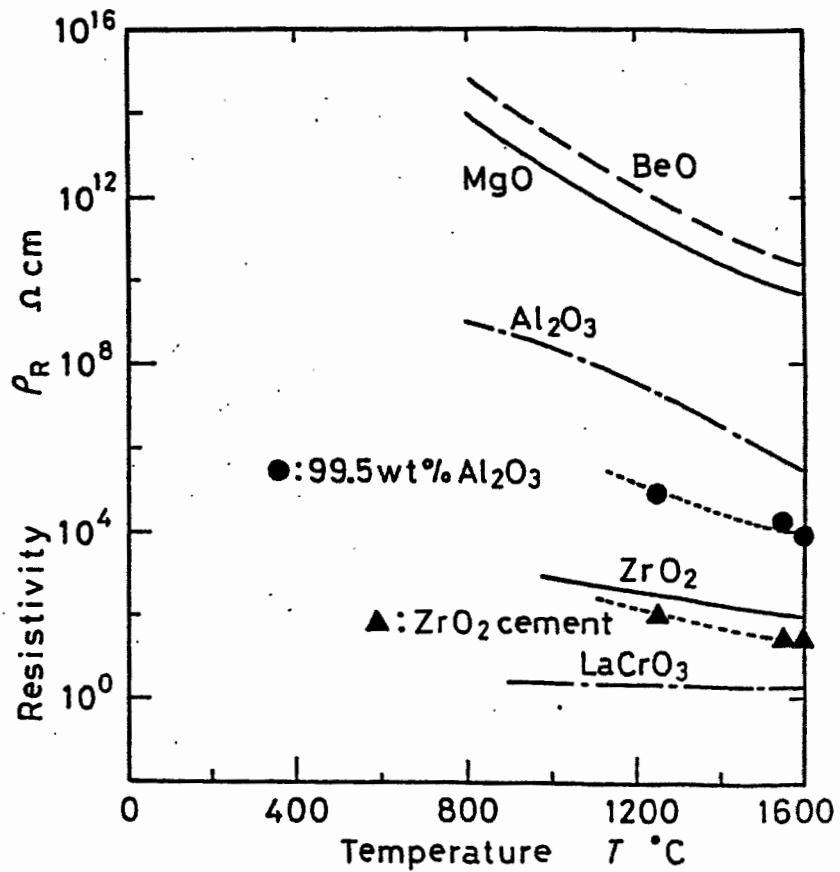


Fig. 1—Resistivity for various refractory materials at high temperature.

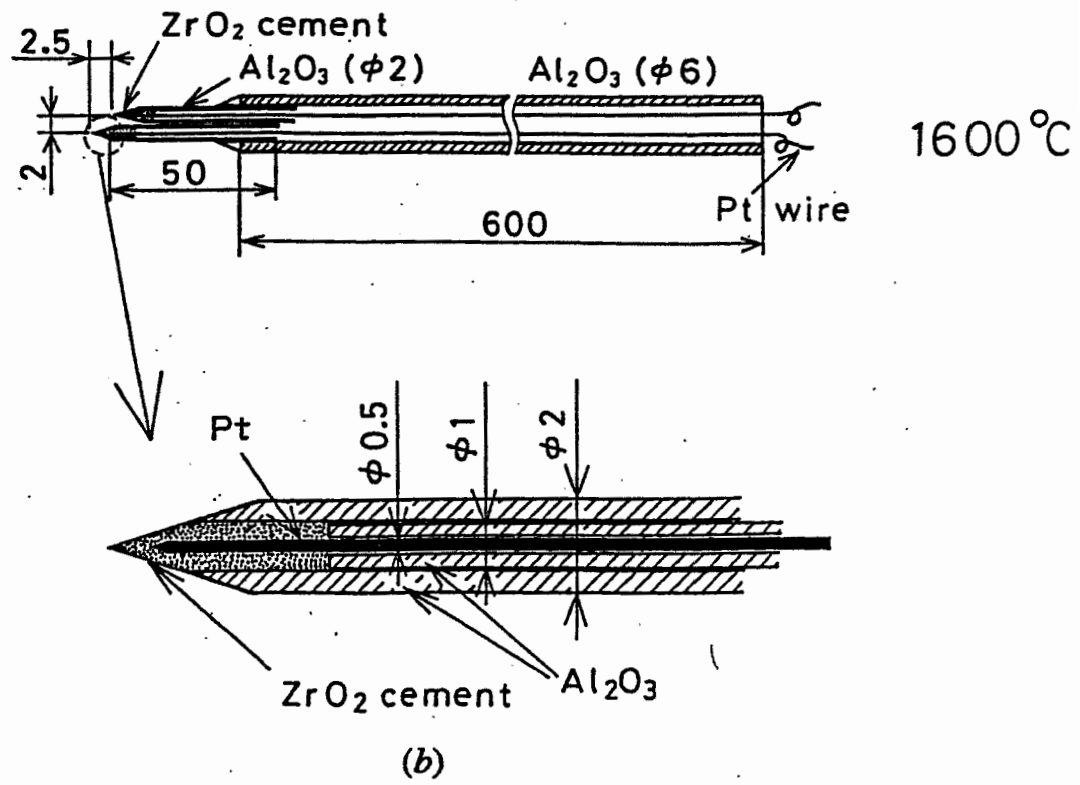
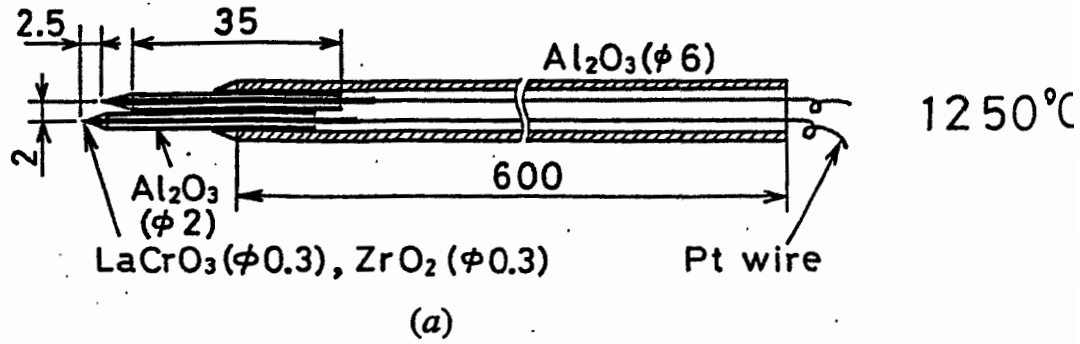


Fig. 2—Electroresistivity probe for measuring bubbles in molten iron bath: (a) probe applicable to 1250 °C (mm) and (b) probe applicable to 1600 °C (mm).

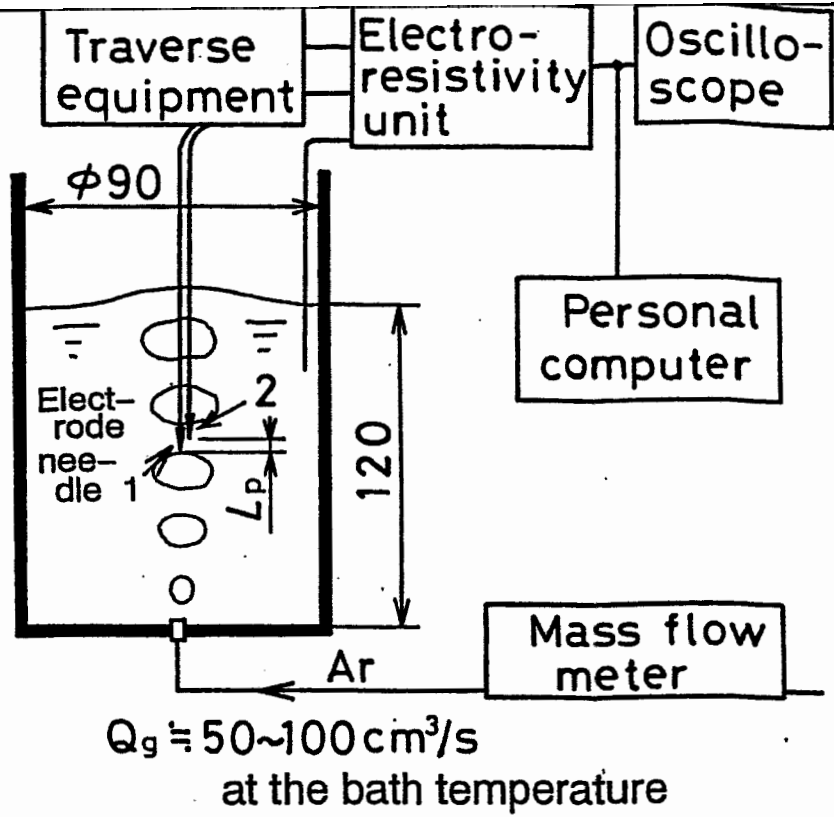


Fig. 3— Experimental apparatus for measuring bubble characteristics in molten iron bath (mm).

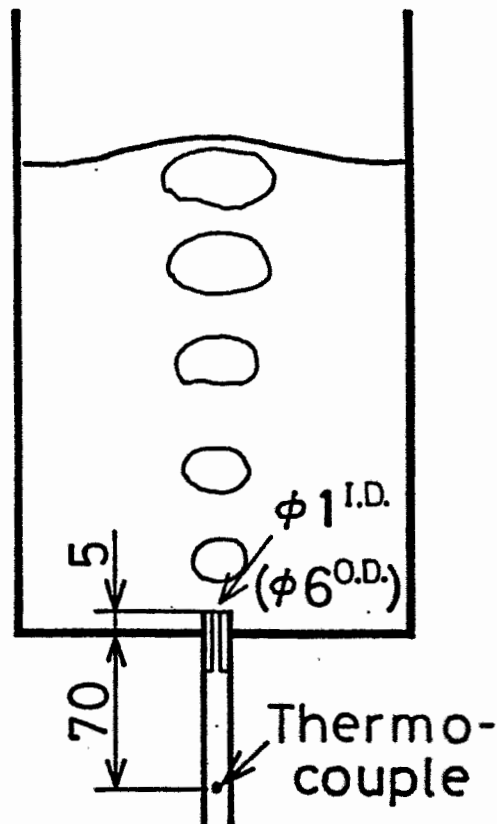


Fig. 4— Shape of bottom blowing nozzle and measurement position of argon gas temperature (mm).



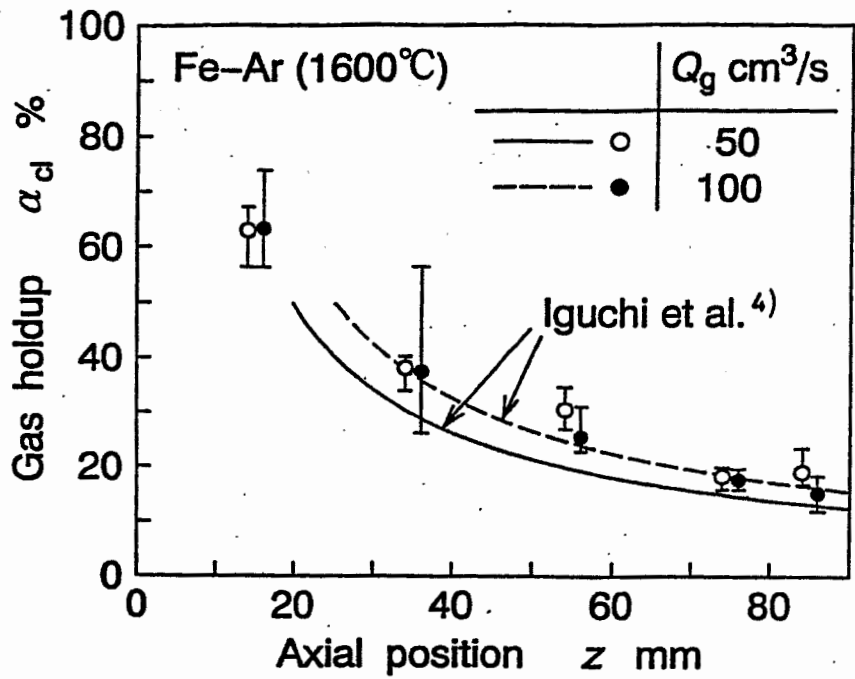


Fig. 6—Axial distributions of gas holdup  $\alpha_{cl}$  on the centerline of molten iron bath with bottom blowing.

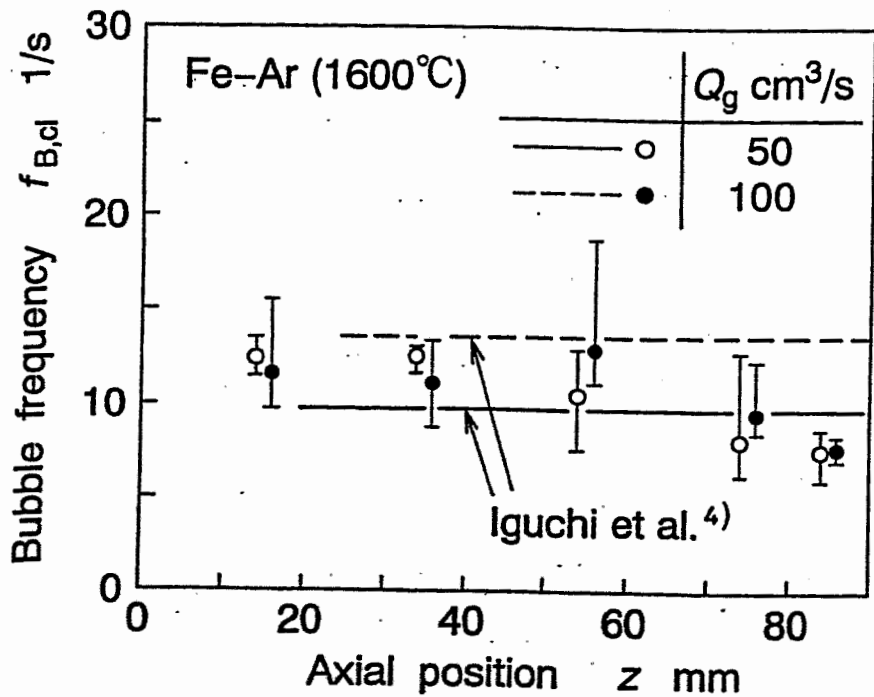


Fig. 7—Axial distributions of bubble frequency  $f_{B,cl}$  on the centerline of molten iron bath with bottom blowing.

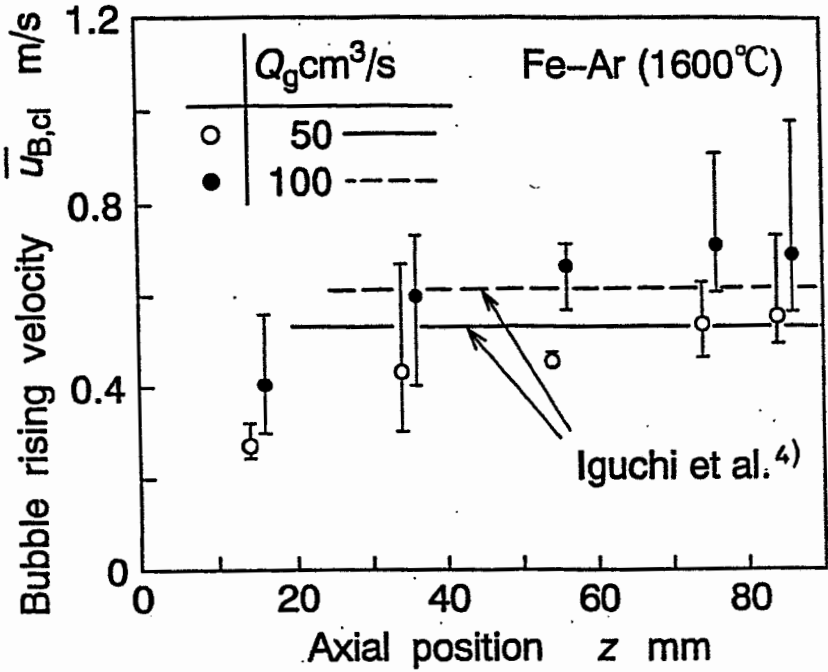


Fig. 8—Axial distributions of bubble rising velocity  $\bar{u}_{B,cl}$  on the centerline of molten iron bath with bottom blowing.

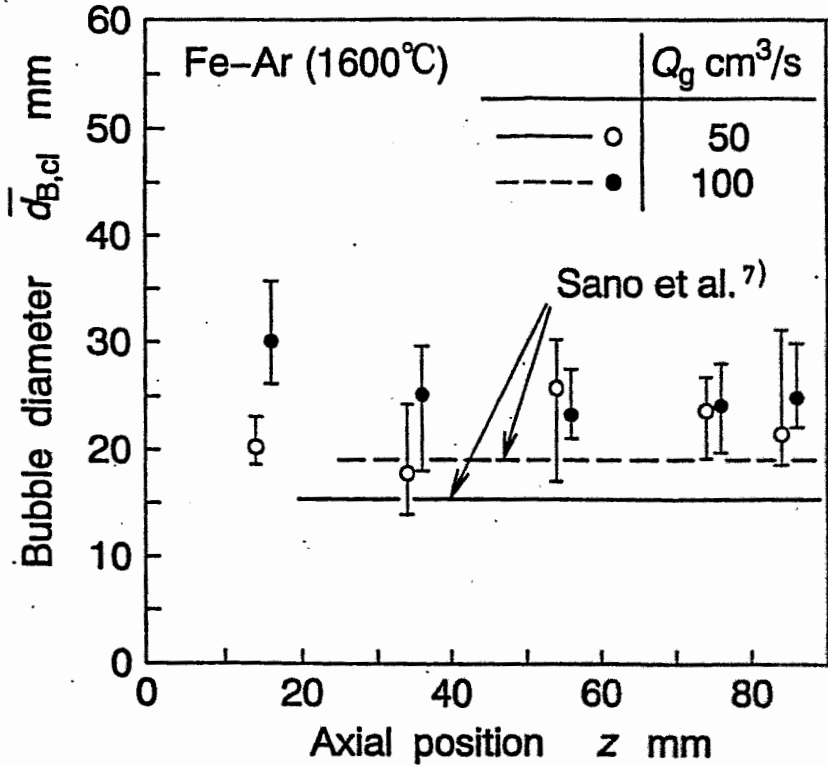


Fig. 9—Axial distributions of bubble diameter  $\bar{d}_{B,cl}$  on the centerline of molten iron bath with bottom blowing.

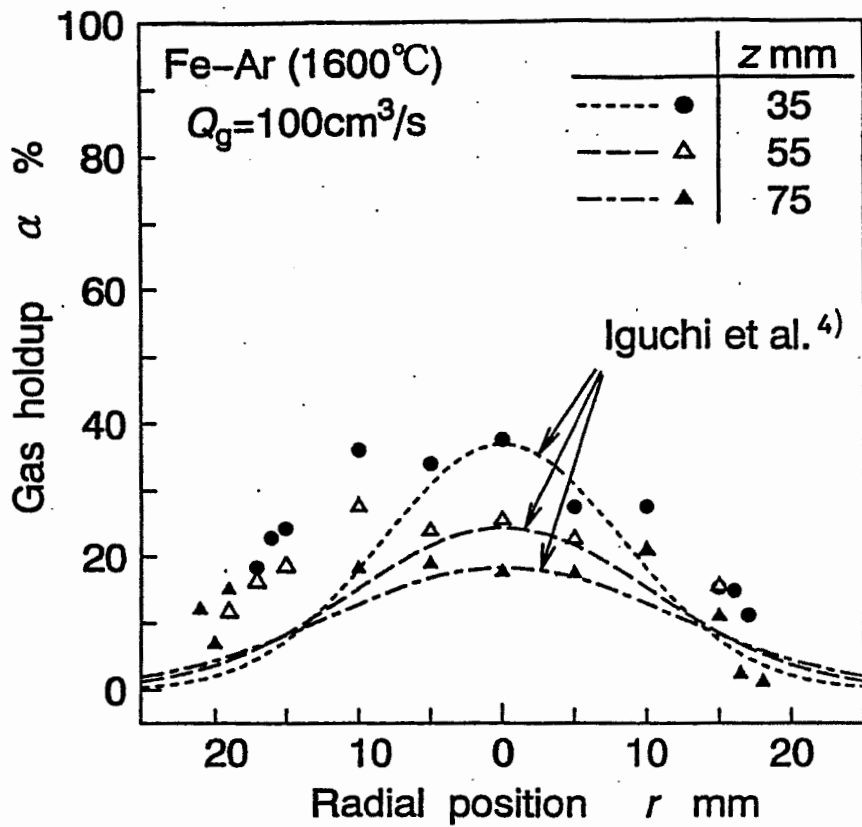


Fig. 10—Radial profiles of gas holdup  $\alpha$  at different axial positions in molten iron bath with bottom blowing.

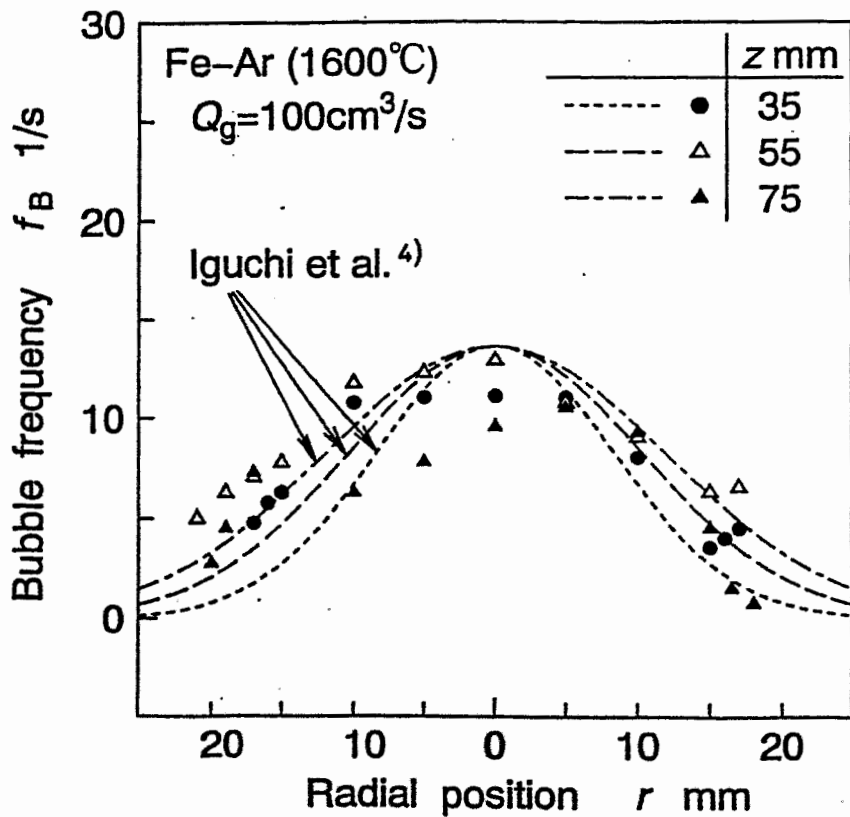


Fig. 11—Radial profiles of bubble frequency  $f_B$  at different axial positions in molten iron bath with bottom blowing.

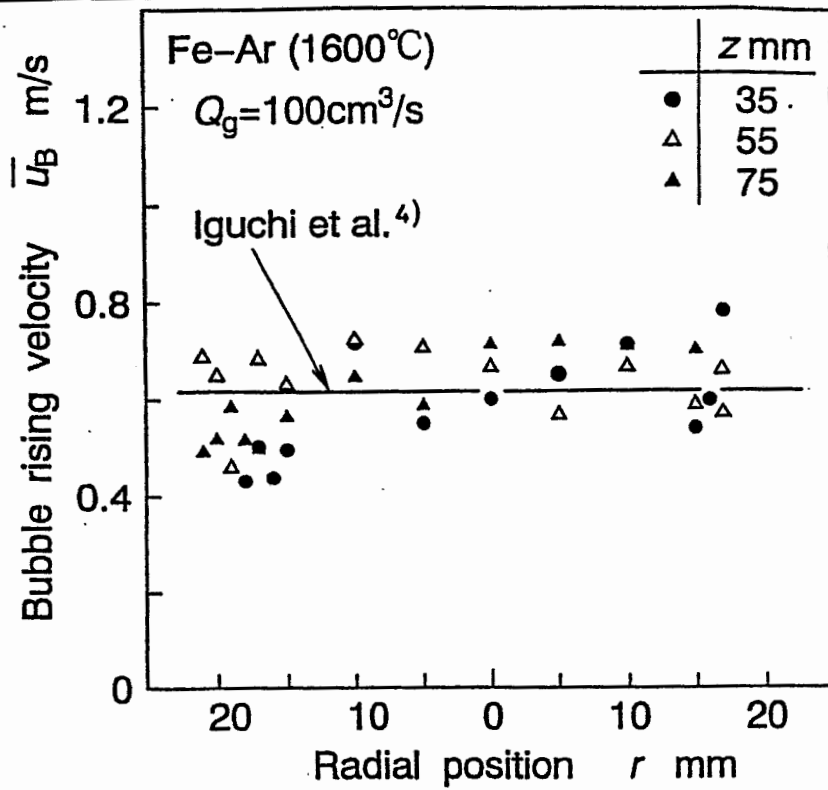


Fig. 12—Radial profiles of bubble rising velocity  $\bar{u}_B$  at different axial positions in molten iron bath with bottom blowing.

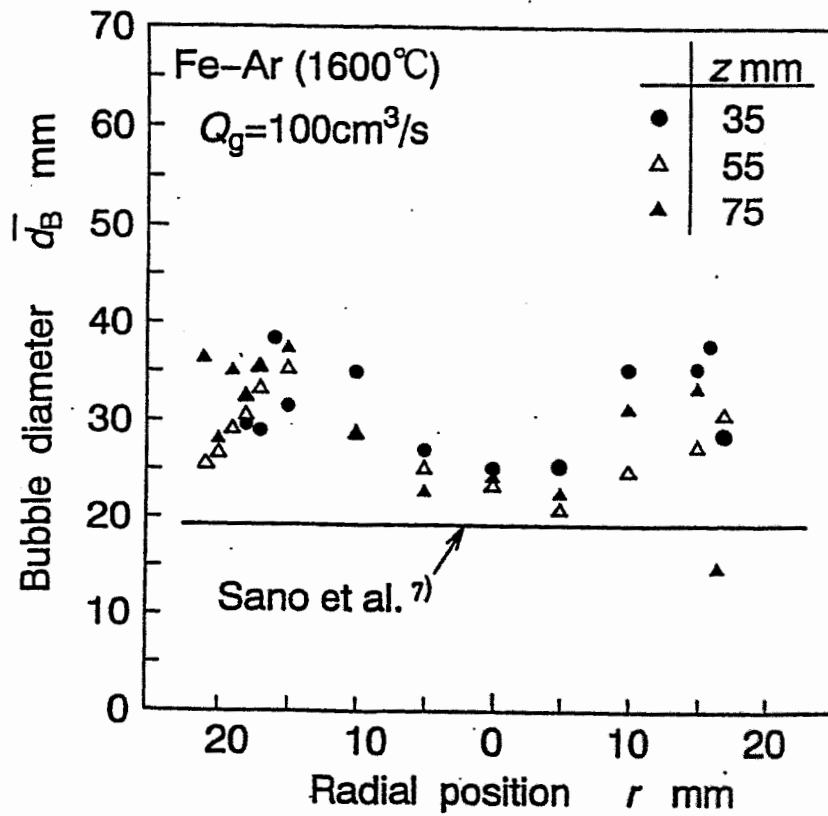


Fig. 13—Radial profiles of bubble diameter  $\bar{d}_B$  at different axial positions in molten iron bath with bottom blowing.

**Empirical equations for bubble characteristics derived for low temperature molten metal baths were found to be applicable for very high temperature molten metal baths.**

# Bubble shape measurement

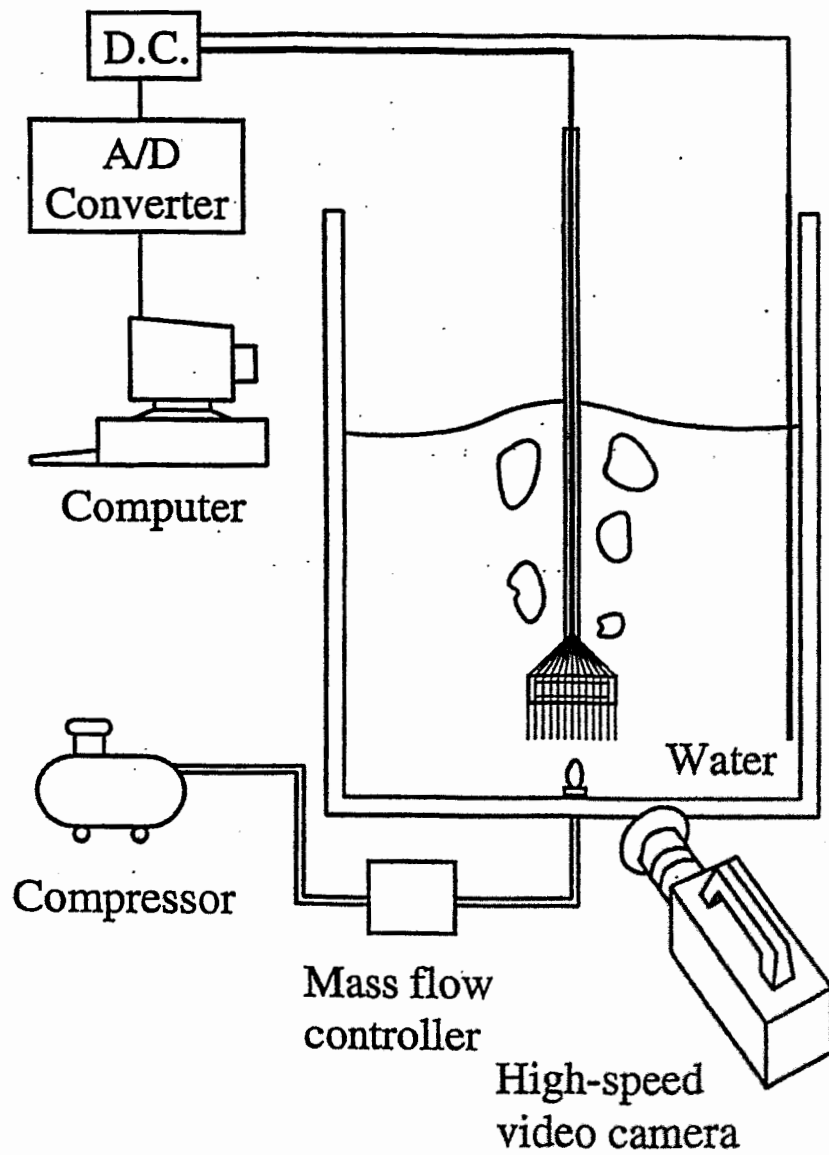


Fig. 1—Experimental apparatus for water-air system.

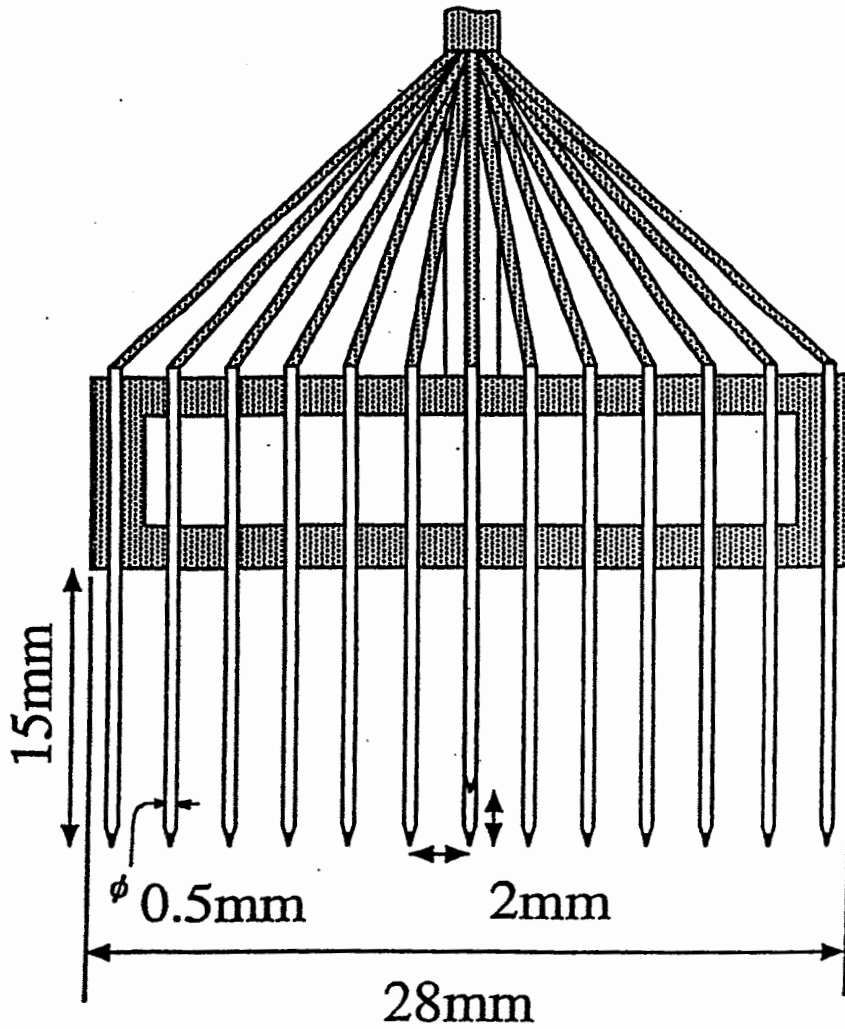
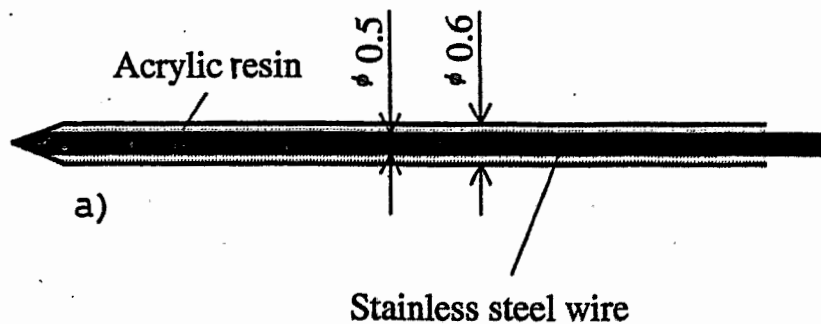


Fig. 3—Schematic of multineedle electroresistivity probe.

Water



Wood's metal ( $100^{\circ}\text{C}$ )

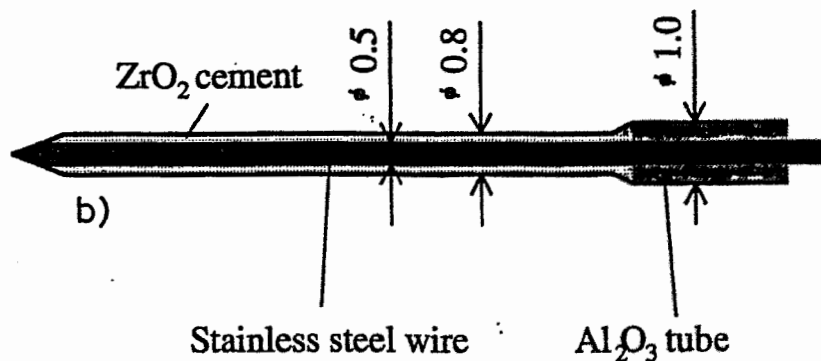


Fig. 2—Schematic of electrode needle: (a) water-air system and (b) Wood's metal-He system.



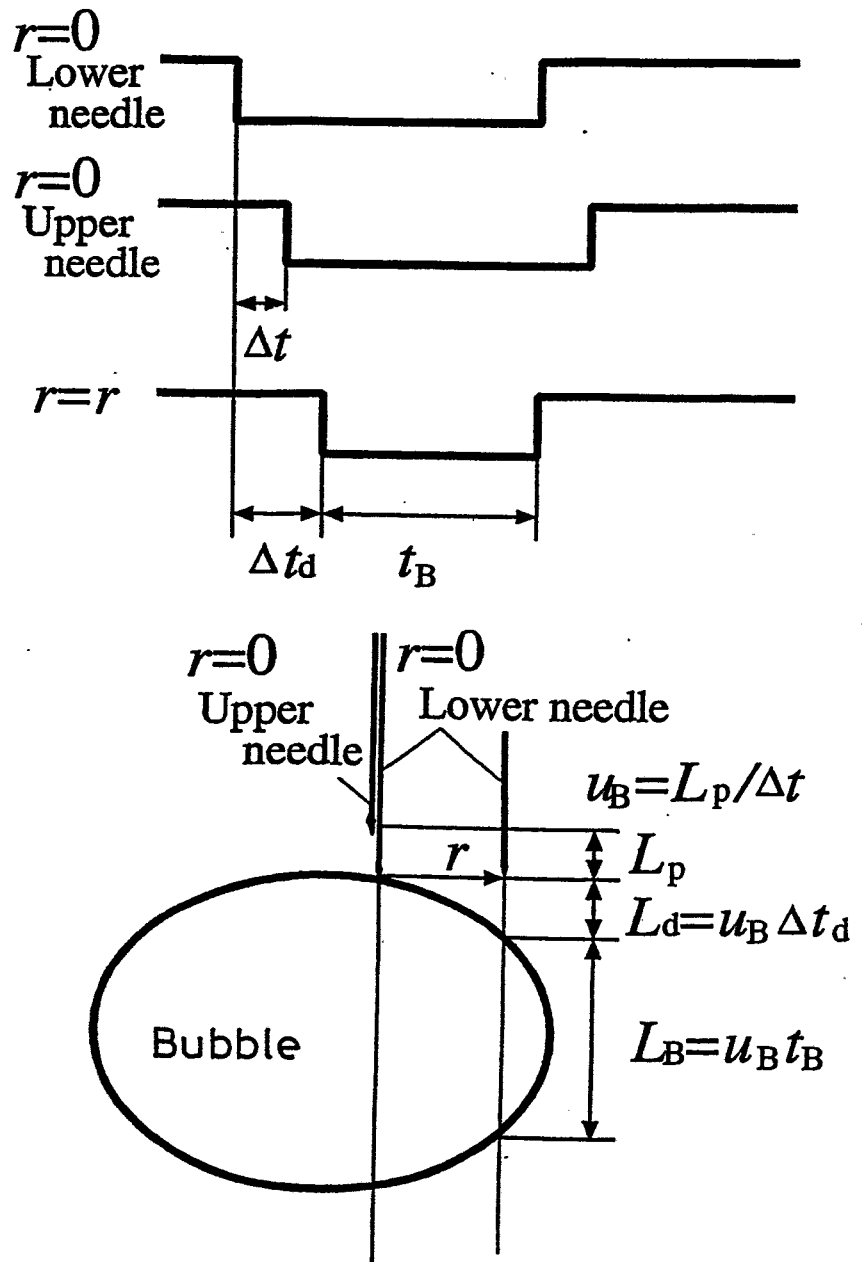


Fig. 4—Measurement method of bubble shape.

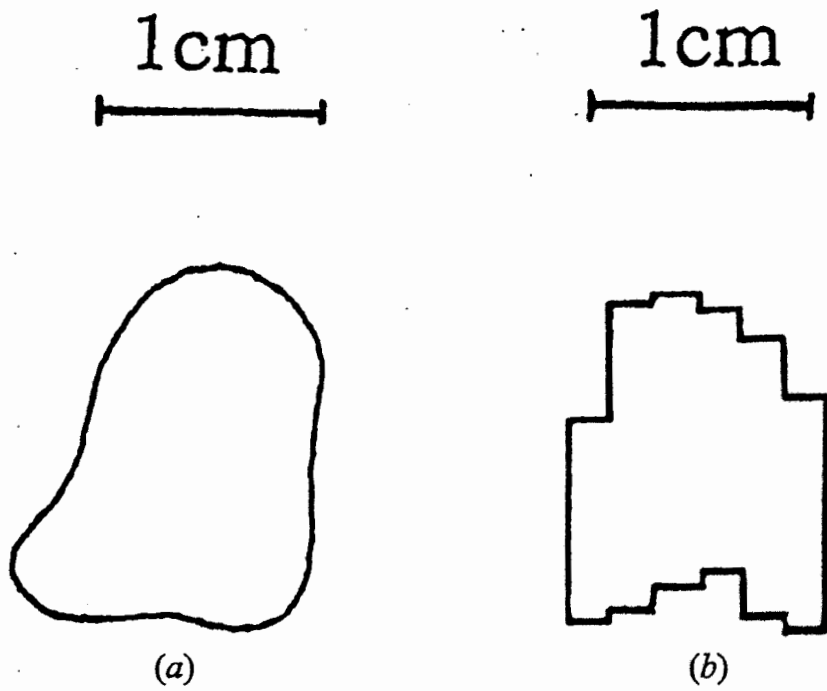


Fig. 12—Measured bubble shape for water-air system: (a) high-speed video camera and (b) multineedle electroresistivity probe.

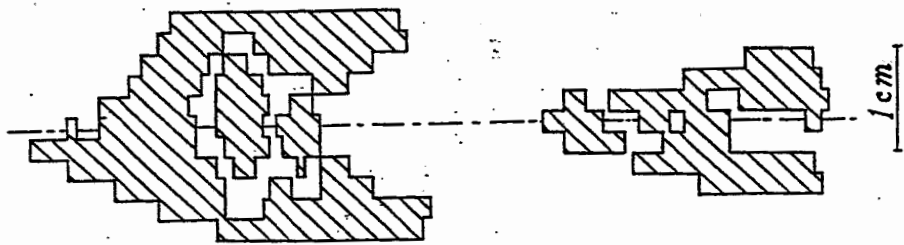


Fig. 8—Measured bubble shape in Wood's metal- $N_2$  system at  $z = 5$  cm.

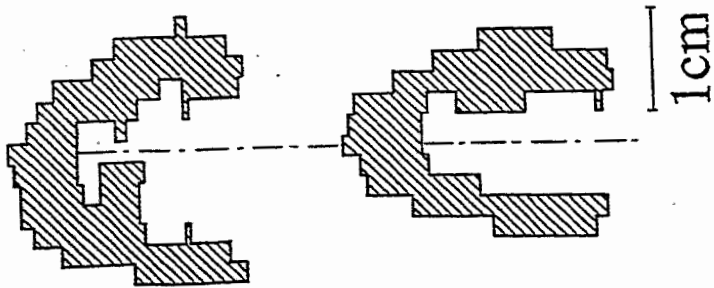


Fig. 5—Measured bubble shape in Wood's metal-He system at  $z = 5$  cm.

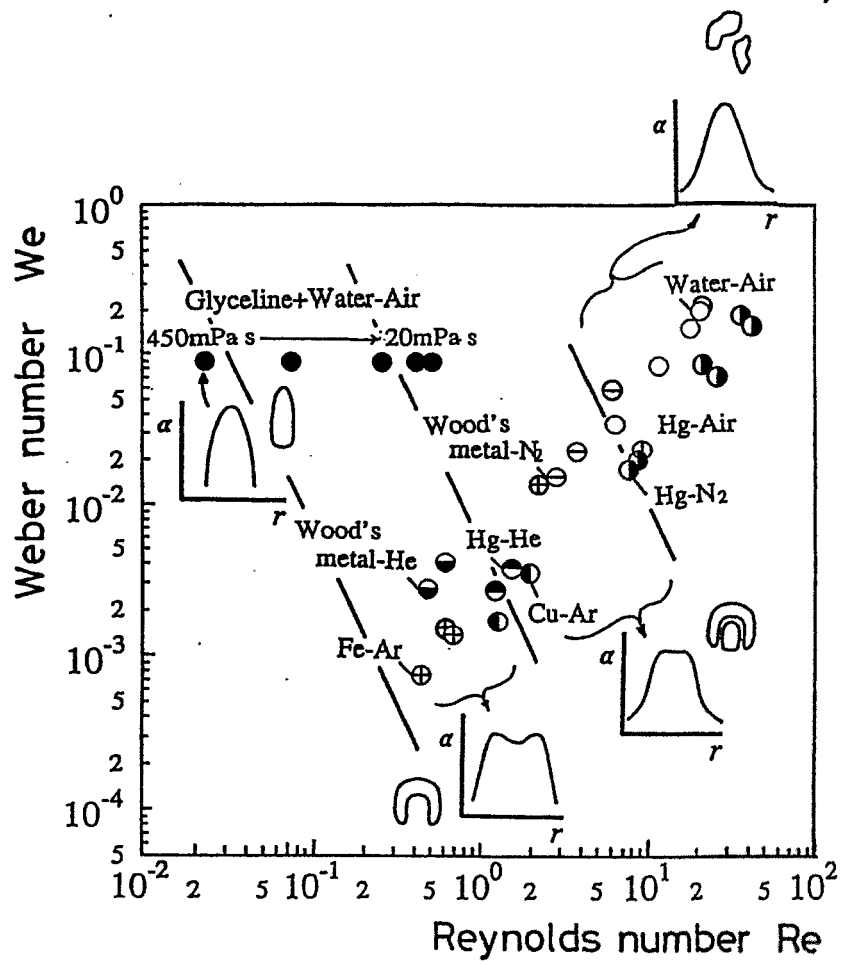


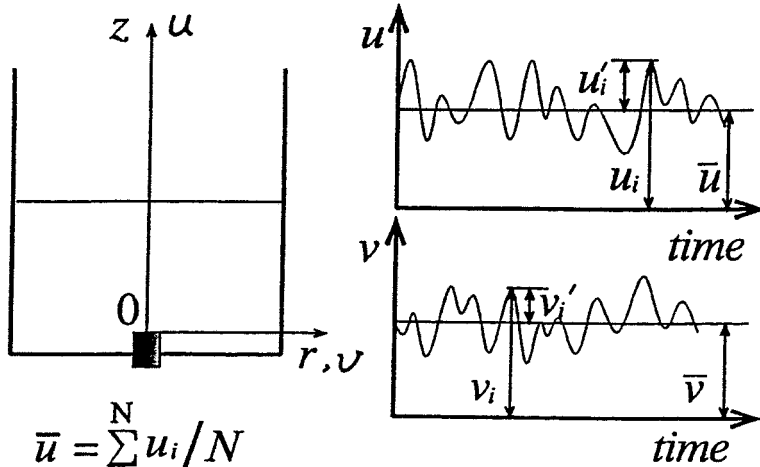
Fig. 15—Classification of bubble shapes (water-air,<sup>[1,2,4,5,9,10]</sup> glyceline + water-air,<sup>[13]</sup> Fe-Ar<sup>[8,15,16]</sup> Cu-Ar,<sup>[8,17]</sup> Hg-air,<sup>[12]</sup> Wood's metal-N<sub>2</sub>,<sup>[7,14]</sup> the present Hg-He, Hg-N<sub>2</sub>, Wood's metal-N<sub>2</sub>, and Wood's metal-He systems are also included.)

$$Re = (\rho_g/\rho_L) \bar{d}_B \bar{u}_B / \nu_L$$

$$We = (\rho_g/\rho_L) \rho_L \bar{d}_B \bar{u}_B^2 / \sigma$$

# Measurements of molten metal flow

- (1) Mean velocity components
- (2) Turbulence components



$$\bar{u} = \sum_{i=1}^N u_i / N$$

$$\bar{v} = \sum_{i=1}^N v_i / N$$

$$\overline{u'v'} = \sum_{i=1}^N u_i' v_i' / N$$

$$u'_{\text{rms}} = \sqrt{\sum_{i=1}^N u_i'^2 / N}$$

$$v'_{\text{rms}} = \sqrt{\sum_{i=1}^N v_i'^2 / N}$$

$N$  ; number of sampling data ( $> 50,000$ )

$\bar{u}$  ; mean value of axial velocity component

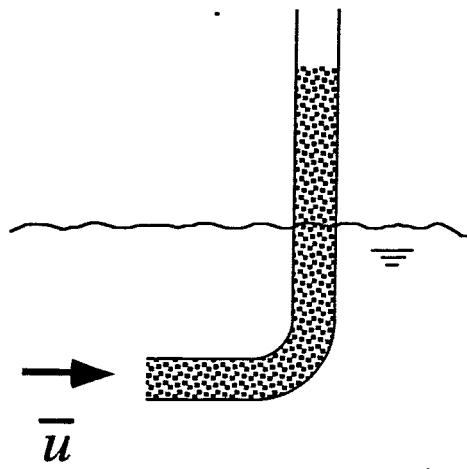
$\bar{v}$  ; mean value of radial velocity component

$\overline{u'v'}$  ; Reynolds shear stress

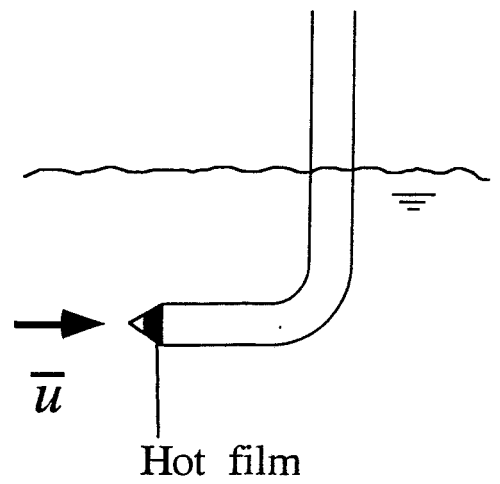
$u'_{\text{rms}}$  ; root mean square value of axial fluctuating component

$v'_{\text{rms}}$  ; root mean square value of radial fluctuating component

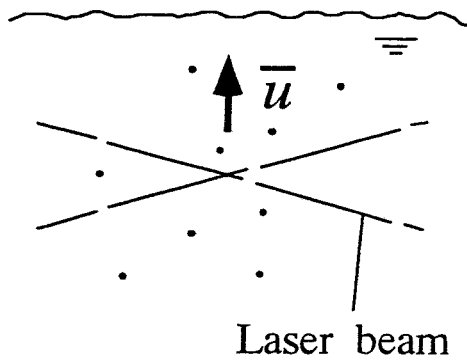
- (a) Pitot tube**
- (b) Hot wire / film anemometer**
- (c) Laser Doppler velocimeter**
- (d) Reaction probe**  
**(Measurement of drag force)**
- (e) Vives probe**
- (f) Mass transfer probe**
- (g) Karman's vortex probe**



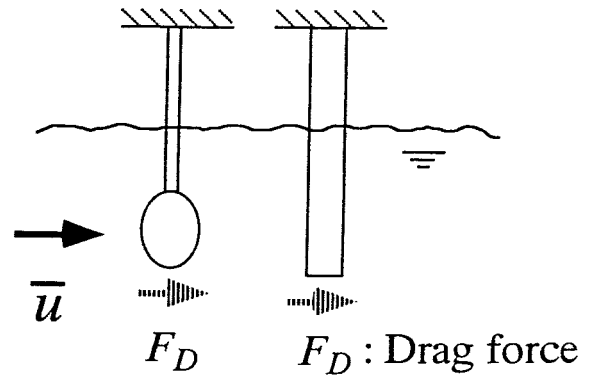
(a) Pitot tube



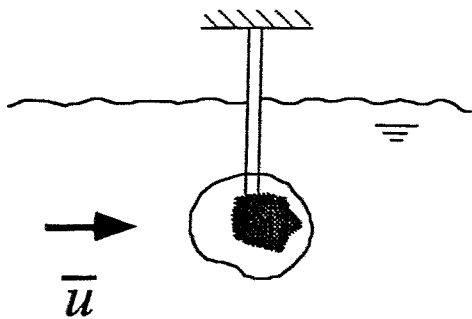
(b) Hot film anemometer



(c) LDV



(d) Reaction probe



(e) Mass transfer probe

(Dr. Julius et al )

(f) Magnet probe

# Vives probe ( Magnet probe )

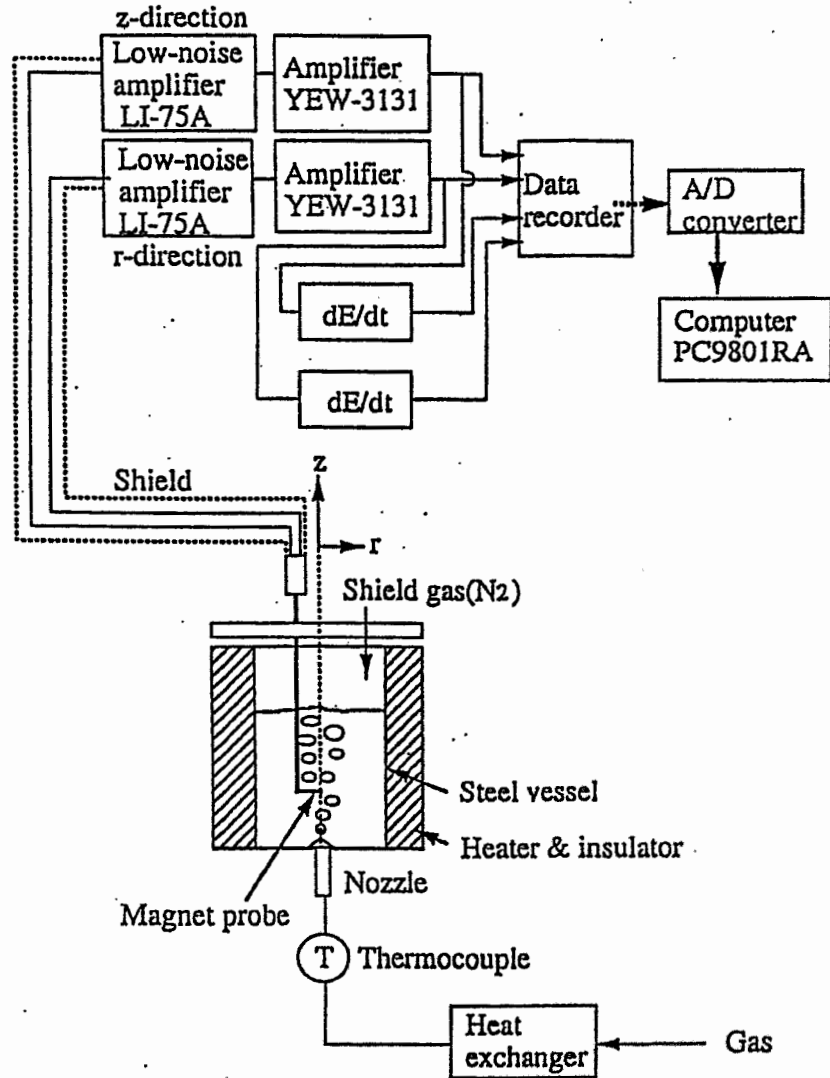


Fig. 1—Experimental apparatus.



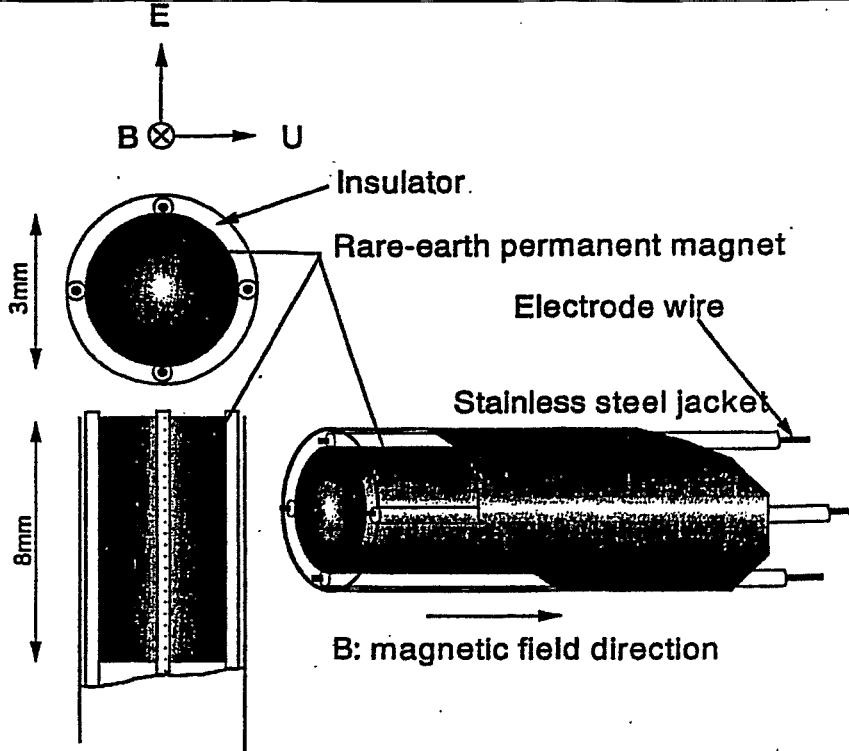


Fig. 2—Schematic illustration of magnet probe.

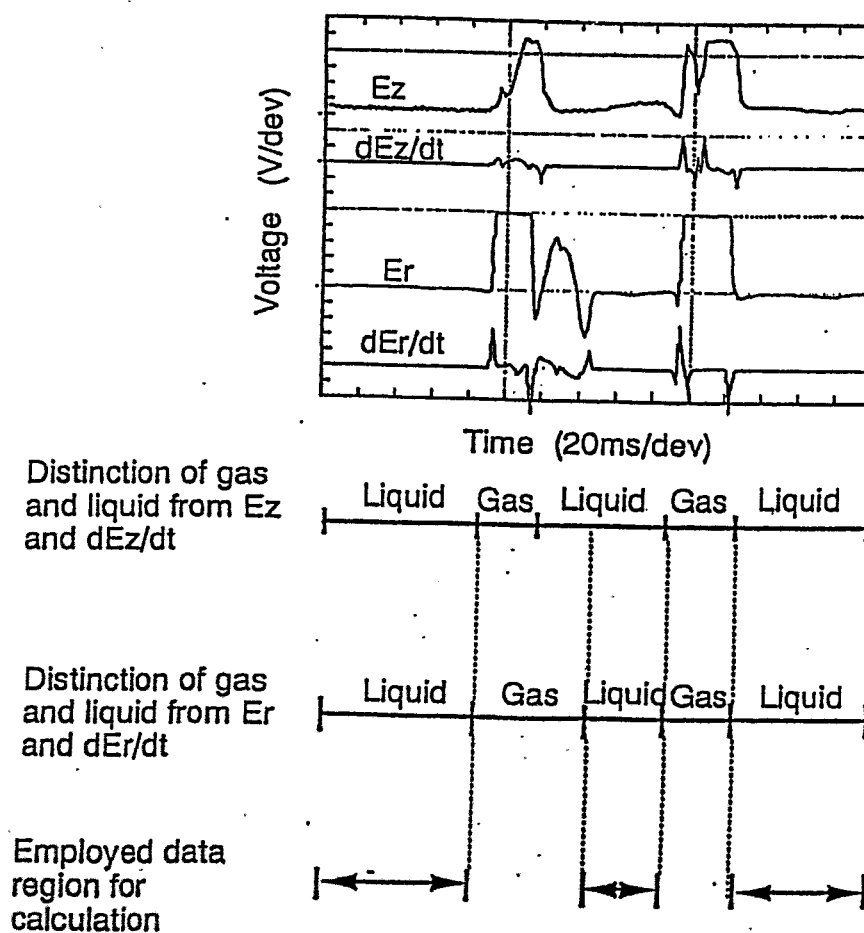


Fig. 3—Discrimination of gas and liquid signals.

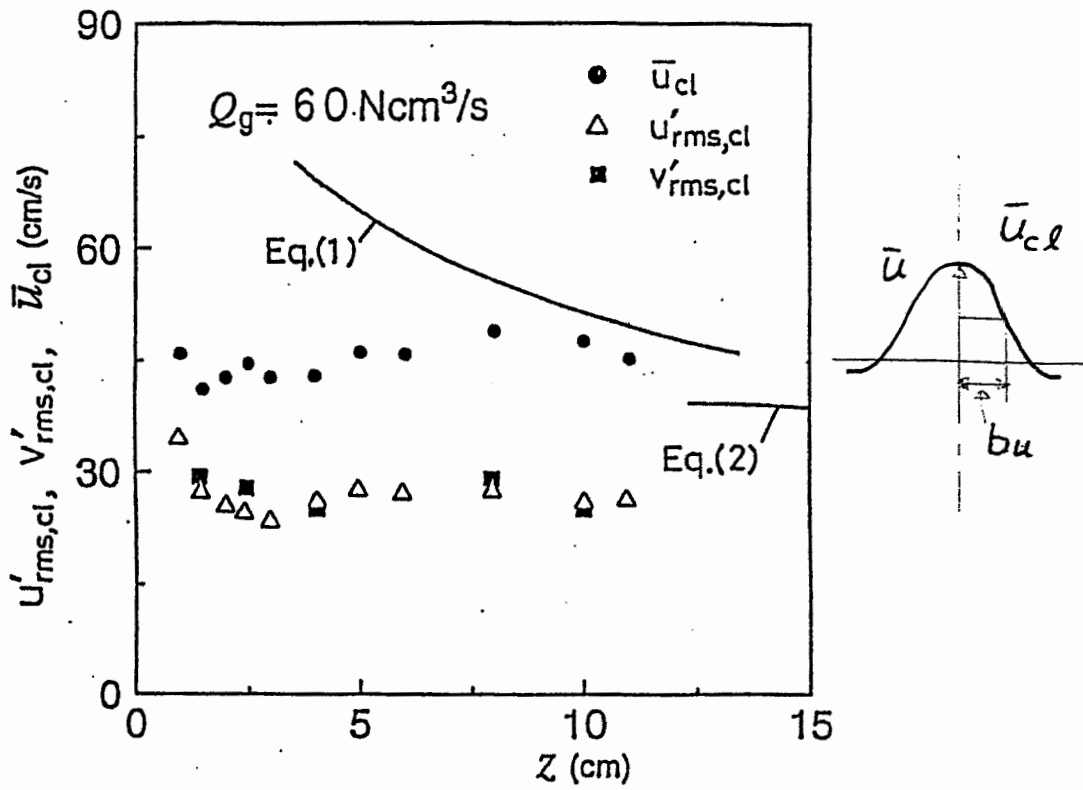


Fig. 14—Axial mean velocity and the rms values of turbulence components on the centerline as functions of axial distance.

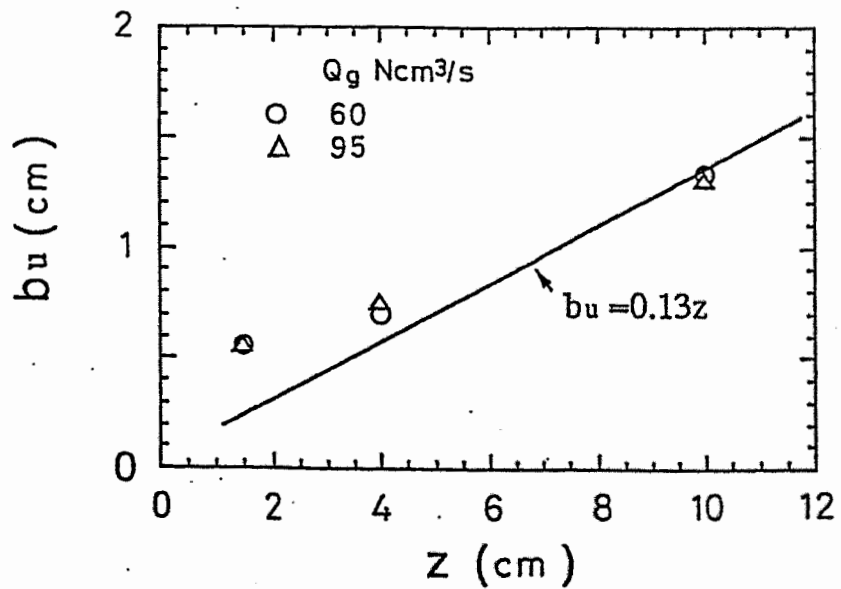


Fig. 15—Relation between half-value radius and axial distance.

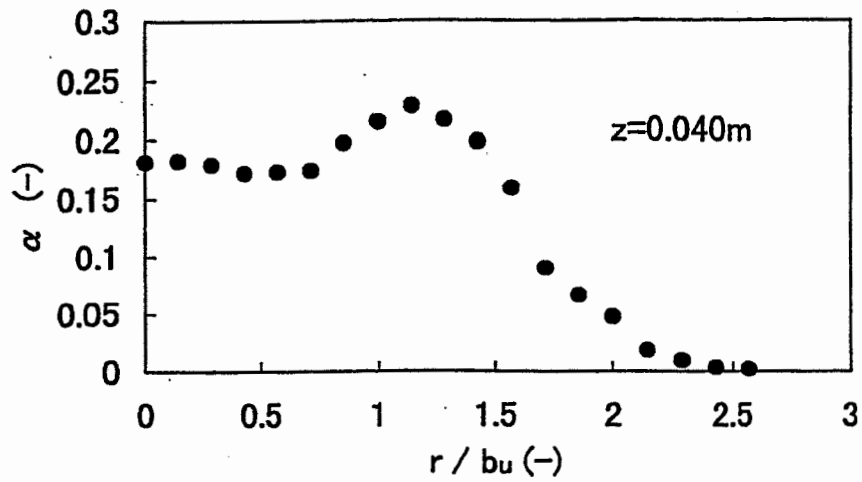


Fig. 3—Radial distribution of gas holdup at  $z = 0.040$  m.

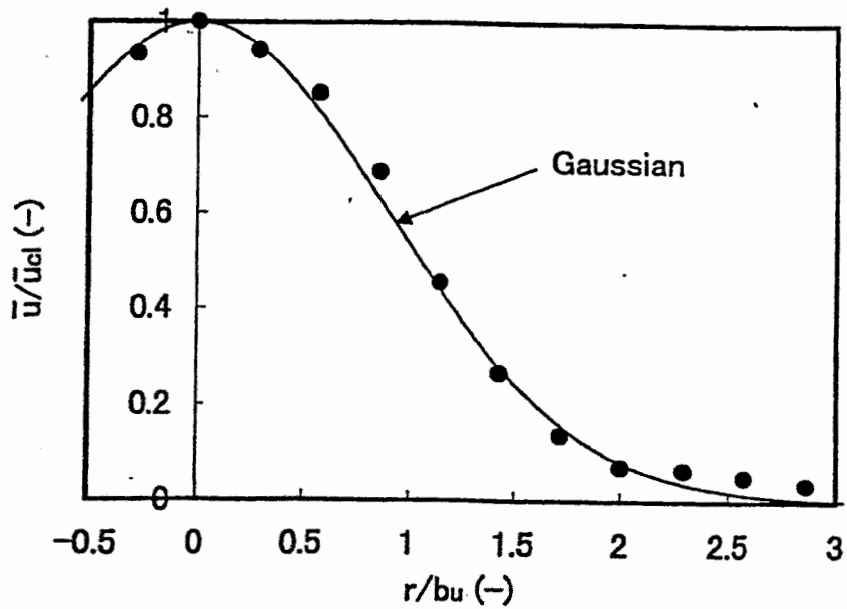


Fig. 6—Radial distribution of normalized axial mean velocity  $\bar{u}/\bar{u}_c$ .

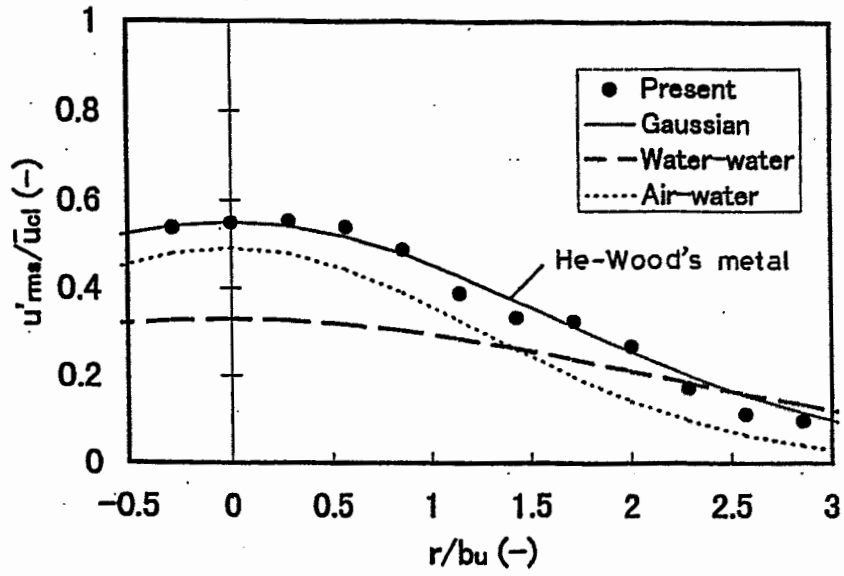


Fig. 7—Radial distribution of nondimensionalized rms values of axial turbulence component  $u'_{rms}/\bar{u}_{ci}$ .

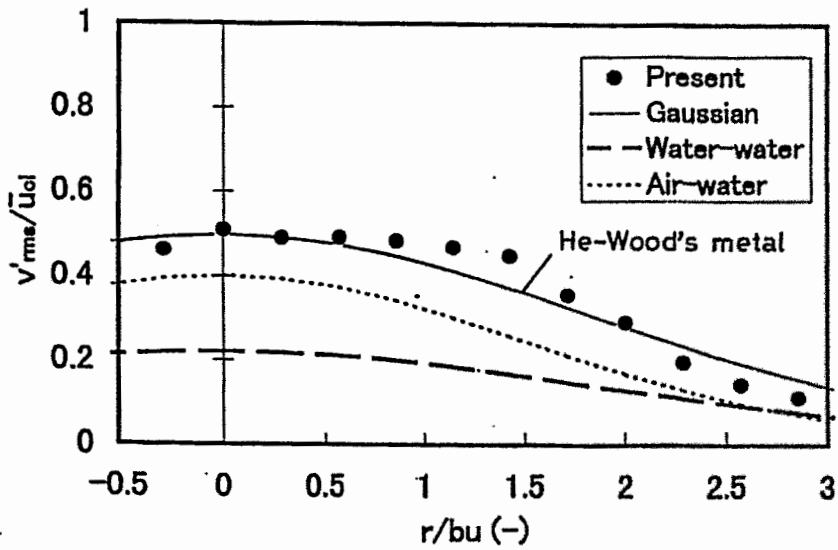


Fig. 8—Radial distribution of nondimensionalized rms values of radial turbulence component  $v'_{rms}/\bar{u}_{ci}$ .

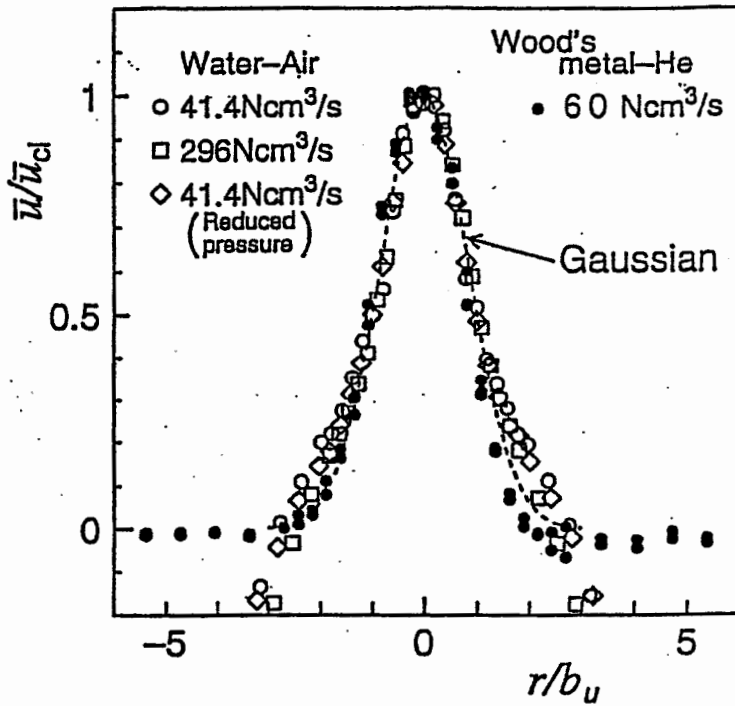


Fig. 17—Comparison of radial distributions of  $\bar{u}$  between Wood's metal-He and water-air systems.

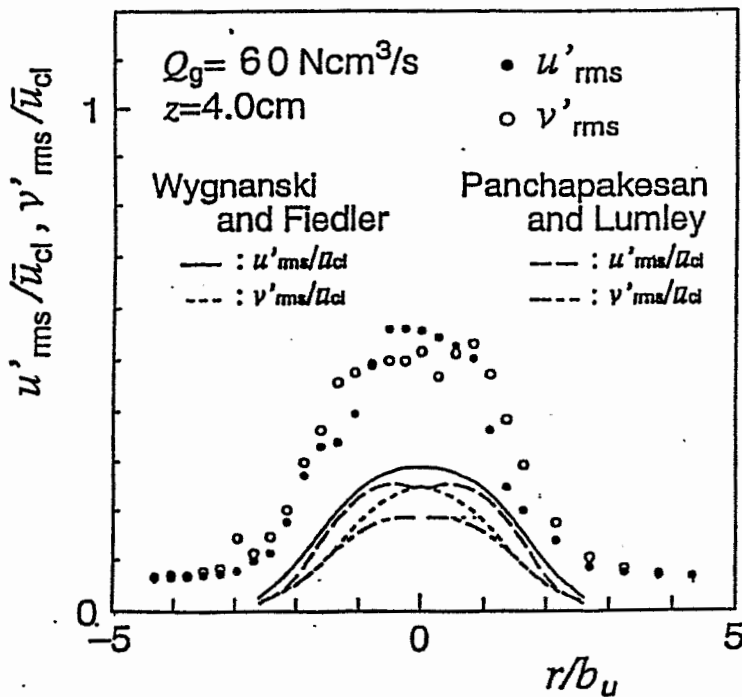
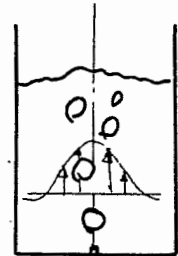
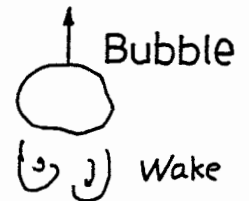


Fig. 18—Radial distributions of the rms values of axial and radial turbulence components.



Particle  
Hetsroni (1989)



$Re_B \geq 400$   
 $Re_B = \frac{(\bar{u}_B - \bar{u}) \bar{d}_B}{\nu}$

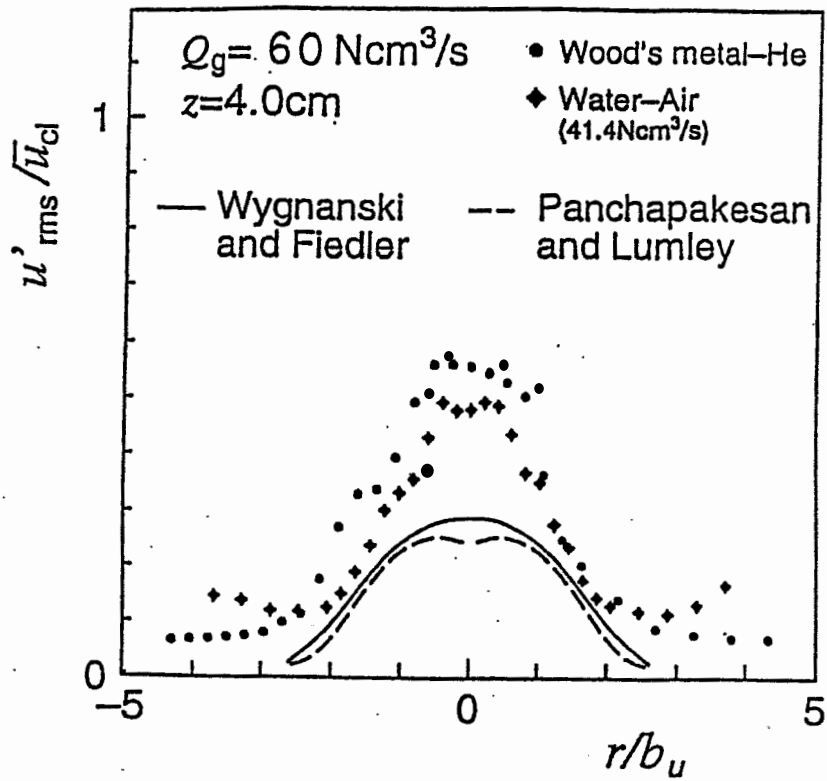


Fig. 19—Radial distributions of the rms values of the axial turbulence component.

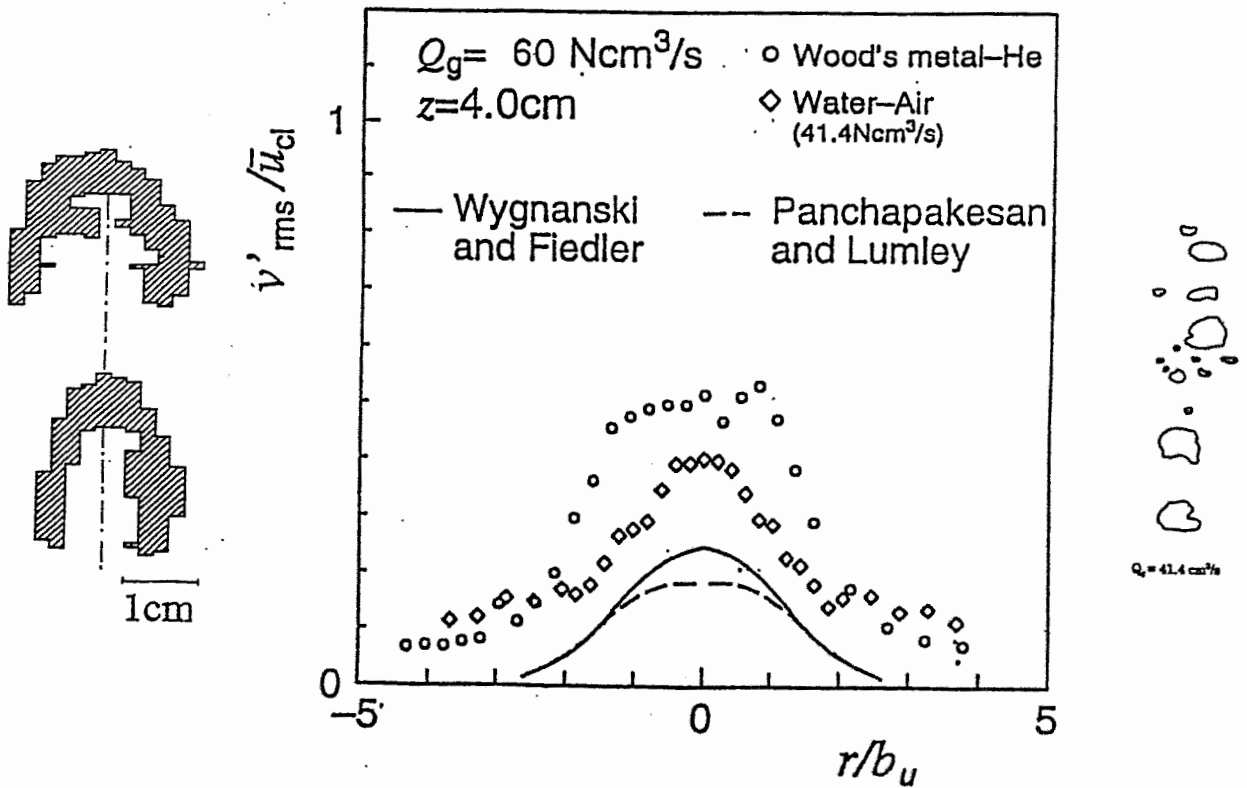


Fig. 20—Radial distributions of the rms values of the radial turbulence component.

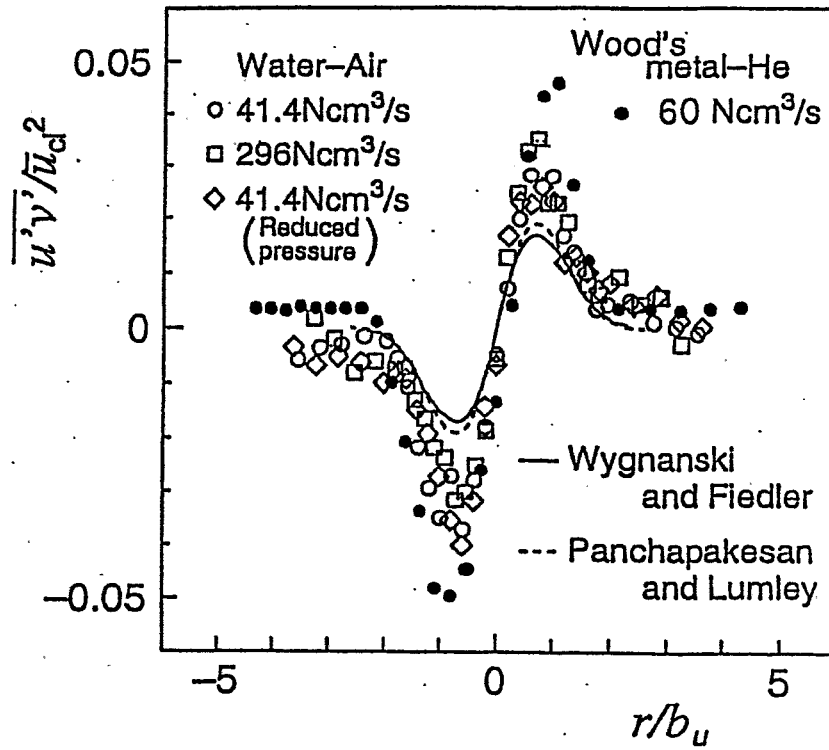


Fig. 21—Radial distributions of the Reynolds shear stress.

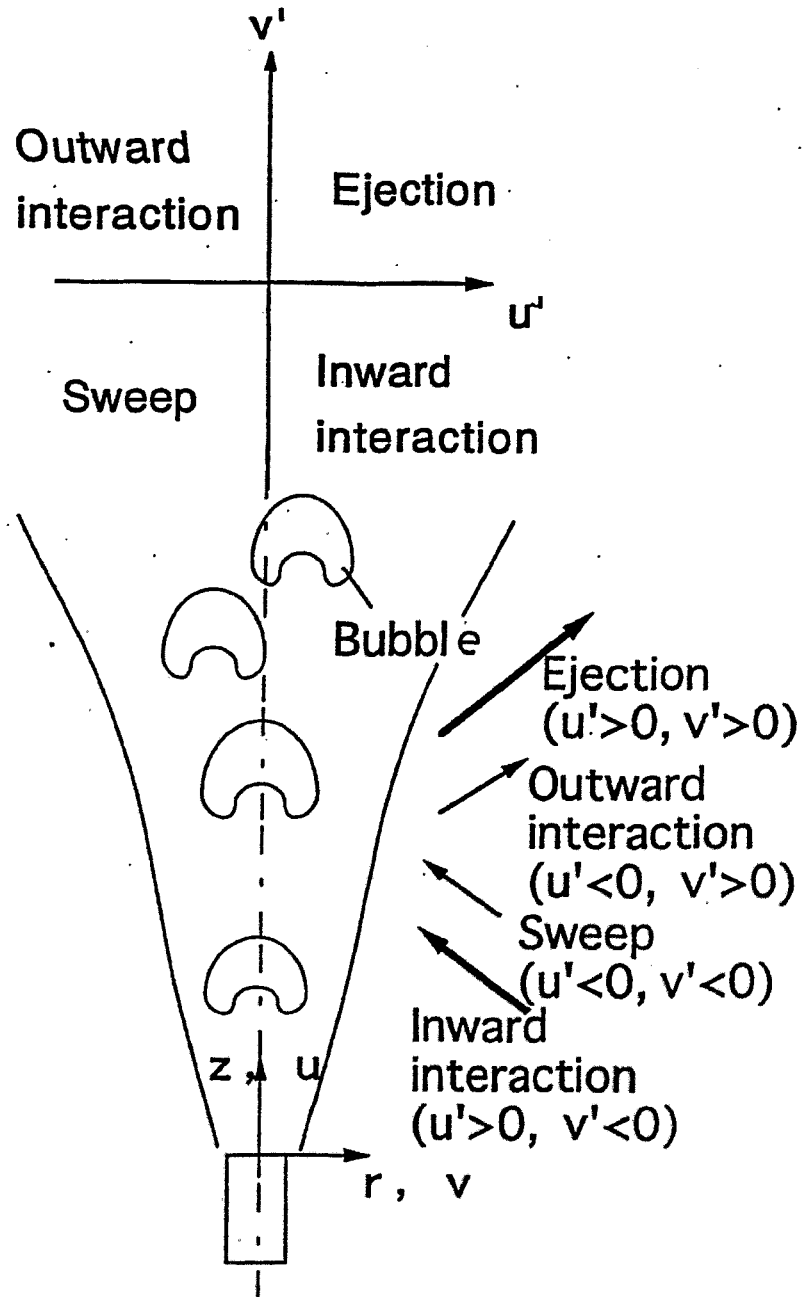


Fig. 10—Classification of turbulent motions.



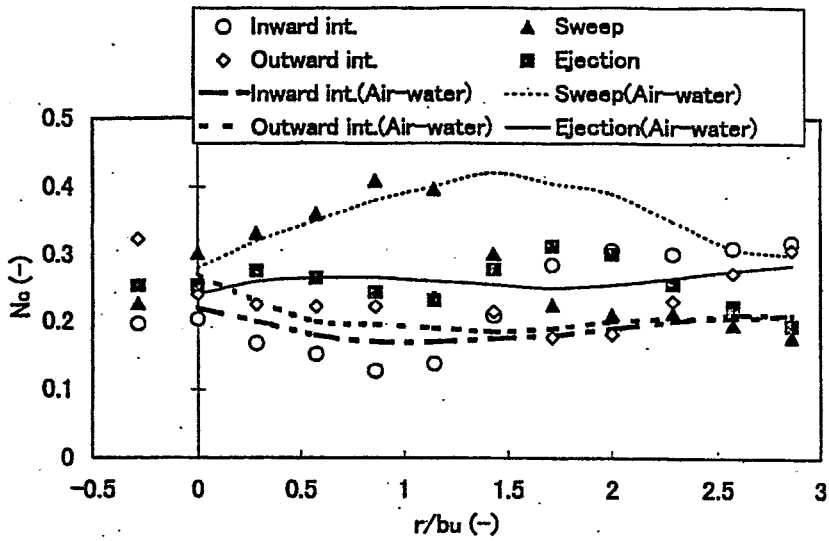


Fig. 11—Relative occurrence frequency  $N_c$ .

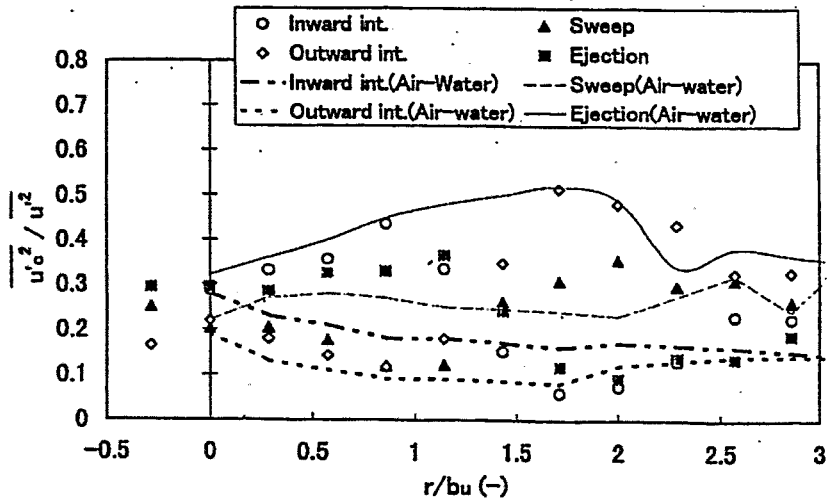


Fig. 13—Contributions of four turbulent motions to the axial turbulence kinetic energy.

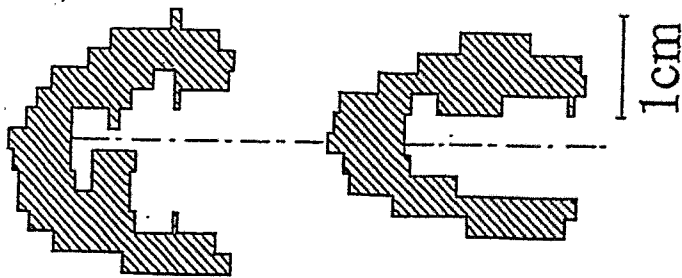


Fig. 5—Measured bubble shape around  $x = 0.040$  in He-Wood's main bubbling jet.



Fig. 4—Shape of bubbles visualized with a high-speed video camera in air-water bubbling jet.

**Kármán vortex probe**

**Continuous casting mold**

$$Re = VD/\nu$$

Re: Reynolds number  
V: flow velocity  
D: diameter of cylinder  
 $\nu$ : kinematic viscosity of fluid

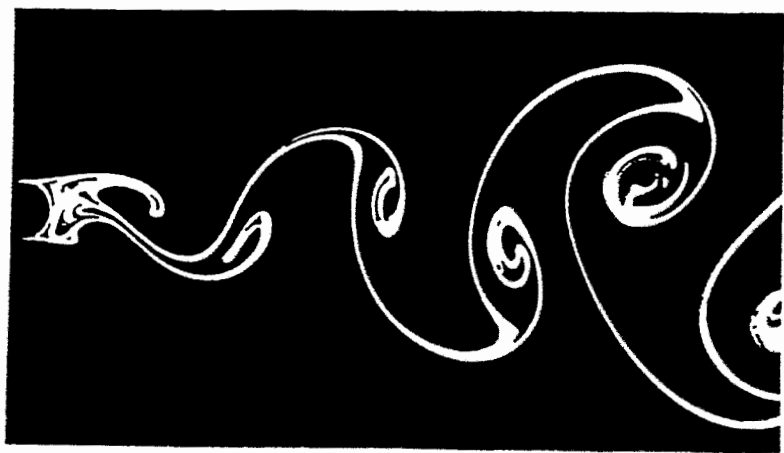
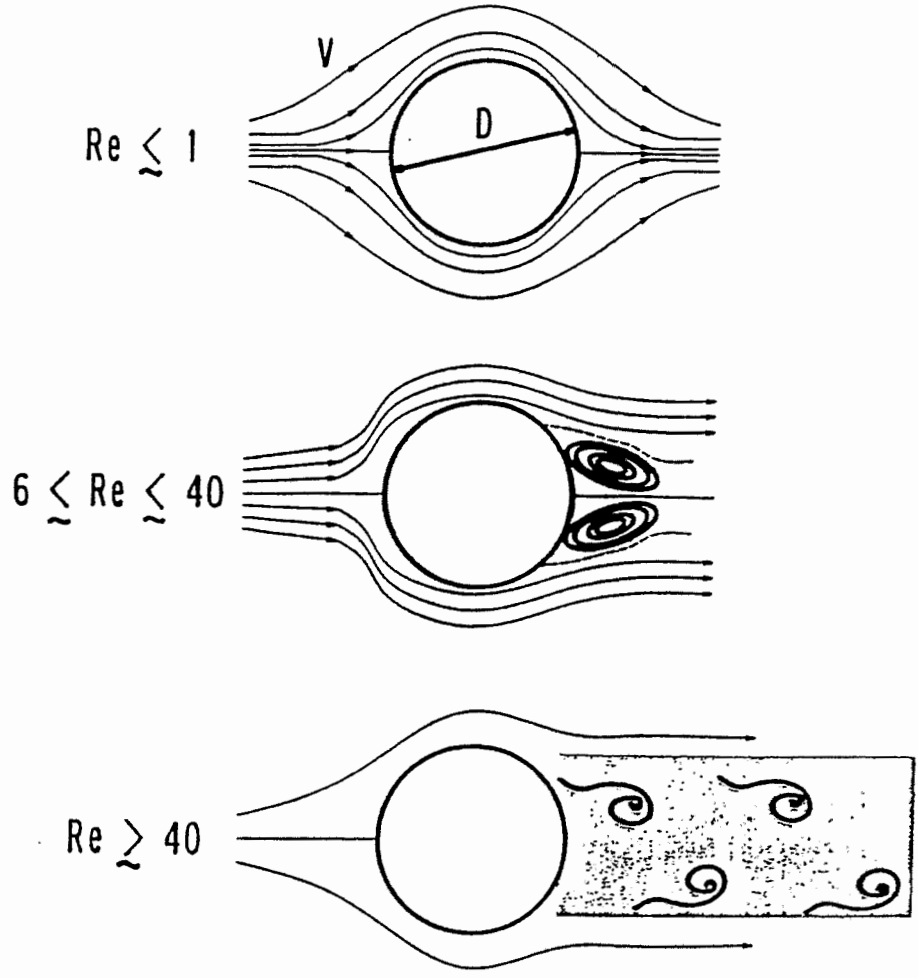


Fig.2 Kármán's vortex street.

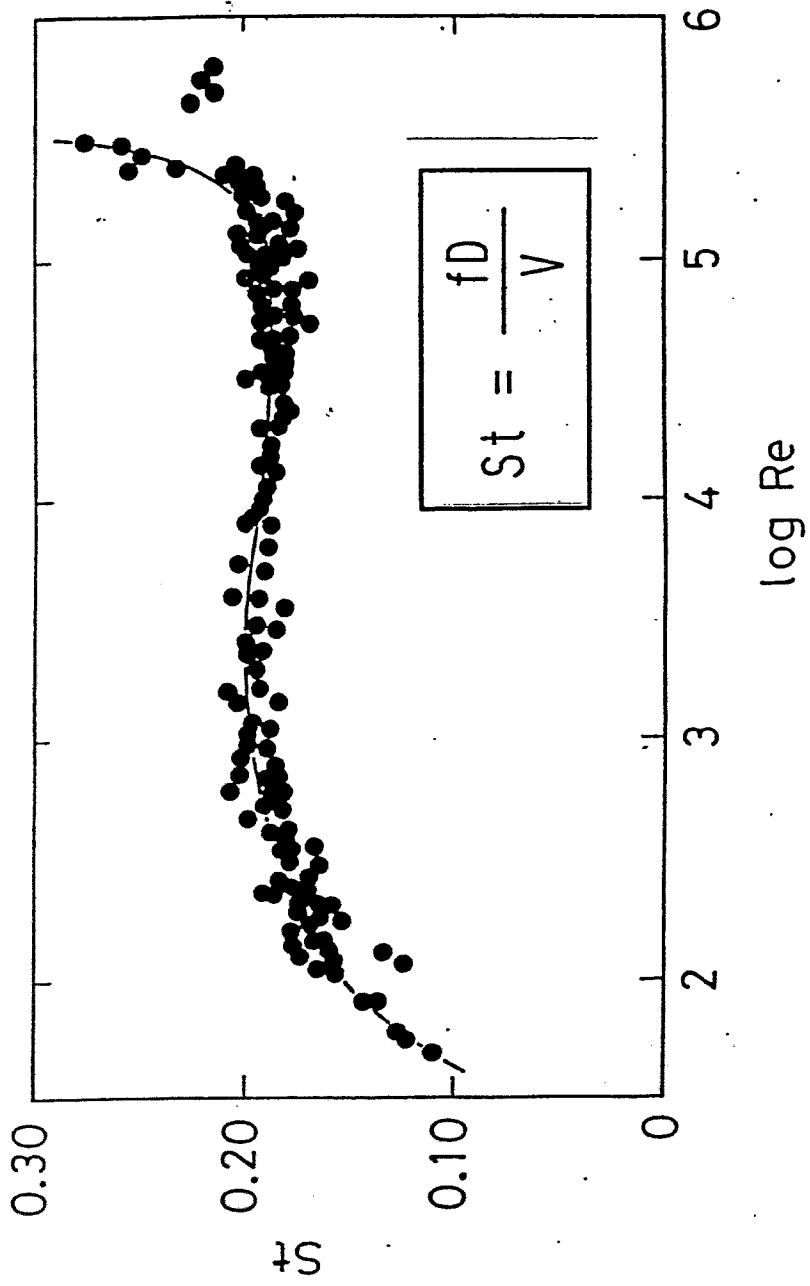


Fig.3 Relation between the Strouhal number and the Reynolds number for the circular cylinder.

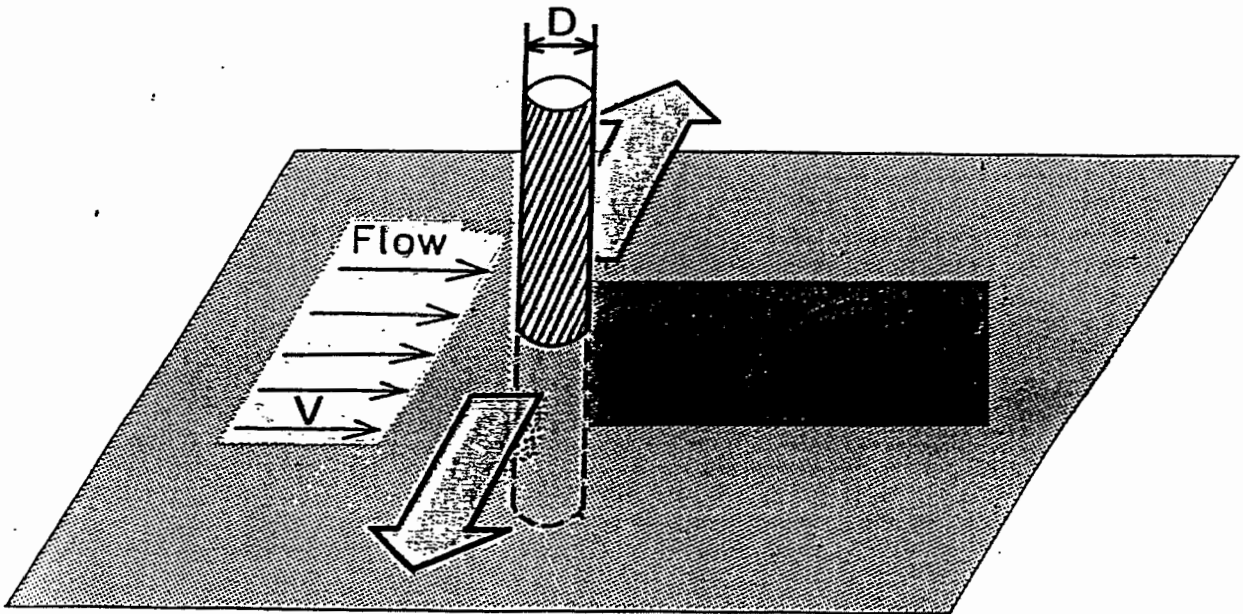
$$Re = VD/\nu$$

Re: Reynolds number

V: flow velocity

D: diameter of the cylinder

$\nu$ : kinematic viscosity of fluid



$$St = \frac{fD}{V}$$

St: Strouhal number

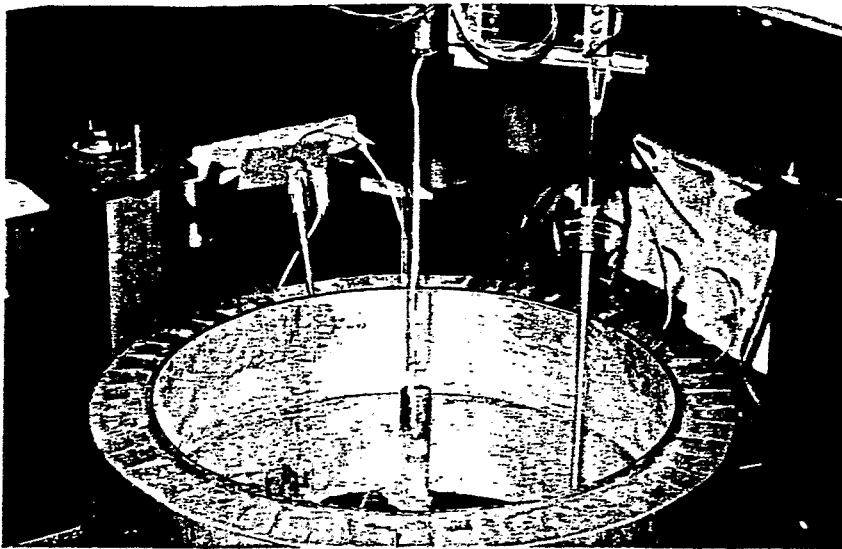
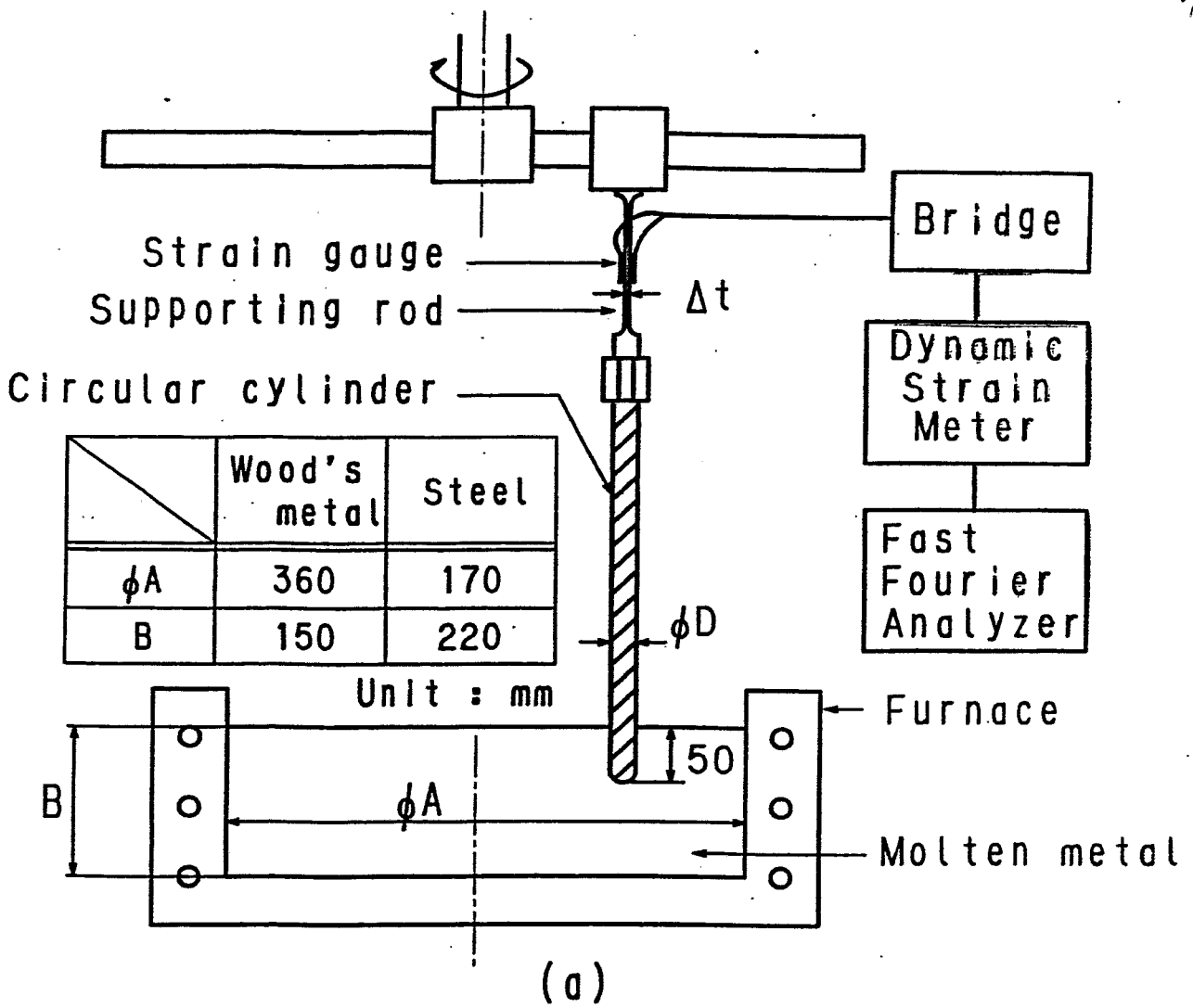
f: the shedding frequency

of Kármán's vortex street

D: the diameter of the cylinder

V: flow velocity

Fig.2 Schematic of the Kármán's vortex street.



(b)

Fig.6 Experimental apparatus.

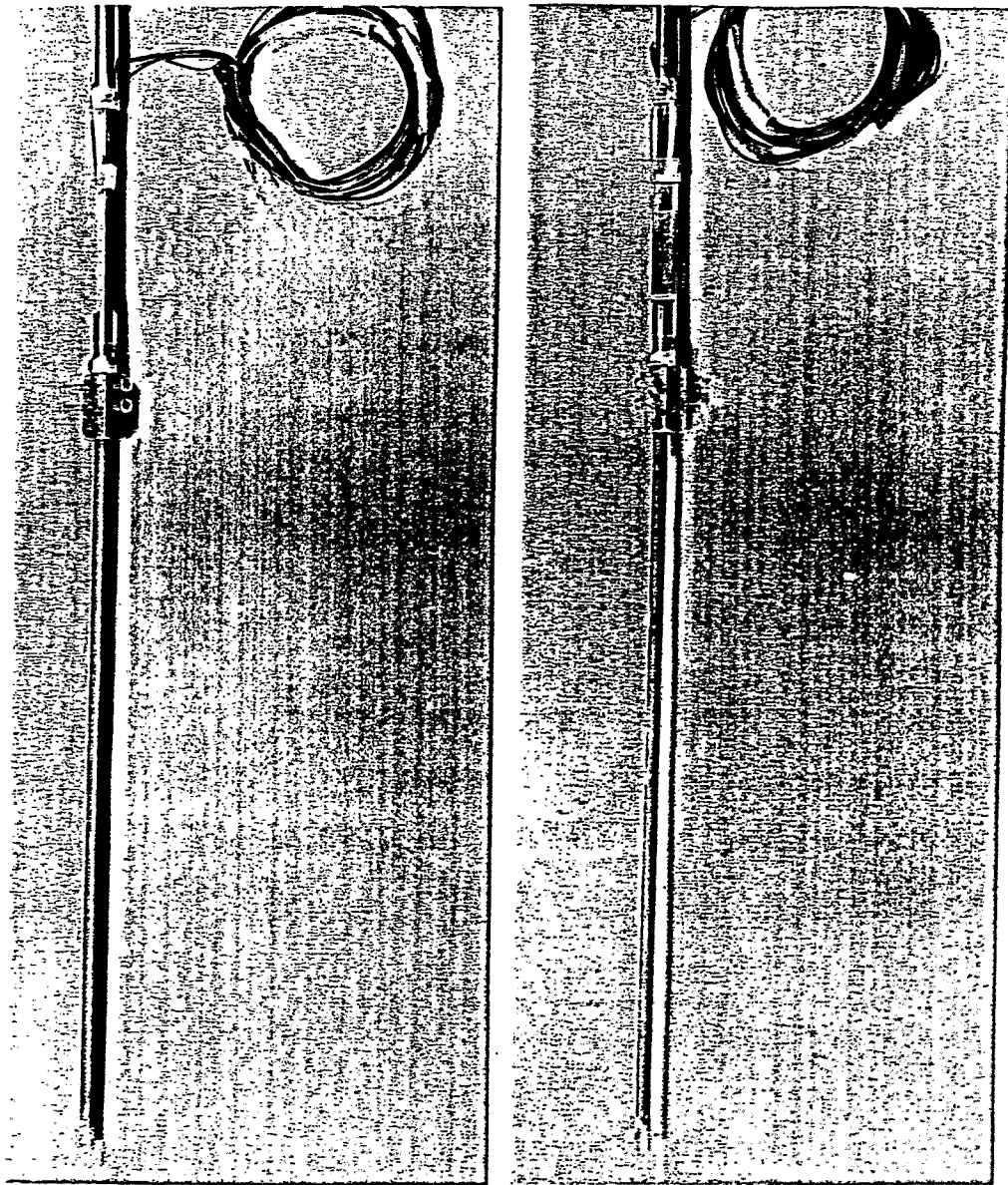
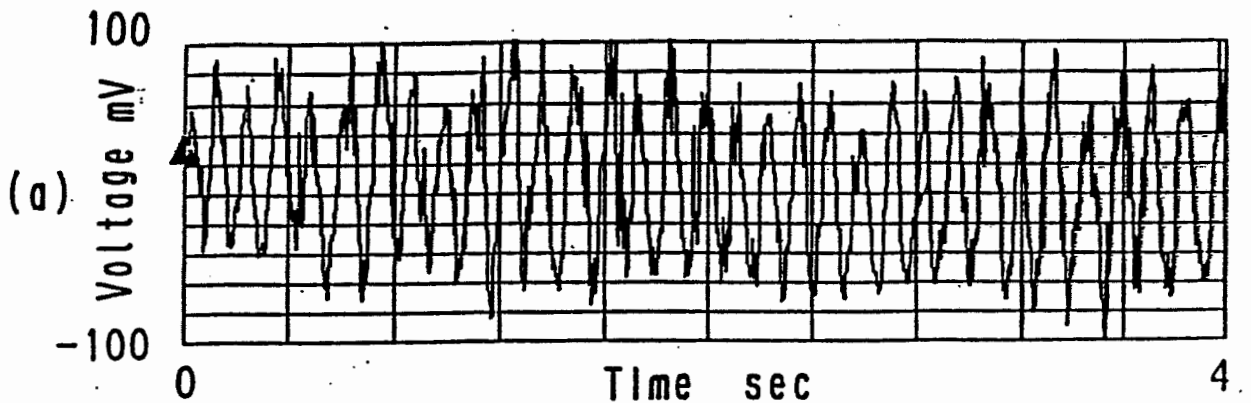


Fig.4 Kármán vortex Probe.





25cm/s

Shedding frequency of Kármán vortex

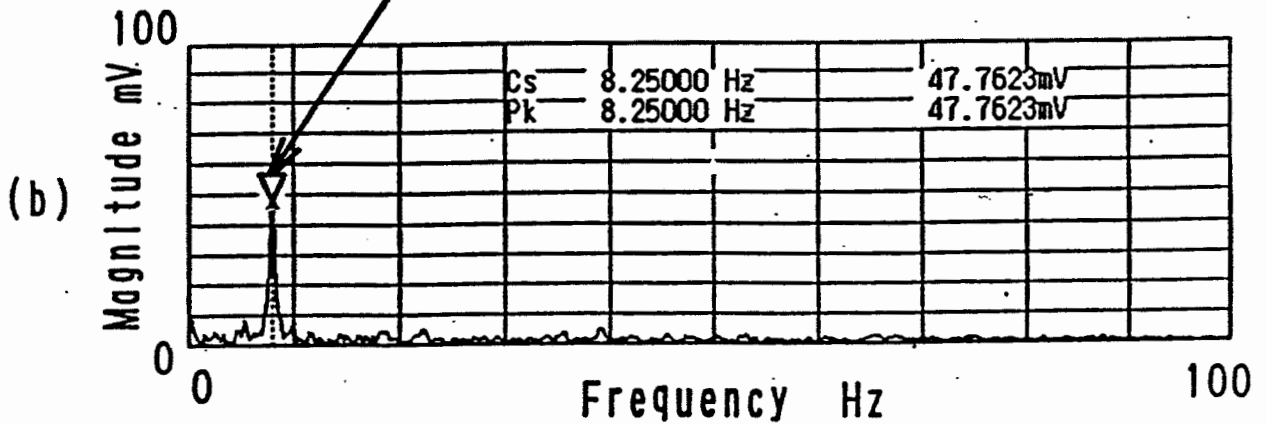


Fig.7 Output signal of strain meter and its power spectrum for Wood's metal bath.

$$f \cdot D = kV$$

k : the proportionality constant

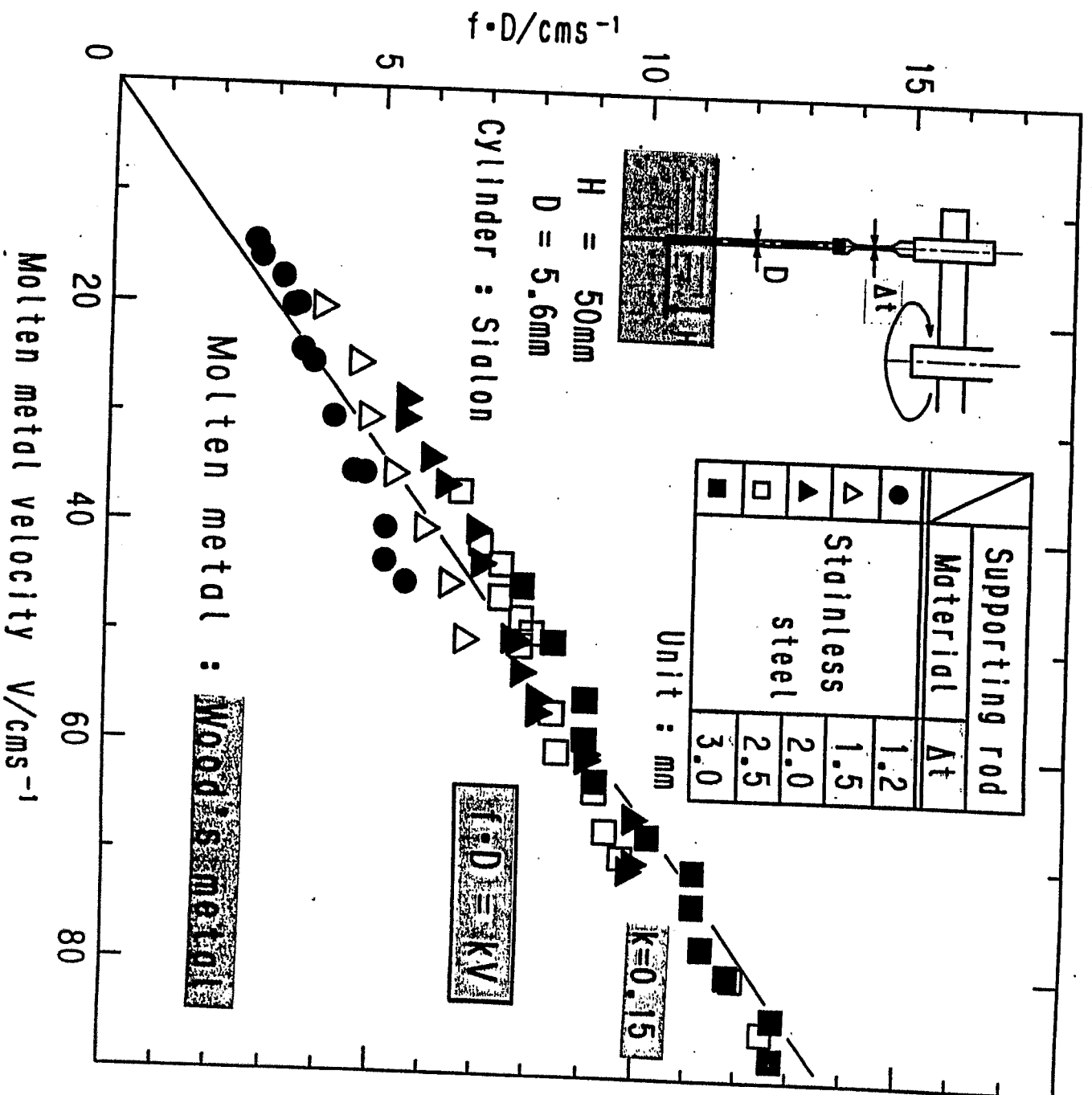


Fig.8 Relation between molten metal velocity and the product of shedding frequency and cylinder diameter.  
 (Effect of supporting rod thickness)

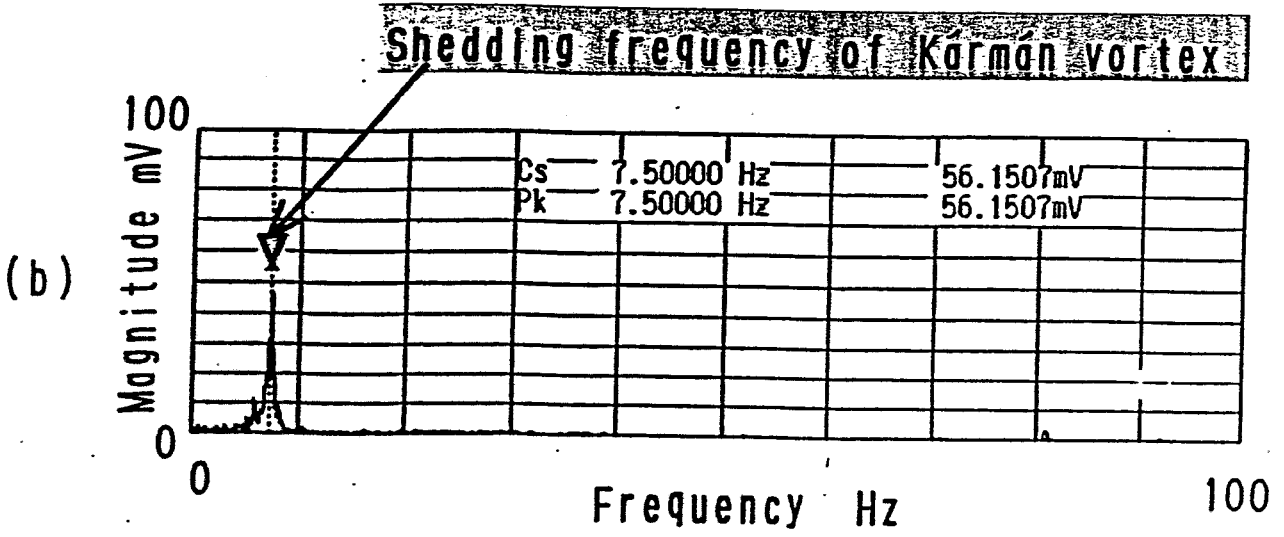
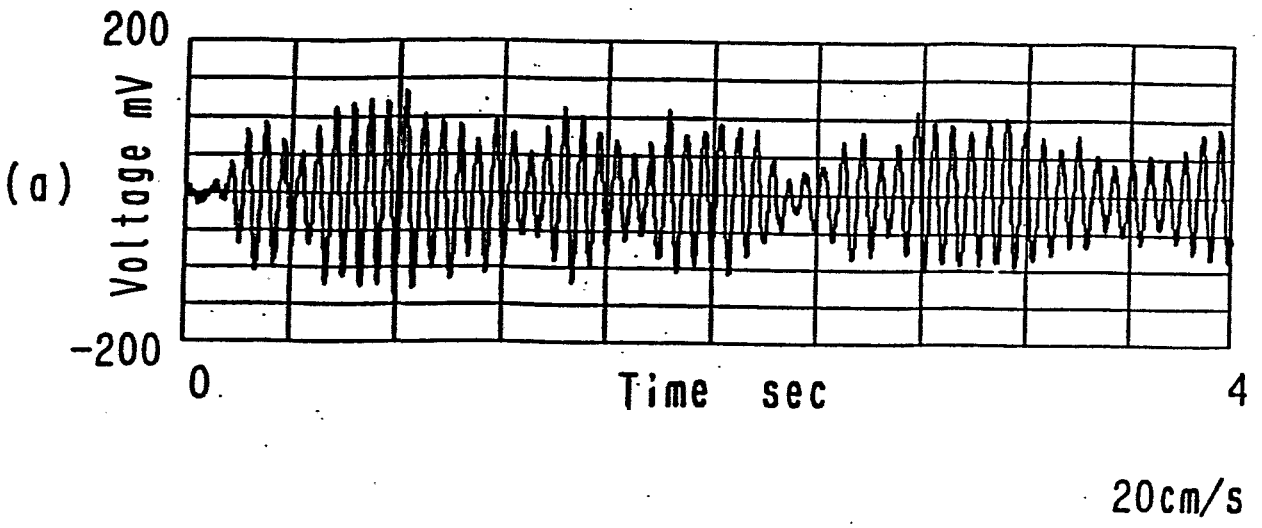


Fig.9 Output signal of strain meter and its power spectrum for molten steel bath.

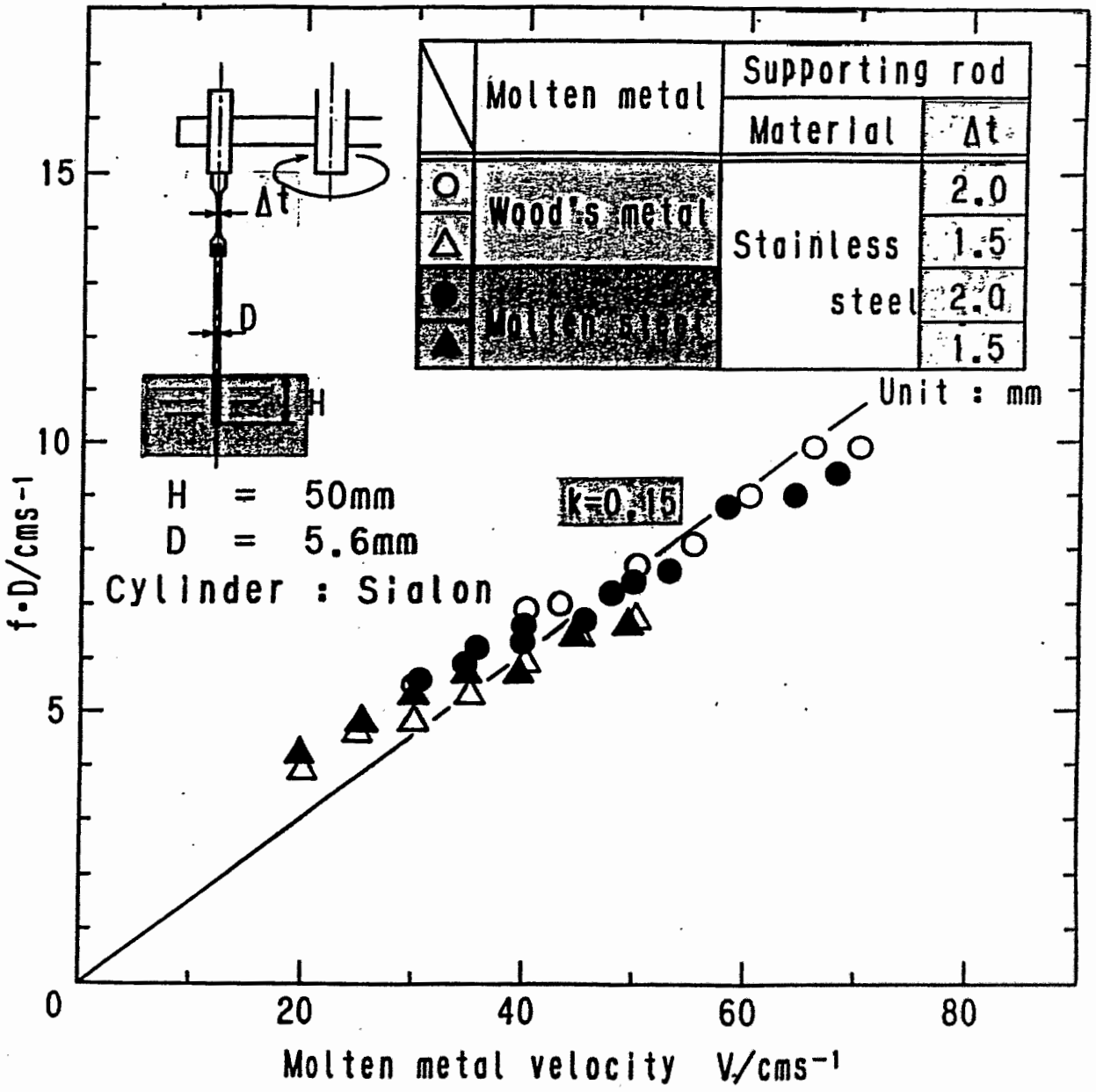


Fig.10 Relation between molten metal velocity and the product of shedding frequency and cylinder diameter.  
 (Comparison between Wood's metal data and molten steel data)

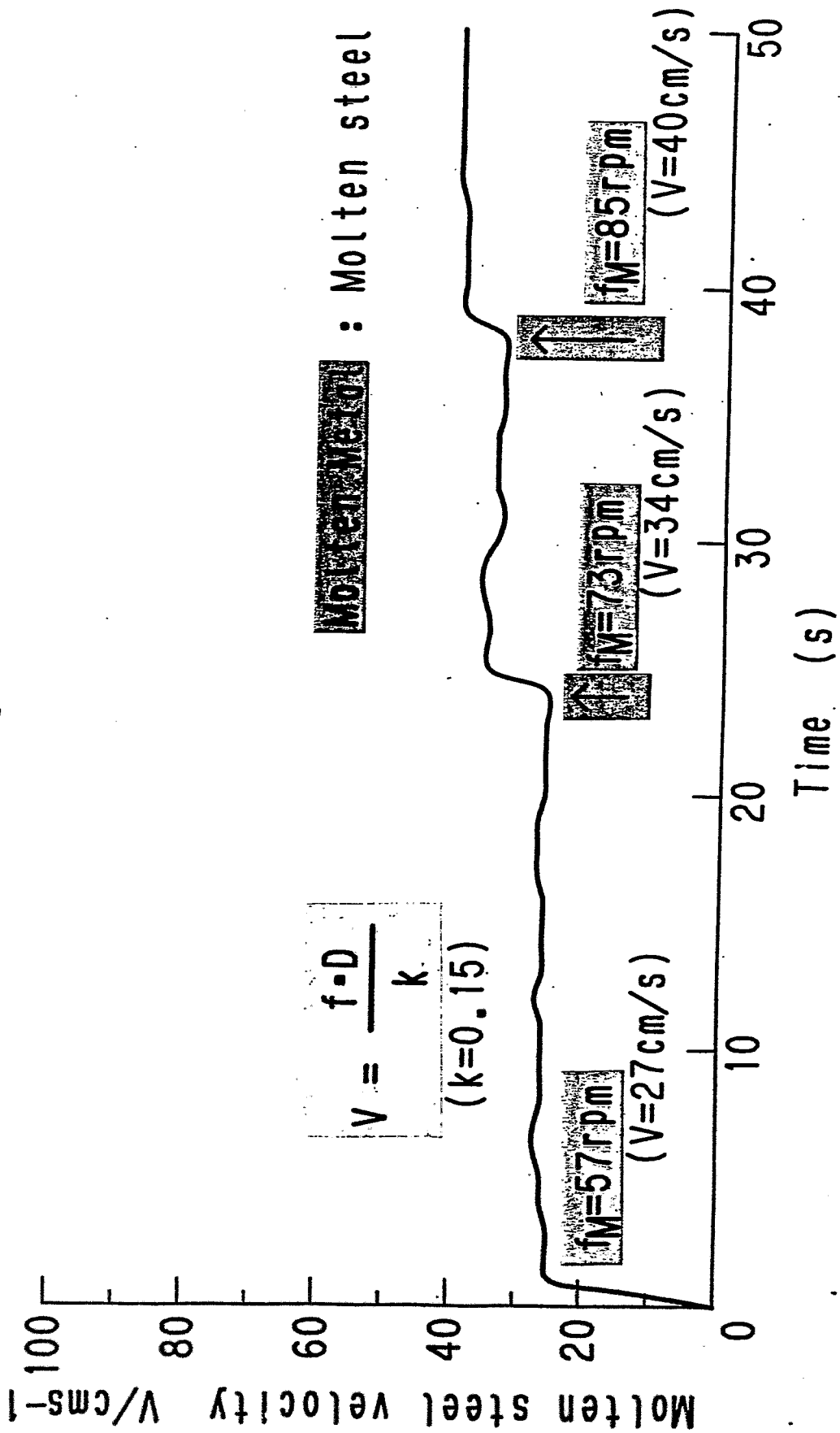


Fig.11 Molten steel velocity with time.

53/69

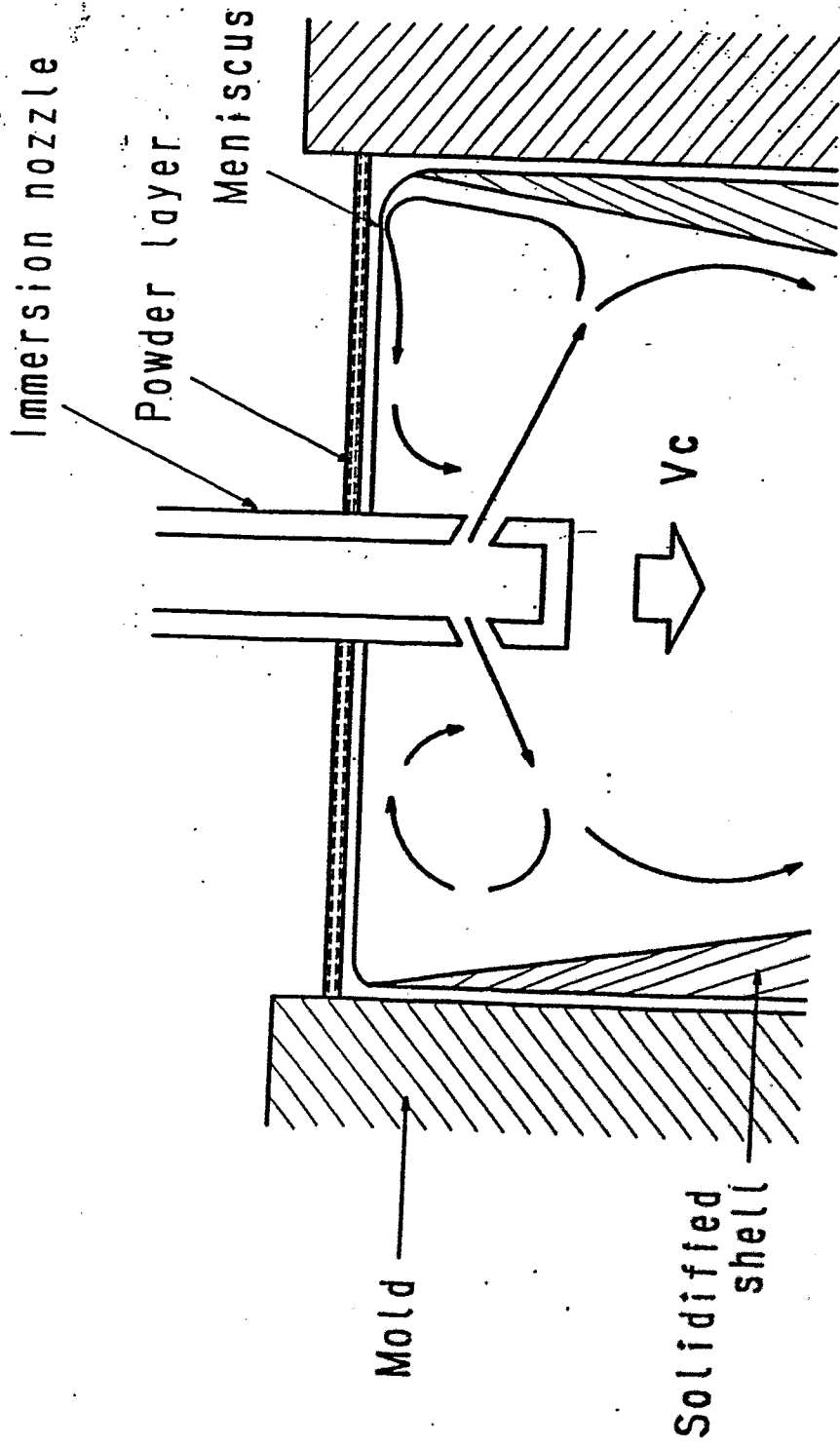


Fig.1 Schematic diagram of mold flows.

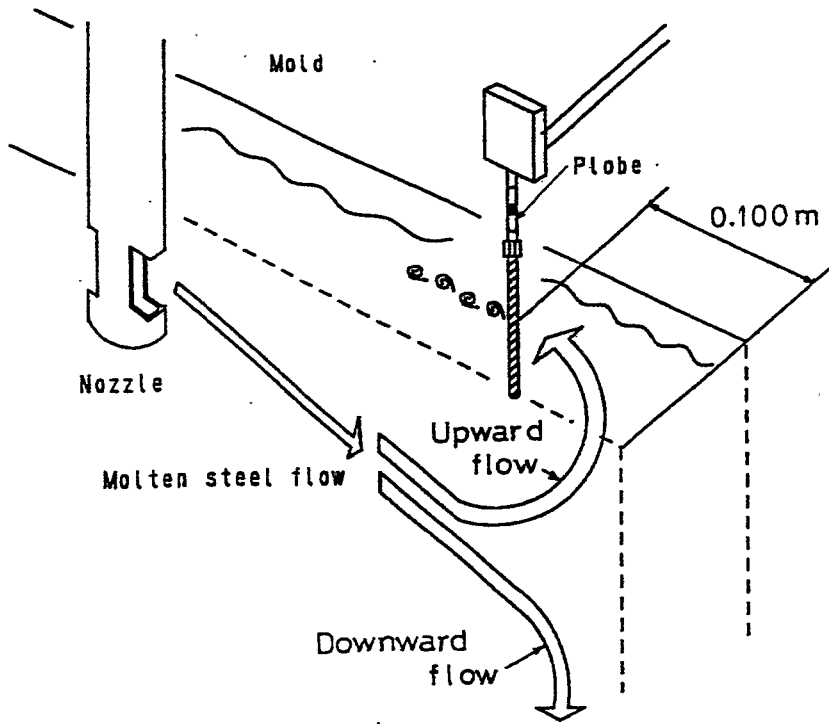
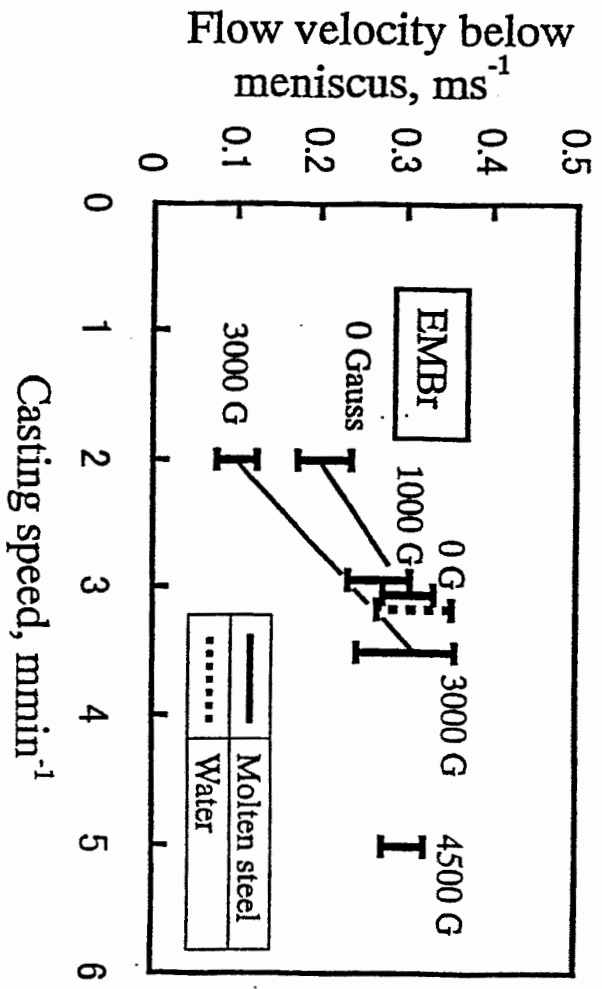


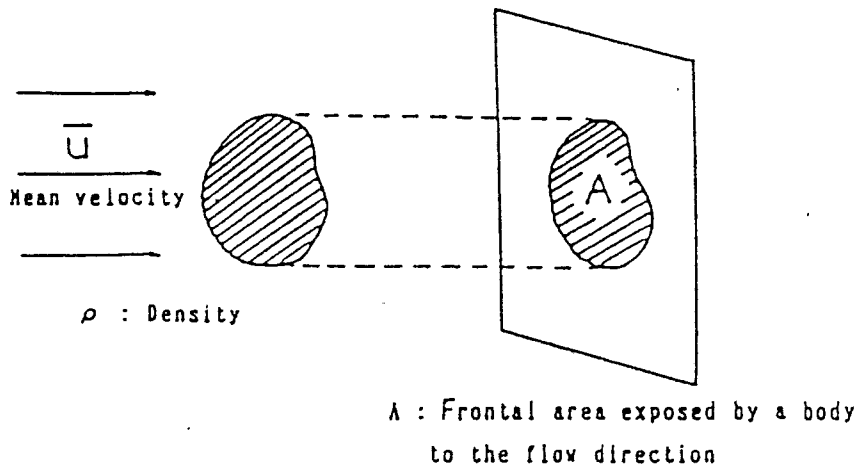
Fig. 12—Schematic view of measurement of meniscus flow velocity.



4/10



# Reaction probe



$$C_D = \frac{2F_D}{A\rho\bar{u}^2}$$

Fig.1 Definition of drag coefficient  $C_D$

$$\bar{u} = \sqrt{\frac{2F_D}{A\rho C_D}}$$

$$C_D = f(\text{Re}, \text{Tu}, \lambda/D)$$

Re: Reynolds number

T: Turbulence intensity

$\lambda$ : Turbulence scale

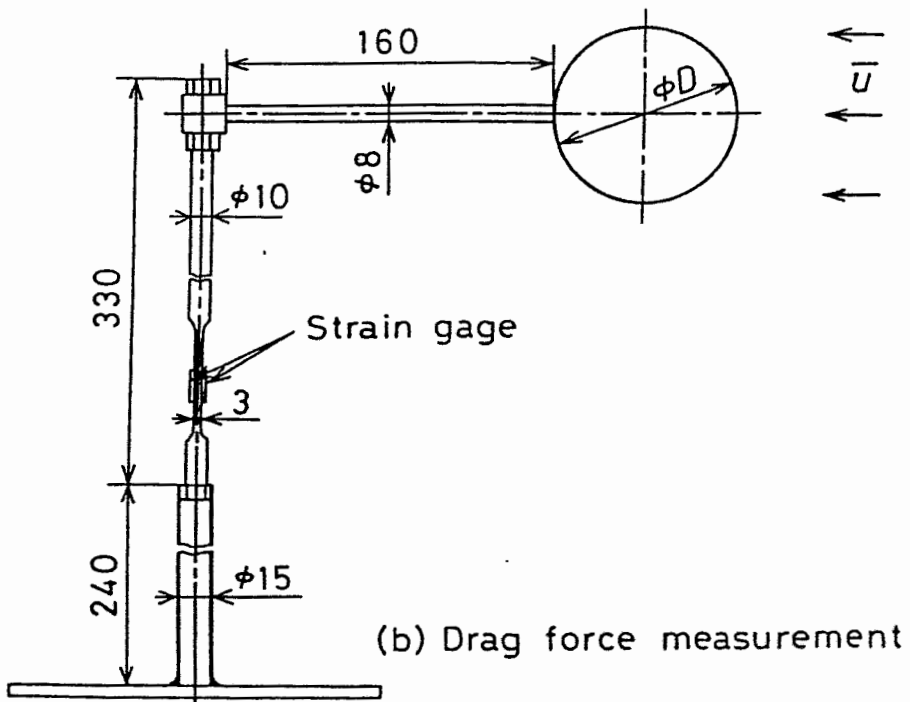
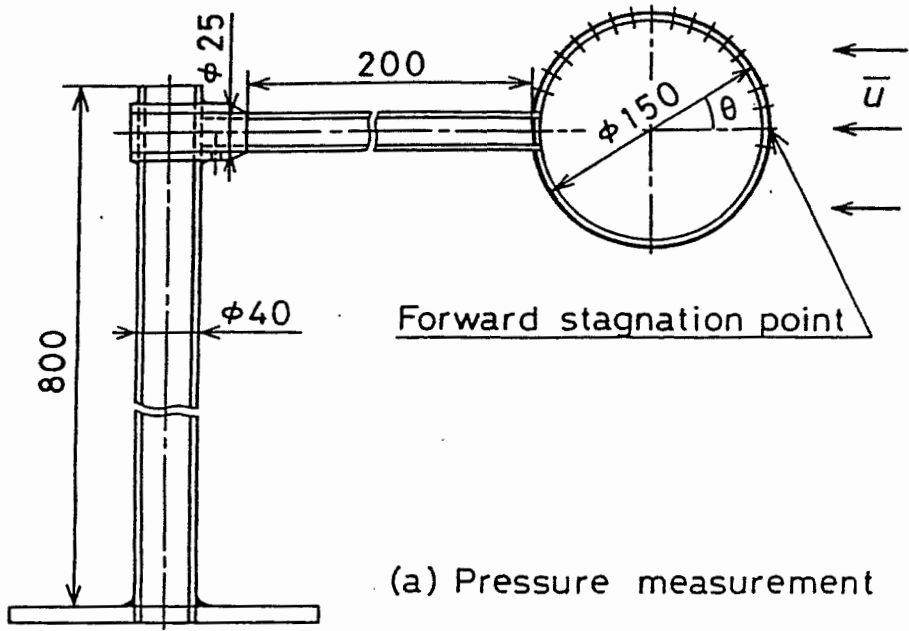


Fig. Test sphere for determining  $C_D$ .  
 (a) Pressure measurement  
 (b) Drag force measurement

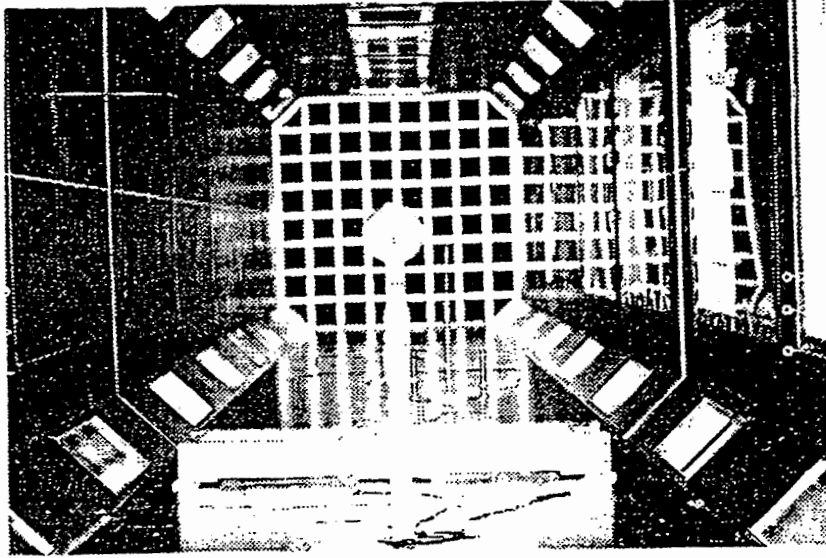


Fig. (a) Inside view of the test section upstream of a test sphere

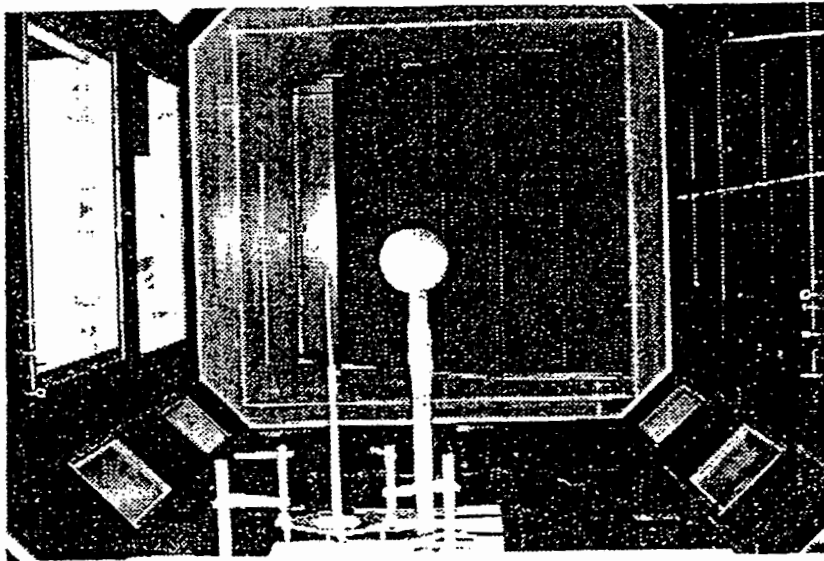


Fig. (b) Inside view of the test section downstream of a test sphere

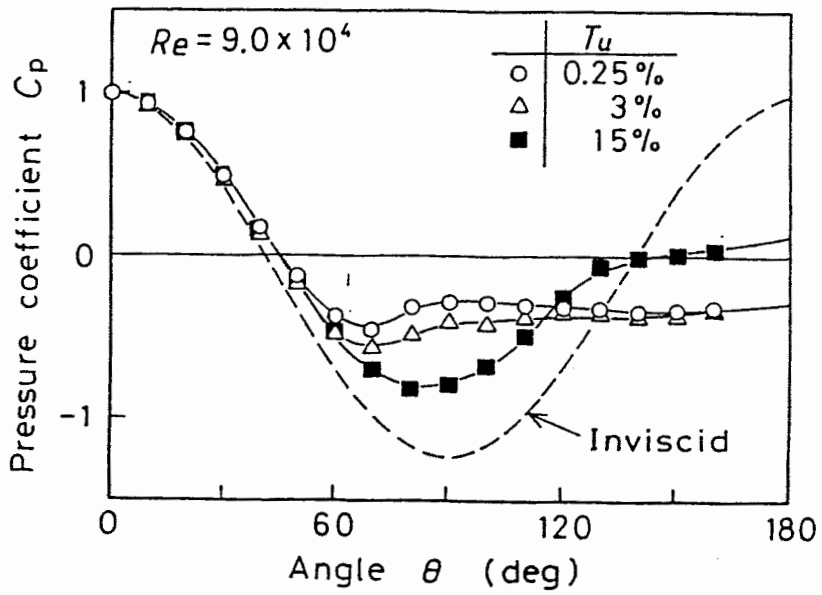


Fig. Pressure coefficient around the sphere for various  $Tu$ .

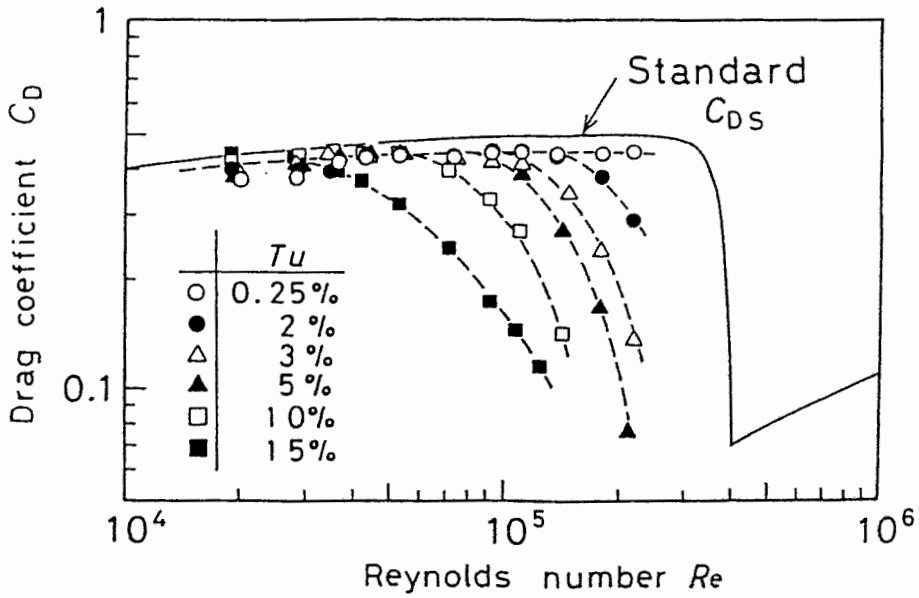


Fig. Drag coefficient of sphere as a function of  $Re$  and  $Tu$ .

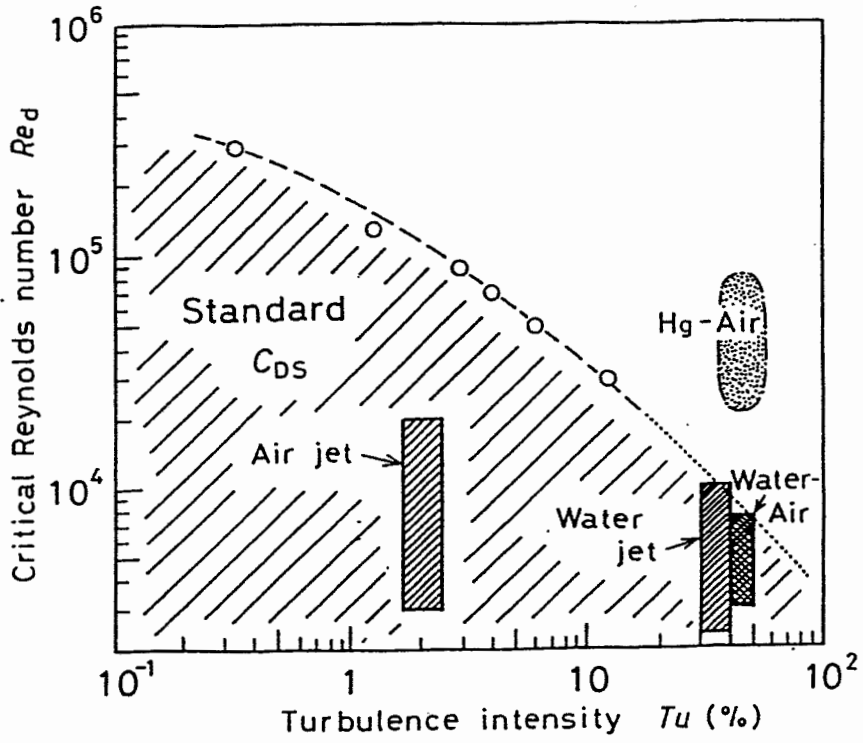


Fig. Diagram showing the present experimental conditions.

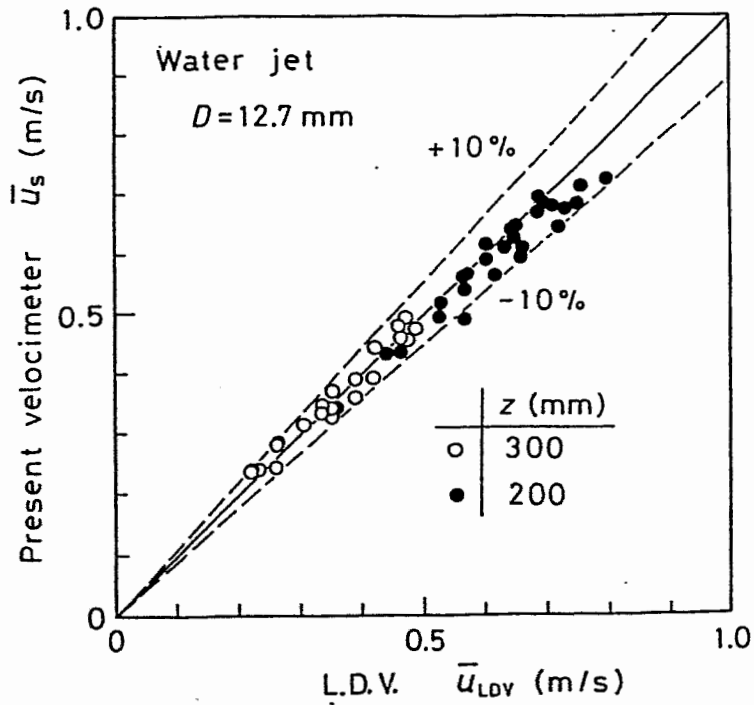


Fig. Relation between  $\bar{u}_s$  and  $\bar{u}_{LDV}$  for water jet.

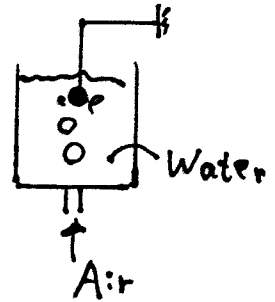
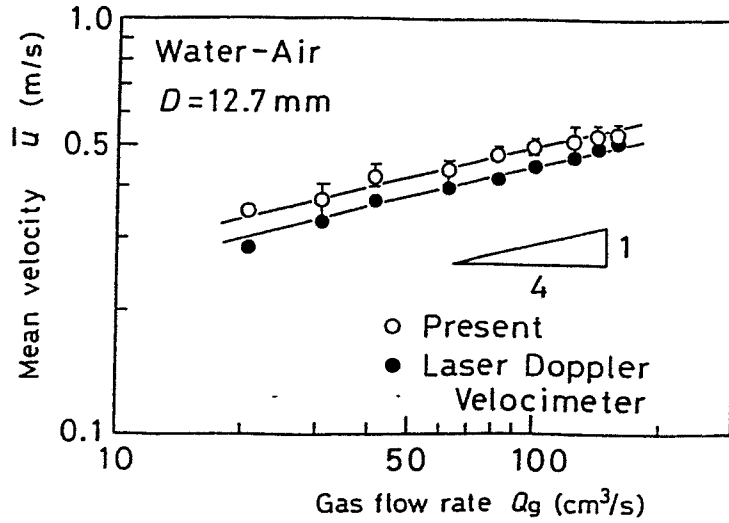


Fig. Relation between  $Q_g$  and  $\bar{u}$  for water-air bubbling jet.

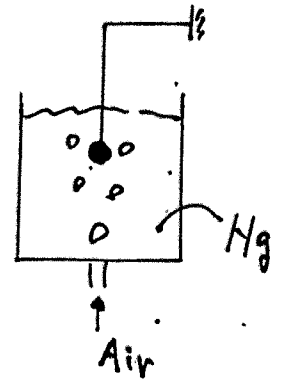
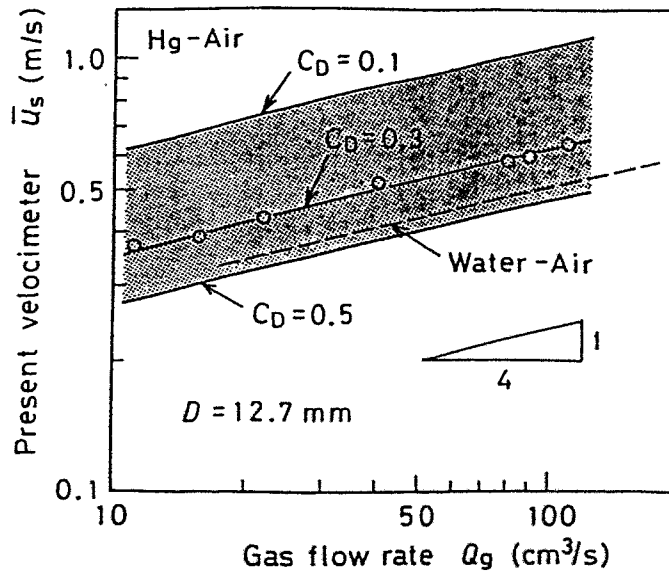


Fig. Relation between  $Q_g$  and  $\bar{u}_s$  for Hg-air bubbling jet.

# Particle imaging velocimetry (PIV)

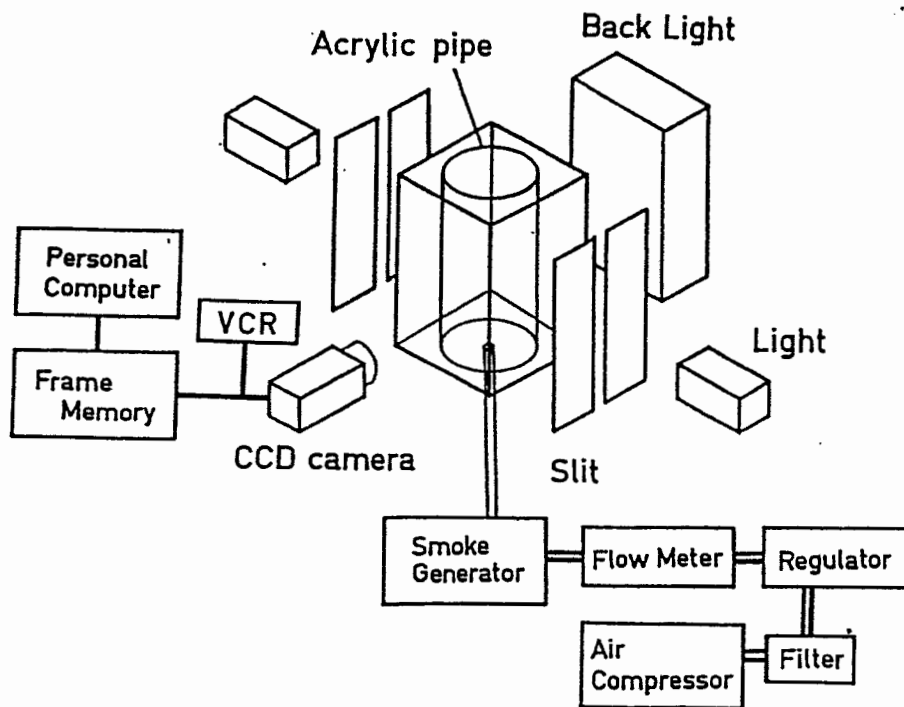
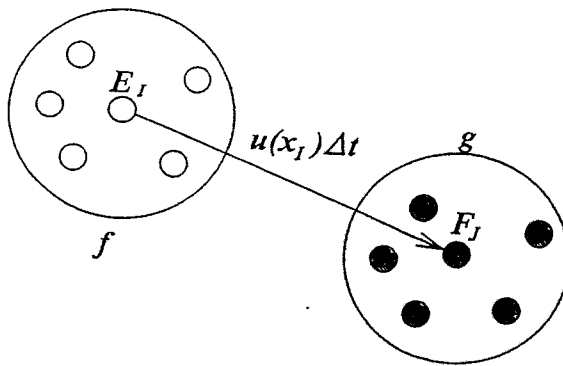
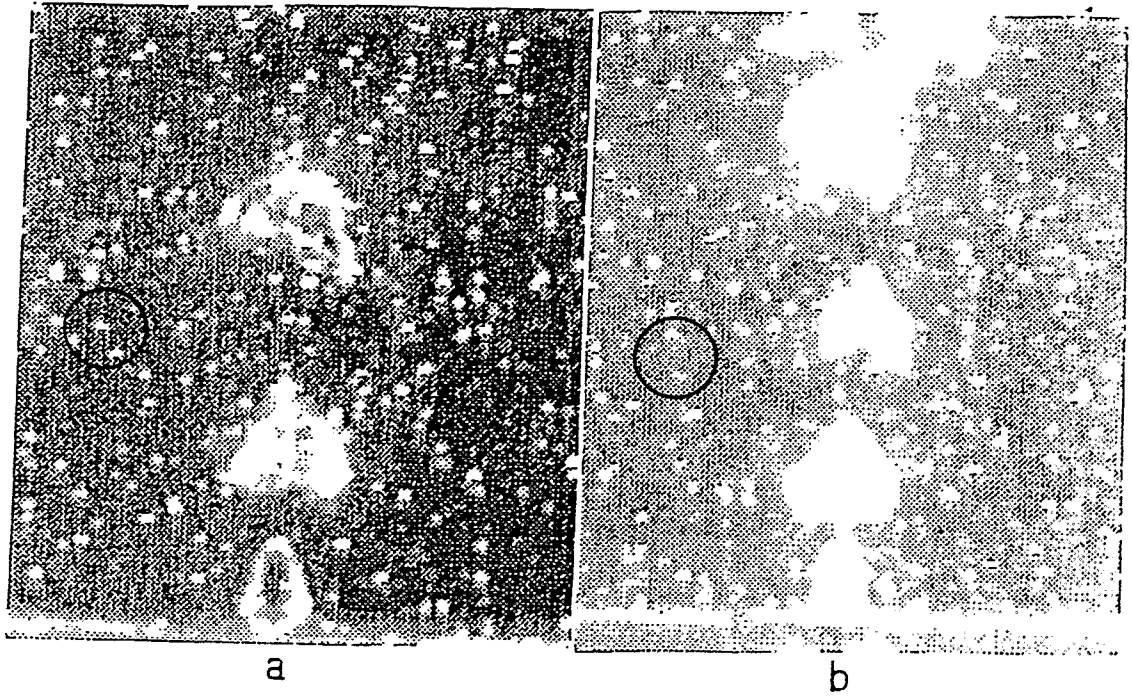


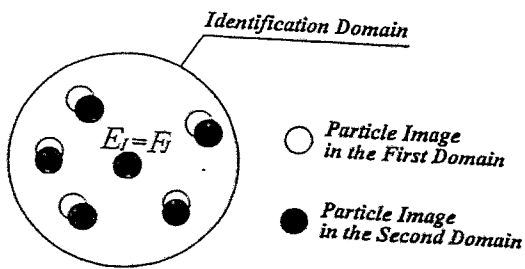
Fig. Schematic display of experimental apparatus.

# 1.8 3 次元動的画像解析

## (1) 2 値化画像相関法

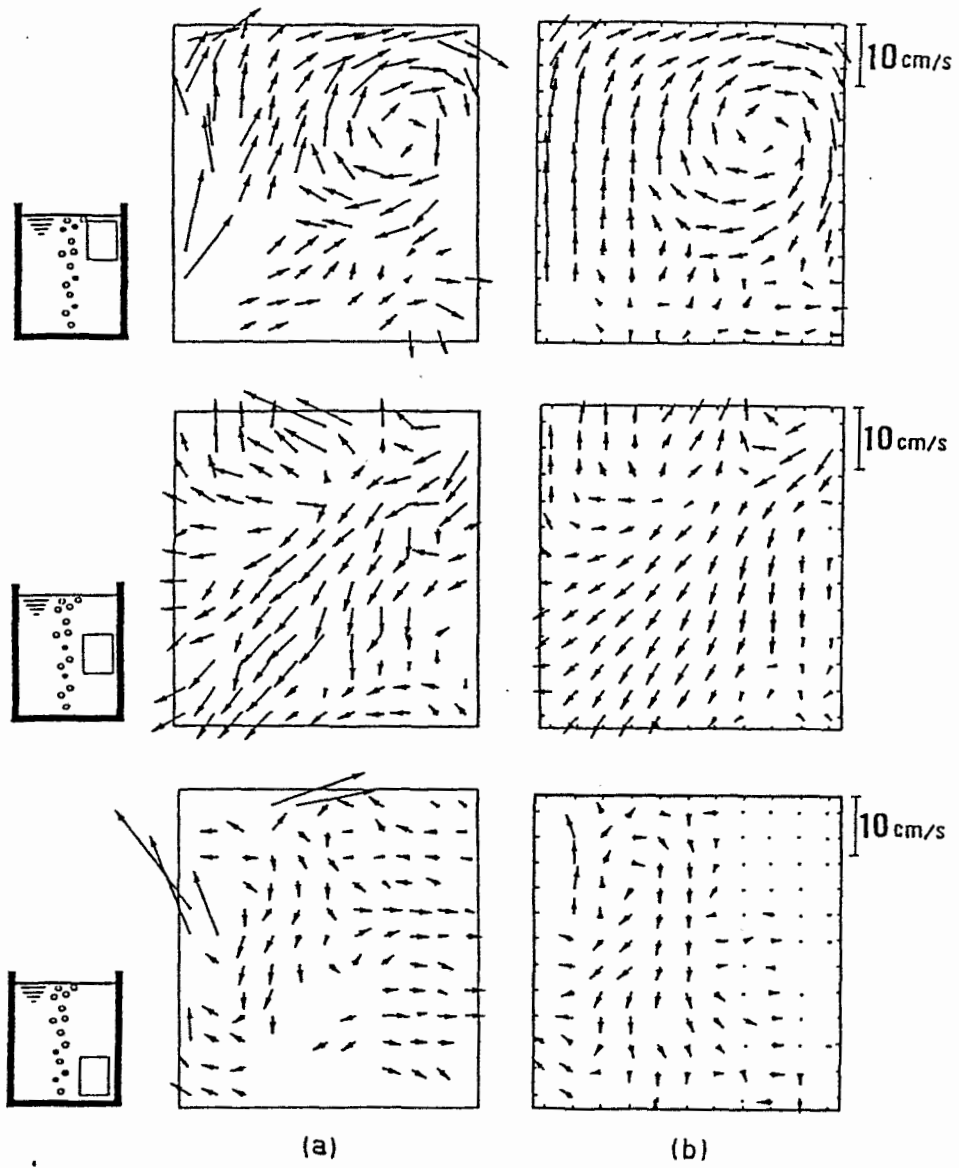


$$C_{fg} = \frac{\sum_{i=1}^n \sum_{j=1}^m \alpha_i \beta_j \mu(E_i \cap F_j)}{\mu(E_i) \sqrt{\sum_{i=1}^n \alpha_i^2} \sqrt{\sum_{j=1}^m \beta_j^2}}$$



$$C_{fg} = \frac{L}{\sqrt{nm}}$$





$Q=2\text{cm}^3/\text{s}$   $h=270\text{mm}$

(a) Instantaneous velocity distributions

(b) Time averaged velocity distributions

Fig. Two kinds of velocity distributions measured by PTV image analysis.

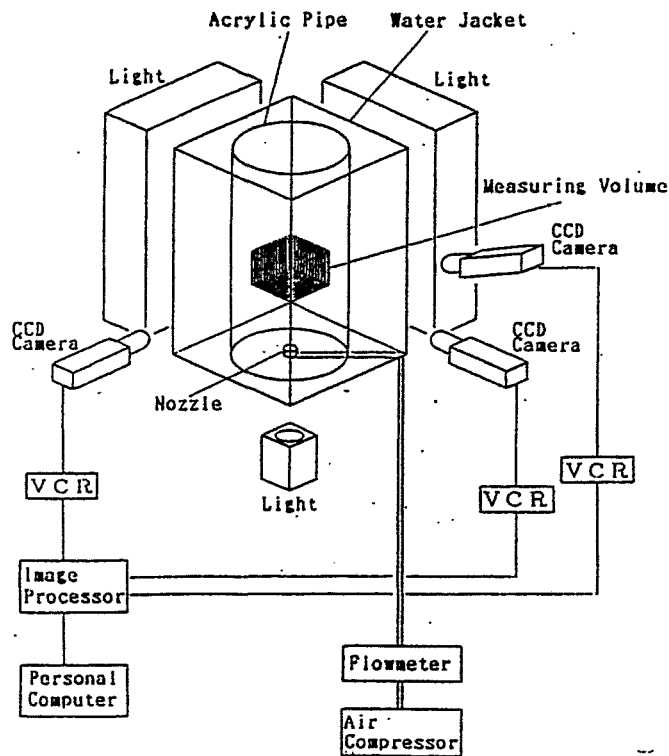


Fig. Outline of experimental apparatus for bubbling jet two-phase flow.

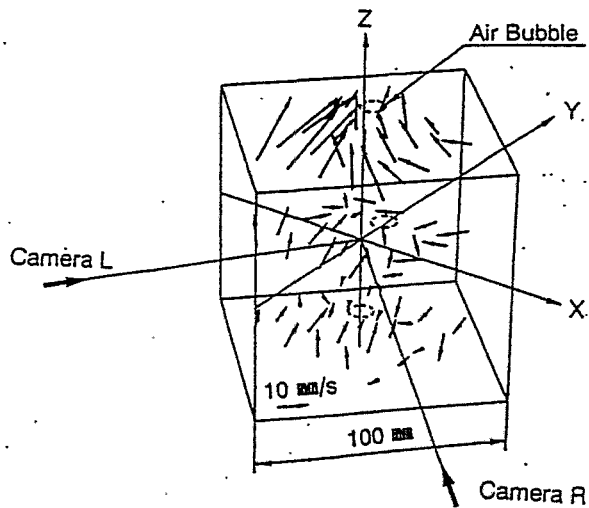


Fig. 3-D velocity vectors of particle in a bubbling jet mixing water vessel.

## **Future study**

- (1) Development of electroresistivity probe applicable in practical applications**
- (2) Development of velocimetry capable of measuring turbulence components in practical applications**

# Measurement of multiphase flow in metallurgy

*I.J. Opstelten*

*Hoogovens R&D, P.O. Box 10000, 1970 CA IJmuiden, The Netherlands*

In many stages during the manufacturing process of steel and aluminium, flow of molten metal, slags and gases is important. In these cases multiphase flow (gas through liquid metal and/or slag on liquid metal) determines the impact of phenomena such as mixing and heat transfer. In the academic world a great deal of research has been done on multiphase flow. The research has, by its focus over the past few years, led to enhanced insight and development tools mainly for application in the petro-chemical industry. The question is still open in how far this insight and these tools (relying on substantial empirical data obtained for the petro-chemical practice) can be translated into multiphase flow in metallurgical processes. It was the main reason for starting the project "multiphase flow in metallurgy", conducted in co-operation between Hoogovens R&D and the University of Twente.

One of the main contributions of Hoogovens R&D is supplying experimental data on multiphase flow in molten metals for validation of numerical models developed at the University of Twente. This initiated the investigation into and development of tools to assess these phenomena. A review of the existing tools will be given as well as the first results of two tools to characterise important factors of a vertical plume of gas in a vessel of molten metal.

---

## Multiphase flow in metallurgy



presentation MTLM Dr L.J. Opstelten  
12 October 1999



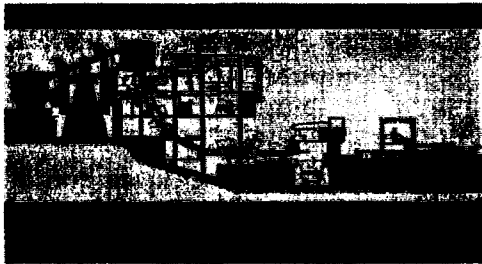
---

## What's this presentation about?

- Relevance multiphase flow to Corus
- Modelling multiphase flow in metals
- Available techniques for liquid metals
- Bubble formation results

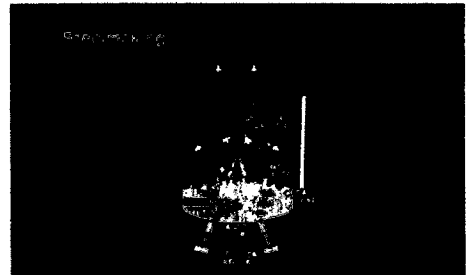
---

## Relevant processes: Continuous casting



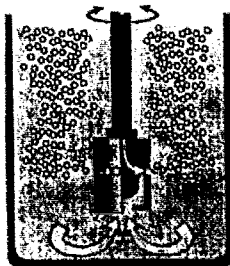
---

## Relevant processes: Steelmaking



---

## Relevant processes: Aluminium refinement



Hydro Aluminium Hycast<sup>®</sup>



---

## Modelling multiphase flow in metals

### physical modelling

- |                                |  |
|--------------------------------|--|
| ▪ Advantages:                  | ▪ Disadvantages:                                 |
| • Safety                       | • Scaling laws                                   |
| • Cost                         | • Empirical relations                            |
| • Visualisation                | • Translation of results<br>(sub-processes only) |
| • Measurement<br>opportunities |  |

## Modelling multiphase flow in metals

### gas-liquid flow properties

- Plume characteristics
  - Gas hold up
  - Void fraction
  - Plume velocity
  - Liquid velocity
  - Precession frequency
- Bubble characteristics
  - Bubble formation
  - Bubble size distribution
  - Bubble velocity
  - Bubble frequency
  - Bubble shape

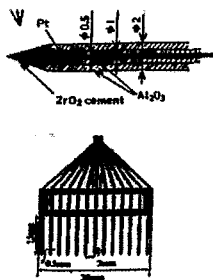


## Available techniques for liquid metals

- Electroresistivity Probe (ERP)
- Magnetic Probe (MP)
- Gamma-ray Attenuation Technique (GAT)
- X-ray Fluoroscopic Observation (XFO)
- Dynamic Gas Disengagement (DGD)
- Ultrasound (US)



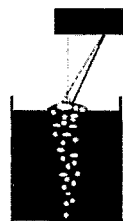
### Electro-resistivity probe



- Two-needle:
  - Axial and Radial gas hold-up
  - Bubble frequency
  - Bubble velocity
  - Bubble size (distribution)
- Multi-needle also:
  - Bubble shape



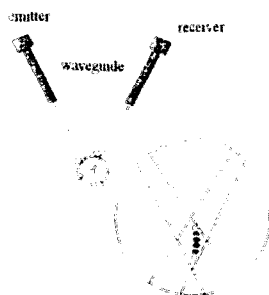
### Dynamic Gas Disengagement



- Distance to meniscus(t)
- Radial gas hold-up
- Bubble frequency
- Bubble exit velocity (?)
- Bubble size (?)
- Plume precession frequency



### Ultrasound



- Direct:
  - Ultrasonic Doppler Velocimetry
- Indirect:
  - Bubble Tracing
    - Bubble formation
    - Bubble velocity
    - Bubble frequency
    - Bubble size (?)



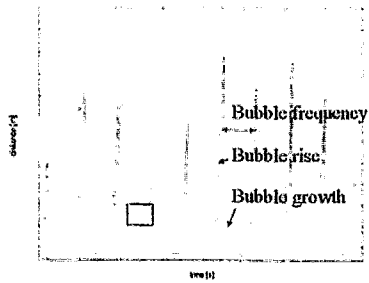
## Available techniques for liquid metals

### advantages/disadvantages

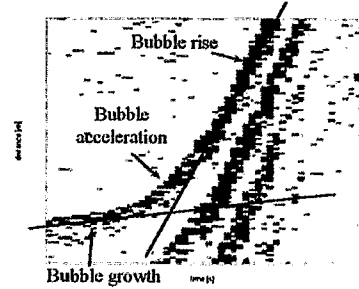
No	++	+	+	+	+/+	+/+
No	+/-	+	+	-	-	-
Yes	+/-	+	+	+	+	+
Yes	+/-	-	-	+	+	-
Yes	+	-	-	+	+	-
Yes	+	+/-	+	+	+/-	+/-



## Bubble formation results: Ultrasound



## Bubble formation results: a close-up



## Conclusions

- Multiphase flow important in metallurgy
- Need for know-how physical scaling MFM
- Measuring Techniques MFM crucial
- Ultrasound successfully applied to Aluminium
- Next step: Ultrasound in Steel?!



# Investigation of liquid metal two phase flow characteristics by means of local resistivity probes and X-ray screening technique

*S. Eckert<sup>1</sup>, G. Gerbeth<sup>1</sup>, B. Guttek<sup>2</sup>, H. Stechemesser<sup>2</sup>  
and O. Lielausis<sup>3</sup>*

<sup>1</sup> *Forschungszentrum Rossendorf (FZR), P.O.Box 510119, D-01314 Dresden, Germany*

<sup>2</sup> *Forschungszentrum Jülich (FZJ), D-52425 Jülich, Germany*

<sup>3</sup> *Latvian Academy of Science, Institute of Physics, Miera iela, LV-2169 Salaspils, Latvia*

In many technologies such as the refinement of metallic melts the injection of gas bubbles is used to drive some liquid motion, enhance transport processes or to control the rate of chemical reactions. The resulting flow structure strongly depends on two phase flow parameters such as bubble size, bubble distribution or the local void fraction. Magnetic fields can be used to control the characteristics of a liquid metal bubbly flow.

We present experimental investigations of the bubble formation in heavy liquid metals as well as the influence of external magnetic fields on the turbulent dispersion of gas bubbles and the slip ratio in liquid metal bubbly flows, respectively.

## **a) Bubble formation**

If gas bubbles are injected into a liquid metal characterised by a large surface tension one should be care to get a good wetting between the fluid and the surface of the gas injector. Otherwise, the gas would try to spread out along this interface to form gas layers. A control of the bubble size and formation rate becomes difficult. The comparison between experiment and theoretical models describing bubble formation processes requires an ideal wetted gas injector.

The bubble formation in mercury and the eutectic alloy InGaSn has been studied by means of several methods of gas injection, for instance through single orifices or injectors made from sintered metals with a mean porosity of a few microns. X-ray measurements have been used to directly observe the resulting gas bubbles rising in the liquid metal. In the case of an single orifice the influence of electromagnetic forces on the bubble frequency has been demonstrated.

## **b) Turbulent bubble dispersion, slip ratio**

The transport properties of small argon bubbles have been studied in turbulent upwards channel flows of sodium and mercury. The bubbles were injected by a single orifice located in the centre of the channel cross section. After a distinct distance the local void fraction and the bubble velocity has been measured by means of electrical resistivity probes. The flow has been exposed to external magnetic fields directed transverse or longitudinal to the mean flow direction.

We will present and discuss measuring results showing the effect of the magnetic field strength and direction on the horizontal gas distribution and the ratio between gas and liquid velocity.



**Investigation of liquid metal  
two-phase flow characteristics by  
means of local resistivity probes and  
X-ray screening technique**

*S. Eckert, G. Gerbeth  
Forschungszentrum Rossendorf, Germany*

*B. Guttek, H. Stechemesser  
Forschungszentrum Jülich, Germany*

*O. Lielausis  
Institute of Physics Riga, Latvia*

**International Workshop on  
Measuring Techniques for Liquid Metal Flows (MTLM)**

Rossendorf, October 11-13, 1999

# Liquid metal two phase flow

- metallurgical/chemical industry:
  - mixing and homogeneization
  - melt refinement
  - control reaction kinetics
  - reduce clogging in tundish nozzles
- liquid metal targets for neutron spallation sources
- MHD generator

## Measuring quantities

- void fraction
- bubble size, interfacial area
- bubble velocity

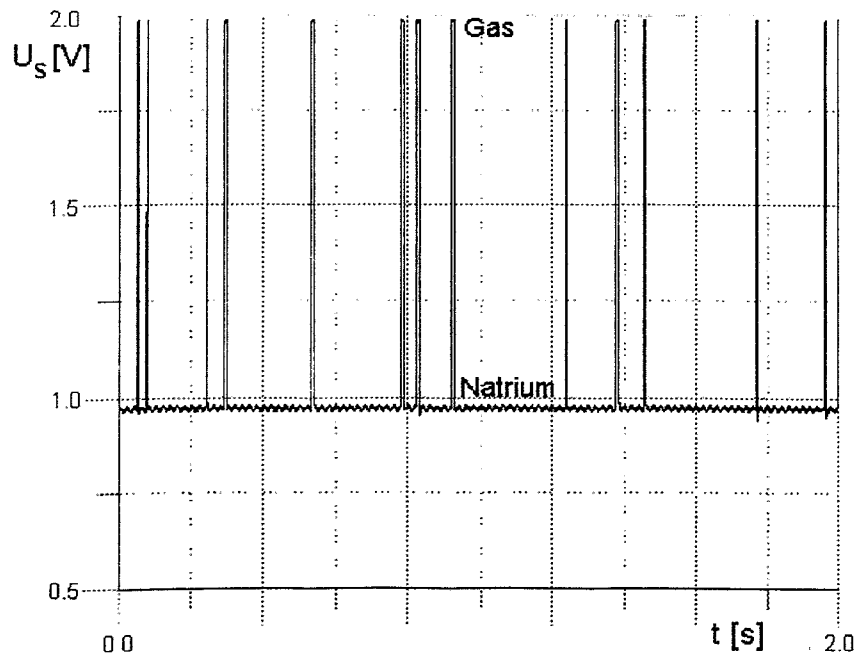
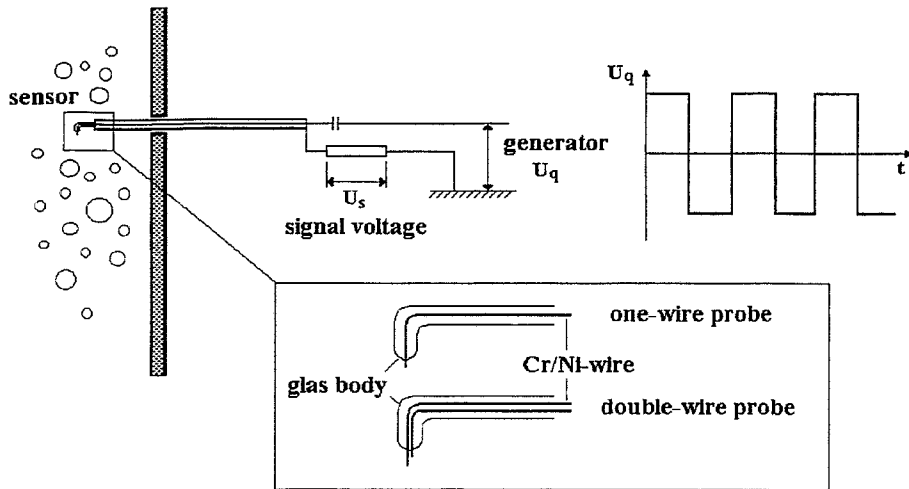
## Fields of interest

- Influence of an external magnetic field on the properties of liquid metal two-phase flows (void fraction distribution, slip ratio)
- Formation process of gas bubbles in liquid metals

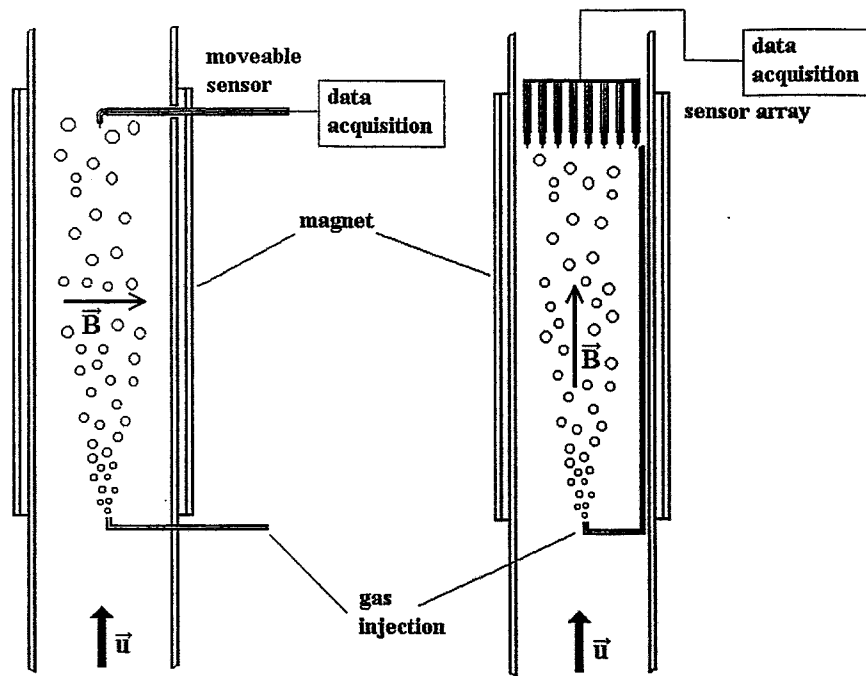
## Methods

- single- and double wire resistivity probes (FZR)
- X-ray screening technique (FZJ)

# Measuring Principle Resistivity Probe



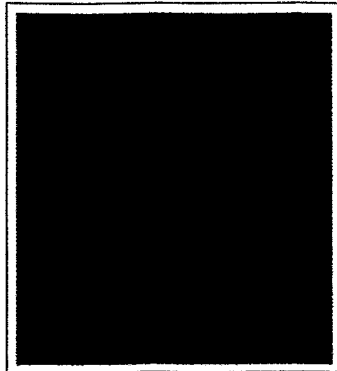
# Experiment: Liquid Metal MHD Two-Phase Flow in a rectangular channel



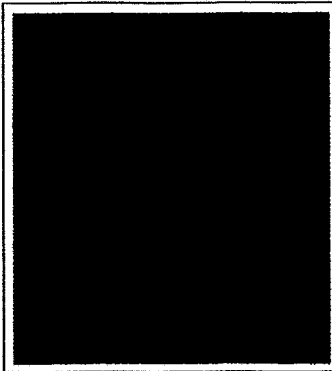
a) transverse magnetic field

b) longitudinal magnetic field

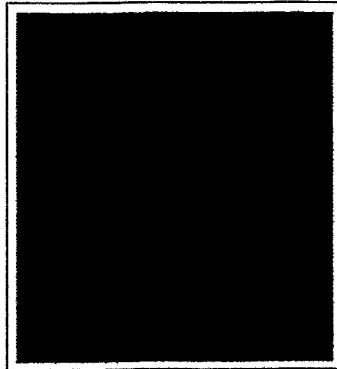
# Local void fraction distribution (transverse magnetic field)



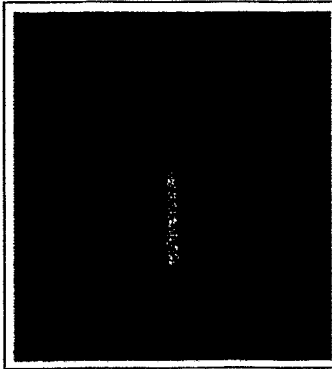
a)  $Ha = 0, N = 0$



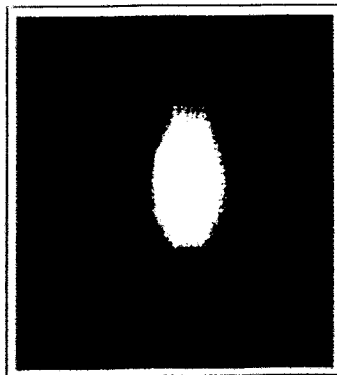
b)  $Ha = 600, N = 19$



c)  $Ha = 1200, N = 78$



d)  $Ha = 1505, N = 122$

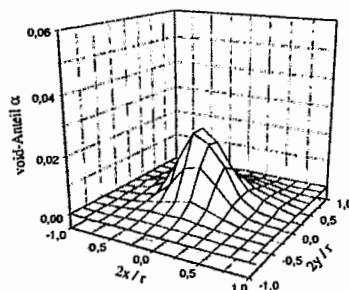
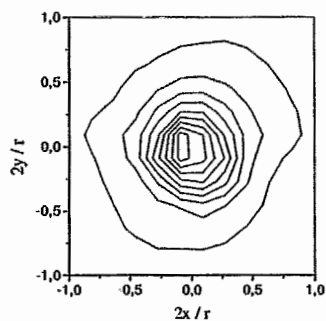


e)  $Ha = 2110, N = 239$

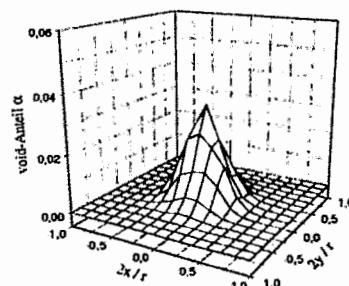
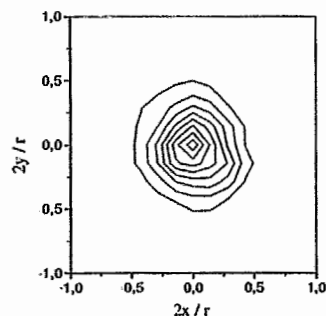


→ B-field direction →

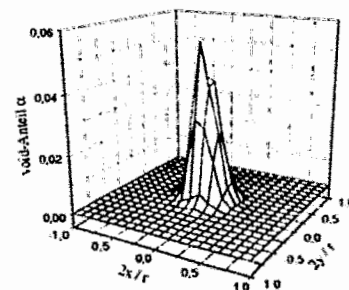
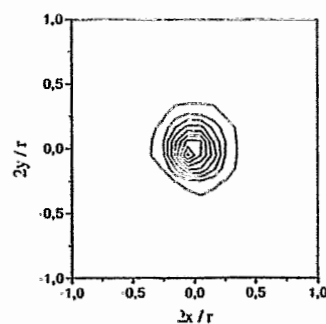
# Local void fraction distribution (longitudinal magnetic field)



Ha = 0, N = 0

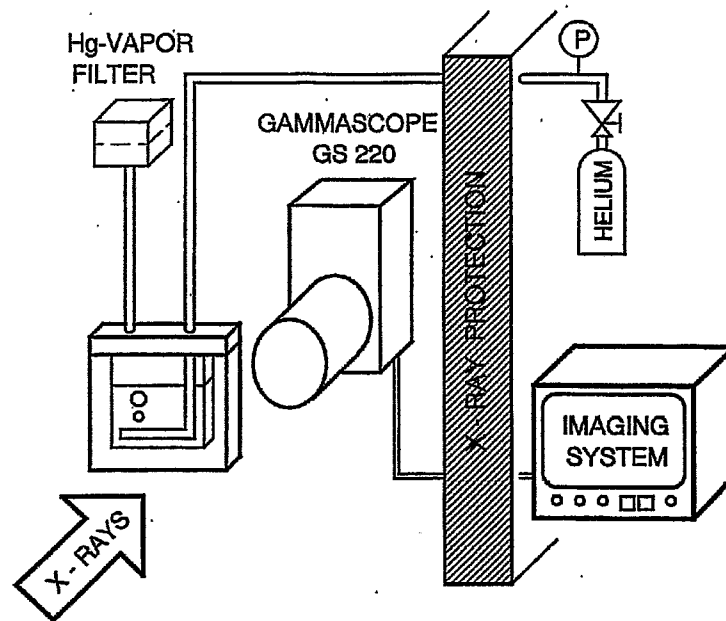


Ha = 770, N = 7



Ha = 2320, N = 66

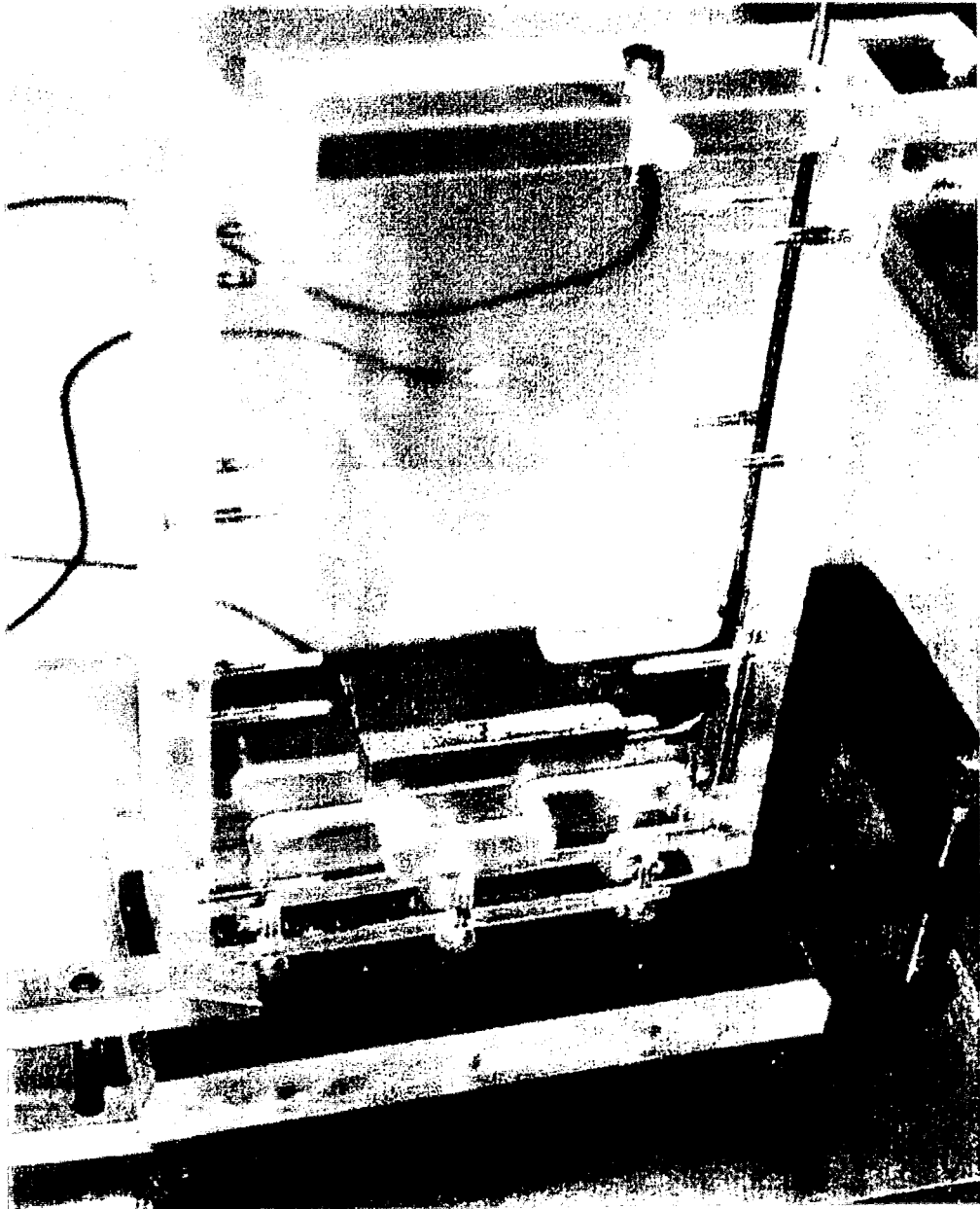
# Measuring Principle X-ray Radiography



- High-voltage X-ray tube (450kV, 12mA)
- Fluid inside a Plexiglass container  $H = 10\text{cm}$ ,  
 $D = 6\text{mm}$  (mercury, 450kV), 10mm (InGaSn, 147kV)
- Flow is depicted by a flouroscope

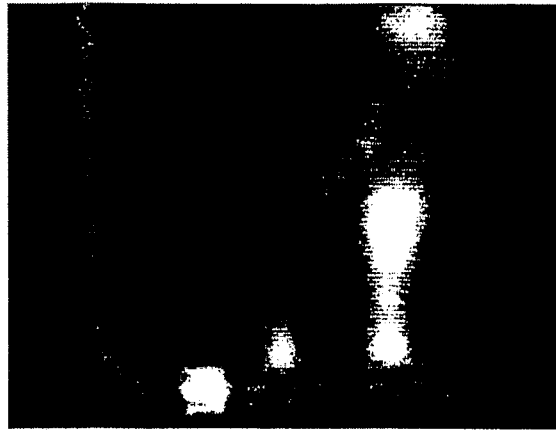


# Fluid container with gas injector (porous material)

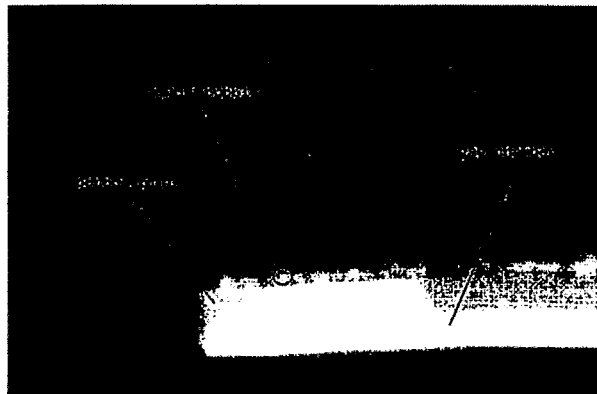


# Gas injection through a porous plate

- high surface tension → process of bubble detachment is very sensitive on the wetting conditions

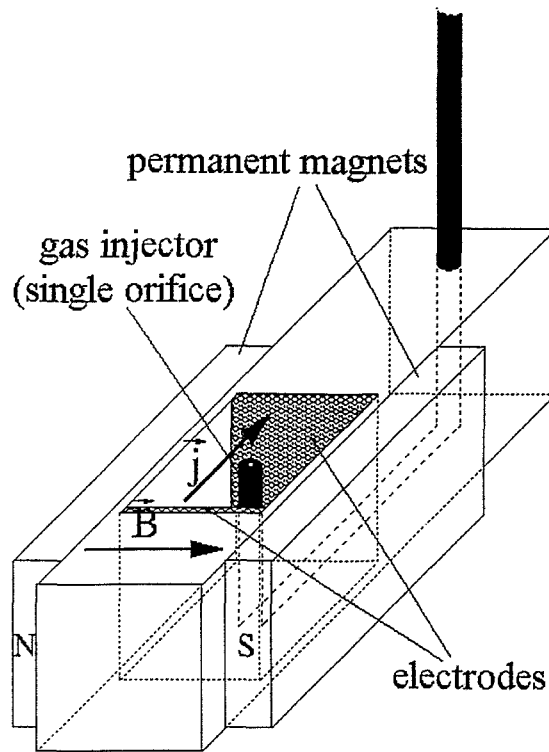


- nonwetted injector  
→ formation of gas layers around the injector  
→ detachment of large bubbles



- wetted injector  
→ detachment of small gas bubbles ( $\approx 1-2$  mm)

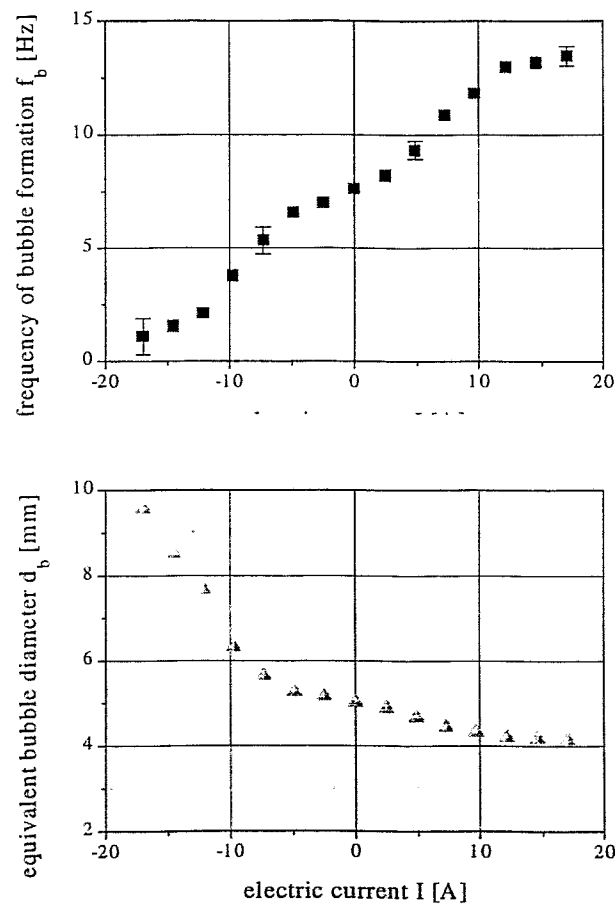
# MHD injector in a vertical channel



- Supplementary force to promote an early bubble detachment
- Idea: to control the bubble size or the volumetric gas flow rate
- Tuning parameter: amplitude of the electric current

# Influence of an electromagnetic force on the bubble formation

- MHD-injector placed inside a container filled with InGaSn
- Injection of single bubbles at constant gas flow rate
- Measurement of the bubble frequency by means of resistivity probes



# Evaluation of the methods

## Resistivity probe

- simple and robust
- clear signals

Problems: - invasive method  
- detection of small bubbles  
- stability of insulating materials

## X-ray Radiography

- non-invasive
- visualisation of the flow

Problems: - limitation of the fluid domain  
- detection of small bubbles  
- observation of rapid transient phenomena  
- large technical effort

# Void Profile Studies in Vertical Upward Co-Current Churn Mercury-Nitrogen Flows

P. Satyamurthy<sup>1</sup>, N. S. Dixit<sup>1</sup>, A. M. Quraishi<sup>1</sup> and N. Venkatramani<sup>2</sup>

<sup>1</sup> Laser and Plasma Technology Division, Bhabha Atomic Research Centre, Mumbai-400085, India

<sup>2</sup> Department of Physics, Aligarh Muslim University, Aligarh-202002, India

Liquid Metal Magnetohydrodynamic (LMMHD) power converters of gravity type have been proposed for various heat sources [1]. In these systems, two-phase flows consisting of steam and high density liquid metal (lead, lead-bismuth alloys etc.) take place in the riser and liquid metal flows in the downcomer containing MHD generator.

In general, the flow consists of multibubble, churn and slug as void fraction varies from around 0.1 to 0.8. Due to large diameter of the riser and high gas flow rates, significant length of the riser will have churn flow. The parameters of two-phase flow critically decide the overall efficiency of conversion. This requires detailed knowledge of void distribution across the cross-section.

Neal and Bankoff have studied void profiles for slug flow and developed an empirical relation for void fraction as a function of ratio of volumetric flux and Froude number of the liquid metal flow [2]. In this paper, void profiles for churn flows are studied. Empirical relations similar to that of Neal and Bankoff are developed.

Experiments have been carried out in a nitrogen-mercury simulation LMMHD loop operating at ambient temperature. The system consists of mixer, riser pipe, separator, downcomer and MHD flow meter. Nitrogen is introduced through the mixer and a two-phase mixture is established in the riser. This gives rise to density difference between the riser and downcomer and leads to the circulation of liquid metal in the loop. Nitrogen is separated and is let out to the ambient. Mercury flows through the downcomer. Gamma ray attenuation method has been employed for determining radial void profile using <sup>60</sup>Co of activity 2775 MBq at two locations in the riser [3].

For low flow rates, the flow was bubbly and the void exhibited oscillating profile as a function of radial co-ordinate [4]. However, for gas flow rates above 4.7 g/s, the flow was churn [5] and the void profile exhibited monotonic variation with maximum value at the center.

Void fraction profile ( $\alpha$ ) for churn flow has been expressed as a function of power law as follows:

$$\alpha = \left( \frac{r}{R} \right)^p \quad \text{EMBED Equation.2} \quad (1)$$

where  $r$  is the radial distance from entrance.  $R$  is the internal radius of the pipe.  $p$  is given by EMBED Equation.2 (2)

$C_1$  and  $C_2$  are constants determined based on the best fitted  $p$  value. ( $\alpha$ ,  $N_{fr}$  are the fraction of the volumetric flow rate of the gas and Froude number of the liquid metal respectively.

Best fitted  $p$  values for the experimental data varied from 2.75 to 4.75 for different flow rates. For slug flow this value is in the range of 10.9 and 12.7. The smaller values for  $p$  indicate that void fraction profiles for churn flows are less steep than those of slug flow near the walls.

The difference in the profile shape can be attributed to the difference in the flow structure between slug and churn. The slug flow consists of large bullet shaped voids extending right up to the walls of the pipe followed by bubbles distributed across the cross section. Because of the bullet shaped

void, the time averaged void fraction near the walls will be larger than that for churn, making the profiles steeper.

Both C1 and C2 have been separately varied to fit with experimental values. C1 varied in the narrow range of 3.5 to 4.5. On the other hand, C2 varied from 1.19 to 2.11 for the entire flow conditions and locations. These values are five times or more as compared to those for slug flow.

## References

- [1] Branover, H. 1993 Liquid metal MHD research and development in Israel energy convention and Magnetohydrodynamic flows, Progress in Astronautics and Aeronautic, Edited by H .Branover and Y .Unger, 18, 209-221.
- [2] Neal, L. G. and Bankoff, S. G., 1965 Local parameters in cocurrent mercury-nitrogen flow, A. I. Ch. E. Journal, 11, 624-635.
- [3] Thiyagarajan, T. K., Satyamurthy, P., Dixit, N. S., Venkatramani, N., Garg, A. and Kanvinde, N. R. 1995 Void fraction profile measurements in the two-phase mercury-nitrogen flow s using gamma-ray attenuation method, Experimental Thermal and Fluid Sciences, 10, 347-354.
- [4] Satyamurthy, P., Dixit, N. S., Thiyagarajan, T. K., Venkatramani, Quraishi, A. M. and Mushtaq, A., 1998, Two-fluid model studies for high density two-phase liquid metal vertical flows, Int. J. of Multiphase Flow, 24, 721-737.
- [5] Taitel, Y., Bornea, D. and Duckler, A. E. 1980 Modeling flow pattern transition for steady upward gas-liquid flow in vertical tubes, A. I. Ch. E. Journal, 26, 345-354.

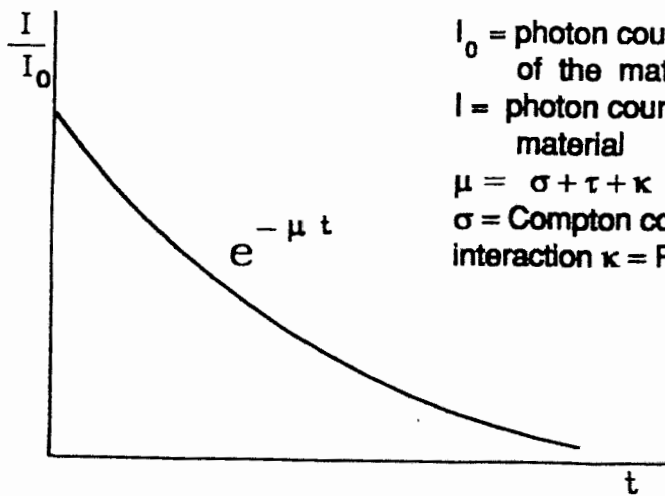
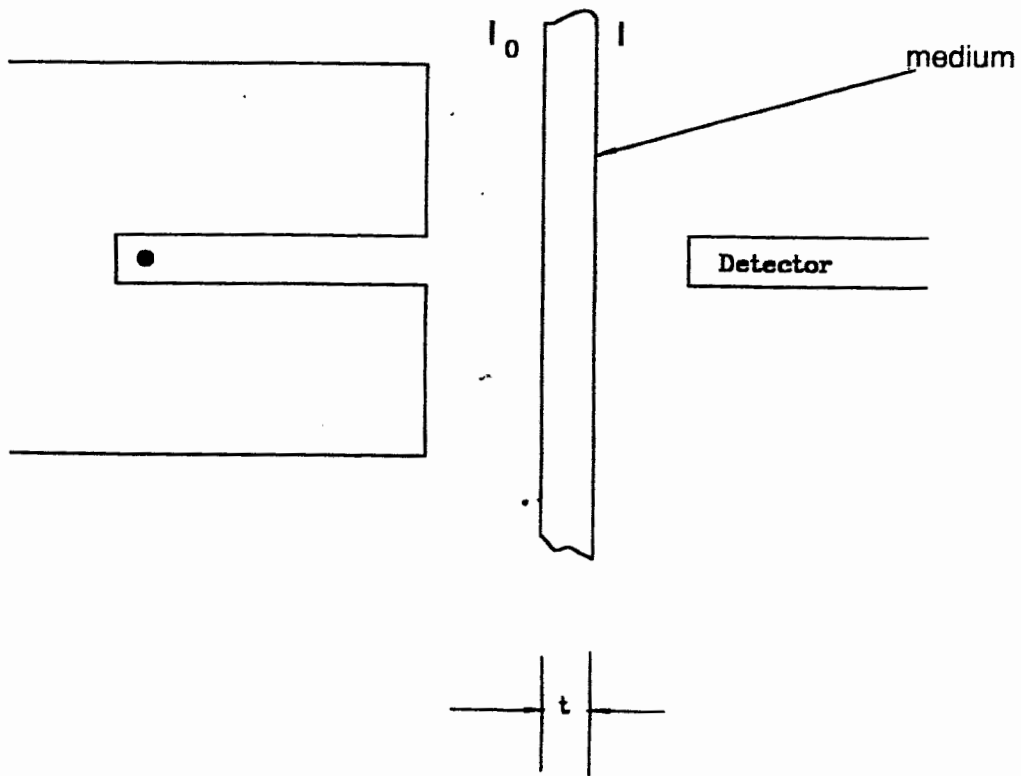
**VOID PROFILE STUDIES IN VERTICAL  
UPWARD CO-CURRENT CHURN MERCURY-  
NITROGEN FLOWS**

**P. Satyamurthy,  
Liquid Metal MHD Section,  
Laser and Plasma Technology Division,  
Bhabha Atomic Research Centre,  
Mumbai-400085, India**

**International Workshop on  
'Measurement Techniques for Liquid Metal Flows'  
October 11-13, 1999, Dresden, Germany**



# GEOMETRY



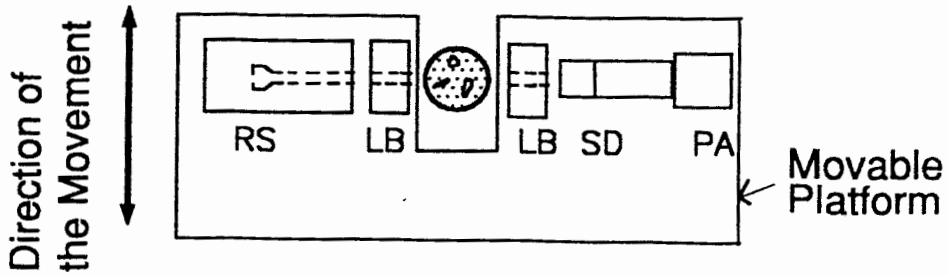
$I_0$  = photon counts per unit time at the entrance of the material

$I$  = photon counts per unit time at exit of the material

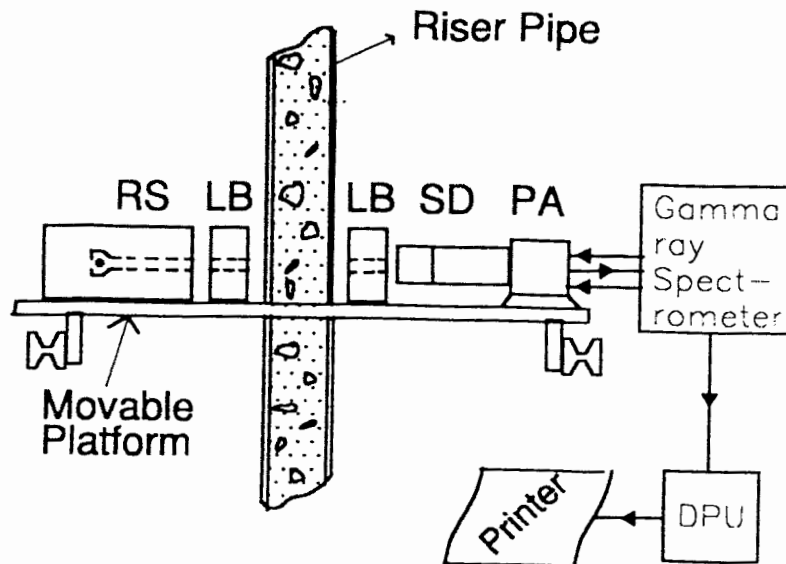
$\mu = \sigma + \tau + \kappa$  where

$\sigma$  = Compton collision,  $\tau$  = Photo electric interaction  $\kappa$  = Pair production

## Top view

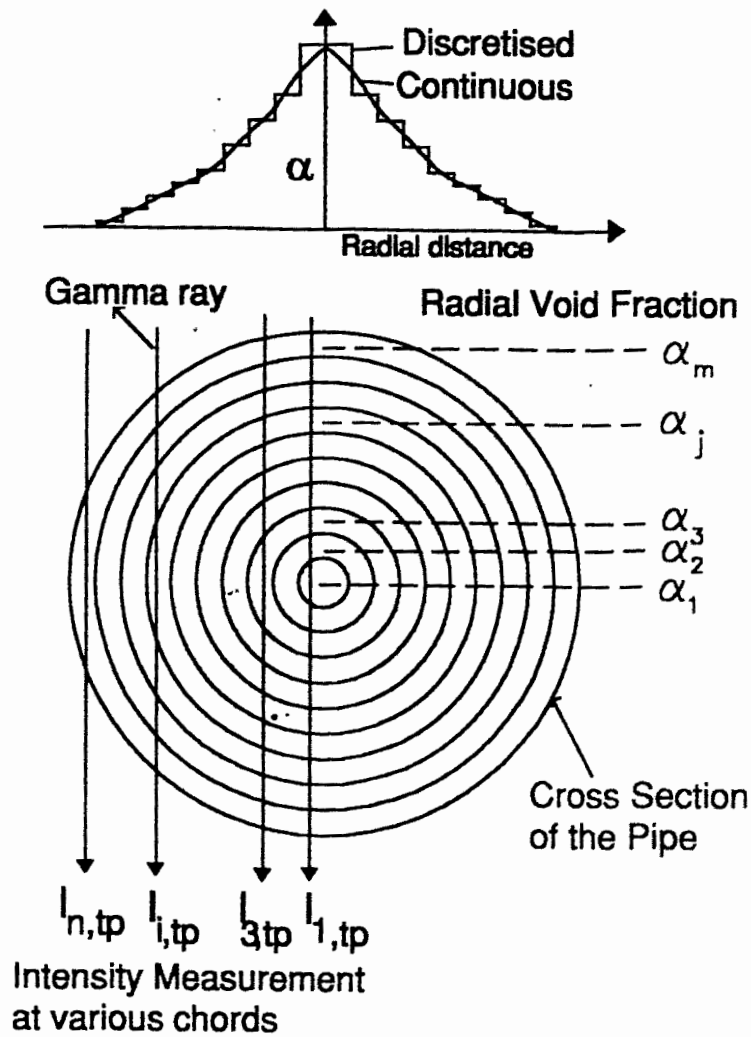


## Front View



RS - Radioactive Source    LB - Lead Block  
SD - Scintillation Detector    PA - Pre-Amplifier

# Void Fraction Measurement System



Scheme for the measurement of  $\alpha$ -profile

$$\bar{\beta}_i = \frac{\ln\left(\frac{l_{i,tp}}{l_{i,l}}\right)}{\ln\left(\frac{l_{i,g}}{l_{i,l}}\right)} = \sum_{j=1}^m \frac{d_{i,j}}{c_i} \alpha_j$$

$d_{i,j}$  is the length of the  $j^{\text{th}}$  zone intercepted by  $i^{\text{th}}$  beam and  $c_i$  is the total length of the  $i^{\text{th}}$  beam in the flow

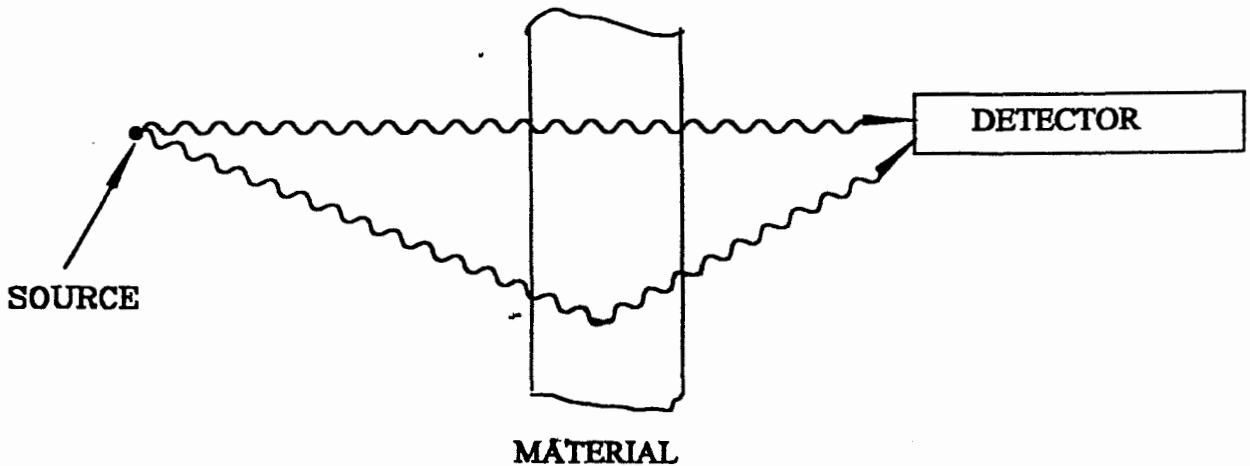
## **Phenomena Associated With Void Fraction Measurements by Radiation Attenuation Method**

- 1) System Configuration**
- 2) Appropriate Radio Active Source Selection**
  - Photon Energy
  - Intensity of the Source
  - Beam diameter
- 3) Number of counts for each measurement ( Poisson's Corruption )**
- 4) Background Counts**
- 5) Geometry**
- 6) Dynamic Void Fraction Fluctuations**
- 7) Cylindrical Symmetry Assumption ( Fully developed flows in the pipes )**
- 9) Detector Efficiency, Dead-time, Summation Effects etc..**

## **Co<sup>60</sup> radio-active source**

- 1) High gamma ray energy ( 1.332 MeV ) suitable for 80 mm mercury path length**
- 2) Commercially available**
- 3) Relatively smaller lead shielding for 60 – 100 mCi source**
- 4) Half-life is 5.26 years**

# BUILDUP



HERE, THE DETECTOR WILL RESPOND TO THE GAMMA RAYS DIRECTLY FROM THE SOURCE, TO THE GAMMA RAYS AFTER HAVING SCATTERED IN THE ABSORBER OR TO OTHER TYPE OF SECONDARY PHOTONS SO THE MEASUREMENT DETECTOR SIGNAL WILL BE LARGER THAN THAT RECORDED UNDER EQUIVALENT GOOD GEOMETRY CONDITIONS. THIS STATE CAN BE CALLED AS BROAD BEAM OR BAD GEOMETRY MEASUREMENT. IN THIS CASE WE WILL HAVE :

$$\frac{I}{I_0} = B(t, E_\gamma) e^{-\mu t}$$

WHERE, THE FACTOR  $B(t, E_\gamma)$  IS CALLED THE BUILDUP FACTOR.

## Dynamic Fluctuation Effect

Time and Path Averaged Void Fraction is given by

$$\bar{\beta}_{\text{measured}} = \frac{\ln\left(\frac{\bar{I}_{\text{two-phase}}}{\bar{I}_{\text{liquid-only}}}\right)}{\ln\left(\frac{\bar{I}_{\text{gas-only}}}{\bar{I}_{\text{liquid-only}}}\right)}$$

$\bar{I}$  is the number of attenuated photon counts per unit time

$$\bar{\beta}_{\text{actual}} = \frac{\int \beta(t) dt}{\int dt}$$

However since

$$\bar{I}_{\text{two-phase}} = \text{constant} \left[ \frac{\int e^{\beta(t)} dt}{\int dt} \right]$$

We always have

$$\bar{\beta}_{\text{actual}} \leq \bar{\beta}_{\text{measured}}$$

We require detailed fluctuation pattern for determining actual void fraction from measured one

# Computer Tomography

What we measure by gamma ray attenuation is time and line averaged void fraction  $\beta$ .

In order to obtain void fraction distribution ( $\alpha$ ), we require tomographic algorithms.

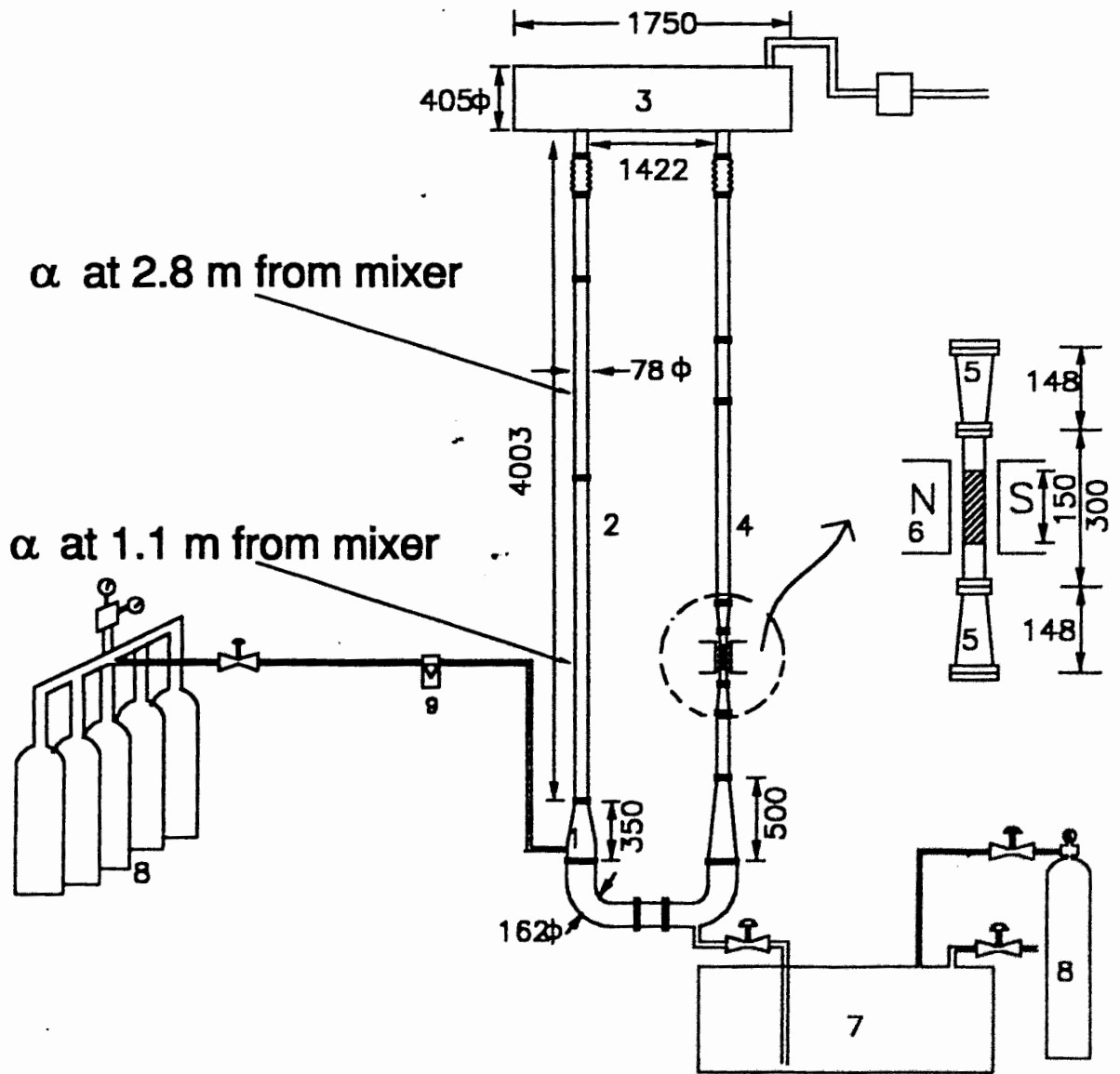
Non-Cylindrical Symmetric Distribution ( $\alpha(r, \theta)$ ), we have

- ART (Algebraic Reconstruction Techniques)
- MART (Multiplicative Algebraic Reconstruction Techniques)

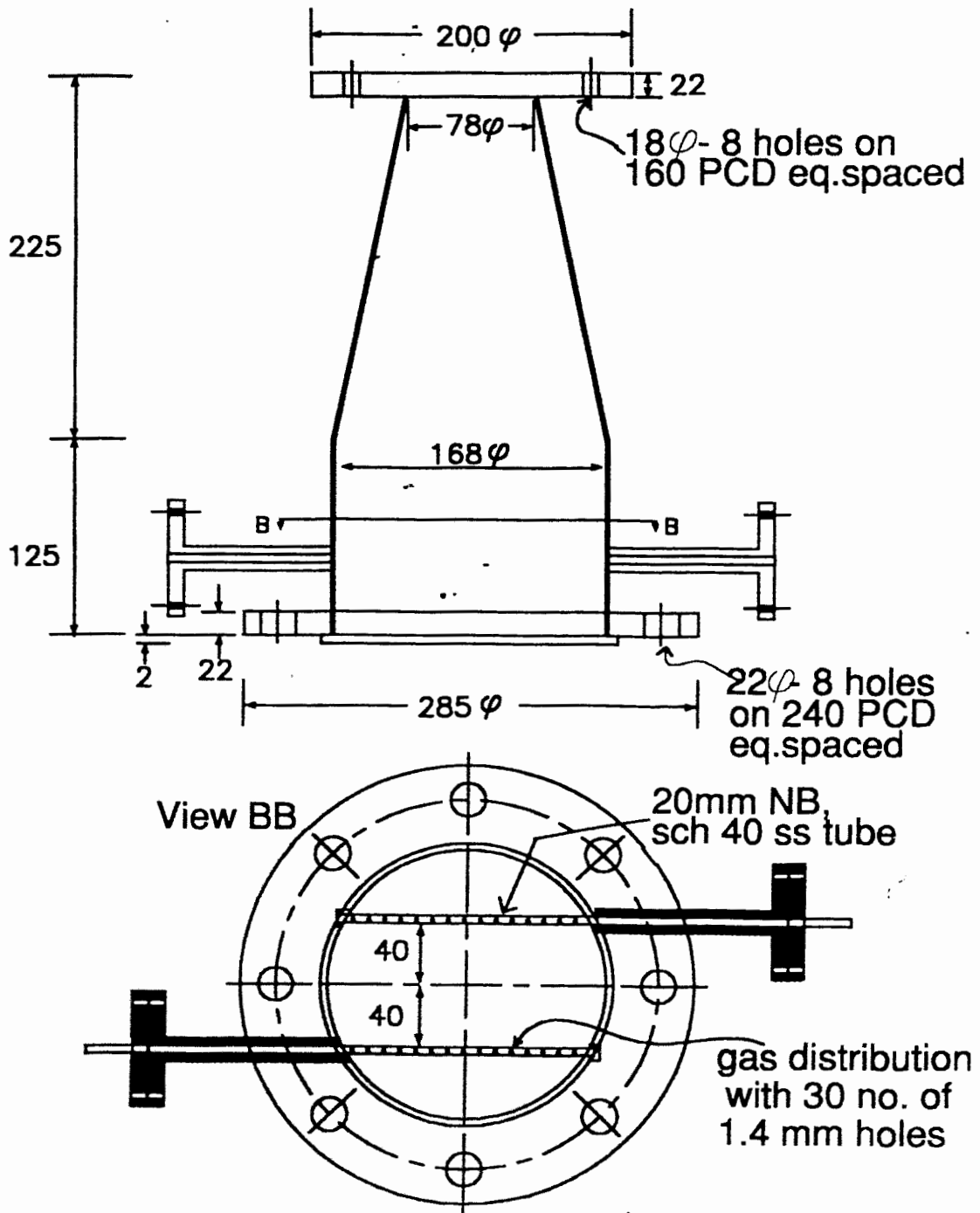
Cylindrical Symmetric Distribution ( $\alpha(r)$ )

- Chord Segment Inversion Techniques
- Least Square Solution Techniques
- Radial Polynomial Techniques
- Bessel Function Algorithms

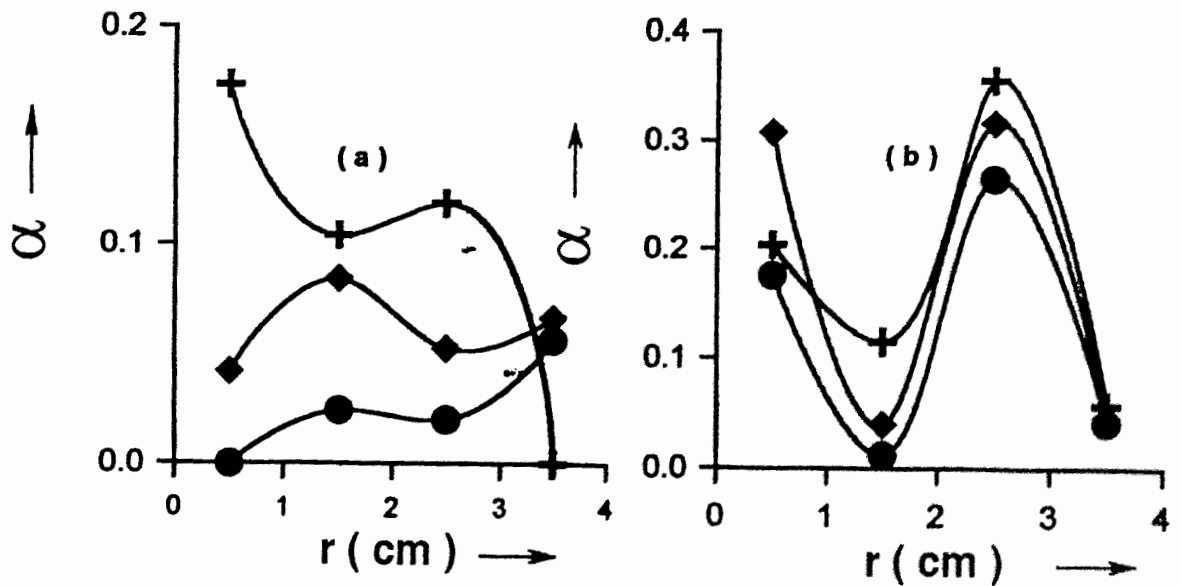




**Schematic of the nitrogen-mercury LMMHD Facility**

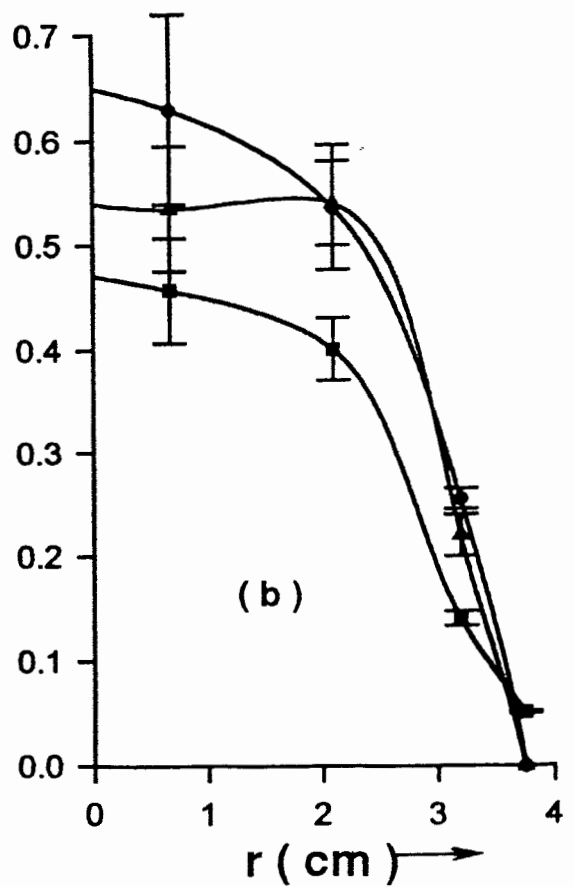
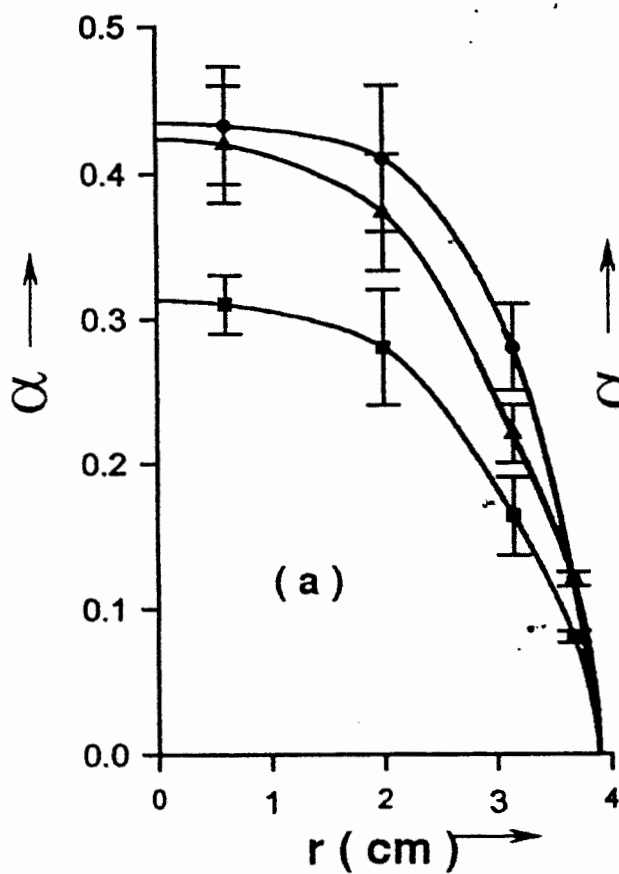


**Details of the Mixer**



Sym.	Nitrogen flow rate (g/s)	Mercury flow Rate (kg/s)
●	0.6	26.4
◆	1.3	28.9
+	2.5	35.2

Measured void fraction profiles for low gas flow rates at two location in the riser  
 (a)  $z = 1.1$  m (b)  $z = 2.8$  m



Sym.	Nitrogen flow rate (g/s)	Mercury flow rate (kg/s)
■	4.7	43.0
▲	9.0	54.8
●	11.0	58.6

Measured void fraction profiles for higher flow rates at two locations in the riser ( a )  $z = 1.1\text{m}$  (  $\xi = 14.0$  ) ( b )  $z = 2.8\text{m}$  (  $\xi = 35.9$  )

Void-profile is expressed as;

$$\frac{\alpha(r) - \alpha(R)}{\alpha(0) - \alpha(R)} = \left(1 - \frac{r}{R}\right)^{\frac{1}{P_{NB}}}$$

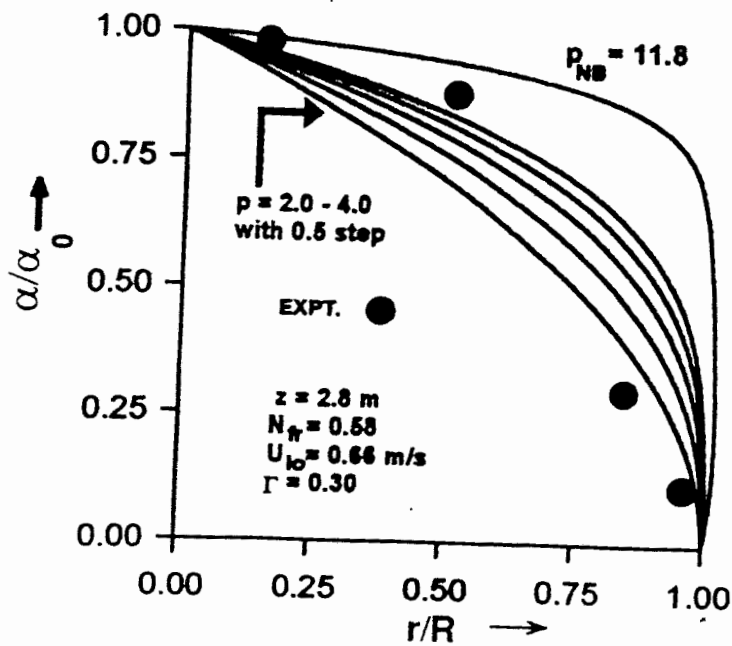
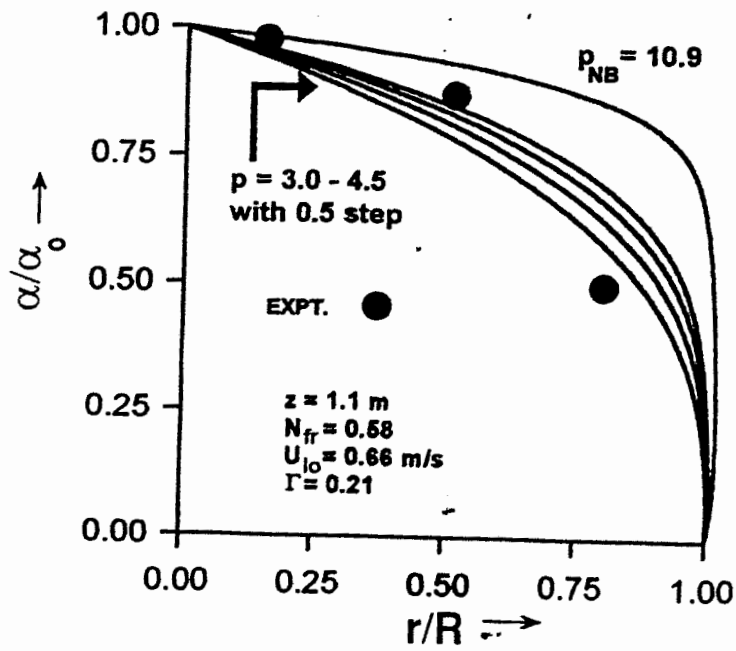
For Slug flows Neal and Bankoff have obtained the following relation for  $P_{NB}$ :

$$P_{NB} = C_1 \left( \frac{\Gamma}{N_{fr}^{0.5}} \right)^{C_2} \quad C_1 = 15 \text{ and } C_2 = 0.25$$

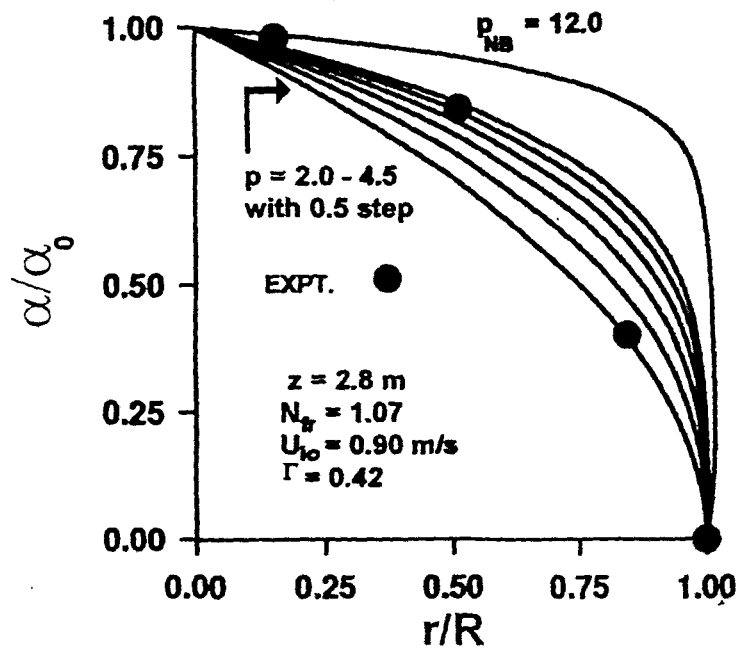
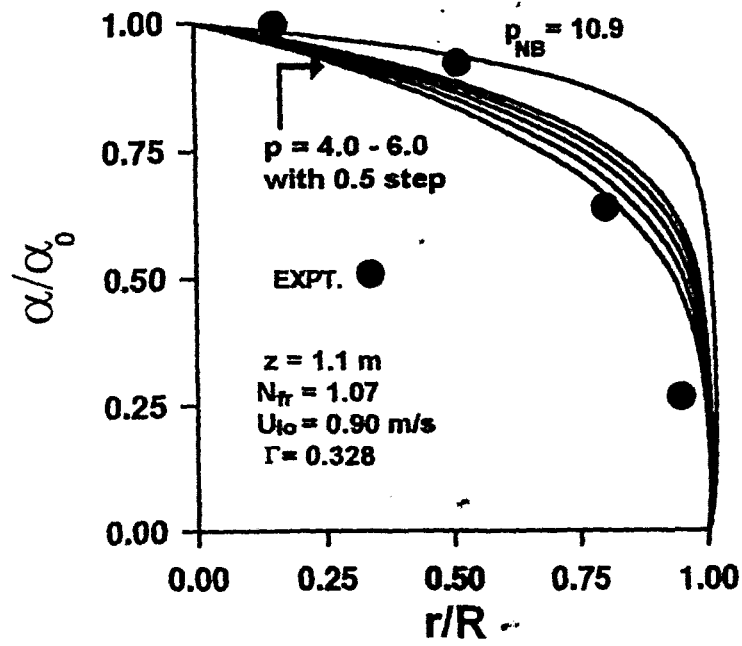
$$N_{fr} = \left( \frac{u_{lo}^2}{2gR} \right)$$

$$\Gamma = \frac{Q_g}{Q_l + Q_g}$$

$r$  is radial co-ordinate and  $R$  is the radius of the riser pipe,  $u_{lo}$  is the superficial liquid velocity,  $g$  is the acceleration due to gravity and  $\Gamma$  is the gas flow volumetric concentration.



Comparison of non-dimensionalized experimental void fraction profile with Neal and Bankoff relation and profiles based on different  $p$  values. ( $\dot{m}_g = 4.7 \text{ g/s}$ )



Comparison of non-dimensionalized experimental void fraction profile with Neal and Bankoff and profiles based on different  $p$  values. ( $m_g = 11.0 \text{ g/s}$ )

**Table - 1**

**' p ' values which match with experimental data**

<b>Nitrogen flow rate ( kg/s )</b>	<b>Mercury flow rate ( g/s )</b>	<b>Distance from the mixer (m) And ( <math>\xi</math> )</b>	<b>P<sub>NB</sub></b>	<b>P<sub>ex</sub> ( value which f with exp. data</b>
4.73	43.0	1.1 ( 14.0 )	10.9	3.25
4.73	43.0	2.8 ( 35.9 )	11.8	2.75
9.0	54.8	1.1 ( 14.0 )	11.5	3.25
9.0	54.8	2.8 ( 35.9 )	12.7	3.75
11.07	58.6	1.1 ( 14.0 )	11.2	4.75
11.07	58.6	2.8 ( 35.9 )	12.0	2.75

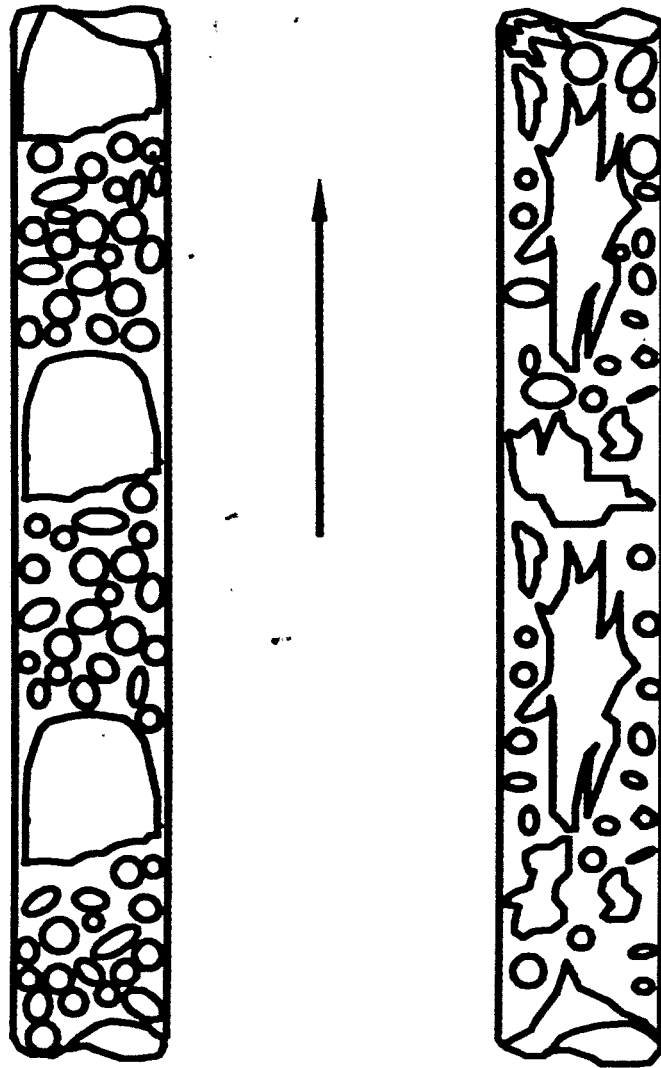


**Table – 2****Required  $C_1$  to fit experimental ' p ' value (for  $C_2 = 0.25$ )**

<b>Nitrogen flow rate ( g/s )</b>	$\xi$	$p_{ex}$	$p_{NB}$	$\frac{\Gamma}{N_{fr}^{0.5}}$	$C_{1ex}$
4.73	14.0	3.25	10.9	0.277	4.47
4.73	35.9	2.75	11.8	0.386	3.49
9.0	14.0	3.25	11.5	0.342	4.24
9.0	35.9	3.75	12.7	0.519	4.43
11.07	14.0	4.75	11.2	0.315	6.36
11.07	35.9	2.75	12.0	0.417	3.44

**Table - 3****Required  $C_2$  to fit experimental ' p ' value (for  $C_1 = 15$ )**

<b>Nitrogen flow rate ( g/s )</b>	$\xi$	$p_{ex}$	$p_{NB}$	$\frac{\Gamma}{N_{fr}^{0.5}}$	$C_{2ex}$
4.73	14.0	3.25	10.9	0.277	1.19
4.73	35.9	2.75	11.8	0.386	1.78
9.0	14.0	3.25	11.5	0.342	1.42
9.0	35.9	3.75	12.7	0.519	2.11
11.07	14.0	4.75	11.2	0.315	1.00
11.07	35.9	2.75	12.0	0.417	1.94



Slug Flow

Churn Flow

**Structure of slug and  
churn-turbulent flow.**

## **Conclusions**

**Empirical relation developed by Neal and Bankoff for slug flows has been extended for co-current, upward churn flows. The void profile was less steep for churn flow near the walls. Experimental values were fitted with Neal and Bankoff equation by modifying the coefficients. These modified coefficients substantially deviated from that of slug flow indicating significant difference in void fraction distribution along the radial direction in circular pipes.**

# ULTRASONIC MEASUREMENTS OF THE MOTION OF GAS BUBBLES RISING IN A LIQUID METAL

*B. Hofmann<sup>1</sup>, S. Eckert<sup>2</sup>, G. Gerbeth<sup>2</sup> and E. Kaiser<sup>1</sup>*

<sup>1</sup> *Technische Universität Dresden, Institute of Energiemaschinen und Maschinenlabor,  
D-01062 Dresden, Germany*

<sup>2</sup> *Forschungszentrum Rossendorf e.V., Institute of Safety Research, D-01314 Dresden, Germany*

The ultrasonic detection of argon bubbles rising in a liquid metal caused by buoyancy forces is the topic of this paper. The metal is an eutectic alloy of In, Ga and Sn having a melting point of about 283,7°K (+10,5°C). Therefore, it is liquid at normal laboratory temperatures. Bubbles can be generated by different sparking facilities on the bottom of circular-cylindrical vessels consisting of stainless steel, mineral or plastical glass.

The aim of the investigations is the determination of the bubble detaching frequencies and the estimation of the void and bubble size distributions over the cross section of the vessels at different levels above the vessel bottom as functions of the typ of the sparking facility.

For the experimental determination of these two-phase flow parameters the ultrasonic pulse-echo method well known from the non-destructive material testing technology is used. A piezoceramic narrow band straight-beam probe having an ultrasonic resonance frequency of 15 MHz transmits short bursts with regular intervalls of about 2 kHz and receives the echoes. The probe is clamped outside of the vessel by means of a special assembling device allowing a comfortable installation of the probe at different positions on the vessel wall. The ultrasonic waves penetrate the wall and the liquid metal as a slim sonic cone perpendicularely to the inner wall of the vessel and will be reflected by the phase boundary between liquid metal and a gas bubble moving inside the sound cone. The detectibility of the bubbles is limited by their minimal size, by the sound attenuation in the liquid metal, by the unavoidable signal noise and other effects.

The ultrasonic probe is triggered by an electronic device generating the transmitting pulses as well as receiving and amplifying the sonic echo waves reflected by the bubbles. The amplitude and the time of flight of the sonic echoes will be transfered into two analogue electric voltage signals. These signals can be pre-storaged and recorded as functions of time by a digital storage oscilloscope (DSO).

For further data processing using the software tool FAMOS and final storing the measured signal data are transfered to a PC using the software code TRANSITION. By means of different FAMOS functions like *HISTOGRAM*, *FFT* and others the distribution of the echo amplitudes of bubbles, the detaching frequencies at the bubble generating process and the bubble distances from the vessel wall can be determined. From this results, to the relative bubble sizes, bubble shapes, bubble velocities, local bubble positions and void distributions in the vessel can be concluded.

B. Hofmann <sup>1)</sup>, S. Eckert <sup>2)</sup>, G. Gerbeth <sup>2)</sup> and E. Kaiser <sup>1)</sup>

## **ULTRASONIC MEASUREMENTS OF THE MOTION OF GAS BUBBLES RISING IN A LIQUID METAL**

1. Introduction
2. The principle of the ultrasonic pulse-echo technique for two-phase flow measurements
3. Experimental set-up
4. The liquid metal
5. Small theory
6. Results
  - Analysis of the sonic echoes of single bubbles
  - Analysis of bubble streams
7. Conclusions

---

<sup>1)</sup> Technische Universität Dresden, Institute of Energiemaschinen und Maschinenlabor, Chair of Measurement and Automation Technology, D-01062 Dresden, Germany

<sup>2)</sup> Forschungszentrum Rossendorf e.V., Institute of Safety Research, D-01314 Dresden, Germany

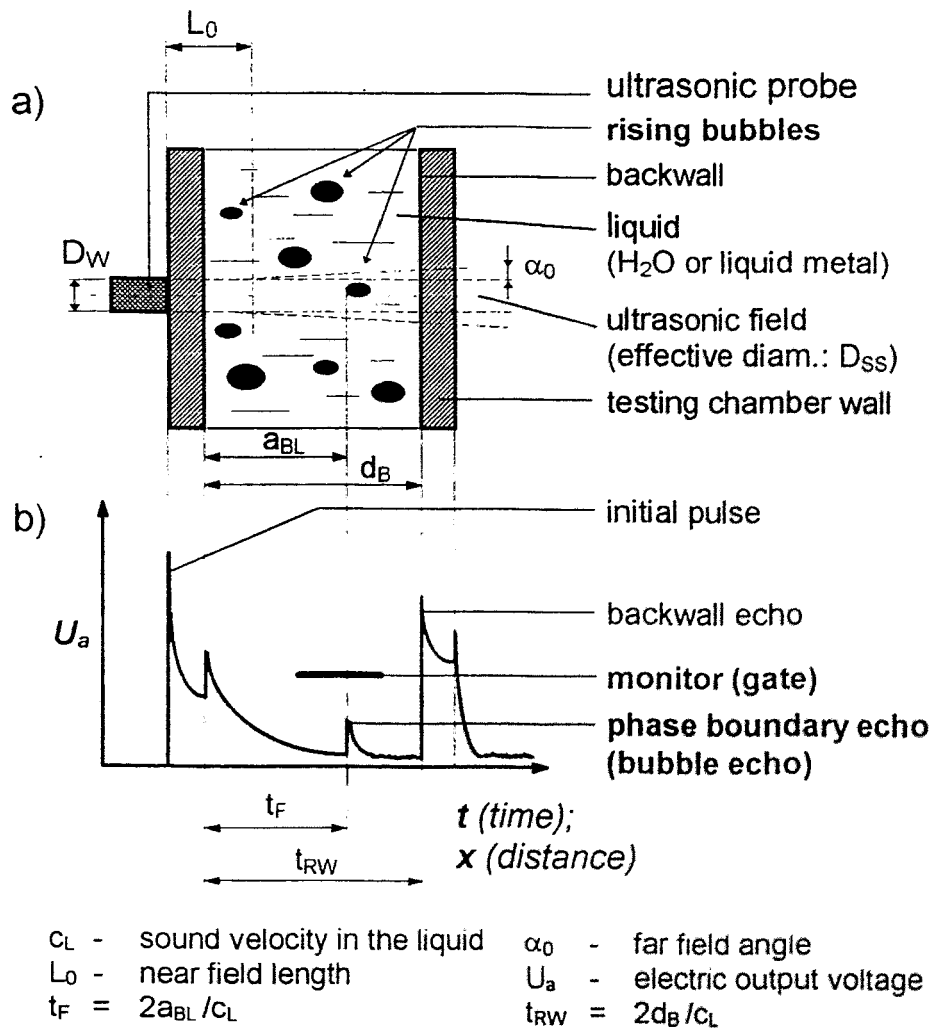
B. Hofmann , S. Eckert , G. Gerbeth and E. Kaiser

**ULTRASONIC MEASUREMENTS OF THE MOTION OF GAS  
BUBBLES RISING IN A LIQUID METAL**

**- INTRODUCTION -**

The ultrasonic detection of argon bubbles rising in a liquid metal caused by buoyancy forces is the topic of this paper. The metal is an eutectic alloy of indium (In), gallium (Ga) and tin (Sn) which is liquid at normal laboratory temperatures. Bubbles are generated by different sparking facilities on the bottom of circular-cylindrical chambers consisting of stainless steel, ceramic or plastical glass.

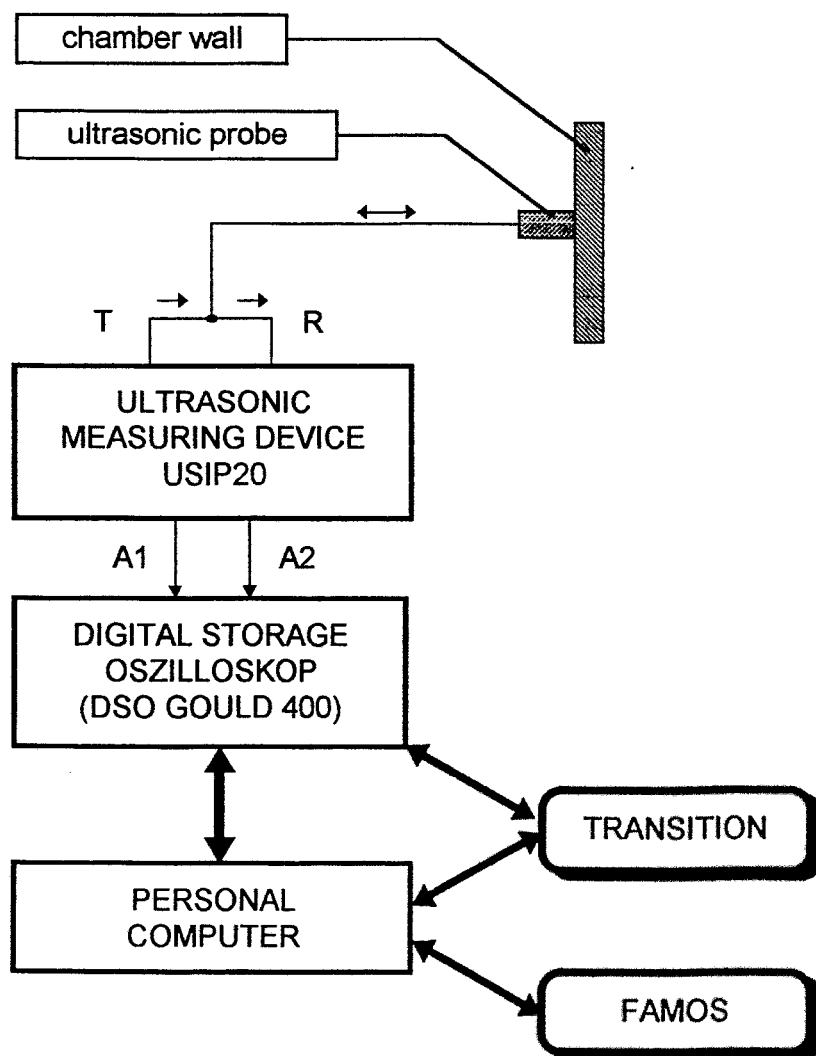
The aim of the investigations is the determination of the bubble detaching frequencies and the estimation of the void and bubble size distributions over the cross section of the chambers at different levels above the chambers bottom as functions of the type of the sparking facility.



The principle of the ultrasonic pulse-echo technique for two-phase flow measurements (a - schematic diagram, b - echograph)







TRANSITION, FAMOS: Software tools

**Experimental Setup:**  
 Block diagram of the measuring and data processing equipment

PROPERTIES	VALUES	REMARKS
Compounds (eutectical):	In 20,5% Ga 67,0% Sn 12,5 %	mass parts
Melting temperature / °C	+10,5±0,1	
Boiling temperature / °C	> +2000	
Density / kg m <sup>-3</sup>	≈ 6363	ϑ=20°C
Sound velocity / m s <sup>-1</sup>	≈ 2747	ϑ=20°C

Reference liquid (water<sup>\*)</sup>):

PROPERTIES	VALUES	REMARKS
Density / kg m <sup>-3</sup>	≈ 1000	ϑ=20°C
Sound velocity / m s <sup>-1</sup>	≈ 1482	ϑ=20°C

\* delivered by the common supply conduit system, free of gas and particles nearly, laboratory temperature (≈ +23°C)

**The Liquid Metal:**  
**Properties of the Alloy In Ga Sn used with the**  
**experiments**

Acoustic transmission factor (pulse-echo method):

$$T_{GES} = T_T \cdot T_B = 4 \cdot Z_L \cdot Z_S / (Z_L + Z_S)^2$$

where

Z - Acoustic impedance of a material in general:  
 $Z = \rho \cdot c$  ( $\rho$  - density,  $c$  - sound velocity)

$Z_L$  - Acoustic impedance of the liquid to be tested

$Z_S$  - Acoustic impedance of the wall material (solid)

$$T_T = 2 \cdot Z_L / (Z_L + Z_S)$$

$$T_B = 2 \cdot Z_S / (Z_L + Z_S)$$

$T_T$  - Transmission factor „THERE“  $T_B$  - Transmission factor „BACK“

COMBINATION MATERIAL-LIQUID	H <sub>2</sub> O-V2A (reference)	H <sub>2</sub> O-PLG	FLM-V2A	FLM-PLG	FLM-GLA
$Z_L / 10^6 \text{ Ns m}^{-3}$	1,5		17,5		
$Z_S / 10^6 \text{ Ns m}^{-3}$	45,0	3,2	45,0	3,2	11,5
$T_{GES} / \%$	12,5	87	81	52	96
<b>EVALUATION:</b>	very bad	fine	fine	bad	excellent

where means:

FLM - liquid metal (In Ga Sn)

GLA - glass

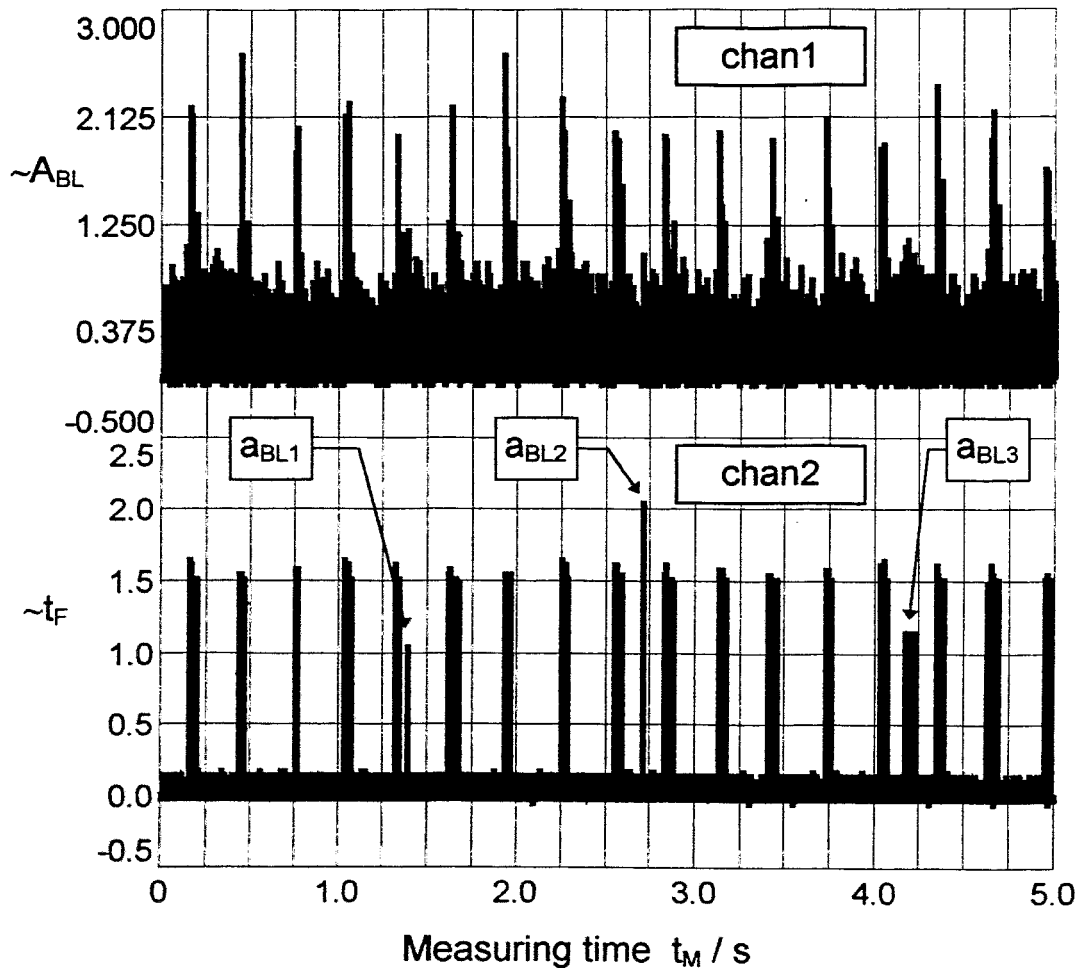
H<sub>2</sub>O - water

PLG - plastical glass

V2A - stainless steel

Acoustic properties of different combinations of chamber wall materials and liquids

$U_a/V$



Vertical coordinates  $U_a/V$  are proportional:

**chan 1:** to the *amplitude*  $A_{BL}$ ,

**chan 2:** to *time of flight*  $t_F$  of the bubble echoes, where:

- $t_F$  is a measure for the *distance*  $a_{BL}$  between a bubble and the vessel wall.
- $a_{BL1}$ ,  $a_{BL2}$ ,  $a_{BL3}$  : small bubbles *in front of* ( $a_{BL1}$ ,  $a_{BL3}$ ) and *behind* ( $a_{BL2}$ ) the nozzle.

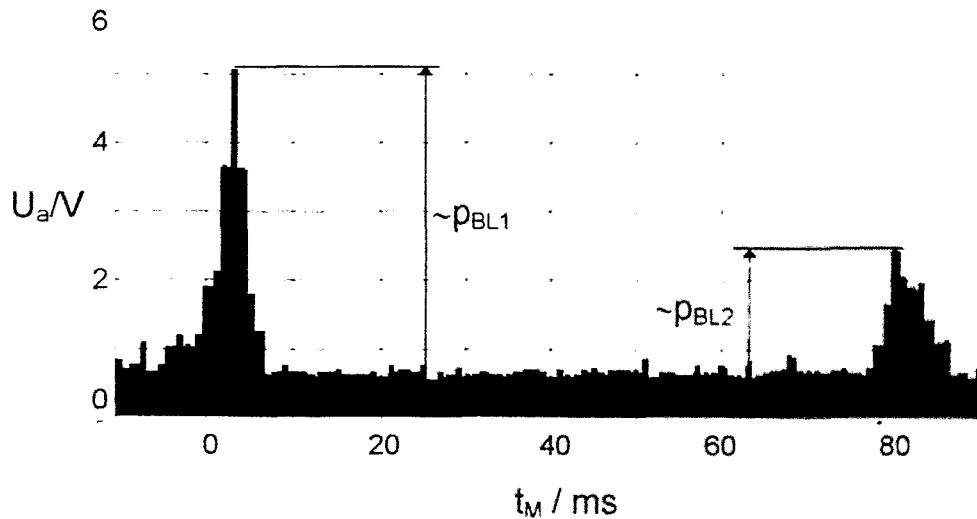
The principle of the evaluation of ultrasonic echo signals of a sequence of argon bubbles in liquid InGaSn

1. The **amplitude** of the ultrasonic **echo signal** (sound pressure) is proportional to the **bubble diameter** in principle:

$$p_{BL} \sim d_{BL}$$

2. By means of a special ultrasonic measurement device the amplitude of the ultrasonic echo pressure can be transmitted into an **electric voltage** in the range of (0 ...5)VDC e.g. :

$$U_a \sim p_{BL} \sim d_{BL}$$



Determination of the relative bubble size  
( $t_M$ : measuring time)

### 1. Bubble velocity:

Influence is negligible.

The reason is the large quotient of sound and bubble velocities in the liquid ( $c_L/c_{BL} > 700$ ).

### 2. Bubble shape:

With increasing size and velocity the bubbles become more and more oblate (see R. CLIFT et al, e.g.). That means, bending radius  $r_K$  at the reflecting point and, consequently, sonic echo amplitude of the bubble changes with the bubble shape. Models to describe this effect are not known so far.

### 3. Bubble distance:

With increasing distance  $a_{BL}$  between probe and bubble its size seems to become smaller, because the sonic echo amplitude decreases by sound attenuation proportionally to raising distance (influence reducable by „distance-amplitude-correction“ - DAC).

### 4. Bubble position:

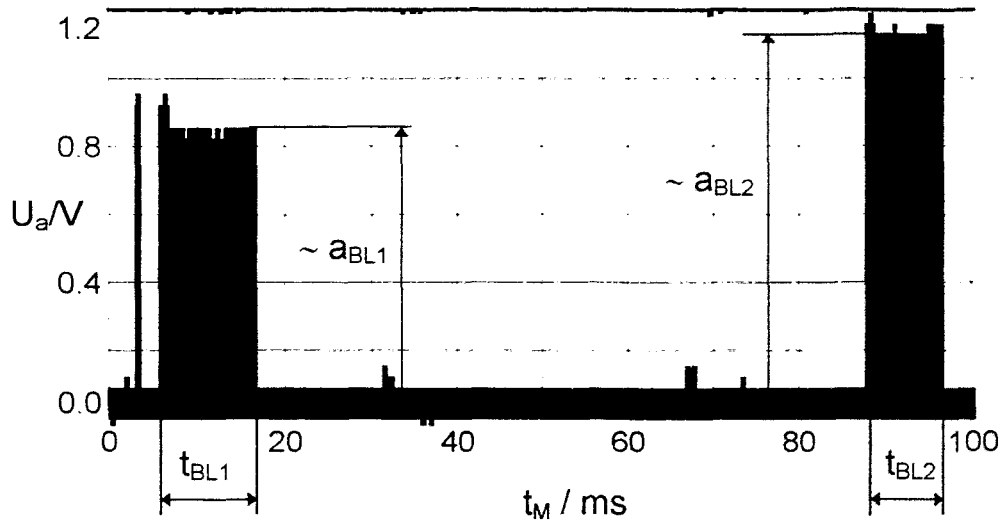
In case a bubble passes the sound beam laterally, the amplitude of sonic echo reaching the probe again decreases. Therefore, the bubble size seems to be reduced.

### 5. Bubble covering:

At a homogeneous bubble distribution, the medium probability  $w_M$  of the covering of two bubble columns increases with bubble diameter  $d_{BL}$  and frequency  $f_{BL}$  (through a nozzle) and decreases with bubble velocity  $c_{BL}$ :  $w_M \approx f_{BL} * d_{BL} / c_{BL}$

(Example: For  $d_{BL}=4\text{mm}$ ,  $c_{BL}=0.3\text{m/s}$  and  $f_{BL}=10\text{Hz}$  follows  $w_M \approx 13\%$ .)

Geometric influences disturbing the ultrasonic determination  
of the bubble size



a) **Distance:**  $\frac{a_{BL}}{\text{mm}} \approx 40 \cdot \frac{U_a}{V} - 1.0$  (error  $\approx \pm 0,5\text{mm}$ )

b) **Velocity:**  $\frac{c_{BL}}{\text{m} \cdot \text{s}^{-1}} \approx \frac{D_{SS}}{\text{mm}} / t_{BL} / \text{ms}$  (error  $\approx \pm 0,15 \text{ms}^{-1}$ )

From these equations follows:

$a_{BL1} \approx 33,0 \text{ mm}$	$a_{BL2} \approx 43,8 \text{ mm}$
$t_{BL1} \approx 10,8 \text{ ms}$	$t_{BL2} \approx 8,8 \text{ ms}$
$c_{BL1} \approx 0,37 \text{ ms}^{-1}$	$c_{BL2} \approx 0,46 \text{ ms}^{-1}$

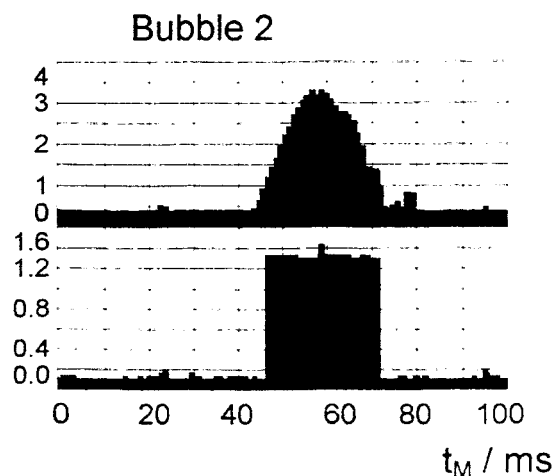
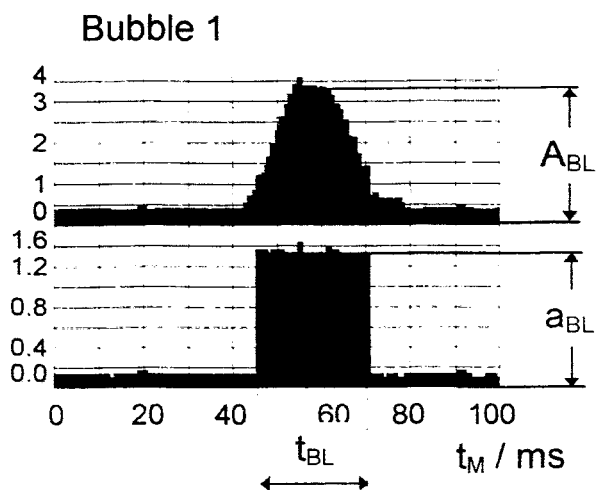
Evaluation:

- Left bubble is generated by the *front* nozzle. *right* by the *medium* one
- The medium velocity of both bubble is about  $0.42 \text{ms}^{-1}$

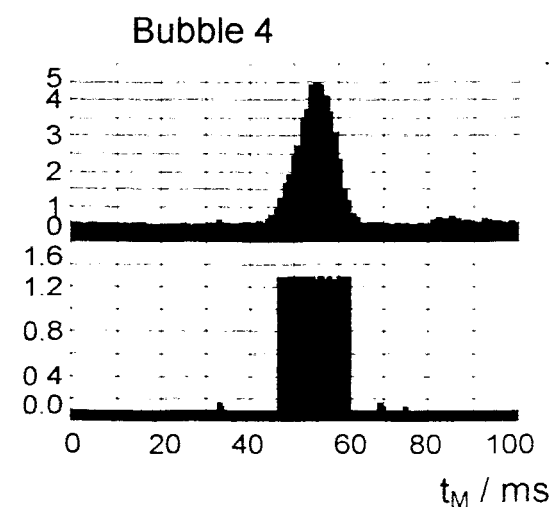
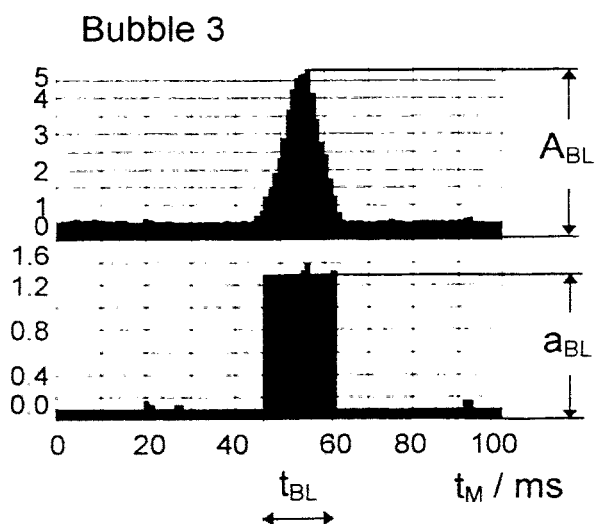
### Estimation of the bubble distance $a_{BL}$ from the inner vessel wall as well as the bubble velocity $c_{BL}$

(Combination vessel material - liquid: V2A - H2O; measuring time  $t_M$ ; effective diameter of the sonic cone (on bubble position)  $D_{SS} \approx 4\text{mm}$  height of the ultrasonic probe above the bubble generator (type G2, 3 nozzles)  $h_1 \approx 50\text{mm}$ )

a)  $h_1 \approx 10\text{mm}$



b)  $h_1 \approx 50\text{mm}$



### Ultrasonic echo signals of single bubbles of a bubble stream

(Combination vessel material - liquid: PLG - FLM; measuring time:  $t_M$ ;  
 $h_1$ : height of the ultrasonic probe above the bubble generator type G6 / sintered  
ceramic plate, pore width  $2\mu\text{m}$ ; argon flow:  $Q \approx 3\text{l/h}$ )



## Ultrasonic echo signals of single bubbles of a bubble stream

- Results of the measurements in liquid metal InGaSn -

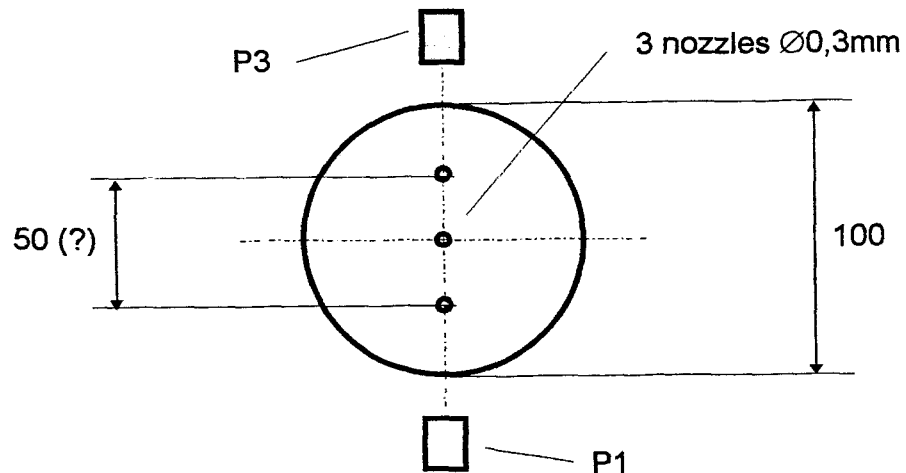
In case of increasing  $h_1$  results in accordance with theory:

- bubble *diameter* (echo amplitude  $A_{BL}$ ) *increases*
- bubble *shape* changes from *spherical* to *ellipsoidal* (amplitude echoes becomes more narrow)
- bubble stream *position* (distance  $a_{BL}$ ) *does not change* nearly
- bubble *velocity*  $c_{BL}$  *increases* (echo width  $t_{BL}$  *decreases*)

Parameters of these measurements:

- Combination vessel material - liquid: PLG - FLM
- argon flow:  $Q \approx 3l/h$
- $h_1$ : height of the ultrasonic probe above the bubble generator type G6 / sintered ceramic plate, pore width  $2\mu m$

a) Bubble generator G2 and measurement positions P of ultrasonic probe



b) Comparison of the results of measurement positions P1 and P3

PARAMETER	P1 (0°)	P3 (180°)
bubble main frequency $f_{BL}$ / Hz	6,2	3,6
harmonics <sup>1)</sup> / Hz	-	7,0 and 10,6
bubble size range (relative)	0,9 - 3,0	0,8 - 4,2
main size ranges (relative)	2,2 - 2,5	0,8 - 1,2 and 3,2 - 4,2
bubble distance <sup>2)</sup> range $a_{BL}$ / mm	30 -34	17,5 - 22,5
main distance <sup>2)</sup> $a_{BL}$ / mm	30	20

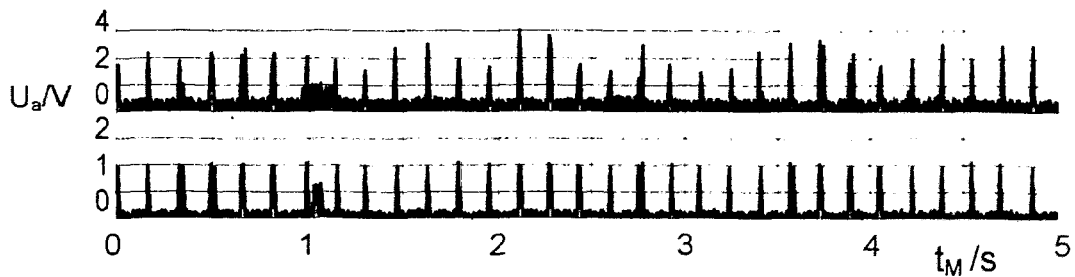
<sup>1)</sup> in the range (1 -11)Hz;

<sup>2)</sup> measured from the inner vessel wall

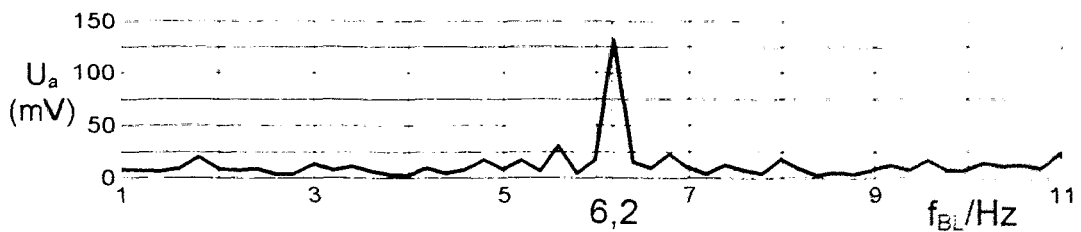
**Comparison of the experimental results of ultrasonic watching of two argon bubble streams generated by the bubble generator G2 rising in the liquid metal InGaSn**

(Vessel material: plastical glass; probe height  $h_1 \approx 10$ mm above the bubble generator; measuring time:  $t_M=5$ s; argon gas flow:  $Q \approx 15$ l/h)

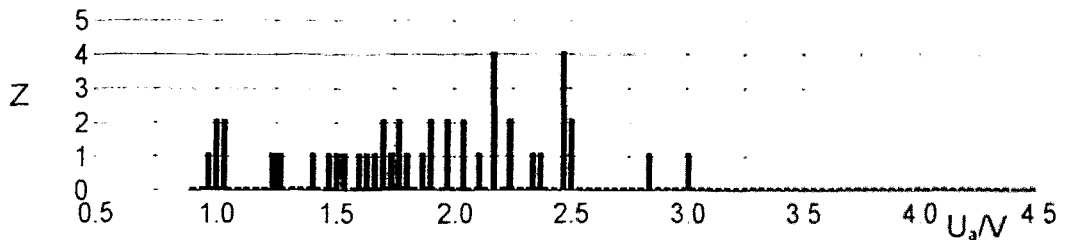
a) Sequence of the bubble echoes (upper plot: bubble sizes, lower: distances)



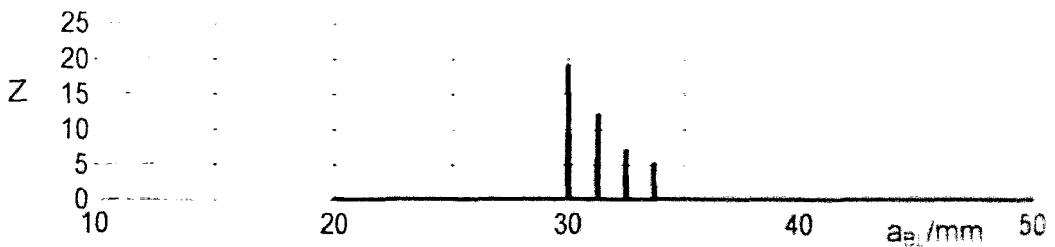
b) FAMOS-FFT of the bubble echoes sequence ( $f_{BL}$ : bubble sequence frequency)



c) FAMOS-histogram of the bubble echo amplitudes  $A_{BL}$  (distribution of the bubble sizes)



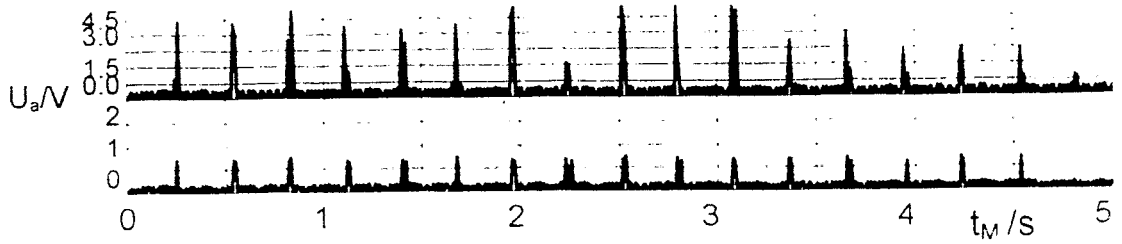
d) FAMOS-histogram of the times of flight  $t_F$  of the bubble echoes (distribution of the bubble distances  $a_{BL}$  from the inner vessel wall)



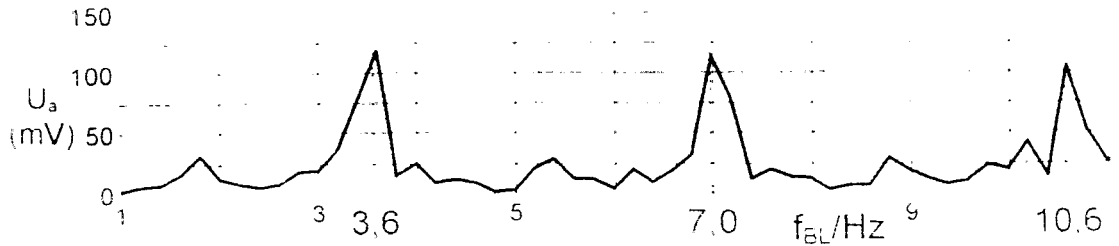
### Analysis of an argon bubble stream rising in liquid metal InGaSn using ultrasonic pulse-echo method (probe pos. P1)

(Combination vessel material - liquid: PLG - FLM; measuring time  $t_M = 5s$  probe height  $h_1 \approx 10mm$  above the bubble generator type G2 / 3 nozzles  $\varnothing 3mm$ , probe circumference position: P1=0°; argon gas flow:  $Q \approx 15l/h$ )

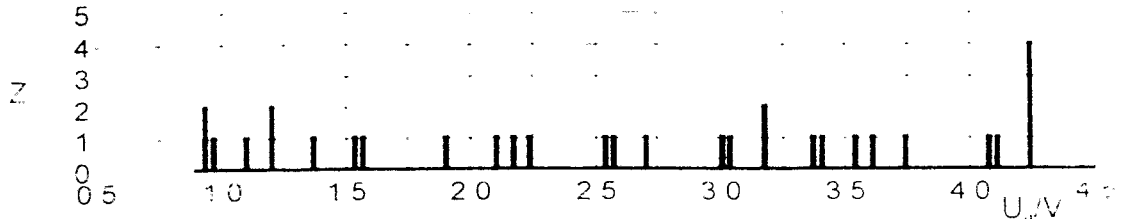
a) Sequence of the bubble echoes (upper plot: bubble sizes, lower: distances)



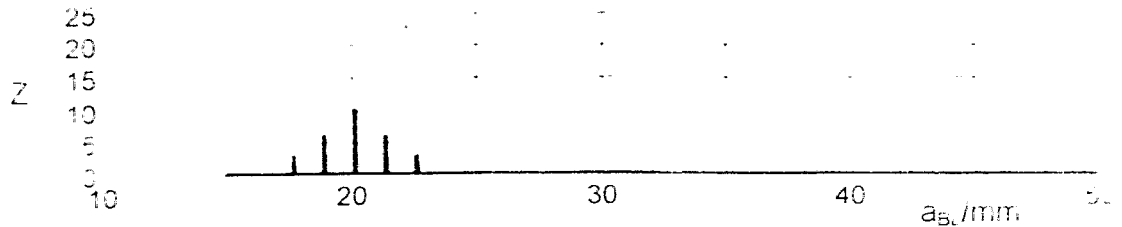
b) FAMOS-FFT of the bubble echoes sequence ( $f_{BL}$ : bubble sequence frequency)



c) FAMOS-histogram of the bubble echo amplitudes  $A_{BL}$  (distribution of the bubble sizes)



d) FAMOS-histogram of the times of flight  $t_F$  of the bubble echoes (distribution of the bubble distances  $a_{BL}$  from the inner vessel wall)



## Analysis of an argon bubble stream rising in liquid metal InGaSn using ultrasonic pulse-echo method (probe pos. P3)

(Combination vessel material - liquid: PLG - FLM; measuring time  $t_M = 5s$  probe height  $h_p \approx 10mm$  above the bubble generator type G2 / 3 nozzles  $\varnothing 0.3mm$  probe circumference position  $P3=180^\circ$ , argon gas flow:  $Q \approx 15l/h$ )

B. Hofmann <sup>1)</sup>, S. Eckert <sup>2)</sup>, G. Gerbeth <sup>2)</sup> and E. Kaiser <sup>1)</sup>

## ULTRASONIC MEASUREMENTS OF THE MOTION OF GAS BUBBLES RISING IN A LIQUID METAL

### - CONCLUSIONS -

- The tests have shown that argon bubbles rising in a liquid can be detected in water as well as in the liquid metal InGaSn with a sufficient time and local resolution.
- The distribution of the bubble echo amplitudes and of the bubble distances over the cross-section of the testing chamber were estimated by means of the histogram function of the software tool FAMOS.
- The bubble detaching frequencies from the different sparkling units was determined by means of the FFT-function of FAMOS.
- From these results conclusions were drawn to the relative bubble size, the bubble shape and velocity as well as to the positions of the bubbles and to the local void distributions inside the testing chamber.
- The detectibility of the bubbles is limited by their minimal size, the sound attenuation in the liquid metal and an unavoidable signal noise.
- The reason of an additional damping of the sonic echoes in the liquid metal could not be found out so far. This can be caused possibly by crystallizing effects as well as gaseous or oxide layers in the liquid alloy.

---

<sup>1)</sup> Technische Universität Dresden, Institute of Energiemaschinen und Maschinenlabor, Chair of Measurement and Automation Technology, D-01062 Dresden, Germany

<sup>2)</sup> Forschungszentrum Rossendorf e.V., Institute of Safety Research, D-01314 Dresden, Germany

**Ultrasonic measuring techniques suitable for high temperature melts  
for Doppler imaging, for the determination of densities and temperatures  
and for the growth rate of the solidified fraction**

*Wolfgang Grill, Michael Schmachtl, Jens Jahny*

*Institut für Experimentelle Physik II der Universität Leipzig  
Linnestraße 5, D-04103 Leipzig, Germany*

Ultrasonic detection schemes based on phase sensitive detection respectively correlation techniques have been developed for the spatially resolved characterization of solidifying melts. With the aid of guided ultrasonic waves, the position of the solid-liquid interface of metallic alloys has been detected with high resolution under directional solidification conditions. Detection schemes based on focusing transducers suitable for Doppler imaging at 100 MHz with a resolution of the fluid velocity of typically 1 mm/s are demonstrated. Special probe configurations suitable for the detection of the density and the temperature of the liquid fraction and possible applications of synthetic aperture techniques for spatially resolved detection are discussed. The presentation of a variety of novel ultrasonic detection schemes has the aim to identify possible applications demanded for the processing of semiconductors, metals respectively alloys and other optically non-transparent media.

# Ultrasonic measuring techniques suitable for high temperature melts (for Doppler imaging, for the determination of densities and temperatures, and for the growth rate of solidified fractions)

Wolfgang Grill, Michael Schmachtl, Jens Jahny  
Institut für Experimentelle Physik II  
Universität Leipzig  
Linnéstr. 5  
D 04103 Leipzig  
Germany

Tel.: 0341 / 97-32681  
Fax : 0341 / 97-32699  
E-mail: grill@physik.uni-leipzig.de

## Experimental demonstration of Doppler-imaging and the obtainable resolution

The measurements are performed in water with aluminium particles (typically 10  $\mu\text{m}$  flakes with a rather large variation of the size) as reflecting tracers. Observation is restricted to the focal region of a focusing transducer. The observation is conducted in reflection. The centre frequency of the ultrasonic pulses is 100 MHz.

The measurement concerning the resolution is conducted for a fixed position with movements of the fluid introduced simply by stirring. Imaging demonstrated here for one dimensional scanning can also be based on two- or three-dimensional scanning.

The spatial resolution is determined by the size of the focal volume (ellipsoid, Gaussian point spread function) of about 20  $\mu\text{m}$  diameter (FWHM) and a length of about 30  $\mu\text{m}$  which beside of geometrical conditions has also been restricted by temporal gating.

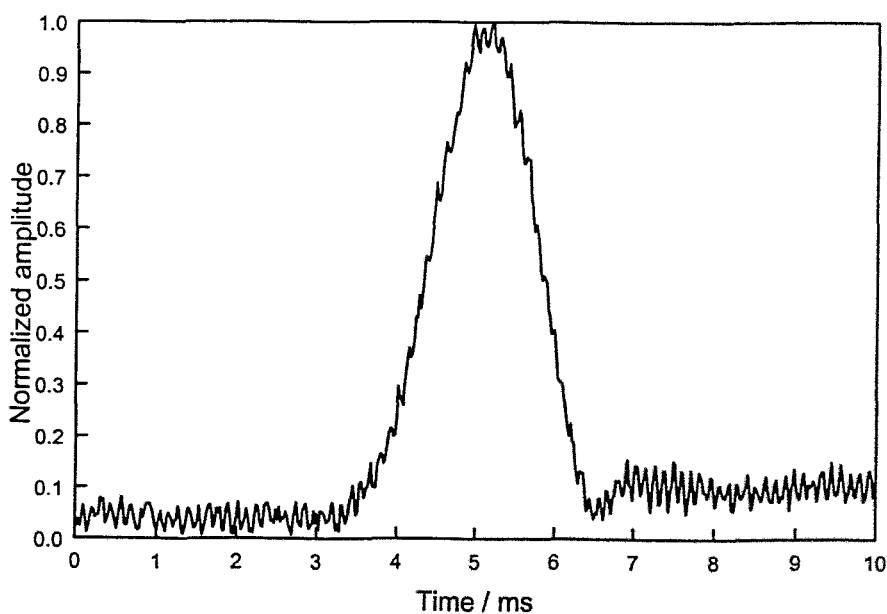


Figure 1: Time dependence of the observed amplitude (normalised to the maximum) of ultrasonic waves reflected from a silver flake accidentally crossing the focal volume.

The velocity resolution is demonstrated by the position versus time graph (figure 2) for a particle accidentally crossing the focal volume. The amplitude for this event is demonstrated on identical times in the normalised amplitude versus time graph (figure 1). The velocity can simply be derived from the maximum slope of the position versus time graph (about  $1.1 \mu\text{m}/\text{ms} = 10^{-3} \text{ m/s}$ ). The resolution for the velocity (equivalent to the minimum detectable velocity) is at least  $\pm 10^{-4} \text{ m/s}$ .

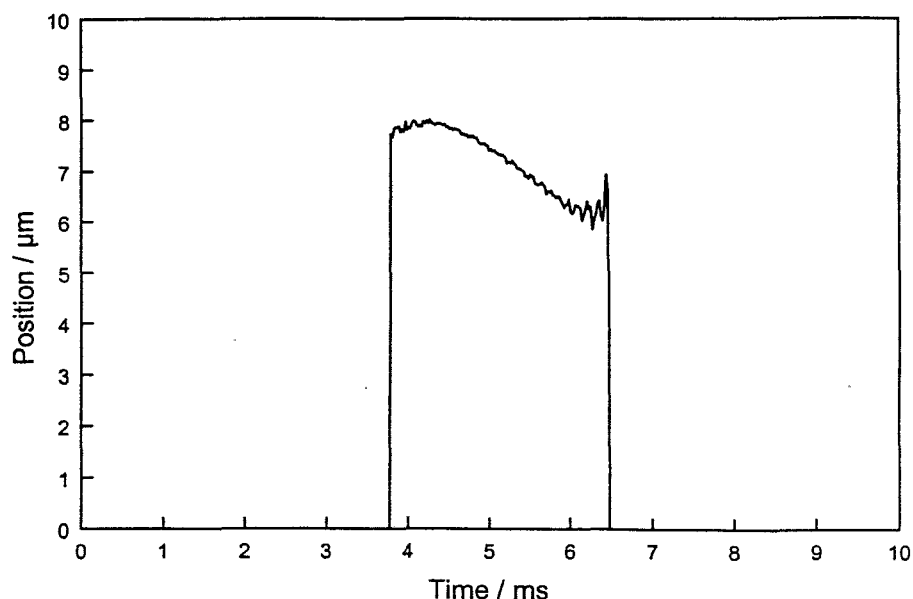


Figure 2: Position in axial direction derived by Doppler detection for the same particle respectively event observed also with respect to the amplitude in figure 1 (the vertical lines in the graph are an artefact of the representation and should be ignored)

Depending on the methods used for signal processing and bandwidth of the transducers a maximum velocity of 100 m/s is at least (for the actual existing and available system) detectable. This leads to a dynamic range for the detectable velocities of at least  $10^6$  ( $10^4 \text{ m/s}$  to 100 m/s)

Depending on the speed of scanning, three dimensional images can be collected with a minimum acquisition time per voxel of about 2 ms (see graphs).

Non-avoidable limits on the working distance respectively depth of the three dimensional volume are caused only by the absorption of the actual fluid used (assumed that adequate focusing transducers are manufactured). This is typically at least 10 mm if not 100 mm for liquid metals at a frequency of 100 MHz (similar to the frequency used here for demonstration in water).

A graph (figure 3) demonstrating the results obtained for a one dimensional scan across the flow emitted from a valve is included to demonstrate that spatial resolution can be obtained. A three dimensional scan would deliver the respective data for each voxel of the volume under observation. The expected resolution can not be demonstrated with the data presented here for



a line scan, since the opening of the (currently) available valve (diameter: 0.5 mm) is too large to probe the expected resolution.

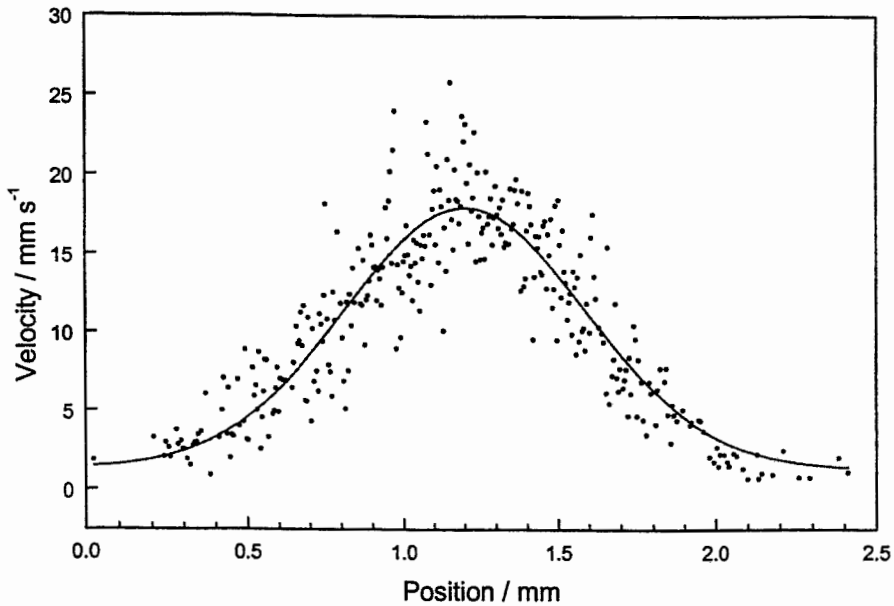


Figure 3: linear scan for a localised flow emitted by a valve. The dots represent velocities derived from single or multiple events as demonstrated in figures 1 and 2 for each position of the scan.

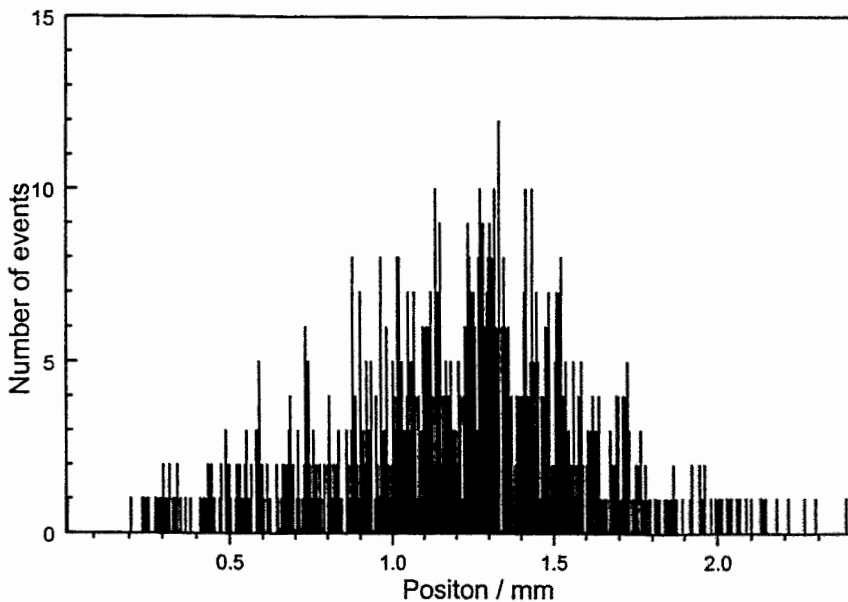


Figure 4: Histogram for the number of events contributing to the determination of the velocities at each pixel of the scan. In regions with small velocities the number of events observed per unit time is also small (as to be expected under the given conditions).

The observed variation (scatter) of the velocity is probably caused by a turbulent respectively fluctuating flow. It may also be influenced by the dependence of the inertial

forces of the particles on their size (the aluminium flakes used in the experiment have a large variation concerning the distribution of the individual sizes). A Gaussian profile has been fitted to the data (figure 3) to demonstrate the time averaged velocity under the assumption that the flow can be represented by such a profile, which seems to be adequate for the measurement. The number of events (number of particles crossing the focal volume) used to determine the velocity for any position of the line-scan is demonstrated in figure 4.

### **Directional Solidification**

Applications involving the monitoring of directional solidification and related applications at temperatures up to 1500 °C as well as a description of the developed technologies are accessible in the publications listed below:

Ultrasonic Detection of the Solid-Liquid Interface in High Temperature Solidification Experiments

G. Zimmermann, A. Schievenbusch, W. Grill, M. Schmachtl, A. Lundström, M. Braun  
Experimental Methods for Microgravity Materials Science. eds. R. A. Schiffmann, J. B. Andrews, The Minerals and Material Society, 27-31 (1994)

Bestimmung der Erstarrungsrate bei der gerichteten Erstarrung mittels Ultraschall

G. Zimmermann, A. Schievenbusch, A. Drevermann, W. Grill, M. Schmachtl  
Herausgeber: F. Aldiger, H. Mughrabi, Werkstoffwoche '96, Band 7, 167 (1997)

Bestimmung der Position und der Geschwindigkeit der Erstarrungsfront bei der gerichteten Erstarrung durch die Emission von Ultraschall an der Fest-Flüssig-Phasengrenze

G. Zimmermann, A. Schievenbusch, W. Grill, M. Schmachtl  
11. Kolloquium Schallemission, Band 58, 21-28 (1997)

Determination of elastic moduli for high temperature materials by an ultrasonic method

W. Grill, T. J. Kim, M. Schmachtl, P. Busse, A. Schievenbusch  
Proc. of the 5th European Conference on Advanced Materials, Processes and Applications, Vol. 4, 279 (1997)

Determination of the crystallization rate during directional solidification by ultrasound

G. Zimmermann, A. Schievenbusch, A. Drevermann, W. Grill, M. Schmachtl  
Proc. of the 5th European Conference on Advanced Materials, Processes and Applications, Vol. 4, 155 (1997)

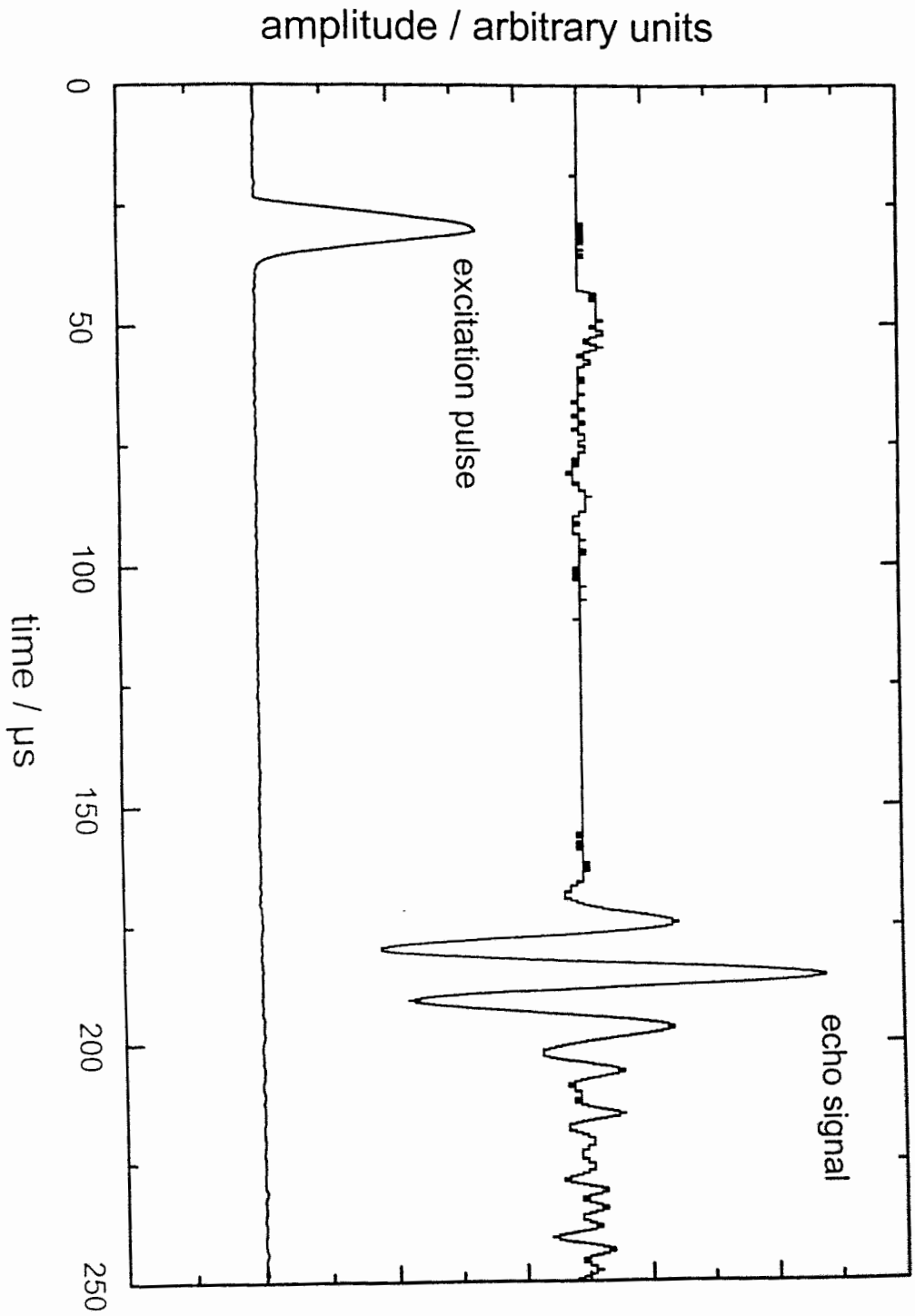
Determination of the Position and Velocity of the Solid-Liquid Interface During Directional Solidification of Metals based on Guided Ultrasonic Waves

T. J. Kim, M. Schmachtl, W. Grill, A. Schievenbusch, G. Zimmermann  
J. Acoust. Soc. Korea 17, 79-83 (1998)

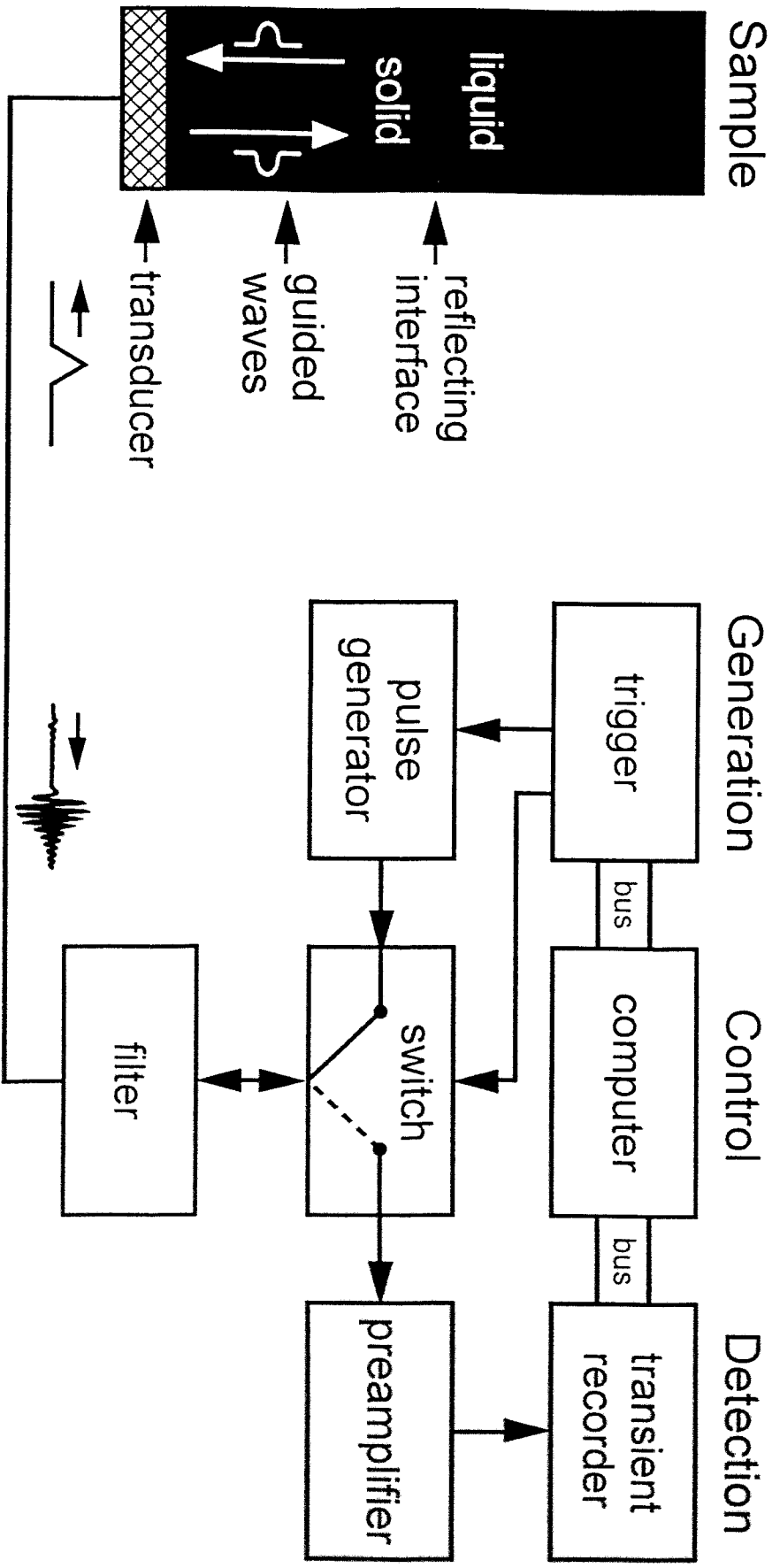
Crystallization process control during directional solidification in a high-temperature-gradient furnace by guided ultrasonic waves and real-time signal evaluation

M. Schmachtl, A. Schievenbusch, G. Zimmermann, W. Grill  
Ultrasonics 36, 291 (1998)

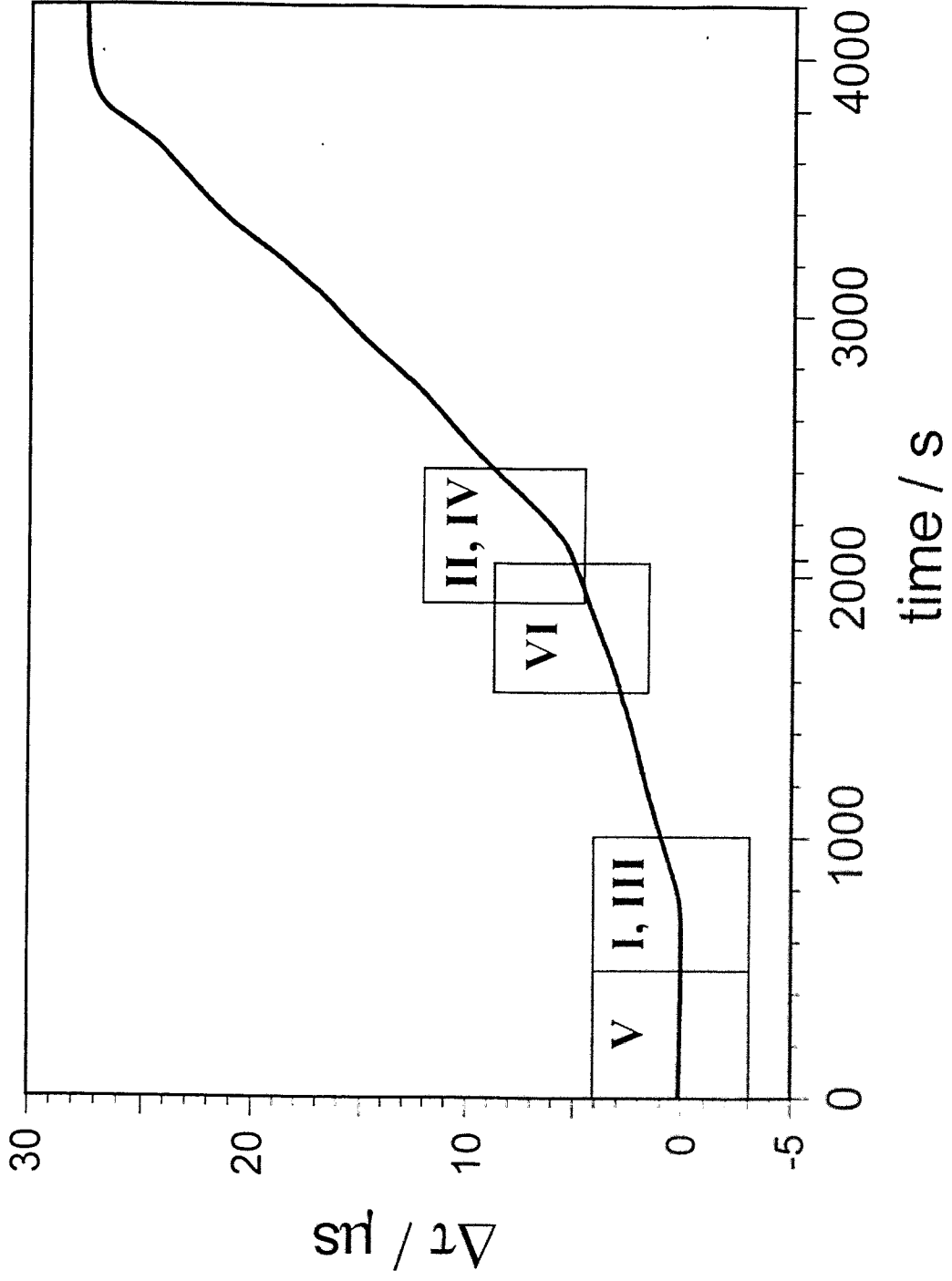
Typical excitation pulse and detected ultrasonic echo signal



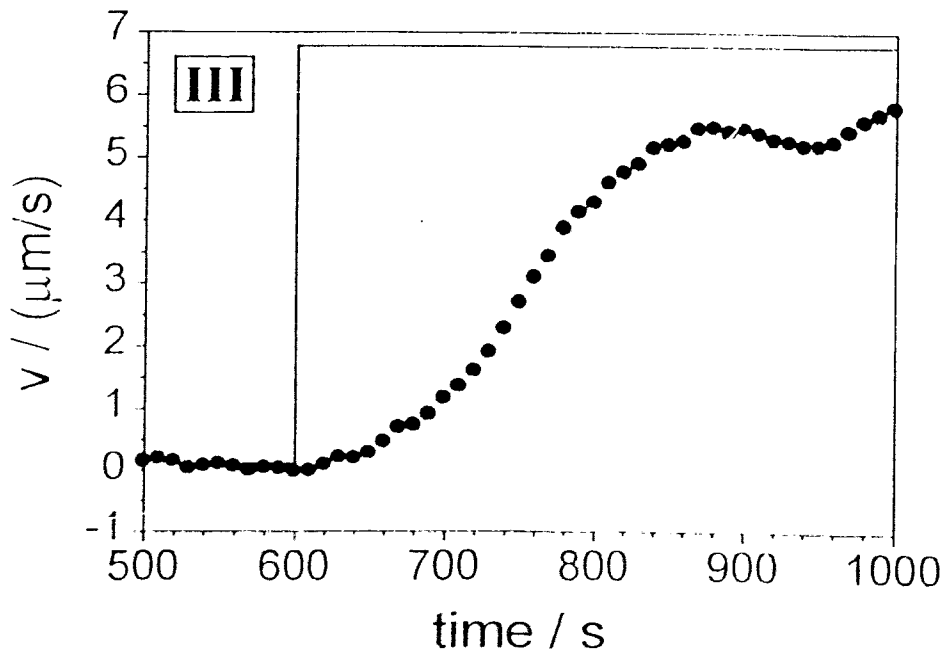
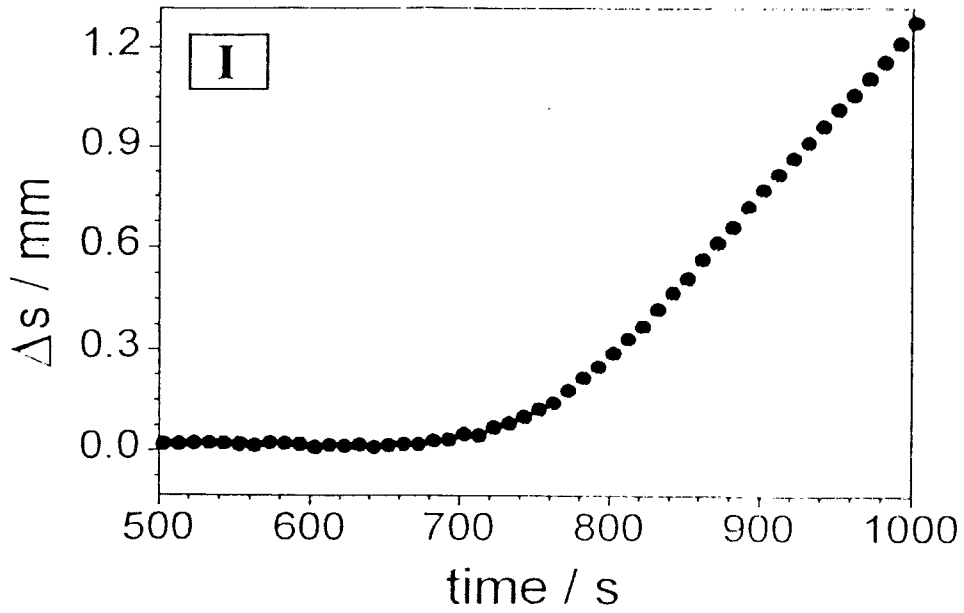
# Electronic set-up



Measured time-of-flight during solidification process

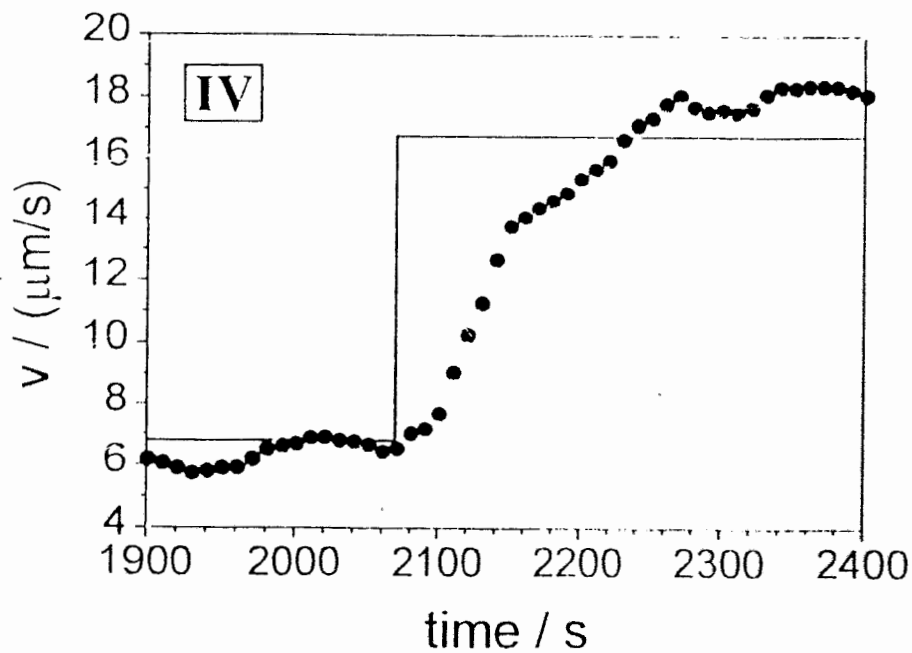
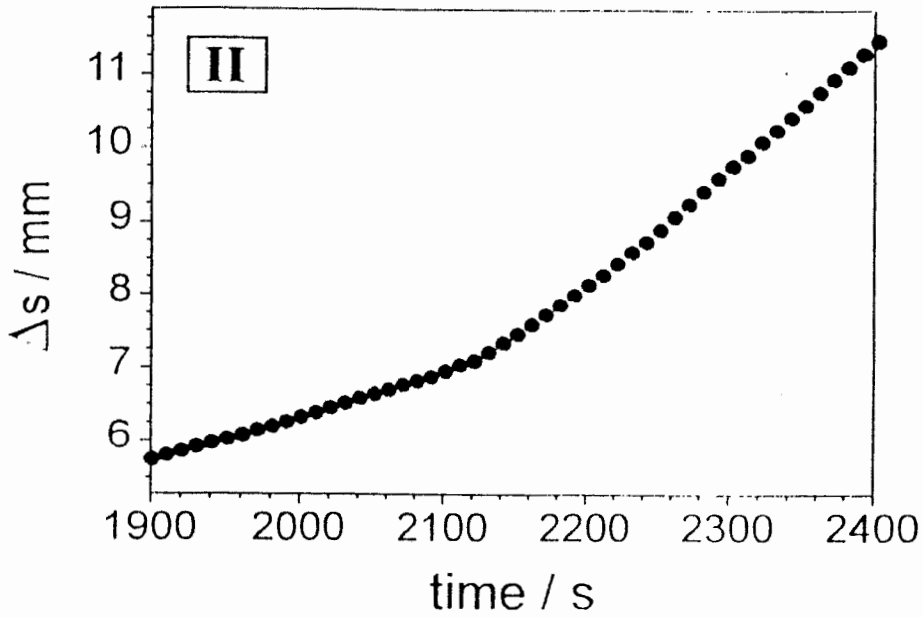


# Position and velocity of the interface during the onset of solidification



(straight line – furnace velocity)

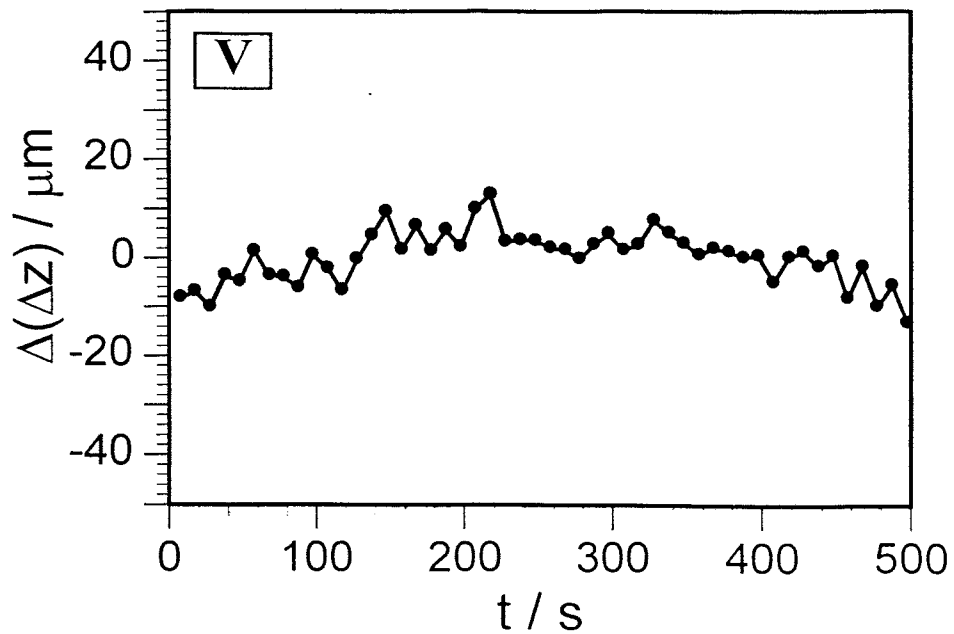
# Position and velocity of the interface during the change of the furnace velocity



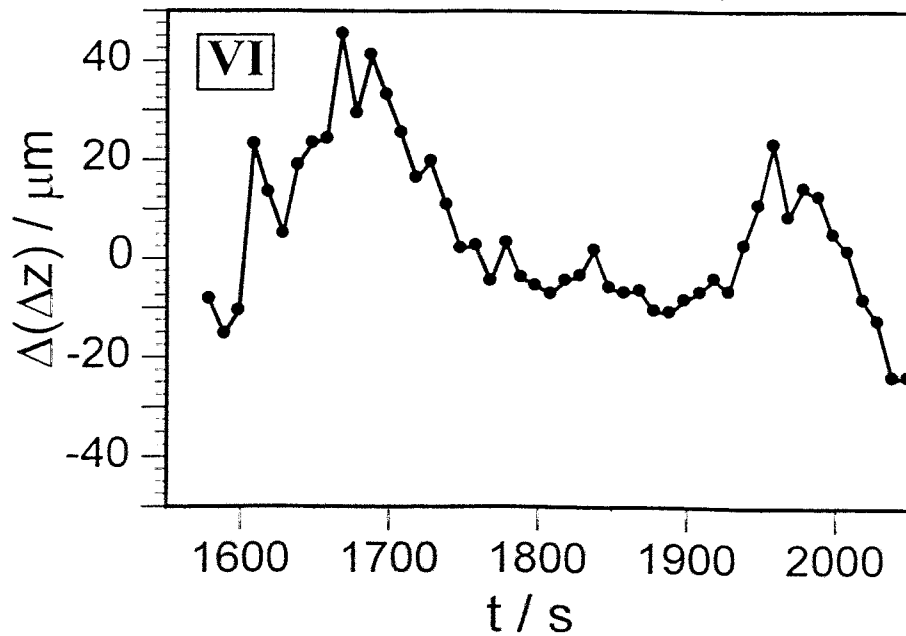
(straight line – furnace velocity)

# Determination of the interface position

without furnace movement



constant furnace velocity





## Scientific Programme

**October 12, 1999 (Tuesday)**

### **Afternoon Session**

**14.00 Invited Lecture**

*Y. Takeda (Paul-Scherrer-Institute, Switzerland)*

Ultrasonic Doppler method for velocity profile measurements: Application to the mercury flow

**14.45 *D. Brito, H.-C. Nataf, O. Szydlo, P. Cardin (Universite J. Fourier Grenoble, France)***

Ultrasonic Doppler velocity measurements in liquid gallium

**15.05 *J.-C. Willemetz (Signal Processing Lausanne, Switzerland)***

Ultrasonic Doppler Velocimetry applied to high temperature liquids

## **Ultrasonic Doppler method for velocity profile measurements: Application to the mercury flow**

*Y. Takeda (Paul-Scherrer-Institute, Switzerland)*

The Ultrasonic Doppler method for flow measurement has been developed at PSI, especially aiming at its application to liquid metal flow. This method has three major advantages over the conventional measuring techniques :

- (1) Spatio-temporal information about the flow field can be obtained.
- (2) It can be applied to opaque liquids, as well as for opaque container materials.
- (3) As a line measurement, measurement is efficient for obtaining spatial information and thus flow mapping is practically performed.

The principle and practice of this method will be presented, together with results of a variety of confirmation experiments.

The mercury flow in the SINQ target geometry has been fully investigated using this method at Riga, Latvia. The flow was studied by measuring average flow fields with different geometries as well as for various flow rates, in the form of vector field. The investigation was extended to obtain the time dependent vector fields.

These results will be presented to show the this method might be a powerful tool for flow investigation of liquid metal.

---

International Workshop on Measuring Techniques  
for Liquid Metal Flows (MTLM)  
Dresden, October 11-13, 1999

**Ultrasonic Doppler method for velocity profile measurements  
- Application to mercury flow**

**Y.Takeda  
Paul Scherrer Institute, Switzerland**

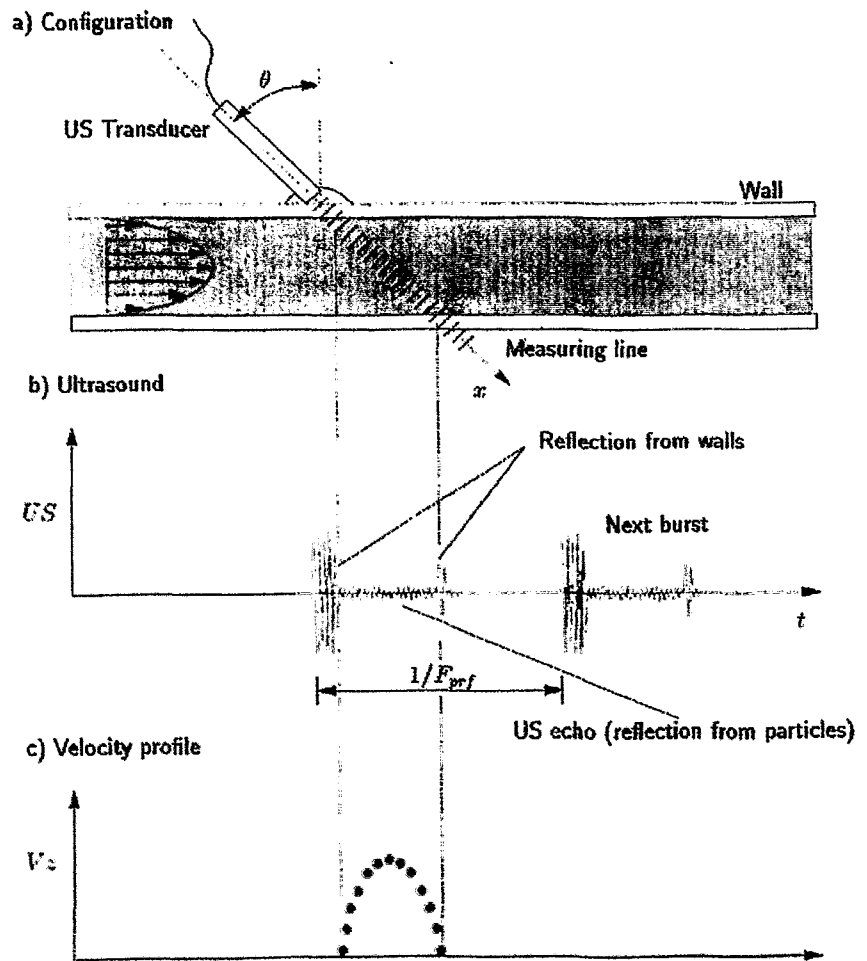
**I : UVP**

- \* Principle
- \* Advantages
- \* Application limit
- \* Accuracy

**II : Applications**

- \* Spatio-temporal
  - \* Flow Mapping
  - \* Mercury flow
  - \*
-

# Working principle of UVP method



*Flow transition in a rotating Couette system*

## **UVP : Working principle**

◆ Echographic relation

$$x = 2t/c$$

◆ Doppler relation

$$V_x = cf_D / 2f_0$$

$f_D$ : instantaneous frequency

## Ultrasonic Doppler Method

- ◆ US echo

$$R(t) = A(t) \cos \omega_0 t + B(\tau) \cos\{\omega_0 + \omega_D(\tau)\}t$$

- ◆ Decomposition

Phase shift + Demodulation

Low pass filtering :  $f_0 \gg f_D$

$$S_1(t) = Q_1(t) + D_1(\tau) \cos \omega_D(\tau) t$$

$$S_2(t) = Q_2(t) + D_2(\tau) \sin \omega_D(\tau) t$$

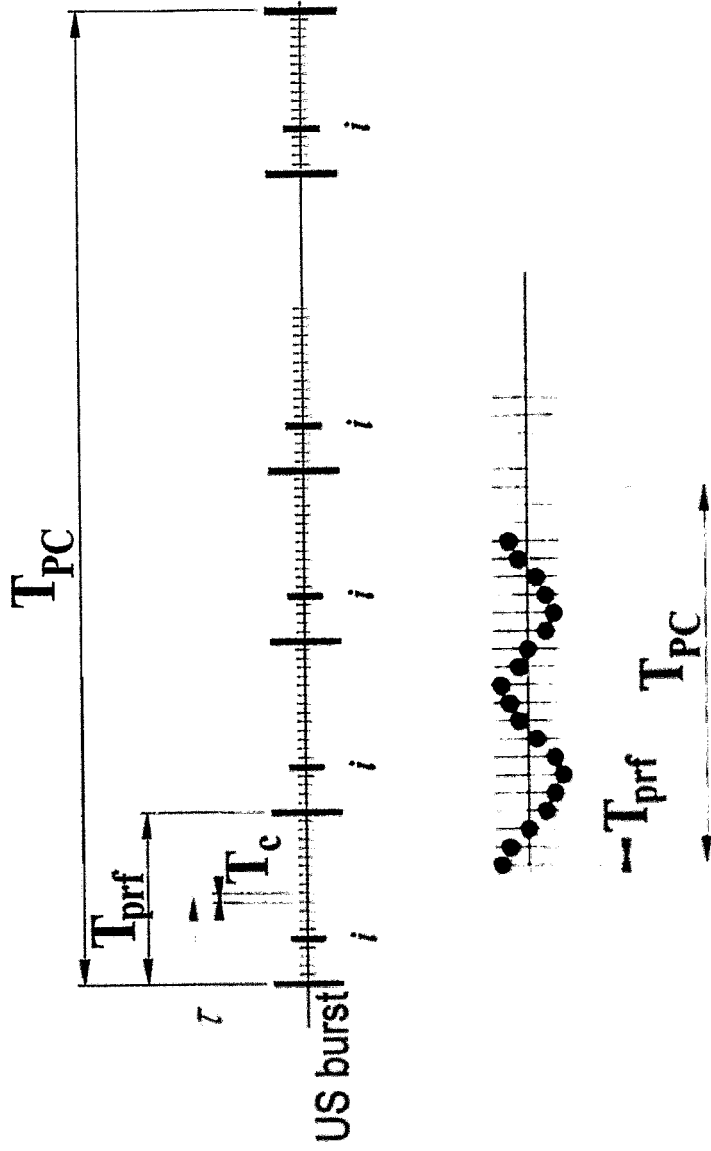
- ◆ With an ideal filter

$$F_1(t) = D_1(\tau) \cos \omega_D(\tau) t$$

$$F_2(t) = D_2(\tau) \sin \omega_D(\tau) t$$

## Ultrasonic Doppler Method

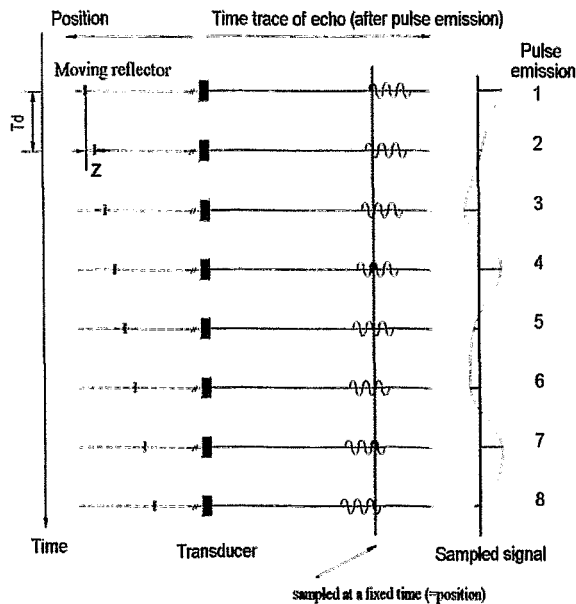
### Detection of instantaneous Doppler frequency



$$D(\tau_i) \cos \omega_D(\tau_i) t$$

# Ultrasonic Doppler Method

## Detection of Doppler frequency



$$\phi = f_0 T_d$$

$$d\phi/dt = f_0 dT_d/dt$$

$$T_d = 2z/c$$

$$dT_d/dt = (2/c) dz/dt = 2v/c$$

$$d\phi/dt = 2vf_0/c = f_D$$



---

## *Ultrasonic Doppler Method*

### **Measurement limitation**

- ◆ From Nyquist sampling theorem

$$f_{D \max} < f_{\text{prf}}/2 \Rightarrow V_{\max} < cf_{\text{prf}}/4f_0$$

- ◆ Maximum depth

$$P_{\max} = c/2f_{\text{prf}}$$

- ◆ Measurement constraint

$$V_{\max} P_{\max} < c^2/8f_0$$

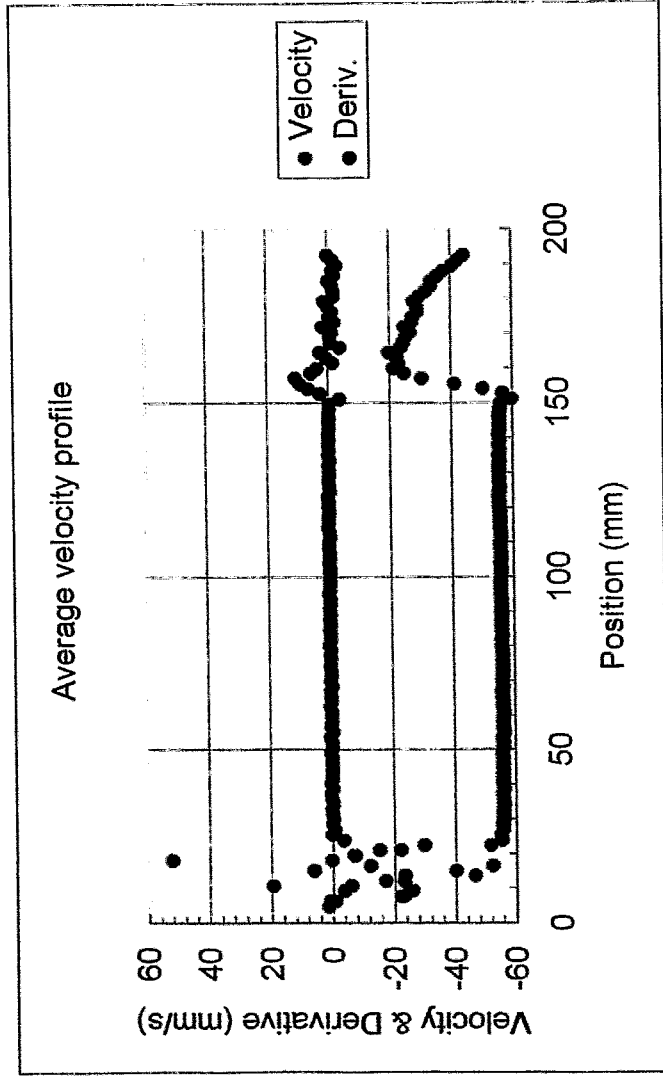
---

# UVP : Accuracy - Velocity and Position

## Velocity profile in a rotating cylinder

**Average velocity**  
 Rotation 52.32 sec 30 rotation  
 rps= 0.57339  
 Y= 111.00  
 Y0= 126.5  
 Average= -55.7  
 Vth= -55.84  
 Diff= 0.3%

**Position**  
 Pos. = 139.1 mm  
 Dtheo= 141.6 mm  
 Diff = 1.8%



---

**Ultrasonic Doppler Method**

***Advantages***

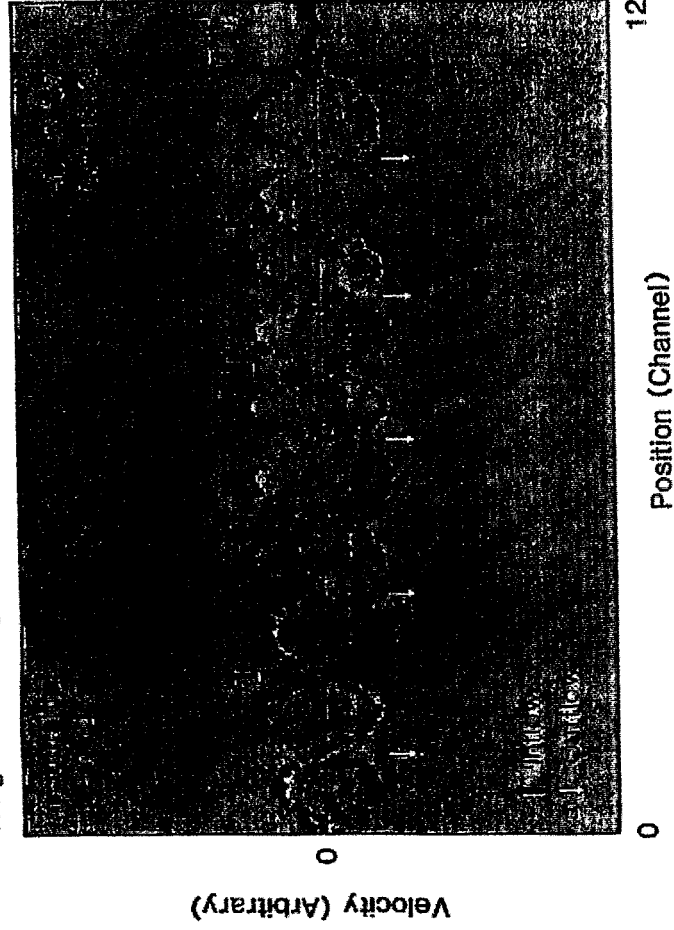
- ◆ Safe
- ◆ Operates in situ
- ◆ Efficient
- ◆ Non-invasive



## *Flow transition in a rotating Couette system*

# Time averaged velocity profiles : $V_z$

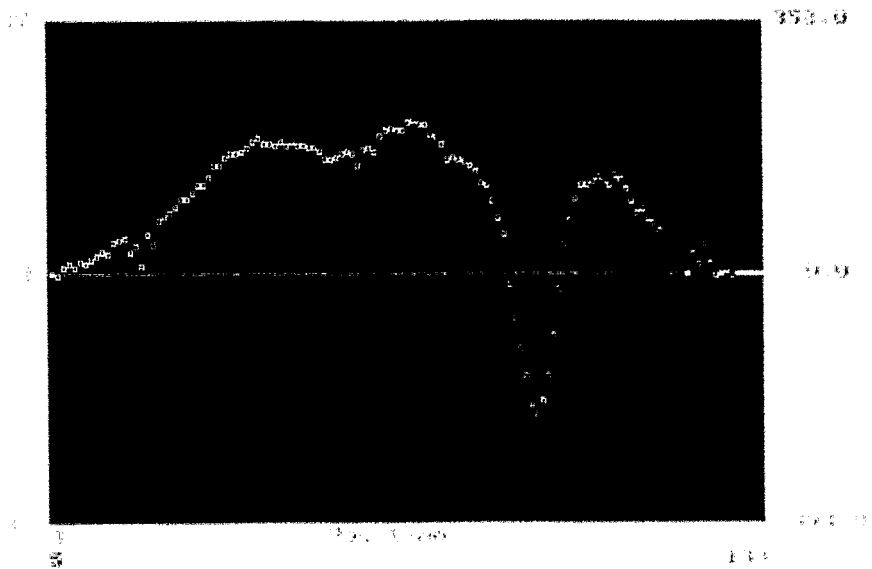
Weighted Average Profile



$$\eta=0.65$$

# Velocity profile

(0.6 Ltr/s, 30° )

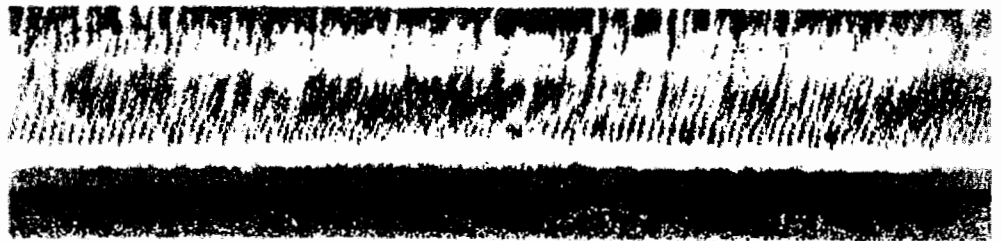


Flow Measurement Instruments - SIM

MET-FLOW S.A. - Lausanne - Switzerland

# *Chaotic behavior of Hg flow*

(0.6 Ltr/s, 30°)

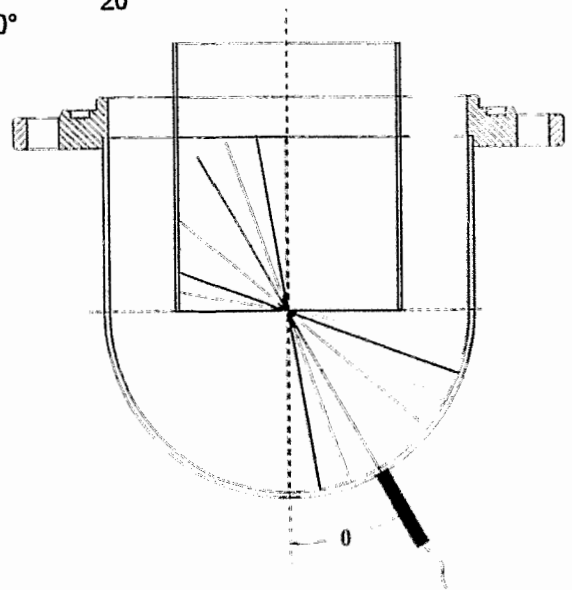
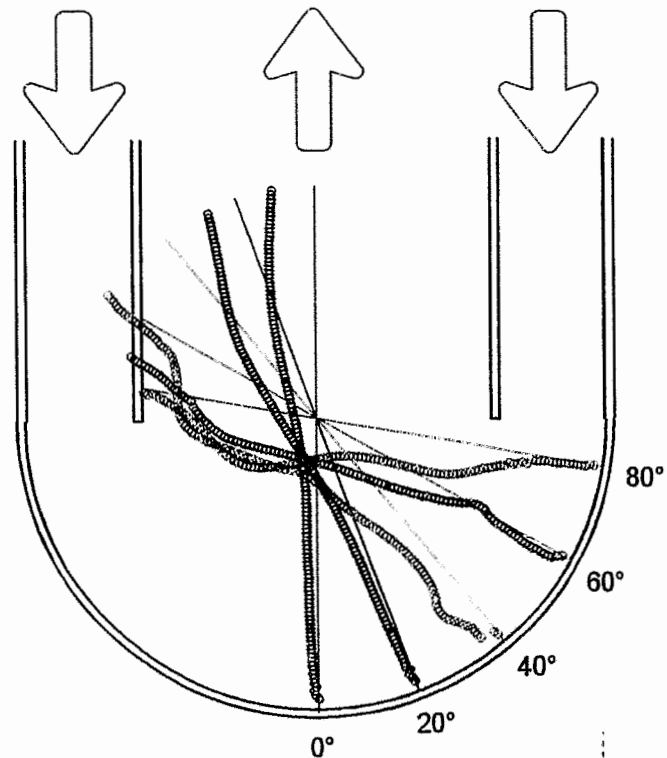


Flow visualization of Hg flow

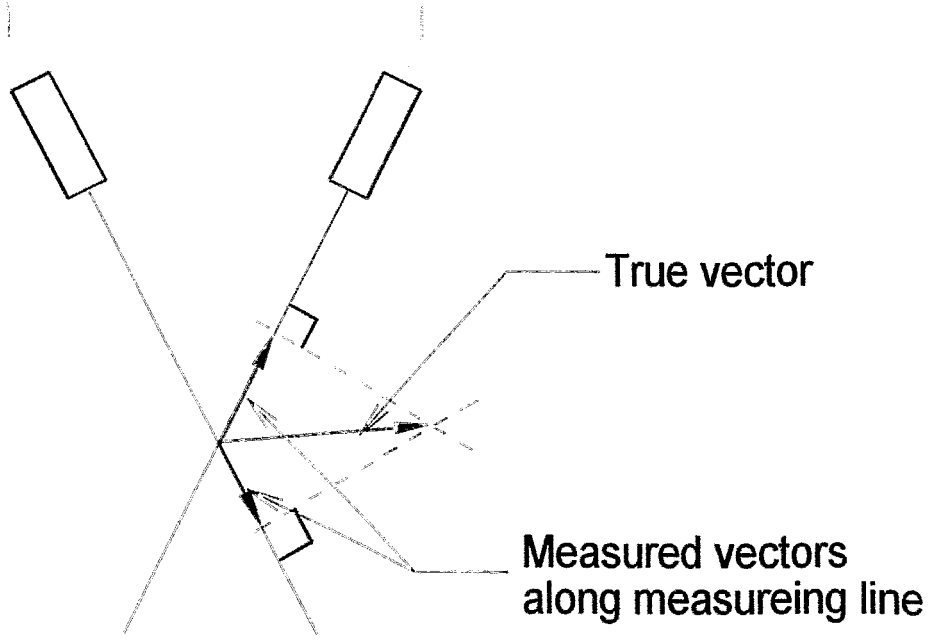
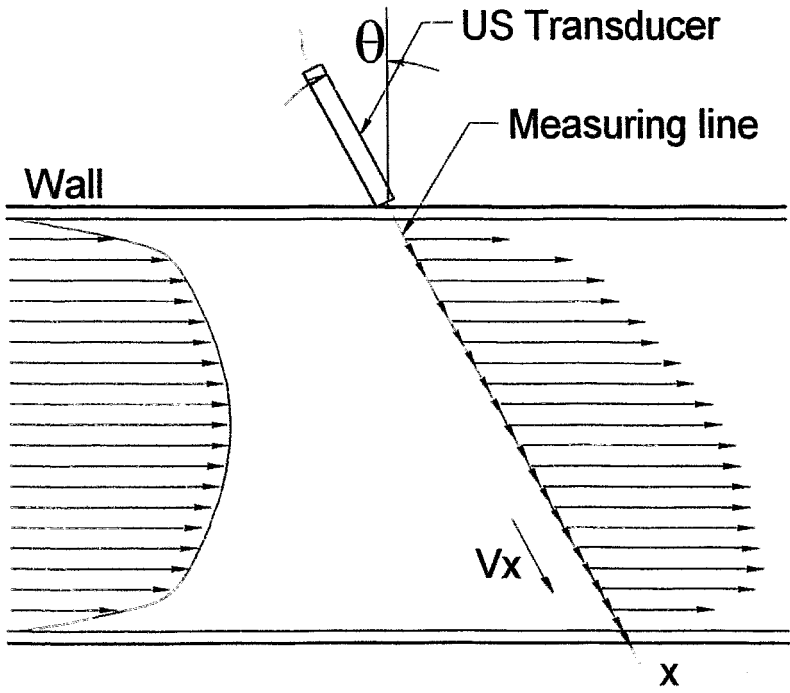
MEI-FLOW S.A. Lausanne Switzerland

# Velocity profiles of mercury flow

Hg flow in SINQ : 1.2 Ltr/s

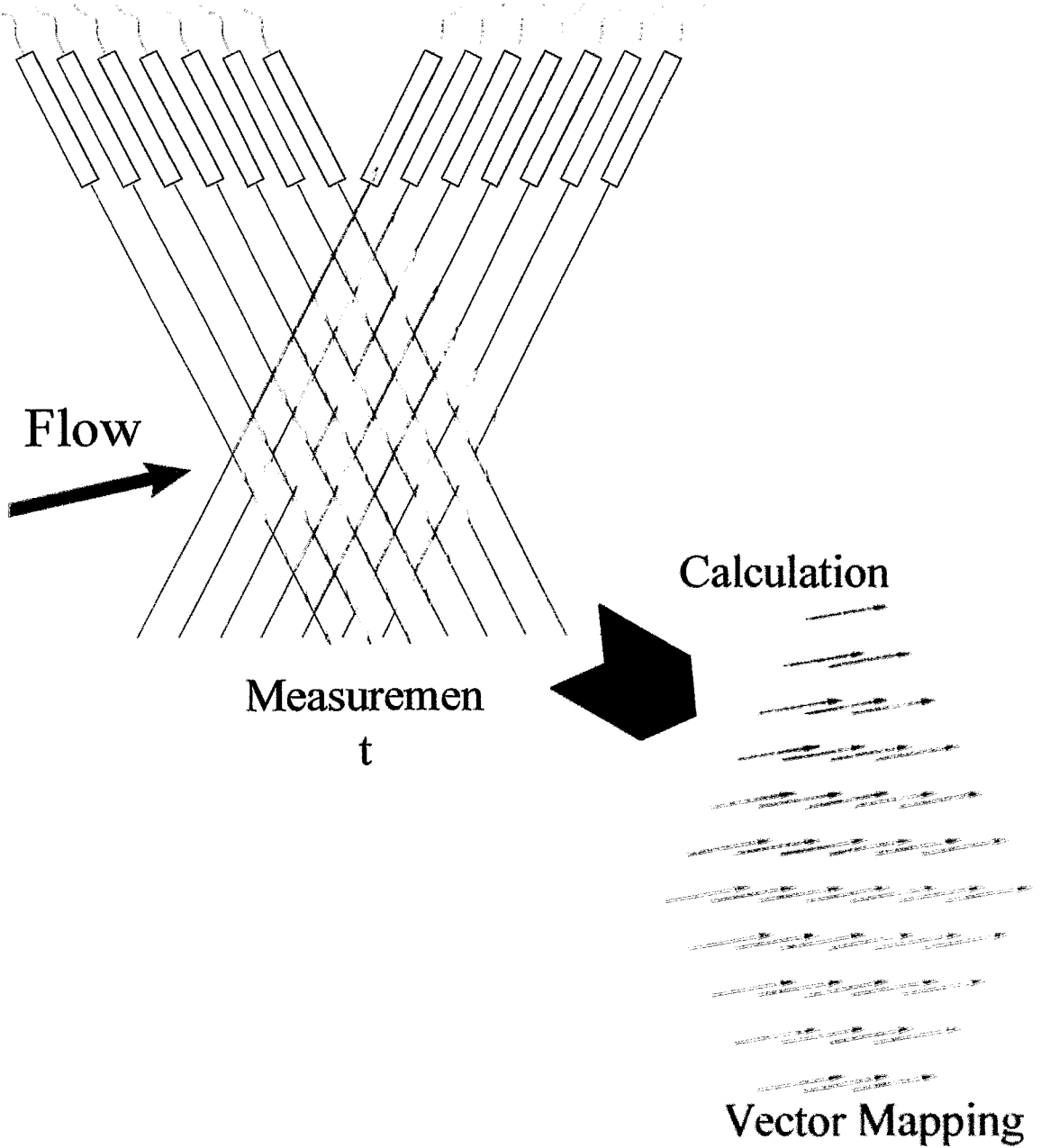


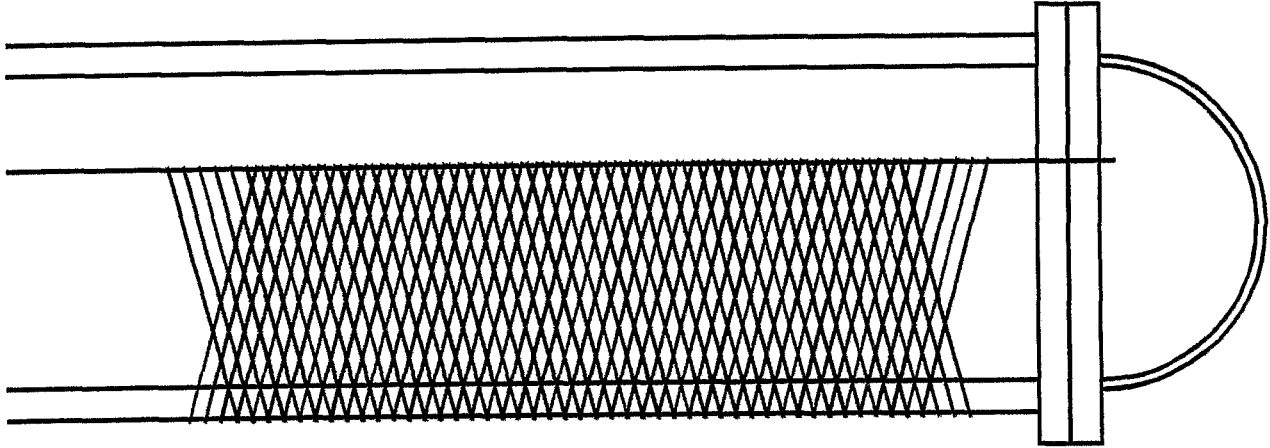
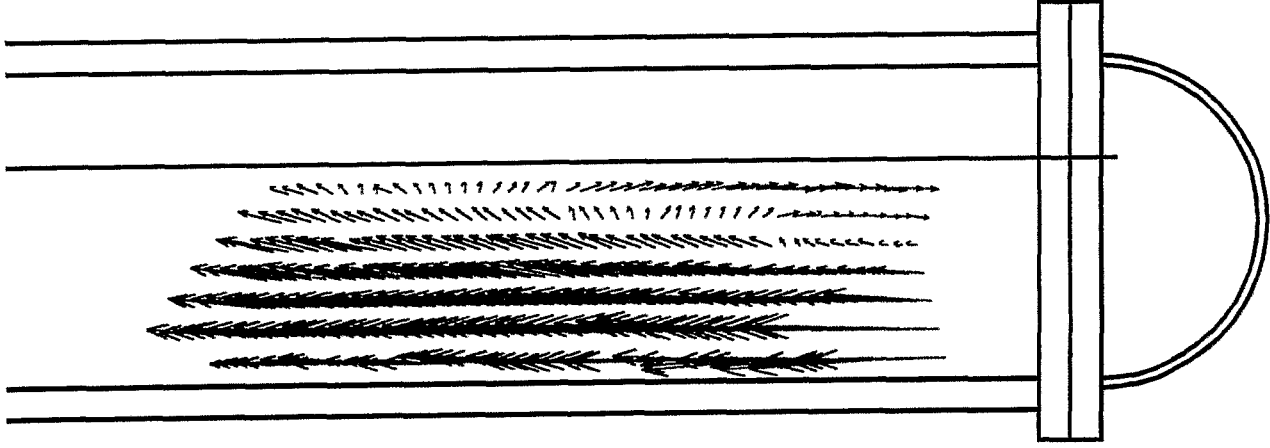
# Forming a true vector





# Flow mapping

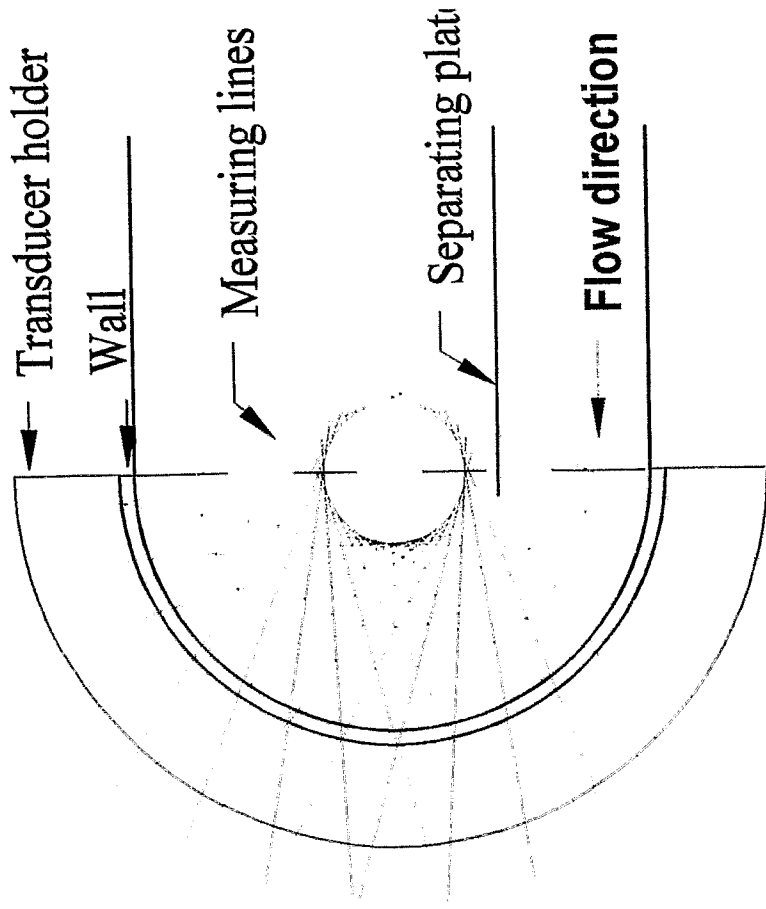




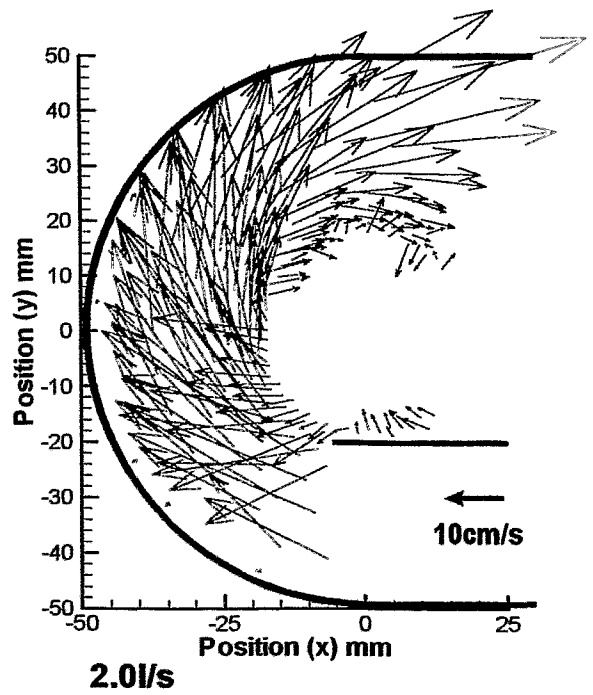
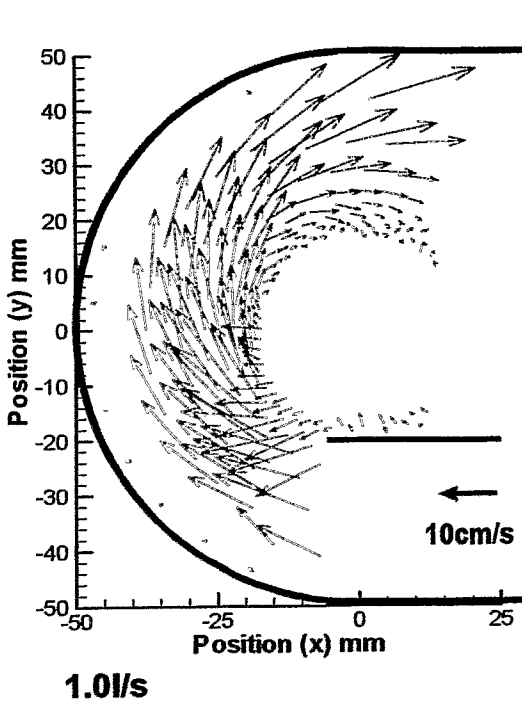
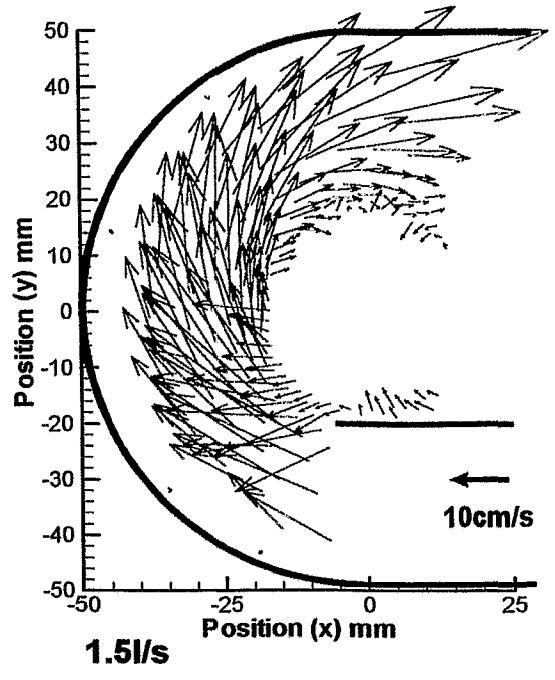
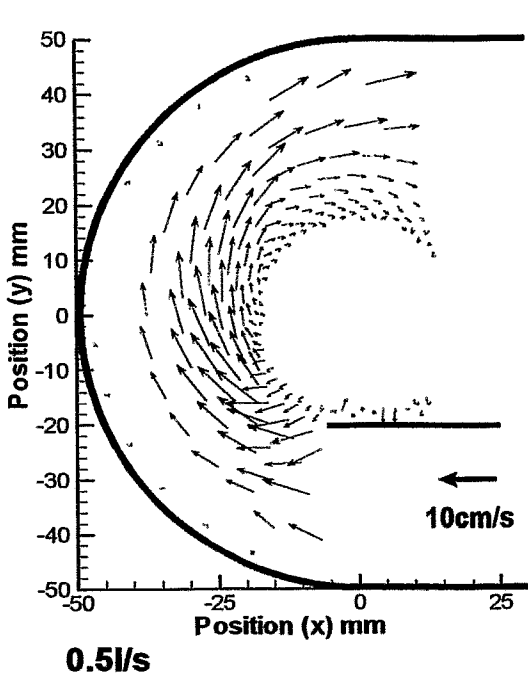
ESS 2D : Flow mapping

# ESS Horizontal Target : Flow Mapping

## *Transducer arrangement*

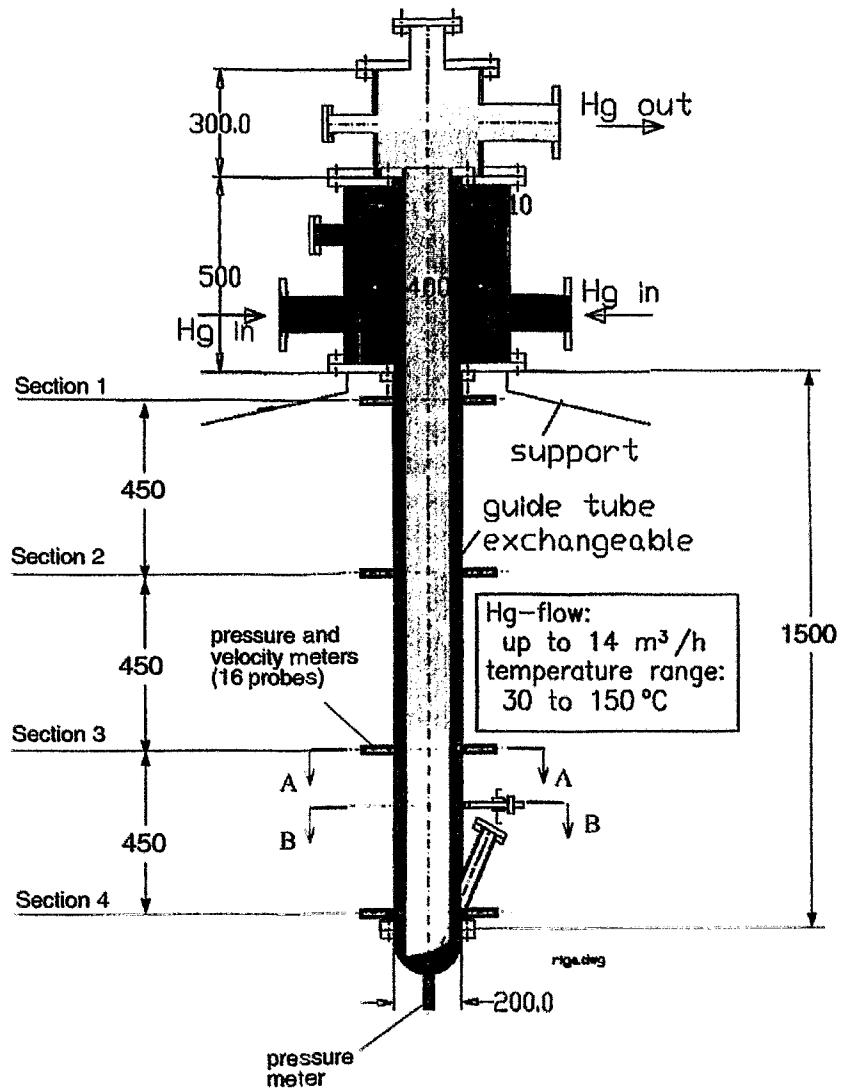


# ESS 2D : Vector plots for various flow rate

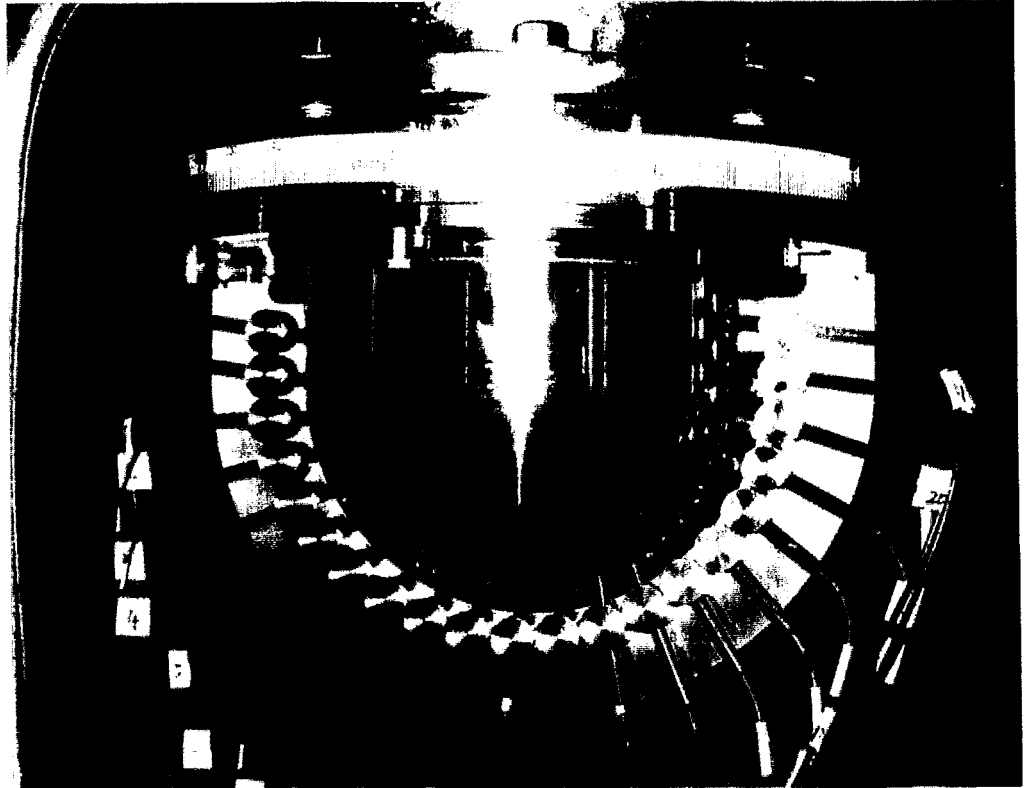


# Riga Experiment 97 SINQ configuration

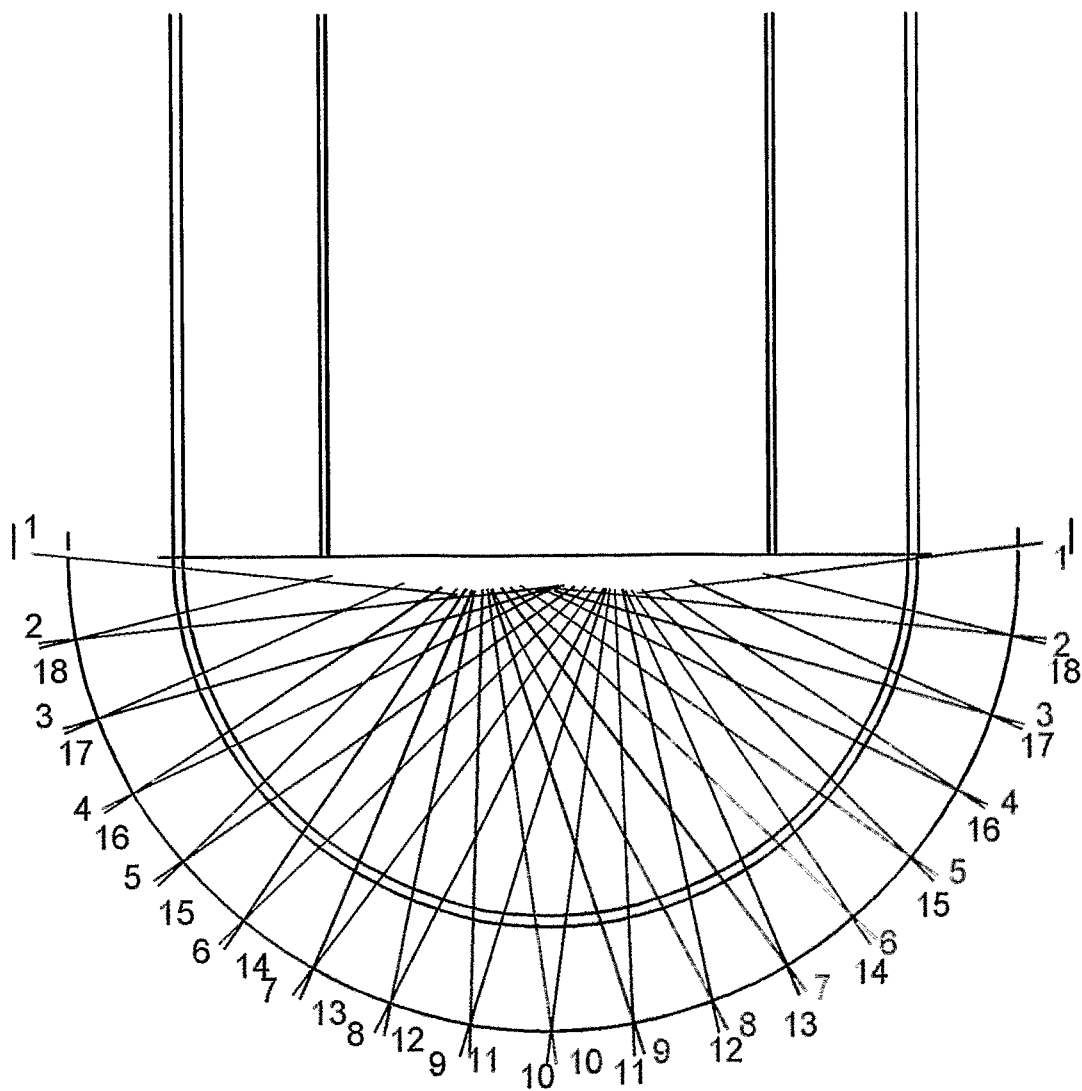
Schematic of SINQ-Target Mockup



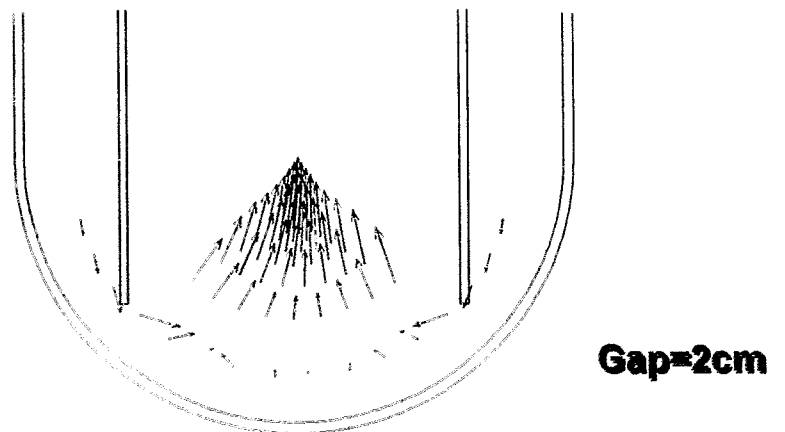
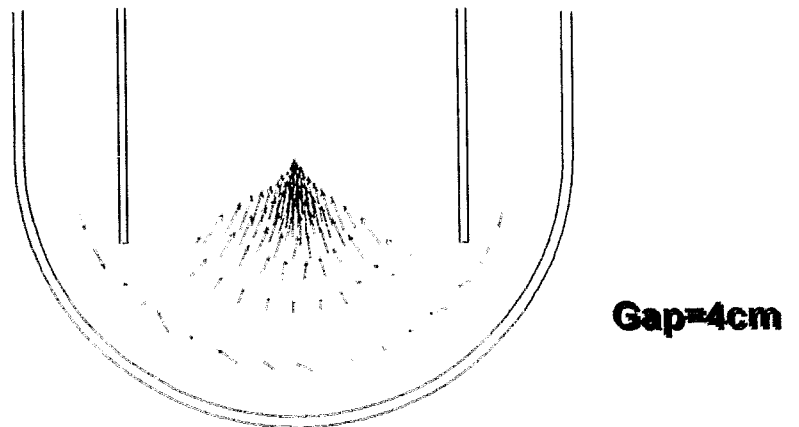
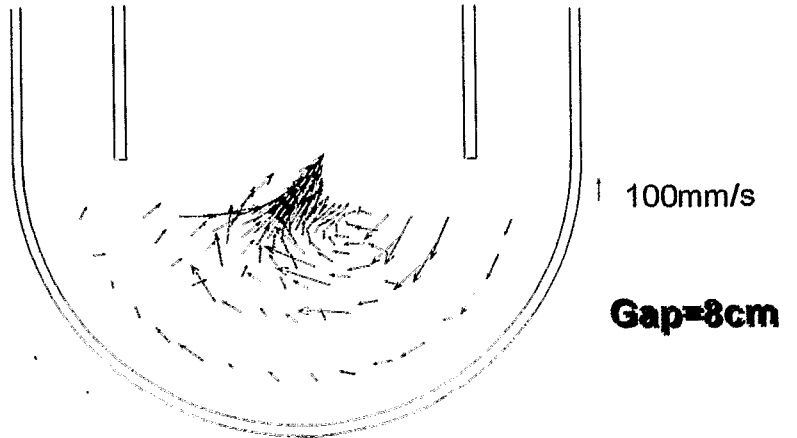
## *Transducer set up on the Window*



# Measuring line for time-averaged measurement

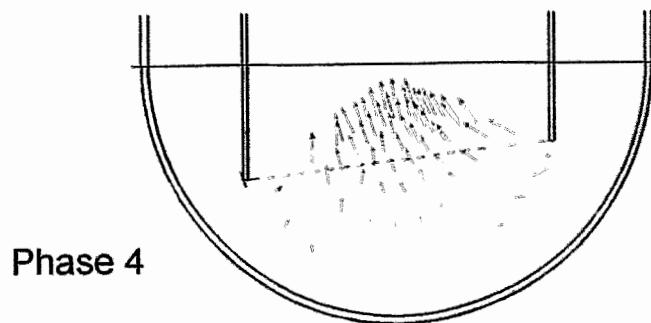
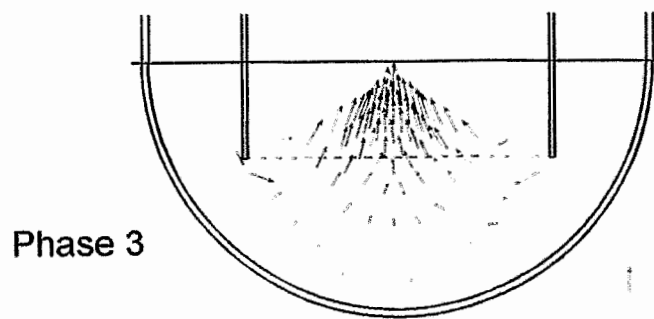
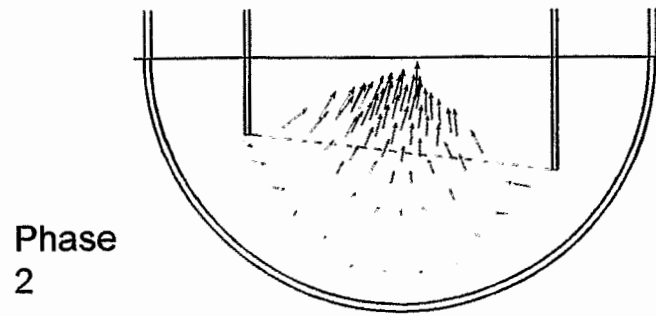
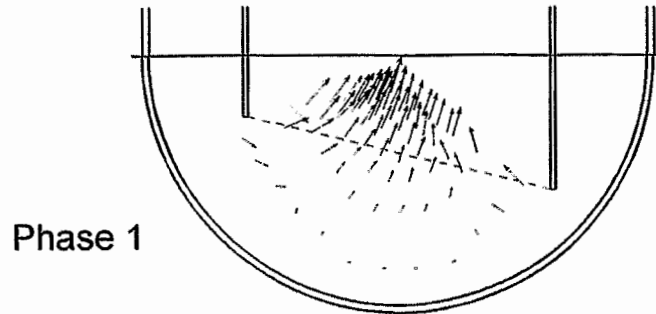


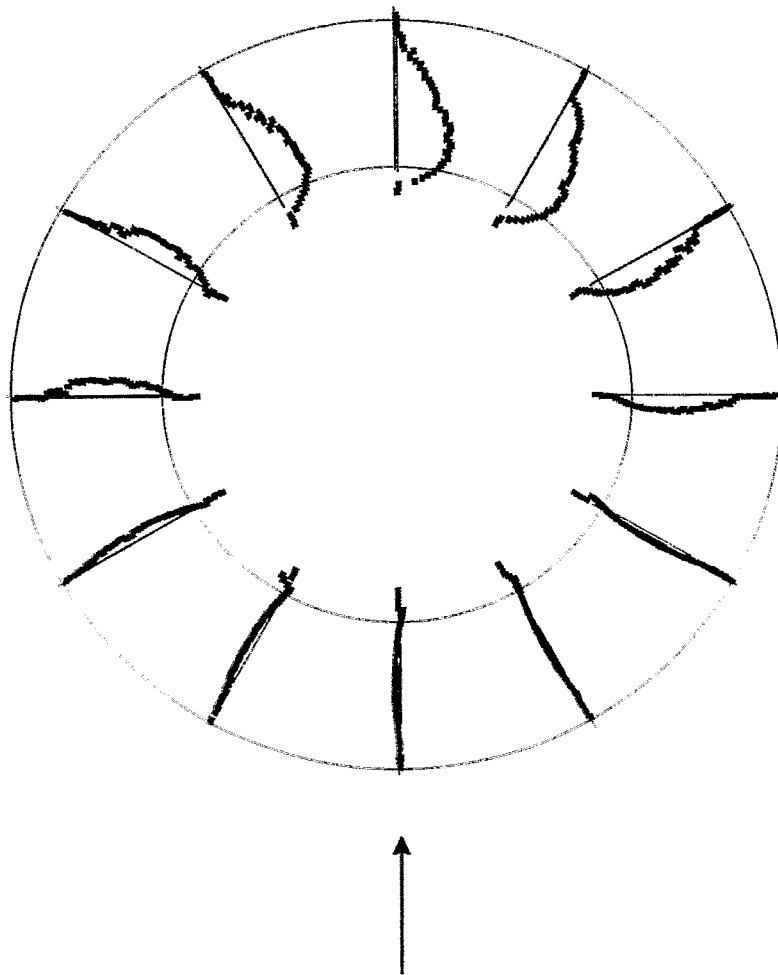
# Measured vector flow field for different gap distances





*Flow mapping (GAP 4, Q=0.6l/s)*

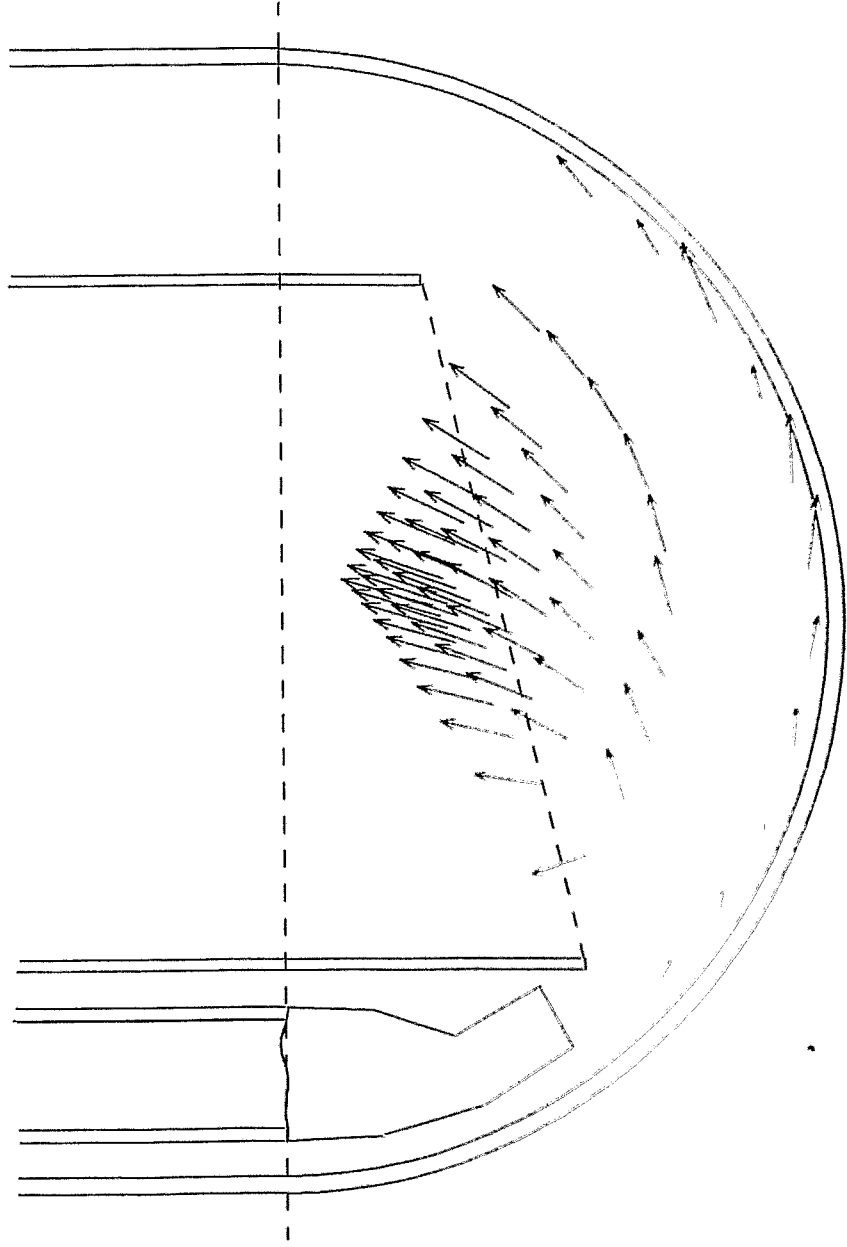




Velocity profiles of annular flow(GAP 8)

# SINQ Riga : Additional Jet

## Nozzle C2



*ULTRASONIC DOPPLER  
VELOCITY MEASUREMENTS  
IN LIQUID GALLIUM*

Daniel BRITO. Henri-Claude NATAF & Philippe CARDIN

Equipe Géodynamo  
*LGIT - Observatoire de Grenoble*  
*FRANCE*

International Workshop for Liquid metal Flows - Dresden  
October 12, 1999

# Ultrasonic Doppler velocity measurements in liquid gallium

*D. Brito, H-C. Nataf, O. Szydlo and Ph. Cardin*

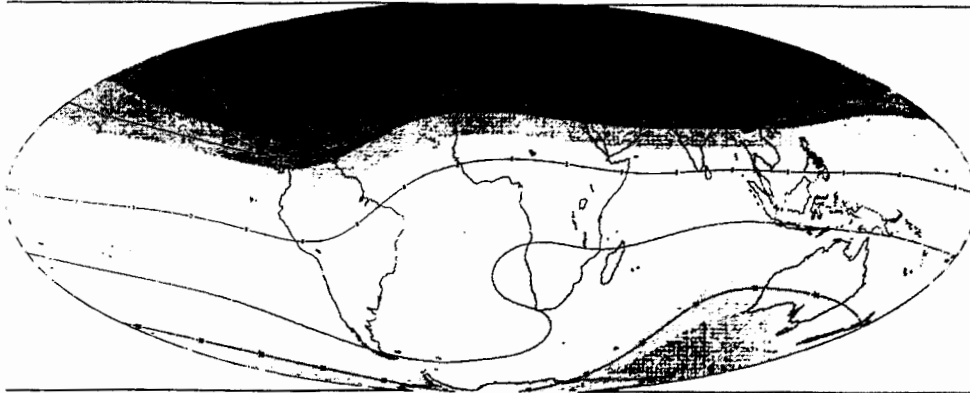
*Universite J. Fourier, LGIT-CNRS, Bat IRIGM, BP 53, 38041 Grenoble Cedex 9, France*

We have developed methods to measure flow velocities in metallic liquid gallium. We use the DOP 1000 ultrasonic Doppler apparatus from Signal Processing. Our test configuration consists in a cylinder filled with gallium. The cylinder is 80 mm in diameter and 130 mm high. A 40 mm-diameter crenelated disk spins at the top of the cylinder, with angular velocities up to 3000 rpm. 8 mm-diameter ultrasonic transducers are placed on the outside walls of the cylinder, on flat portions machined at some angle from tangent. We therefore retrieve profiles of the velocity along a line of sight that is a cord of the cylinder.

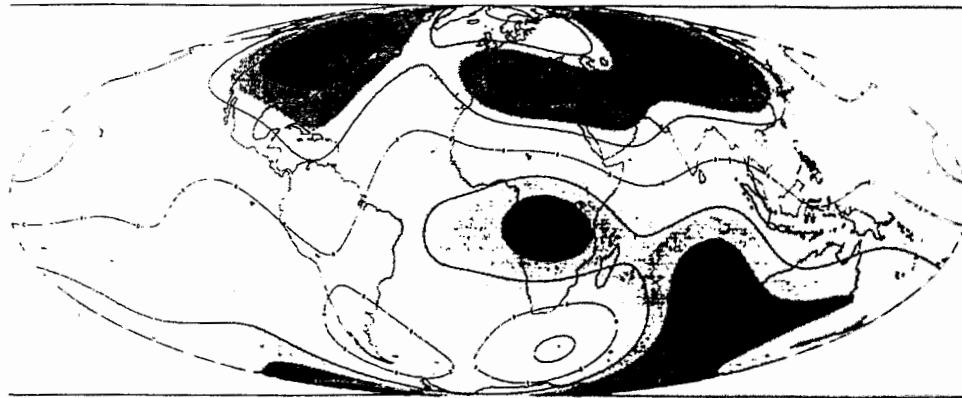
We have obtained very nice such profiles for various disk velocities. The observed bell-shaped profile is consistent with the expected flow pattern. The maximum measured velocity is proportional to the disk velocity. The profiles are perfectly superposable with profiles measured with water in the same cylinder. A comparison with velocities derived from streak photographs in water shows very good agreement.

In order to obtain profiles in liquid gallium, we have had to overcome a number of technical problems. The main problem is due to the very fast oxidation of gallium. Apparently, oxides tend to cluster on the walls of the container, thereby making it impossible for 4 MHz ultrasonic waves to probe the inside. The first step to overcome this problem is to clean the gallium with an HCl-ethanol mixture. However, once oxides stick to the walls, it is very difficult to get rid of them. We therefore had to give up using polycarbonate, nylon, and copper for the cylinder. Good and lasting results were obtained using copper coated with a cataphoretic black deposit.

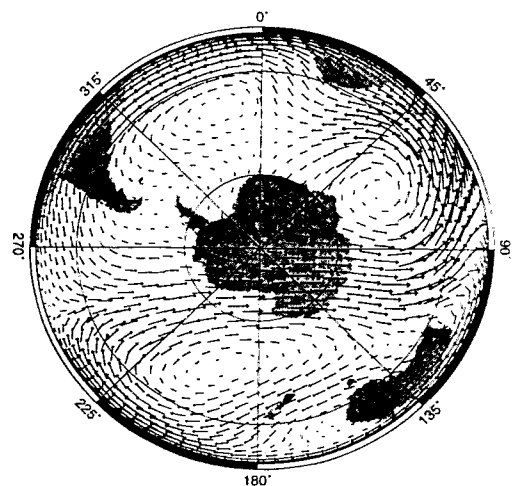
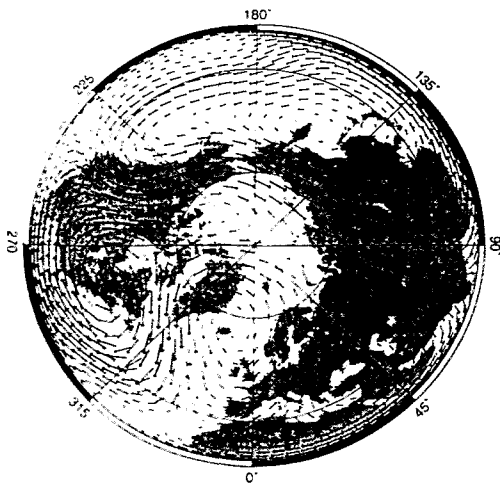
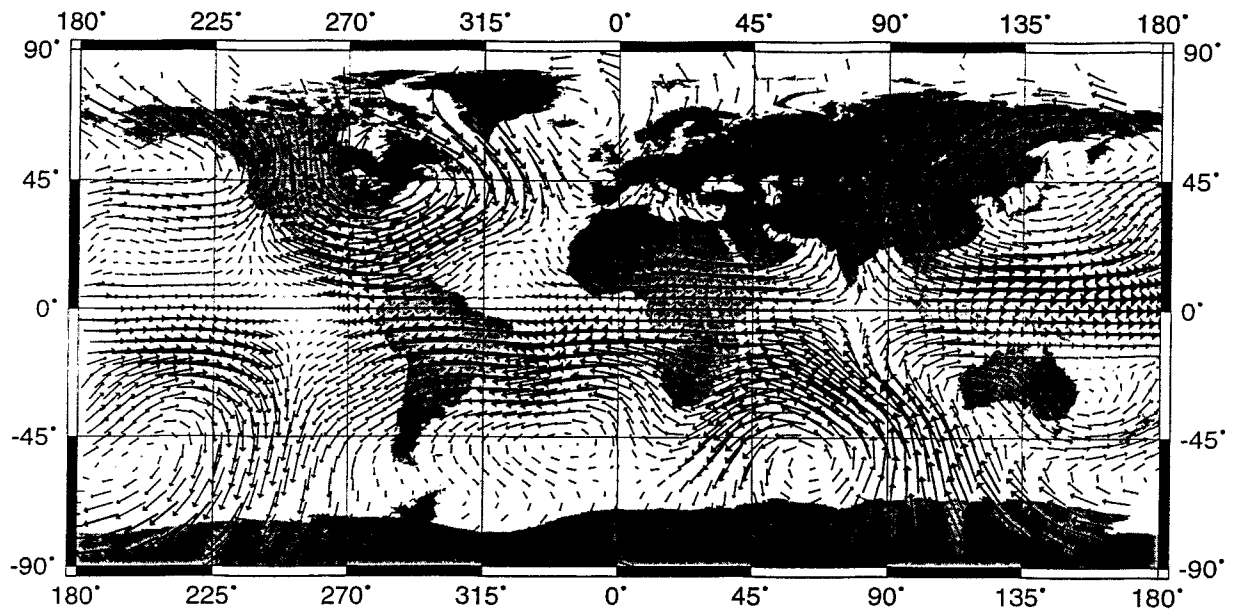
We will report on our latest results and recipes.



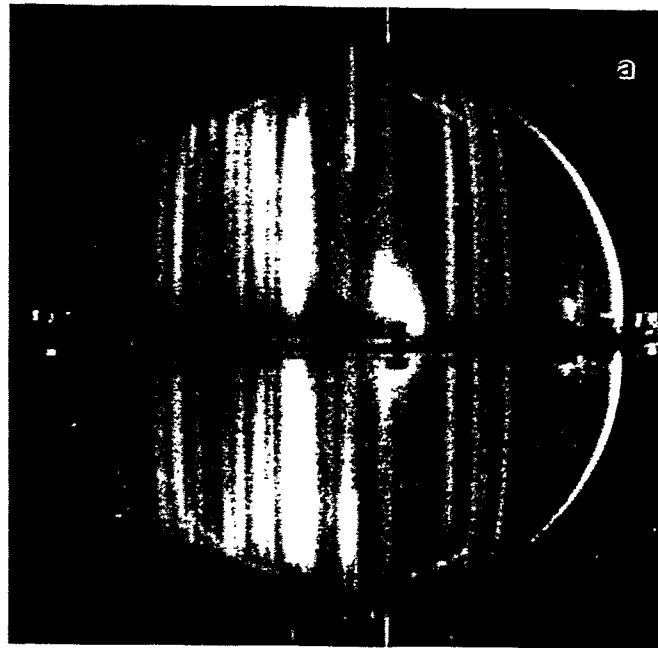
Radial component of the magnetic field at the surface of the Earth



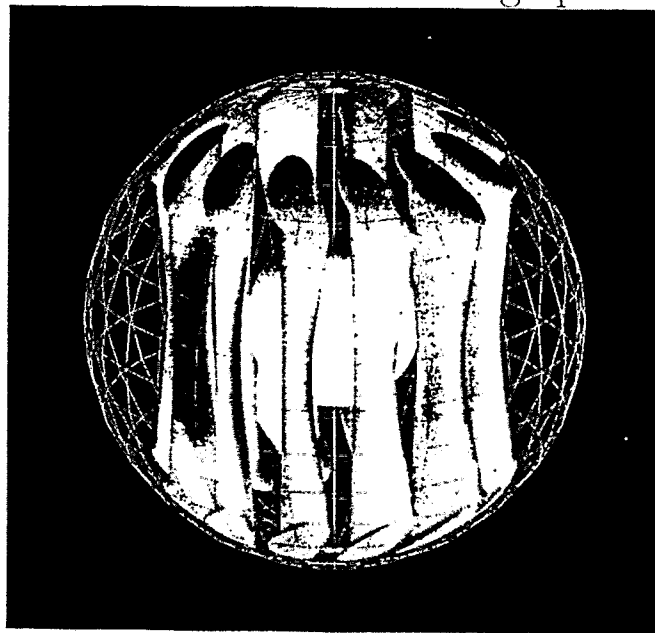
Radial component of the magnetic field at the core mantle boundary



Velocity field at the top of the Earth's Core deduced from the secular variation of the magnetic field



Thermal convection of water in a rotating sphere <sup>1</sup>

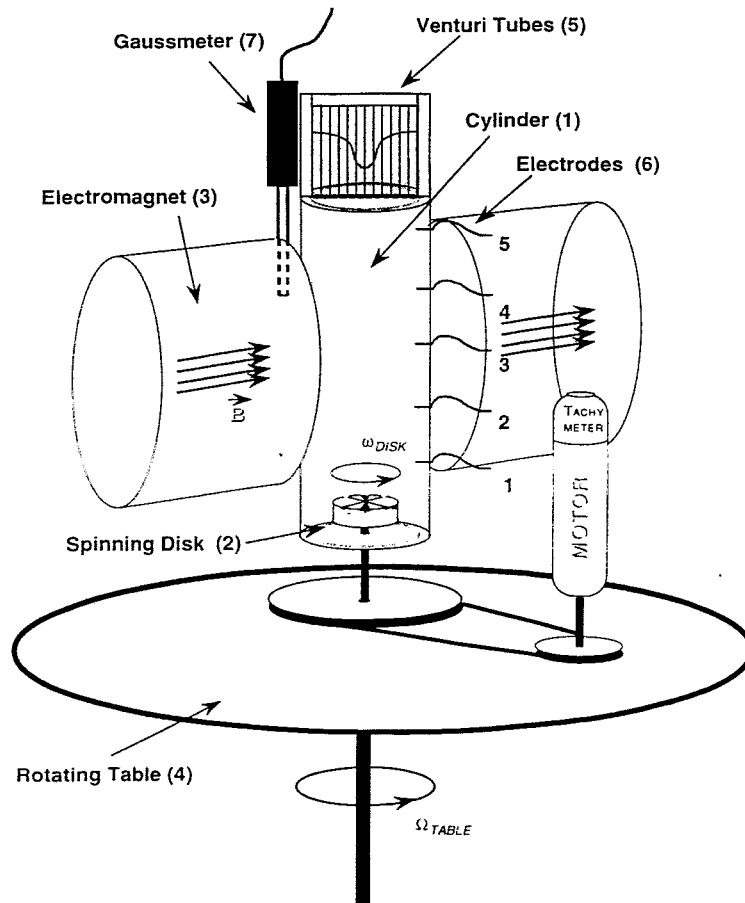


Numerical modeling of convective columns <sup>2</sup>

<sup>1</sup>Chaotic thermal convection in a rapidly rotating spherical shell: consequences for flow in the outer core. Carlini P. and P. Ois in Physics of the Earth and Planetary Interiors, 82, 235-259, 1994

<sup>2</sup>Modélisation numérique de la dynamo terrestre. E. Dormy, thèse Institut de physique du Glaci, France

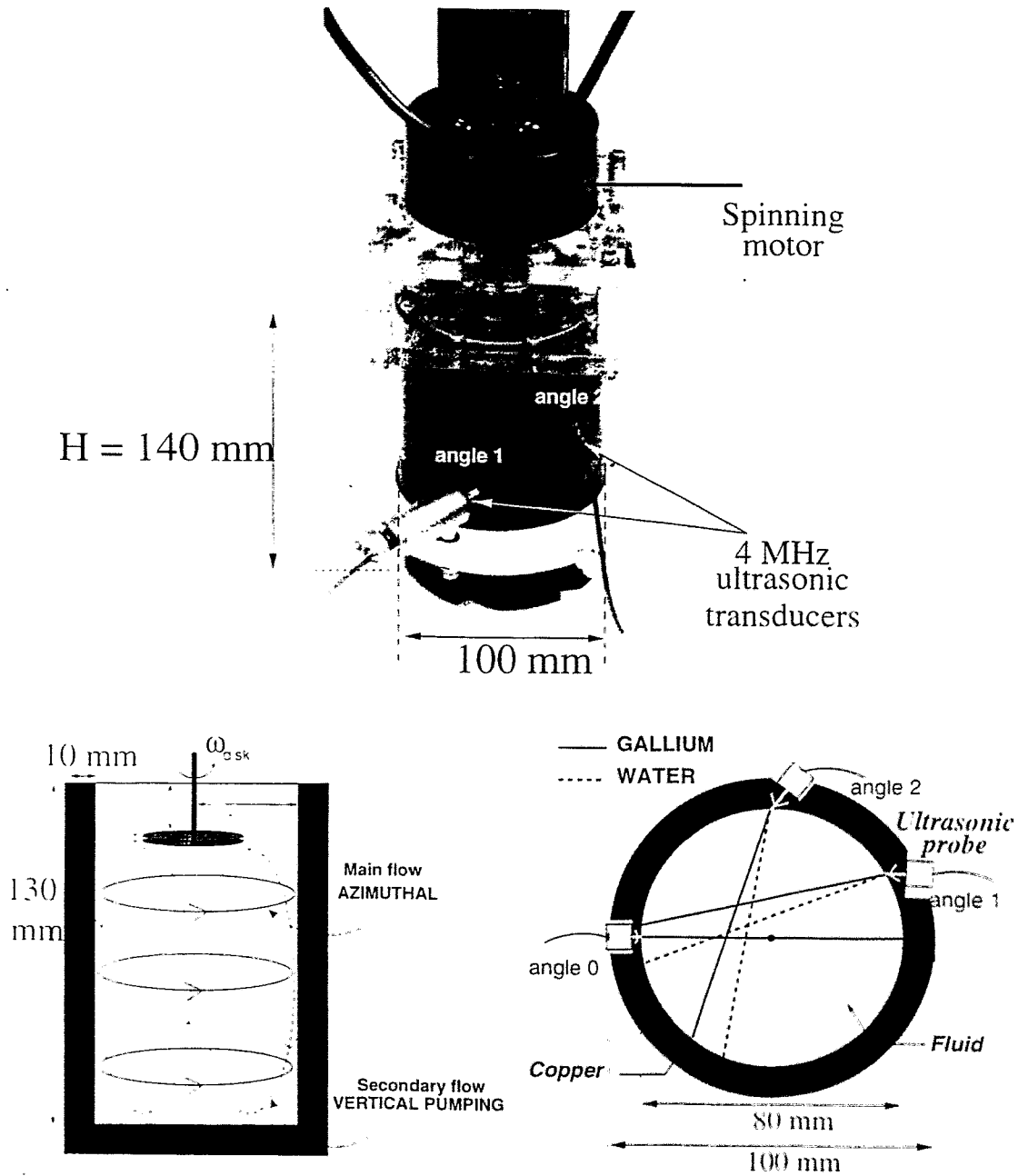




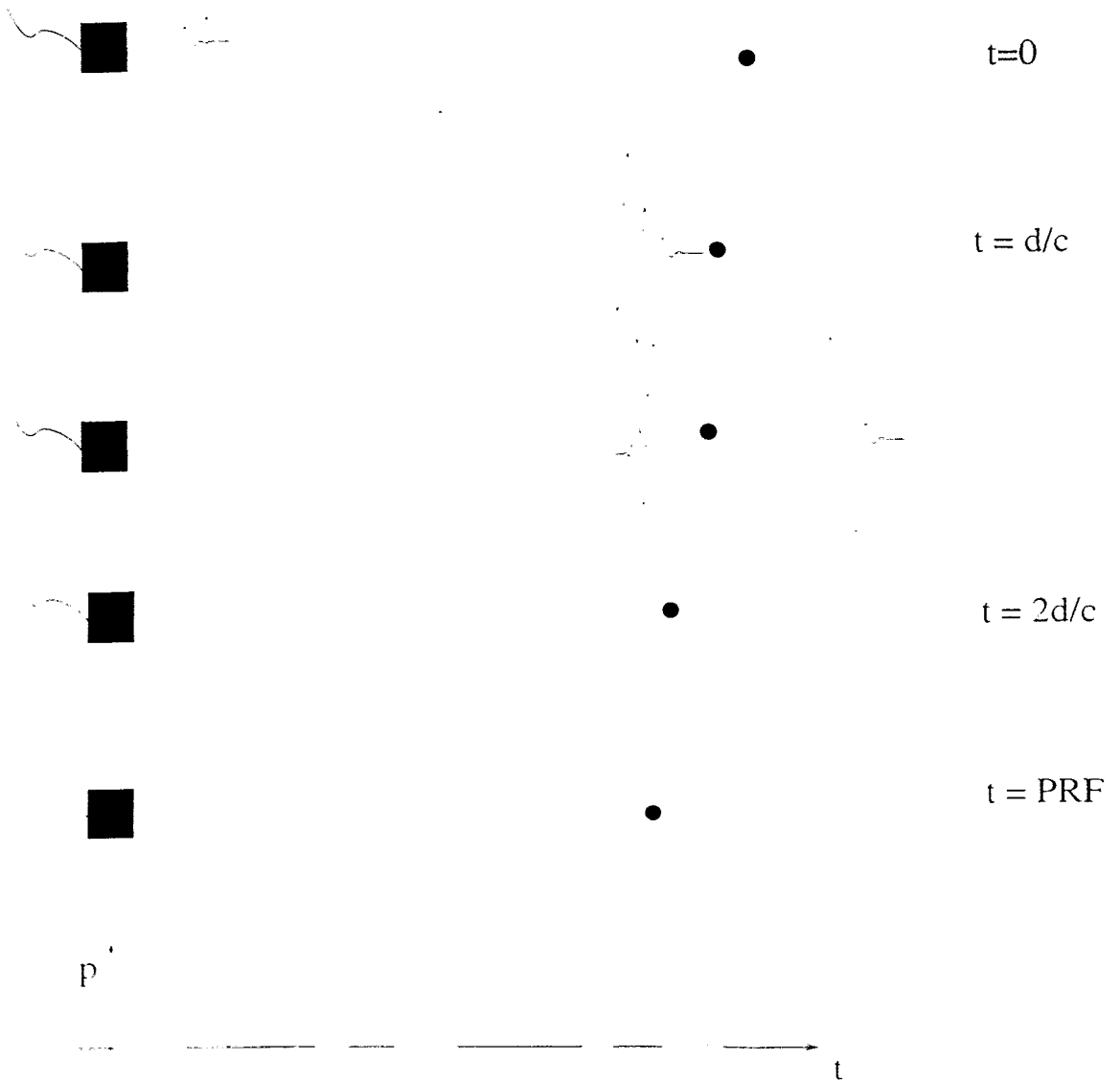
MHD experiment on a rotating table<sup>3-4</sup>

<sup>3</sup> Experimental study of a geostrophic vortex of gallium in a transverse magnetic field. Brito D., Cardin P., Nataf H.C. and G. Moret. *Physics of the Earth and Planetary Interiors*, 91, 77-98, 1995.

<sup>4</sup> Experiments on double-rotating and the intensity of the Earth's magnetic field. Brito D., Cardin P., Nataf H.C. and P. Olson. *Geophysical Journal International*, 127, 339-347, 1996.

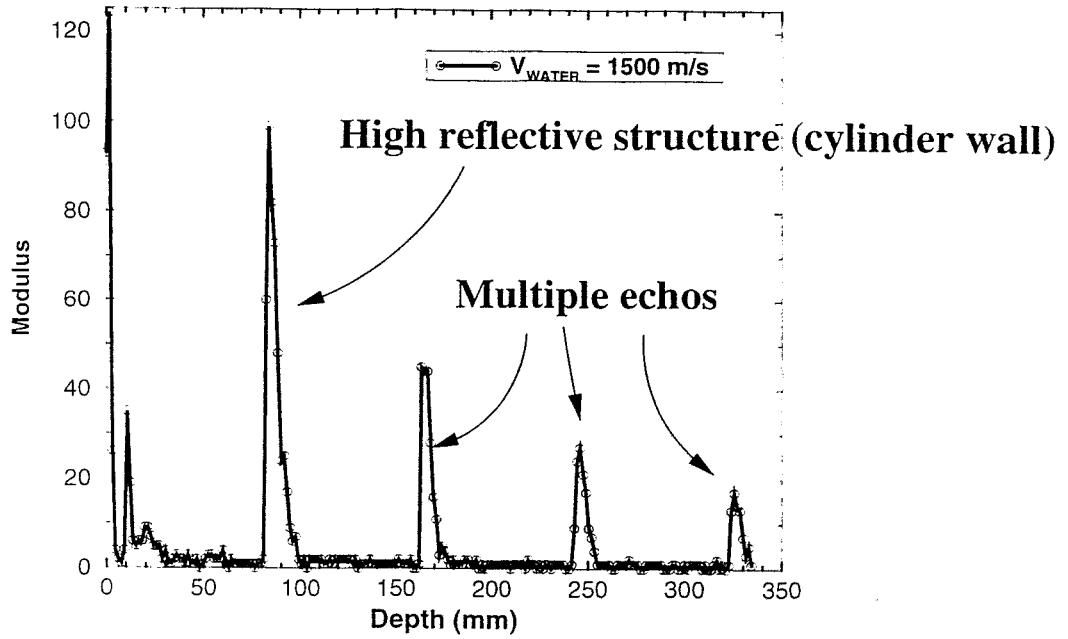


## EXPERIMENTAL SET-UP

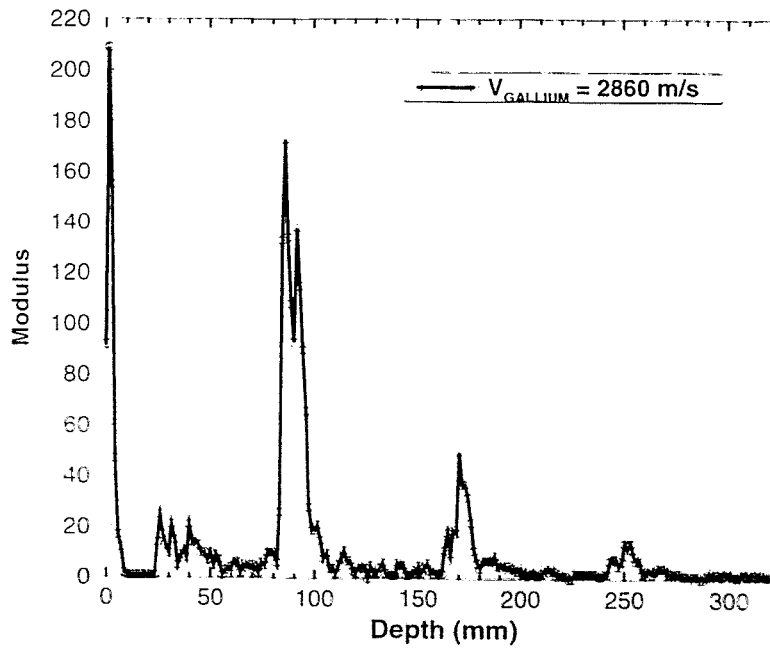


Principle of Doppler effect

### ECHO MODULUS IN WATER

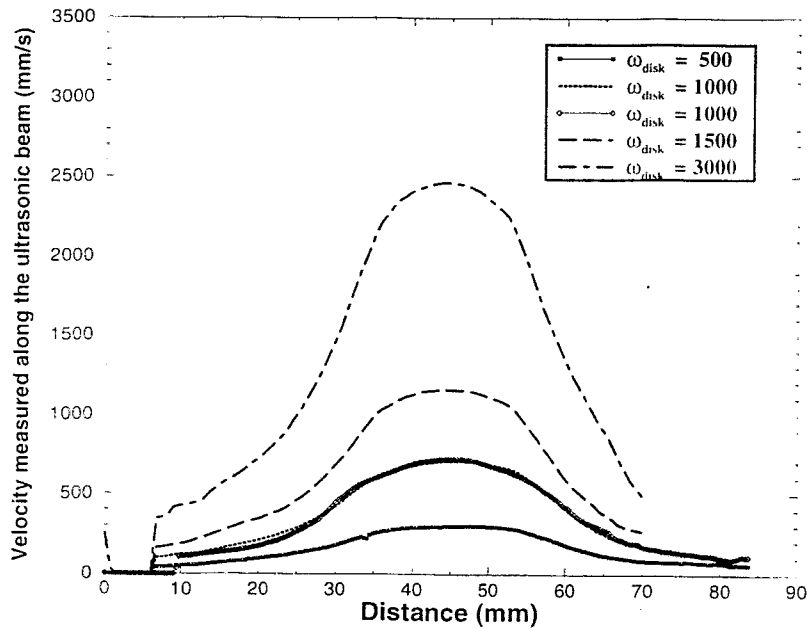


### ECHO MODULUS IN GALLIUM

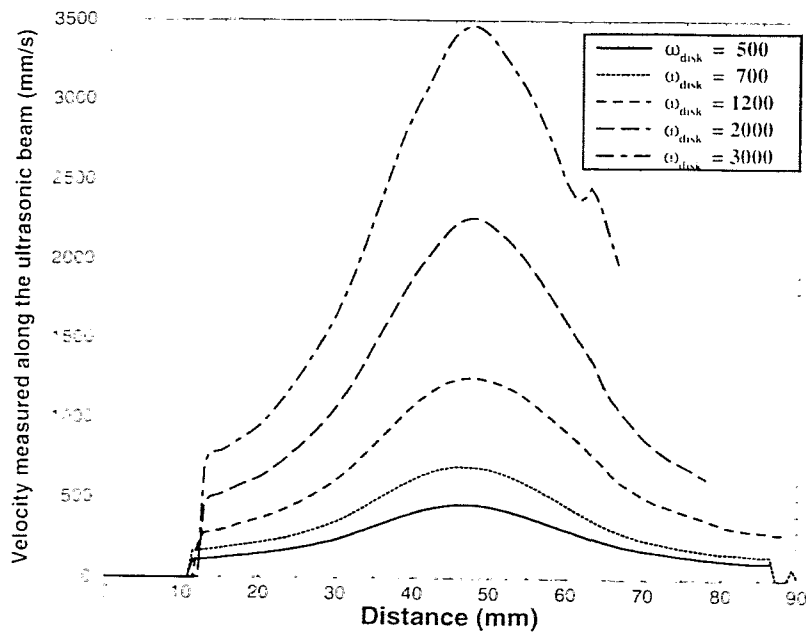


ECHO MODE

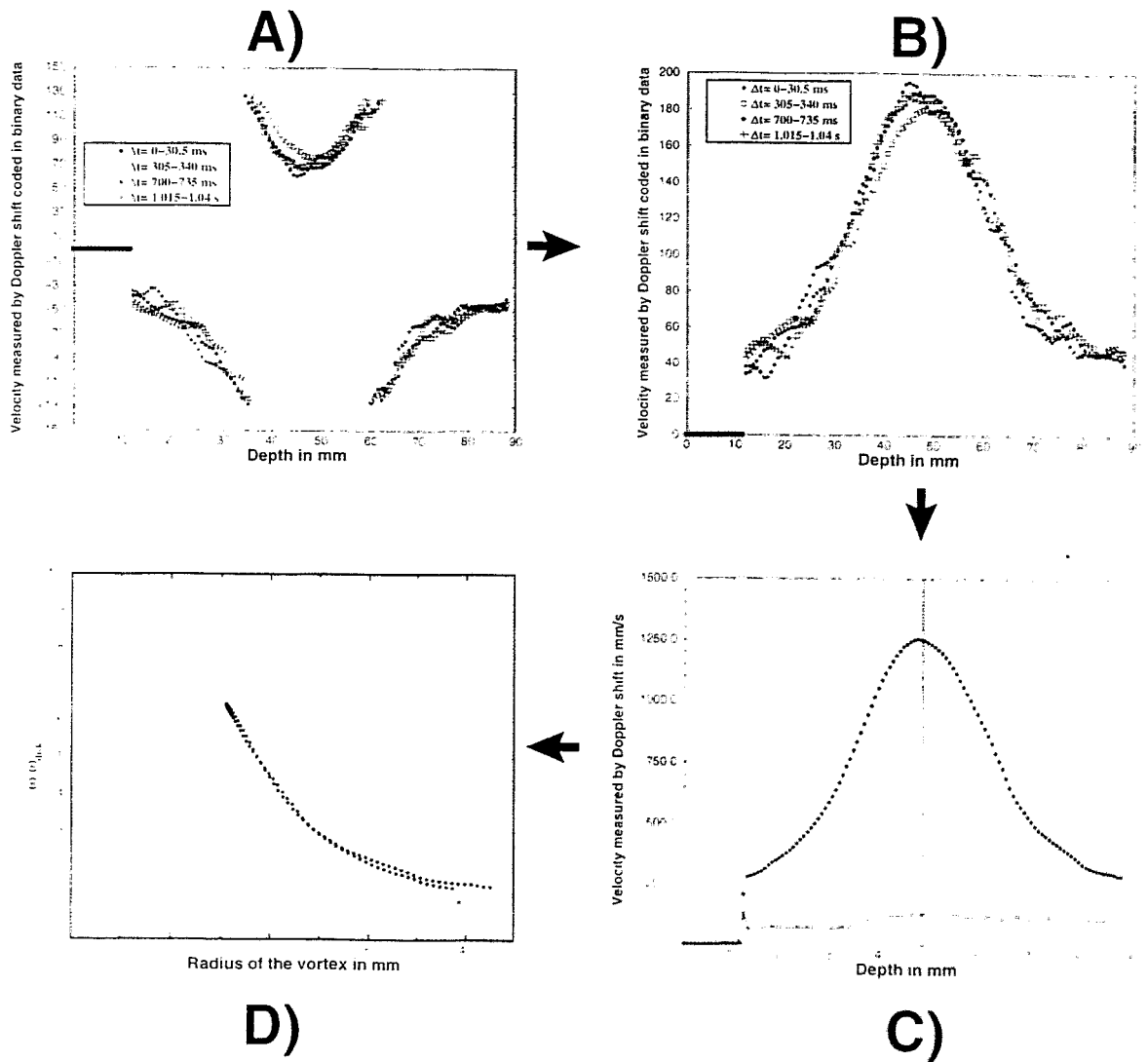
### Velocity profiles in WATER



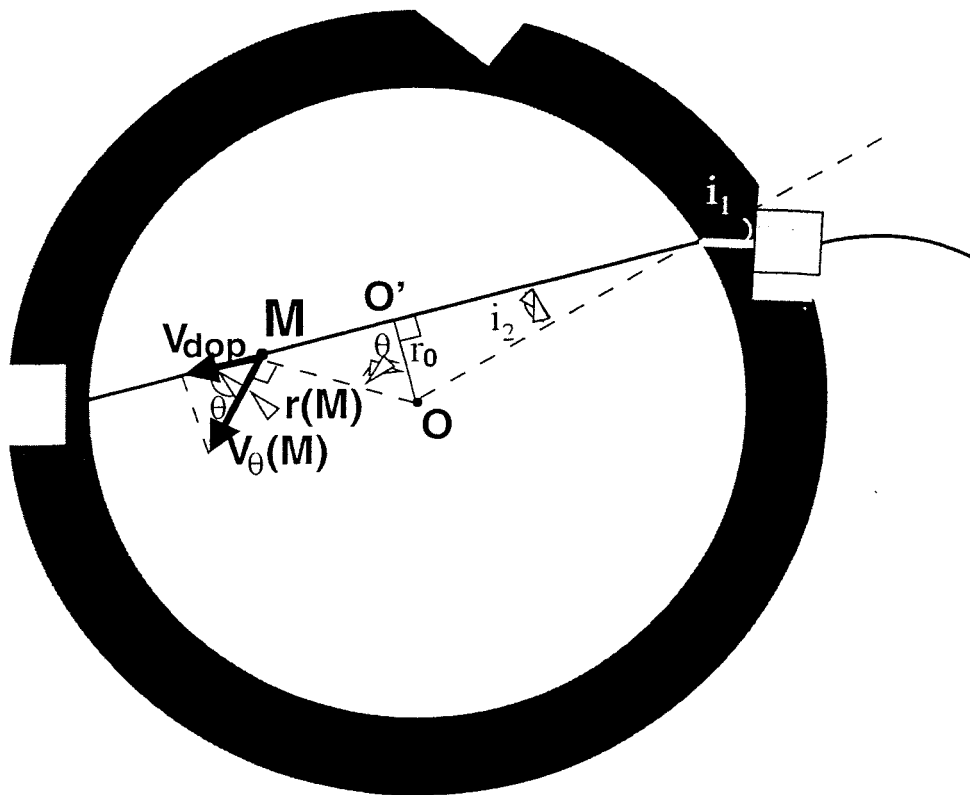
### Velocity profiles in GALLIUM



VELOCITY MODE



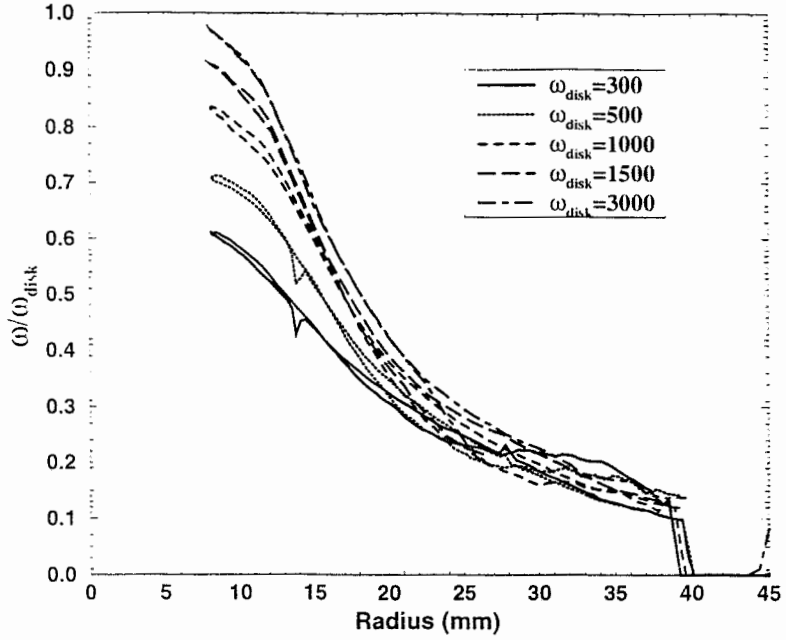
## TREATMENT OF VELOCITY PROFILES



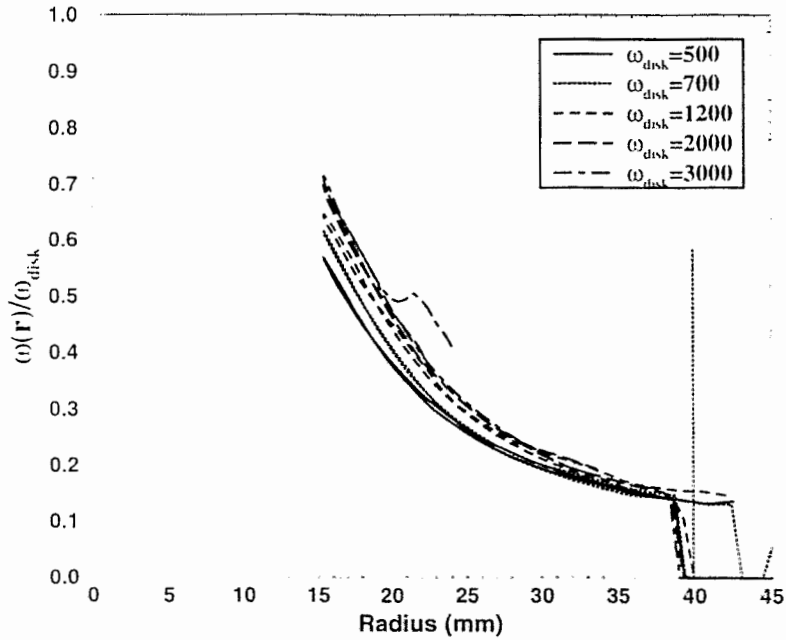
$$V_{\theta}(M) = V_{dop}(M) \cdot \frac{r(M)}{r_0}$$

DETERMINATION OF THE AZIMUTHAL COMPONENT

### Angular velocity in WATER



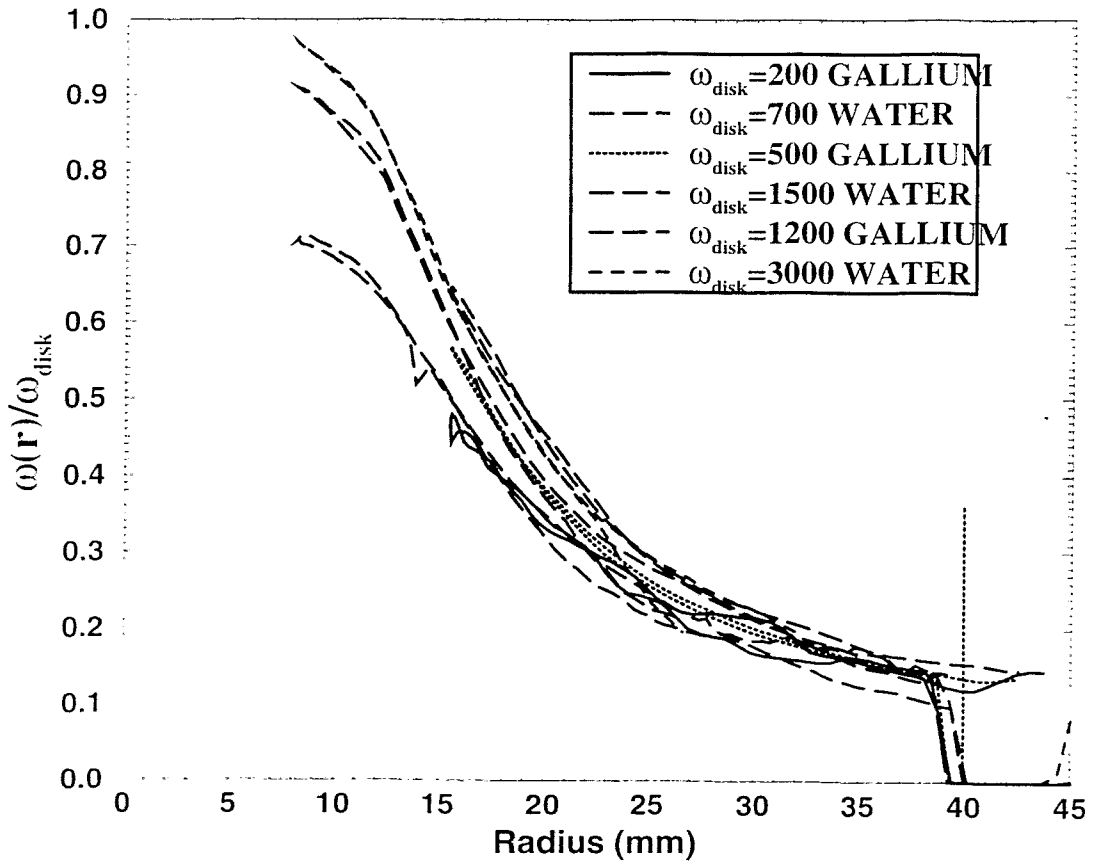
### Angular velocity in GALLIUM

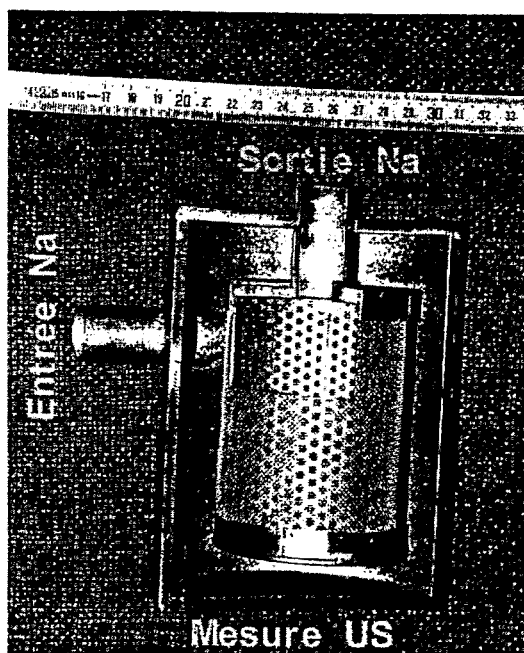


ANGULAR VELOCITY  $\omega(r)$  IN THE VORTEX

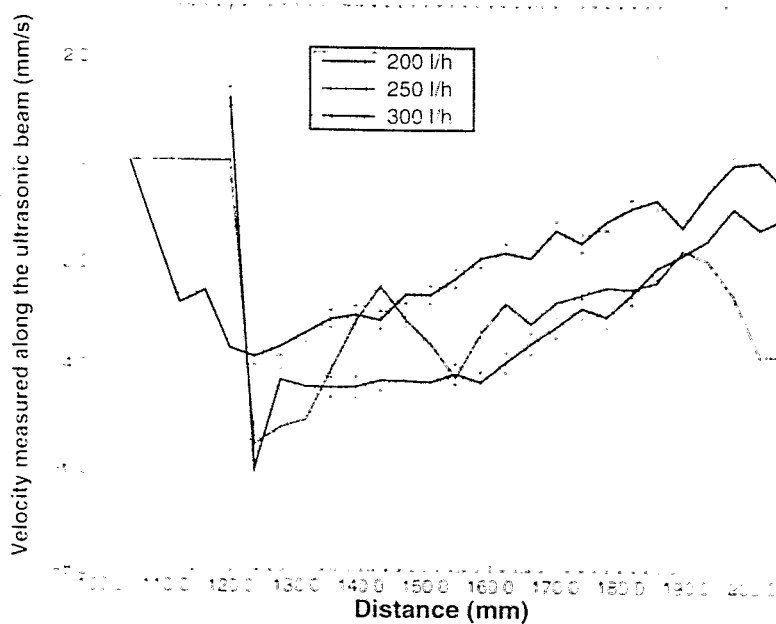


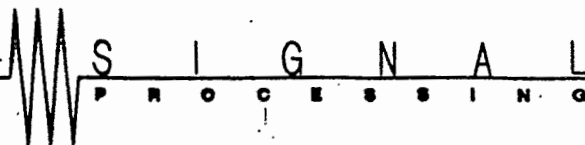
### Comparison of angular velocity in WATER and GALLIUM





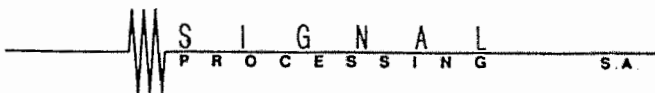
### Velocity profiles in SODIUM





# Technique and applications of pulsed ultrasonic Doppler velocimetry

Dr. J.-Cl. Willemetz



**Jean-Claude Willemetz**

Docteur ès-sciences  
Directeur

Signal Processing SA  
rue du Maupas 51  
1004 Lausanne  
Switzerland

Tel: (+41-21) 683 17 17  
Fax: (+41-21) 683 17 18  
E-mail: [jcw@signal-processing.com](mailto:jcw@signal-processing.com)  
Web: [www.signal-processing.com](http://www.signal-processing.com)

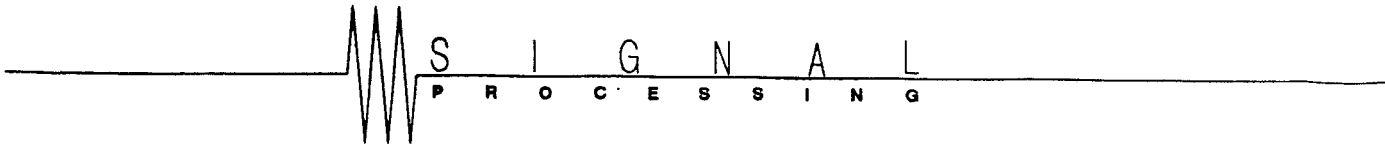
# **Ultrasonic Doppler Velocimetry applied to high temperature liquids**

*Jean-Claude Willemetz*

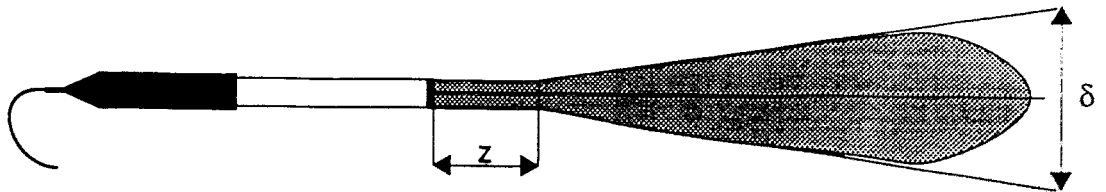
*Signal Processing Lausanne, Switzerland*

Application of ultrasonic Doppler velocimetry to high temperature liquid is today limited by some technological aspects, like the availability of high temperature ultrasonic transducers, but by also some physical aspects, like crossing wall, influences of high temperature gradient, injection of US energy into the analysed medium, type and sizes of ultrasonic reflectors. A good knowledge of the ultrasonic field is also an important aspect.

In order to profit from the main advantage of pulsed ultrasonic Doppler velocimetry, which is a depth resolution, it is of utmost importance to have a good understanding of these physical limitation. The aim of my talk is not to give solution to these problems, but to point out some of the challenges that have to be solved in order to apply high temperature ultrasonic Doppler velocimetry to real industrial applications.



## Ultrasonic field



$$z = \frac{a^2}{\lambda}$$

$$\delta = 2 \times \arcsin\left(\frac{0.61\lambda}{a}\right)$$

$a$  = radius of the transducer

$\lambda$  = wave length



**Table 1: Near field value in mm  
( $c=1500$  m/s)**

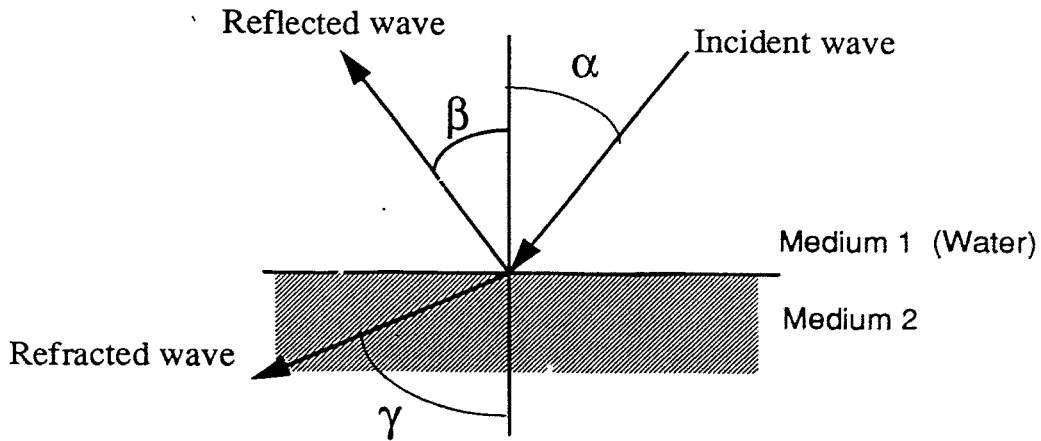
Frequency Mhz	Transducer diameter in mm							
	2	3	4	5	8	10	12	16
1	0.6	1.5	2.6	4.1	10.6	16.6	24.0	42.7
2	1.3	3.0	5.3	8.3	21.3	33.3	48.0	85.3
4	2.7	6.0	10.7	16.7	42.7	66.7	96.0	170.7
5	3.3	7.5	13.3	20.8	53.3	83.3	120.0	213.3
8	5.3	12.0	21.3	33.3	85.3	133.3	192.0	341.3
10	6.7	15.0	26.7	41.7	106.7	166.7	240.0	426.7

**Table 2: Directivity in degrees (half-angle)  
( $c=1500$  m/s)**

Frequency Mhz	Transducer diameter in mm							
	2	3	4	5	8	10	12	16
1	66.2	37.5	27.2	21.5	13.2	10.5	8.8	6.6
2	27.2	17.6	13.2	10.5	6.6	5.2	4.4	3.3
4	13.2	8.8	6.6	5.2	3.3	2.6	2.2	1.6
5	10.5	7.0	2.6	5.2	2.6	2.1	1.7	1.3
8	6.6	4.4	3.3	2.6	1.6	1.3	1.1	0.8
10	5.2	3.5	2.6	2.1	1.3	1.0	0.9	0.7



# S I G N A L P R O C E S S I N G



$$\text{refraction angle} = \gamma = \text{asin} \left( \frac{c_2 \sin \alpha}{c_1} \right)$$

Critical angle  $\alpha$  ( $\gamma=90^\circ$ )

C = Sound velocity

Z = Acoustic impedance  
( $Z = \rho c$ )

Plexiglas:  $33^\circ$       Aluminium:  $14^\circ$       Steel:  $15^\circ$

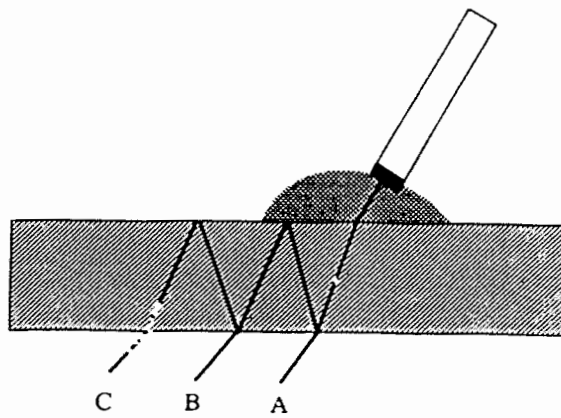
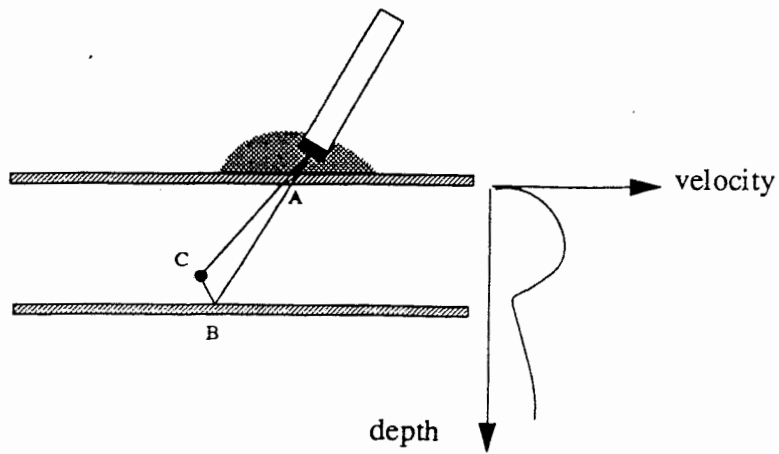
$$\text{Reflexion coefficient} = R = \frac{[z_2 \cos \alpha - z_1 \cos \gamma]^2}{[z_2 \cos \alpha + z_1 \cos \gamma]^2}$$

$$\text{Refraction coefficient} = D = \frac{4z_1 z_2 \cos \alpha \cos \delta}{(z_2 \cos \alpha + z_1 \cos \gamma)^2}$$

Examples: (medium 1 = water)

Plexiglas:	$\alpha=30^\circ$	$\gamma=66^\circ$	R= 0.42	D=0.58	$\alpha_{\max}=33^\circ$
	$\alpha=27^\circ$	$\gamma=56^\circ$	R= 0.30	D=0.69	
	$\alpha=25^\circ$	$\gamma=50^\circ$	R= 0.26	D=0.74	
	$\alpha=20^\circ$	$\gamma=38^\circ$	R= 0.20	D=0.80	
	$\alpha=25^\circ$	$\gamma=18^\circ$	R= 0.15	D=0.85	
Steel:	$\alpha=14^\circ$	$\gamma=69^\circ$	R= 0.95	D=0.047	$\alpha_{\max}=15^\circ$
	$\alpha=12^\circ$	$\gamma=53^\circ$	R= 0.92	D=0.077	
	$\alpha=10^\circ$	$\gamma=42^\circ$	R= 0.90	D=0.094	
	$\alpha=8^\circ$	$\gamma=32^\circ$	R= 0.89	D=0.11	
	$\alpha=4^\circ$	$\gamma=15^\circ$	R= 0.88	D=0.12	

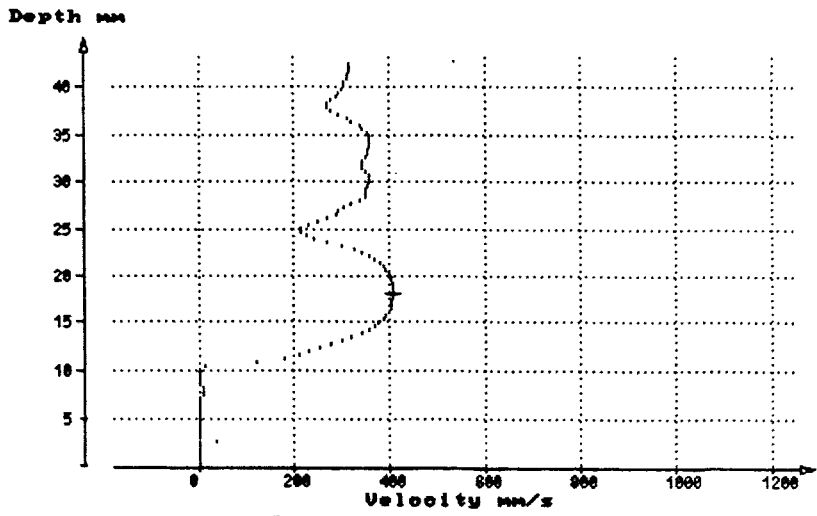
# Wall effects





S I G N A L  
P R O C E S S I N G

Velocity profile in a tube  
Plexiglas tube: wall thickness 13 mm, 4 MHz, high Doppler angle (73 degrees)



B: Gate

C: Used value

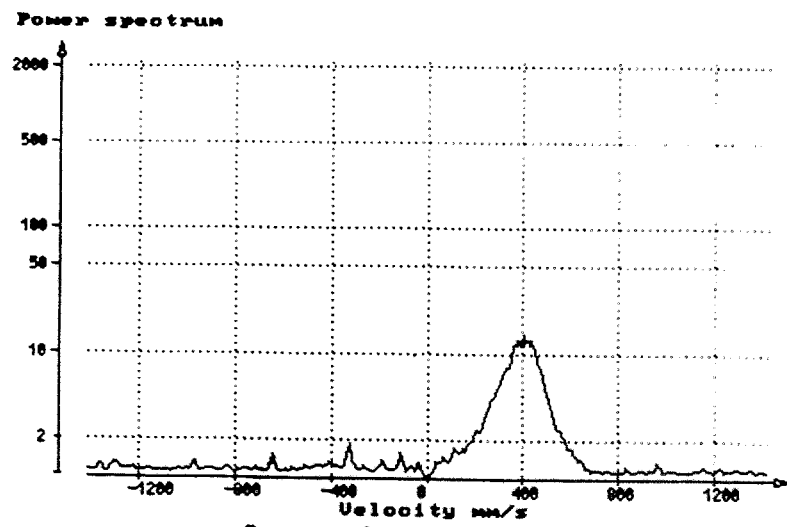
E: Display Profile

Status  
PRF: 198mm .264us  
Resolution .3mm .5us  
Sound speed 1500 m/s  
Angle: 0  
Profile: 28  
Buffer: full

Cursor 1  
Depth : 18.0 mm  
Size : .3 mm  
Mean : 404.8 mm/s  
St. dev. : 22.0 mm/s

Cine mode  
File: F\_PRO2.DOP  
VER: 5.17 T2

FFT of one channel placed in the middle



B: Cursor On/Off

C: FFT average

Status  
PRF: 198mm 264us  
Resolution .3mm .5us  
Sound speed 1500 m/s  
Angle: 0  
Profile: 28  
Buffer: full

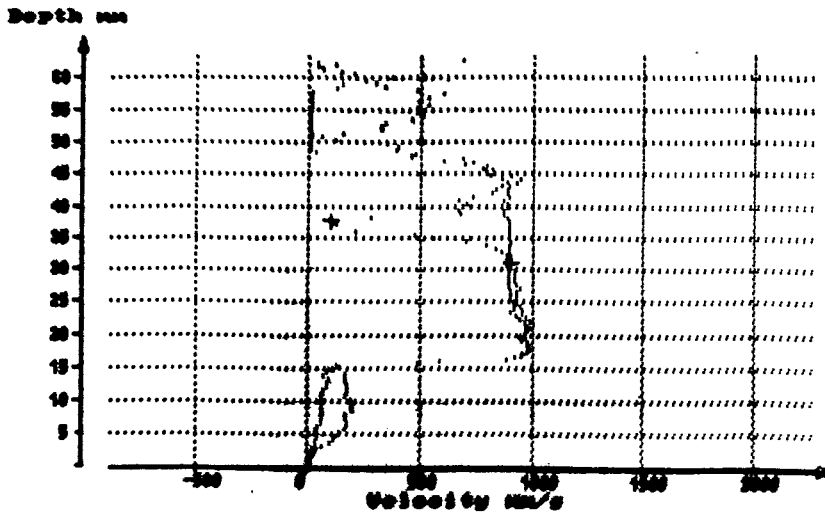
Cursor 1  
Velocity : 410 mm/s  
Power : 13

Cine mode  
File: I\_FFTB1.DOP  
VER: 5.17 T2



# S I G N A L P R O C E S S I N G

## Rotating cylinder, 8 MHz Influence of an external perturbation



Cine mode  
File: C\_FT00.DOP  
VER: 8.17 T2

Cursor 1	
Depth	19.0 mm
Size	1.0 mm
Mean	100.1 mm/s
St. dev.	15.2 mm/s

B: Gate

C: Used value  
64 profile

D: Display  
Profile

Status

PRF: 96.4mm 176us

Resolution .5mm 1.0us

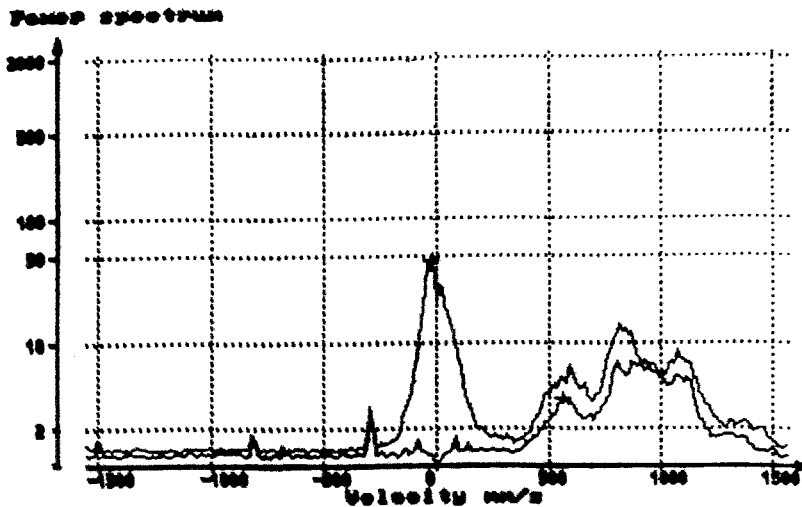
Sound speed 1500 m/s

Angle: 47

Profile: 59

Buffer: full

## FFT of one channel placed at the location of the perturbation



Cine mode  
File: C\_FFT02.DOP  
VER: 8.17 T2

Cursor 1	
Velocity	1580 mm/s
Power	165

B: CURSOR  
On/Off

C: FFT average

Status

PRF: 96.4mm 176us

Resolution .5mm 1.0us

Sound speed 1500 m/s

Angle: 47

Profile: 60

Buffer: full



## Conclusions

- Measurements through walls are possible but a careful analysis of the measurement have to be realized
- A good understanding of the ultrasonic in field is a required
- Advance real-time processing capabilities of the measuring instrument allows to detect and analyze artifacts
- New real-time processing technic would allows to extend the capabilities of the ultrasonic Doppler velocimeter

## Scientific Programme

**October 13, 1999 (Wednesday)**

### **Morning Session**

- 9.30 *S. Makarov, R. Ludwig, D. Apelian (Worcester Polytechnic Institute, USA)*  
Electromagnetic detection and optical visualization techniques for non-metallic inclusions in molten metal
- 9.50 *B. Fischer, U. Hilburger, J. Friedrich, G. Müller (University Erlangen, Germany)*  
Temperature and velocity analysis in vertical melt cylinders under the influence of rotating magnetic fields and buoyant convection
- 10.10 *Y.-S. Lee, Ch.-H. Chun (Pohang University of Science and Technology, South Korea)*  
Spatio-Temporal Temperature Measurement in Liquid Metal of a Rotating System
- 10.30 Coffee break
- 10.50 *P. Dold and K.W. Benz (University of Freiburg, Germany)*  
Flow Velocities in Liquid Gallium as a Function of an Applied Rotating Magnetic Field
- 11.10 *A. Bojarevics, Y. Gelfgat (Institute of Physics Riga, Latvia)*  
*Y. Fautrelle (EPM-MADYLAM Grenoble, France)*  
Limitations of permanent magnet incorporated potential difference probe for liquid metal flow
- 11.30 *B. Dumont (IRSID Metz, France)*  
*R. Haettel, J. Hamburger, R. Bolcato, J. Etay (EPM MADYLAM Grenoble, France)*  
A Resistive Probe for Continuous Measurement of Electroconductive Liquid Level faced to Electromagnetic Fields
- 11.50 *S. Khripchenko, S. Denisov, V. Dolgikh (Institute of Continous Media Mechanics Perm, Russia)*  
Electrovortex Flow in Flat Channels
- 12.10 Round table discussion, Concluding remarks

## **Electromagnetic detection and optical visualization techniques for non-metallic inclusions in molten metall**

*Sergey Makarov, Reinhold Ludwig<sup>1</sup>, and Diran Apelian*

*Metal Processing Institute, Department of Mechanical Engineering,  
<sup>1</sup>Electrical and Computer Engineering Department,  
Worcester Polytechnic Institute, Worcester, MA 01609-2280.*

The role of detecting non-metallic and weakly-conducting inclusions in hot melts is of major importance during the manufacturing process in that every aspect of quality is affected by the presence of secondary phases. However, the weak link is how one quantitatively determines the level of inclusions. In this paper, we present a theoretical model and preliminary experimental results for a magnetic force-based detection system to monitor small inclusions of micron-size. The idea is to force these non-conducting inclusions to a detection location (the free melt surface) by electromagnetic Archimedes forces. Further, an optical imaging system can then be applied to detect them visually. The theoretical modeling efforts include the force model, the surface concentration model, and the escape model of the submerged inclusions.

The developed technique potentially has the best resolution performance when compared to other on-line methods. The application area includes hot melts of metals and other high-conductive non-transparent fluids. Low-temperature experimentation with liquid gallium has been conducted to prove this nondestructive measurement concept.

# Electromagnetic Detection and Optical Visualization Techniques for Non-Metallic Inclusions in Molten Metals

Sergey Makarov, Reinhold Ludwig, Diran Apelian  
and Joshua Resnik

Metal Processing Institute

WPI, Worcester, MA 01609, USA

October 12, 1999

International Workshop on  
Measuring Techniques for Liquid Metal Flows (MTLM)

Dresden, Germany



## Sensor concept - General

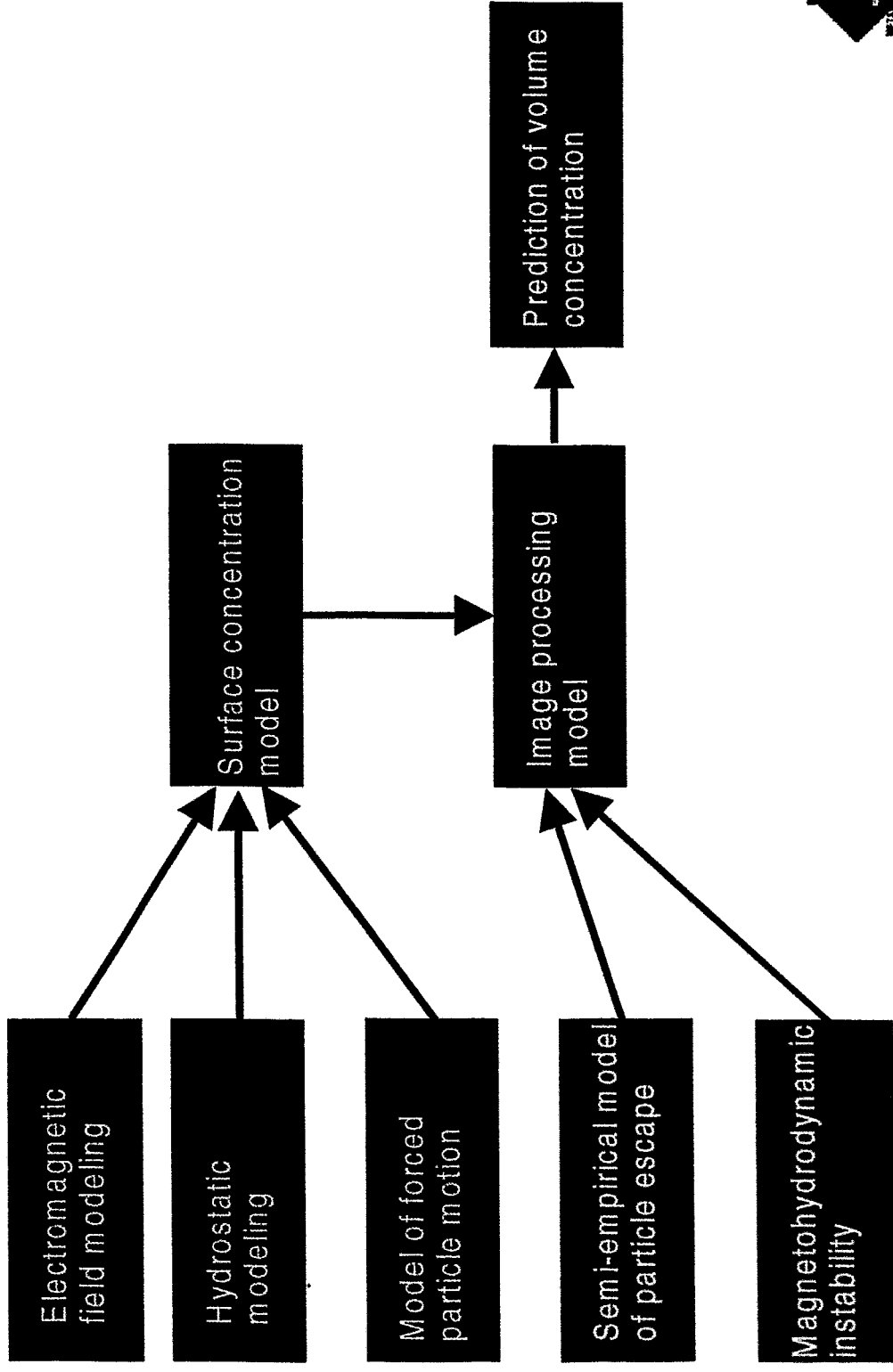
---

- High Lorentz force density is created in a small volume
- As a reaction to this force particles are moved to an inspection location: free melt surface
- Melt surface is appropriately conditioned to improve detection
- Particles are counted and classified using an optical image system



# Sensor concept - Theory

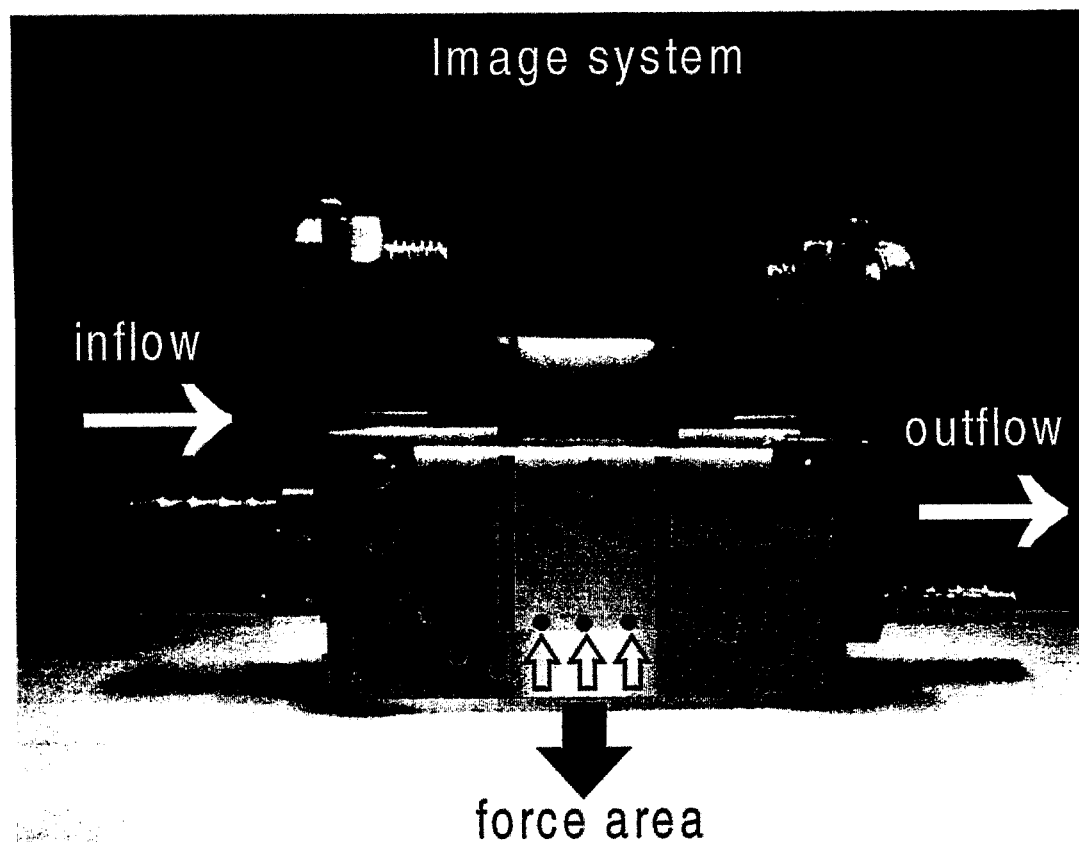
---





# Sensor concept - Close-up view

---



- Lorentz force density is created by a DC current and a super-imposed magnetic flux density vector field



## Sensor concept - Forced particle motion (a)

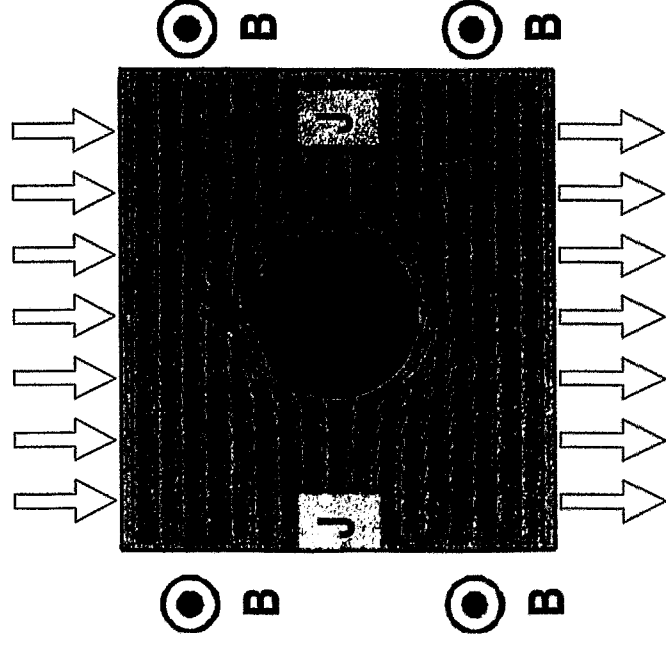
---

- The Lorentz force density  $\mathbf{f}$  in the inspection volume is 10-100 times the gravitation force density on liquid metal

- Archimedes electromagnetic force density is the opposite of  $\mathbf{f}$

$$\mathbf{f}_a = -\phi \mathbf{f}, \phi = \frac{3}{2} \frac{\sigma - \sigma_i}{2\sigma + \sigma_i}$$

- Particles of lower conductivity are pushed upwards with "rise velocity"  $u$ .



## Sensor concept - Forced particle motion (b)

---

- Particle motion from the rest state at small and moderate Reynold's numbers

$$m \dot{u} = -\frac{v}{2} \rho_f \dot{u} - \frac{1}{2} C_D \rho_f s u^2 + v f_a + \frac{3}{2} \sqrt{\pi \rho_f \eta} \int_{-\infty}^t \frac{du/d\tau}{\sqrt{t-\tau}} d\tau$$

$m$  = inclusion mass,  $s$  = inclusion projected area,  $v$  = particle volume,  $\eta$  = shear viscosity

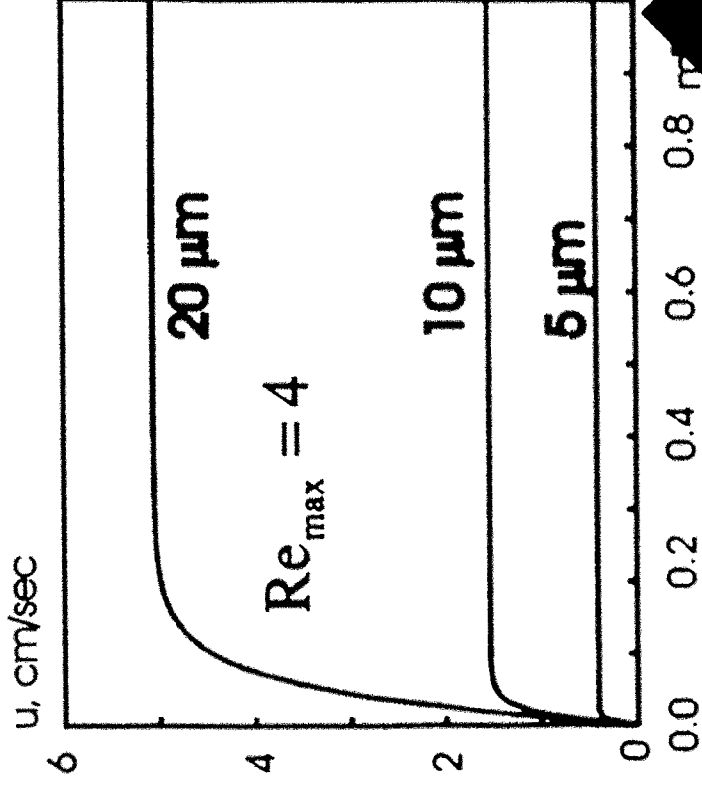
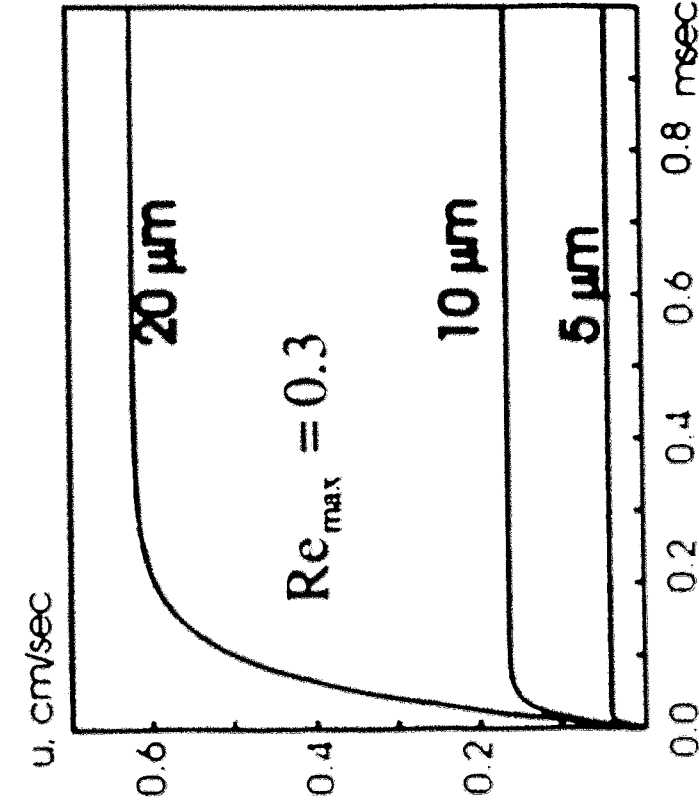
- Drag coefficient (Schiller and Naumann,  $Re = \rho_f du/d\eta < 800$ )

$$C_D = \frac{24}{Re} (1 + 0.15 Re^{0.687})$$



## Sensor concept - Forced particle motion (c)

- Rise velocity (SiC particle in Ga; present force density is  $6 \times 10^5 \text{ N/m}^3$ )
- Rise velocity (SiC particle in Ga; desired force density is  $6 \times 10^6 \text{ N/m}^3$ )



# Sensor concept - Particle escape (a)

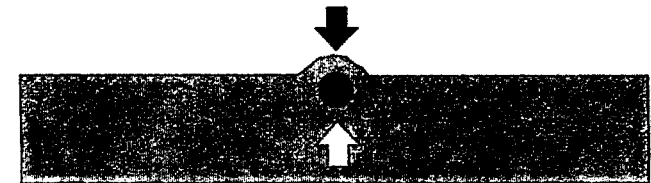
- Surface tension hinders escape

Liquid	$\sigma$ , N/m
Ga (50 °C)	0.706
Al (800 °C)	0.850
Water (20 °C)	0.073

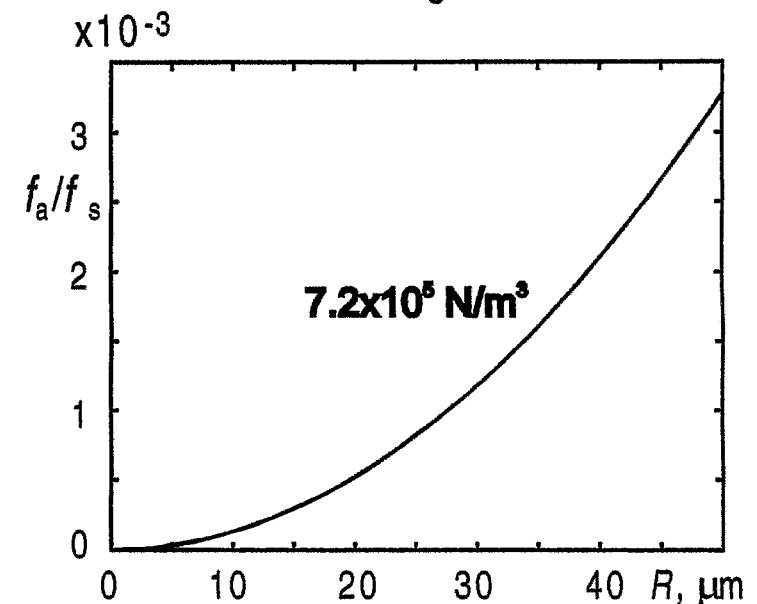
- Lorentz force density is too small to guarantee escape:

$$\frac{f_a}{f_s} = \frac{3/4 v f}{\pi d \sigma} \ll 1$$

Surface tension force



Electromagnetic force

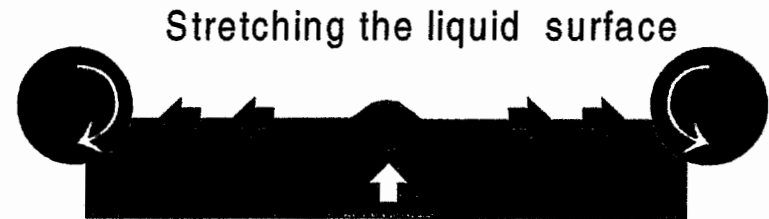


# Sensor concept - Particle escape (b)

---

- Additional mechanism is necessary to enable particle escape on the free surface

- Mechanical breakdown



- Acoustic breakdown

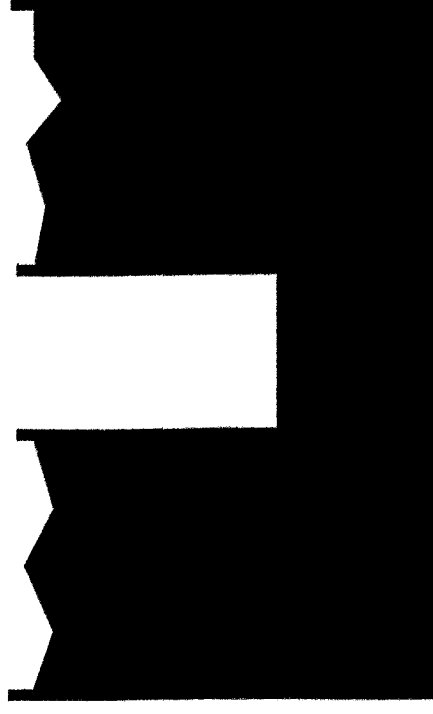
Shaking the liquid surface (16-30 Hz)



## Sensor concept - Magnetohydrodynamic instability

---

- Instability of a liquid metal surface appears after switching on the current
  - The oscillation frequencies are 3-20 Hz
  - The instability is much lower in the central section
- 



- First possible mechanism: vortex velocity fluctuation
- Second possible mechanism: magnetohydrodynamic instability of the free surface in the alternating EM field



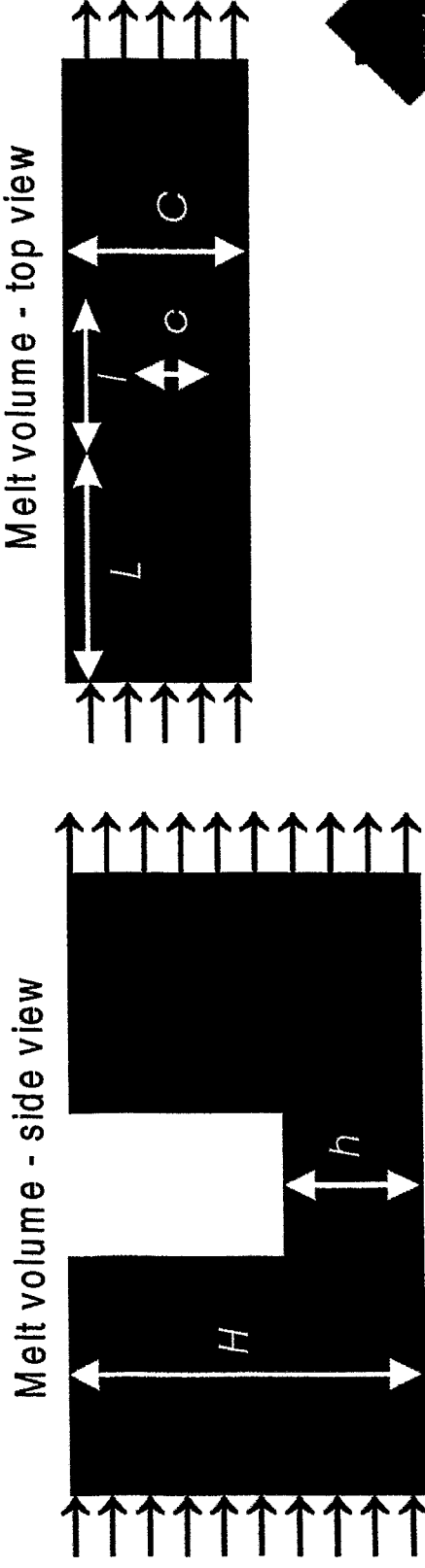
# Sensor concept - Hydrostatic modeling

---

- Higher Lorentz force density in the central section creates a lower metal level
- Melt level adjustment; useful formula:

$$H - h = \frac{IB}{\rho_f g} \left[ \frac{1}{c} - \frac{1}{C} \right]$$

$I$  = total current,  $B$  = magnetic field,  $\rho_f$  = melt density



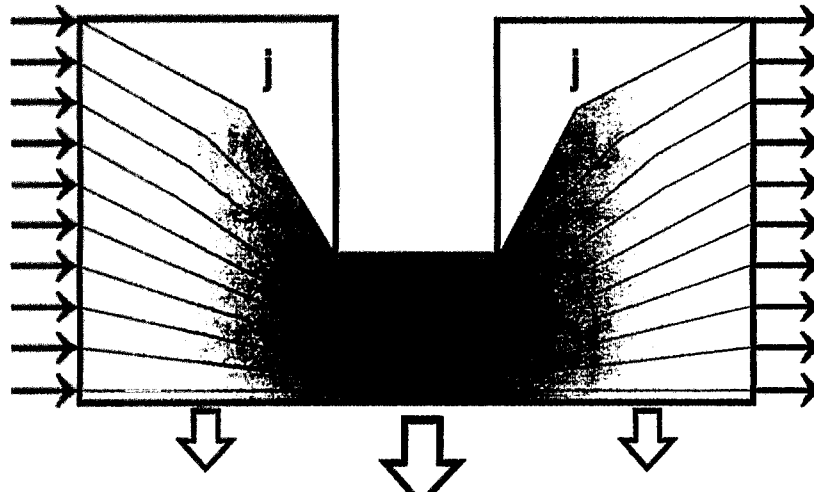


# Sensor concept - Electromagnetic modeling

- Magnetic and electric field calculations (Green's function approach, FEM)
 
$$\mathbf{f} = \mathbf{j} \times \mathbf{B}, \mathbf{B} \approx \mathbf{B}_0, \mathbf{j} = -\sigma \nabla \phi$$

$$\nabla \nabla \phi = 0, S: \partial \phi / \partial \mathbf{n} = \left\{ \begin{array}{l} 0 \\ \mathbf{j}_0 / \sigma \end{array} \right\}$$
- Current/force density appears nearly uniform in the central section

Current(force) density - side view



Current(force) density - top view

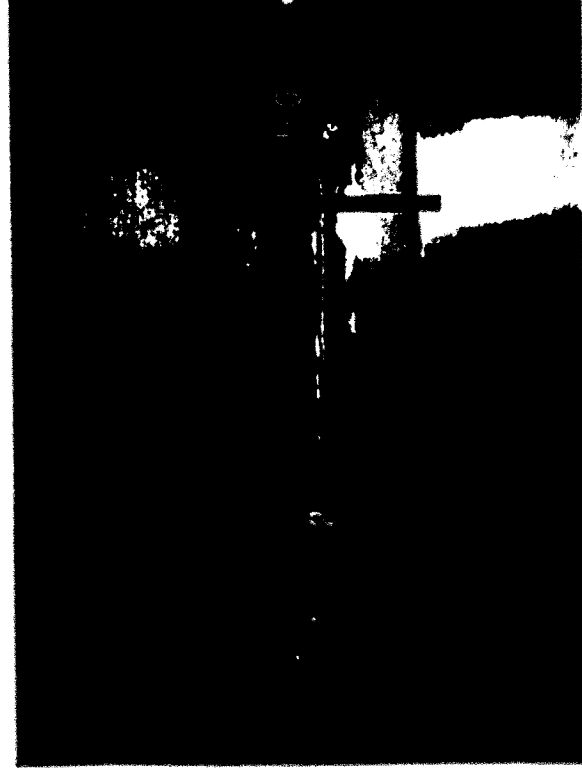


# Sensor concept - Proof

---

- Proof of the sensor concept for large ceramic particles

No current



Current is switched on



# Experimental setup: General comments

---

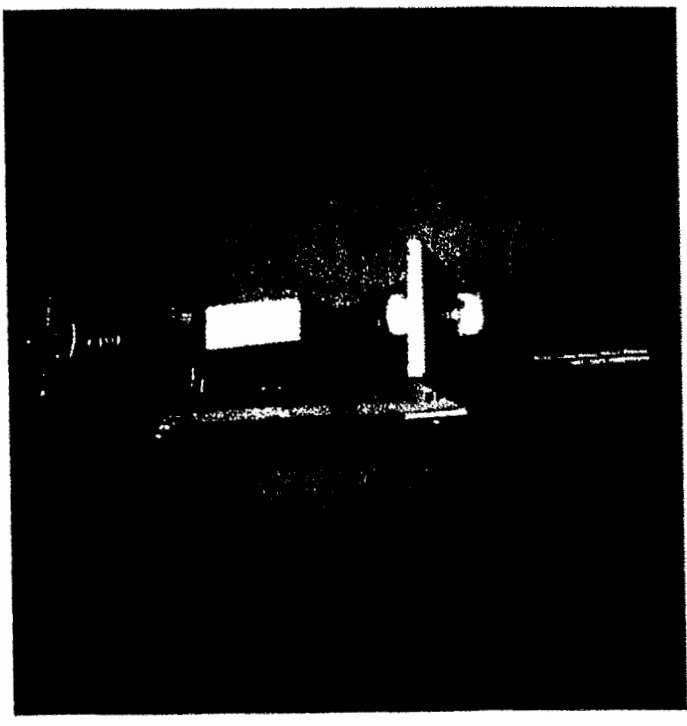
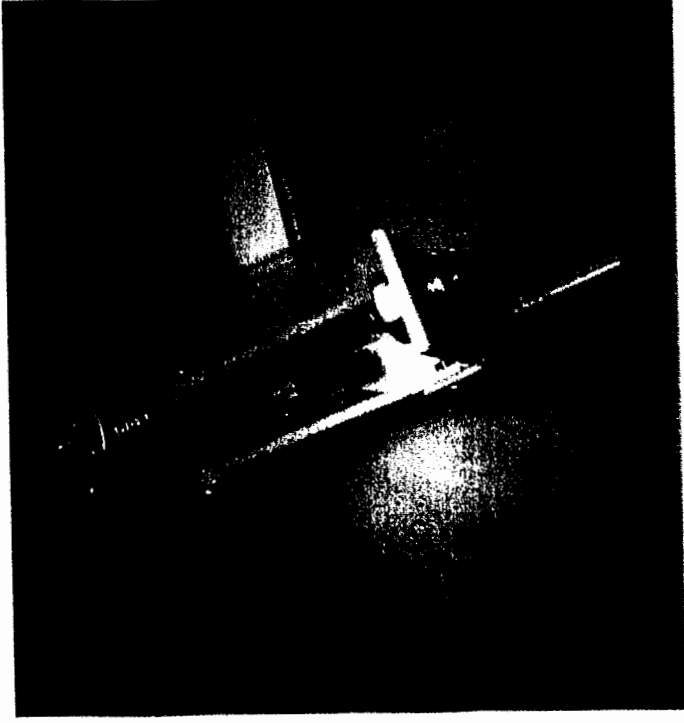
- Low-temperature modeling: **liquid gallium** with a melting point of 30° C
- Total current is 120 A; current density in the sensing domain of **0.5 cm<sup>2</sup>** cross-section is **2.4x10<sup>6</sup> A/m<sup>2</sup>**
- Lorentz force density in the sensing domain is **6x10<sup>5</sup> N/m<sup>3</sup>**
- Magnetic flux density in the sensing domain is **0.25 Tesla**



# Experimental set-up: Container

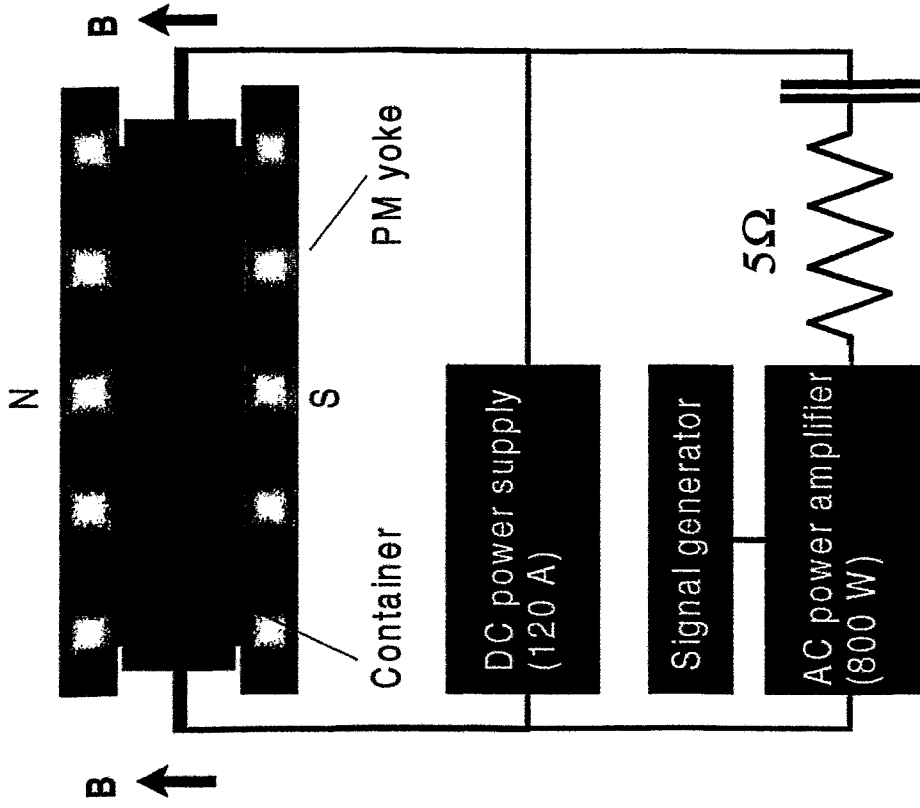
---

- Includes: two electrodes, central section, and ceramic roller

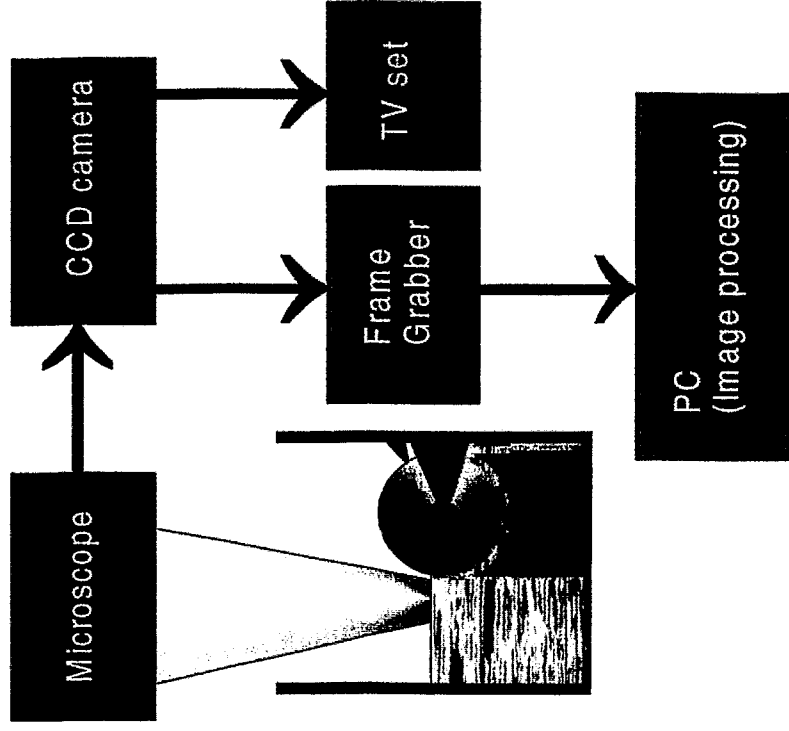


# Experimental setup: System overview

## Electric Scheme

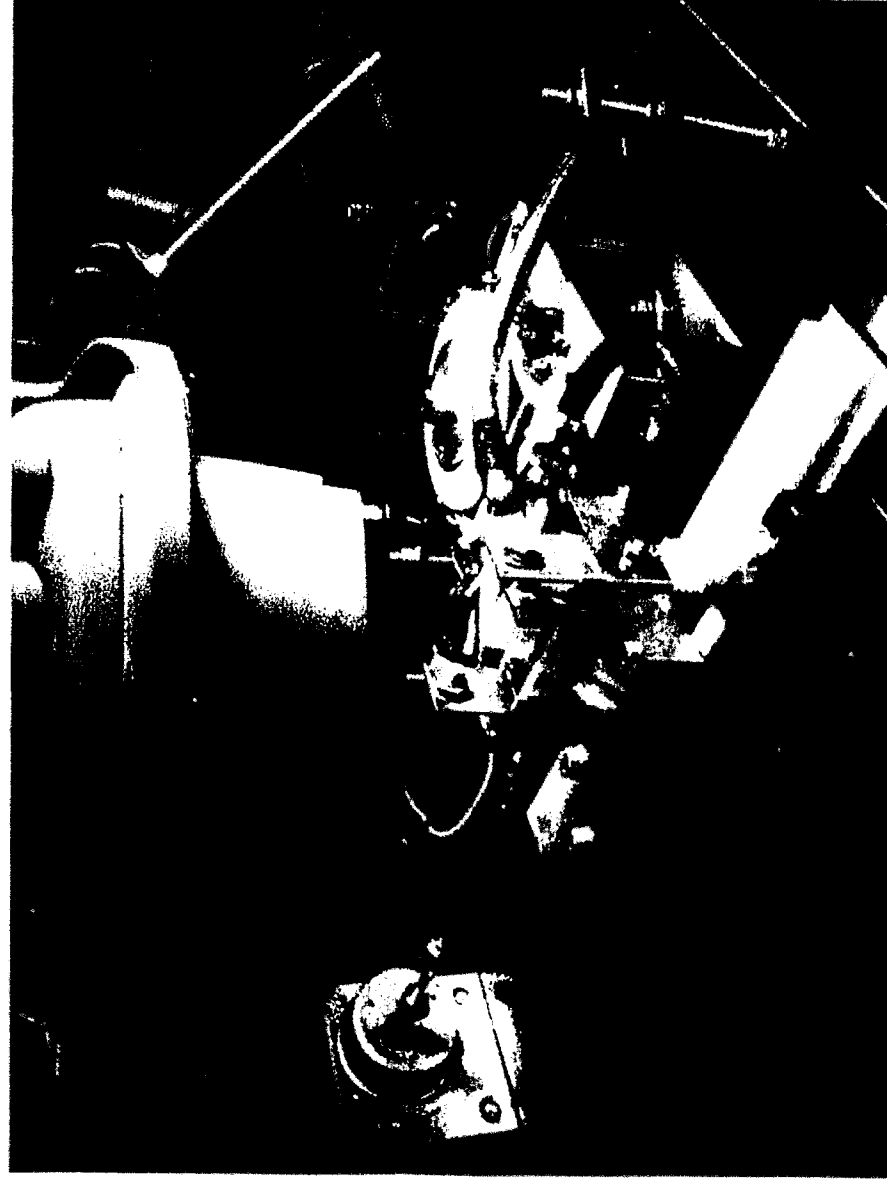


## Optical Scheme



# Experimental setup: Sensor in operation

---

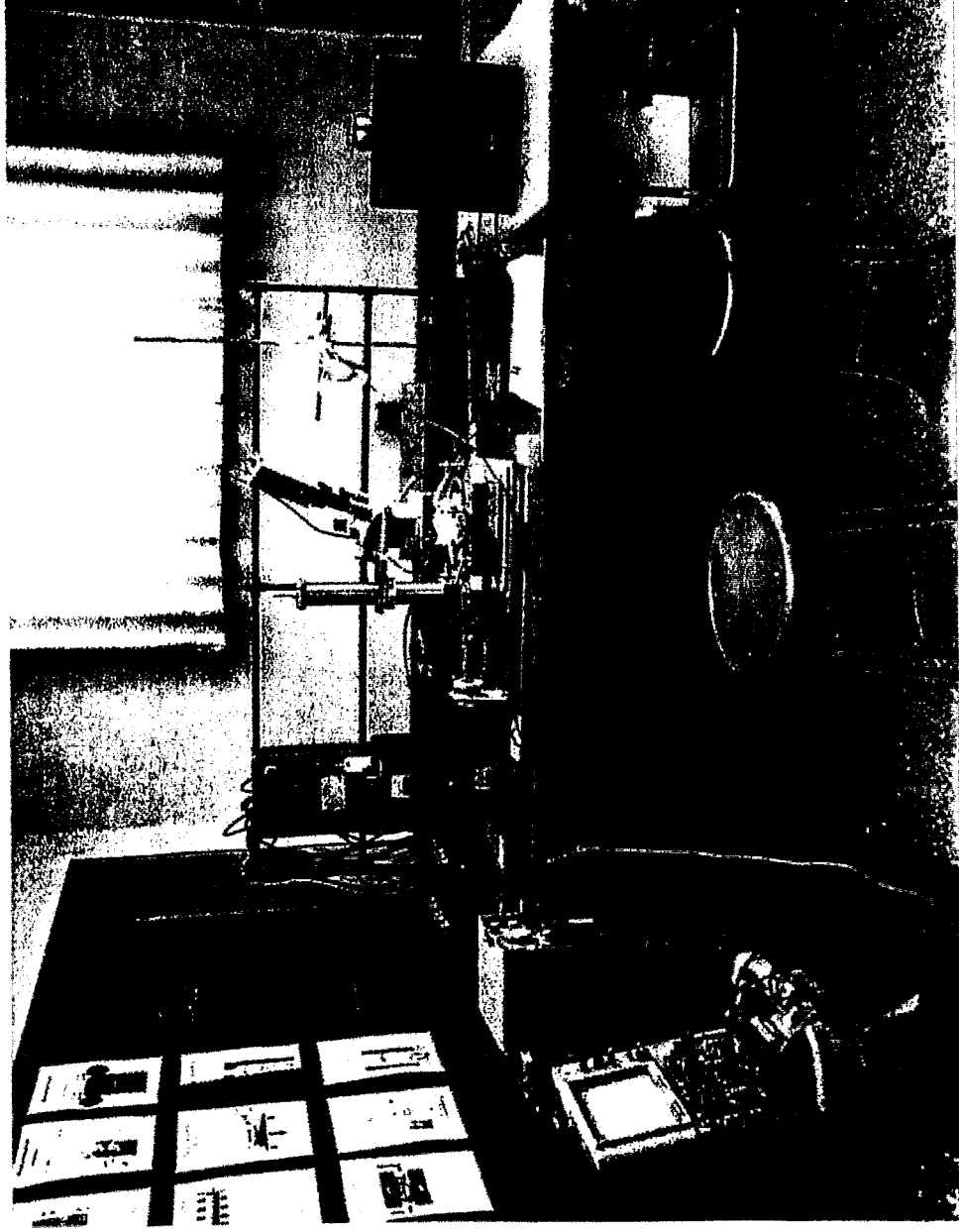


**Includes:**

- **Container**
- **PM yoke**
- **Peristaltic pump**
- **Electromotor**
- **Microscope**

# Experimental setup - Measuring system

---



Includes:

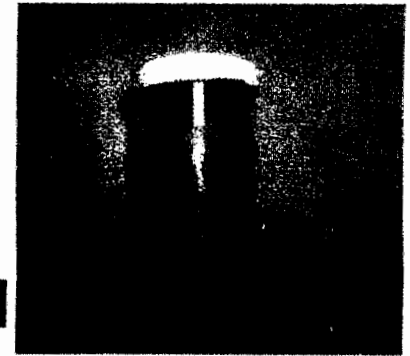
- Sensor
- DC power supply
- AC power supply
- CCD camera
- TV-set



## Measurements results - General

---

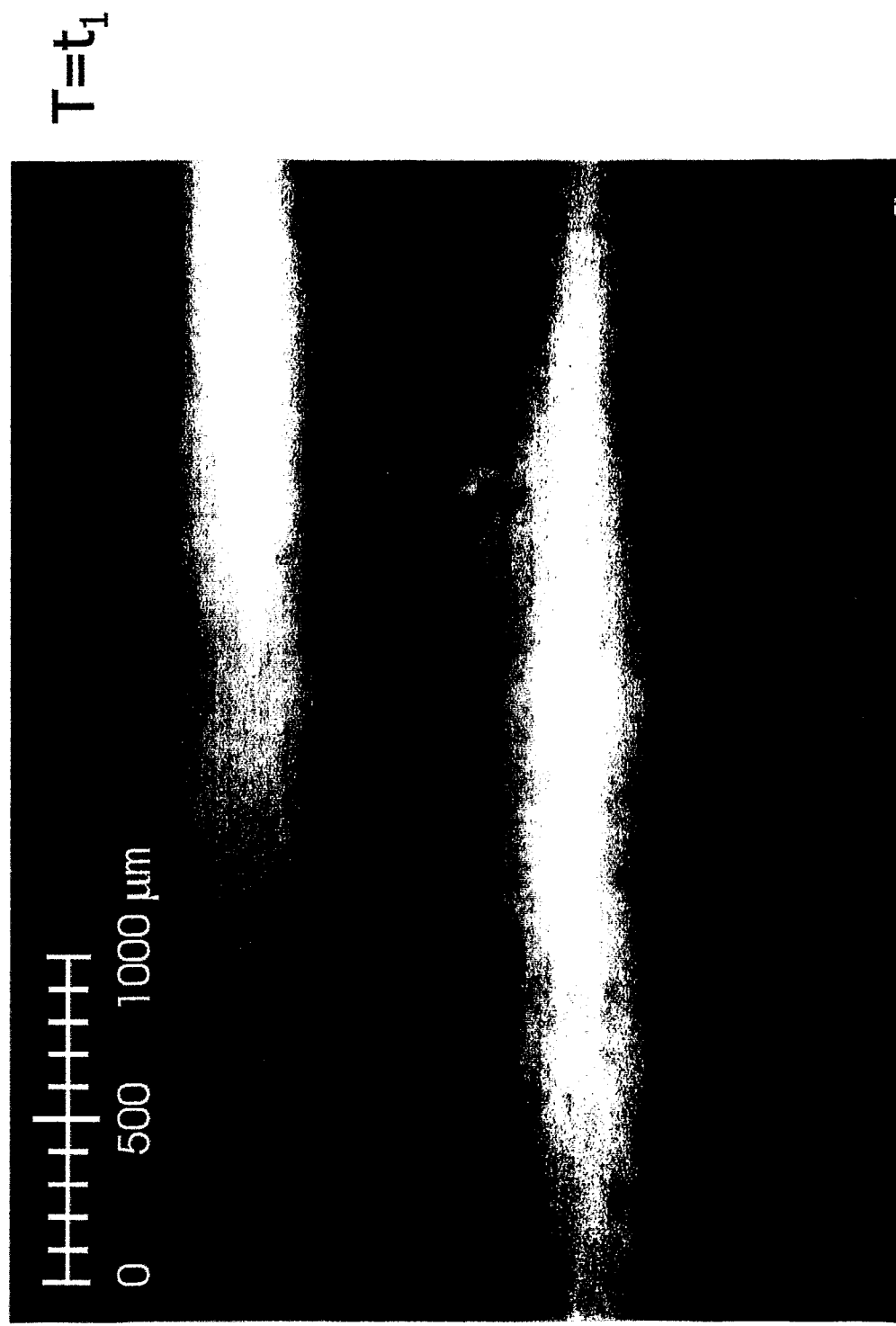
- Particles: SiC of different sizes: 5-160  $\mu\text{m}$ .
- Clusters: gallium oxide  $\text{Ga}_2\text{O}_3$  , air dust, unknown oxides, together with embedded SiC particles
- The estimated concentration: 10-1000 SiC particles and foreign inclusions per cubic centimeter.
- Flow rate: 150 g per minute





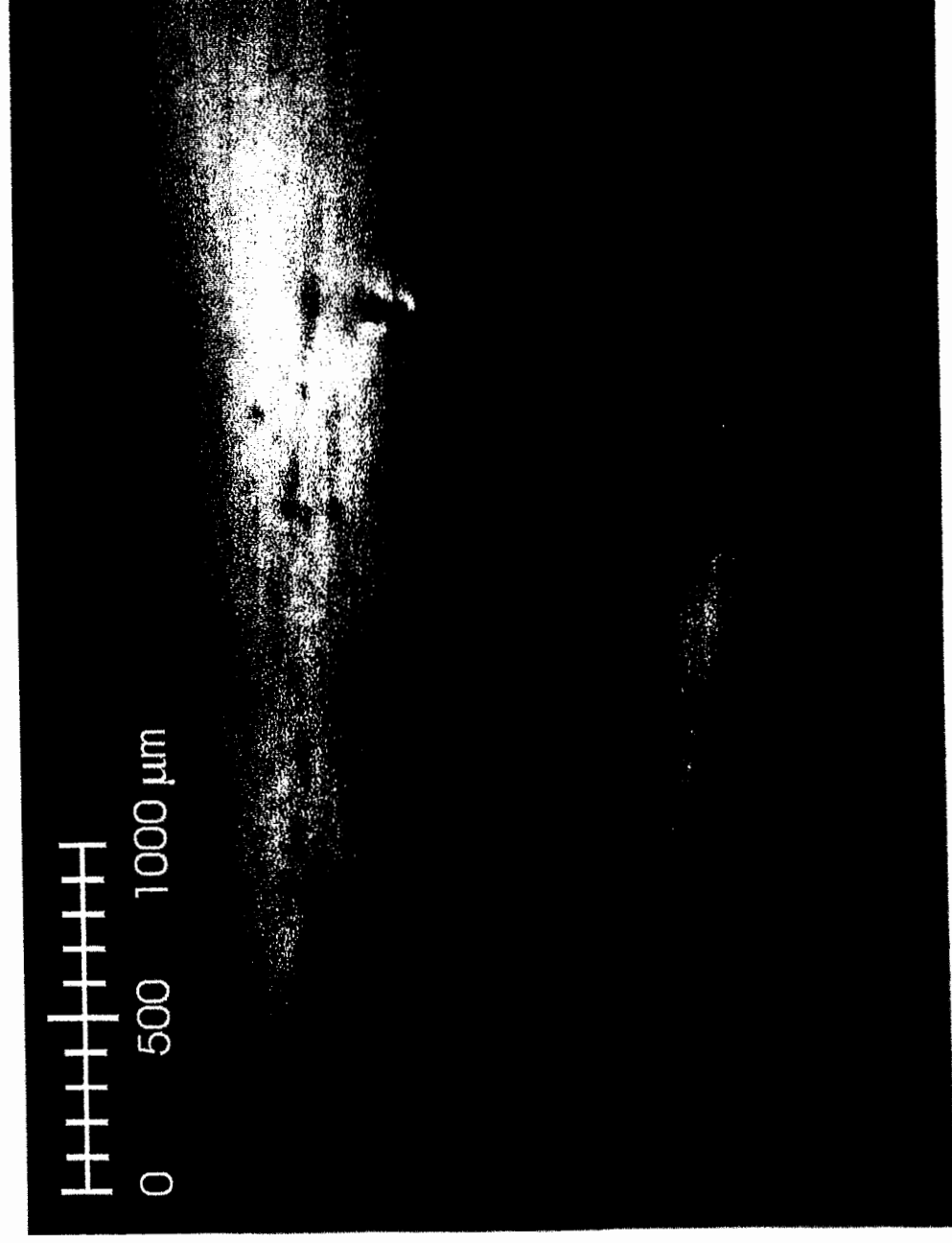
# Measurements results - Particle appearance (a)

---



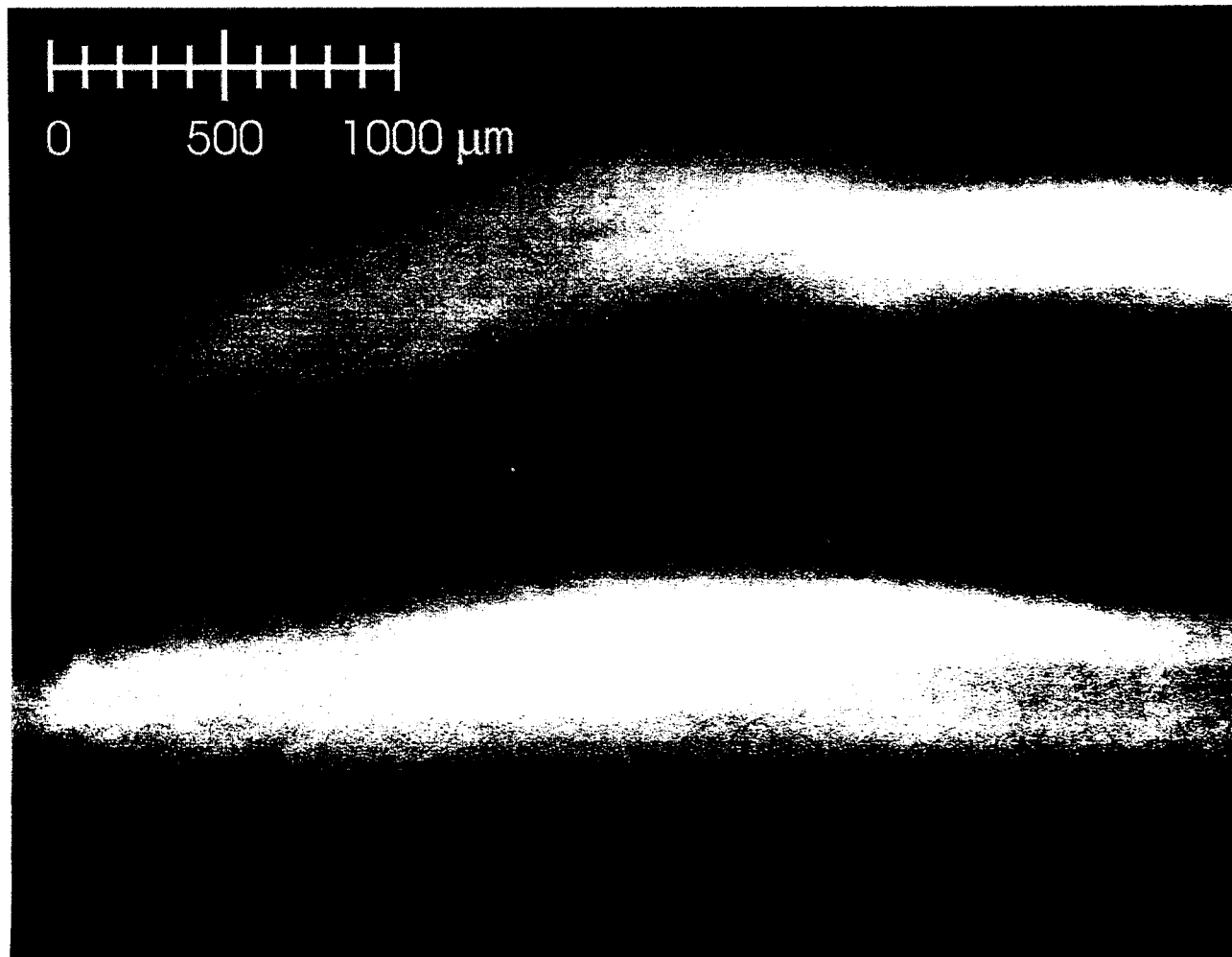
# Measurements results - Particle appearance (b)

---



# Measurements results - Cluster appearance (a)

---

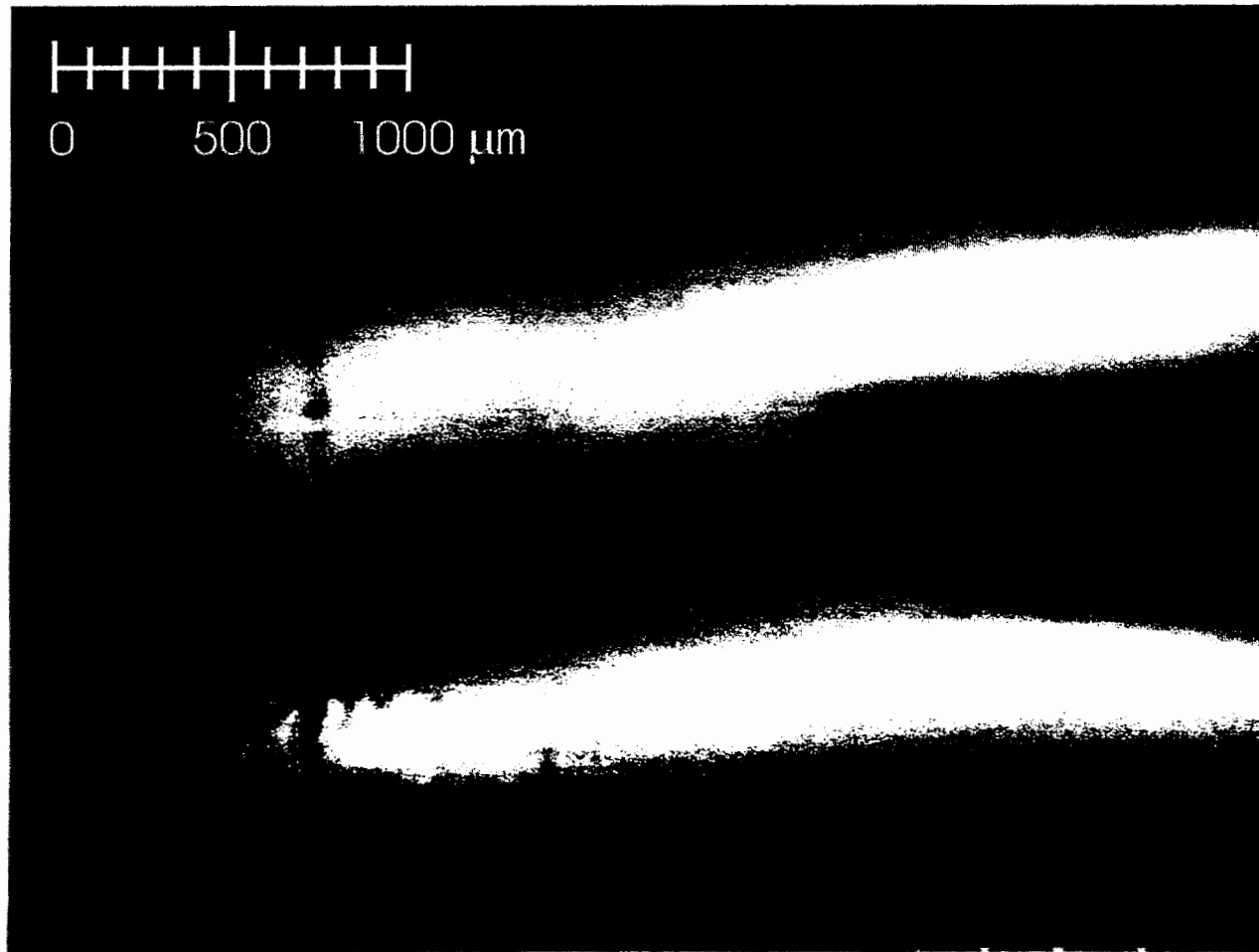


$T=t_1$



# Measurements results - Cluster appearance (b)

---



$T=t_1+2\text{ s}$



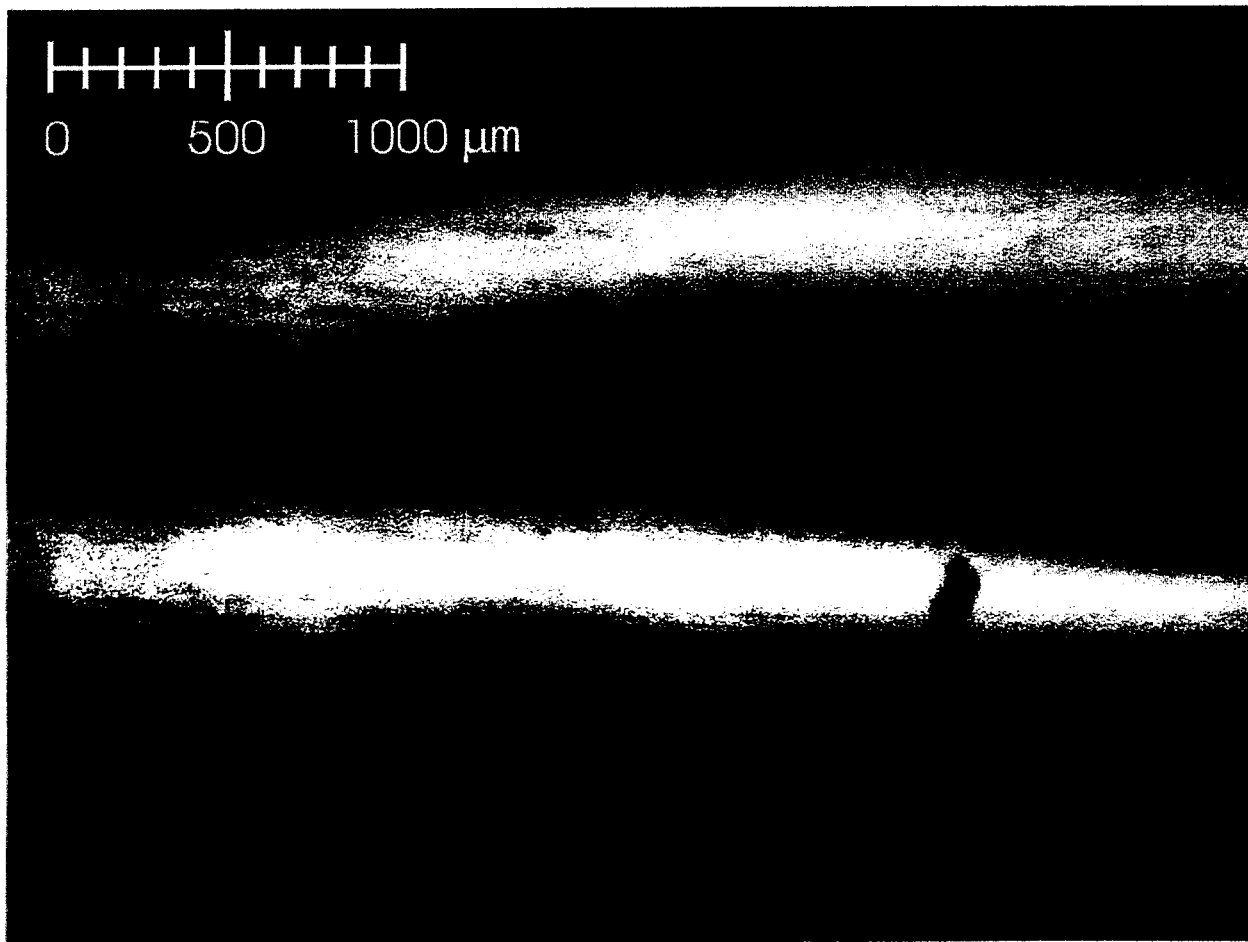
# Measurements results - Cluster appearance (c)

---



# Measurements results - Clustered particle (below) and sludge cluster (above) (a)

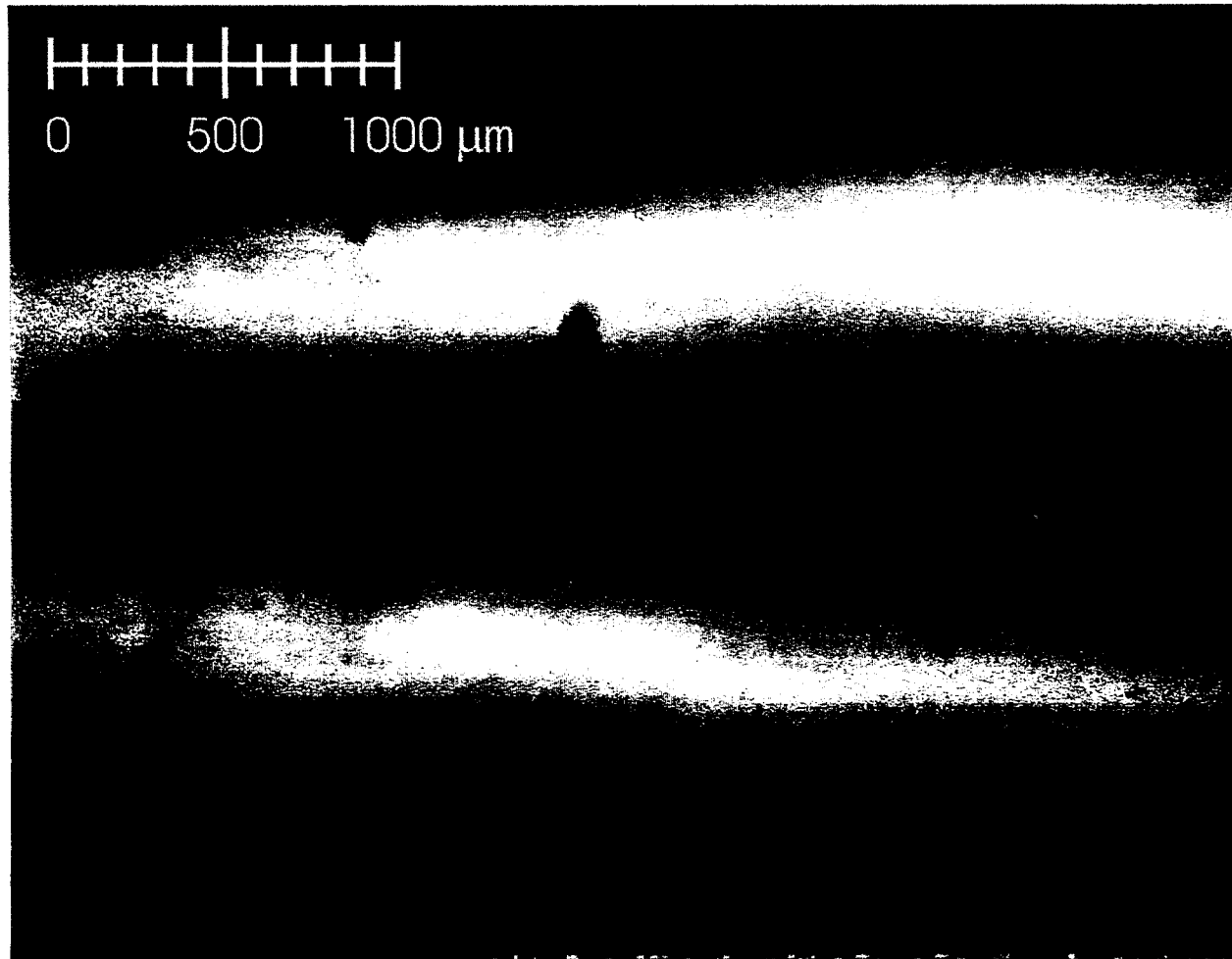
---



$T=t_1$

# Measurements results - Clustered particle (below) and sludge cluster (above) (b)

---

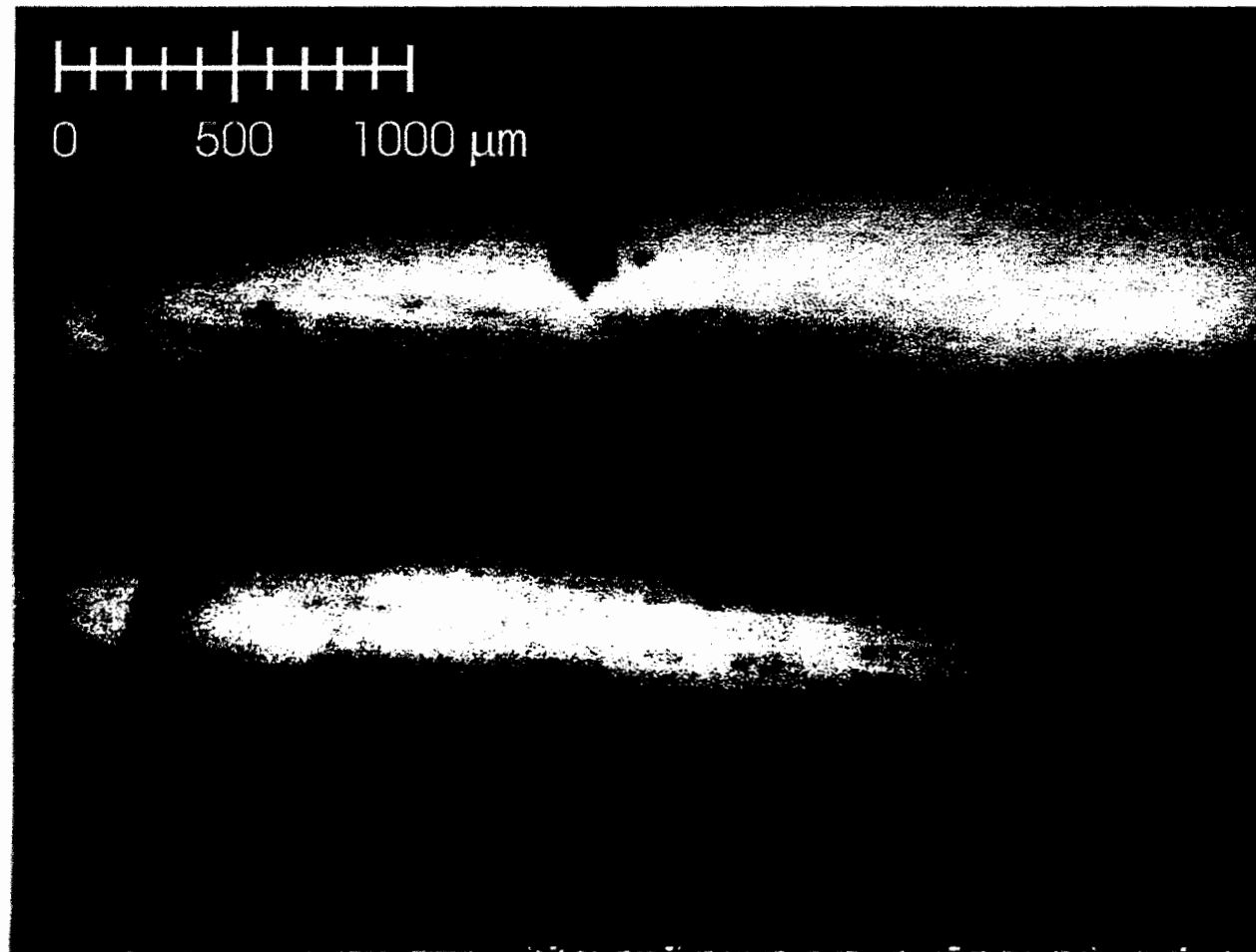


$T=t_1+2\text{ s}$



# Measurements results - Clustered particle (below) and sludge cluster (above) (c)

---

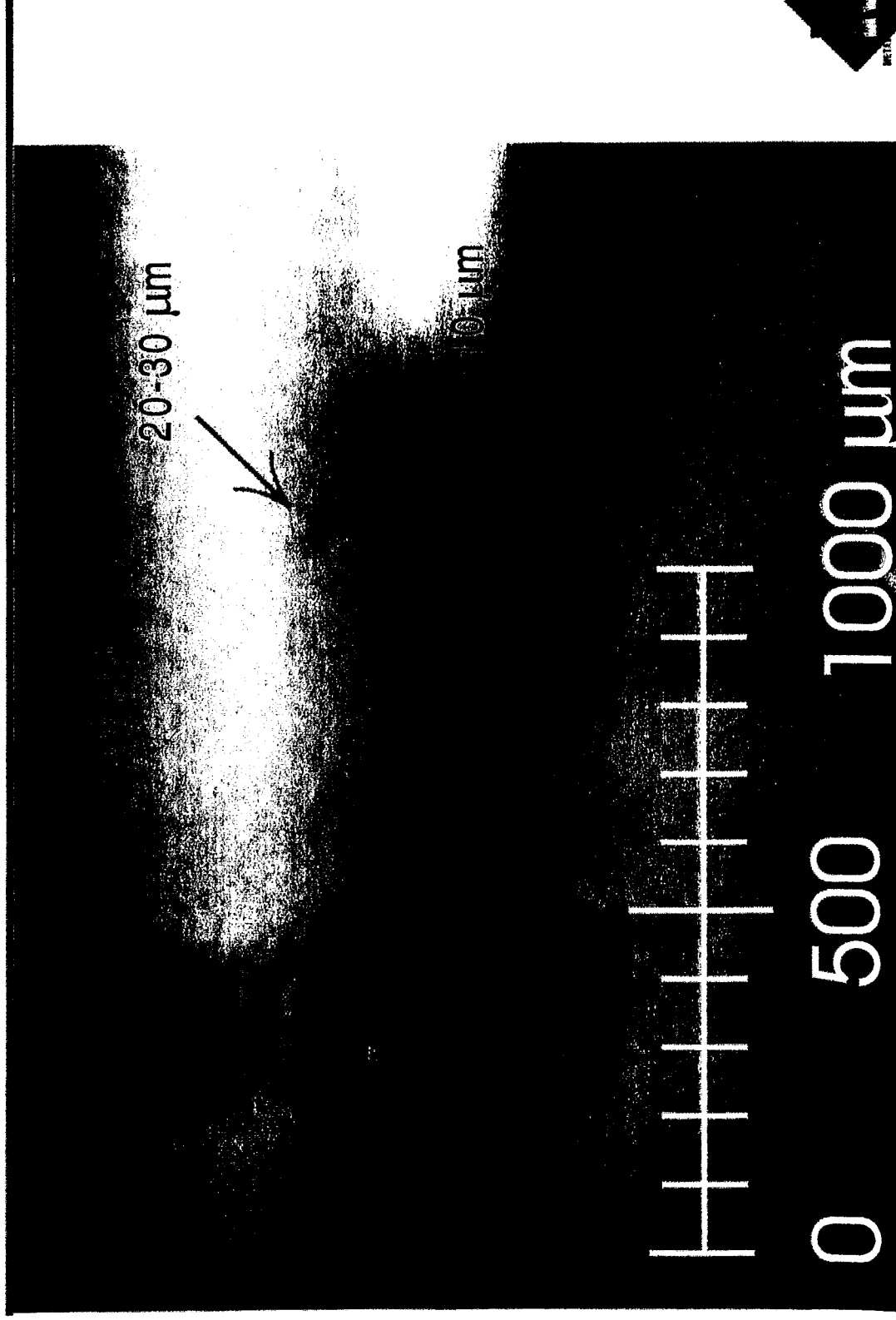


$T=t_1+4\text{ s}$

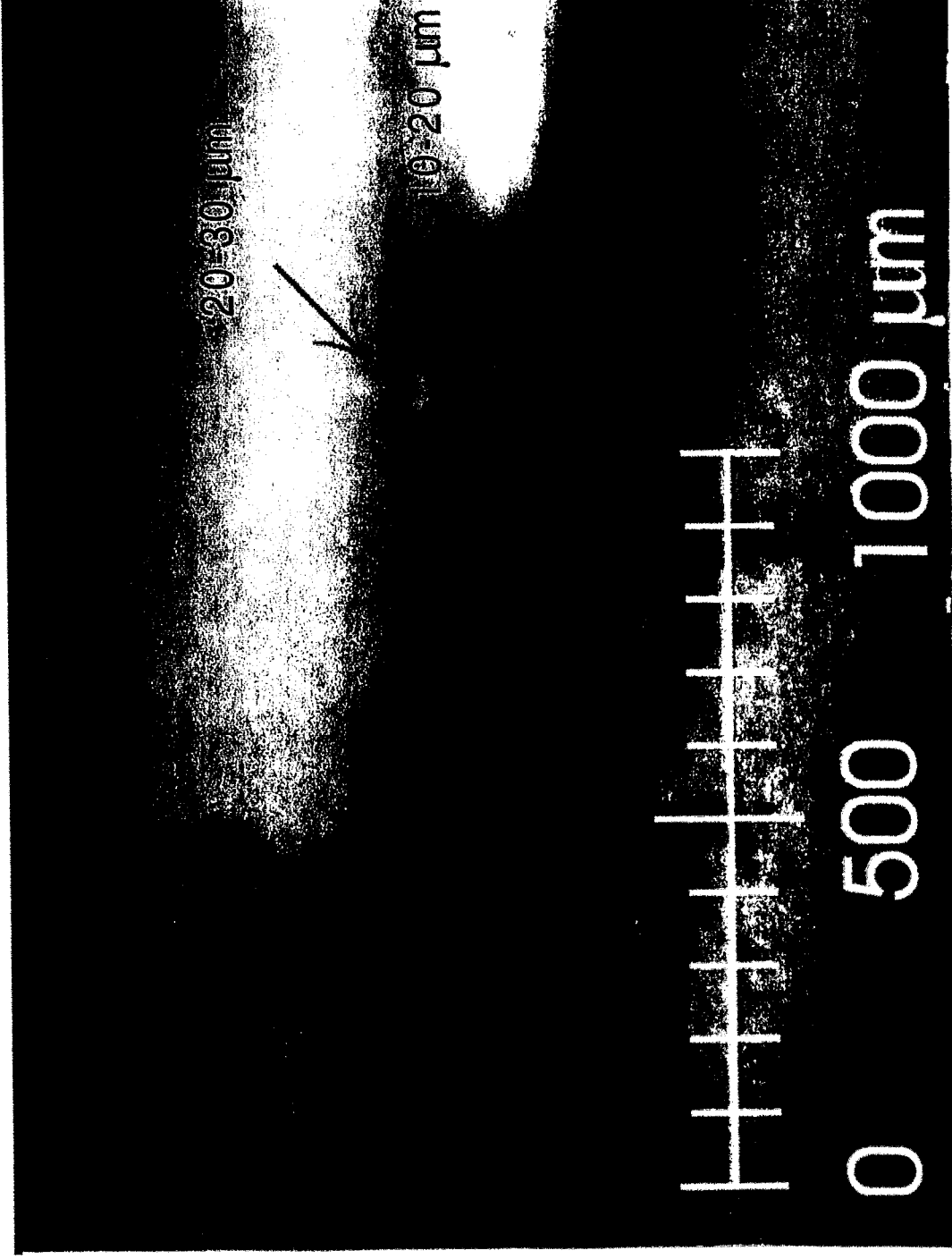




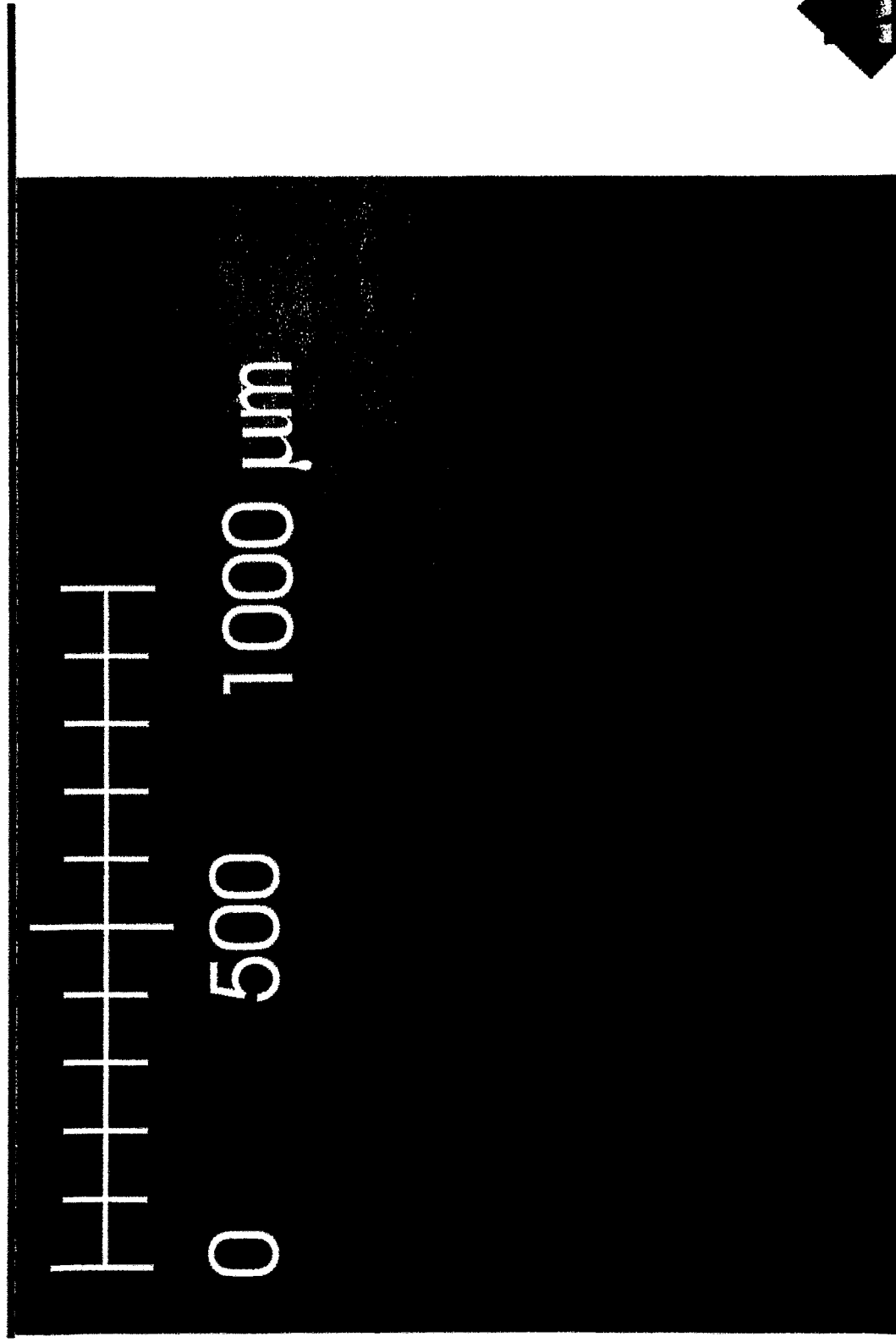
# Measurements results - Image resolution (a)



# Measurements results - Image resolution (b)

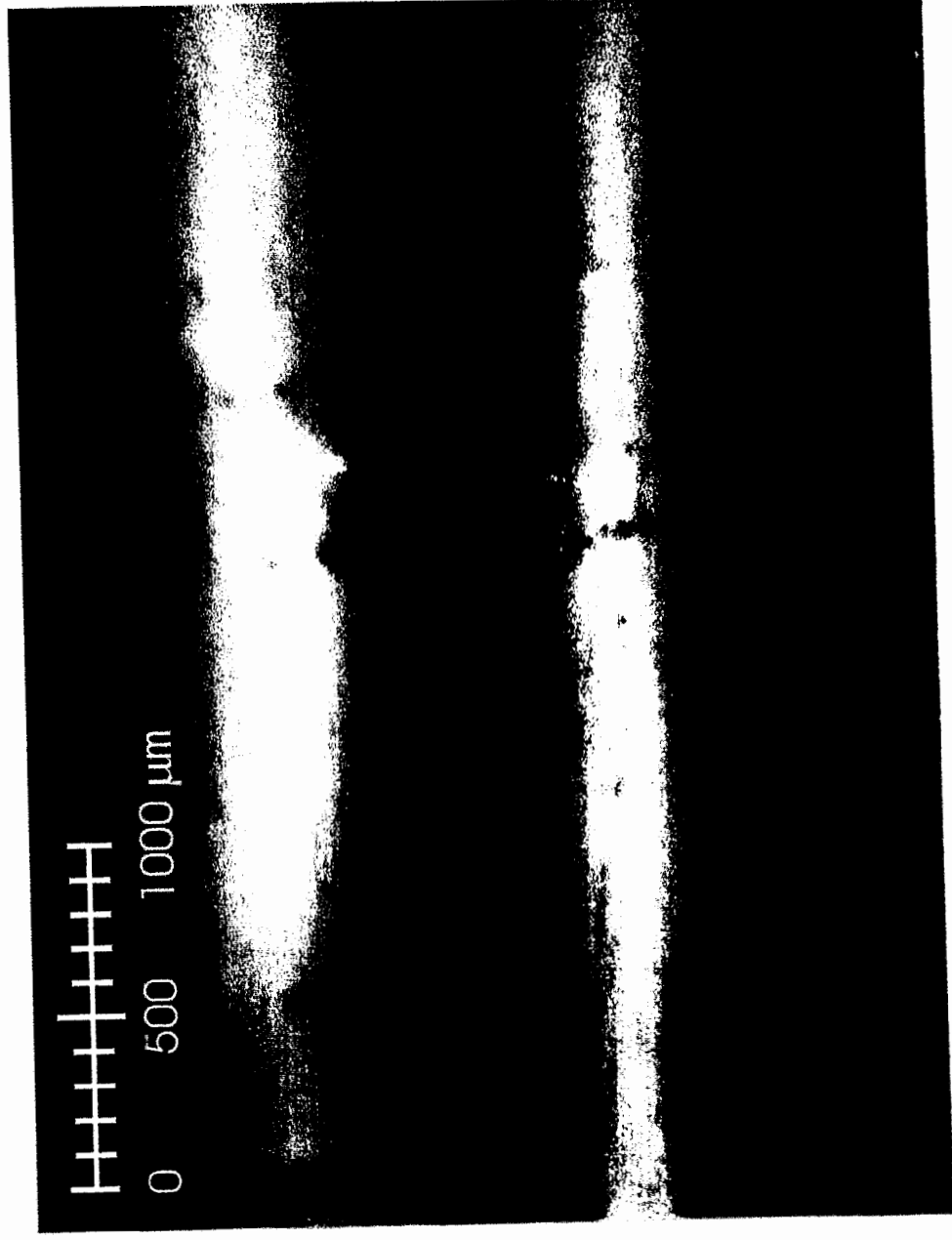


# Measurements results - Image resolution (c)



# Measurements results - Hidden particles and escaped particles

---



## Discussion - Advantages of sensor

---

- Current resolution performance:  $\sim 10\ \mu\text{m}$  large particles
- Ability to discriminate between particles and clusters
- **Ability to explore clusters**
- Identify gas bubbles: small bubbles are not counted
- Possible ability to identify chemical content of particles
- Low-cost



## Discussion - Challenges

---

- A mechanical element (externally driven ceramic roller) is an important part of the present construction
- External pump is still necessary to create steady-state melt flow through the container
- Lorentz force density has not yet reached the desired magnitude
- Current experimentation is restricted to liquid Ga; no research has yet been carried out with molten Al
- Additional electrical and mechanical refinements are needed to make the sensor industrially viable

## Future work - Low-temperature modeling (a)

---

- Increase sensor capacity (Lorentz force density) by a factor of at least 10. Requirements:
  - PM magnet of **1.0-1.3 Tesla** (Alnico 5, 5cc)
  - DC power supply of **300-700 A**
  - Switched power supply
- Implement self-pumping concept (an electromagnetic pump) with variable velocity rate
  - Electrode asymmetry creates the pumping force component
  - Velocity rate is proportion to the asymmetry magnitude

## Future work - Low-temperature modeling (b)

---

- Identify a final sensor construction
- Explore an alternative to the externally driven roller
  - Hydrodynamic treatment
  - Electric treatment
- Develop an intelligent image acquisition approach
  - image acquisition
  - image storage and processing
  - image analysis (Neural network counter/classifier)



# Temperature and velocity analysis in vertical melt cylinders under the influence of rotating magnetic fields and buoyant convection

*B. Fischer, U. Hilburger, J. Friedrich\* and G. Müller*

*Crystal Growth Lab, Dept. of Material Science WW6, University of Erlangen-Nürnberg,  
Martensstr. 7, D-91058 Erlangen, Germany*

*\* Crystal Growth Lab, Fraunhofer Institute IIS-B, Schottkystraße 10, D-91058 Erlangen, Germany*

Rotating magnetic fields (RMFs) offer an efficient possibility to control the convective heat and mass transport in electrically conducting fluids, in metallurgy as well as in the field of semiconductor crystal growth. In this study we report on the influence of the magnetic induction and frequency of a RMF on the flow in cylindrical Rayleigh-Benard configurations for various system parameters (thermal boundary conditions, aspect ratio). Both experiments and numerical simulations were carried out.

Cylindrical test cells with diameter  $D = 34$  mm and different heights  $H$  or aspect ratios  $H/D = 0.5, 1.0, 2.0$ , respectively, are completely filled with liquid gallium (melting point at  $30$  °C). The test cells consist of a plexiglas tube as the vertical cylinder wall. Copper plates on top and bottom of the cylinder (each connected to a thermostat water circuit) are establishing the thermal boundary conditions, in the case of this study a type of Rayleigh-Benard temperature profile with hot bottom and cold top. NTC temperature sensors are fixed at various positions in the vertical cylinder wall, reaching about 4 mm into the melt. A series of three sensors at the same height ( $\frac{1}{3}H$  and  $\frac{2}{3}H$ , respectively), which are azimuthally separated by  $90^\circ$ , allows to determine the azimuthal phase shift of the recorded temperature signals. The RMF is generated by a 3-phase stator (number of pole pairs  $p = 2$ ) with an inner diameter of 16 cm and a height of 17 cm, where the test cells are centered coaxially.

The behaviour of the flow is analysed by using the frequency, amplitude and phase shift of the time-dependent temperature signals at the different positions near the cylinder wall. The chosen parameters are: temperature difference  $\Delta T = 2, 5, 10, 20$  K, frequency  $\Omega/2\pi = 7.5, 25, 50, 100$  Hz, and the magnetic induction was varied from 0 to 10 mT. In addition to the experiments we carried out three-dimensional time-dependent numerical simulations. The combined results of experiments and simulations give a clear picture of the flow regimes, flow patterns, velocities, rotation frequencies, and time-dependent behaviour.

We find hybrid flow patterns which are significantly influenced by both buoyancy and RMF with different wave numbers, preceeding in the same azimuthal direction as the RMF. For dominating RMF a nearly axisymmetric rotational motion of the fluid with flattened isotherms results in an axial heat transport similar to the case of pure diffusion.

This study is supported by the german space agency, DLR, contract 50WM9455.

# Temperature and Velocity Analysis in Vertical Melt Cylinders under the Influence of Rotating Magnetic Fields and Buoyant Convection

B. Fischer, U. Hilburger, J. Friedrich\*, G. Müller

Crystal Growth Lab, Dept. of Material Science WW6,  
University of Erlangen-Nürnberg, Germany

\* Crystal Growth Lab, Fraunhofer Institute for Integrated  
Circuits IIS-B, Erlangen, Germany

- Introduction
- Experimental Setup
- Theory
- Results of the Measurements
- Numerical Simulations
- Conclusions

# Introduction

- Topic:  
Influence of rotating magnetic fields on the flow in cylindrical Rayleigh-Bénard-like configurations
- Motivation:  
Basic understanding of interaction of buoyant and electromagnetically driven flow  
⇒ model experiments in simplified configurations  
⇒ variation of system parameters  
⇒ variation of container shape → aspect ratio
- How to get information on the flow?
- Flow analysis with temperature sensors  
⇒ absolute temperature values  
⇒ amplitudes/frequencies of T-fluctuations
- Arrangements of temperature sensors  
⇒ phase shifts between temperature signals  
⇒ flow velocities  
⇒ wavenumbers of velocity and temperature fields

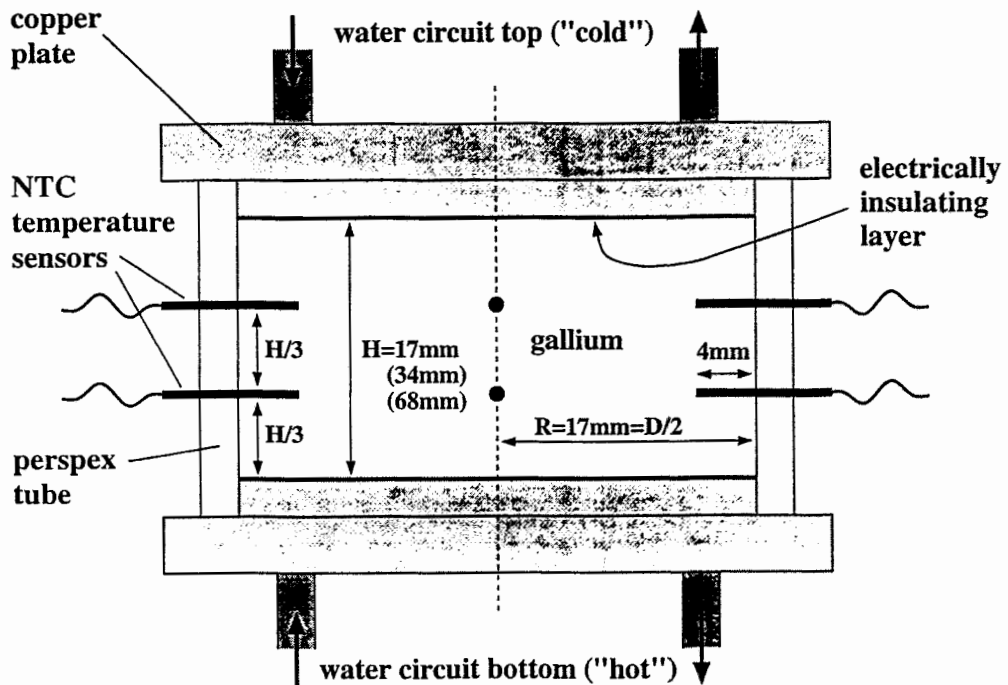
Analysis of experimental temperature signals

+

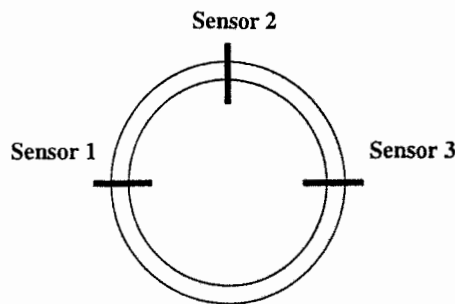
Numerical simulation

⇒ Understanding of the flow

# Experimental Setup



from above:



- rotating magnetic field ( $p = 2$ ) generated by stator of an electric motor:  
 $B = 0 \dots 10 \text{ mT}$ ,  $\frac{\omega}{2\pi p} = 7.5, 25, 50, 100 \text{ Hz}$
- test cells filled with liquid gallium
- cylindrical cavities with radius  $R = 17 \text{ mm}$  and heights  $H = 17, 34, 68 \text{ mm}$   
 $\Rightarrow$  aspect ratios  $\frac{H}{D} = \frac{H}{2R} = 0.5, 1.0, 2.0$
- temperature difference between hot bottom and cold top  $\Delta T = 2, 5, 10, 20 \text{ K}$

# Theory

- Assumptions:
  - neglect influence of melt flow on magnetic field
  - neglect skin effect
- Externally applied rotating magnetic field:

$$\vec{B}(r, \varphi, z) = \begin{pmatrix} B \left(\frac{r}{R}\right)^{p-1} \sin(p\varphi - \omega t) \\ B \left(\frac{r}{R}\right)^{p-1} \cos(p\varphi - \omega t) \\ 0 \end{pmatrix}$$

- Current density  $\vec{j}$  from Ohm's law:

$$\vec{j} = \sigma \left( -\vec{\nabla}\Phi - \frac{\partial \vec{A}}{\partial t} \right)$$

- Time-averaged Lorentz force density

$$\langle \vec{f} \rangle = \langle \vec{j} \times \vec{B} \rangle = \langle f_\varphi \rangle \cdot \vec{e}_\varphi \propto B^2 \omega$$

$r, \varphi, z$ : cylindrical coordinates

$t$ : time

$B$ : amplitude of rotating magnetic field at  $r = R$

$\frac{\omega}{2\pi p}$ : frequency of rotating magnetic field

$p$ : number of pole pairs

$\Phi$ : scalar electric potential

$\vec{A}$ : magnetic vector potential,  $\vec{B} = \vec{\nabla} \times \vec{A}$

$\sigma$ : electrical conductivity

# Characterization of the System

- Prandtl number  $Pr = \frac{\nu}{\kappa}$
- Grashof number

$$Gr = \frac{\beta g \Delta T H^3}{\nu^2}$$

- Magnetic Taylor number

$$Ta_m = \frac{B^2 R^4 \sigma \omega}{2\rho \nu^2 p}$$

- Interaction parameter

$$N_{rot} = \frac{Ta_m}{Gr} \propto \frac{B^2 \omega}{\Delta T}$$

Varied parameters:  $B, \omega, \Delta T$ , aspect ratio  $\frac{H}{D} = \frac{H}{2R}$

$H$ : height of the cylinder

$R$ : radius of the cylinder

$\nu$ : kinematic viscosity

$\kappa$ : thermal diffusivity

$\beta$ : thermal expansion coefficient

$\rho$ : density

$\sigma$ : electrical conductivity

$g$ : gravitational acceleration

$\Delta T$ : temperature difference between hot bottom  
and cold top

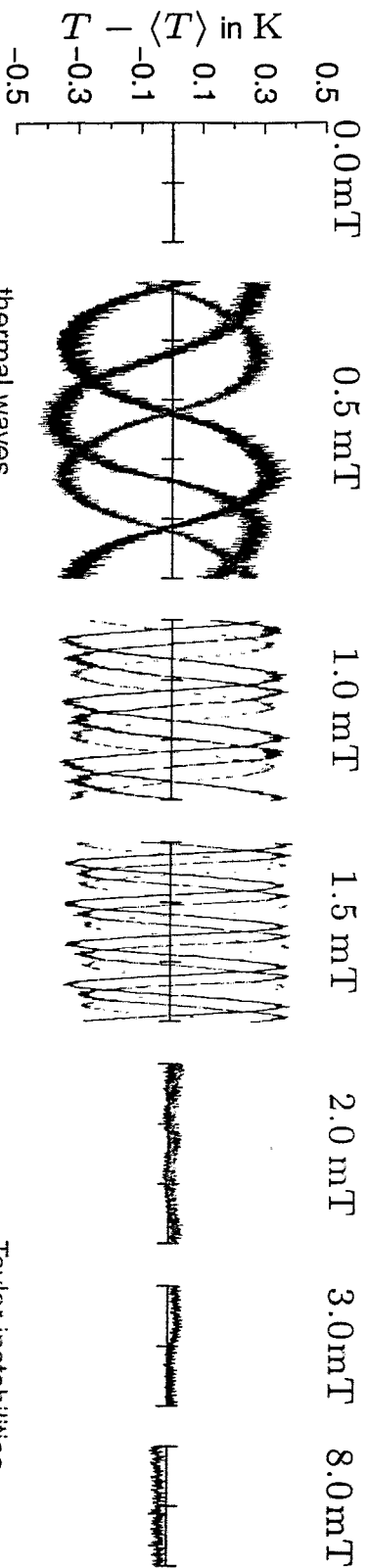
$p$ : number of pole pairs

$\frac{\omega}{2\pi p}$ : frequency of rotating magnetic field

# Temperature Fluctuations: Typical Results

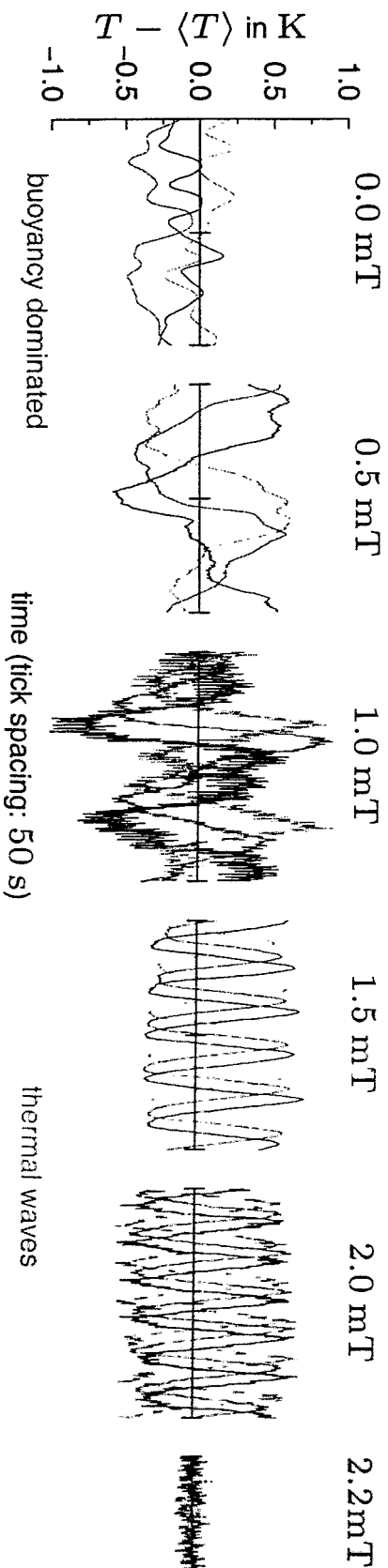
**H/D=1.0**

$$\Delta T = 2 \text{ K}, \frac{\omega}{2\pi p} = 25 \text{ Hz}$$

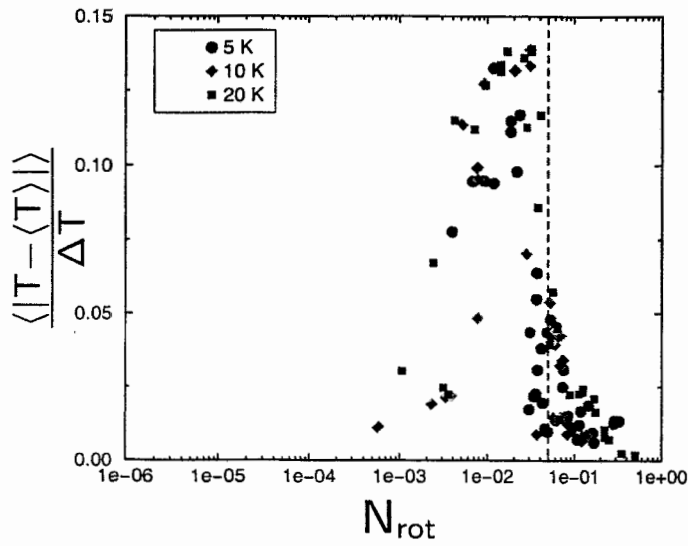


**H/D=2.0**

$$\Delta T = 5 \text{ K}, \frac{\omega}{2\pi p} = 25 \text{ Hz}$$



H/D=0.5

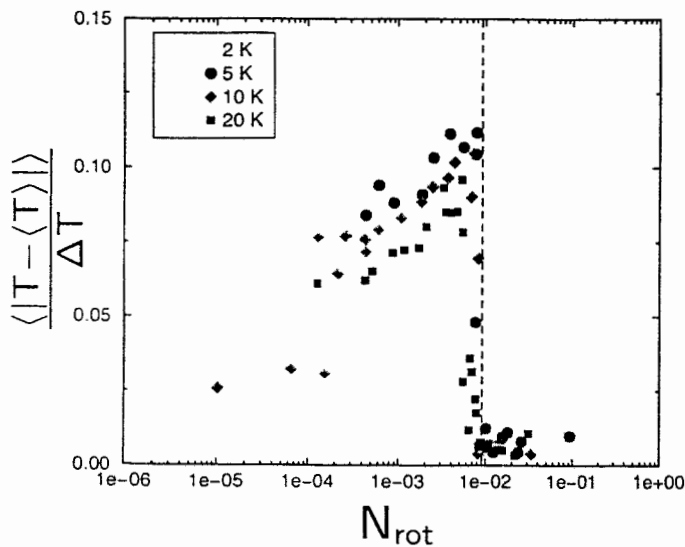


## Amplitude of temperature fluctuations

measure for amplitude: average deviation  $A$ , normalized by  $\Delta T$ :

$$A = \frac{\langle |T - \langle T \rangle| \rangle}{\Delta T}$$

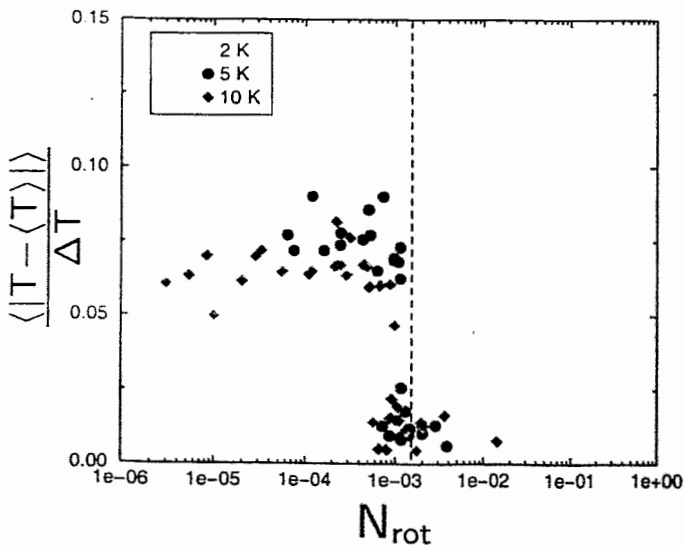
H/D=1.0



interaction parameter:

$$N_{rot} = \frac{Ta_m}{Gr} \propto \frac{B^2 \omega}{\Delta T}$$

H/D=2.0

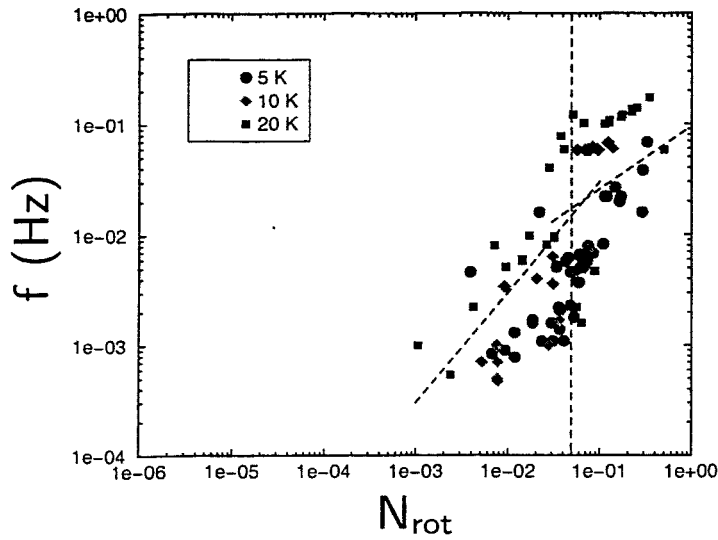


different thermal boundary conditions  $\Delta T$  distinguished by colour

vertical dashed lines: step decrease of amplitude  $\Rightarrow$  flow transition



H/D=0.5



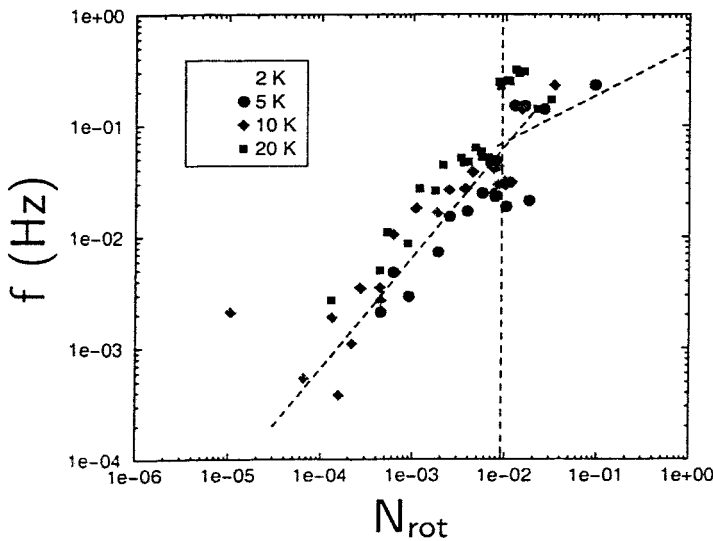
Frequency of temperature fluctuations

dominating frequency  $f$  determined from Fourier spectra

interaction parameter:

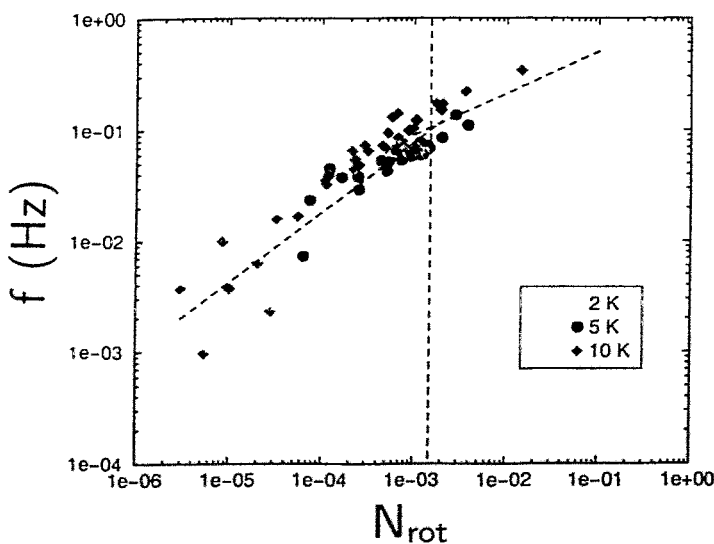
$$N_{\text{rot}} = \frac{\text{Ta}_m}{\text{Gr}} \propto \frac{B^2 \omega}{\Delta T}$$

H/D=1.0



different thermal boundary conditions  $\Delta T$  distinguished by colour

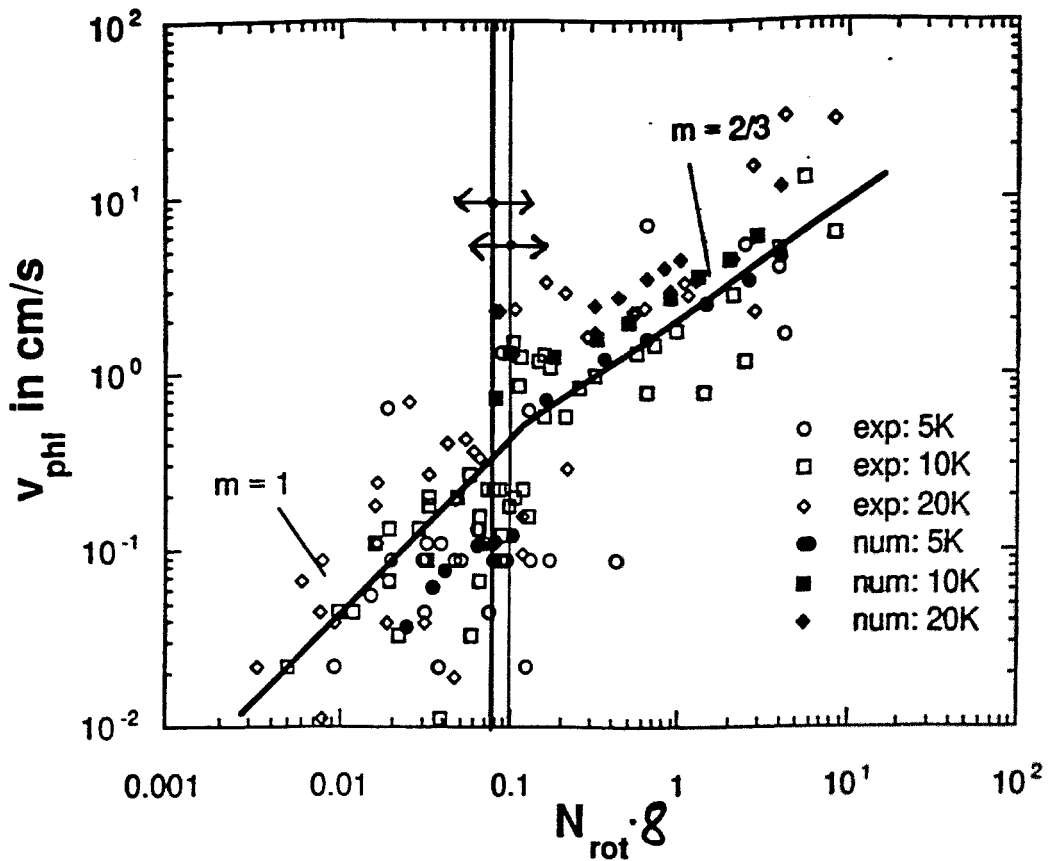
H/D=2.0



change of slope at flow transition: velocity of temperature field precession  $\rightarrow$  velocity of fluid flow

# Earlier Studies for $\frac{H}{D} = 1.0$ :

Friedrich et al., Physics of Fluids 11 (1999) 853



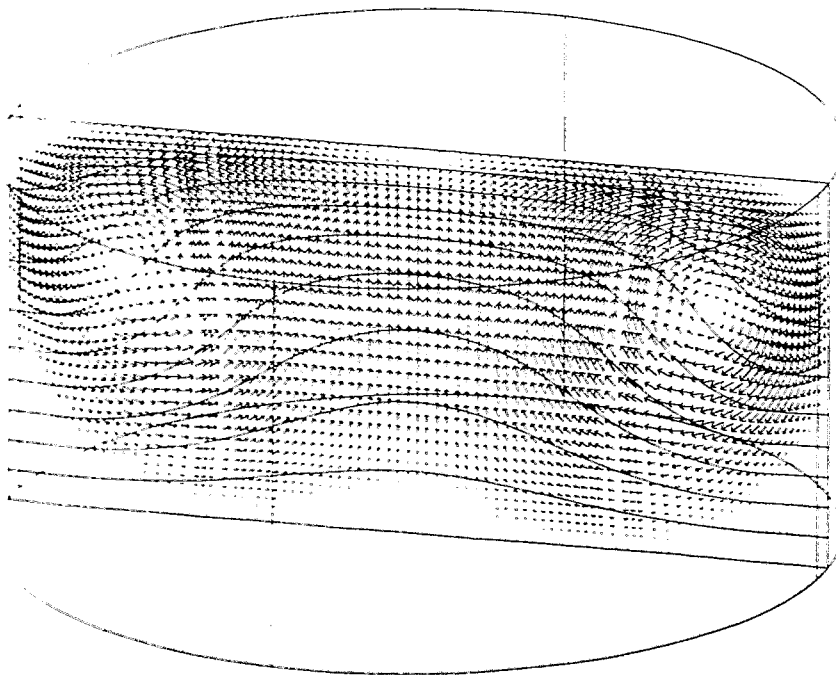
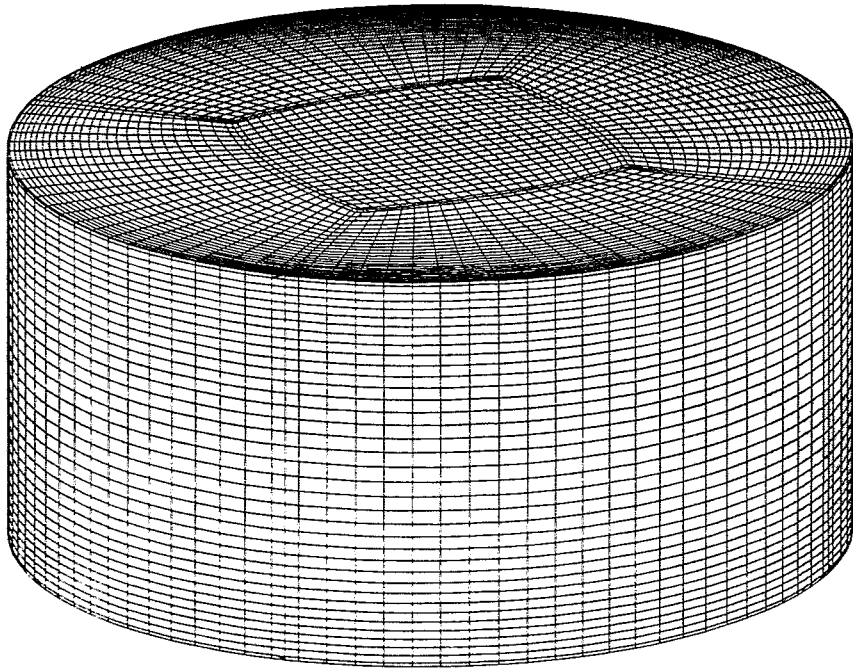
— transition in Friedrich et al.  
(different test cell)

— transition for aspect ratio 1.0  
in this work

⇒ results reproducible

⇒ numerical simulations reliable

# Simulation of 3D Time-Dependent Convective Phenomena in Melt Cylinders by STHAMAS 3D



$$\Delta T = 10 \text{ K}, B = 0 \text{ mT}$$

STHAMAS 3D:

- finite volume method
- equations for heat and mass transport
- equations for rotating magnetic field

numerical grid:

- block-structured
- 130.000 control volumes

cylinder:

- $H = 1.7 \text{ cm}$
- $D = 3.4 \text{ cm}$
- aspect ratio  $\frac{H}{D} = 0.5$

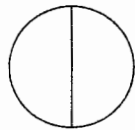
thermal boundary conditions:

- top/bottom: fixed temperatures
- vertical wall: adiabatic

# Numerical Simulation

- $\Delta T = 10 \text{ K}$
- $\frac{\omega}{2\pi p} = 25 \text{ Hz}$
- $B = 1.3 \text{ mT}$

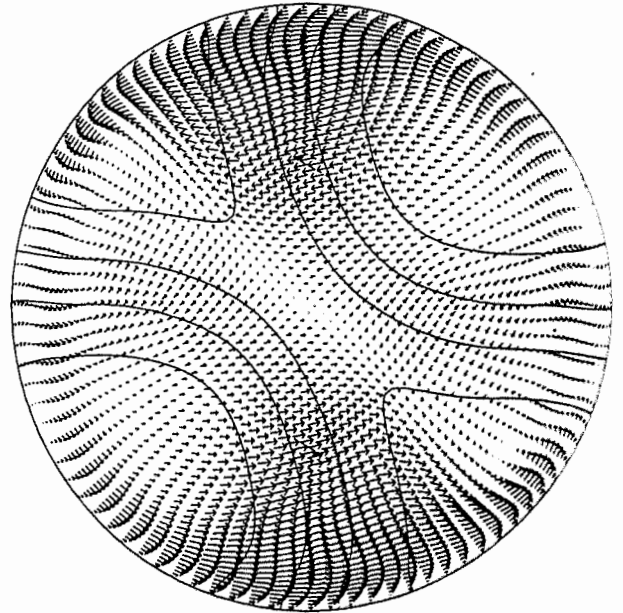
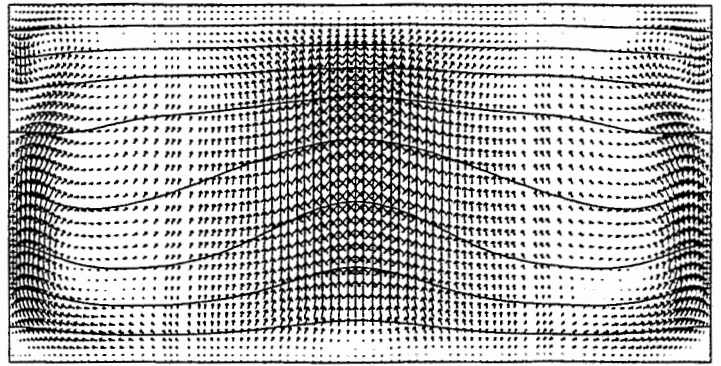
Top:  
velocity and isotherms  
(spacing: 1.1 K) in  
vertical cross section



Centre:  
horizontal cross  
section at  $z = \frac{H}{3}$

Bottom:  
temperature signals,  
sensors at  $z = \frac{H}{3}$ ,  
 $r = R - 4 \text{ mm}$ ,  
azimuthal spacing:  $90^\circ$

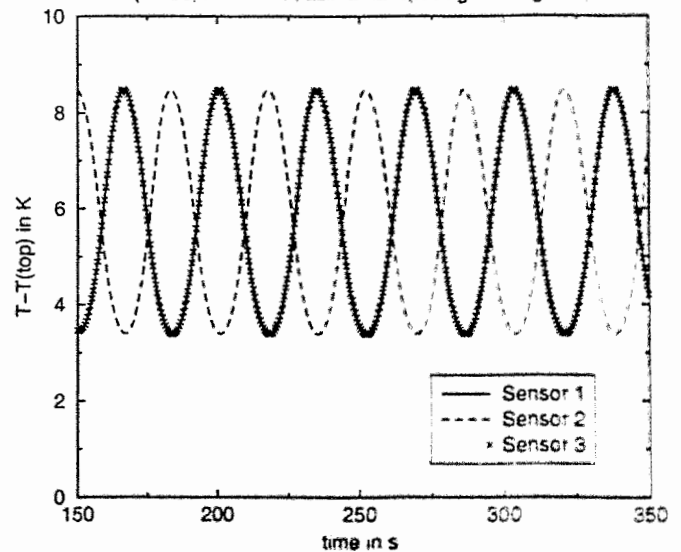
$\Rightarrow$  wavenumber 2

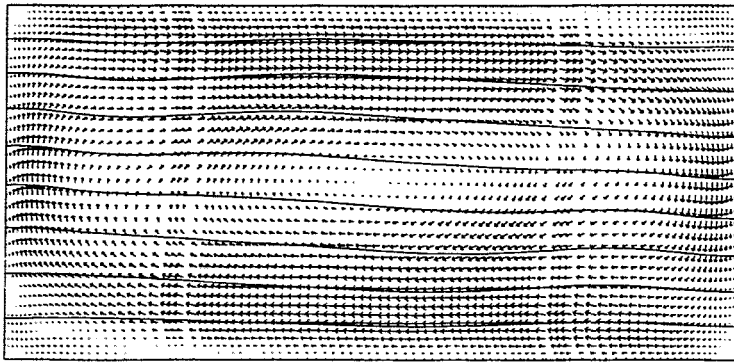


$$v_r = 0.53 \frac{\text{cm}}{\text{s}}, v_\varphi = 0.99 \frac{\text{cm}}{\text{s}}, v_z = 1.06 \frac{\text{cm}}{\text{s}}$$

temperature T at 3 monitor points

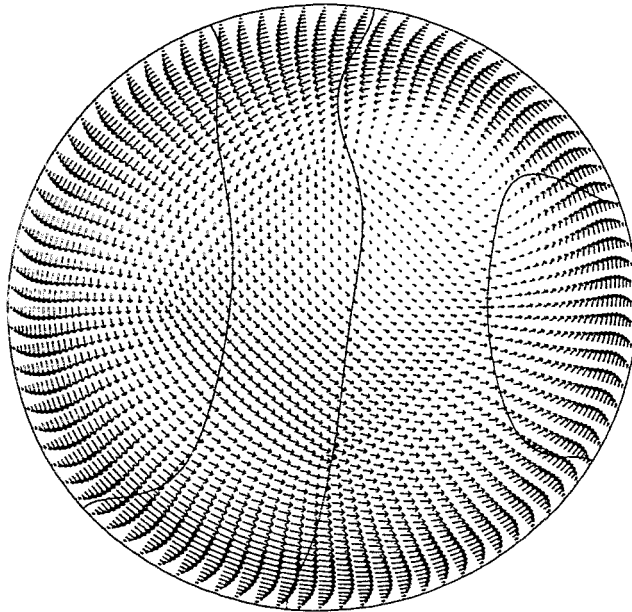
( $z=H/3$ ,  $r=R-4\text{mm}$ , azimuthal spacing:  $90^\circ$ )



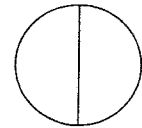


## Numerical Simulation

- $\Delta T = 10 \text{ K}$
- $\frac{\omega}{2\pi p} = 25 \text{ Hz}$
- $B = 1.7 \text{ mT}$



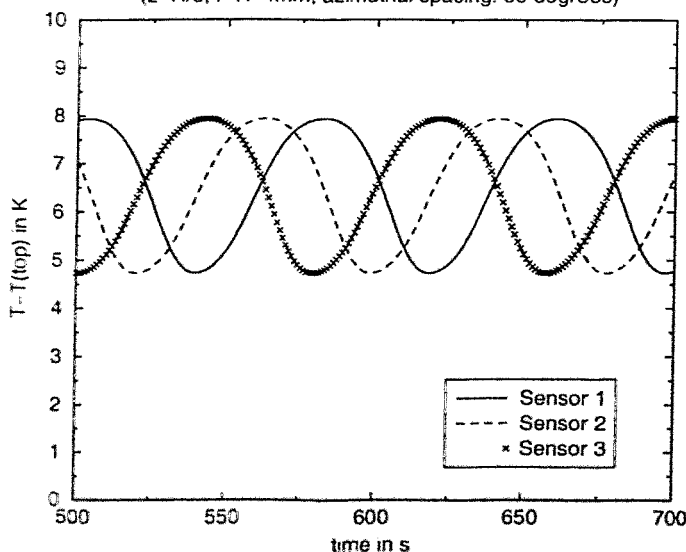
Top:  
velocity and isotherms  
(spacing: 1.1 K) in  
vertical cross section



$$v_r = 0.65 \frac{\text{cm}}{\text{s}}, v_\varphi = 0.80 \frac{\text{cm}}{\text{s}}, v_z = 0.43 \frac{\text{cm}}{\text{s}}$$

Centre:  
horizontal cross  
section at  $z = \frac{H}{3}$

temperature T at 3 monitor points  
( $z=H/3$ ,  $r=R-4\text{mm}$ , azimuthal spacing: 90 degrees)



Bottom:  
temperature signals,  
sensors at  $z = \frac{H}{3}$ ,  
 $r = R - 4 \text{ mm}$ ,  
azimuthal spacing:  $90^\circ$   
 $\Rightarrow$  wavenumber 1

## Conclusions

- experimental and numerical variation of system parameters and aspect ratio
- temperature signals analyzed concerning amplitude and frequency
- efficient damping of temperature fluctuations by suitable rotating magnetic field
- flow regimes investigated in detail
- combination of analysis of experimental temperature signals and numerical simulation delivers a clear picture of flow patterns and regime transitions

# **Spatio-Temporal Temperature Measurement in Liquid Metal of a Rotating System**

*Y.-S. Lee<sup>\*</sup>, Ch.-H. Chun*

*Pohang University of Science and Technology, Department of Mechanical Engineering,  
San 31 Hyoja Dong, Pohang, 790-784, South Korea*

*\* present address: ZARM - University of Bremen,  
Am Fallturm, 28359 Bremen, Germany*

Spatio-temporal temperature fluctuation measurements are carried out to investigate oscillatory convection of mercury melts induced by coupling of natural convection with the rotations of crystal disk and crucible in a Czochralski crystal growing configuration.

Thermocouple probes rotating together with the crystal disk and crucible are used in order to minimize adverse effects occurred by placing fixed objects in a rotating flow. Many thermocouples(28) are used to study the relationship among the outputs, especially their phase relations, on the basis of which one can deduce the overall convection pattern and flow structure. Two slip ring assemblies are integrated to provide rotating electrical contacts. Thermocouple signals measured are amplified by a factor of 2201 by a linear thermocouple-amplifier before passing the slipring, to maximize the ratio of signal to noise induced by a mechanical brush of the slip ring. Without rotation, a platinum resistance thermometer(Pt100) is used to measure the temperature of a reference junction which is embedded in an isothermal copper block. With the rotations of disk or crucible, an electronic thermometer with junction compensator is used. A high resolution(<0.02K) temperature measurement in a rotating liquid metal has been successfully accomplished.

MTLM in Dresden, Germany: 11-13 Oct. 1999

## **Spacio-Temporal Temperature Measurement in Liquid Metal of a Rotating System**

You-Seop Lee and Ch.-H. Chun

Dept. of Mech. Engg., Pohang University of Science and Technology, Korea

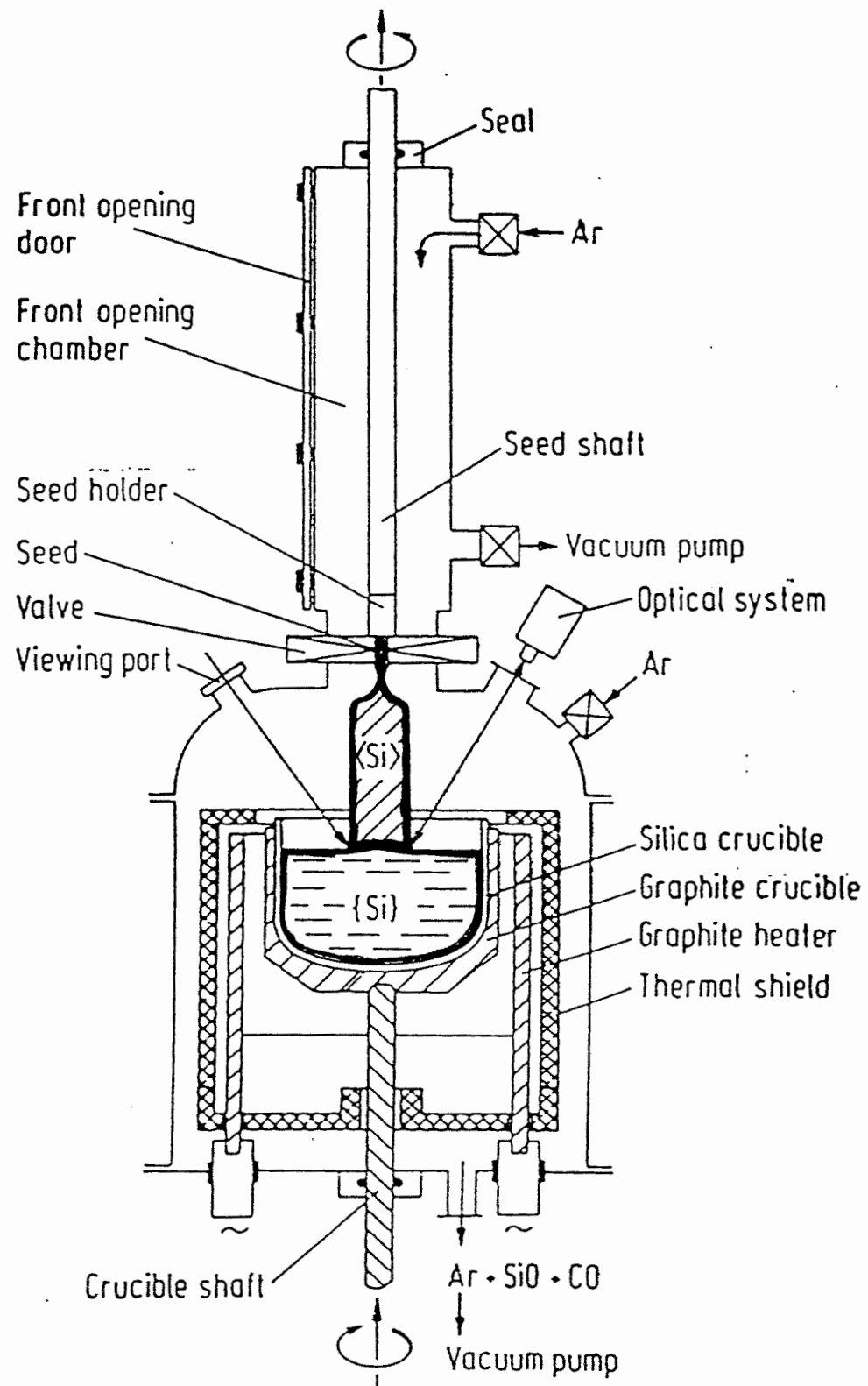
- **Motivation:**

- **Unsteady flows** arising during **Czochralski crystal growth** are not still well understood.
- A spatio-temporal temperature data measured in a **rotating frame** could be used to investigate the flow instability mechanism caused by the rotations of crystal and crucible.

- **Objective:**

- To clarify various flow regimes caused by the rotations of crystal and crucible in Czochralski crystal growth





Czochralski pulling apparatus  
 for the growth of silicon crystals.

## Description of Experiment

### 1. Boundary Conditions

- Working fluid : mercury ( $Pr \approx 0.025$ )
- The crystal-disk ( $D= 64\text{mm}$ ) and crucible ( $D= 160 \text{ mm}$ ) were made of aluminum and anodized in order to be electrically insulated and also to prevent amalgamation with the mercury.
- The free surface of mercury ( $H=32\text{-}80\text{mm}$ ) was covered with a water layer of 10 mm to prevent mercury evaporation. The influence of the water layer on the convection of the mercury can be neglected, due to the large difference in densities.
- Two thermostat-baths are used to maintain the driving temperature difference,  $\Delta T$  between the disk wall and the crucible side wall. The bottom wall of the crucible was adiabatically insulated by a honey comb base filled with polyurethane foam.

## 2. Thermocouple temperature measurement

- 28 copper-constantan (T type) thermocouples are used to study the relationship among the outputs, especially their phase relations, on the basis of which one can deduce the overall convection pattern and flow structure.
- Traveling waves are sensed by these thermocouples, which are separated azimuthally by the angle of  $\Phi = \frac{1}{6}\pi$  rad. The wave numbers and the angular velocity of the regular wave patterns are determined from the relative wave phases sensed by the adjacent probes.
- The junctions of the thermocouples were soldered and enameled with a thin coat of insulating materials.

## 3. Effects of protrusions of the TC probes

- Geometrical change effect of the container
- An effect of increased viscosity (Fowles, 1974)
- Use of relatively thin copper-constantan (T type) TC probes (0.1 mm diameter with 0.5 mm sheath diameter, OMEGA-CLAD) to reduce such an increased viscosity effect in connection with a relatively large dimension of crucible diameter (160 mm).
- To investigate the effects of the thermocouples protrusion, we used two sets of thermocouples underneath the crystal disk, of which protrusion depths are 1 mm and 2 mm, resp. There was no evidence of a significant change in characteristics of the thermal wave due to the different protrusion depths.

#### **4. Adverse effects occurred by placing fixed probes in a rotating flow**

- Kaiser (1969) observed that as one temperature probe traversed through the fluid, the temperature of the other fixed probe changed by the order of 15%.
- Use of TC probes rotating with crucible and crystal.
- Rotating electrical contact : Two slipring assemblies made of brass and mechanical carbon brushes (Schleifring GmbH)

#### **5. Cold junction compensation method**

- Use of a rotating isothermal copper block in which TC junction (copper-constantan) are embedded.
- Without rotation: the reference temperature of the copper block is measured by using platinum resistance thermometer (Pt 100) without rotation.
- With rotation: an electronic thermometer with cold junction compensator (AD595, ANALOG DEVICES) is used to measure the temperature of a chromel-alumel thermocouple which is also embedded inside the isothermal copper block.

#### **6. Electrical noise induced by the mechanical carbon brush of the slipring**

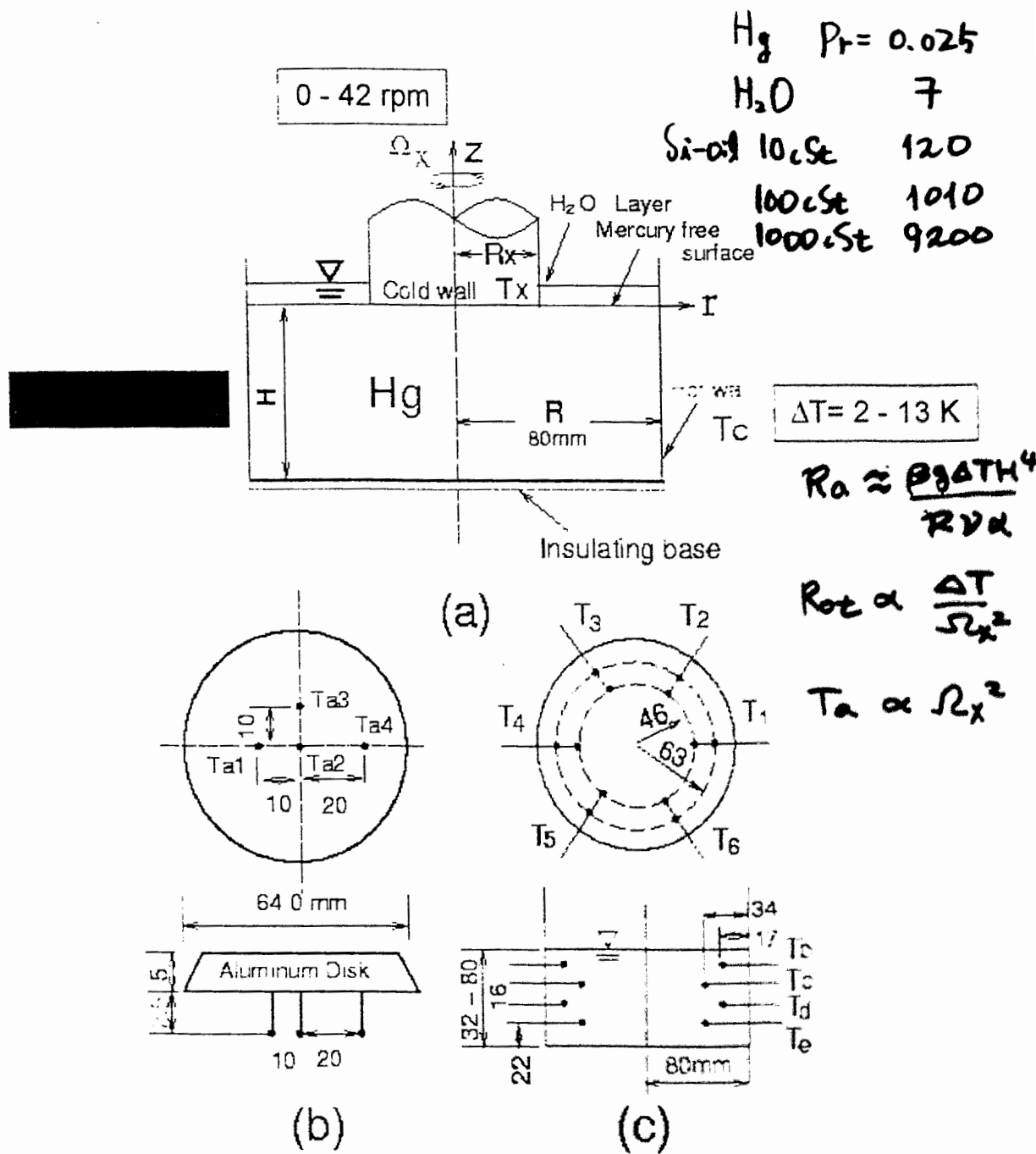
- TC signals are amplified by a factor of 2201 by a linear amplifier before passing the slipring, to maximize the ratio of signal to noise induced by a mechanical brush of the slip ring.

## 7. Probes interference

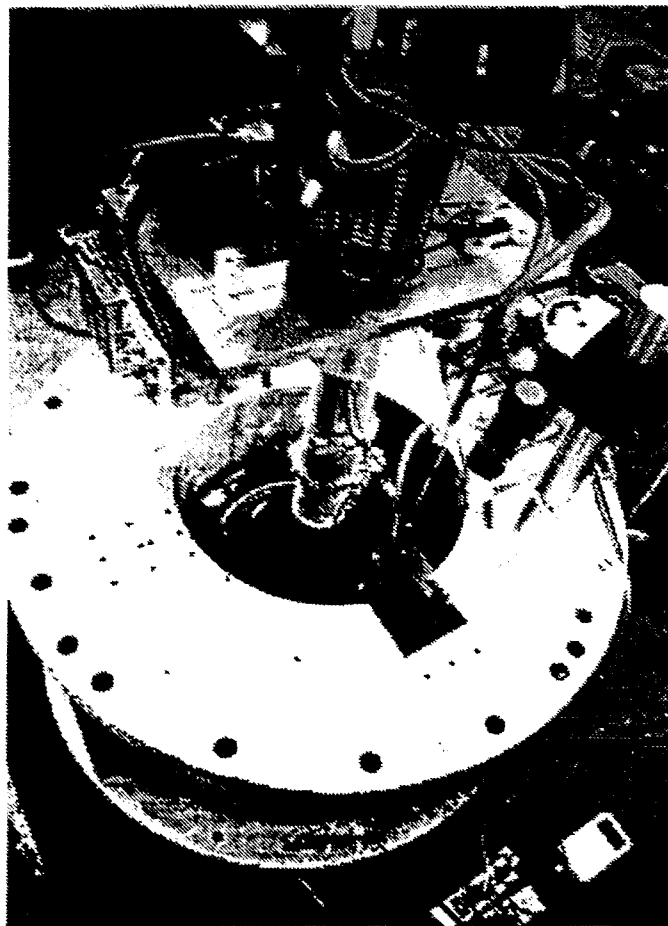
- It can be expected that a upstream probe causes to produce a wake, which affects a downstream probe. Supposed that the Reynolds number based on the probe diameter can be estimated to be about order of 100, the shedding frequency of vortex behind the probe in the present study can be estimated to be greater than approximately 4 Hz.
- Typical frequency components of concern in the present study are less than 1 Hz. So, it can be expected that the disturbing effect of the probes is not so serious as to result in a misleading temperature fluctuation measurement.

## 8. Data acquisition

- The amplified signals are converted into 12-bit digital signal by DT-2805 (DATA TRANSLATION) A/D converting board at a sampling frequency of 2 Hz and stored in a personal computer. For each sampling, data are taken 50 times and an averaged value is taken.
- The resolution of the temperature measurement was about  $0.02^{\circ}C$ .



Schematic diagram(a) of the model crucible and crystal and thermocouples arrangement underneath the model crystal(b) and in the crucible(c).



A photograph of the experimental apparatus.

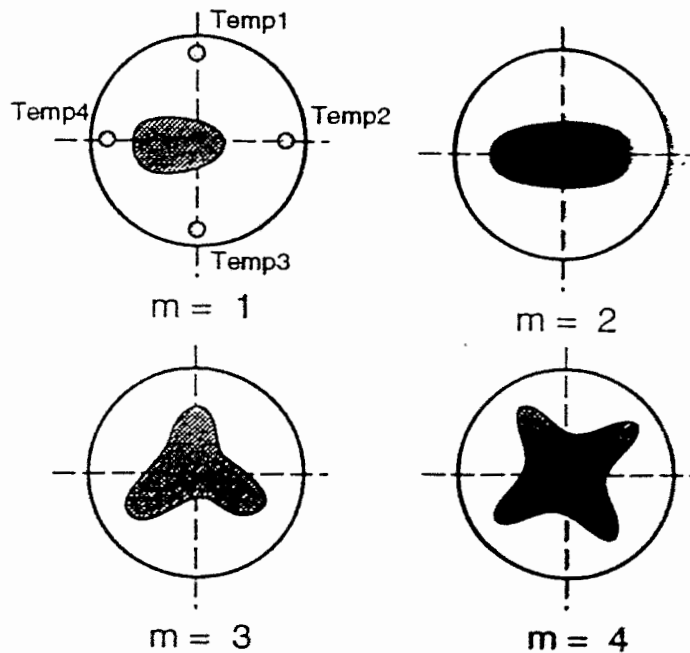
Table 1: Dimensionless governing parameters

$H/R$	Aspect ratio	$0.4 - 1.0$
$Pr = \nu/\alpha$	Prandtl number	$0.025$
$Ra = \beta g \Delta T H^4 / \nu \alpha$	Rayleigh number	$3 \times 10^4 - 2 \times 10^7$
$Gr = Ra / Pr$	Grashof number	
$Ro_T = \frac{g \beta \Delta T H}{\omega_c^2 (R - R_S)^2}$	Thermal Rossby number	$0.08 - 1.6$
$Ta = \frac{\omega_c^2 (R - R_S)^2}{\nu \beta H}$	Taylor number	$9.5 \times 10^7 - 1.5 \times 10^9$
$Ha = BH(\sigma/\mu_0)^{1/2}$	Hartmann number	$0 - 600$

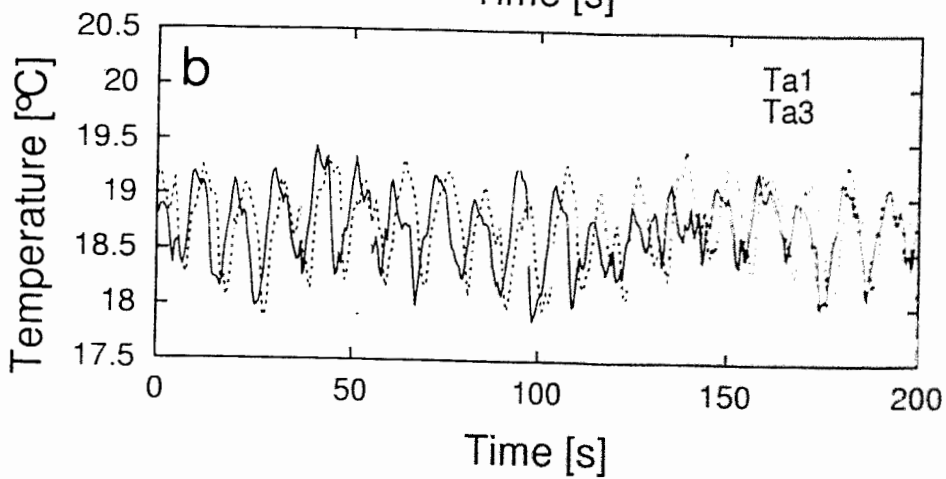
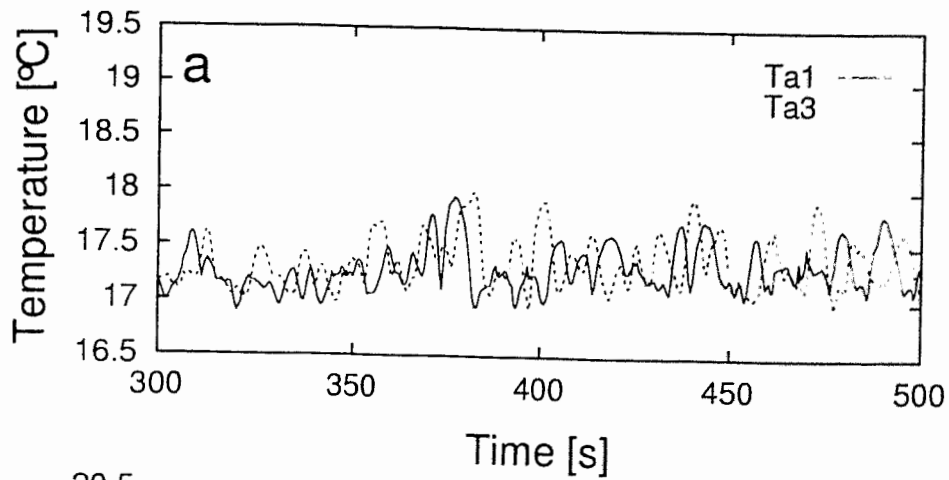
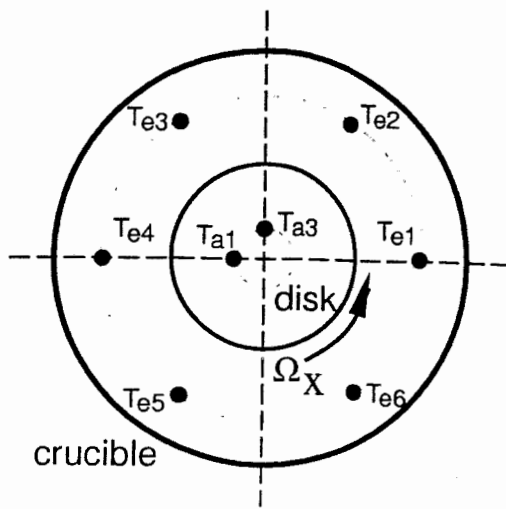


## Data Reduction

- Temperature signal,  $T$ .
- The **standard deviation**,  $S$  of the temperature fluctuations:  $S = \left[ \frac{1}{n-1} \sum_{i=1}^n (T_i - \bar{T})^2 \right]^{1/2}$ .
- The **frequency**,  $f$  of the temperature fluctuations: obtained by a Fourier transformation.
- The **phase difference**,  $\Delta t$  between the temperature signals of two thermocouples which are separated by  $\Phi$ : obtained by calculating a cross spectrum between these signals.
- The **phase velocity**,  $V_p = \Phi / \Delta t$ .
- The **wavenumber**,  $m = 2\pi f / V_p$ .

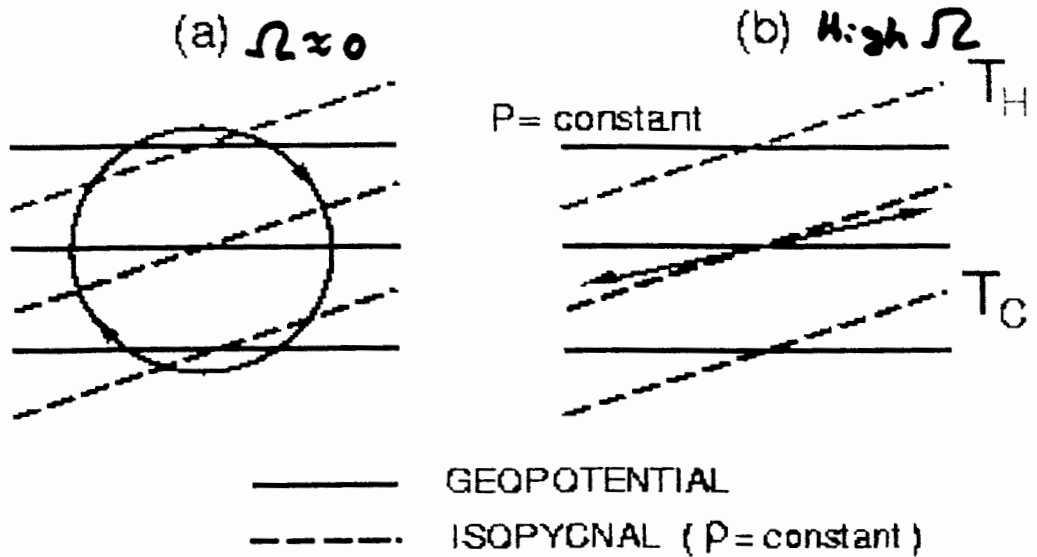


Schematic View of "isotherm" on the horizontal plane for each wave number



Mercury,  $\Delta T = 3.63$  K,  $\Omega_r = 6$  rpm ( $Re_r = 5590$ ). (Wave propagation underneath the disk, observed in a rotating frame); (a)  $H/R = 0.4$ ; (b)  $H/R = 0.8$ .

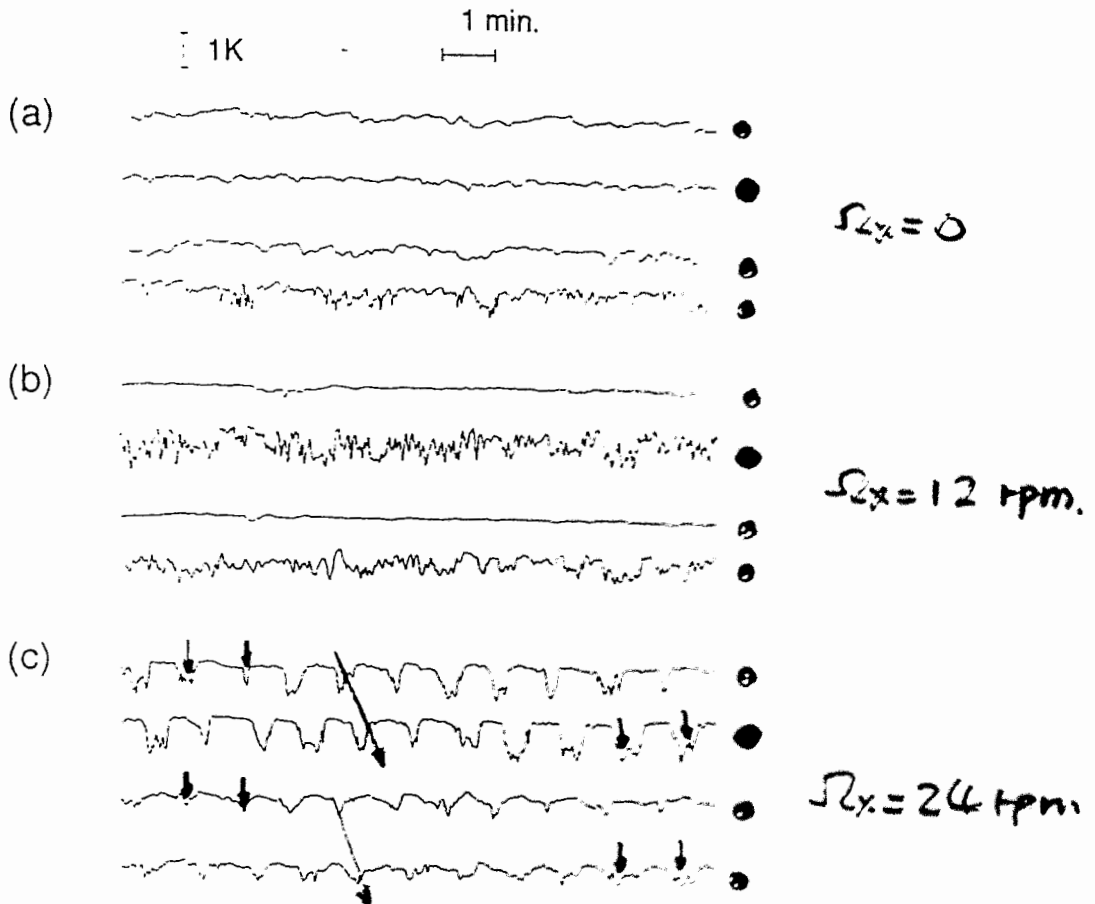
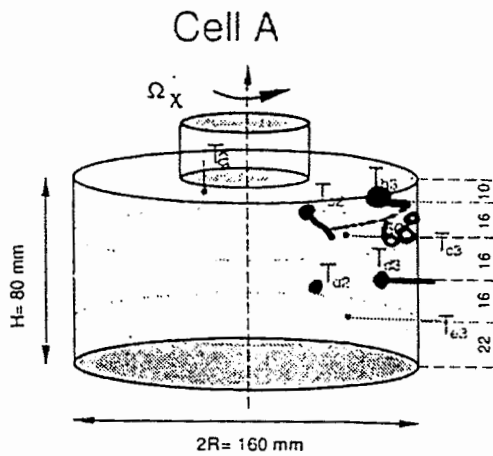
'Sloping convection' in a rotating fluid.



Potential energy of density field  $\rightarrow$  Kinetic energy

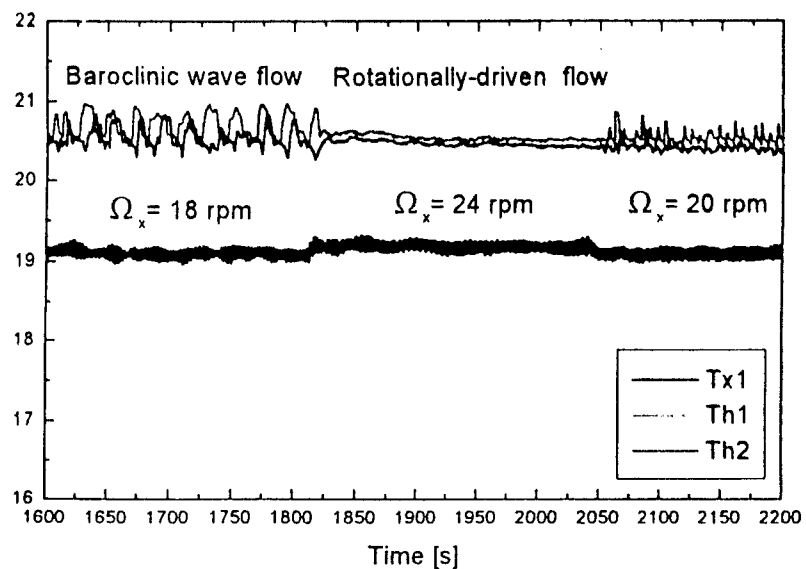
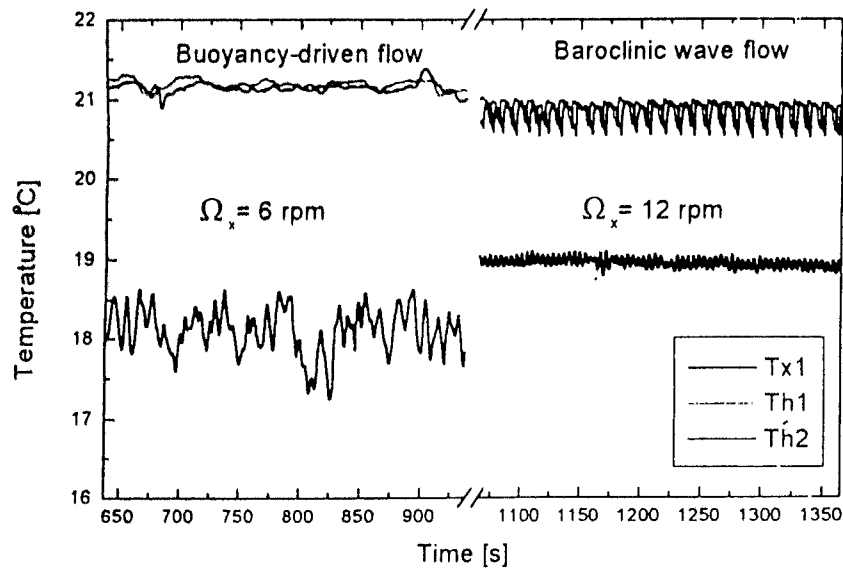
$\downarrow$

**Generation of baroclinic wave**

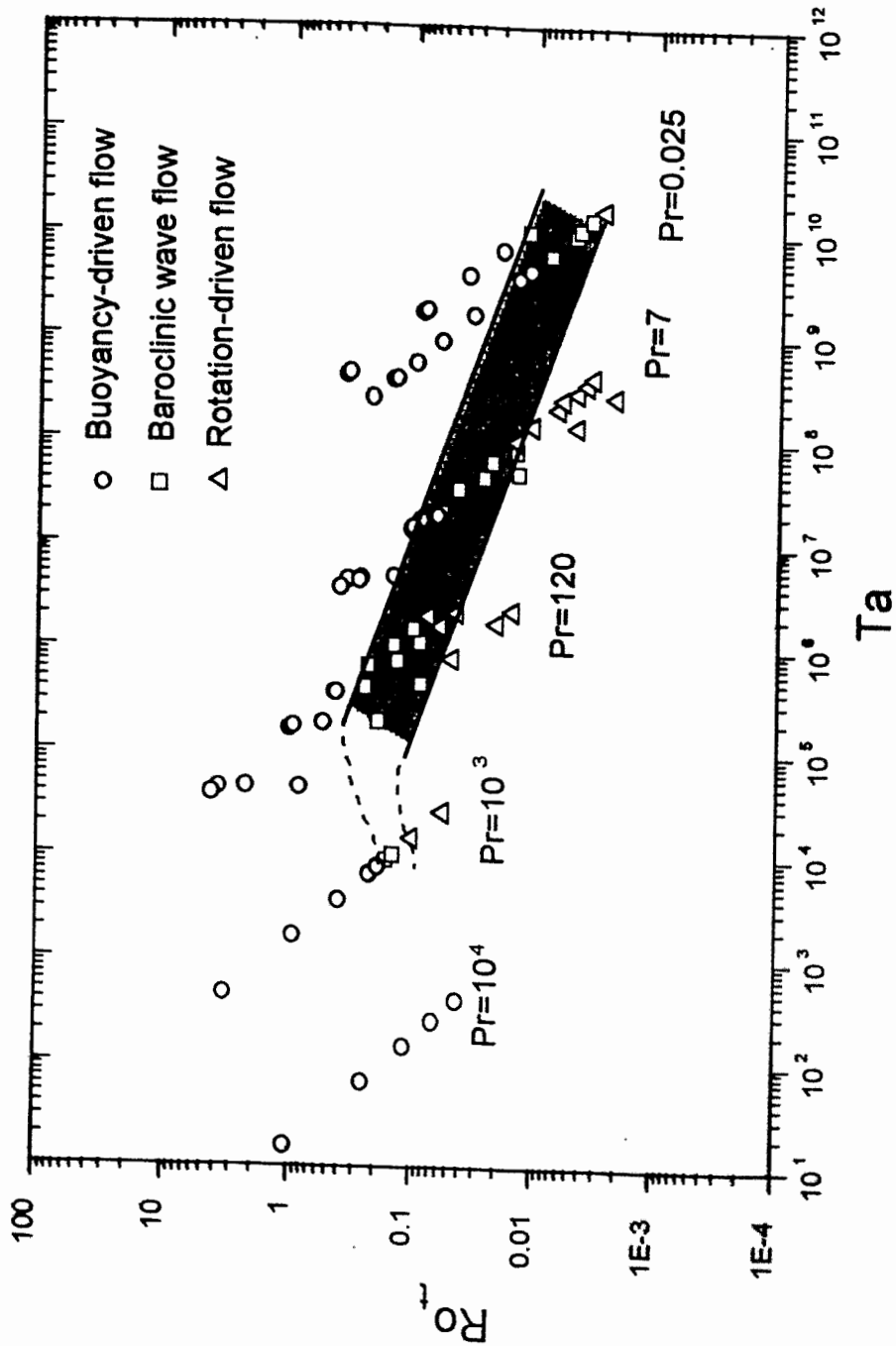


"Perfect correlation in the vertical."

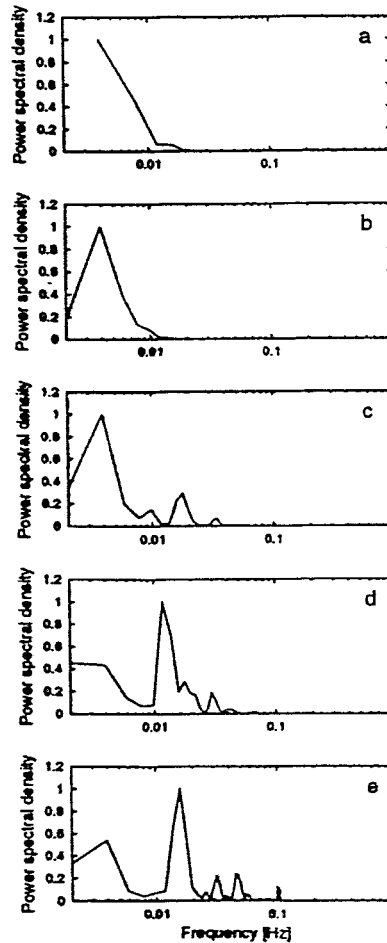
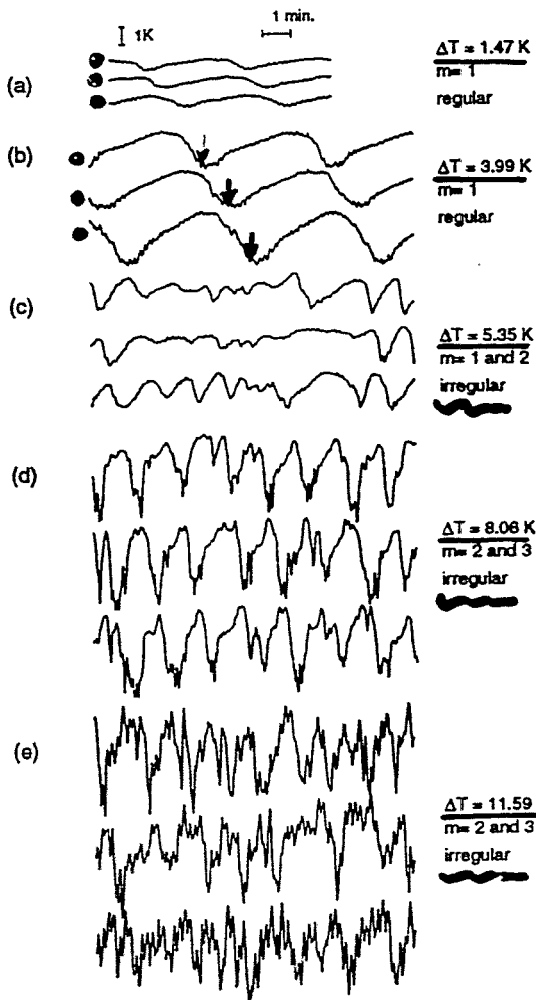
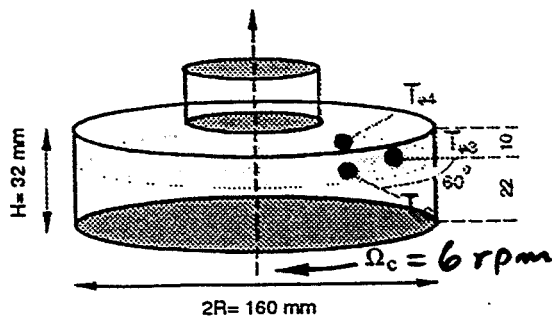
Mercury,  $H/R = 1.0$ ,  $\Delta T = 3.43 \text{ K}$  ( $Ra = 5.57 \times 10^6$ ); (a) without rotation  
 (b)  $\Omega_X = 12 \text{ rpm}$ ; (c)  $\Omega_X = 24 \text{ rpm}$ .



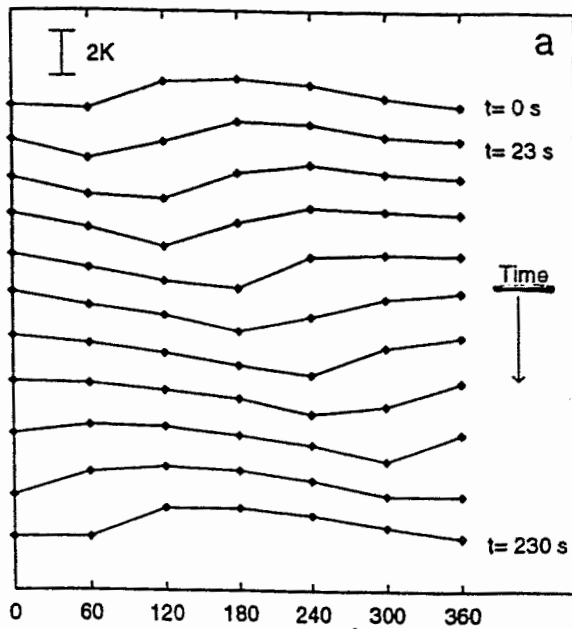
Water,  $H/R=0.4$ ,  $\Delta T=6.7 - 5.4$  K



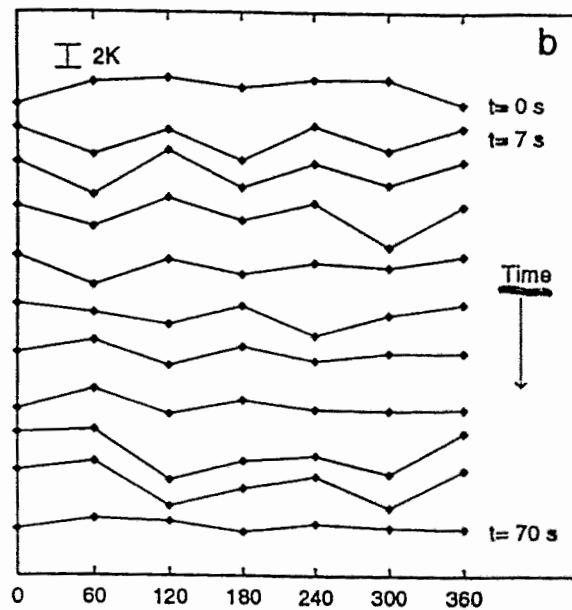
Flow regime diagram of buoyancy-driven baroclinic wave, and rotation-driven flows for different  $Pr$  fluids.  $H/R = 1.0$ .



Temperature signals of three adjacent thermocouples  $T_{e2}$ ,  $T_{e3}$ , and  $T_{e4}$ , and the corresponding power spectra of  $T_{e2}$  signal under conditions: Mercury,  $H/R = 0.4$ ,  $\Omega_c = 0.628 \text{ rad/s}$ .



$\Delta T = 3.99 \text{ K}$   
 (regular wave)  
 $m = 1$



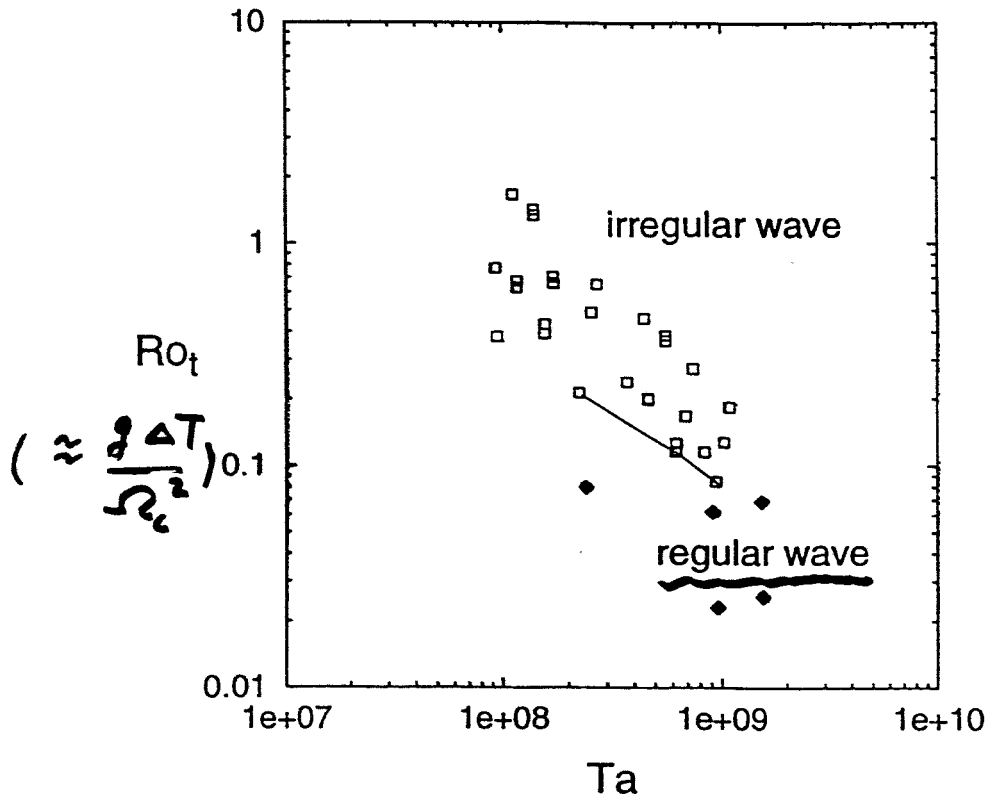
$\Delta T = 11.59 \text{ K}$   
 (irregular wave)  
 $m = 2$   
 $m = 3$

↓  
 $m = 2$

Measuring position,  $\theta$  [deg.]

Space-time plots of the traveling thermal waves in the azimuthal direction:  $H/R = 0.4$ ,  $\Omega_c = 0.628 \text{ rad/s}$ ; (a)  $\Delta T = 3.99 \text{ K}$ , wave number  $m = 1$ ; (b)  $\Delta T = 11.59 \text{ K}$ , wave number variations from  $m = 2$  to  $m = 3$  and again to  $m = 2$ .





An experimental flow regime diagram for the existence of regular and irregular waves.

## CONCLUSIONS

1. A high resolution ( $< 0.02\text{K}$ ) temperature measurement in a rotating mercury melt has been successfully accomplished.
2. A Spacio-temporal temperature fluctuation measurement is applied to investigate oscillatory convection of the mercury melt induced by coupling of natural convection with the rotations of crystal disk and crucible in a Czochralski crystal growing configuration.
3. The generation of a **regular baroclinic thermal wave** and the **transition to an irregular wave** are experimentally verified in a rotating frame when the **crucible rotation** is applied.
4. It is found that a traveling thermal wave is produced when the **rotation of crystal disk** is applied. **Three distinct flow regimes** are shown to exist, which are **buoyancy driven flow, baroclinic wave flow, and rotationally-driven flow.**



Kristallographisches Institut  
Albert-Ludwigs-Universität Freiburg  
Hebelstr.25, D-79104 Freiburg i. Br.

# Flow Velocities in Liquid Gallium as a Function of an Applied Rotating Magnetic Field

MTLM

October 11-13, 1999, Dresden

P. Dold and K.W. Benz

Kristallographisches Institut  
Albert-Ludwigs-Universität Freiburg  
Hebelstraße 25  
79104 Freiburg, Germany

## Content:

- Motivation
- Rotating magnetic field: theory and hardware
- Tracer Velocity on an isothermal surface
- Azimuthal transport of temperature fluctuations

# Flow Velocities in Liquid Gallium as a Function of an Applied Rotating Magnetic Field

*P. Dold and K.W. Benz*

*Kristallographisches Institut, Universität Freiburg, Hebelstr. 25, D-79104 Freiburg*

Rotating magnetic fields (RMF) are an effective tool to homogenize liquid metals or semi-conductors as well as to stabilize solidification processes and the solid-liquid interfaces.

To determine the induced flow velocity as a function of the RMF, two different approaches have been applied, in both cases, gallium served as a model liquid, enclosed in cylindrical quartz glass containers. The range of the investigated Taylor number was  $0 \leq Ta \leq 4 \cdot 10^7$ , or expressed in terms of the magnetic induction and the frequency of transverse rotating magnetic field it was  $0 \leq B \leq 11 \text{ mT}$  and  $5 \leq f \leq 400 \text{ Hz}$ .

## I. Tracking of tracer particles on an oxide-free melt surface.

The experiments have been performed under isothermal conditions at room temperature, the Taylor number was  $Ta \leq 6.5 \cdot 10^4$ . The measured radial velocity profiles have been used to validate corresponding numerical simulations. Therefore, reliable information about the flow field was obtained not only at the surface but also in the bulk of the melt.

## II. High resolution temperature measurements in a closed cylinder.

Up to three sapphire sensors have been inserted into the melt, the temperature range of the measurements was between 700 and 900°C, and the investigated range of the Rayleigh number was  $-10^6 \leq Ra \leq 10^6$ . In the case of  $Ra < 0$ , the onset of Taylor instabilities was observed. For  $Ra > 10^5$  (i.e. time dependent buoyancy convection), the velocity of the superimposed flow due to the RMF can be extracted from the time-lag of corresponding temperature signals. For a certain Ra-number, the transition point where the flow regime is dominated by the RMF (and where the time-dependent temperature fluctuations are suppressed to a high degree) can be described as a function of the Rayleigh-number and the square root of the Taylor-number:  $Ra \sim \sqrt{Ta}$ .

## **Co-workers**

Dr. Th. Kaiser

Dipl.-Phys. Ing. St. Rothenbacher

Fr. L. Rees-Isele

## **Cooperation**

Prof. E. Bänsch, University of Bremen  
(numerical simulation)

## **Financial Support**

Deutsches Zentrum für Luft-  
und Raumfahrt e.V. (DLR)

European Space Agency (ESA)



# Motivation

Growing semiconductor crystals (e.g. Si or Ge) from the melt:

- > variation of the composition in the micro- and macroscale due to time-dependent convection (buoyancy, thermocapillary etc.)
- > control of these convective flows by the use of external fields
- > optimization of the field strength and the configuration requires the knowledge of the corresponding flow velocity

# Growth of FZ-Si in a rotating magnetic field

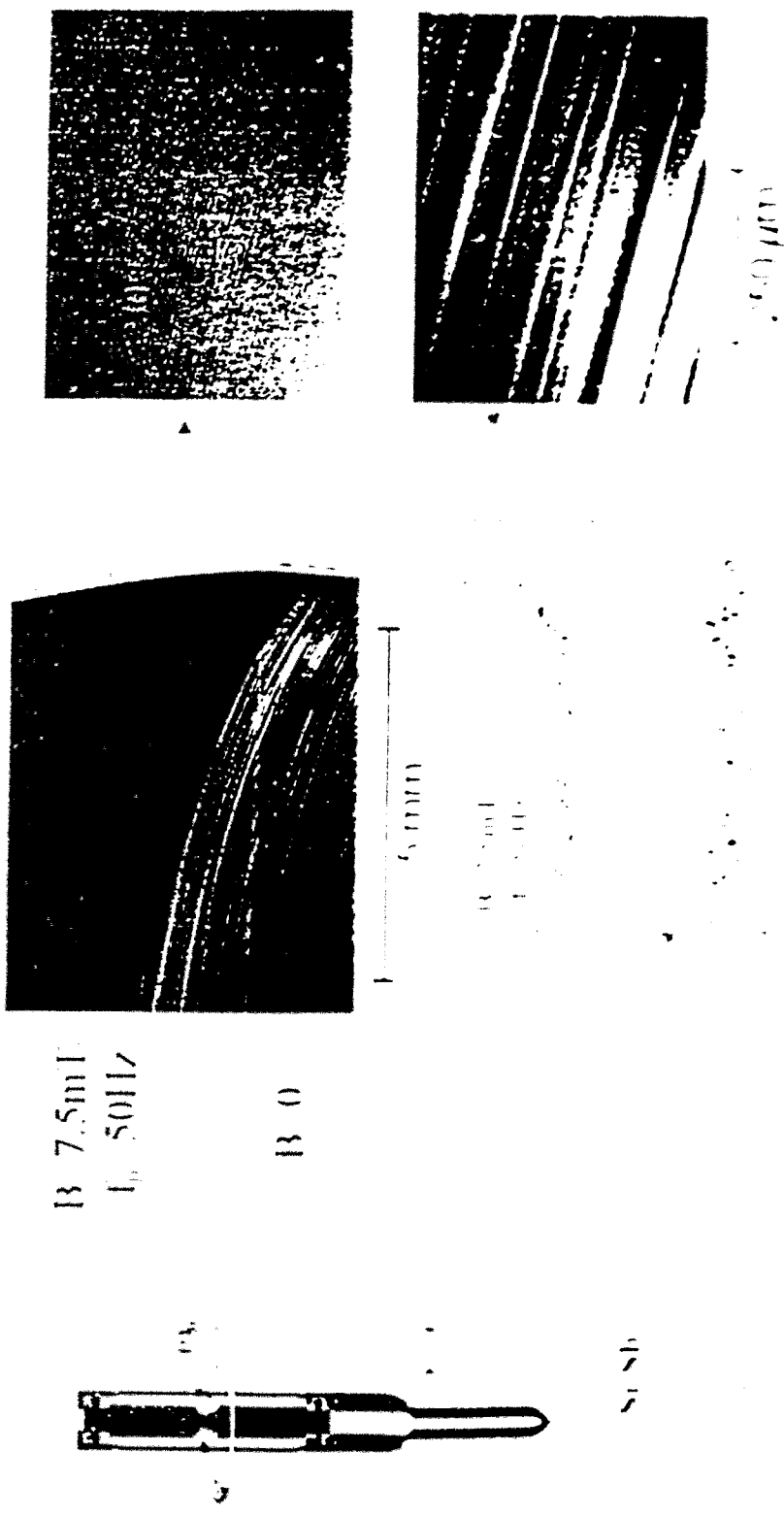


Fig. 1. Growth of FZ-Si in a rotating magnetic field.

Received August 15, 1988; revised manuscript received October 10, 1988.

# Material Properties

Silicon:

- $T_m = 1415^\circ\text{C}$
- in the liquid state, silicon reacts with every known material

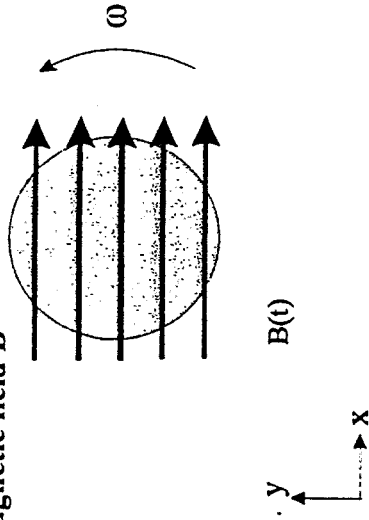
Gallium:

- liquid over a wide temperature range  
( $T_m = 29.8^\circ\text{C}$ ,  $T_b = 2403^\circ\text{C}$ )
- below  $1000^\circ\text{C}$ , the vapor pressure is neglectible
- material parameters are relatively well known

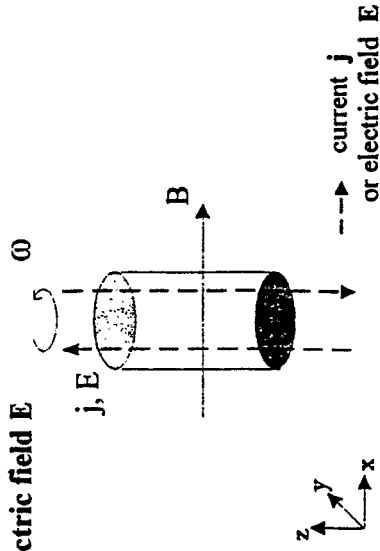


# Effect of rotating magnetic field on electrically conducting melts

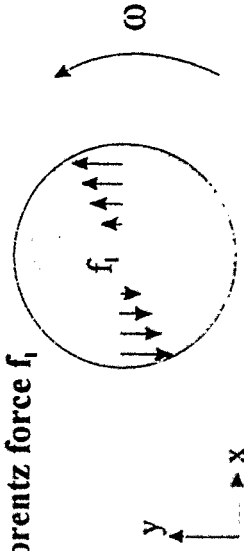
I. magnetic field  $B$



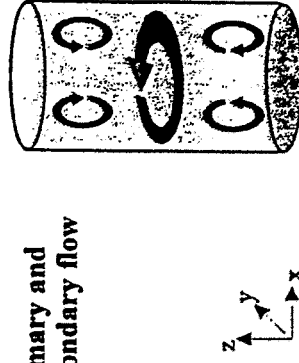
II. electric field  $E$



III. Lorentz force  $f_l$



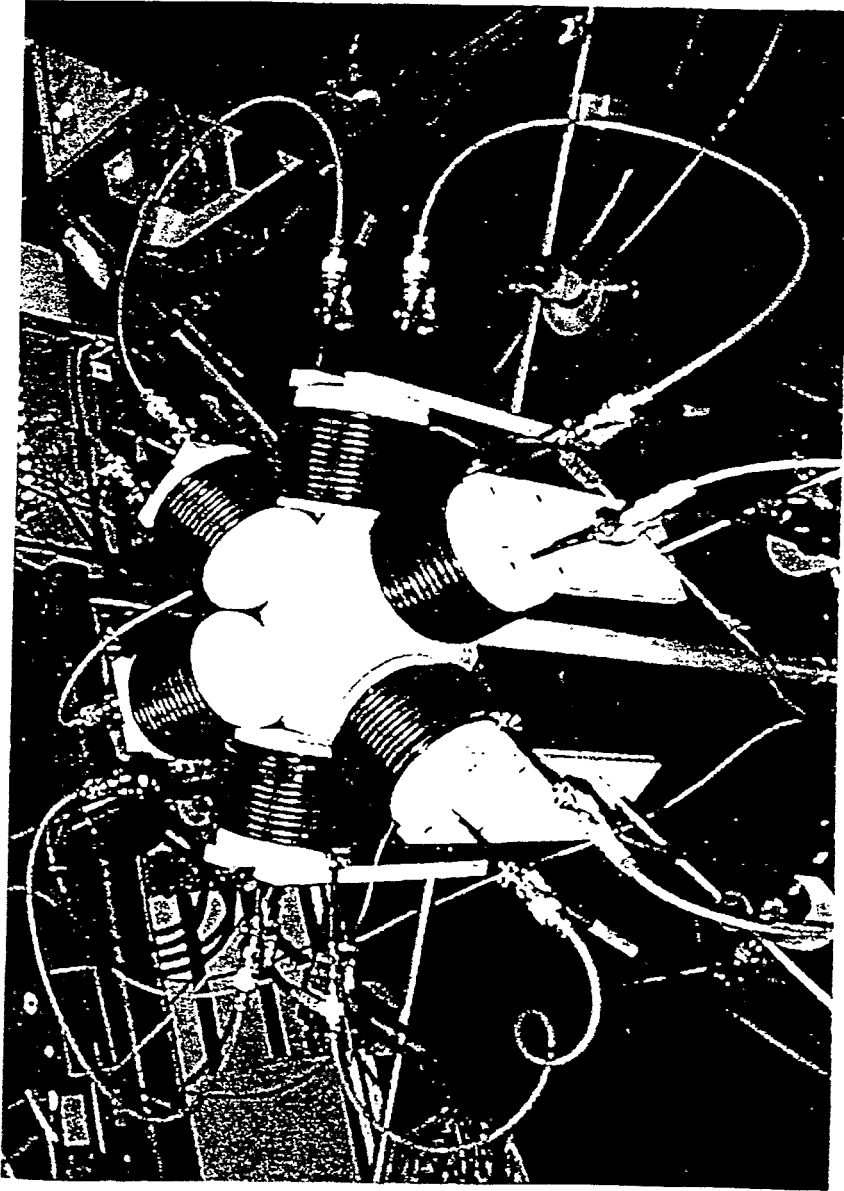
IV. primary and secondary flow



Kristallographisches Institut  
 Albert-Ludwigs-Universität Freiburg  
 Hebelstr. 25, D-79104 Freiburg i. Br.

Effect of rotating magnetic field on  
 electrically conducting melts  
 P. Dold, K.W. Benz

# Rotating magnetic fields: hardware



$B_{\text{max}} = 10 \text{ mT}$  (dep. on the diameter),  $f = 50 \text{ Hz}$  (KI)



Kristallographisches Institut  
Albert-Ludwigs-Universität Freiburg  
Herbertstr. 25, D-79104 Freiburg i. Br.

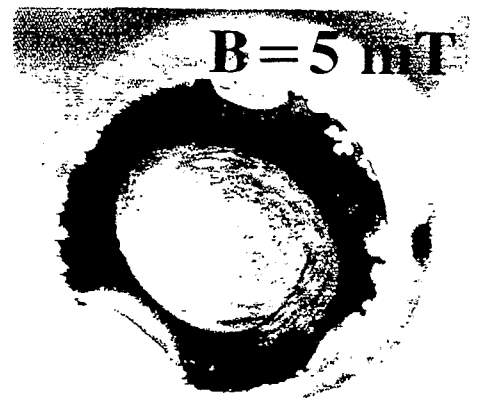
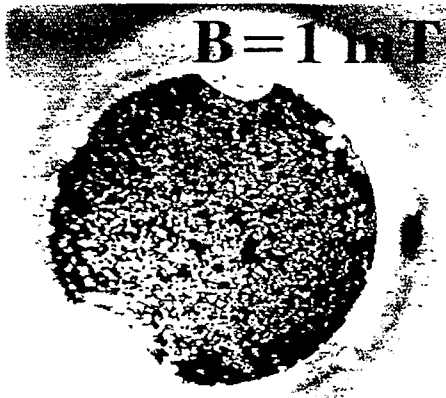
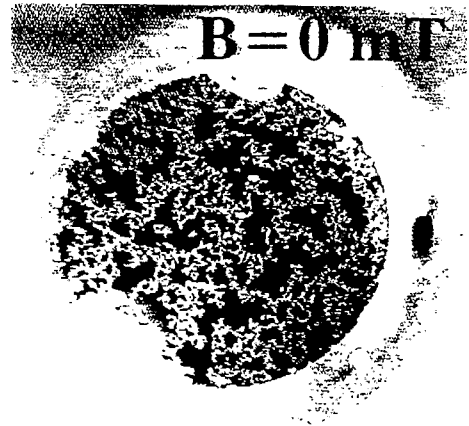
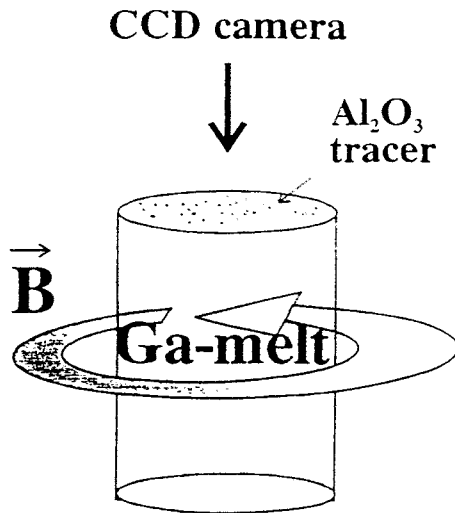
Rotating magnetic fields: hardware  
P. Dold, M. Schweizer, K.W. Benz

# Set-up I: Flow velocity of tracer particles

- \* cylindrical gallium melt,  $r=12.5\text{mm}$ ,  $h=50\text{mm}$ , enclosed in quartz-glass ampoules
  - => oxid-free melt surface
- \* observation of  $\text{SiO}_2$  /  $\text{Al}_2\text{O}_3$ -particles by CCD-camera
- \* isothermal conditions (room temperature)
  - => no additional buoyancy convection
- \* restricted to the azimuthal component of the surface velocity

# Fluid flow observation

- free gallium surface with tracer particles



$f = 20 \text{ Hz}$

10 mm

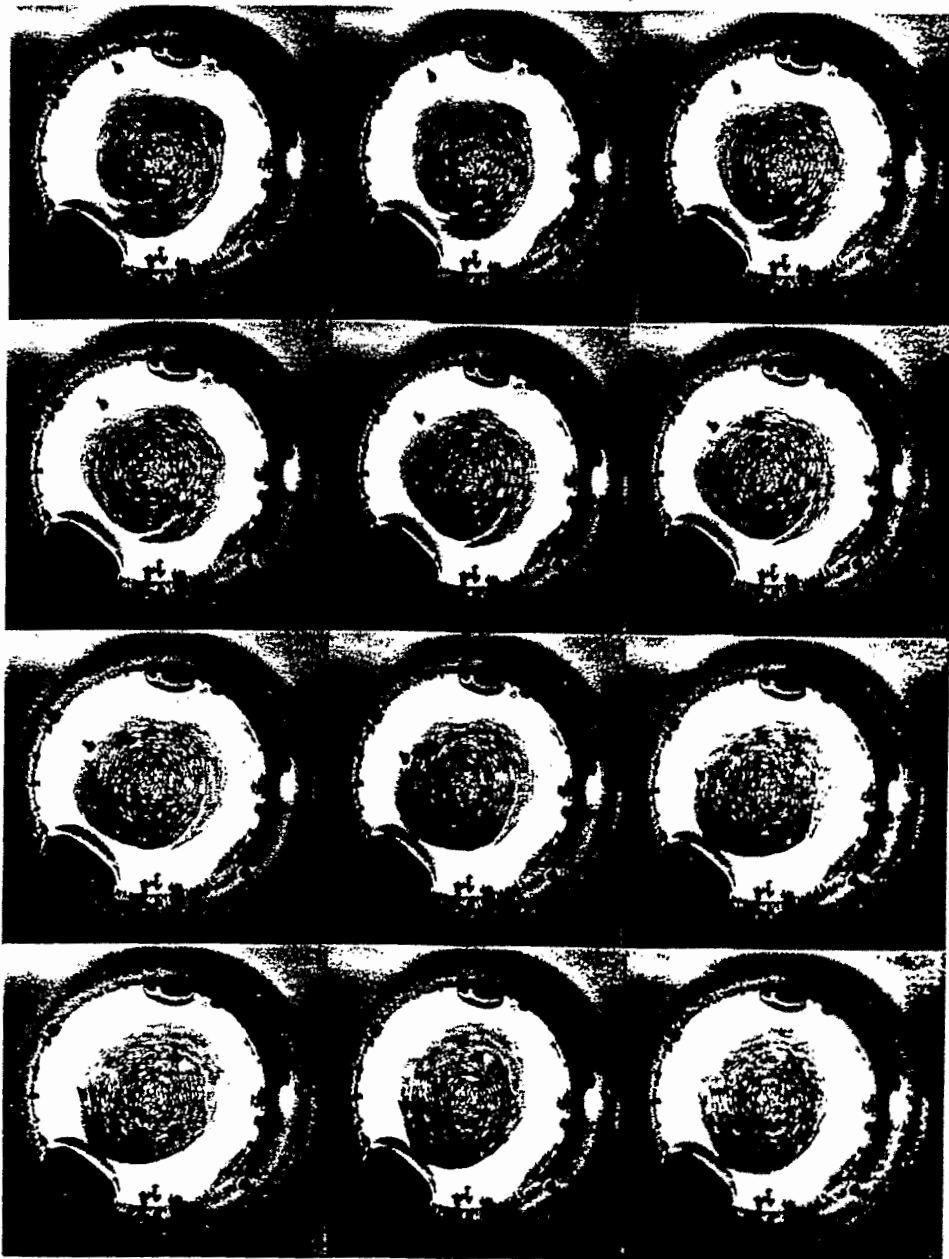


Kristallographisches Institut  
Albert-Ludwigs-Universität Freiburg  
Hebelstr. 25 D-79104 Freiburg, Br

MDT 2 - Fluid flow observation  
P. Dold, K.W. Benz

# Fluid flow observation

Gallium:  $B=1$  mT,  $\omega=400$  Hz,  $\Delta t=0.04$  sec/image



—|—|—  
10 mm

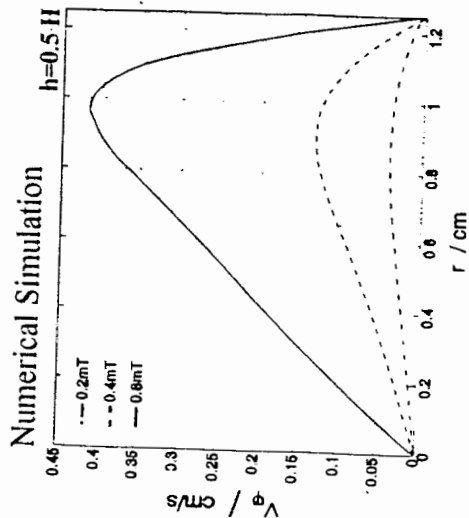
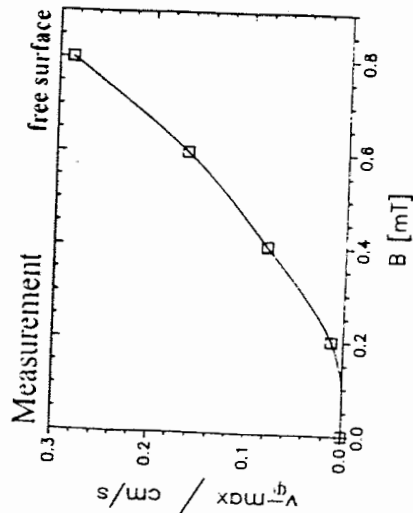
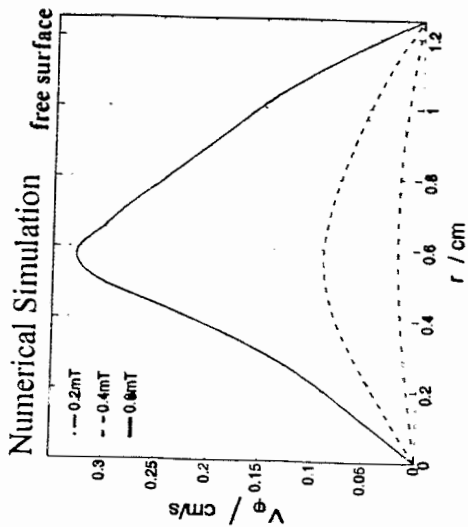
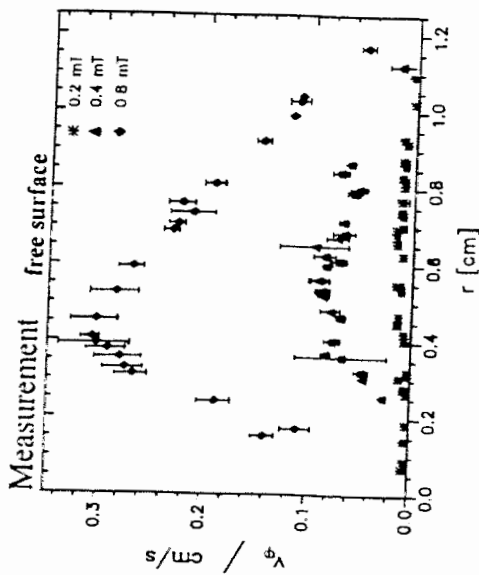


Kristallographisches Institut  
Albert-Ludwigs-Universität Freiburg  
Herzstr. 25, D-79104 Freiburg i. Br.

MDT 2 - Fluid flow observation  
P. Deid, S. Boscher

# Rotating magnetic fields: numerical simulation

$f_B = 20 \text{ Hz}$



Kristallographisches Institut  
 Albert Ludwigs Universität Freiburg  
 Hebelstr. 25 D-79104 Freiburg i. Br.

Rotating magnetic fields: numerical simulation

M Tenhaeff, F Bänisch, Th. Kaiser, PDold, K.W Benz

## Results

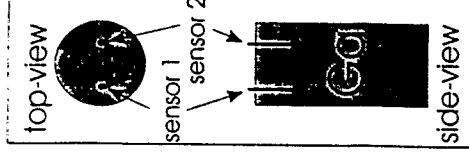
- with  $B=0.8\text{mT} / f_g=20\text{Hz}$ , a maximum flow velocity of 3mm/s was measured
- on the free surface, the flow maximum is shifted in direction to the center (compared to analytical solutions for infinite cylinders)
- good agreement with numerical simulations (Th. Kaiser, E. Bänsch); in the bulk of the melt, the maximum flow velocity is approx. 30% higher than on the surface, the position of the maximum is near the container wall



## Set-up II:

### Temperature measurements inside the melt

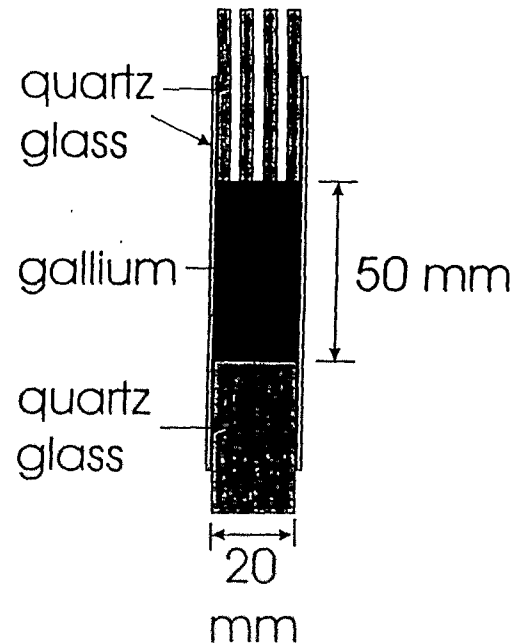
- \* cylindrical gallium melt,  $r=10\text{mm}$ ,  $h=50\text{mm}$
- \* high resolution sapphire rods were used for temperature measurements (black body)
  - 2 sensors at  $r=0.5R$  and  $r=-0.5R$ ,  $z=10\text{mm}$
- \* temperature range:  $700 - 900^\circ\text{C}$ , Rayleigh numbers:  $Ra=-10^6$  to  $10^6$
- \* magnetic field:  $B < 8.6\text{mT}$ ,  $5 < f_b < 400\text{Hz}$



Temperature fluctuations caused by buoyancy or by Taylor instabilities are transported in azimuthal direction by the rotating magnetic field



# Measurements of convective temperature fluctuations



## Gallium

$$Pr = 2.5 \cdot 10^{-3}$$

Ra between  $-10^6$  and  $10^6$

aspect ratio: 2 and 2.5

magnetic fields:

static axial field up to 500 mT

rotating field with

f between 5 and 400 Hz

and B up to 30 mT

---

Measurement of the temperature directly in the melt, either with thermocouples or sapphire sensors

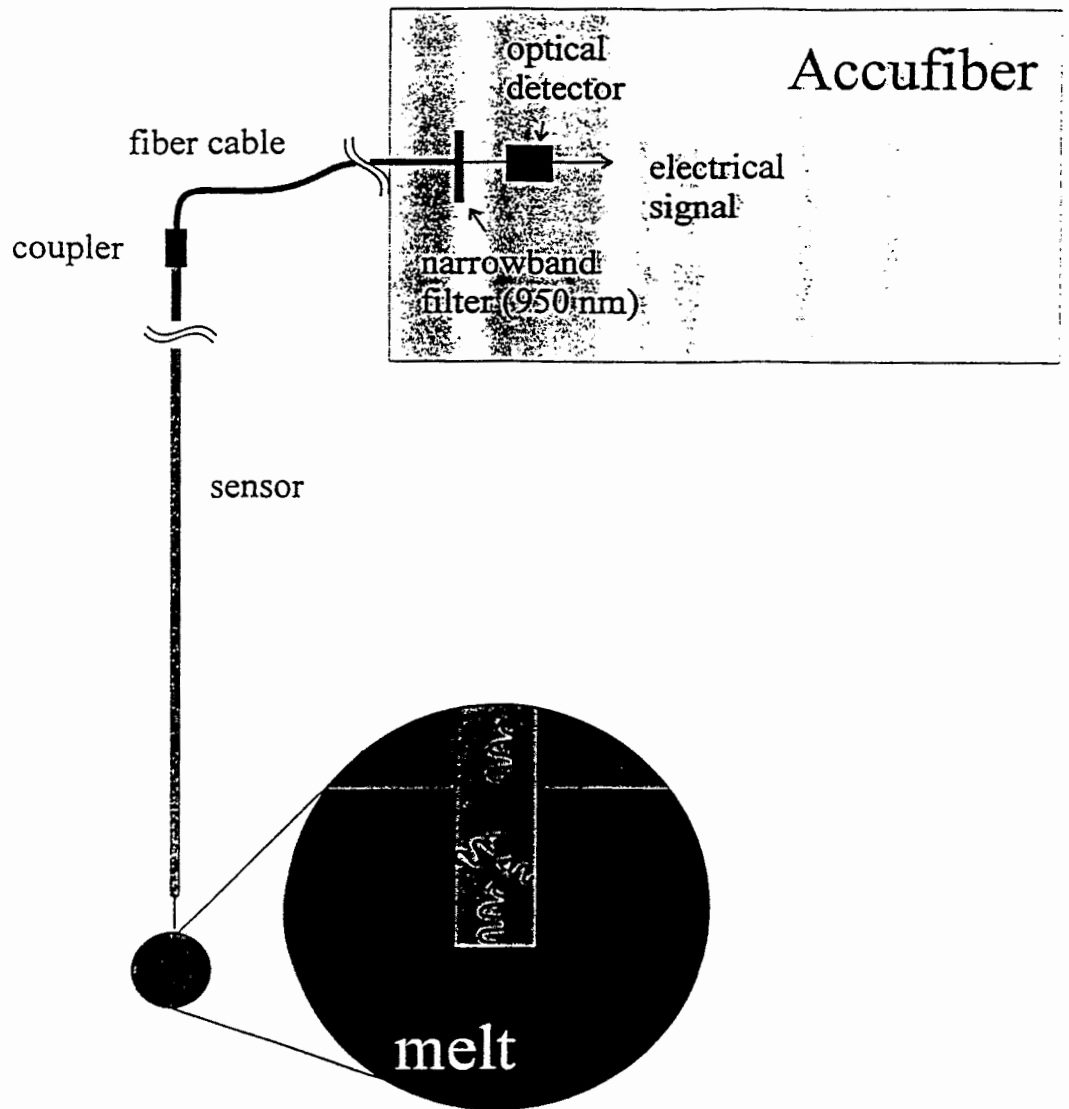


Kristallographisches Institut  
Albert-Ludwigs-Universität Freiburg  
Kerstch 25, D-79104 Freiburg, BR

Measurements of temperature fluctuations in gallium

P. Dold, K.W. Benz

# Optical Fiber Thermometry

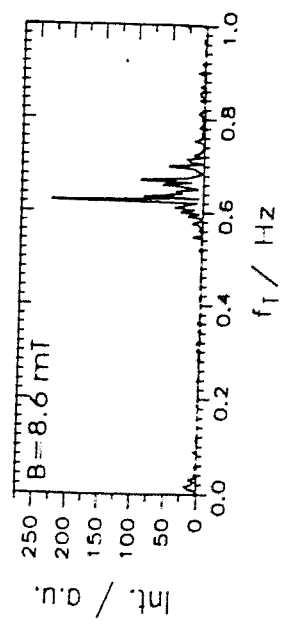
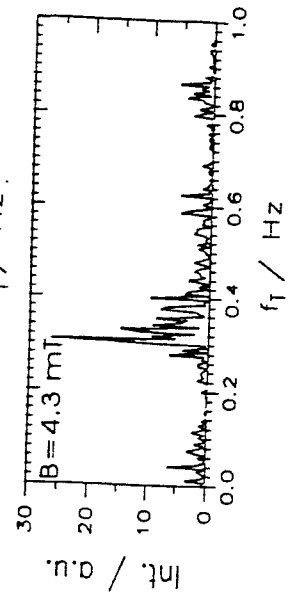
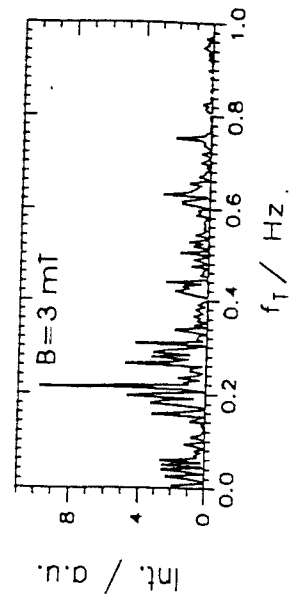
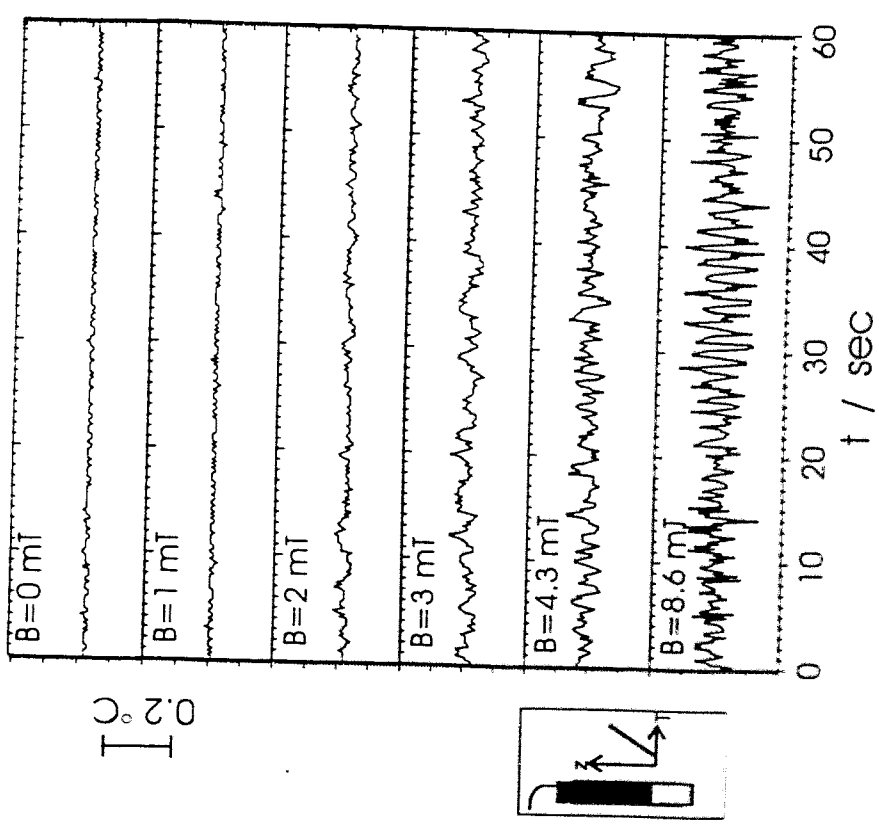


- temperature range: 400-1900°C (sapphire)  
400-1500°C (quartz-glass)
- resolution: 0.01°C
- accuracy: 0.2% at 1000°C (sapphire)
- high chemical resistivity



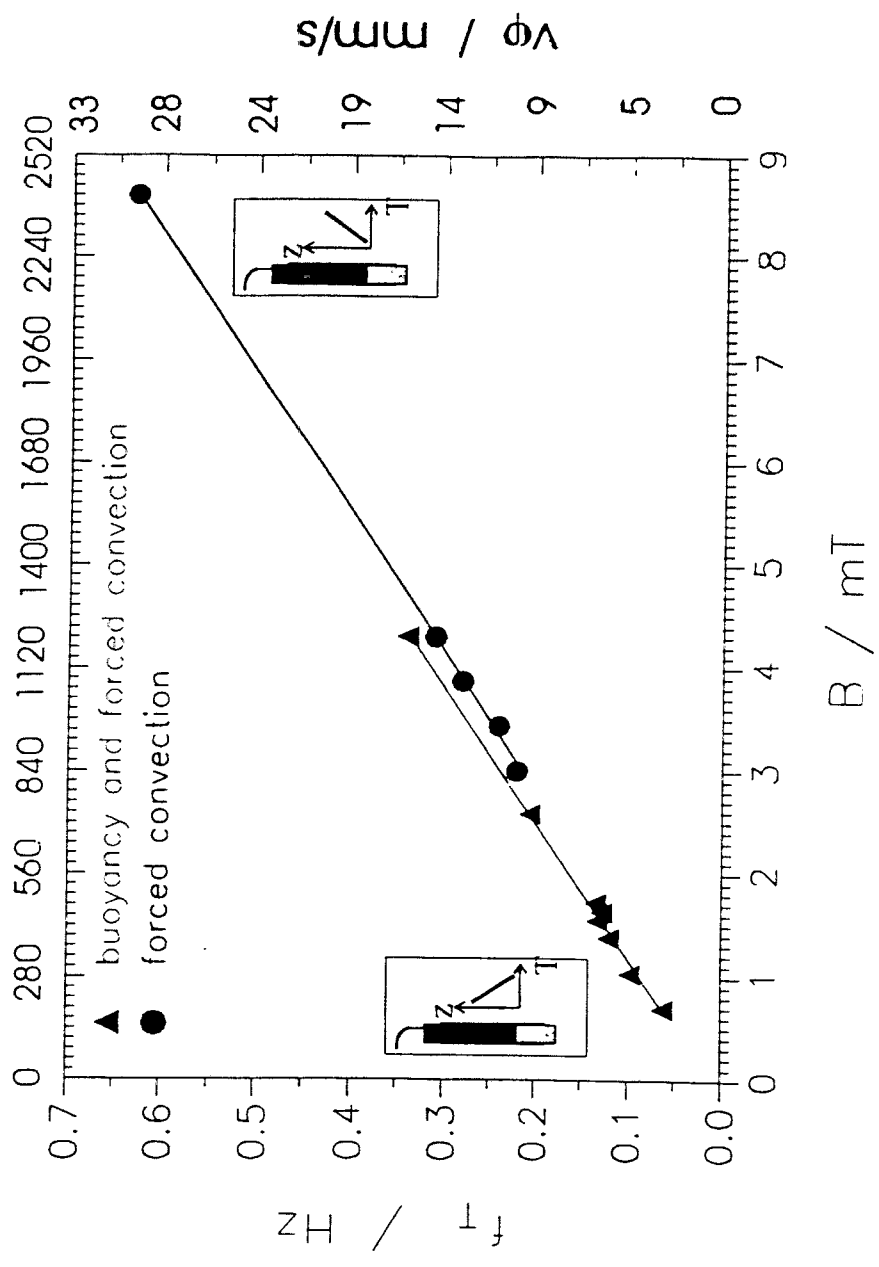
# Rotation frequency and strength of Taylor vortices

$f_b = 20\text{Hz}$



# Rotation frequency of temperature fluctuations and deduced flow velocities

$$\sqrt{Ta} \quad f_b = 20 \text{ Hz}$$



## Results

- $Ra = -10^\circ$  (stable density gradient): first flow instabilities (Taylor vortices) have been detected at  $B = 1.2 \text{ mT} / f_B = 20 \text{ Hz}$ ;
- temperature fluctuations:  $0.01$  to  $0.02^\circ \text{C}$
- azimuthal flow velocity:  $\approx 5 \text{ mm/sec}$
- $B = 8.6 \text{ mT} / f_B = 20 \text{ Hz}$ :  $v_\phi \approx 30 \text{ mm/sec}$  (i.e. the melt rotates with  $0.6 \text{ Hz}$ )
- $Ra = 10^\circ$  (unstable density gradient) buoyancy convection leads to temperature fluctuations up to  $3^\circ \text{C}$ , these could be reduced with the rotating magnetic field by more than one order of magnitude

# **Limitations of permanent magnet incorporated potential difference probe for liquid metal flow investigations in presence of the AC magnetic field**

*A. Bojarevics<sup>\*</sup>, Y. Fautrelle<sup>#</sup>, Yu. Gelfgat<sup>\*</sup>*

*<sup>\*</sup> Latvian Academy of Science, Institute of Physics, Miera iela, LV-2169 Salaspils, Latvia*

*<sup>#</sup> EPM-MADYLAM ENSHMG BP 95 38402 St Martin d'Hères Cedex, France*

The permanent magnet incorporated potential difference probes (PMP) has been tested for liquid metal local velocity measurements in flows driven by AC magnetic field at frequencies ranging from 5 to 50 Hz and at much higher frequency 2400 Hz.

Magnetic force density acting on the rare earth permanent magnet in AC magnetic field may reach extremely high values. Resulting demands to mechanical properties of the probe support should be regarded.

Account should be taken of the local fluid flow perturbation generated by electromagnetic forces resulting from: 1) AC current interaction with permanent magnet DC magnetic field; and 2) DC current interaction with AC magnetic field.

Caution should be taken with the AC signal component induced in the loop formed, on the one hand, by the fork of the probe electrodes and, on the other hand, closed via liquid metal. The AC signal component, regarded as a noise for velocity measurement, may be even for orders higher than the fluid velocity information carrying DC signal. Without proper signal conditioning procedure the signal preamplifier may become saturated by high amplitude AC signal.

The PMP was found to be applicable for investigations of liquid metal under impact of AC magnetic field, but only with thorough critical analysis of probe limitations under specific conditions of actual experiment.

## Limitations of permanent magnet incorporated potential difference probe for liquid metal flow investigations in presence of the AC magnetic field

*Andris Bojarevics\**, *Yves Fautrelle\*\**, *Yu. Gelfgat\**

\* *Institute of Physics, University of Latvia, Miera st. 32, LV-2169 Salaspils, Latvia*

\*\* *EPM-MADYLAM ENSHMG BP 95 384 St Martin d'Herès Cedex, France*

Incorporated permanent magnet velocity probe (PMP) for investigation of liquid metal flow has been described:

1. *R. Ricou and C. Vives. Local velocity and mass transfer measurement in molten metals using an incorporated magnet probe. Int. J. Heat Mass Transfer 25, 1579-1588 (1982).*

2. *T. von Weissenfluh. Probes for local velocity and temperature measurements in liquid metal flow. Int. J. Heat Mass Transfer 28, 1563-1574 (1985).*

In MADYLAM the PMP was tested for applicability to measure liquid Mercury flow induced by low frequency (10 - 40 Hz) AC magnetic field, with induction reaching 0.1 Tesla.

In the Institute of Physics, Riga, the PMP was used to investigate the flow in a model of the 2400 Hz induction furnace.

The PMP has been used in Riga for 12 years during many experiments on low temperature liquid metal flow investigations.

### Principle of the velocity measurement

During a liquid metal flow in presence of steady magnetic field induction the electrical potential distribution in the liquid may reflect the flow velocity field:

$$\vec{j}/\sigma = \text{grad}\phi + \vec{v} \times \vec{B}$$

Assumption

$$\vec{j}/\sigma \ll \text{grad}\phi$$

Actually it should be proved by solving a system of equations for potential, current density and velocity at a fixed magnetic field distribution.

### Permanent magnets

Magnetic field around a rare earth permanent magnet could easily be found, because magnetic permeability of the material, magnetised in up to 5 T field to saturation, is very near to 1. With this assumption the magnetic field may be calculated from the virtual surface current density  $i$ , which coincides with the coercive force of the magnet  $H_c$ .

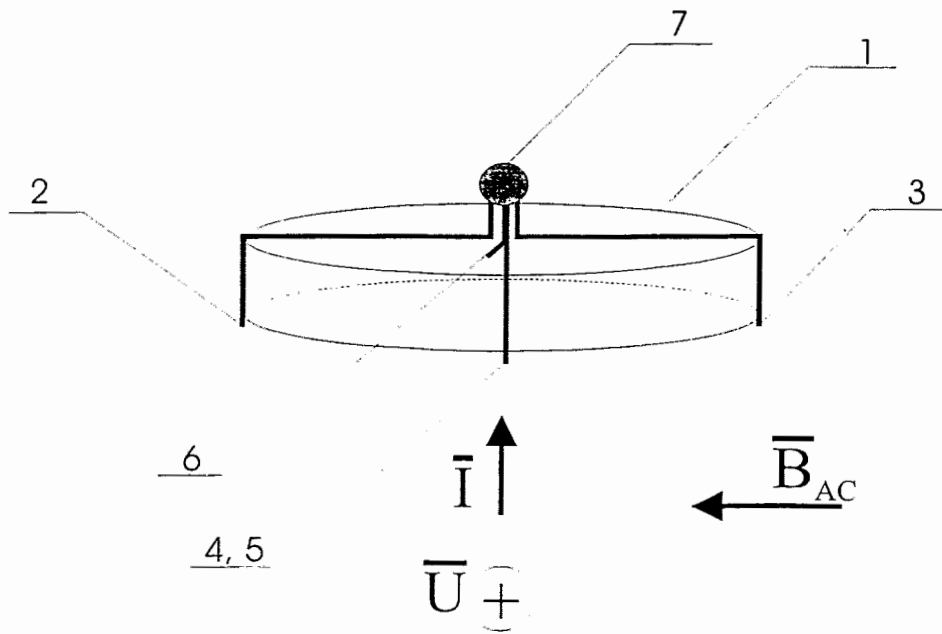
Nd-Fe-B and Sm-Co magnets are produced from a powder. Each of the particles form a single magnetic domain, which after magnetisation up to full saturation do not demagnetise in external field. Single domain particles are sintered into the necessary shape, while magnetisation field and pressure is applied. Resulting material consists of single domain particles frozen in the piece of the magnet.

*Sintered Nd-Fe-B:  $\max H_c = 1.2 \cdot 10^6 \text{ A/m}$ ,  $\max \text{ working } t' = 180 \text{ }^\circ\text{C}$*

*Sintered Sm-Co:  $\max H_c = 0.85 \cdot 10^6 \text{ A/m}$ ,  $\max \text{ working } t' = 350 \text{ }^\circ\text{C}$*

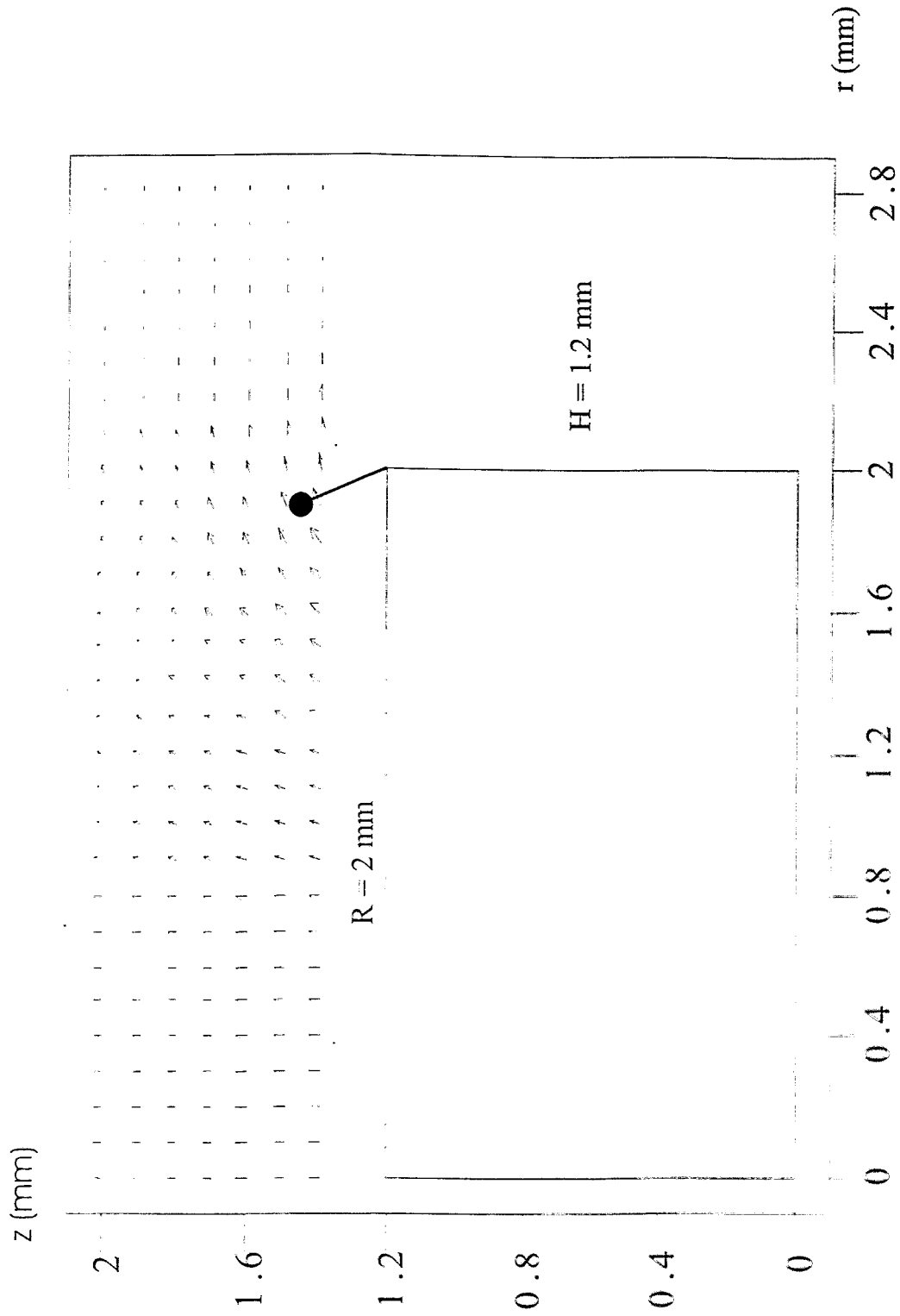
*Casted Al-Ni-Co:  $\max H_c = 0.16 \cdot 10^6 \text{ A/m}$ ,  $\max \text{ working } t' = 540 \text{ }^\circ\text{C}$*





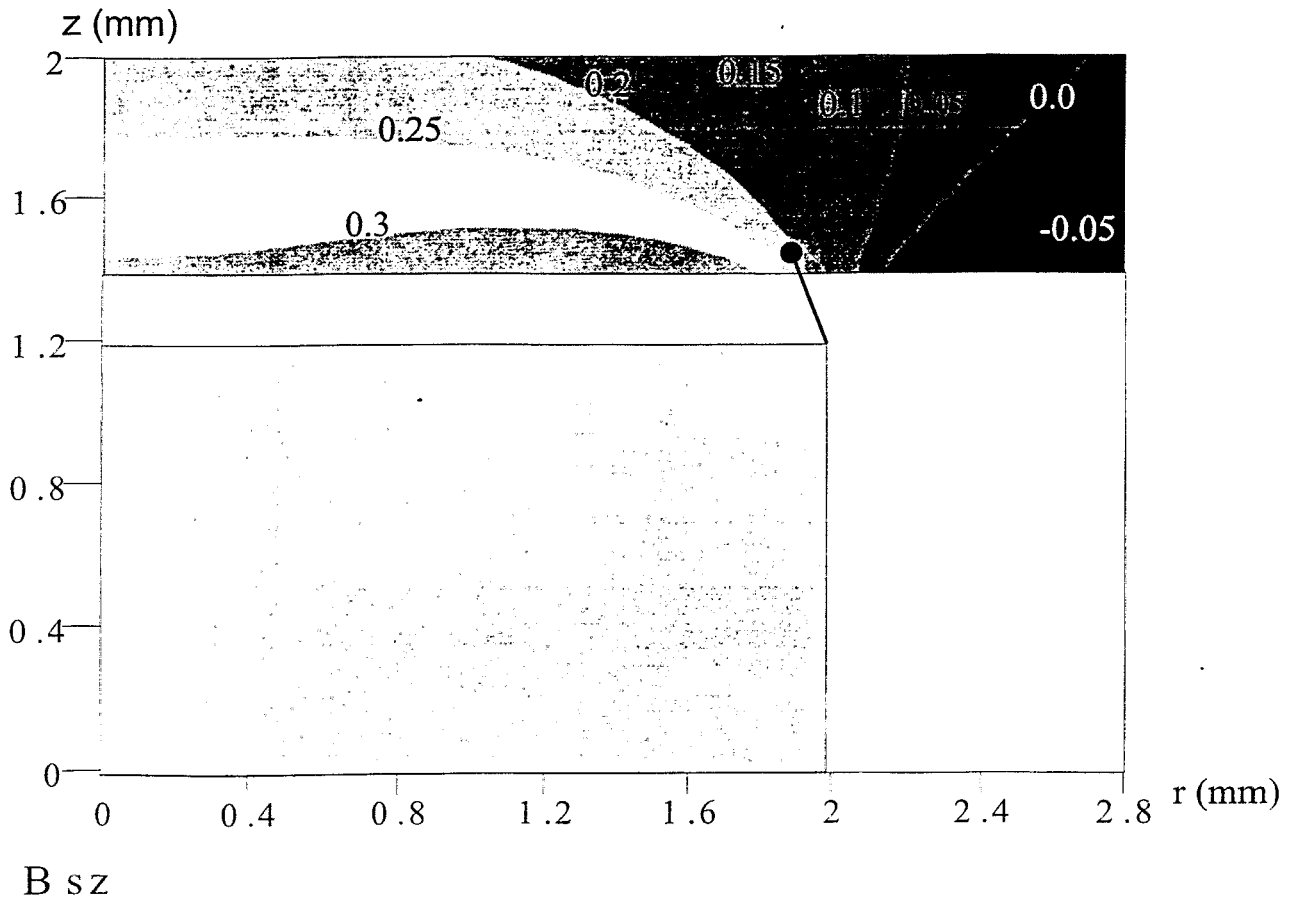
Schematic of an incorporated permanent magnet velocity probe. Diameter 4 mm, height 1.2 mm, magnet - Nd-Fe-B,  $H_c = 10^6$  A/m.

1. Cylindrical permanent magnet,  $I$  - magnetization vector.
- 2., 3. Signal electrodes to measure one component of velocity.
- 4., 5. Signal electrodes to measure the second component of velocity.
6. Reference electrode.
7. Stainless steel capillary

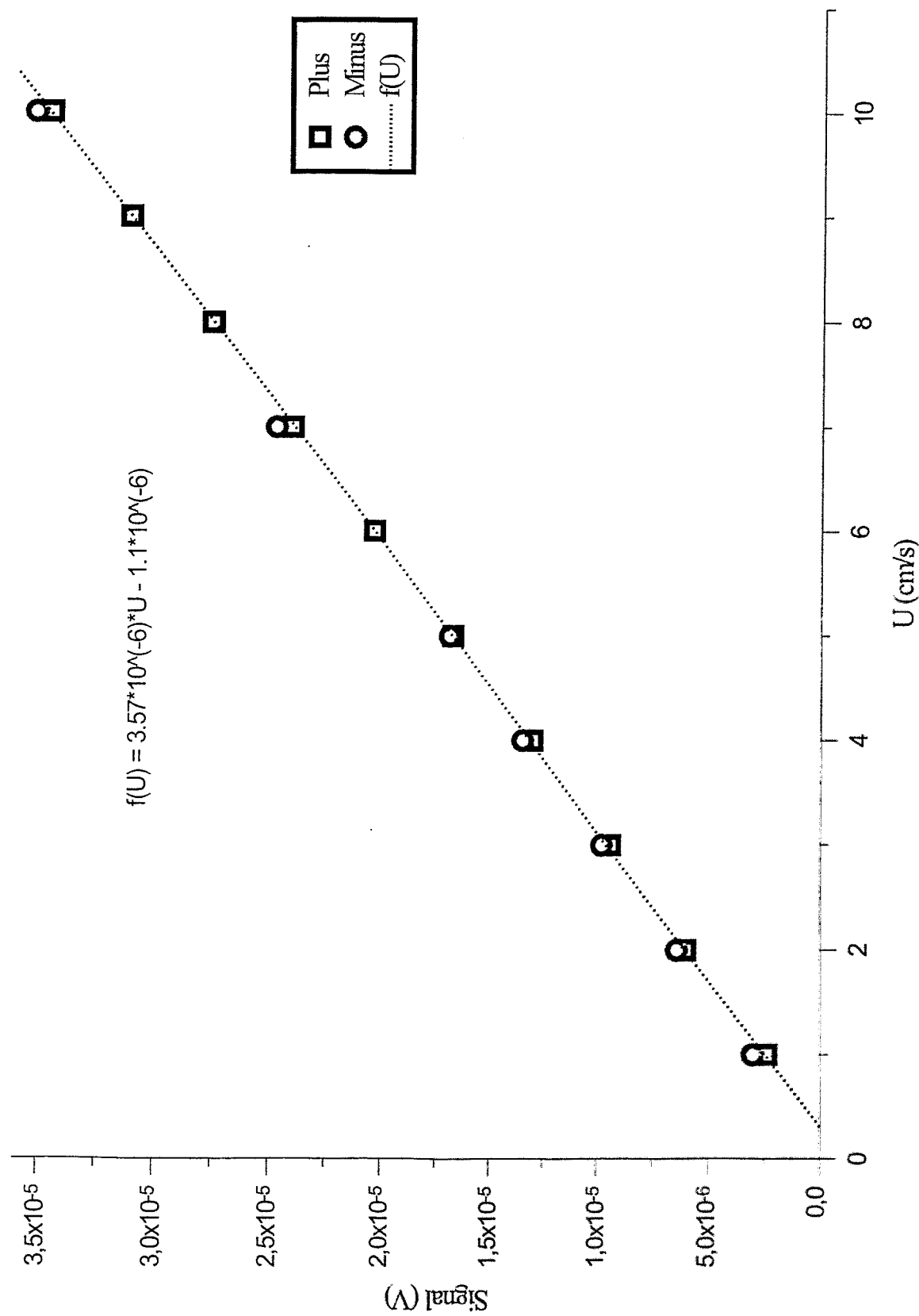


**B**

Vector plot of the magnetic field at the end of a cylindrical permanent magnet.



Isolines of the magnetic field induction vertical component  $B_z$  at the end of a cylindrical magnet



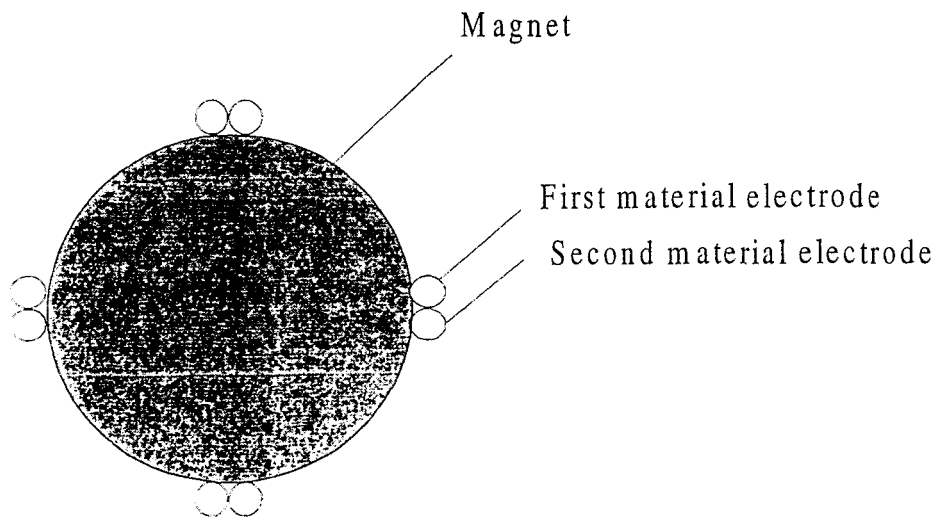
Permanent magnet calibration. Reduced electrode length. U - velocity in cm/s  
 "Plus" - velocity direction inducing positive voltage diff. "Minus" - velocity direction inducing negative voltage diff.

## Electrodes

- Stability of the electrode material in the liquid metal.
- Thermoelectric power of the electrode material should match that of the liquid metal. Otherwise in a presence even of not too high temperature gradient the probe signal would be perturbed.

Differential thermocouple electrode-melt-electrode

*T. von Weissenfluh* proposed a PMP which allows measurements of velocity in nonisothermal conditions. Such probe was also tested in Riga.



$$S_1 \quad S_{\text{melt}} \quad S_2$$

The double electrodes from two materials with different absolute thermoelectric powers  $S_1$  and  $S_2$  should be chosen so that the temperature signal would be of the same order as the velocity signal.

$$S_1 - S_{\text{melt}} \approx S_{\text{melt}} - S_2$$

### Measurable simultaneously:

- 1) local temperature at 4 points;
- 2) two components of velocity;
- 3) two components of temperature gradient.

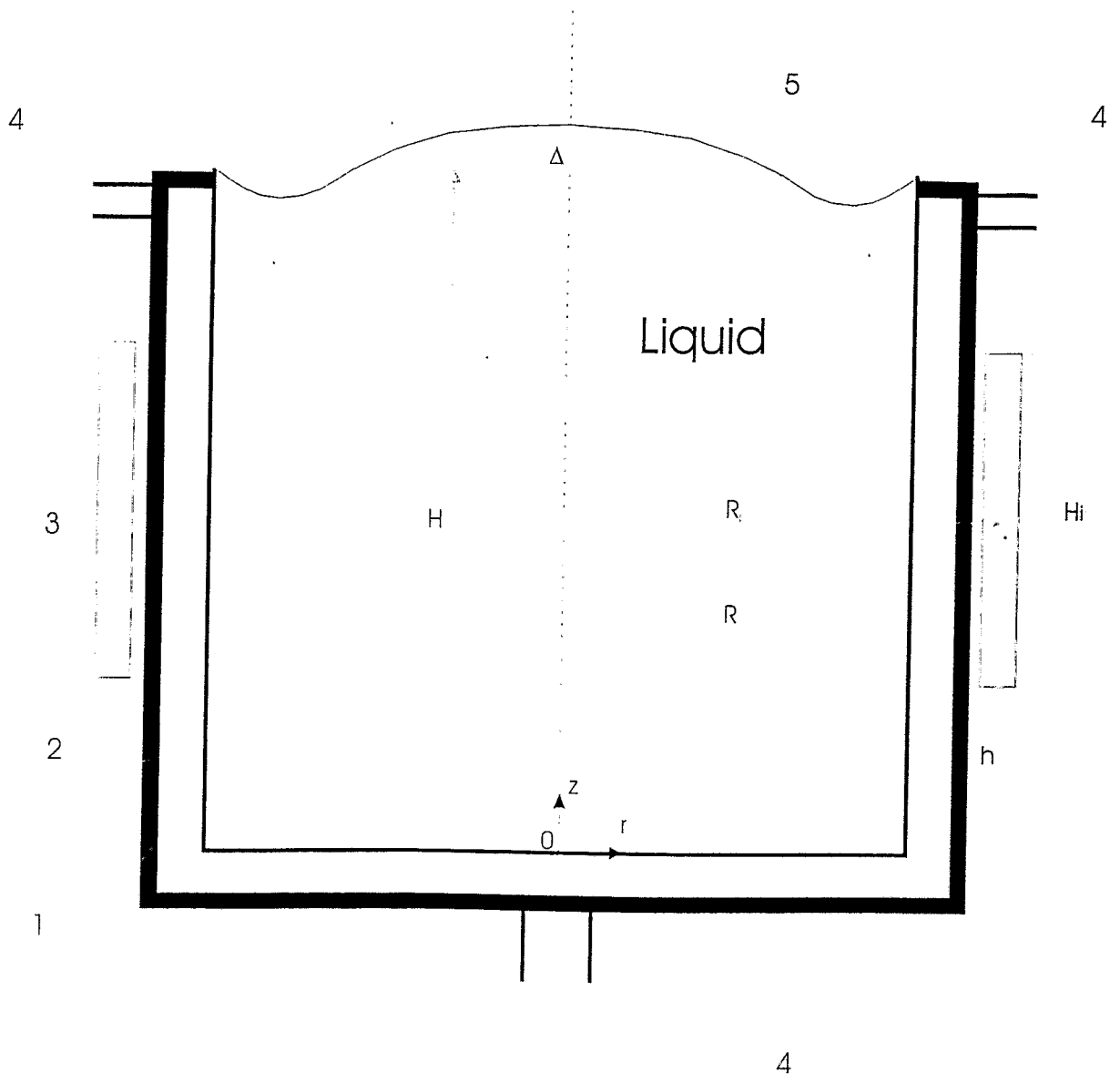


Fig. 1. A schematic of the experimental set-up.

- 1. Stainless steel crucible.
- 2. Dielectric jacket.
- 3. Inductor.
- 4. Cooling water inlet and outlets.
- 5. Liquid metal free surface profile in time averaged sense.

$H = 11$  cm  
 $R = 5.5$  cm  
 $H_i = 5.5$  cm  
 $R_i = 6.5$  cm  
 $h = 2.75 \dots 6.75$  cm

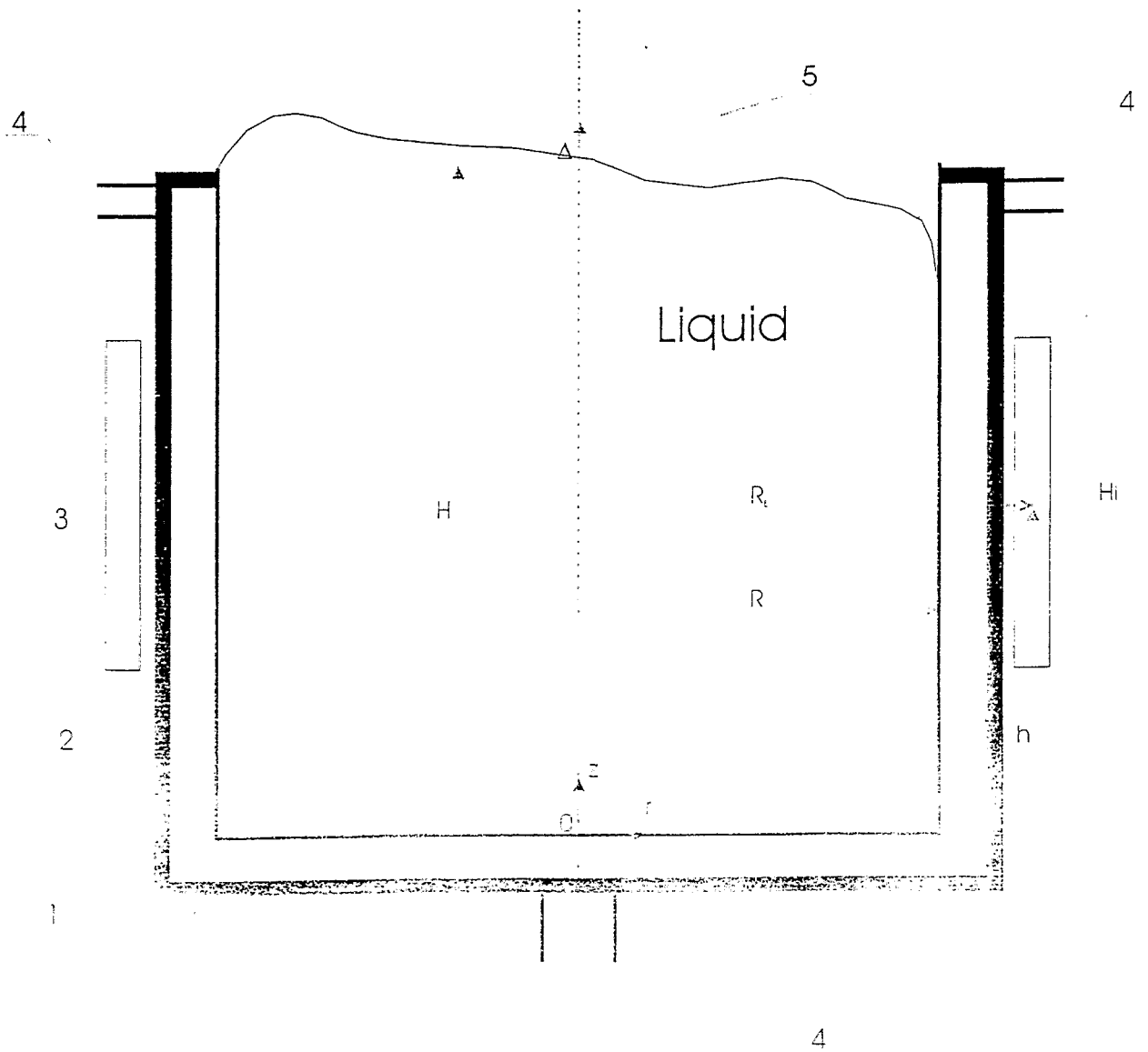


Fig. 1. A schematic of the experimental set-up.

1. Stainless steel crucible.
2. Dielectric jacket.
3. Inductor.
4. Cooling water inlet and outlets.
5. Liquid metal free surface profile in time averaged sense.

$H = 11$  cm

$R = 5.5$  cm

$H_i = 5.5$  cm

$R_i = 6.5$  cm

$h = 2.75 \dots 6.75$  cm

Fig. 15. Velocity signal at  $r = 0$ ,  $z = 9$  cm, inductor position  $z = 6.75$  cm and  $I = 150$  A.

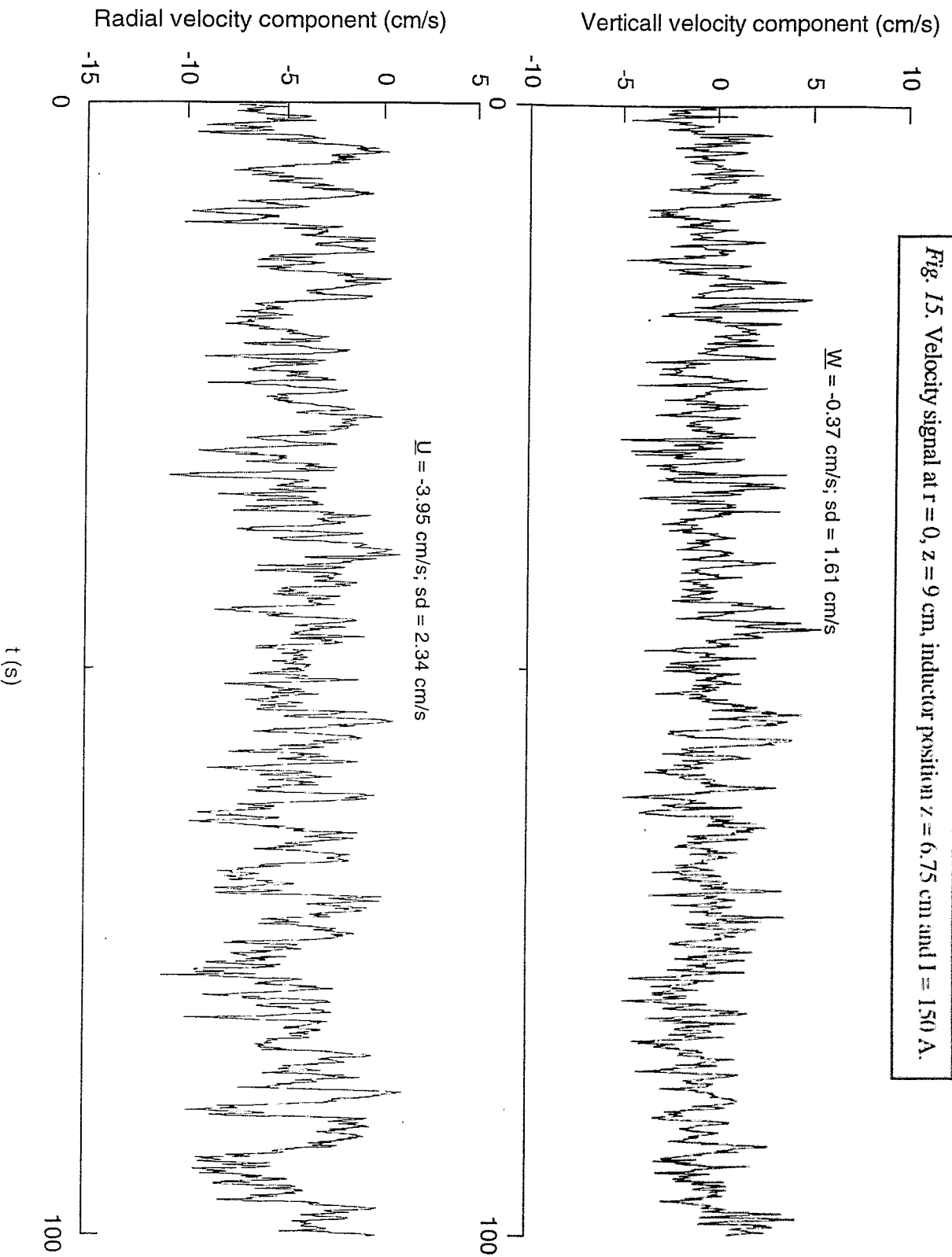
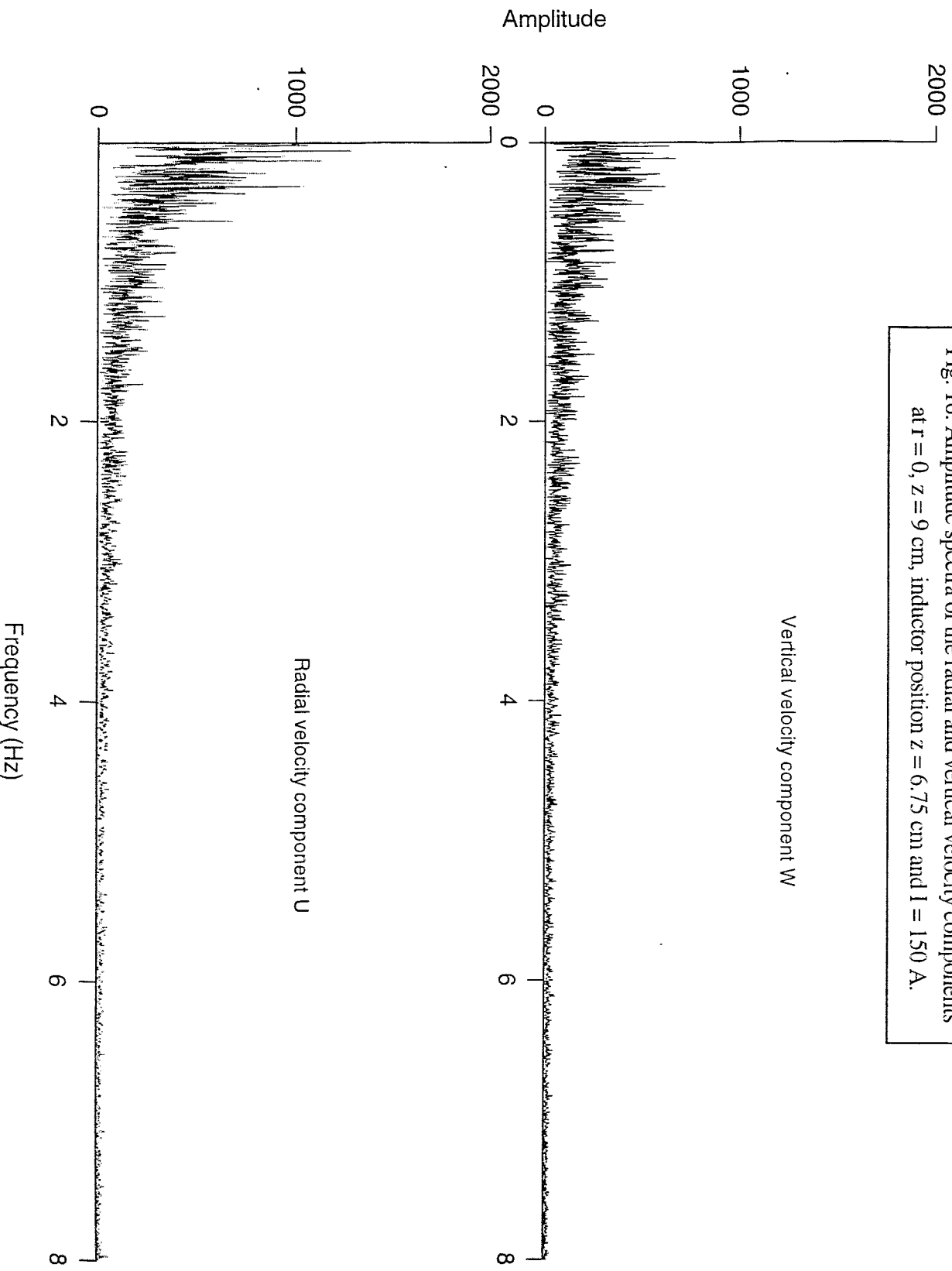
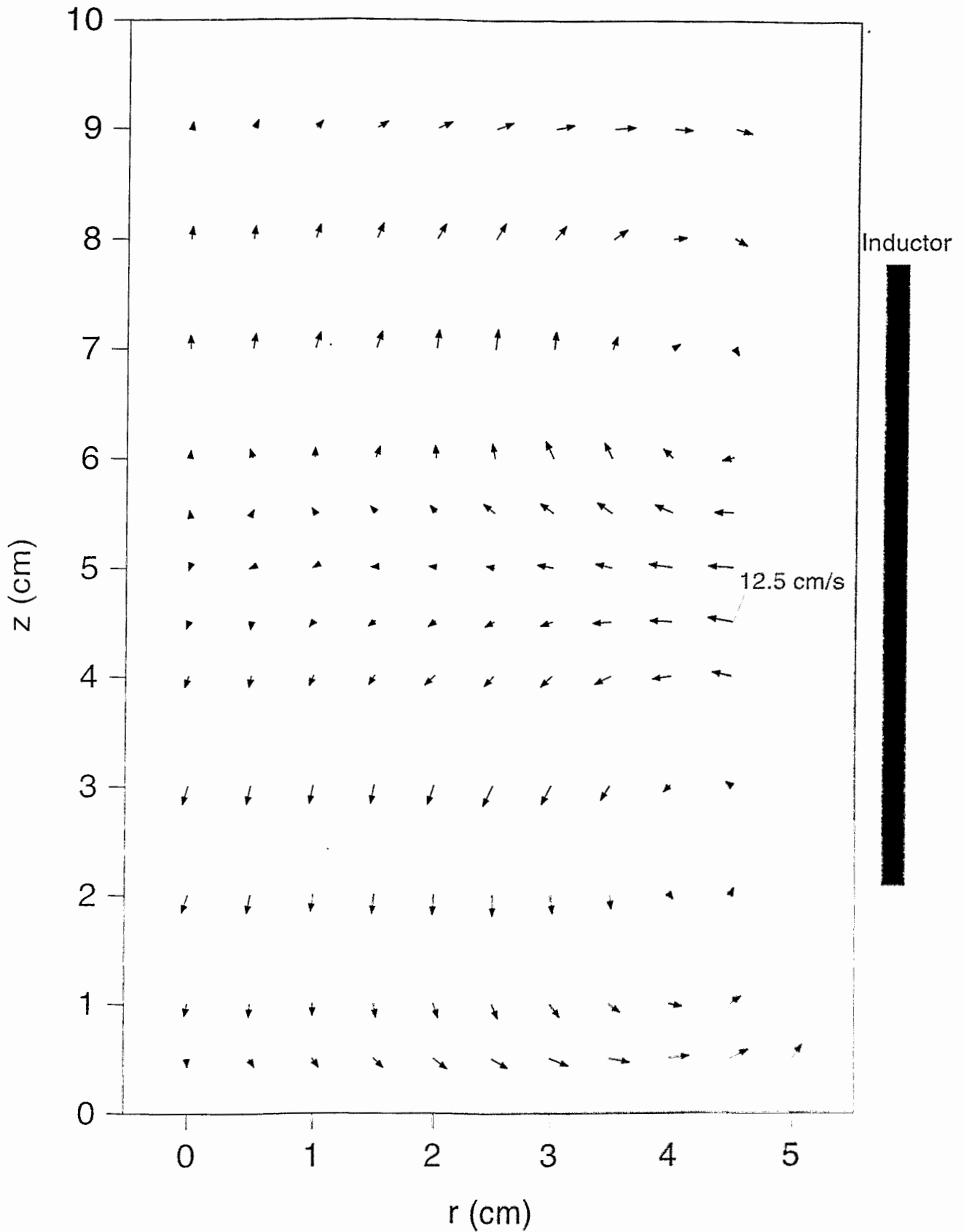


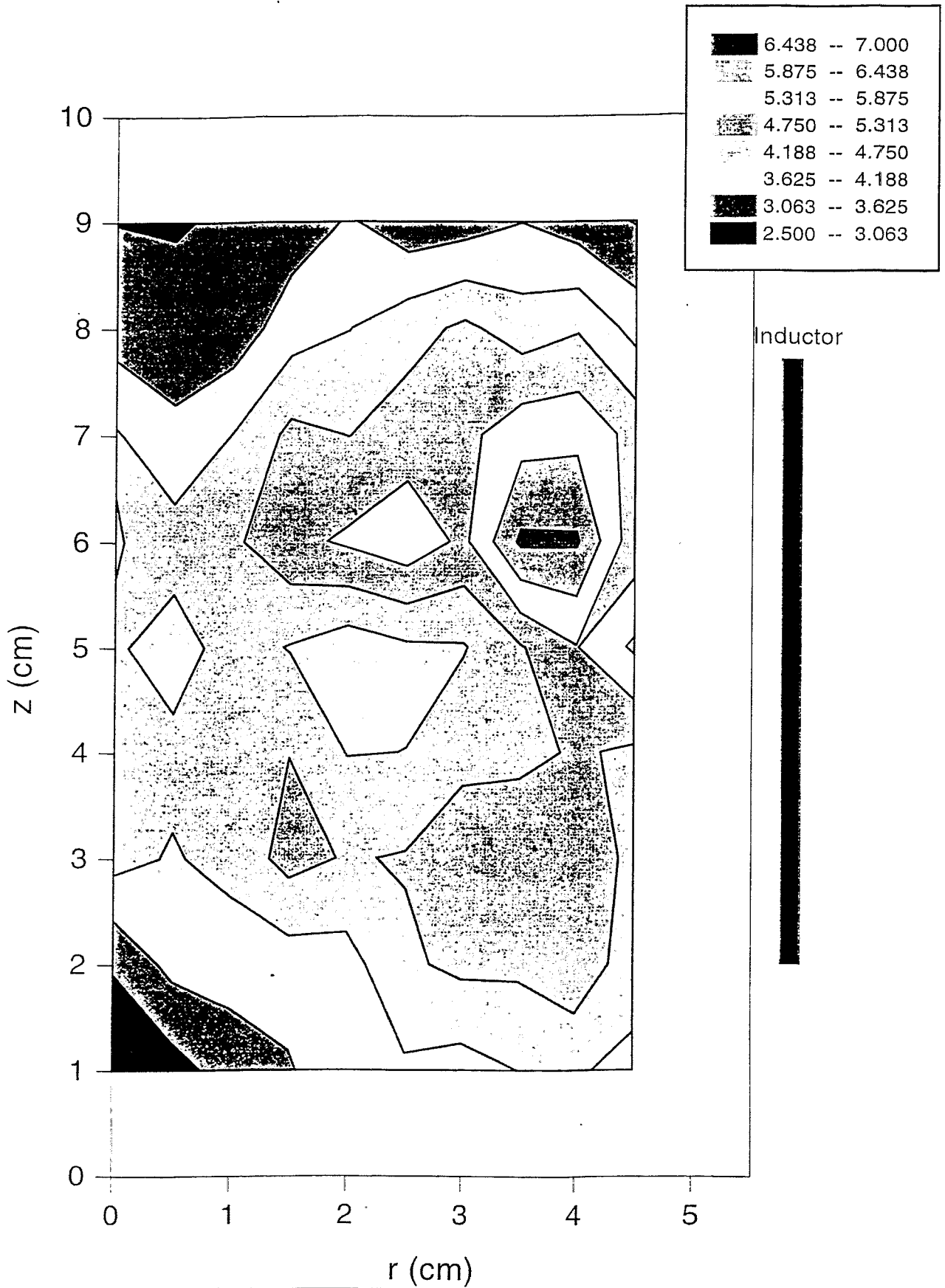


Fig. 16. Amplitude spectra of the radial and vertical velocity components at  $r = 0$ ,  $z = 9$  cm, inductor position  $z = 6.75$  cm and  $I = 150$  A.



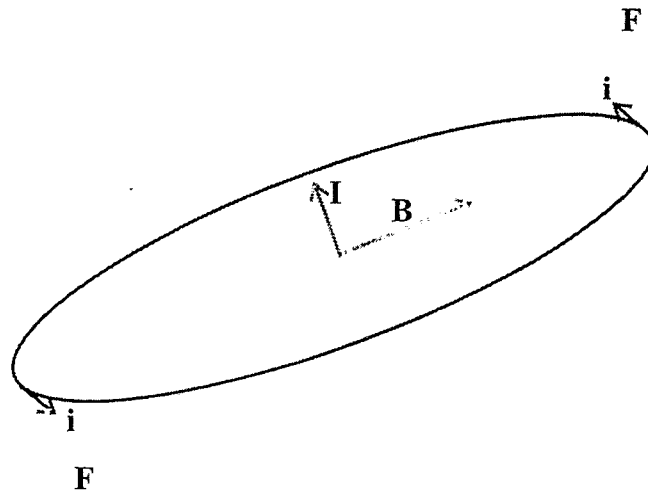


Velocity field measured by a PMP during In-Ga-Sn flow induced by 2.4 kHz current. Measurements were impossible near to inductor, where  $B_{ac} > 2$  mT.

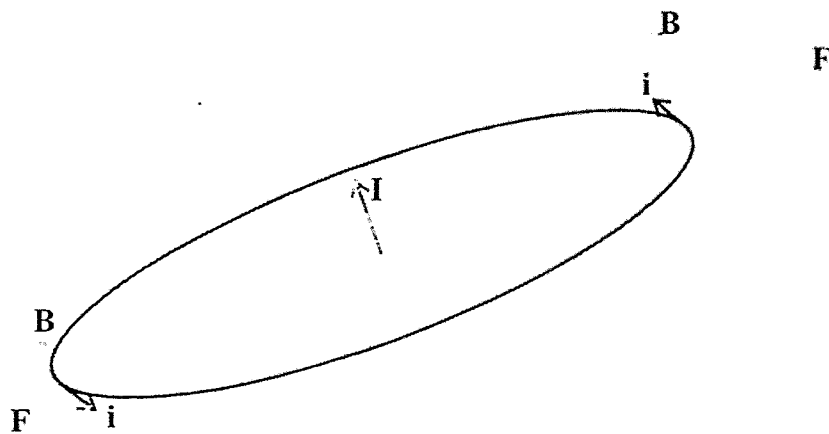


*Fig. 10.* Map of velocity pulsation intensity (standard deviation in cm/s) for flow at  $I = 150$  A

If external magnetic field  $\mathbf{B}$  is applied so, that there is a component normal to the magnetization vector  $\mathbf{I}$ , there appears a torque, acting till the magnet aligns to the direction of  $\mathbf{B}$ . Where  $i$  is equivalent surface current density, and  $F$  - equivalent surface force density.



If the external magnetic field  $\mathbf{B}$  has a nonuniform component parallel to  $\mathbf{I}$ , then there would be a resulting force acting on the magnet.



In an external AC magnetic field both effects - aligning and displacing, would change sign with the external AC field. The permanent magnet in PMP is fixed to a support. These magnetic forces acting on PMP in the AC field result in vibrations.

## Conclusions

PMP in external magnetic fields may be used on conditions:

- 1) the magnitude of the external field is not too high (mT range);
- 2) magnetisation direction of the permanent magnet is aligned as near as possible to the direction of the external field;
- 3) PMP support design should be considered regarding strength and resonance frequencies.

PMP with thermocouple electrodes is a powerful tool allowing to measure simultaneously:

- 1) two components of the velocity;
- 2) temperature at four points;
- 3) two components of the temperature gradient;
- 4) and correlation among any couple of these variables.

PMP strongly perturbs the fluid flow. Reduction of the permanent diameter and height up to 1mm both, allows to reduce this perturbation, but leads to decreased sensitivity. A set of DC nanovolt preamplifiers are rather costly.

Measuring techniques for liquid metal flows (MTLM)  
Dresden, Germany, October 11-13, 1999

## **A resistive probe for continuous measurement of electroconductive liquid level faced to electromagnetic fields**

**B. DUMONT\***, **R. HAETTEL\*\***, **J. HAMBURGER\*\***,  
**R. BOLCATO\*\*** and **J. ETAY\*\***

*\* IRSID Voie Romaine BP 320 57214 Maizières lès Metz Cedex*

*\*\* EPM-MADYLAM ENSHMG BP 95 38402 St Martin d'Hères Cedex  
France*

- 1 - Target
- 2 - Presentation of the equipment
- 3 - Description of the probe
- 4 - Results
- 5 - Conclusions

# Conclusions

## Resistive probe

- mercury (18->70°C) and Gallium (50°C)
- answer
  - linear
  - $f \leq 6 \text{ Hz}$
  - no thermal shift (when using Constantan)
- allows parallel measurements
- used in the presence of 20 magnetic field
- precision better on absolute level  $> \pm 0.5 \text{ mm}$
- for fluctuations  $\pm 0.2 \text{ mm}$
- cheap

but

- contact probe  $\Leftrightarrow$  size problem
- sensitive to the presence of oxides

- for  $Velocity_{\text{freesurface}} \geq 20 \text{ cm} \cdot \text{s}^{-1}$



## Purpose :

- Shape of a rectangular free surface in the presence of 20 kHz field,
- fluctuations - spectra

# A Resistive Probe for Continuous Measurement of Electroconductive Liquid Level faced to Electromagnetic Fields

B. DUMONT\*, R.HAETTEL\*\*, J. HAMBURGER\*\*, R. BOLCATO\*\* and J. ETAY\*\*

\* IRSID Voie Romaine BP 320 57214 Maizières lès Metz Cedex - France

\*\* EPM-MADYLAM ENSHMG BP 95 38402 St Martin d'Hères Cedex - France

We study the experimental device shown on figure 1.

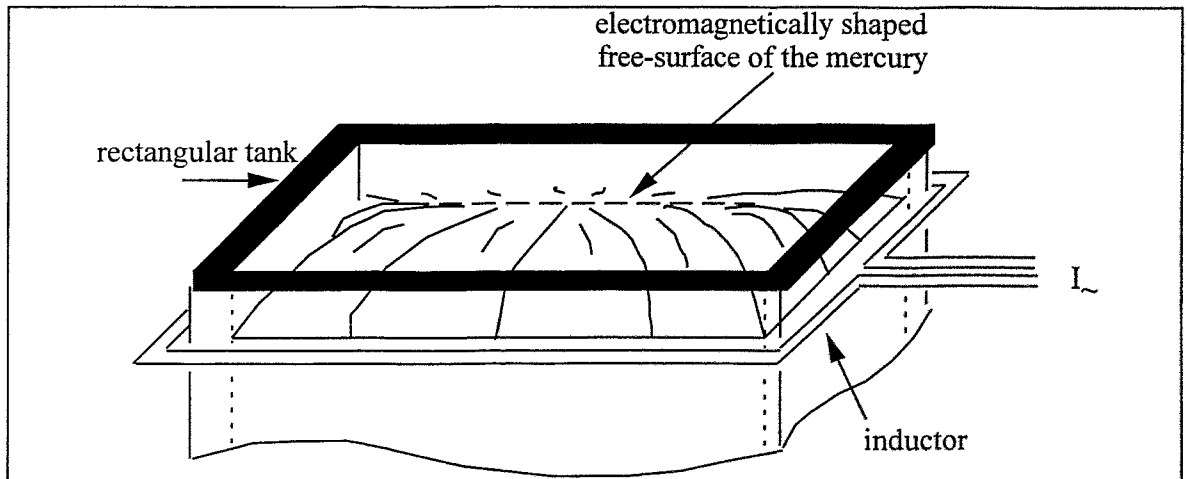


Figure 1 : view of the experimental device

A rectangular tank containing a liquid metal is put in an alternating electromagnetic field generated by an inductor. When the frequency of the current increases, the irrotational part of the induced electromagnetic forces acts on the shape of the meniscus by repulsion forces. Thanks to the efforts made in research on cold crucibles and ladle furnaces, this phenomenon was well studied in an axisymmetric configuration.

We intend to measure the electromagnetic shaping  $h = h(x,y,t)$  of a mercury free surface in a rectangular configuration ( $x, y$  are the horizontal co-ordinates and  $t$  is the time). To this aim, we developed a specific probe which measures  $h$  continuously at a fixed point. This is a resistive probe, connected to a Wheatstone bridge. It was designed so as to :

- be insensitive to the perturbations of the electromagnetic environment,
- allow parallel multiple measurements,
- be insensitive to the dirtying due to the presence of mercury.

The probe and its electronic wiring are described below. The resistive wire is short-cutted by the mercury. Then its resistivity and the electronic signal vary with the height  $h$ . A calibration of the probe is performed to find the law  $\Delta h = \alpha \Delta V$ .



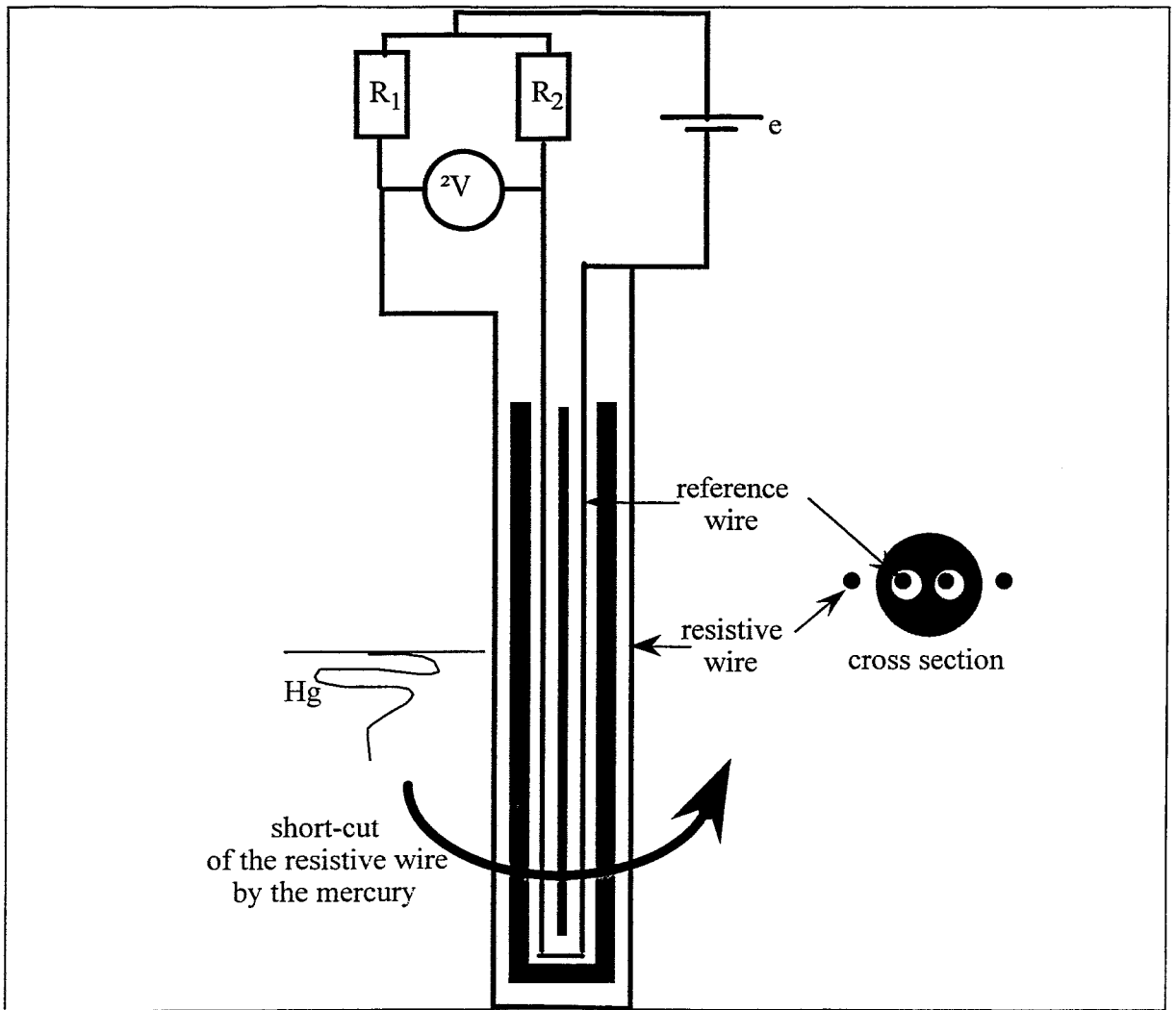


Figure 2 : Principle and wiring of the level probe

## **Electrovortex Flow in Flat Channels**

*S.Khripchenko, S.Denisov and V.Dolgikh*

*Institute of Continuous Media Mechanics, Korolev 1, 614061, Perm, RUSSIA*

While the electric current flows through the bulk of a conducting liquid the electromagnetic forces are generated due to the interaction between the current and its magnetic field. These forces comprise the potential and vortex parts. The vortex forces cause in the liquid a motion that is called an electrovortex flow. As known, the condition of the electrovortex flow generation is the non-uniformity of the electric current distribution over the bulk of the liquid. Therefore, the calculation work in designing a variety of technological devices reduces to a solution of a problem, how a conducting liquid flows in a flat layer or channel with the electric current. In the flat geometry the conditions of the electrovortex flow onset differ from those for the three-dimensional case.

The electrovortex flow in a flat layer with a ferromagnetic core has its peculiarities. On the one hand, it might set out even when the current distribution over the layer is uniform. On the other hand, it might be absent despite the current distribution is non-uniform.

In our talk we describe several new effects predicted theoretically and verified experimentally for the electrovortex flow in a flat MHD channel. These effects could turn out to be useful in the metallurgical device design.

## ELECTROVORTEX FLOW IN FLAT CHANNEL.

It is a well-known fact that an electric current passing through conducting liquids generates electromagnetic forces. These forces are provoked by the interaction between the electric current and its magnetic field. At no homogeneous volume distribution of current density the electromagnetic force has a vortex component.

The vortex force produces the liquid motion named ELECTROVORTEX FLOW or E.V.F.

There are technological MHD-problems, which can be reduced to the problem of the flow of a conducting liquid in a flat channel. It is different from the 3D case when the electric current passes through the volume of a conducting liquid. For instance, E.V.F. can appear at constant density of a current in a plane layer.

Let us consider the plane layer of a conducting liquid placed in the gap between two ferromagnetic blocks (Fig.1). In this case the electric current passes in plan of the layer and his magnetic field has one transverse component only, which is constant across the gap.

The gap averaged Maxwell equation can be written as  
 $\text{rot } \mathbf{B} = \mathbf{j} d/\delta$ , where  $d$  is the layer thickness, and  $\delta$  is the gap thickness.  
 In this case the electromagnetic force rotor consists of one component.

$$\text{rot}_z \mathbf{f}_{em} = (B_z/\mu_0) [ \partial B_z/\partial y \partial(\delta/d)/\partial x - \partial B_z/\partial x \partial(\delta/d)/\partial y ]$$

It is seen that if  $\delta/d$  is constant, then the rotor of the electromagnetic force is zero and no electrovortex flow can appear. Here the magnetic field is constant along the electric current line.

$$\text{rot}_z \mathbf{f}_{em} = -j_y \partial B_z/\partial y - j_x \partial B_z/\partial x = 0.$$

To produce the vortex force,  $\delta/d$  need to be changed along the current line.

Now let us consider a conducting liquid thin layer with a current. This layer is surrounded by solid boundaries. Ferromagnetic plates (Fig.2) occupy some part of the channel. So, the gap near the edges of these plates increases greatly, which causes the appearance of the vortex force. Thus, the ferromagnetic plate edges generate the vortex flow. This effect is very important because it can be used for stirring castings in metallurgy.

The induction frees approximation for thin layers placed between ferromagnetic blocks differ from the ordinary case.

The gap-averaged equation of magnetic field diffusion can be written as  
 $v_x \partial B_z/\partial x + v_y \partial B_z/\partial y = Bt^{-1} \Delta [ B \delta/d ]$ , where  $Bt = \sigma \mu_0 v$ ,  
 $v/d$ ..the velocity scale, and  $a$  is the channel size in plan.

Therefore, for  $v_x, v_y \ll \delta/(Bt a)$  we can ignore the convection members of this equation.

This means that the conducting liquid motion does not influence the magnetic field.

This is possible when  $v_x, v_y \ll \delta/(Bt a)$  or  $Re_m \ll \delta/a$ .

So, the induction free approximation for electrovortex flows in thin layers is stricter than that for ordinary case. Our statement is supported by the phenomena of isothermal MHD-instability predicted by Zimin and Khripchenko and experimentally verified by Barannikov.

As an example of this phenomenon let us consider a conducting liquid rectangular thin layer surrounded by solid boundaries. An electric current of constant cross-sectional density passes through the layer located in the wedge-like gap. The vector of current density is directed normally to the gap change direction.  $\delta/d$  is constant along the electric current line. The layer electromagnetic forces are potential. When perturbation appears in the form of a plane vortex motion, it distorts electric current lines. Thereafter the current density component directed along the gap change appears. This is the condition for existence of the vortex electromagnetic force. This force intensifies perturbation.

Thus, at vortex perturbation the potential electromagnetic force becomes the vortex force, the isothermal MHD-instability can be realised in a layer, and the induction free approximation is not valid.

Let us consider the other case of instability of a conducting liquid thin layer, that is, when the electric current passes in plan

through the layer located in a plane-parallel gap. The layer surface is free. We assume that the small surface layer perturbation  $\zeta$  takes place. In this case, the current density is the function of perturbation  $\zeta$ . So, as the surface perturbation appears, the vortex forces appear to. These forces generate the electrovortex flow, which can intensify the surface layer perturbation.

Our numerical experiments showed that the layer surface instability could take place in some cases.

The interaction between the electric current and its magnetic field is the basic principle of "windingless" MHD pumps for liquid metals. These pumps usually represent a piece of stainless pipe with rectangular cross-section. A ferromagnetic core (Fig.5) surrounds it.

The electromagnetic force induced by the interaction of the electric current and its magnetic field influences the liquid metal.

But for pumping the metal, the electromagnetic forces need to be directed along the streamline of a liquid in the channel. For this, the electricity current line must cross the streamline of the metal, which can be usually achieved by injecting the electric current through the channel walls by special copper conductors.

We discovered a new effect and called it a "skin layer mechanism" This effect allows us not to use the traditional current conductors any more and to supply the electric current by the pump pipe. Let us illustrate this effect. The flat channel with a liquid metal is placed in the wedge-shaped gap. The channel axis is directed along the gap change.

The lines of an alternating current are distorted and forced out from the region covered with ferromagnetic plates (Fig.6). The transverse component appears in the channel. The interaction between the current transverse component and its magnetic

field produces the electromagnetic force, which is directed along the channel axis. We believe this effect can be used in different technological processes.

Let us consider the last case. A permanent electric current runs along the "metalloconductor" of the pump. In this case the electric current line and the liquid metal streamline usually coincide and the electromagnetic force component directed along the streamline is absent. However, when the electrovortex flow exists in the channel, it distorts the streamline. Thereafter the electromagnetic force component directed along the streamline may appear (Fig.7).

We have designed several constructions of MHD-pumps based on the principle of interaction of the electric current and its magnetic field. These pumps were tested for liquid magnesium at metallurgical plant.

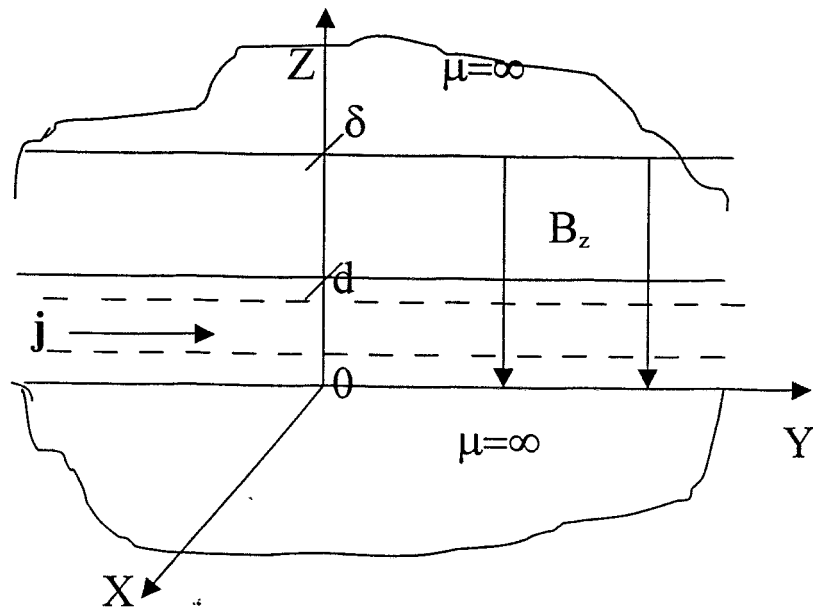


Fig.1

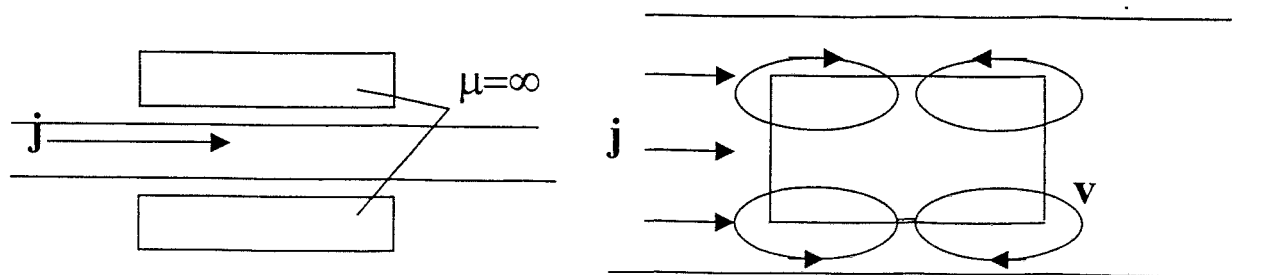


Fig. 2.

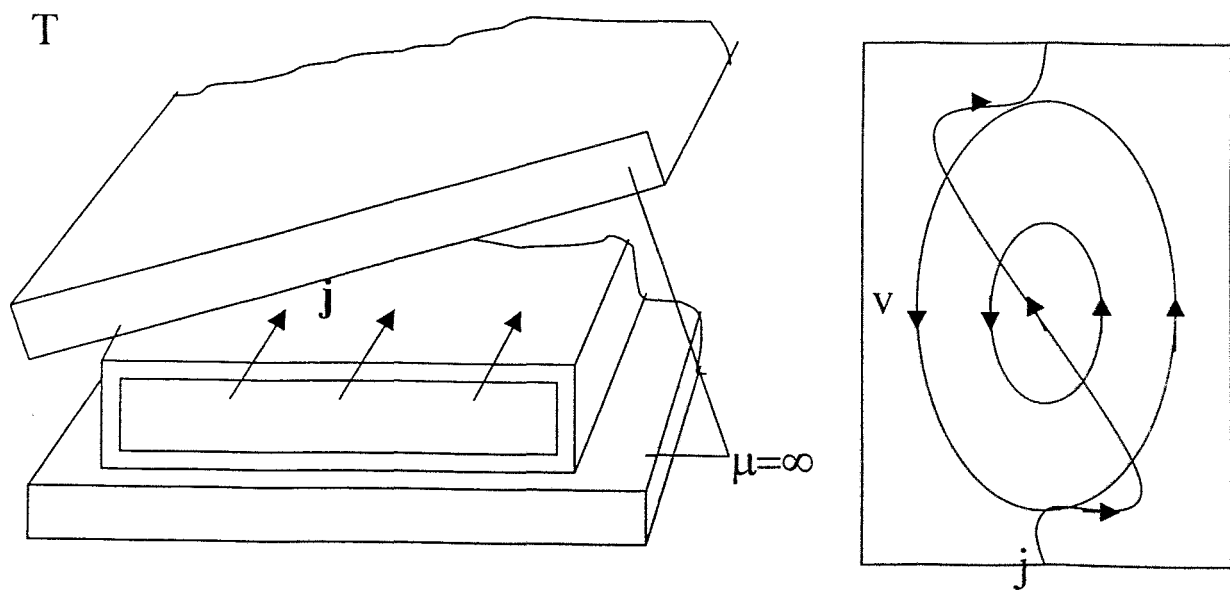


Fig.3

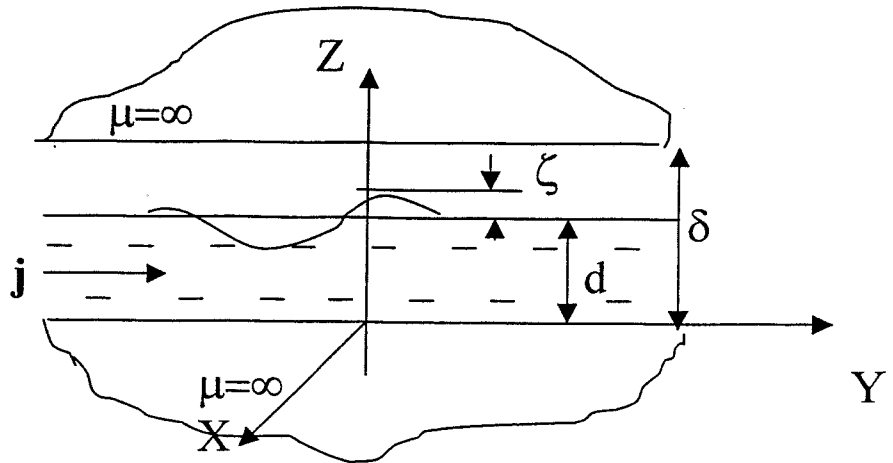
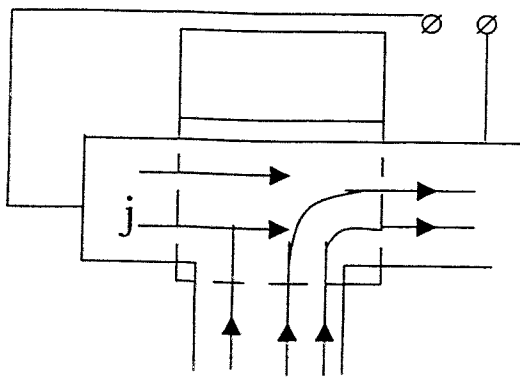


Fig.4



v  
Fig.5

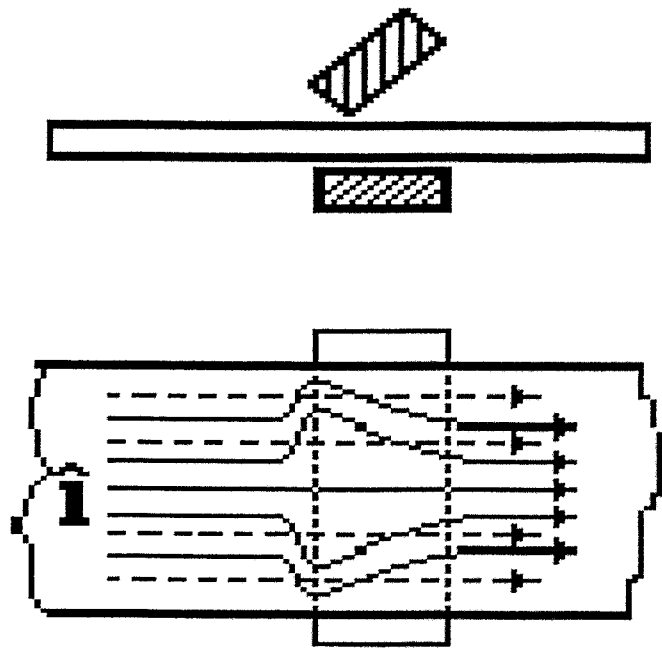


Fig.6

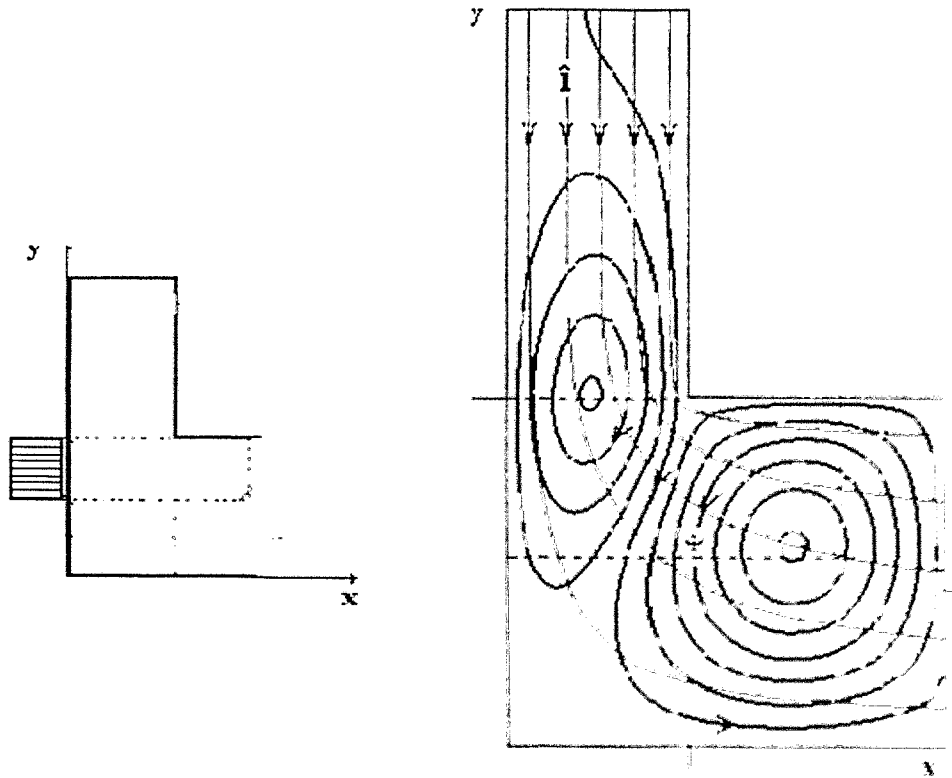


Fig.7